



POLITECNICO DI TORINO  
Repository ISTITUZIONALE

Spatial damping identification and control of mechanical systems

*Original*

Spatial damping identification and control of mechanical systems / Lisitano, Domenico. - (2019 May 31), pp. 1-338.

*Availability:*

This version is available at: 11583/2734827 since: 2019-06-07T15:36:46Z

*Publisher:*

Politecnico di Torino

*Published*

DOI:

*Terms of use:*

openAccess

This article is made available under terms and conditions as specified in the corresponding bibliographic description in the repository

*Publisher copyright*

(Article begins on next page)



**ScuDo**  
Scuola di Dottorato ~ Doctoral School  
WHAT YOU ARE, TAKES YOU FAR



Doctoral Dissertation  
Doctoral Program in Management, Production and Design Engineering (31<sup>st</sup> Cycle)

# **Spatial damping identification and control of mechanical systems**

**Domenico Lisitano**

\* \* \* \* \*

## **Supervisors**

Prof. Elvio Bonisoli, Supervisor, Politecnico di Torino  
Prof. John E. Mottershead, Co-Supervisor, University of Liverpool

## **Doctoral Examination Committee:**

Prof. J. Slavič, Referee, University of Ljubljana  
Prof. M. Ghandchi Tehrani, Referee, University of Southampton  
Prof. N. M. M. Maia, Universidade de Lisboa  
Prof. A. Fregolent, Università di Roma Sapienza  
Prof. A. Vigliani, Politecnico di Torino

Politecnico di Torino  
May 31, 2019



This thesis is licensed under a Creative Commons License, Attribution - Noncommercial - NoDerivative Works 4.0 International: see [www.creativecommons.org](http://www.creativecommons.org). The text may be reproduced for non-commercial purposes, provided that credit is given to the original author.

I hereby declare that, the contents and organisation of this dissertation constitute my own original work and does not compromise in any way the rights of third parties, including those relating to the security of personal data.

.....  
Domenico Lisitano  
Turin, May 31, 2018





# Acknowledgment

This thesis represents the result of three years of research at Politecnico di Torino. Although this period was very demanding, it was highly formative and rich of personal satisfactions. It would not have been such without the presence of numerous people, whom I would like to thank.

My biggest thanks to my supervisor prof. E. Bonisoli, who convinced me to undertake this research period in Politecnico. He started me in the world of research, transmitting his passion for this work. His experience, constant support, confidence in my research choices and the incitement to overcome my limitations were of fundamental importance during this long period.

I would also like to acknowledge my co-supervisor prof. J. E. Mottershead, who gave me the opportunity of join his research group at the University of Liverpool as research student, sharing his vast experience and innovative ideas. In his research group, I had the possibility to quickly expanding my knowledge. His guidance and suggestions were crucial to achieve the results.

I would like to thank you both my supervisors, prof. E. Bonisoli and prof. E. Mottershead, for their extreme willingness and appreciation for my work, this helped me to improve myself more and more.

I would like to thank prof. M. Velardocchia, prof. A. Vigliani and prof. E. Galvagno for welcoming me in the Vehicle Dynamics Group and for involving me in their academic and industrial research activities.

A special thanks to the colleagues and friends of Politecnico: Marco, Nicolò, Matteo, Gianmarco, Luca, Antonio, Guido, Mattia, Hamid, Simone, Christian, Valerio, Marco, Angelo. Thanks to them, many hours spent at the Politecnico are more pleasant and cheerful, including all the hilarity moments and coffee breaks.

A recognition deserves to Dr. S. Jiffri, who supported me during the research period in Liverpool, and Dr. S. Fichera who was always ready to provide suggestions and support. I would also thank them, along with all the other people I met in Liverpool, for nice evenings spent together, which cheered my stay in Liverpool.

Un ringraziamento va a tutti gli amici conosciuti a Torino, ormai in parte dispersi per il modo: Loro hanno allietato la mia lunga permanenza a Torino regalandomi momenti di svago spensierati e divertenti. Un pensiero spetta anche agli amici di sempre, con i quali è un grosso piacere ritrovarsi puntualmente durante le vacanze.

Infine, ma non per importanza, ringrazio i miei genitori, Giuseppe e Carmelina, e mia sorella Ivana che nonostante la lontananza sono stati sempre presenti e di grande supporto in tutti questi anni lontano da casa.

# Abstract

This dissertation addresses two research questions: 1) spatially identify dissipations in mechanical systems and 2) actively control the dissipation spatial distribution. Dissipation is here intended as the transformation of mechanical energy in another form of energy, irrecoverably lost.

In structural dynamics dissipations are usually known as the effects of damping. The inverse problem of damping identification and modelling is still not completely solved in literature, with huge space for research, while inertial and elastic properties of mechanical systems are well understood.

The thesis focusses on direct spatial damping identification for enhanced damping layouts. A brief explanation of the keywords is required to fully understand the thesis aims: “Direct” means using straightway experimental measures of the system behaviour, acquired with standard techniques to make the procedure feasible in all the contexts; “Spatial” stands for damping matrices identification, to be distinguished from damping identification in terms of modal properties; “Damping Identification” focus the attention on the inverse problem of extrapolate the dissipations properties from real structures, in particular: to identify the most accurate damping model able to describe the dissipations in the system, to localise the dissipation sources within the structure and to quantify their dissipation levels; finally “Enhanced Damping Layouts” suggests improvements of the dissipation level and distribution, i.e. the damping layout, imposing the desired dynamic behaviour to the system, without changing its structural design.

The identification of the damping matrix is achieved by a novel damping matrices identification method, called Stabilised Layers Method. The presented method belongs to the receptances based methods, it can identify “physical” linear viscous and structural damping matrices of a mechanical system using standard experimental frequency response functions and the system geometry, which is usually known.

The Stabilised Layers Method identifies non-classical damping matrices, introducing non-proportional and localised damping sources. Non-classical

damping matrices have the advantage of representing better the system behaviour than classical proportional damping, although it introduces a complication in the mathematical model.

The damping matrices identified using Stabilised Layers Method are the closest to the real dissipation distribution in the system, among the infinite energetically equivalent possible identification solutions.

The Stabilised Layers Method is also extended to the identification of systems with a localised amplitude dependent damping nonlinearity.

The design of systems vibrational behaviour and damping layout in different working condition is achieved applying real time active control on the already identified system. The system desired behaviour is assigned, without changing the structural design, using real time active control. Two different control strategies are experimentally implemented to assign the desired poles to the system. The control laws not only allow to change the damping distribution, but also to assign convenient natural frequencies to the system. The first control strategy is state space feedback linearisation, which requires an accurate identification of the system model. The other strategy is a receptances based version of the feedback linearisation, which allows to obtain the same results requiring only the experimental open loop response of the system.

The Stabilised Layers Method is validated against experimental applications. A simple three degrees of freedom test-rig is identified in several configurations, to assess the robustness of the method. The identified results are very close to the reference values. The Stabilised Layers Method is applied to the identification of damping distribution of an industrial body in white car chassis. The identified damping distribution is realistic, and the quantification of suspensions system damping is perfectly aligned with the reference values.

The extension to nonlinear damping identification is applied in the experimental identification of a nonlinear magnetic damping test-rig. The nonlinear damping force identification results agree with the literature knowledge.

The damping layout of the already identified three degrees of freedom system is experimentally modified using input-output feedback linearisation control. The desired dynamic behaviour is assigned to the system validating both the classical feedback linearisation applied to non-smooth nonlinear system and the receptances based feedback linearisation.

# Contents

1. Introduction .....	1
1.1 Main contributions .....	3
1.2 Organisation of the thesis .....	4
2. Vibrations and control of mechanical systems .....	7
2.1 SDOF systems.....	8
2.1.1 Undamped systems.....	8
2.1.2 Viscous Damped systems.....	14
2.1.3 Structural damped systems.....	21
2.1.4 Other forms of damping .....	26
2.2 MDOF systems .....	27
2.2.1 Undamped systems.....	28
2.2.2 Proportional viscous damping .....	33
2.2.3 Non-classical viscous damping .....	36
2.2.4 Structural damping .....	44
2.3 Vibration control.....	46
2.3.1 Pole placement .....	47
2.4 Conclusions.....	50
3. Review of passive damping matrix identification and active vibration suppression methods .....	53
3.1 FRF based damping matrix identification .....	54
3.1.1 Chen-Ju-Tseui's method .....	54
3.1.2 Lee-Kim's Method .....	55
3.1.3 Arora's Method .....	56
3.1.4 Instrumented variable method .....	56
3.1.5 Adhikari's method.....	57
3.1.6 Phani-Woodhouse's method .....	59
3.1.7 Lancaster's method .....	60
3.1.8 Okuma-Shi-Oho's method .....	61
3.1.9 Leuridian-Brown-Allemang's method .....	63
3.1.10 Link's method.....	64

## Contents

---

3.1.11	Minas-Inman's method.....	65
3.1.12	Local equation of motion method.....	66
3.1.13	Other methods .....	68
3.2	Damping identification for vibration design.....	68
3.3	Vibration suppression by active control .....	69
3.3.1	Method of receptances .....	70
3.3.2	State space feedback linearisation.....	75
3.3.3	Feedback linearisation via method of receptances.....	82
3.4	Conclusions.....	87
4.	Stabilised Layers Method .....	89
4.1	Layers formulation for damping matrices .....	89
4.1.1	Layers selection.....	94
4.2	Direct spatial damping identification.....	96
4.2.1	Damping matrices identification via Layers Method.....	99
4.2.2	Considerations on unknowns number .....	102
4.2.3	Considerations on the normal FRM .....	103
4.3	Solution regularization and stability .....	104
4.3.1	Stability test and optimal solution.....	106
4.3.2	Considerations on the range span.....	107
4.4	Conclusions.....	109
5.	Enhancing methods for direct identification .....	111
5.1	Synthesis of FRM from modal parameters .....	112
5.1.1	Modal models identification .....	113
5.2	Mode shapes expansion and smoothing.....	115
5.3	Properness condition for complex modes .....	117
5.4	Conclusion .....	119
6.	Test-rig for spatial damping matrix identification and nonlinear vibration control .....	121
6.1	The three DOFs test-rig lumped parameters test-rig .....	121
6.2	Test-rig damped configuration.....	122
6.3	Test-rig non-smooth nonlinear configuration .....	125
6.4	Conclusions.....	126

---

7.	Experimental direct damping identification in a lumped parameters system	127
7.1	SLM for viscous damped system.....	127
7.2	Experimental setup .....	128
7.3	Experimental viscous damping identification.....	129
7.3.1	Undamped configuration.....	130
7.3.2	Configuration D3 .....	134
7.3.3	Configuration D12 L1 .....	137
7.3.4	Configuration D12 L2 .....	141
7.3.5	Configuration D12 L3 .....	145
7.3.6	Configuration D12 L4 .....	149
7.3.7	Configuration D3 & D12 L1 .....	153
7.3.8	Configuration D3 & D12 L2 .....	156
7.3.9	Configuration D3 & D12 L3 .....	160
7.3.10	Configuration D3 & D12 L4 .....	163
7.4	Identification comparison .....	167
7.5	Conclusions.....	171
8.	Experimental direct spatial damping identification of a car chassis .....	173
8.1	BIW car chassis .....	174
8.1.1	Hammer tip choice .....	176
8.2	Shock absorbers effects on chassis dynamic behaviour .....	177
8.2.1	Configuration MK.....	177
8.2.2	Configuration MCK 1.2 bar .....	180
8.2.3	Configuration MCK 2.4 bar .....	181
8.3	Experimental mode shapes expansion and filtering .....	183
8.4	Shock absorber effects on global flexible modes .....	185
8.5	Damping matrices identification.....	190
8.5.1	Layers selection.....	190
8.5.2	Consideration on normal FRM extraction.....	191
8.5.3	Spatial matrix identification results .....	193
8.5.4	Quantification of the front shock absorber viscous damping.....	197
8.6	Conclusions.....	199
9.	Stabilised Layers Method for nonlinear damping identification .....	201
9.1	Nonlinearly damped system.....	201
9.2	Nonlinear damping identification .....	202

---



## Contents

---

9.2.1	Layers formulation of the nonlinear damping force .....	206
9.2.2	Nonlinearly damped system identification via Layers Method .....	207
9.3	Application to numerical nonlinearly damped system .....	208
9.4	Conclusions.....	215
10.	Identification of a nonlinear magnetic damped system .....	217
10.1	Three DOFs magnetic damped test rig .....	218
10.1.1	Experimental setup .....	219
10.2	Nonlinear damping force .....	219
10.3	Nonlinear SLM application .....	220
10.4	Identification results .....	221
10.4.1	Nonlinear damping with 17 mm air-gap .....	221
10.4.2	Nonlinear damping with 22 mm air-gap .....	226
10.5	Identification results comparison.....	231
10.6	Conclusions.....	233
10.7	Identification of nonlinear system and active design of vibrational behaviour .....	234
11.	Feedback linearisation of non-smooth nonlinear systems .....	235
11.1	Feedback linearisation of non-smooth nonlinear systems .....	236
11.1.1	Limitations for lumped mass systems .....	237
11.2	Active control experimental setup .....	238
11.3	System model.....	240
11.3.1	Tuning the linear parameters .....	242
11.3.2	Tuning the nonlinear parameters .....	244
11.4	Application of partial feedback linearisation.....	246
11.4.1	Internal dynamics .....	247
11.4.2	Stability of the zero dynamics .....	249
11.4.3	Dynamics of the partially linearised system.....	251
11.5	Partial feedback linearisation results .....	252
11.5.1	Internal dynamics .....	257
11.5.2	Control of the input force .....	259
11.6	Conclusions.....	260
12.	Feedback linearisation via method of receptances .....	263
12.1	Non-smooth system receptance-based model.....	264

---

12.1.1	Describing function of the nonlinear damping force.....	266
12.2	Experimental linearisation via method of receptances .....	269
12.2.1	Zero dynamics stability .....	269
12.2.2	Computation of the actual input .....	272
12.2.3	Close loop results .....	274
12.3	Comparison between classic and receptance based feedback linearisation.....	280
12.4	Conclusions.....	282
13.	Conclusions.....	283
13.1	Future developments.....	286
14.	List of publications .....	289
15.	References.....	291



# List of Tables

Table 4.1 - Identification unknowns number.....	102
Table 6.1 - Identified test-rig configurations.....	124
Table 6.2 - Reference damping coefficients.....	125
Table 7.1 - Non-viscosity index of the test-rig configurations.....	130
Table 7.2 - Identified damping coefficients values of undamped configuration.....	134
Table 7.3 - Identified damping coefficients values of the configuration D3.....	137
Table 7.4 - Identified damping coefficients values of the conf. D12 L1.....	141
Table 7.5 - Identified damping coefficients values of the conf. D12 L2.....	145
Table 7.6 - Identified damping coefficients values of the conf. D12 L3.....	149
Table 7.7 - Identified damping coefficients values of the conf. D12 L4.....	152
Table 7.8 - Identified damping coefficients values of the conf. D3 & D12 L1...156	
Table 7.9 - Identified damping coefficients values of the conf. D3 & D12 L2...160	
Table 7.10 - Identified damping coefficients values of the conf. D3 & D12 L3.....	163
Table 7.11 - Identified damping coefficients values of the conf. D3 & D12 L4.....	167
Table 7.12 - Identified damping coefficients comparison.....	171
Table 8.1 - Configuration MK EMA identified modes: $f_{n,i}$ [Hz], $\zeta_i$ [%].....	179
Table 8.2 - Conf. MCK 1.2 bar EMA identified modes: $f_{n,i}$ [Hz], $\zeta_i$ [%].....	181
Table 8.3 - Conf. MCK 1.2 bar EMA identified modes: $f_{n,i}$ [Hz], $\zeta_i$ [%].....	182
Table 8.4 - Expanded eigenvectors number of DOFs of the at each iteration.....	183
Table 8.5 - Triplets of matched modes: MK (green)-MCK 1.2 bar (blue)- MCK 2.4 bar (red)-MACX3.....	187
Table 8.6 - Patterns and Layers for damping matrices building.....	191
Table 9.1 - Identified damping coefficients values.....	214
Table 10.1 - Identified damping coefficients values, air-gap $\Delta = 17$ mm.....	226
Table 10.2 - Identified damping coefficients values, air-gap $\Delta = 22$ mm.....	231
Table 10.3 - Comparison between identified damping coefficients $c_{nl,i}$ of the nonlinear damping force.....	232
Table 10.4 - Comparison of identified $c_{eq}$ damping values with literature.....	233
Table 11.1 - Parameters of the linear system.....	243
Table 12.1 - Coefficients of the fitted DSM $\mathbf{Z}$ terms.....	273



# List of Figures

Figure 2.1 - Undamped SDOF system model.....	8
Figure 2.2 - Free response of a SDOF undamped system. ....	10
Figure 2.3 - Receptance FRF $H$ of a SDOF undamped system. ....	12
Figure 2.4 - Relative transmissibility $T_r$ of a SDOF undamped system.....	13
Figure 2.5 - Viscous damped SDOF system model.....	14
Figure 2.6 - Free response of underdamped SDOF system. ....	16
Figure 2.7 - Free response of a critically damped SDOF system. ....	17
Figure 2.8 - Free response of SDOF system response changing damping ratio....	17
Figure 2.9 - Receptance FRF $H$ of a SDOF system changing damping ratio. ....	18
Figure 2.10 - Transmissibility FRF $T_r$ of a SDOF system. ....	21
Figure 2.11 - Structural damped SDOF system model.....	22
Figure 2.12 - Inertance FRF $H$ of a structural damped SDOF system.....	23
Figure 2.13 - Comparison between viscous and structural damped system with equivalent dissipation: $\zeta = 5\%$ , $\eta = 10\%$ (left) and $\zeta = 75\%$ , $\eta = 150\%$ (right). ....	24
Figure 2.14 - Transmissibility FRF $T_r$ of a structural damped SDOF system. ....	26
Figure 2.15 - Real modal analysis of MDOF undamped system.....	30
Figure 2.16 - Free response of a MDOF system.....	31
Figure 2.17 - Receptance matrix $\mathbf{H}$ of an undamped system .....	33
Figure 2.18 - Real modal analysis on MDOF proportionally damped system. ....	34
Figure 2.19 - Free response of a MDOF proportionally damped system: modal coordinates (left) and physical coordinates (right). ....	35
Figure 2.20 - Receptance matrix $\mathbf{H}$ of a proportionally damped system.....	36
Figure 2.21 – Effects of real modal analysis on non-proportional damped system. ....	40
Figure 2.22 - Complex modal analysis uncoupling effect. ....	41
Figure 2.23 - Free response of a MDOF non-classical viscous damped system. ..	42
Figure 2.24 - Receptance matrix $\mathbf{H}$ of 3 DOF non-classically damped system. ..	43
Figure 2.25 - Receptance matrix $\mathbf{H}$ of a 3 DOF structural damped system. ....	46

## List of Figures

---

Figure 2.26 – Inertance FRF of the open and close loop system.....	49
Figure 2.27 – Free response of open and controlled system.....	50
Figure 2.28 – Input force required for pole placement. ....	50
Figure 4.1 - Absolute (left) and relative (right) dampers.....	91
Figure 4.2 - Matrix building process by Layers Method. ....	92
Figure 4.3 - Schematic of an example 4 DOFs system.....	95
Figure 4.4 - Normal FRF changing $g$ :normal FRF (left) and error (right).....	104
Figure 4.5 - Normal and damped FRF.....	105
Figure 4.6 - Frequency range (left) and spectral lines changing $\tilde{k}$ (right).....	106
Figure 4.7 - Singularity diagram in terms of $(r_0, \tilde{k})$ .....	108
Figure 5.1 - Synthesised and experimental FRF.....	113
Figure 5.2 - Synthesised FRF using pLSFC and ML-MM. ....	114
Figure 5.3 - Incomplete mode shapes (left) and expanded mode shape (right)...	116
Figure 5.4 - Effects of mode shape expansion and filtering on FRF.....	117
Figure 5.5 - Synthesised FRF imposing proper condition. ....	119
Figure 6.1 - Three DOFs lumped parameters test-rig (left) and CAD model (right). ....	122
Figure 6.2 - Three DOFs damping configurable test-rig. ....	123
Figure 6.3 - Dampers activated (top) and excluded (bottom): relative damper $c_{12}$ (left) and absolute damper $c_3$ (right).....	123
Figure 6.4 - Schematic of the dampers test setup: extension - retraction (left), expected damping coefficients values (right). ....	124
Figure 6.5 - Non-smooth nonlinear test-rig(left), nonlinear spring (right).....	125
Figure 6.6 - Nonlinear spring: model (left) and characteristic (right). ....	126
Figure 7.1 - Experimental laboratory setup: A - test rig; B - laser displacement DOF 1; C - laser displacement DOF 2; D - laser displacement DOF 3.....	129
Figure 7.2 - Experimental and synthesised FRM of the conf. undamped. ....	131
Figure 7.3 - Damping coefficient $c_1$ : quantification (left) , stability (right).....	131
Figure 7.4 - Damping coefficient $c_2$ : quantification (left) , stability (right). ....	132
Figure 7.5 - Damping coefficient $c_3$ : quantification (left) , stability (right).....	132
Figure 7.6 - Damping coefficient $c_{1,2}$ : quantification (left) , stability (right).....	132
Figure 7.7 - Damping coefficient $c_{2,3}$ : quantification (left) , stability (right). ....	132
Figure 7.8 - Normalised residuum (left) and global stability diagram (right). ....	133
Figure 7.9 - Identified viscous damping matrix of the conf. undamped.....	133
Figure 7.10 - Experimental and synthesised FRM of the configuration D3.....	134
Figure 7.11 - Damping coefficient $c_1$ : quantification (left) , stability (right).....	135
Figure 7.12 - Damping coefficient $c_2$ : quantification (left) , stability (right). ....	135
Figure 7.13 - Damping coefficient $c_3$ : quantification (left) , stability (right).....	136

---

Figure 7.14 - Damping coefficient $c_{1,2}$ : quantification (left) , stability (right)....	136
Figure 7.15 - Damping coefficient $c_{2,3}$ : quantification (left) , stability (right). ..	136
Figure 7.16 - Normalised residuum (left) and global stability diagram (right)...	136
Figure 7.17 - Identified viscous damping matrix of the configuration D3. ....	137
Figure 7.18 - Experimental and synthesised FRM of the conf. D12 L1.....	138
Figure 7.19 - Damping coefficient $c_1$ : quantification (left) , stability (right).....	139
Figure 7.20 - Damping coefficient $c_2$ : quantification (left) , stability (right). ....	139
Figure 7.21 - Damping coefficient $c_3$ : quantification (left) , stability (right).....	139
Figure 7.22 - Damping coefficient $c_{1,2}$ : quantification (left) , stability (right)....	139
Figure 7.23 - Damping coefficient $c_{2,3}$ : quantification (left) , stability (right). ..	140
Figure 7.24 - Normalised residuum (left) and global stability diagram (right). ..	140
Figure 7.25 - Identified viscous damping matrix of the configuration D12 L1...	141
Figure 7.26 - Experimental and synthesised FRM of the conf. D12 L2.....	142
Figure 7.27 - Damping coefficient $c_1$ : quantification (left) , stability (right).....	143
Figure 7.28 - Damping coefficient $c_2$ : quantification (left) , stability (right). ....	143
Figure 7.29 - Damping coefficient $c_3$ : quantification (left) , stability (right).....	143
Figure 7.30 - Damping coefficient $c_{1,2}$ : quantification (left) , stability (right)....	143
Figure 7.31 - Damping coefficient $c_{2,3}$ : quantification (left) , stability (right). ..	144
Figure 7.32 - Normalised residuum (left) and global stability diagram (right). ..	144
Figure 7.33 - Identified viscous damping matrix of the configuration D12 L2...	145
Figure 7.34 - Experimental and synthesised FRM of the conf. D12 L3.....	145
Figure 7.35 - Damping coefficient $c_1$ : quantification (left) , stability (right).....	146
Figure 7.36 - Damping coefficient $c_2$ : quantification (left) , stability (right). ....	147
Figure 7.37 - Damping coefficient $c_3$ : quantification (left) , stability (right).....	147
Figure 7.38 - Damping coefficient $c_{1,2}$ : quantification (left) , stability (right)....	147
Figure 7.39 - Damping coefficient $c_{2,3}$ : quantification (left) , stability (right). ..	147
Figure 7.40 - Normalised residuum (left) and global stability diagram (right). ..	148
Figure 7.41 - Identified viscous damping matrix of the configuration D12 L3...	148
Figure 7.42 - Experimental and synthesised FRM of the conf. D12 L4.....	149
Figure 7.43 - Damping coefficient $c_1$ : quantification (left) , stability (right).....	150
Figure 7.44 - Damping coefficient $c_2$ : quantification (left) , stability (right). ....	150
Figure 7.45 - Damping coefficient $c_3$ : quantification (left) , stability (right).....	151
Figure 7.46 - Damping coefficient $c_{1,2}$ : quantification (left) , stability (right)....	151
Figure 7.47 - Damping coefficient $c_{2,3}$ : quantification (left) , stability (right). ..	151
Figure 7.48 - Normalised residuum (left) and global stability diagram (right). ..	152
Figure 7.49 - Identified viscous damping matrix of the configuration D12 L4...	152

---



## List of Figures

---

Figure 7.50 - Experimental and synthesised FRM of the conf. D3 & D12 L1....	153
Figure 7.51 - Damping coefficient $c_1$ : quantification (left) , stability (right).....	154
Figure 7.52 - Damping coefficient $c_2$ : quantification (left) , stability (right). ....	154
Figure 7.53 - Damping coefficient $c_3$ : quantification (left) , stability (right).....	154
Figure 7.54 - Damping coefficient $c_{1,2}$ : quantification (left) , stability (right)....	155
Figure 7.55 - Damping coefficient $c_{2,3}$ : quantification (left) , stability (right). ..	155
Figure 7.56 - Normalised residuum (left) and global stability diagram (right). ..	155
Figure 7.57 - Identified viscous damping matrix of the config. D3 & D12 L1...	156
Figure 7.58 - Experimental and synthesised FRM of the conf. D3 & D12 L2....	157
Figure 7.59 - Damping coefficient $c_1$ : quantification (left) , stability (right).....	157
Figure 7.60 - Damping coefficient $c_2$ : quantification (left) , stability (right). ....	158
Figure 7.61 - Damping coefficient $c_3$ : quantification (left) , stability (right).....	158
Figure 7.62 - Damping coefficient $c_{1,2}$ : quantification (left) , stability (right)....	158
Figure 7.63 - Damping coefficient $c_{2,3}$ : quantification (left) , stability (right). ..	158
Figure 7.64 - Normalised residuum (left) and global stability diagram (right). ..	159
Figure 7.65 - Identified viscous damping matrix of the config. D3 & D12 L2...	159
Figure 7.66 - Experimental and synthesised FRM of the conf. D3 & D12 L3....	160
Figure 7.67 - Damping coefficient $c_1$ : quantification (left) , stability (right).....	161
Figure 7.68 - Damping coefficient $c_2$ : quantification (left) , stability (right). ....	161
Figure 7.69 - Damping coefficient $c_3$ : quantification (left) , stability (right).....	161
Figure 7.70 - Damping coefficient $c_{1,2}$ : quantification (left) , stability (right)....	162
Figure 7.71 - Damping coefficient $c_{2,3}$ : quantification (left) , stability (right). ..	162
Figure 7.72 - Normalised residuum (left) and global stability diagram (right). ..	162
Figure 7.73 - Identified viscous damping matrix of the config. D3 & D12 L3...	163
Figure 7.74 - Experimental and synthesised FRM of the conf. D3 & D12 L4....	164
Figure 7.75 - Damping coefficient $c_1$ : quantification (left) , stability (right).....	164
Figure 7.76 - Damping coefficient $c_2$ : quantification (left) , stability (right). ....	165
Figure 7.77 - Damping coefficient $c_3$ : quantification (left) , stability (right).....	165
Figure 7.78 - Damping coefficient $c_{1,2}$ : quantification (left) , stability (right)....	165
Figure 7.79 - Damping coefficient $c_{2,3}$ : quantification (left) , stability (right). ..	165
Figure 7.80 - Normalised residuum (left) and global stability diagram (right). ..	166
Figure 7.81 - Identified viscous damping matrix of the config. D3 & D12 L4...	166
Figure 7.82 - FRM of configurations undamped and D12 Lx.....	167
Figure 7.83 - FRM of configurations D3 and D3 & D12 Lx.....	168
Figure 7.84 - Normal FRM of configurations undamped and D12 Lx.....	168
Figure 7.85 - Normal FRM of configurations D3 and D3 & D12 Lx.....	169

---

Figure 7.86 - Identified viscous damping matrices.....	169
Figure 7.87 - Expected and identified dashpot viscous damping coefficients.....	170
Figure 8.1 - Experimental setups configurations: MK (left) and MCK (right). ..	174
Figure 8.2 - Hanging points: front and rear, right and left (left to right). .....	175
Figure 8.3 - Test grid (top) and accelerometers location (bottom). .....	175
Figure 8.4 - FRF (left) and PSD (right) with different hammer tips. ....	176
Figure 8.5 - Configuration MK Auto-MACX matrix. ....	178
Figure 8.6 - Configuration MCK 1.2 bar Auto-MACX matrix. ....	180
Figure 8.7 - Configuration MCK 2.4 bar Auto-MACX matrix. ....	182
Figure 8.8 - MACX identified and expanded modes, conf. MK. ....	184
Figure 8.9 - MACX identified and expanded modes, conf. MCK 1.2 bar. ....	184
Figure 8.10 - MACX identified and expanded modes, conf. MCK 2.4 bar. ....	184
Figure 8.11 - MACX between configurations MCK 1.2 bar and MCK 2.4 bar. ....	186
Figure 8.12 - MACX between configurations MCK 1.2 bar and MK. ....	186
Figure 8.13 - MACX between configurations MCK 2.4 bar and MK. ....	186
Figure 8.14 - Natural frequency comparison of the triplet of matched modes. ....	188
Figure 8.15 - Damping ratio comparison of the triplet of matched modes. ....	188
Figure 8.16 - MPC comparison of the triplet of matched modes. ....	188
Figure 8.17 - Experimental FRF comparison between the three setups. ....	189
Figure 8.18 - Normal FRM with classical inversion. ....	192
Figure 8.19 - Normal FRM using Marquardt-Levenberg inversion. ....	193
Figure 8.20 - Identified damping matrices of conf. MK: viscous (left), structural (right). ....	195
Figure 8.21 - Identified damping matrices of conf. MCK 1.2 bar: viscous (left), structural (right). ....	196
Figure 8.22 - Identified damping matrices of conf. MCK 2.4 bar: viscous (left), structural (right). ....	197
Figure 8.23 - Front shock absorbers viscous damping coefficient. ....	198
Figure 9.1 - Schematic of the nonlinear damped system. ....	208
Figure 9.2 - Numerical noisy FRF with different oscillations amplitude. ....	210
Figure 9.3 - Damping coefficient $c_1$ : quantification (left) , stability (right). ....	211
Figure 9.4 - Damping coefficient $c_2$ : quantification (left) , stability (right). ....	211
Figure 9.5 - Damping coefficient $c_3$ : quantification (left) , stability (right). ....	211
Figure 9.6 - Damping coefficient $c_4$ : quantification (left) , stability (right). ....	211
Figure 9.7 - Damping coefficient $c_5$ : quantification (left) , stability (right). ....	212
Figure 9.8 - Damping coefficient $c_{1,2}$ : quantification (left) , stability (right). ....	212
Figure 9.9 - Damping coefficient $c_{2,3}$ : quantification (left) , stability (right). ....	212
Figure 9.10 - Damping coefficient $c_{3,4}$ : quantification (left) , stability (right). ..	212

---

## List of Figures

---

Figure 9.11 - Damping coefficient $c_{4,5}^{id}$ : quantification (left) , stability (right). ..	213
Figure 9.12 - Damping coefficient $c_{nl,1}$ : quantification (left) , stability (right). ..	213
Figure 9.13 - Damping coefficient $c_{nl,2}$ : quantification (left) , stability (right)...	213
Figure 9.14 - Normalised residuum (left) and global stability diagram (right). ..	214
Figure 9.15 - Identified damping matrices: $C$ (left), $C_{nl,1}$ (middle) and $C_{nl,2}$ (right). .....	214
Figure 10.1 - Three DOFs magnetic damped test rig. ....	218
Figure 10.2 - Measured and synthesised FRFs changing oscillation amplitude. ....	222
Figure 10.3 - Effects of nonlinearity with air-gap $\Delta = 17$ mm. ....	222
Figure 10.4 - Damping coefficient $c_1$ : quantification (left) , stability (right).....	223
Figure 10.5 - Damping coefficient $c_2$ : quantification (left) , stability (right). ....	223
Figure 10.6 - Damping coefficient $c_3^{id}$ : quantification (left) , stability (right). ...	224
Figure 10.7 - Damping coefficient $c_{1,2}$ : quantification (left) , stability (right)... ..	224
Figure 10.8 - Damping coefficient $c_{2,3}$ : quantification (left) , stability (right). ..	224
Figure 10.9 - Damping coefficient $c_{nl,1}$ : quantification (left) , stability (right). ..	224
Figure 10.10 - Damping coefficient $c_{nl,2}$ : quantification (left) , stability (right). ..	225
Figure 10.11 - Normalised residuum (left) and global stability diagram (right). ..	225
Figure 10.12 - Identified damping matrices: $C_{lin}$ (left), $C_{nl,1}$ (middle) and $C_{nl,2}$ (right). .....	226
Figure 10.13 - Measured and synthesised FRFs changing oscillation amplitude. ....	227
Figure 10.14 - Effects of nonlinearity with air-gap 22 mm. ....	227
Figure 10.15 - Damping coefficient $c_1$ : quantification (left) , stability (right)....	228
Figure 10.16 - Damping coefficient $c_2$ : quantification (left) , stability (right). ..	228
Figure 10.17 - Damping coefficient $c_3^{id}$ : quantification (left) , stability (right). ..	229
Figure 10.18 - Damping coefficient $c_{1,2}$ : quantification (left) , stability (right)..	229
Figure 10.19 - Damping coefficient $c_{2,3}$ : quantification (left) , stability (right). ..	229
Figure 10.20 - Damping coefficient $c_{nl,1}$ : quantification (left) , stability (right). ..	229
Figure 10.21 - Damping coefficient $c_{nl,2}$ : quantification (left) , stability (right). ..	230
Figure 10.22 - Normalised residuum (left) and global stability diagram (right). ..	230
Figure 10.23 - Identified damping matrices: $C_{lin}$ (left), $C_{nl,1}$ (middle) and $C_{nl,2}$ (right). .....	231
Figure 10.24 - Equivalent identified damping coefficients: configurations $\Delta = 17$ mm (left) and $\Delta = 22$ mm (right). ....	232
Figure 10.25 - Reference and identified equivalent damping coefficients. ....	233

---

Figure 11.1 - Close-loop experimental setup: A) suspended shaker, B) Load cell, C) left gap $g_1$ , D) right gap $g_2$ , E) Accelerometers (one for each DOF), F) laser on $x_1$ , G) laser on $x_2$ and H) laser on $x_3$ .	239
Figure 11.2 - Schematic of the three DOFs non-smooth nonlinear system.	240
Figure 11.3 - Experimental and numerical FRM comparison.	243
Figure 11.4 - MAC between numerical and experimental mode shapes.	244
Figure 11.5 - Nonlinear experimental FRF for different levels of excitation:	244
Figure 11.6 - Experimental vs. numerical FRFs, changing force amplitude: $f_0 = 0.1$ N -1 <sup>st</sup> row, $f_0 = 0.2$ N -2 <sup>nd</sup> row, $f_0 = 0.3$ N -3 <sup>rd</sup> row, $f_0 = 0.4$ N -4 <sup>th</sup> row.	245
Figure 11.7 - Several numerical simulations of the zero dynamics.	249
Figure 11.8 - Schematic of the control strategy.	253
Figure 11.9 - Closed-loop FRFs: experimental (left) and numerical (right).	254
Figure 11.10 - Feedback linearisation, desired $f_{n,d} = 9.7, 13.5, 16, 19$ Hz: actual natural frequencies (left) and actual damping ratios (right).	255
Figure 11.11 - Effect of the output saturation on close-loop dynamics.	256
Figure 11.12 - Comparison between experimental (dashed line) and numerical (solid line) closed-loop FRFs with $\zeta_d = 5\%$ .	256
Figure 11.13 - Experimental closed loop FRFs phases.	256
Figure 11.14 - Time domain $\chi_1$ , $f_n = 16$ Hz	257
Figure 11.15 - Internal dynamics numerical and experimental closed loop FRFs.	258
Figure 11.16 - Experimental time domain response of the internal dynamics $f_{n,d} = 16$ Hz and increasing values of damping: $\chi_3$ (left) and $\chi_4$ (right).	259
Figure 11.17 - Commanded and achieved input $u(t)$ with $f_{n,d} = 16$ Hz: $\zeta_d = 0.5\%$ (left) and $\zeta_d = 5\%$ (right).	259
Figure 11.18 - Commanded and achieved input for $f_{n,d} = 19$ Hz: $\zeta_d = 5\%$ (left) and $\zeta_d = 35\%$ (right).	260
Figure 12.1 - Nonlinear damping force.	266
Figure 12.2 - Nonlinear FRM $\mathbf{H}_{nl}(X_3, \Omega)$ changing oscillation amplitude $X_3$ .	270
Figure 12.3 - Zero dynamics FRM changing $X_3$ amplitude.	271
Figure 12.4 - Zero dynamics poles: real (left) and imaginary (right) parts.	272
Figure 12.5 - Zoomed view of poles: real (left) and imaginary (right) parts.	272
Figure 12.6 - Fitting of the required DSM $\mathbf{Z}$ terms.	273
Figure 12.7 - Schematic of the control logic.	275
Figure 12.8 - Close-loop FRF: experimental (left) and numerical (right).	276
Figure 12.9 - Desired and actual poles of the linearised system.	277
Figure 12.10 - Experimental closed loop FRFs phases.	277

---

## List of Figures

---

Figure 12.11 - Time domain responses for $f_{n,d} = 13.5$ Hz: $z_1$ (left), $z_2$ (middle) and $z_3$ (right).....	278
Figure 12.12 - Time domain responses for $f_{n,d} = 16$ Hz: $z_1$ (left), $z_2$ (middle) and $z_3$ (right). ....	278
Figure 12.13 - Time domain responses for $f_{n,d} = 19$ Hz: $z_1$ (left), $z_2$ (middle) and $z_3$ (right). ....	279
Figure 12.14 - Close-loop internal dynamics $\mathbf{H}_{1,2}$ : experimental (left) and numerical (right). ....	279
Figure 12.15 - Close-loop internal dynamics $\mathbf{H}_{1,3}$ : experimental (left) and numerical (right). ....	280
Figure 12.16 - Error in the assigned natural frequency (left) and damping ratio (right) using the two methods. ....	281

# List of Acronyms

BIW	Body in white
DF	Describing function
DOF	Degree of freedom
DSM	Dynamic stiffness matrix
EMA	Experimental modal analysis
FE	Finite element
FEM	Finite element method
FRF	Frequency response function
FRM	Frequency response matrix
ISSPA	Identification of structural System Parameters
IV	Instrumented variable
l.h.s.	Left hand side
LSCE	Least squares complex exponential
LSCF	Least-Squares Complex Frequency-domain
LSRF	Least-squares rational function estimation method
MAC	Modal assurance criterion
MACX	Modal assurance criterion complex
MPC	Modal phase collinearity
MDOF	Multi degrees of freedom
ML-MM	Maximum likelihood modal parameter identification
NVH	Noise, vibration and harshness
pLSCF	Polyreference least-squares complex frequency-domain method
ODE	Ordinary differential equation
PD	Proportional derivative
PSD	Power spectral density
r.h.s.	Right hand side
SDOF	Single degree of freedom
SISO	Single-input single-output
SLM	Stabilised Layers Method



# List of Symbols

$a$	Dissipation square amplitude proportionality constant of the material
$a_{ij}$	DSM fitting coefficients of $s^2$ terms
$a_r$	Modal constant in complex modal analysis
$a_{r,new}$	Modal constant after the expansion and filtering process
$A$	Oscillations amplitude in amplitude-controlled sweeps
$A, A_1, A_2$	Integration constant
$\mathbf{A}$	Duncan coefficients matrix of state derivative vector
$b_{i,j}$	DSM fitting coefficients of $s$ terms
$b_r$	Modal constant in complex modal analysis
$B$	Integration constant
$B_r$	Magnetic residual induction
$\mathbf{B}$	Duncan matrix coefficients of state vector or Input location matrix
$\tilde{\mathbf{B}}$	Perturbation theory matrix of coefficients to express the eigenvectors imaginary part
$c$	Viscous damping coefficient
$c_{eq}$	Equivalent viscous damping coefficients
$c_{i,j}$	DSM fitting coefficients of known terms
$c_j$	Viscous damping coefficient of the $j^{th}$ Layer
$c_{nl,i}$	Coefficient of the polynomial nonlinear force fitting
$C_D$	Drag coefficient
$C_{el}^A$	Absolute damper elementary matrix
$\mathbf{c}_A$	Vector of absolute viscous damping coefficients unknowns
$\mathbf{c}_R$	Vector of relative viscous damping coefficients unknowns
$\mathbf{c}_p$	Position gain vector for feedback control
$\mathbf{c}_v$	Velocity gain vector for feedback control
$\mathbf{C}$	Viscous damping matrix



## List of Symbols

---

$\mathbf{C}_{el,j}$	Elementary viscous damping matrix of the $j^{th}$ Layer
$\mathbf{C}_{el}^R$	Relative damper elementary matrix
$\mathbf{C}_j$	$j^{th}$ Layer of the viscous damping matrix
$\mathbf{C}_{lin}$	Viscous damping matrix including linear part of the nonlinear damping force describing function approximation
$\mathbf{C}_{nl,i}$	$i$ order matrix of the nonlinear damping force DF
$\mathbf{C}_p$	Position gain matrix for feedback control
$\mathbf{C}_v$	Velocity gain matrix for feedback control
$\tilde{\mathbf{C}}$	Modal viscous damping matrix
$\tilde{\mathbf{C}}_d$	Diagonal terms of the modal viscous damping matrix
$\tilde{\mathbf{C}}_o$	Off-diagonal terms of the modal viscous damping matrix
$d$	Structural damping coefficient
$d_j$	Structural damping coefficient of the $j^{th}$ Layer
$\tilde{d}_r$	Modal structural damping
$\mathbf{d}_A$	Vector of absolute structural damping coefficients unknowns
$\mathbf{d}_R$	Vector of relative structural damping coefficients unknowns
$\mathbf{D}$	Structural damping matrix
$\mathbf{D}_{el,j}$	Elementary structural damping matrix of the $j^{th}$ Layer
$\mathbf{D}_j$	$j^{th}$ Layer of the damping viscous damping matrix
$E_E$	Potential energy
$E_K$	Kinetic energy
$E_{tot}$	Total energy
$E_{\%}$	Normalised residuum
$\mathbf{e}_i$	$i^{th}$ column of the identity matrix
$\mathbf{E}$	Error matrix
$f$	Objective function
$f(t)$	Excitation force
$f_{C,nl}$	Nonlinear damping force
$f_n$	Natural frequency
$f_{n,d}$	Desired natural frequency
$\hat{f}$	Peak frequency
$F_{C,nl}(A, \Omega)$	DF approximation of the nonlinear damping force
$F_D$	Damping force
$F_0$	Amplitude of sinusoidal excitation force
$\mathbf{f}$	Generalised excitation force vector
$\mathbf{f}(\mathbf{x}, \dot{\mathbf{x}})$	Nonlinear dynamic vector in second order formulation
$\mathbf{f}_{Cnl}$	Vector of nonlinear damping forces
$\mathbf{f}_{Knl}$	Vector of nonlinear stiffness forces

---

$\mathbf{f}_{nl}$	Nonlinear force
$\mathbf{f}_0$	Vector of harmonic excitations amplitudes
$\underline{\mathbf{f}}$	Dynamic vector in state space formulation
$\mathbf{F}$	Vector for generalised load in Duncan formulation
$\mathbf{F}(\mu_{i,d})$	Control gain matrix in receptance method
$g_{c,i}$	Tuning parameters
$g_1$ and $g_2$	Gaps in the nonlinear piecewise spring
$\mathbf{g}$	Selection vector
$\mathbf{G}$	Transformation matrix between normal and complex FRM or Input matrix in second order formulation
$\mathbf{G}(\mu_{i,d})$	Control gain matrix in receptance method
$\underline{\mathbf{G}}$	Input matrix in states space formulation
$h$	Aluminium beam thickness
$H$	Receptance for SDOF system
$\mathbf{H}$	Frequency response matrix
$\mathbf{H}^{Exp}$	Experimental frequency response matrix
$\mathbf{H}_m$	Frequency response matrix of a proportionally damped system in modal coordinates
$\mathbf{H}_{nl}$	Nonlinear FRM
$\mathbf{H}^N$	Normal frequency response matrix
$\mathbf{H}_{nl}^{Exp}$	Experimental nonlinear frequency response matrix
$\mathbf{H}_{nl,R}$	Real part of the nonlinear FRM
$\mathbf{H}_{nl,I}$	Imaginary part of the nonlinear FRM
$\mathbf{H}_{syn}$	Synthesised FRM
$\mathbf{H}_{nl,syn}$	Synthesised nonlinear FRM
$\mathbf{H}_R$	Real part of the complex FRM
$\mathbf{H}_I$	Imaginary part of the complex FRM
$\tilde{\mathbf{H}}_{nl}$	Nonlinear FRM in linearised coordinates
$k$	Stiffness coefficient
$k_r$	Modal stiffness
$k_2$	Stiffness at closed gaps
$\tilde{k}$	Number of spectral lines around each FRM peak
$\tilde{k}_r$	Modal stiffness in structural damped systems
$\tilde{k}^*$	Number of spectral lines per mode of the optimal solution
$K$	Total number of spectral lines considered in the identification
$\mathbf{K}$	Stiffness matrix
$i$	Imaginary unit
$I$	Number of inputs

---

## List of Symbols

---

$I_{xx}, I_{yy}, I_{zz},$ $I_{yx}, I_{zx}, I_{zy}$	Rigid body inertia
<b>I</b>	Identity matrix
$l$	Aluminium beam length
$l_2$	Setting spring length
$L_s$	Work of structural damping forces
$L_v$	Work of viscous damping forces
<b>L</b>	Imaginary part of the complex modal matrix
$\mathbf{L}_r$	Imaginary part of complex $r^{th}$ eigenvector
$m$	Mass in SDOF system
$m_r$	Modal mass
$\tilde{m}_r$	Modal mass in structural damped system
$M$	Number of actuators
$M_p$	Magnification factor
<b>M</b>	Mass matrix
$\mathbf{M}_{rigid}$	Rigid body mass matrix
$n$	Number of nodes physically connected to node $U$
$n_p$	Real term of a describing function
$n_q$	Imaginary term of a describing function
$N$	Number of DOFs
$N_p$	Number of repetitions of the $p^{th}$ absolute layer
$N_q$	Number of repetitions of the $q^{th}$ relative layer
$NA$	Number of distinct absolute layers
$NL$	Total number of Layers
$NR$	Number of distinct relative layers
$NA^*$	Total number of absolute layers
$NR^*$	Total number of relative layers
$o$	Number of overdamped modes
$O$	Number of outputs
$p$	Marquardt-Levenberg coefficient
$\mathbf{P}_j$	Pattern of the $j^{th}$ damping element
$\mathbf{P}_j^A$	Pattern of the $j^{th}$ absolute damping element
$\mathbf{P}_j^R$	Pattern of the $j^{th}$ relative damping element
$\mathbf{P}_{nl}$	Pattern of nonlinear terms
$\bar{\mathbf{P}}$	Patterns matrix
$\tilde{\mathbf{P}}$	Block-diagonal matrix of the pattern matrices
<b>Q</b>	Known term matrix of transformation matrices
$\mathbf{Q}(A)$	Known term matrix of transformation matrices for nonlinear damping identification
$\mathbf{Q}^*$	Unitary and orthogonal matrix in QR decomposition
$\tilde{\mathbf{Q}}$	Known term matrix of transformation matrices including

---

	different constant level of oscillations for nonlinear damping identification
$\bar{\mathbf{Q}}$	Conditioned known term matrix of transformation matrices
	Normalised excitation ratio
$r$	or
	Relative degree
$rb$	Number of rigid body motion
$r_e$	Electric resistance
$r_{\%}$	Range percentage in the stabilisation diagram
$r_{\%}^*$	Range percentage of the optimal solution
$r_{\%asympote,i}$	Range value of the asymptotes relative to the $i^{th}$ modes in the stabilisation diagram
$R$	Number of identified modes
$\mathbf{R}^*$	Upper triangular matrix in QR decomposition
	System pole
$s$ or $s_r$	or
	Laplace variable
$\tilde{s}_r$	Pole of structural damped system
$\mathbf{S}$	Complex spectral matrix
$\mathbf{S}_i$	Stability Boolean matrix of the $i^{th}$ coefficient of the solution
$\bar{\mathbf{S}}$	Global stability Boolean matrix
$t$	Time
$T$	Order of the polynomial fitting the nonlinear damping force
$T_a$	Absolute transmissibility FRF
$T_r$	Relative transmissibility FRF
	Houseolder transformation matrix
$\mathbf{T}$	or
	Transformation matrix between nonlinear and linearised DOFs
$\mathbf{T}_j$	Localisation matrix of the $j^{th}$ Layer
$\mathbf{T}_{pl}$	Transformation matrix between original and linearised coordinates in partial feedback linearisation
$\mathbf{T}_j^A$	Localisation matrix of the $j^{th}$ absolute Layer
$\mathbf{T}_j^R$	Localisation matrix of the $j^{th}$ relative Layer
$U_d$	Response of the node $U$ in direction $d$
$U_{j,d}$	Response of the $j^{th}$ node physically connected to node $U$ in direction $d$
$\mathbf{u}$	Unknowns vector in SLM
$\mathbf{u}^*$	Optimal solution
$\mathbf{u}(t)$	Vector of physical input
$\bar{\mathbf{u}}(t)$	Virtual input
$v_0$	Velocity initial condition
$V$	Lyapunov function

---

## List of Symbols

---

$\mathbf{v}$	States vector
$\dot{\mathbf{v}}$	States derivatives vector
$\mathbf{v}_0$	Vector of velocity initial condition
$\mathbf{V}$	Coefficients matrix of normal FRM or Transformation matrix to uncouple the internal dynamic from the controlled states
$\mathbf{V}(A)$	Coefficients matrix of normal FRM for nonlinear damping identification
$\tilde{\mathbf{V}}$	Coefficients matrix of normal FRM including different level of oscillations for nonlinear damping identification
$\bar{\mathbf{V}}$	Conditioned coefficients matrix of normal FRM
$w$	Aluminium beam width
$\mathbf{w}$	Artificial variable for simplex method
$\mathbf{W}$	Instrumented variable
$\mathbf{W}_i$	Conditioning matrix for known terms
$x(t)$	Displacement
$\dot{x}(t)$	Velocity
$\ddot{x}(t)$	Acceleration
$x_b(t)$	Base excitation displacement
$\ddot{x}_b(t)$	Base excitation acceleration
$x_g$	Centre of gravity $x$ coordinate
$x_p(t)$	Particular solution
$x_0$	Displacement initial condition
$\mathbf{x}$	Displacement vector
$\dot{\mathbf{x}}$	Velocity vector
$\ddot{\mathbf{x}}$	Acceleration vector
$\mathbf{x}_0$	Vector of displacement initial condition
$X$	Oscillation amplitude
$X_{b0}$	Amplitude of sinusoidal base excitation
$X_0$	Initial amplitude of oscillation
$\mathbf{X}_0$	Vector of oscillations amplitudes
$y(t)$	Relative displacement
$\dot{y}(t)$	Relative velocity
$\ddot{y}(t)$	Relative acceleration
$y_g$	centre of gravity $y$ coordinate
$Y$	Amplitude of the relative displacement
$\mathbf{y}$	First order formulation states vector or Output vector
$\dot{\mathbf{y}}$	State vector derivative

---

$\mathbf{Y}_0$	Amplitudes of the states harmonic response
$z_g$	Centre of gravity $z$ coordinate
$z_i$	Gain coefficients resulting from DF approximation
$\mathbf{z}$	Second order formulation linearised DOFs vector
$\mathbf{z}_{in}$	Internal dynamics vector
$\mathbf{z}_{zd}$	Zero dynamics vector
$\mathbf{Z}$	Dynamic stiffness matrix
$\mathbf{Z}_i$	Conditioning matrix for coefficients matrix
$\mathbf{Z}_{nl}$	Nonlinear dynamic stiffness matrix
$\mathbf{Z}_0$	Constant amplitude of oscillation in linearised coordinates
$2a$	Dimension of the magnet along $y$
$2b$	Dimension of the magnet along $x$
$2c$	Dimension of the magnet along $z$
$\alpha$	Mass viscous damping proportionality coefficient
$\alpha_j$	Weight coefficient for mode shapes expansion
$\beta$ or $\beta_r$	Stiffness viscous damping proportionality coefficient
$\chi$	Normalised gap ratio
$\boldsymbol{\chi}$	First order formulation linearised DOFs vector
$\boldsymbol{\chi}_{eq}$	Equilibrium point displacements
$\boldsymbol{\chi}_{id}$	Internal dynamics vector
$\boldsymbol{\chi}_{zd}$	Zero dynamics vector
$\delta f_k$	Frequency distance between spectral lines inside the $k^{th}$ frequency range
$\boldsymbol{\delta}$	Lagrange Multiplier matrix
$\tilde{\boldsymbol{\delta}}$	Disturb vector
$\Delta$	Air gap
$\Delta f_i$	Frequency range around $i^{th}$ FRM peak
	Threshold for solution stability check
$\varepsilon$	or Restitution factor for damping nonlinearity
$\boldsymbol{\Phi}$	Modal matrix
$\boldsymbol{\Phi}_r$	Unscaled real mode shape
$\boldsymbol{\Phi}_r$	Unitary modal mass scaled real mode shape
$\gamma_3$	Non-viscous damping index
$\eta$	Structural damping factor
$\eta_r$	Modal displacement of the $r^{th}$ modal coordinate
$\dot{\eta}_r$	Modal velocity of the $r^{th}$ modal coordinate
$\ddot{\eta}_r$	Modal acceleration of the $r^{th}$ modal coordinate
$\boldsymbol{\eta}$	Displacement vector in modal coordinates
$\boldsymbol{\Lambda}$	Spectral matrix
$\tilde{\boldsymbol{\Lambda}}$	Spectral matrix of the second order problem with non-proportional structural damping

---

## List of Symbols

---

$\mu_{i,d}$	Desired pole
$\nu_i$ or $\nu_{ij}$	Control gains
$\varsigma_i$ or $\varsigma_{ij}$	Control gains
$\Theta$	Unscaled modal matrix first order problem
$\Theta_r$	Unscaled complex mode shape
$\tilde{\Theta}$	Unscaled modal matrix second order problem with non-proportional viscous damping
$\hat{\Theta}$	Proper modal matrix
$\hat{\omega}$	Peak angular frequency
$\omega_d$ or $\omega_{d,r}$	Damped natural angular frequency
$\omega_n$ or $\omega_{n,r}$	Natural angular frequency
$\omega_{n,d}$	Desired natural angular frequency
$\tilde{\omega}_r$	Structural damped system natural angular frequency
$\Omega$	Excitation or spectral line angular frequency
$\zeta$ or $\zeta_r$	Damping ratio
$\zeta_d$	Desired damping ratio
$\psi_1$	Switching angle in a cycle between open and close the gaps
$\Psi_e$	Expanded modal matrix
$\Psi_r$	Normalised complex mode shape
$\tilde{\Psi}_r$	Normalised complex mode shape of structural damped system
$\hat{\Psi}_r$	Complex eigenvector normalised as required by Lancaster's formula
$\mathbf{0}$	Zero matrix

# Chapter 1

## 1. Introduction

Vibration theory [1–3] is a particular branch of dynamics focused on cyclic oscillations. Vibrations are defined as the fluctuation of an element around an equilibrium position.

Vibrations of mechanical systems are of interest and widely studied in several engineering industrial application: automotive (suspension systems [4], engine vibration [5], noise vibration and harshness problems (NVH) [6], disc brakes squeal [7]), tooling machine vibrations [8], railway dynamics [9] and structural health monitoring [10] are some example.

In aerospace engineering the vibration problem are of fundamental importance, e.g. cabin noise [11] and flutter instability control [12] are widely studied.

In civil engineering the main application of vibration are earthquake problems [13] or skyscraper and bridges wind-induced vibrations [14].

Recently, vibrations are more and more considered with regards to energetic aspects, in this sense a large branch of research, the so called energy harvester [15], is trying to harvest the energy of residual vibrations, both in micro and macro scale, and convert this energy in a usable form.

The main features of a vibrating system are natural frequencies and mode shapes, which are related to inertia and elastic elements [16,17]. Inertia and elastic forces have been known for a long time: Hooke [18] in 1679 described elastic forces and few years later, in 1687, Newton defined the inertial forces [19].

An additional mechanism is always present in real systems, the so-called damping. Damping is responsible for the energy removal from systems in forms of radiation and dissipation; a definition of damping is provided by Gaul in [17]: *“Energy dissipating property of materials and members undergoing time dependent deformations and/or displacement. Damping is primarily associated with the irreversible transition of mechanical energy into thermal energy.”*



The first attempts to study dissipation are related to Poisson [20], Stokes [21] and Maxwell [22] almost two hundred years later than elastic and inertial forces. Damping has been always seen as a mystery and the related forces are considered complicated and unknown [23], since several mechanisms contribute to dissipations and often they are quite complicated to understand.

Although the damping forces are generally small compared to inertial and elastic forces, their effects have great influence on the dynamic response of systems [17]: displacement amplitude decay, finite vibration amplitude and phase shift when the excitation is close to system resonance frequency and requirement to continuously provide external energy to maintain forced vibration amplitude.

The first mathematical definition of viscous damping is due to Lord Rayleigh [24], his model of damping relates the dissipations in a structure to only the velocity field and it is just a particular case of the general Rayleigh dissipation function. The two most known models for linear damping representation are the viscous and structural damping models. Viscous model relates the damping force to the velocity, and it is in phase with it, while in the structural damping model the damping force is proportional with the displacement but in phase with the velocity. A lot of other damping models exists, as may be found in [25]. Bishop in [23] admits some degree of incompleteness of the damping mathematical theory, which sacrifices the accuracy in representing the physical behaviour of the system in order to preserve the mathematical linearity of the problem. He underlines that any usable mathematical model can give a good approximation of the damping forces, and among all the different possible solutions/models the engineer should select the most suitable case by case. This leads to the loss of correlation between the mathematical damping model and the real dissipations in physical systems.

Usually, the simplest proportional viscous damping model is fitted to experimental measured response of the system, thus, assuming light damping. In this way a dissipation sources equivalent to the real one is included in the system model to consider the main damping effects, but most probably it is not correlated with the real system.

In recent years an increasing demand for not only identification and modelling of damping but also optimisation of damping level and distribution in the structures to comply with working conditions is more and more required [26]. The damping layout should be optimised according to the case of whether vibrations should be avoided or amplified.

In mechanical, aerospace and civil engineering the focus often is in suppressing or attenuating as much as possible the vibrations, to improve system performance; hence a certain level of damping is desirable, for example to reduce structure-borne noise [27], decreases vibration levels [28], increase fatigue life [29] or optimise automotive differential [30].

In other cases instead, system vibrations are desirable for example to maximise efficiency of mechanical gearbox power transmission [31] or in the sound engineering, which is strictly correlated with structural vibration [32]. In

this field vibrations are fundamentals for the proper functionality of the many musical instruments [33] (for example diapason or violin) and speakers. Structural vibrations are exploited to generate acoustics waves to achieve noise reduction or design the acoustic power of musical instruments and speakers.

Moreover, the recent trends are going toward the use of nonlinear system to support the growing necessity for better performing and at the same time lighter systems. The optimal damping distribution in nonlinear system could become even more difficult to be achieved.

## 1.1 Main contributions

The main original contributions achieved by this Ph.D. are here summarised.

### *Spatial damping matrices identification.*

A novel spatial damping identification method is presented, called Stabilised Layers Method (SLM). The main aim is to identify and fit non-classical viscous and structural damping models, considering the physical property of the system. This is achieved by using the usually known physical connectivity of the system to identify the dissipation layout which is the closest to the real damping spatial distribution in the system.

### *Experimental validation of the Stabilised Layers Method.*

The developed identification method is experimentally validated against a three degrees of freedom (DOFs) test rig in several configurations and a body in white (BIW) car chassis with good results.

### *Nonlinear damping force identification.*

The SLM is extended for the identification of system with a single nonlinear damping force acting on a known location. The nonlinearity is identified in frequency domain using sinusoidal input describing function approximation. The coefficients of the nonlinear force are identified together with the linear damping viscous and structural damping matrices.

### *Experimental validation of the SLM for nonlinear damping identification.*

The latter method is validated against a test-rig with a localised nonlinear magnetic damping acting on the system. The coefficients of the amplitude-dependent polynomial nonlinearity are identified and in good agreement with literature values.

### *Design of vibrational behaviour and damping layout via real time control in non-smooth nonlinear systems.*

The desired damping distribution is imposed to non-smooth nonlinear system using active control laws. The system behaviour is modified as convenient

without changing the system structure or optimising the damping material distribution. Once the system is identified in terms of dissipations and a reliable model is build, classical input-output feedback linearisation is used to compute and apply in real time the input force required to achieve the desired dynamics. A receptances based variant of the partial input-output feedback linearisation is implemented to achieve the same results when the system identification is not accurate.

### 1.2 Organisation of the thesis

The thesis is organised as follow:

- Chapter 2: Vibration theory for single degree of freedom (SDOF) and multi degrees of freedom (MDOF) mechanical system is briefly reported. Viscous and structural damping effects on the system behaviour are highlighted in terms of time and frequency domain responses. A brief introduction to a standard method for pole placement in linear mechanical system is presented.
- Chapter 3: A comprehensive literature review on frequency response function (FRF) based spatial damping identification and active control method for linear and nonlinear systems are presented. A review of the damping matrix identification methods based on experimental FRF or from identified system modal parameters is presented, because this is the nature of the SLM proposed in this dissertation. The review of active control strategy is focused on state space feedback linearisation pole placement via method of receptance and their combination, because the extension of these methods to non-smooth nonlinearities will be applied to design the systems vibrational behaviour in the following chapters.
- Chapter 4: The SLM for the identification of linear viscous and structural non-classical damping matrices is presented. The representation of these matrixes via “Layers” is introduced and combined with an FRF-based identification method. Finally, a novel stabilisation diagram for the identification of the optimal solution is presented.
- Chapter 5: Some methods to improve the identification of the damping matrices from experimental data are presented, together with solutions for damping matrix identification from incomplete spatial measures and optimised reconstruction of FRF.
- Chapter 6: A three DOFs configurable lumped parameters test-rig is presented. The different configurations of the test-rig, including non-classical viscous damping and non-smooth nonlinearities, are introduced. On this system both direct spatial damping matrix

identification and real time control to assign the desired vibrational behaviour will be performed.

- Chapter 7: The SLM is validated against the identification of the non-classical damping configuration of the three DOFs test-rig. The viscous damping matrix of the system is identified in ten different configurations of damping levels and distribution. The experimental application validates the SLM and provide an assessment of its robustness.
- Chapter 8: The SLM is applied in the identification of the damping distribution of a body in white (BIW) car chassis with front and rear suspension system. The structure is tested in three different configurations, to maximise/minimise the suspension effects. The focus is on the non-classical damping effect of the global chassis modes and on the suspension damping identification.
- Chapter 9: The SLM is extended to the identification of nonlinear damping forces in MDOF systems with a single nonlinearity. The required measures and the implementation of the algorithm are presented. This nonlinear version of the SLM is tested against damping identification from noisy numerically-generated data of a five DOFs system with a relative damping nonlinearity.
- Chapter 10: The SLM for nonlinear damping identification is experimentally applied for the identification of a three DOFs system with linear viscous damping and a localised magnetic damping nonlinearity. The identification is performed for two levels of magnetic damping and compared to the reference values.
- Chapter 11: In this chapter the non-smooth nonlinear version of the three DOFs system already identified in Chapter 7 is experimentally linearised using input-output feedback linearisation. The desired damping layout is assigned to the controllable DOF. Several levels of damping layout are assigned, together with the desired natural frequency.
- Chapter 12: The same results already achieved in Chapter 11 are obtained using a receptances based feedback linearisation control law, which do not require the system model. Preliminary tests of the system are necessary to obtain the describing function approximation of the nonlinearity and the open loop response of the system, which are required for the linearisation and pole placements.
- Chapter 13: The main conclusions drawn from the work presented in the previous chapters are reported. In addition, insights are given regarding the interesting topics for future developments.



# Chapter 2

## 2. Vibrations and control of mechanical systems

Dynamic studies the relations between the forces applied to a body and its motion. Most of the engineers' efforts are focused on analysis and prediction of dynamics behaviour of physical system. Vibrations are an omnipresent type of dynamics concerning the oscillation around an equilibrium point.

The prediction of systems behaviour needs a mathematical model of the analysed system; usually it is the simplest model able to catch the main features of the systems. The model contains the physical properties of the system, which are called model parameters. For mechanical systems the parameters are mass, stiffness and damping. They describe respectively inertial, elastic and dissipative properties of systems.

Usually physical systems are continuous, with distributed physical properties, however in many cases it possible to build a simple model replacing the continuous properties with lumped parameters. The mathematical models can be divided into two classes: discrete (lumped) and continuous models.

Another classification subdivides systems into SDOF and MDOF systems, depending on the number of variables need to describe the system motion.

Vibrating systems can be also classified with respect to their behaviour. Two main types of systems exist: linear and nonlinear system. A system is said to be linear when the effects superimposition principle holds, otherwise it is nonlinear. Usually the classification between linear and nonlinear system depend on the range of operation: a linear model can describe quite well a system if the working condition stay in certain range, a classical example is the small amplitude oscillations.

Systems can be also classified in passive and active systems. The first group of system respond to excitations with their own dynamics, while the second group

of system include sensors and actuators to change their dynamics according to working condition. These systems are usually known as controlled system.

This chapter focuses on discrete linear systems model for mechanical systems, for both SDOF § 2.1 and MDOF § 2.2 systems. In particular, the dynamics of undamped and damped system is described, focusing on different model of damping. A brief description of active systems control and pole placement is given in § 2.3. The theory presented in this Chapter can be found in many text books, such as [1–3,34–36].

### 2.1 SDOF systems

A SDOF model can be used to describe simple systems where only a variable is enough to predict the motion and behaviour of the physical system. Physical systems are always non-conservative, therefore include dissipations. A brief overview on the dynamics of ideal conservative SDOF systems is presented in § 2.1.1, and the relevant effects of linear and most used dissipation models are described in § 2.1.2 and § 2.1.3; finally a hint on other models of damping is given in § 2.1.4.

#### 2.1.1 Undamped systems

The model of a SDOF undamped mechanical system is sketched in Figure 2.1, where  $m$  and  $k$  are respectively the mass and stiffness parameters of the model,  $f(t)$  and  $x_b(t)$  are respectively the external load and the base excitation.

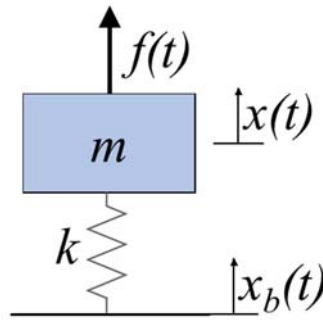


Figure 2.1 - Undamped SDOF system model.

The equation of motion of the system sketched in Figure 2.1 can be obtained using the classical free body diagram [19] or the Lagrange approach [37]

$$m\ddot{x}(t) + kx(t) = f(t) + kx_b(t) \quad (2.1)$$

where  $x(t)$  and  $\ddot{x}(t)$  are the displacement and acceleration of the system induced by the external load  $f(t)$  and the base excitation  $x_b(t)$ .

### Free vibrations

The free vibration response of the system, i.e. the behaviour of the system when it is perturbed from its equilibrium condition, is obtained from the homogenous equation related to Eq. (2.1):

$$m\ddot{x}(t) + kx(t) = 0 \quad (2.2)$$

Eq. (2.2) is a second order ordinary differential equation (ODE), therefore two initial conditions are necessary to find the complete solution.

$$\begin{cases} x(0) = x_0 \\ \dot{x}(0) = v_0 \end{cases} \quad (2.3)$$

The initial conditions in Eq. (2.3) are fundamentals to check that the spring is working in the range where it is linear, thus the linear model is able to predict the physical system response. Eq. (2.2) with two initial condition in Eq. (2.3) possess a unique solution [38] of the form in Eq. (2.4) and the trivial solution  $x(t) = 0$  which is not of interest.

$$x(t) = Xe^{st} \quad (2.4)$$

where  $X$  is the oscillation amplitude and  $s$  is a complex variable associated with the frequency of vibration. Deriving two times Eq. (2.4), substituting in Eq. (2.2) and solving for the poles  $s$  of a system result:

$$s = \pm i\omega_n \quad (2.5)$$

$$\omega_n = \sqrt{\frac{k}{m}} \quad (2.6)$$

where  $i$  is the imaginary unit and  $\omega_n$  is the system angular natural frequency, i.e. the frequency at which the system vibrates once in motion.

The general solution becomes:

$$x(t) = A_1 e^{-i\omega_n t} + A_2 e^{i\omega_n t} \quad (2.7)$$

where  $A_1$  and  $A_2$  are arbitrary complex constant to be determined by the initial conditions. Finally, the solution of the system is:



$$x(t) = x_0 \cos(\omega_n t) + \frac{v_0}{\omega_n} \sin(\omega_n t) \quad (2.8)$$

The response of an SDOF undamped system, with  $f_n = \omega_n / (2\pi) = 2$  Hz, changing the initial conditions  $x_0$  and  $v_0$  is shown in Figure 2.2.

The initial conditions influence the total initial amount of energy  $E_{tot}$  in the system, which does not change in the time evolution because no dissipations are acting. The total amount of energy in the system is given by:

$$E_{tot} = E_K + E_E = \frac{1}{2} m v_0^2 + \frac{1}{2} k x_0^2 \quad (2.9)$$

where  $E_k$  and  $E_E$  are respectively the kinetic and elastic energy of the system. The amplitude of the oscillation  $X$  in Eq. (2.4) can be computed as:

$$X = \sqrt{x_0^2 + \left( \frac{v_0}{\omega_n} \right)^2} \quad (2.10)$$

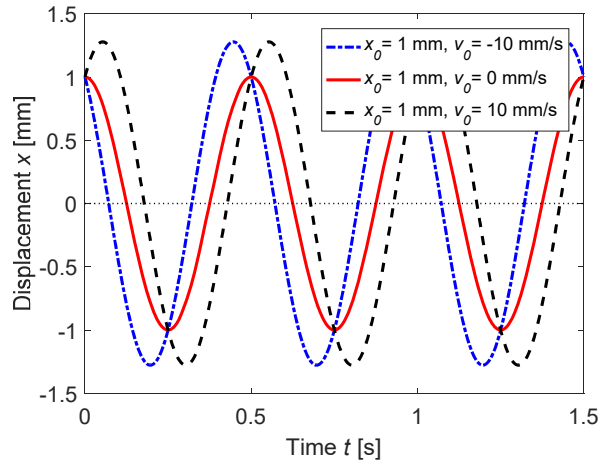


Figure 2.2 - Free response of a SDOF undamped system.

## Harmonic excitation

For linear systems the harmonic excitation response is important, because often periodic vibrations in mechanical devices are induced by rotating machines, motors and other devices. It is common to approximate this excitation as a harmonic excitation of the form:

$$f(t) = F_0 \sin(\Omega t) \quad (2.11)$$

where  $F_0$  is the excitation amplitude and  $\Omega$  is the excitation frequency and the base is fixed, i.e.  $x_b(t) = 0$ .

The solution of Eq. (2.1) under these hypotheses is unique and possess a general solution  $x(t)$ , given in Eq. (2.8), related to the homogeneous system in Eq. (2.2) and a particular solution  $x_p(t)$  which follows the forcing function:

$$x_p(t) = X \sin(\Omega t) \quad (2.12)$$

where  $X$  is the amplitude at the steady state.

The sum of general solution  $x(t)$ , given in Eq. (2.8), and particular solution  $x_p(t)$ , given in Eq. (2.12), is still a solution of the differential equation. The general time domain response of the harmonically forced system is:

$$x(t) = x_0 \cos(\omega_n t) + \frac{x_0}{\omega_n} \sin(\omega_n t) + X \sin(\Omega t) \quad (2.13)$$

For undamped system both the homogenous and particular solution are present in the entire system response. The frequency domain response of the system, it means amplitude  $X$  and phase  $\phi$  of the response at each excitation frequency  $\Omega$ , called inertance FRF  $H$ , can be obtained deriving and substituting Eq. (2.12) in the equation of motion. The inertance FRF for an undamped SDOF system results to be:

$$H(r) = \frac{X}{\frac{F_0}{k}} = \frac{X}{X_{st}} = \frac{1}{1 - \left(\frac{\Omega}{\omega_n}\right)^2} = \frac{1}{1 - r^2} \quad (2.14)$$

where  $X_{st}$  is the static response of the system subjected to a static load  $F_0$ , and  $r = \Omega/\omega_n$  is the ratio between the excitation frequency and the system natural frequency.

Amplitude and phase of the receptance FRF  $H$  result to be:

$$|H(r)| = \frac{1}{|1 - r^2|} \quad (2.15)$$

$$\phi(r) = \tan^{-1}\left(\frac{0}{1 - r^2}\right) \quad (2.16)$$

Some considerations of the SDOF undamped inertance FRF in Figure 2.3 are:

- when the excitation approaches null frequency  $\lim_{r \rightarrow 0} |H(r)| = 1$  and the phase  $\phi = 0^\circ$ , which is the system static response;
- when  $r < 1$ , i.e.  $\Omega < \omega_n$ , the phase  $\phi = 0^\circ$ : the system response is in phase with the excitation;

- when  $r=1$ , i.e.  $\Omega = \omega_n$ , the FRF amplitude  $|H(r)| = \infty$  and the phase  $\phi = -90^\circ$ , this is the system resonance;
- when  $r > 1$ , i.e.  $\Omega > \omega_n$ , the phase  $\phi = -180^\circ$ : the system response is in quadrature with respect the excitation;
- when the excitation frequency approaches infinite  $\lim_{r \rightarrow \infty} |H(r)| = 0$ , the response amplitude vanishes.

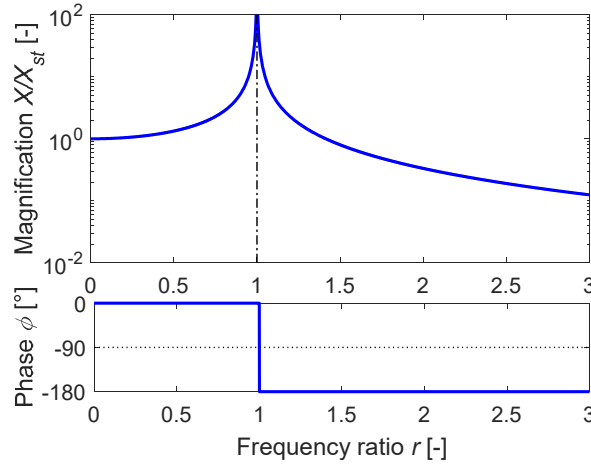


Figure 2.3 - Receptance FRF  $H$  of a SDOF undamped system.

### Base excitation

The base excitation is typical of system in which the excitation is given from the base motion and no direct forces are applied to the system, i.e.  $f(t)=0$  in Eq. (2.1). It is interesting to study the response of the system when the base excitation is harmonic.

$$x_b(t) = X_{b0} \sin(\Omega t) \quad (2.17)$$

where  $X_{b0}$  is the amplitude of the harmonic base excitation.

Performing the coordinate transformation  $y(t) = x(t) - x_b(t)$ , the equation of motion Eq. (2.1) can be rewritten as:

$$m\ddot{y}(t) + ky(t) = m\ddot{x}_b(t) \quad (2.18)$$

and therefore

$$m\ddot{y}(t) + ky(t) = m\Omega^2 x_b(t) \quad (2.19)$$

Assuming null initial conditions, the solution of Eq. (2.19) is of the type:

$$y(t) = Y \sin(\Omega t) \quad (2.20)$$

Substituting Eq. (2.20) in Eq. (2.19) it is possible to evaluate the system FRF. The FRF is in this case called relative transmissibility  $T_r$  and evaluates the ratio between the system response amplitude  $Y$  and the excitation amplitude  $X_{b0}$ .

$$T_r(r) = \frac{Y}{X_{b0}} = \frac{r^2}{1-r^2} \quad (2.21)$$

The relative transmissibility of a SDOF undamped system in amplitude and phase is shown in Figure 2.4.

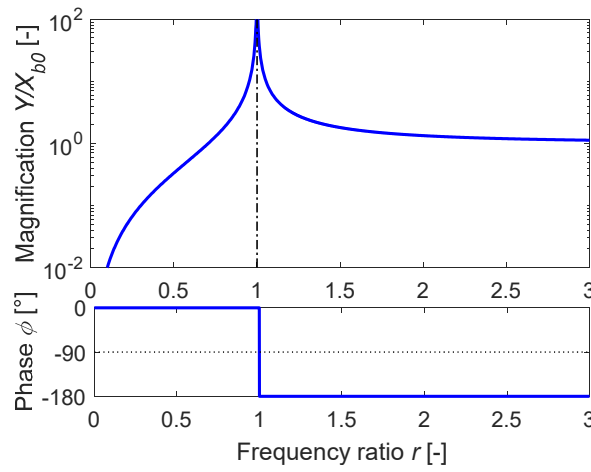


Figure 2.4 - Relative transmissibility  $T_r$  of a SDOF undamped system.

Some considerations on the relative transmissibility  $T_r$  in Figure 2.4 are:

- when  $r \ll 1$ , i.e.  $\Omega \ll \omega_n$ , the relative motion  $y$  is proportional to the amplitude of the acceleration  $X_{b0}\Omega^2$ . The system works as an accelerometer;
- when  $r \gg 1$ , i.e.  $\Omega \gg \omega_n$ , the amplitude of the relative motion is the same amplitude of the base displacement. In the latter case the mass is rested in absolute reference system, while the base moves: this is the concept of the seismograph.

The absolute transmissibility  $T_a$  transfer function can be computed as:

$$T_a(r) = \frac{X}{X_{b0}} = \frac{Y + X_{b0}}{X_{b0}} = T_r(r) + 1 = \frac{1}{1-r^2} \quad (2.22)$$

The absolute transmissibility  $T_a$  has the same behaviour of the inertance FRF  $H$  in Eq. (2.14) and Figure 2.3.

### 2.1.2 Viscous Damped systems

The model of a SDOF viscous damped mechanical system is sketched in Figure 2.5, the viscous damper is now added to model dissipation and  $c$  is the viscous damping coefficient.

The equation of motion of the system sketched in Figure 2.5, can be obtained using the classical free body diagram [19] or the Lagrange approach [37].

$$m\ddot{x}(t) + c\dot{x}(t) + kx(t) = f(t) + kx_b(t) \quad (2.23)$$

where  $\dot{x}(t)$  is the velocity of the mass induced by the external load  $f(t)$  and the base excitation  $x_b(t)$  and all the other variables are already defined in § 2.1.1.

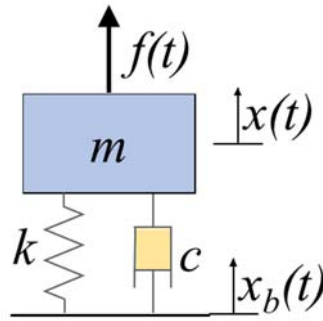


Figure 2.5 - Viscous damped SDOF system model.

### Free vibrations

The free vibration response of the system is obtained from the homogenous equation related to Eq. (2.23):

$$m\ddot{x}(t) + c\dot{x}(t) + kx(t) = 0 \quad (2.24)$$

Two initial conditions are necessary to find the general solution of the second order ODE Eq. (2.24), as for the undamped case.

$$\begin{cases} x(0) = x_0 \\ \dot{x}(0) = v_0 \end{cases} \quad (2.25)$$

The initial conditions in Eq. (2.25) are useful to check that, in addition to the spring, also the damping is working in the range in which it is linear; thus it is correct to use a linear model to predict the physical system response. Eq. (2.24) with two initial conditions in Eq. (2.25) it is known to possess a unique solution [38] of the form in Eq. (2.4) and the trivial solution  $x(t) = 0$ .

$$x(t) = Xe^{st} \quad (2.26)$$

where  $X$  is the oscillation amplitude and  $s$  is a complex variable associated with the frequency of vibration. Deriving two times Eq. (2.26), substituting in Eq. (2.24) and solving for the poles  $s$  of a system, it result:

$$s_{1,2} = -\zeta\omega_n \pm \omega_n\sqrt{\zeta^2 - 1} \quad (2.27)$$

where  $\omega_n$  is defined as in Eq. (2.6) and

$$\zeta = \frac{c}{2\sqrt{km}} \quad (2.28)$$

$$\omega_d = \omega_n\sqrt{1 - \zeta^2} \quad (2.29)$$

$\zeta$  is the damping ratio and  $\omega_d$  is the system damped natural frequency, existing only if  $0 < \zeta < 1$ , i.e. the frequency at which the damped system vibrates once in motion.

The solution of Eq. (2.24) is clearly influenced by the value of the damping ratio  $\zeta$ . There are three cases of interest, analysed in the following.

#### Underdamped

For underdamped systems  $0 < \zeta < 1$  Eq. (2.24) has two complex conjugate poles  $s_{1,2}$ :

$$s_{1,2} = -\zeta\omega_n \pm i\omega_n\sqrt{1 - \zeta^2} \quad (2.30)$$

The solution of Eq. (2.24) is:

$$x(t) = e^{-\zeta\omega_n t} (A \cos(\omega_d t) + B \sin(\omega_d t)) \quad (2.31)$$

where  $A$  and  $B$  are constant of integration in Eq. (2.32), to be found from the initial conditions in Eq. (2.25):

$$A = x_0, \quad B = \frac{\zeta\omega_n x_0 + v_0}{\omega_d} \quad (2.32)$$

Another representation of the solution is

$$x(t) = X_0 e^{-\zeta\omega_n t} \sin(\omega_d t + \phi) \quad (2.33)$$

where  $X_0$  and  $\phi$  are the initial amplitude and phase in Eq. (2.34), to be find from initial conditions in Eq. (2.25).

$$X_0 = \frac{\sqrt{(\zeta\omega_n x_0 + v_0)^2 + (x_0\omega_d)^2}}{\omega_d}, \quad \phi = \tan^{-1}\left(\frac{x_0\omega_d}{\zeta\omega_n x_0 + v_0}\right) \quad (2.34)$$

The response is a decreasing oscillation at the damped natural frequency  $\omega_d$ . The two solutions Eq. (2.31) and Eq. (2.33) are the same, the two expressions are only two different way of write the same quantity: Eq. (2.31) empathises the sinusoidal and co-sinusoidal contribution, Eq. (2.33) focus the attention on the sinusoidal response with a phase delay with respect to the excitation.

The response of an underdamped SDOF system with  $f_n = \omega_n/(2\pi) = 2$  Hz, initial conditions  $x_0 = 1$  mm  $v_0 = 1$  mm/s and different levels of damping ratio  $\zeta$  is shown in Figure 2.6.

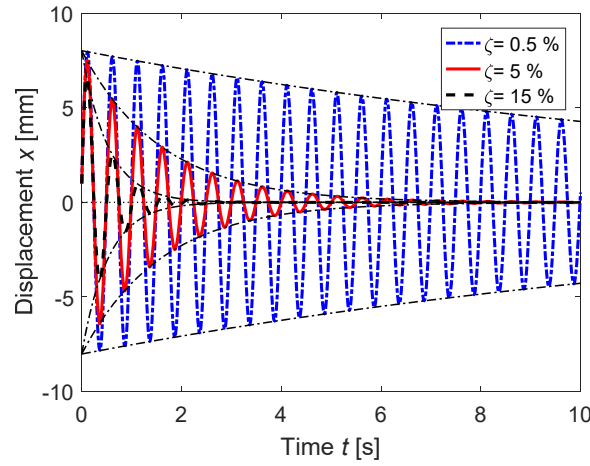


Figure 2.6 - Free response of underdamped SDOF system.

### Critically damped

In critically damped systems  $\zeta = 1$  and Eq. (2.24) has two coincident negative real poles  $s_{1,2}$ .

$$s_{1,2} = -\zeta\omega_n \quad (2.35)$$

The solution of Eq. (2.24) in this case becomes:

$$x(t) = e^{-\omega_n t} [(\omega_n x_0 + v_0)t + x_0] \quad (2.36)$$

Critical damping ratio separates oscillator and non-oscillatory motion, it is the case with minimum damping in which there are not oscillations.

The behaviour of a critically damped system with  $f_n = \omega_n/(2\pi) = 2$  Hz is shown in Figure 2.7, the initial displacement  $x_0$  is kept constant and the initial velocity  $v_0$  changes.

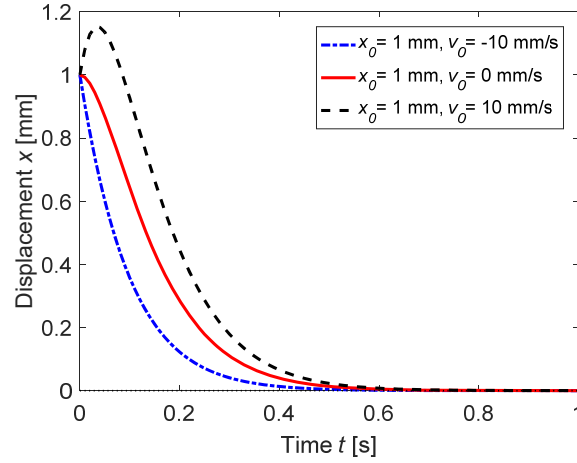


Figure 2.7 - Free response of a critically damped SDOF system.

**Overdamped**

In overdamped system  $\zeta > 1$  and Eq. (2.24) has two real negative poles  $s_{1,2}$ .

$$s_{1,2} = \left( -\zeta \pm \sqrt{\zeta^2 - 1} \right) \omega_n \quad (2.37)$$

The solution of Eq. (2.24) becomes:

$$x(t) = Ae^{(-\zeta + \sqrt{\zeta^2 - 1})\omega_n t} + Be^{(-\zeta - \sqrt{\zeta^2 - 1})\omega_n t} \quad (2.38)$$

where  $A$  and  $B$  are constant to be determined by the initial condition.

$$A = \frac{(-\zeta + \sqrt{\zeta^2 - 1})\omega_n x_0 + v_0}{2\omega_n \sqrt{\zeta^2 - 1}}, \quad B = -\frac{(-\zeta - \sqrt{\zeta^2 - 1})\omega_n x_0 + v_0}{2\omega_n \sqrt{\zeta^2 - 1}} \quad (2.39)$$

An example response of a system with natural frequency with  $f_n = \omega_n / (2\pi) = 2$  Hz and different level of damping ratio  $\zeta$  is shown in Figure 2.8.

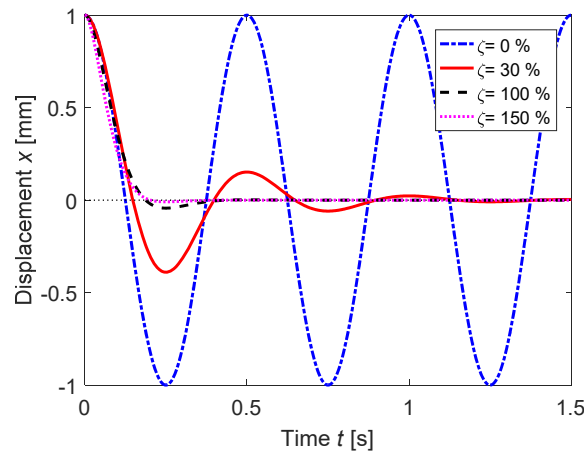


Figure 2.8 - Free response of SDOF system response changing damping ratio.



## Harmonic excitation

A viscous damped SDOF system with harmonic excitation as in Eq. (2.11) and fixed base, i.e.  $x_b(t) = 0$ , is considered. The solution of Eq. (2.23) under these hypotheses is unique and possess a general solution which depends on the damping ratio  $\zeta$  level. The solution is Eq. (2.31) if underdamped, Eq. (2.36) if it is critically damped and Eq. (2.38) if it is overdamped system. The particular solution follows the forcing function:

$$x_p(t) = X \sin(\Omega t + \phi) \quad (2.40)$$

where  $X$  and  $\phi$  are the amplitude and the phase shift at the steady state. The sum of two solutions is still a solution and the general time domain solution of the harmonically forced system for underdamped systems becomes:

$$x(t) = e^{-\zeta\omega_n t} [A \cos(\omega_d t) + B \sin(\omega_d t)] + X \sin(\Omega t + \phi) \quad (2.41)$$

where  $A$  and  $B$  are integration constant defined in Eq. (2.32).

The homogenous response vanishes for large time; hence the steady state solution is represented by the particular solution  $x_p(t)$  only. The frequency domain response of the system can be obtained deriving two times Eq. (2.40) and substituting in the equation of motion Eq. (2.23). The receptance FRF  $H$  for a viscous damped SDOF system is expressed in Eq. (2.42) and the related amplitude and phase in Eq. (2.43) and Eq. (2.44). The bode diagram of the SDOF damped system response for several damping ratio  $\zeta$  is shown in Figure 2.9.

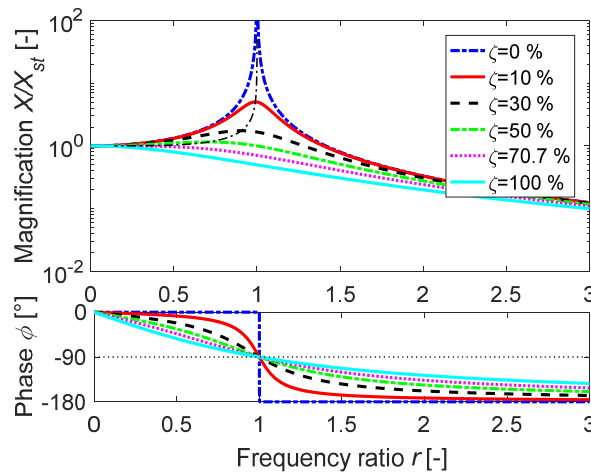


Figure 2.9 - Receptance FRF  $H$  of a SDOF system changing damping ratio.

$$H(r) = \frac{X}{\frac{F_0}{k}} = \frac{X}{X_{st}} = \frac{1}{1 + i2\zeta \frac{\Omega}{\omega_n} - \left(\frac{\Omega}{\omega_n}\right)^2} = \frac{1}{1 + i2\zeta r - r^2} \quad (2.42)$$

$$|H(r)| = \frac{1}{\sqrt{(1-r^2)^2 + (2\zeta r)^2}} \quad (2.43)$$

$$\phi(r) = -\tan^{-1}\left(\frac{2\zeta r}{1-r^2}\right) \quad (2.44)$$

Some considerations on the SDOF viscous damped system inertance FRF  $H$  are:

- when the excitation approaches null frequency  $\lim_{r \rightarrow 0} |H(r)| = 1$  and the phase  $\phi = 0^\circ$ , this is the system static response;
- when  $r < 1$ , i.e.  $\Omega < \omega_n$ , the phase  $0^\circ < \phi < -90^\circ$ : the system response follows the excitation but with a delay depending of the damping ratio  $\zeta$ ;
- when  $r = 1$ , i.e.  $\Omega = \omega_n$ , the FRF amplitude is finite, there are no more discontinuity point and the phase  $\phi = -90^\circ$ , this is the system resonance;
- when  $r > 1$ , i.e.  $\Omega > \omega_n$ , the phase  $-90^\circ < \phi < -180^\circ$ : the system response is out of phase with respect the excitation and with a delay;
- when the excitation frequency approaches infinite  $\lim_{r \rightarrow \infty} |H(r)| = 0$ , the response amplitude vanishes.

It is interesting to identify the peak frequency  $\hat{\omega}$  of the damped FRF and the maximum magnification factor  $M_p$ :

$$\hat{\omega} = \omega_n \sqrt{1 - 2\zeta^2} \quad (2.45)$$

$$M_p = \frac{1}{2\zeta \sqrt{1 - \zeta^2}} \quad (2.46)$$

Eq. (2.45) gives also the condition for the existence of the peak in the damped FRF  $H$ , which is the positiveness of the radicand. The damped system FRF presents a peak up to a defined value of damping ratio  $\zeta$ , given in Eq. (2.47). If the damping ratio is higher, the FRF  $H$  is monotonically decreasing with excitation frequency  $\Omega$ .

$$\zeta < \frac{1}{\sqrt{2}} \quad (2.47)$$

### Base excitation

The response of the damped system when the base excitation is harmonic and no external forces are applied to the system, i.e.  $f(t) = 0$  in Eq. (2.23), is here studied.

$$x_b(t) = X_{b0} \sin(\Omega t) \quad (2.48)$$

Performing the coordinate substitution  $y(t) = x(t) - x_b(t)$ , the equation of the motion, given in Eq. (2.1), can be rewritten as:

$$m\ddot{y}(t) + c\dot{y}(t) + ky(t) = -m\ddot{x}_b(t) \quad (2.49)$$

and therefore

$$m\ddot{y}(t) + c\dot{y}(t) + ky(t) = m\Omega^2 x_b(t) \quad (2.50)$$

Assuming null initial condition the solution is of the type:

$$y(t) = Y \sin(\Omega t + \phi) \quad (2.51)$$

Substituting Eq. (2.51) in Eq. (2.50) it is possible to evaluate the system relative transmissibility FRF  $T_r$ : it evaluates the ratio between the system relative response amplitude and the excitation amplitude.

$$T_r(r) = \frac{Y}{X_{b0}} = \frac{r^2}{1 + i2\zeta r - r^2} \quad (2.52)$$

The amplitude  $|T_r(r)|$  and phase shift  $\phi$  of the latter transfer functions are:

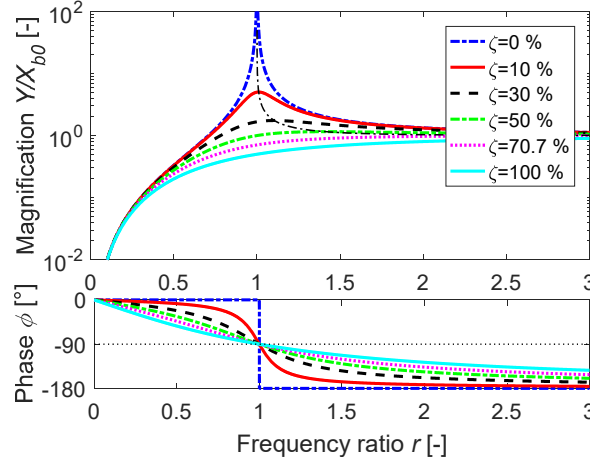
$$|T_r(r)| = \frac{r^2}{\sqrt{(1-r^2)^2 + (2\zeta r)^2}} \quad (2.53)$$

$$\phi(r) = -\tan^{-1}\left(\frac{2\zeta r}{1-r^2}\right) \quad (2.54)$$

It is interesting to identify the peak frequency  $\hat{\omega}$  of the damped FRF  $T_r$  in Figure 2.10 and the maximum magnification factor  $M_p$ :

$$\hat{\omega} = \frac{\omega_n}{\sqrt{1-2\zeta^2}} \quad (2.55)$$

$$M_p = \frac{1}{2\zeta\sqrt{1-\zeta^2}} \quad (2.56)$$

Figure 2.10 - Transmissibility FRF  $T_r$  of a SDOF system.

In the relative transmissibility  $T_r$ , the peak frequency  $\hat{\omega}$  increases with damping ratio  $\zeta$ .

The existence of the peak in the damped relative transmissibility FRF  $T_r$  can be obtained from Eq. (2.55), in particular the radicand has to be positive. The damped FRF has a peak until a defined value of damping ratio  $\zeta$ , given in Eq. (2.57). If the damping ratio is higher the FRF is monotonically increasing with frequency.

$$\zeta < \frac{1}{\sqrt{2}} \quad (2.57)$$

### 2.1.3 Structural damped systems

The ideal stress-strain curve for linear materials does not imply dissipations, however in a real engineering material dissipation exist due to internal planes slide relative to one another and molecular bounds are broken, causing the conversion of strain energy in thermic energy, that will irreversibly lost. This creates a hysteresis loop is created in the force displacement diagram. The area of the hysteresis loop represents the energy dissipated for each cycle. This type of dissipation is called structural damping. The model of a SDOF system with structural damping is shown in Figure 2.11, where  $d$  is the structural damping coefficient.

It has been shown experimentally that the energy dissipated for each cycle in structural damped system is independent of the frequency, contrary to the viscous damping, and proportional to the square of the amplitude.

$$L_v = \pi c \Omega A^2 \quad (2.58)$$

$$L_s = a X^2 \quad (2.59)$$

where  $L_v$ ,  $L_i$  are respectively the dissipative work of viscous and structural damping forces and  $a$  is a constant of the material.

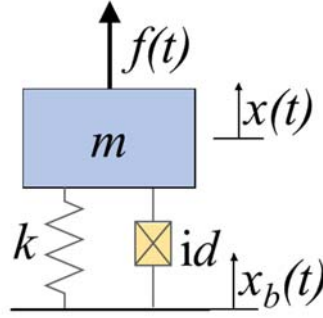


Figure 2.11 - Structural damped SDOF system model.

An equivalent viscous damping coefficient can be obtained to model the hysteresis phenomena. The equivalent viscous damper  $c_{eq}$  has to dissipate the same amount of energy of the structural one, hence  $L_v = L_s$  and  $c_{eq}$  results to be:

$$c_{eq} = \frac{a}{\pi\Omega} \quad (2.60)$$

The equation of motion Eq. (2.23) of the equivalent SDOF system becomes:

$$m\ddot{x} + \frac{a}{\pi\Omega}\dot{x} + kx = f_0 e^{i\Omega t} \quad (2.61)$$

where the system is excited with a harmonic excitation necessary to perform the hysteresis cycle. This model is valid only if the system is forced perform a cycle, otherwise the hypothesis is no more valid. At the steady state the solution will be of the form of the forcing function and the velocity can be written as:

$$\dot{x} = i\Omega x \quad (2.62)$$

Substituting Eq. (2.62) in Eq. (2.61)

$$m\ddot{x} + (k + id)x = f_0 e^{i\Omega t} \quad (2.63)$$

where  $d = a / \pi$  is the structural damping coefficient. Eq. (2.63) is the equation of motion of the system in Figure 2.11.

It is important to highlight again that this model is valid only for harmonic excitation, since the response of the system to driving frequency  $\Omega$  is necessary in the definition of Eq. (2.63). Only harmonic excitation or base excitation can be studied. The model can't be used for the free response of the system.

## Harmonic Excitation

The response of the system in Eq. (2.63) at the steady state will be of the form

$$x(t) = Xe^{i\Omega t + \phi} \quad (2.64)$$

Deriving Eq. (2.64) and substituting in Eq. (2.63), the receptance FRF  $H$  becomes:

$$H(r) = \frac{Xk}{F_0} = \frac{X}{X_{st}} = \frac{1}{1 + i\eta - r^2} \quad (2.65)$$

where  $\eta = d/k$  is called structural damping factor.

The equivalence between the structural damping factor  $\eta$  and the damping ratio  $\zeta$  is:

$$\eta = 2\zeta \frac{\Omega}{\omega_n} \quad (2.66)$$

and because often  $\eta$  is experimental evaluated at the resonance:

$$\eta = 2\zeta \quad (2.67)$$

The amplitude  $|H(r)|$  and phase  $\phi$  of the receptance FRF  $H$  in Eq. (2.65) :

$$|H(r)| = \frac{1}{\sqrt{(1-r^2)^2 + \eta^2}} \quad (2.68)$$

$$\phi(r) = -\tan^{-1}\left(\frac{\eta}{1-r^2}\right) \quad (2.69)$$

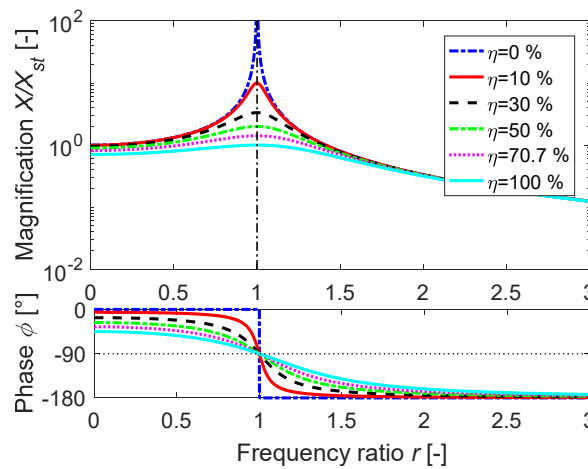


Figure 2.12 - Inertance FRF  $H$  of a structural damped SDOF system.

Some consideration on structural damped system FRF  $H$  in Figure 2.12 are:

- when  $r=0$  the amplitude of the response  $H(0)=1/\sqrt{1+\eta^2} \neq 1$  is no more unitary and the phase  $\phi(0)=\tan^{-1}(\eta) \neq 0$  also when a static load is applied. This delay is due to the model which is wrong if a cycle is not followed.
- when  $r \rightarrow \infty$  the amplitude of the response vanishes;
- The peak is always present for whatever values of structural damping factor  $\eta$ .

The peak of the FRF and the magnification factor  $M_p$  are:

$$\hat{\omega} = \omega_n \quad (2.70)$$

$$M_p = \frac{1}{\eta} \quad (2.71)$$

In the structural damping model, the peak frequency  $\hat{\omega}$  does not change with the structural damping factor  $\eta$ , while the magnification factor  $M_p$  changes.

The comparison between the FRFs of a viscous and structural damped system with equivalent dissipation levels, as in Eq. (2.67), is shown in Figure 2.13. For low dissipation values the two models are quite similar in amplitude  $M_p$  and small differences in the phase  $\phi$  are present. For high level of dissipation viscous and structural models are quite different in both amplitude  $M_p$  and phase  $\phi$ , and only in the resonance condition they are equivalent.

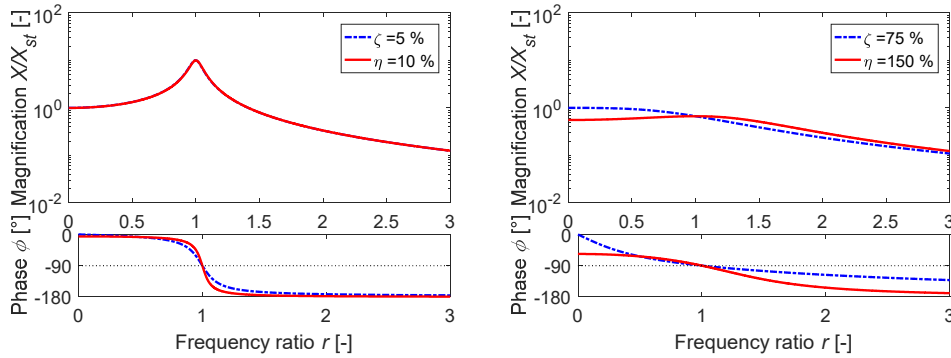


Figure 2.13 - Comparison between viscous and structural damped system with equivalent dissipation:  $\zeta = 5\%$ ,  $\eta = 10\%$  (left) and  $\zeta = 75\%$ ,  $\eta = 150\%$  (right).

### Base Excitation

The equation of motion of a SDOF structural damped system with excitation coming from the base is:

$$m\ddot{x}(t) + (k + id)x(t) = kx_b(t) \quad (2.72)$$

Performing the coordinate substitution  $y(t) = x(t) - x_b(t)$ , the equation of the motion Eq. (2.72) can be rewritten as:

$$m\ddot{y}(t) + (k + id)y(t) = -m\ddot{x}_b(t) \quad (2.73)$$

Considering harmonic excitation of the type:

$$x_b = X_{b0}e^{i\Omega t} \quad (2.74)$$

and assuming null initial condition the solution is of the type:

$$y(t) = Y \sin(\Omega t + \phi) \quad (2.75)$$

Deriving Eq. (2.75) and Eq. (2.74) and substituting in Eq. (2.73) it is possible to evaluate the system relative transmissibility FRF  $T_r$ .

$$T_r(r) = \frac{Y}{X_{b0}} = \frac{r^2}{1 + i\eta - r^2} \quad (2.76)$$

Therefore, the amplitude  $|T_r|$  and phase shift  $\phi$  becomes:

$$|T_r(r)| = \frac{r^2}{\sqrt{(1 - r^2)^2 + \eta^2}} \quad (2.77)$$

$$\phi = -\tan^{-1}\left(\frac{\eta}{1 - r^2}\right) \quad (2.78)$$

The peak frequency  $\hat{\omega}$  and the maximum magnification factor  $M_p$  are:

$$\hat{\omega} = \omega_n \sqrt{1 + \eta^2} \quad (2.79)$$

$$M_p = \frac{\sqrt{1 + \eta^2}}{\eta} \quad (2.80)$$

The peak frequency  $\hat{\omega}$  is always present in the relative transmissibility FRF  $T_r$ , since no limitations have to be assumed in the definition of Eq. (2.79). The transmissibility  $T_r$  FRFs for several damping ratio  $\eta$  are shown in Figure 2.14.



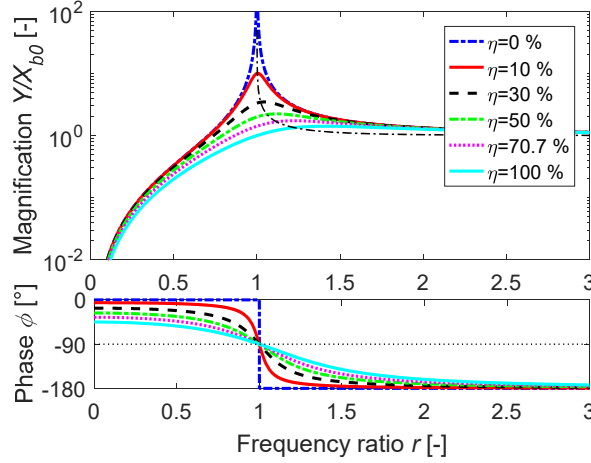


Figure 2.14 - Transmissibility FRF  $T_r$  of a structural damped SDOF system.

### 2.1.4 Other forms of damping

A real mechanical system is generally subjected to other forms of damping such as aerodynamics drag, radiation damping or anelastic damping.

All these models result to be nonlinear and therefore exact close form solutions of the equation of motion with these forms of damping do not exist.

The periodic motion of systems presenting these forms of damping can be developed considering an equivalent viscous damping coefficient. The equivalent viscous damping coefficient can be obtained from the viscous damping coefficient which dissipates the same amount of energy of the considered damping form.

For harmonic motion of the form:

$$x(t) = X \sin(\Omega t) \quad (2.81)$$

the energy dissipated over one cycle due to the generalised damping force  $F_d$  results:

$$\Delta E = \int_0^{\frac{2\pi}{\Omega}} F_d \dot{x} dt = \int_0^{\frac{2\pi}{\Omega}} F_d X \Omega \cos(\Omega t) dt \quad (2.82)$$

Comparing Eq. (2.82) to the energy dissipated by a viscous damper Eq. (2.58), the equivalent viscous damping coefficient  $c_{eq}$  results:

$$c_{eq} = \frac{\Delta E}{\pi \Omega X^2} \quad (2.83)$$

The damping in a system could be eventually the sum of viscous, structural and all the equivalent damping coefficient. Usually viscous damping is

predominant for small amplitude, while for large amplitude of vibration the structural damping can become important.

### **Aerodynamic drag**

Aerodynamic drag force is defined as the force of the wind or air resistance pushing in the opposite direction to the motion of the object. It acts in all real systems; however, its effect is often ignored. The identification and modelling of drag force is a fluid dynamic problem. For high Reynolds number this force can be written as:

$$F_D = C_D \dot{x} |\dot{x}| \quad (2.84)$$

where  $C_D$  is a coefficient depending on the shape of the body.

For moderate Reynolds number the drag force can be expressed as:

$$F_D = C_D \dot{x} |\dot{x}|^\alpha \quad (2.85)$$

where  $0 < \alpha < 1$ .

In both cases the equation of motion is nonlinear.

### **Anelastic damping**

Anelastic damping is typical of viscoelastic materials, e.g. rubber. They obey a constitutive equation in which stress is related to stress and strain rate. For this reason, they present phase lag as viscous damped system.

Usually these materials are modelled using Kelvin-Voigt model [39], where a spring is in parallel with a damper.

### **Radiation damping**

This damping occurs when a body vibrates in the free surface between two fluids. Pressure waves are radiated outward by the vibration, this means a part of energy is transferred from the body to the fluid [17].

## **2.2 MDOF systems**

The number of DOFs  $N$  necessary for describing the vibrational behaviour of a system represents the number of kinematically independent coordinates necessary to predict the motion of each particle in the system. Although the analysis of MDOF system is significantly more difficult and time-consuming than SDOF analysis, it is necessary to model real system. Real systems are continuous and possess infinite number of DOFs. Continuous system requires the solution of partial differential equations, which are much more difficult to solve with respect

to MDOF systems, especially when the geometry is complex. Therefore, the approximation of MDOF systems, i.e. to use a finite number of DOFs, is a good compromise to model mechanical systems.

### 2.2.1 Undamped systems

The equation of motion of an undamped MDOF system can be derived from Newton's laws [19] or Lagrange approach [37] analytically or from commercial finite element (FE) codes.

$$\mathbf{M}\ddot{\mathbf{x}} + \mathbf{K}\mathbf{x} = \mathbf{f} \quad (2.86)$$

where  $\mathbf{x}, \ddot{\mathbf{x}} \in \mathbb{R}^{N \times 1}$  are respectively the generalised displacements and accelerations of the  $N$  DOFs,  $\mathbf{M}, \mathbf{K} \in \mathbb{R}^{N \times N}$  are respectively the mass and stiffness matrices of the system. These matrices are real and symmetric. The mass matrix  $\mathbf{M}$  is strictly positive definite, while the stiffness matrix  $\mathbf{K}$  is positive semidefinite, to allow rigid deformations.  $\mathbf{f} \in \mathbb{R}^{N \times 1}$  is the generalised force vector.

Moreover, if the mass matrix  $\mathbf{M}$  is diagonal and  $\mathbf{K}$  is not diagonal the problem is statically coupled, vice versa the problem is dynamically coupled.

### Eigenproblem

Considering an invariant conservative MDOF system with no external load:

$$\mathbf{M}\ddot{\mathbf{x}} + \mathbf{K}\mathbf{x} = \mathbf{0} \quad (2.87)$$

Looking for a synchronous solution, where all the  $N$  DOFs move with the same time domain law  $g(t)$  and amplitude  $\mathbf{X}_0$ :

$$\mathbf{x} = \mathbf{X}_0 g(t) \quad (2.88)$$

Deriving two times Eq. (2.88) and substituting in Eq. (2.87), it results:

$$\mathbf{M}\mathbf{X}_0 \ddot{g}(t) + \mathbf{K}\mathbf{X}_0 g(t) = \mathbf{0} \quad (2.89)$$

$$\mathbf{X}_0^T \mathbf{M}\mathbf{X}_0 \ddot{g}(t) + \mathbf{X}_0^T \mathbf{K}\mathbf{X}_0 g(t) = 0 \quad (2.90)$$

where  $\mathbf{M}$  is positive defined, therefore it results:

$$\frac{\ddot{g}(t)}{g(t)} = -\frac{\mathbf{X}_0^T \mathbf{K}\mathbf{X}_0}{\mathbf{X}_0^T \mathbf{M}\mathbf{X}_0} = -\omega^2 \leq 0 \quad (2.91)$$

Substituting Eq. (2.91) in Eq. (2.90), it becomes

$$\ddot{g}(t) + \omega^2 g(t) = 0 \quad (2.92)$$

The time domain law  $g(t)$  can be obtained from Eq. (2.92). It is clearly an oscillatory function and Eq. (2.88) can be written as:

$$\mathbf{x} = \mathbf{X}_0 e^{i\omega t + \phi} \quad (2.93)$$

Deriving two times Eq. (2.93) and substituting in Eq. (2.87)

$$(\mathbf{K} - \omega_n^2 \mathbf{M}) \mathbf{X}_0 = \mathbf{0} \quad (2.94)$$

The trivial solution  $\mathbf{X}_0 = \mathbf{0}$  is the static undeformed condition, the others interesting solutions are:

$$|\mathbf{K} - \omega_n^2 \mathbf{M}| = 0 \quad (2.95)$$

Eq. (2.95) is the system characteristic equation, which possess  $N$  solution in  $\omega_n^2$ , called eigenvalues of the systems. The eigenvectors are then evaluated as:

$$(\mathbf{K} - \omega_{n,r}^2 \mathbf{M}) \boldsymbol{\varphi}_r \quad \text{with } r = 1, \dots, N \quad (2.96)$$

The eigenvalues  $\omega_{n,r}^2 \in \mathbb{R}$ , its positive root  $\omega_{n,r}$  is called natural frequency of the system. The eigenvector  $\boldsymbol{\varphi}_r \in \mathbb{R}^{N \times 1}$  is called mode shapes. Natural frequency  $\omega_{n,r}$  and mode shape  $\boldsymbol{\varphi}_r$  are characteristics of the  $r^{th}$  vibration mode.

The spectral matrix  $\boldsymbol{\Lambda} \in \mathbb{R}^{N \times N}$  and modal matrix  $\boldsymbol{\Phi} \in \mathbb{R}^{N \times N}$  are defined collecting all the eigenvalues  $\omega_{n,r}^2$  and eigenvectors  $\boldsymbol{\varphi}_r$  as in Eq. (2.97) and in Eq. (2.98).

$$\boldsymbol{\Lambda} = \text{diag}[\omega_{n,1}, \omega_{n,2}, \dots, \omega_{n,N}] \quad (2.97)$$

$$\boldsymbol{\Phi} = [\boldsymbol{\varphi}_1, \boldsymbol{\varphi}_2, \dots, \boldsymbol{\varphi}_N] \quad (2.98)$$

Fundamental characteristics of the modal matrix  $\boldsymbol{\Phi}$  are the so called M-orthogonality and K-orthogonality [1–3]:

$$\boldsymbol{\Phi}^T \mathbf{M} \boldsymbol{\Phi} = \begin{bmatrix} \ddots & & \\ & m_r & \\ & & \ddots \end{bmatrix} \quad (2.99)$$

$$\boldsymbol{\Phi}^T \mathbf{K} \boldsymbol{\Phi} = \begin{bmatrix} \ddots & & \\ & k_r & \\ & & \ddots \end{bmatrix} \quad (2.100)$$

where  $m_r$  and  $k_r$  are known respectively as modal mass and modal stiffness.

## Eigenvector normalisation

Eigenvector normalisation is necessary to define univocally the modal matrix  $\Phi$ . A useful normalisation for real eigenvectors is the unitary modal mass normalisation:

$$\Phi_r = \frac{\Phi_r}{\sqrt{m_r}} \quad (2.101)$$

where  $\Phi_r$  is the  $r^{th}$  eigenvector unitary modal mass normalised. The result of this choice is a simplification of Eq. (2.99) and Eq. (2.100):

$$\Phi^T \mathbf{M} \Phi = \mathbf{I} \quad (2.102)$$

$$\Phi^T \mathbf{M} \Phi = \Lambda \quad (2.103)$$

## Real modal analysis

Modal analysis is a mathematical tool very useful to solve MDOF system, because it let to uncouple the equation of motion. In particular considering an undamped and unforced system like in Eq. (2.87) it is possible to apply the direct modal transformation:

$$\mathbf{x} = \Phi \boldsymbol{\eta} \quad (2.104)$$

where  $\Phi$  is the modal matrix and  $\boldsymbol{\eta} \in \mathbb{R}^{N \times 1}$  are the displacements in modal coordinates, which are the set of coordinates describing the system with uncoupled equations.

Substituting Eq. (2.104) in Eq. (2.87) and pre-multiplying by  $\Phi^T$  it is possible to obtain  $N$  decoupled SDOF equations:

$$\ddot{\eta}_r + \omega_{n,r}^2 \eta_r = 0 \quad \text{with } r = 1, \dots, N \quad (2.105)$$

The uncoupling effect of the real modal analysis is shown in Figure 2.15.

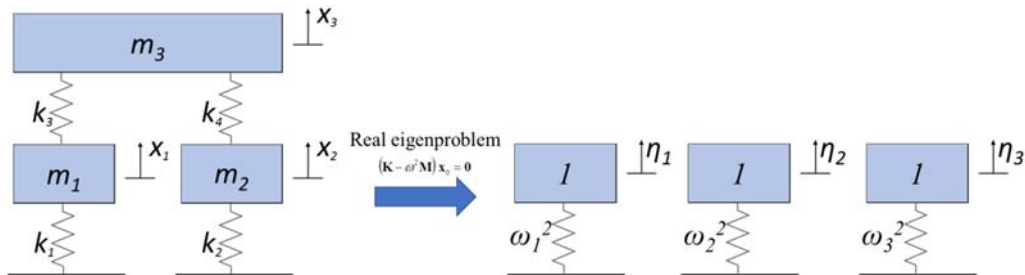


Figure 2.15 - Real modal analysis of MDOF undamped system.

## Free response

The free response a MDOF system with a set of non-null initial conditions, given in Eq. (2.106), can be solved using the modal analysis.

$$\begin{cases} \mathbf{x}(0) = \mathbf{x}_0 \\ \dot{\mathbf{x}}(0) = \mathbf{v}_0 \end{cases} \quad (2.106)$$

The direct modal transformation Eq. (2.104) can be again exploited:

$$\mathbf{x} = \mathbf{\Phi} \boldsymbol{\eta} = \sum_{r=1}^n \mathbf{\Phi}_r \eta_r \quad (2.107)$$

Eq. (2.105) is a SDOF undamped system in modal coordinates, its solution  $\eta_r$  is like Eq. (2.7), therefore Eq. (2.107) becomes:

$$\mathbf{x} = \sum_{r=1}^n \mathbf{\Phi}_r \eta_r = \sum_{r=1}^n \mathbf{\Phi}_r \left( A_r \cos(\omega_{n,r} t) + B_r \sin(\omega_{n,r} t) \right) \quad (2.108)$$

where  $A_r$  and  $B_r$  in Eq. (2.109) depend on the initial conditions in modal coordinates:

$$A_r = \mathbf{\Phi}_r^T \mathbf{M} \mathbf{\Phi}_r^{-1} \mathbf{x}_0, \quad B_r = \frac{\mathbf{\Phi}_r^T \mathbf{M} \mathbf{\Phi}_r^{-1} \mathbf{v}_0}{\omega_{n,r}} \quad (2.109)$$

An example of the free response of a system with  $N=3$  is shown in Figure 2.16.

The system parameters are  $\mathbf{M} = \text{diag}([0.1 \ 0.2 \ 0.3])$ ,  $\mathbf{K} = \text{tridiag}([-2 \ 4 \ -2])$  and initial conditions  $\mathbf{x}_0 = [1 \ 0 \ -1]^T$  mm  $\mathbf{v}_0 = [0 \ 1 \ 0]^T$  mm/s.

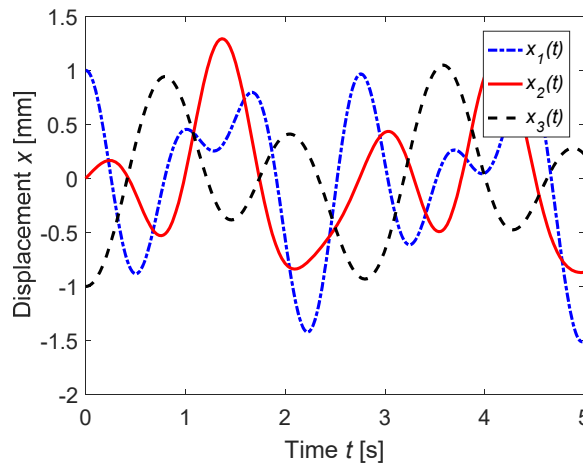


Figure 2.16 - Free response of a MDOF system

## Harmonic excitation

The equation of motion of a MDOF system forced with a harmonic excitation is:

$$\mathbf{M} \ddot{\mathbf{x}} + \mathbf{K} \mathbf{x} = \mathbf{f}_0 e^{i\Omega t} \quad (2.110)$$

where  $\mathbf{f}_0$  is the amplitude vector of harmonic forces acting on different DOFs and all in phase.

Using the direct modal transformation Eq. (2.104) and pre-multiplying Eq. (2.110) times  $\Phi^T$

$$\Phi^T \mathbf{M} \Phi \ddot{\boldsymbol{\eta}} + \Phi^T \mathbf{K} \Phi \boldsymbol{\eta} = \Phi^T \mathbf{f}_0 e^{i\Omega t} \quad (2.111)$$

Eq. (2.111) represents a set of  $N$  uncoupled equations in modal coordinates:

$$(-\Omega^2 + \omega_{n,r}^2) \eta_r = \Phi_r^T \mathbf{f}_0 e^{i\Omega t} \quad \text{with } r=1, \dots, N \quad (2.112)$$

The solution of Eq. (2.112) in modal coordinates is harmonic and therefore

$$\mathbf{x}(t) = \mathbf{X}_0 e^{i\Omega t} = \sum_{r=1}^N \eta_{r0} \Phi_r e^{i\Omega t} \quad (2.113)$$

$$\mathbf{X}_0 = \sum_{r=1}^N \frac{\Phi_r^T \mathbf{f}_0 \Phi_r}{\omega_{n,r}^2 - \Omega^2} \quad (2.114)$$

The receptance FRF  $\mathbf{H}$  of a MDOF system is defined as:

$$\mathbf{H}_{j,k}(\Omega) = \left. \frac{X_{j0}}{f_k} \right|_{f_i=0, \forall i \neq k} \quad (2.115)$$

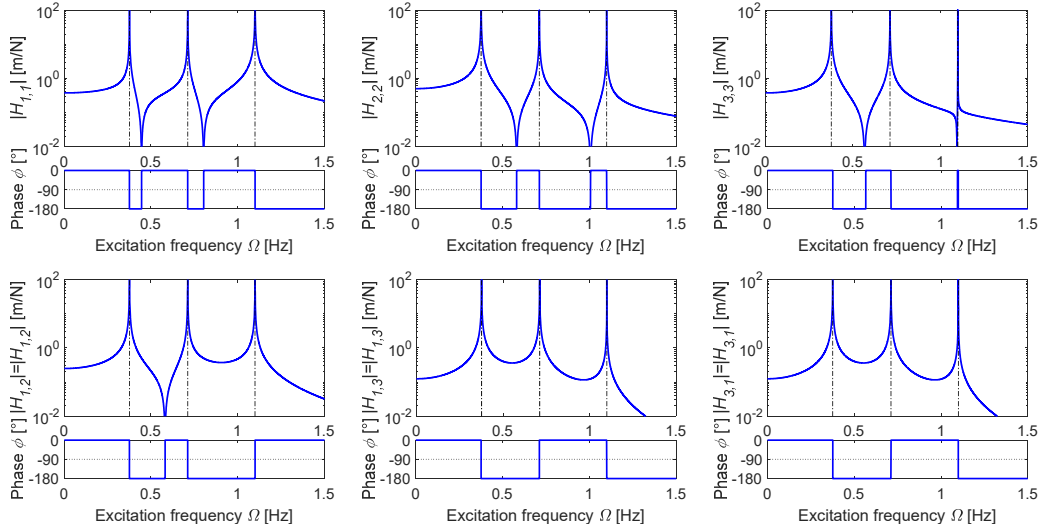
The receptance is computed applying a single force of the  $k^{th}$  DOF and no input on the other DOFs.

Using Eq. (2.114) to compute  $X_{j0}$ , the  $j^{th}$  component of  $\mathbf{X}_0$  when a force  $f_k$  is applied on the  $k^{th}$  DOF, and substituting in Eq. (2.115), the receptance FRF  $\mathbf{H}_{j,k}$  results:

$$\mathbf{H}_{j,k}(\Omega) = \sum_{r=1}^N \frac{\Phi_{j,r} \Phi_{k,r}}{\omega_{n,r}^2 - \Omega^2} \quad (2.116)$$

and the complete receptance matrix:

$$\mathbf{H}(\Omega) = \sum_{r=1}^N \frac{\Phi_r \Phi_r^T}{\omega_{n,r}^2 - \Omega^2} \quad (2.117)$$

Figure 2.17 - Receptance matrix  $\mathbf{H}$  of an undamped system

The receptance matrix  $\mathbf{H}$  of the same example system used in the previous paragraph is shown in Figure 2.17.

The receptance FRFs  $\mathbf{H}$  of an undamped MDOF system, as in Figure 2.17, possess the same characteristics of a SDOF undamped system. The response is infinite at the resonance frequencies  $\omega_{n,r}$  and vanishes in the anti-resonance frequencies. The phase is  $-90^\circ$  in the resonance and in phase or out of phase with respect to the excitation for other frequencies  $\Omega$ .

### 2.2.2 Proportional viscous damping

Modal analysis is a quite powerful tool in the case of undamped system, because lets to uncouple the equations of motion. However, real systems have always a certain amount of dissipation:

$$\mathbf{M}\ddot{\mathbf{x}} + \mathbf{C}\dot{\mathbf{x}} + \mathbf{K}\mathbf{x} = \mathbf{f} \quad (2.118)$$

where  $\mathbf{C}$  is the viscous damping matrix.

The simplest model of damping is proportional viscous damping, which let to uncouple the equation of motion.

The requirements for proportional viscous damping were theorised by Caughey and O'Kelly [40]:

$$\mathbf{K}\mathbf{M}^{-1}\mathbf{C} = \mathbf{C}\mathbf{M}^{-1}\mathbf{K}, \quad \mathbf{M}\mathbf{K}^{-1}\mathbf{C} = \mathbf{C}\mathbf{K}^{-1}\mathbf{M}, \quad \mathbf{M}\mathbf{C}^{-1}\mathbf{K} = \mathbf{K}\mathbf{C}^{-1}\mathbf{M} \quad (2.119)$$

The second and third expressions in Eq. (2.119) can't be used if the stiffness  $\mathbf{K}$  and damping  $\mathbf{C}$  matrices are singular, i.e. if the system possesses rigid body motions. Eq. (2.119) is the generalization of the well knows Rayleigh [24] proportional viscous damping matrix  $\mathbf{C}$ :



$$\mathbf{C} = \alpha \mathbf{M} + \beta \mathbf{K} \quad (2.120)$$

where  $\alpha$  and  $\beta$  are the viscous damping proportionality coefficients.

When proportional viscous damping is used the eigenvectors of the undamped system, given in Eq. (2.94), uncoupled also the damped system equation on motion Eq. (2.118). The modal viscous damping matrix  $\tilde{\mathbf{C}}$  result to be:

$$\tilde{\mathbf{C}} = \mathbf{\Phi}^T \mathbf{C} \mathbf{\Phi} = \begin{bmatrix} \ddots & & \\ & 2\zeta_r \omega_{n,r} & \\ & & \ddots \end{bmatrix} \quad (2.121)$$

where  $\mathbf{\Phi}$  is the modal matrix of the undamped system, normalised to unitary modal mass.

The system equation of motion in Eq. (2.118) is uncoupled from real modal analysis and in modal coordinates becomes:

$$\ddot{\eta}_r + 2\zeta_r \omega_{n,r} \dot{\eta}_r + \omega_{n,r}^2 \eta_r = 0 \text{ with } r = 1, \dots, N \quad (2.122)$$

The uncoupling effects of real modal analysis on a MDOF proportionally damped system are shown in Figure 2.18.

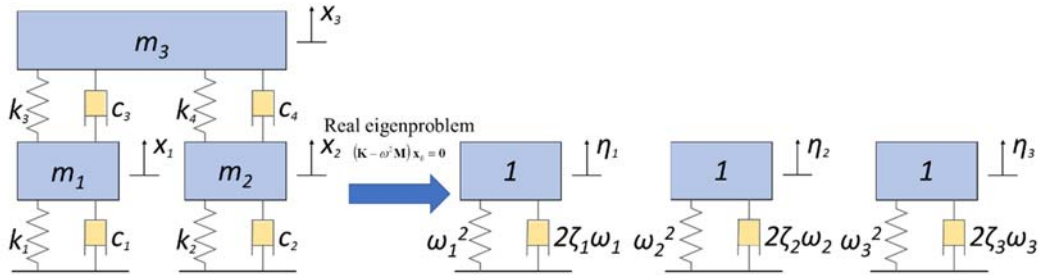


Figure 2.18 - Real modal analysis on MDOF proportionally damped system.

## Free response

The free response a MDOF proportional viscous system with a set of non-null initial conditions, given in Eq. (2.106), can be solved using the direct modal transformation Eq. (2.104).

$$\mathbf{x} = \mathbf{\Phi} \boldsymbol{\eta} = \sum_{r=1}^N \mathbf{\Phi}_r \eta_r \quad (2.123)$$

where  $\eta_r$  can be computed from Eq. (2.122) and it represents a SDOF damped system. The solution for the  $r^{th}$  modal coordinated depends on the damping ratio  $\zeta_r$ . In particular when  $0 < \zeta_r < 1$ ,  $\eta_r$  is described with Eq. (2.31) with integration

constant in Eq. (2.32); when  $\zeta_r = 1$ ,  $\eta_r$  is described with Eq. (2.36) and finally if  $\zeta_r > 1$ , Eq. (2.38) and Eq. (2.39) are used.

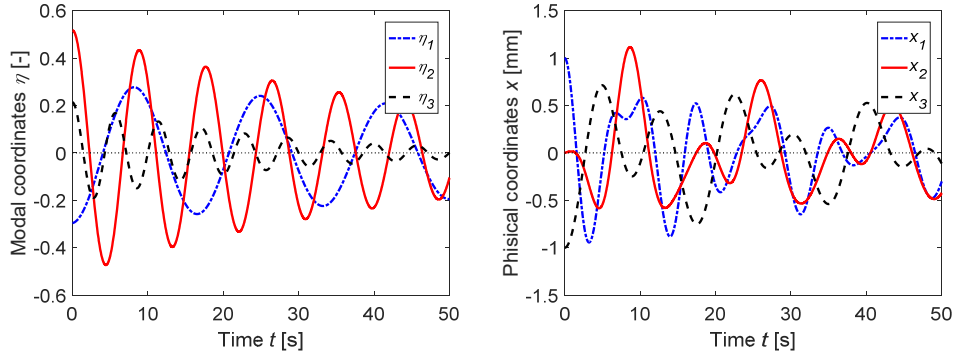


Figure 2.19 - Free response of a MDOF proportionally damped system: modal coordinates (left) and physical coordinates (right).

The free response of the system in § 2.2.1 with added viscous damping is shown in Figure 2.19. The proportional viscous damping coefficients are set to  $\alpha = 0.05$  and  $\beta = 0.01$ . The time domain evolution of the system in modal coordinates  $\eta_r$ , in Figure 2.19 (left), represents three uncoupled damped SDOF systems, while the physical coordinates  $x_r$ , in Figure 2.19 (right), are the composition of the modal coordinates.

## Harmonic excitation

The equation of motion of a MDOF system forced with a harmonic excitation is:

$$\mathbf{M}\ddot{\mathbf{x}} + \mathbf{C}\dot{\mathbf{x}} + \mathbf{K}\mathbf{x} = \mathbf{f}_0 e^{i\Omega t} \quad (2.124)$$

where  $\mathbf{f}_0$  is the amplitude vector of harmonic forces acting on different DOFs and all in phase.

Using the direct modal transformation Eq. (2.104) and pre-multiplying by  $\Phi^T$

$$\Phi^T \mathbf{M} \Phi \ddot{\boldsymbol{\eta}} + \Phi^T \mathbf{C} \Phi \dot{\boldsymbol{\eta}} + \Phi^T \mathbf{K} \Phi \boldsymbol{\eta} = \Phi^T \mathbf{f}_0 e^{i\Omega t} \quad (2.125)$$

For proportional viscous damping the undamped system eigenvector diagonalise also the damping matrix  $\mathbf{C}$ , as in Eq. (2.121), hence Eq. (2.125) represents a set of  $N$  uncoupled equations in modal coordinates.

$$(-\Omega^2 + i2\zeta_r \omega_{n,r} + \omega_{n,r}^2) \eta_r = \Phi_r^T \mathbf{f}_0 e^{i\Omega t} \quad (2.126)$$

The solution of Eq. (2.126) in modal coordinates is harmonic and therefore

$$\mathbf{x}(t) = \mathbf{X}_0 e^{i\Omega t} = \sum_{r=1}^N \eta_{r0} \Phi_r e^{i\Omega t} \quad (2.127)$$

$$\mathbf{X}_0 = \sum_{r=1}^N \frac{\Phi_r^T \mathbf{f}_0 \Phi_r}{\omega_{n,r}^2 + i2\zeta_r \omega_{n,r} - \Omega^2} \quad (2.128)$$

The receptance FRF  $H$  of a MDOF proportionally viscous damped system is defined in Eq. (2.115). Using Eq. (2.128) to compute  $X_{j0}$ , the  $j^{\text{th}}$  component of  $\mathbf{X}_0$  when a single force  $f_k$  is applied on the  $k^{\text{th}}$  DOF and substituting in Eq. (2.115), the receptance FRF  $\mathbf{H}_{j,k}$  results:

$$\mathbf{H}_{j,k}(\Omega) = \sum_{r=1}^N \frac{\Phi_{j,r} \Phi_{k,r}}{\omega_{n,r}^2 + i2\zeta_r \omega_{n,r} - \Omega^2} \quad (2.129)$$

The complete receptance matrix  $\mathbf{H}$  can be computed as:

$$\mathbf{H}(\Omega) = \sum_{r=1}^N \frac{\Phi_r \Phi_r^T}{\omega_{n,r}^2 + i2\zeta_r \omega_{n,r} - \Omega^2} \quad (2.130)$$

The receptance FRFs  $\mathbf{H}$  of the example system in § 2.2.1 are shown in Figure 2.20 for increasing values of stiffness viscous damping proportionality coefficient  $\beta$ . The blue dashed lines represent the undamped configuration.

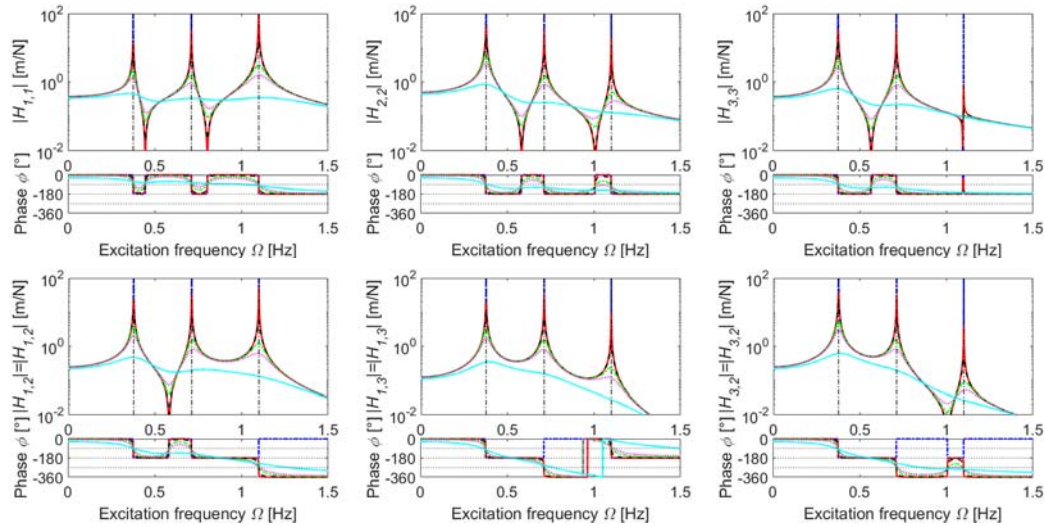


Figure 2.20 - Receptance matrix  $\mathbf{H}$  of a proportionally damped system.

### 2.2.3 Non-classical viscous damping

Non-classical viscous damping is the more general case of viscous damping. It includes localised dampers, thus damping matrix  $\mathbf{C}$  that do not respect the Eq. (2.119). This case is the most common in real structures, but it is

mathematically more difficult to solve, since the damping matrix is not diagonalised from the eigenvectors of the undamped system:

$$\Phi^T C \Phi = \tilde{C} \quad (2.131)$$

where  $\tilde{C}$  is not diagonal.

Real modal analysis does not uncouple the equation of motion Eq. (2.124) and it must be treated by Foss's method [41]:

$$\begin{bmatrix} \mathbf{C} & \mathbf{M} \\ \mathbf{M} & \mathbf{0} \end{bmatrix} \dot{\mathbf{y}} + \begin{bmatrix} \mathbf{K} & \mathbf{0} \\ \mathbf{0} & -\mathbf{M} \end{bmatrix} \mathbf{y} = \begin{Bmatrix} \mathbf{f}_0 \\ \mathbf{0} \end{Bmatrix} e^{i\Omega t}, \quad \mathbf{y} = \begin{Bmatrix} \mathbf{x} \\ \dot{\mathbf{x}} \end{Bmatrix} \quad (2.132)$$

and in compact form:

$$\mathbf{A} \dot{\mathbf{y}} + \mathbf{B} \mathbf{y} = \mathbf{F} e^{i\Omega t} \quad (2.133)$$

where  $\mathbf{A}, \mathbf{B} \in \mathbb{R}^{2N \times 2N}$  are symmetric matrices,  $\mathbf{F} \in \mathbb{R}^{2N \times 1}$  and  $\mathbf{y} \in \mathbb{R}^{2N \times 1}$ . Eq. (2.133) is a first order differential equation with  $2N$  DOFs.

### Complex eigenproblem

Considering the homogenous equation related to Eq. (2.132)

$$\mathbf{A} \dot{\mathbf{y}} + \mathbf{B} \mathbf{y} = \mathbf{0} \quad (2.134)$$

the solution of Eq. (2.134) will be of the type:

$$\mathbf{y} = \mathbf{Y}_0 e^{st} \quad (2.135)$$

where  $s \in \mathbb{C}$ . Deriving Eq. (2.135) and substituting in Eq. (2.134) it results:

$$(s\mathbf{A} + \mathbf{B}) \mathbf{Y}_0 = \mathbf{0} \quad (2.136)$$

Eq. (2.136) is an eigenproblem. The trivial solution  $\mathbf{y}_0 = \mathbf{0}$  is the static undeformed condition, the others interesting solutions are given by the zeros of the characteristic equation:

$$|s\mathbf{A} + \mathbf{B}| = 0 \quad (2.137)$$

which possess  $2N$  solutions in  $s$ , called eigenvalues or poles of the system. The poles  $s$  can be real or complex conjugated. The eigenvectors are then evaluated as:

$$(s_r \mathbf{A} + \mathbf{B}) \boldsymbol{\Theta}_r = \mathbf{0} \text{ with } r = 1, \dots, 2N \quad (2.138)$$

The eigenvectors  $\Theta_r \in \mathbb{C}^{2N \times 1}$  are the mode shapes of the system. They will be also real or complex and conjugated depending on the corresponding pole  $s_r$ . The complex spectral matrix  $\mathbf{S} \in \mathbb{C}^{2N \times 2N}$  and modal matrix  $\Theta \in \mathbb{C}^{2N \times 2N}$  are defined collecting all the eigenvalues and eigenvectors:

$$\mathbf{S} = \text{diag}[s_1, s_2, \dots, s_{2N}] \quad (2.139)$$

$$\Theta = [\Theta_1, \Theta_2, \dots, \Theta_{2N}] \quad (2.140)$$

Eq. (2.140) can be written also as:

$$\Theta = \begin{bmatrix} \tilde{\Theta} & \tilde{\Theta}^* \\ \tilde{\Theta}\tilde{\Lambda} & \tilde{\Theta}^*\tilde{\Lambda}^* \end{bmatrix} \quad (2.141)$$

where  $\tilde{\Theta} \in \mathbb{C}^{N \times N}$  and  $\tilde{\Lambda} \in \mathbb{C}^{N \times N}$  are the modal matrix and spectral matrix of the problem in Eq. (2.124) with non-proportional viscous damping. They can be obtained solving the eigenproblem of the second order formulation, which is computationally very expensive. A very useful property of the modal matrix  $\Theta$  is the so-called A and B orthogonality:

$$\Theta^T \mathbf{A} \Theta = \begin{bmatrix} \ddots & & \\ & a_r & \\ & & \ddots \end{bmatrix} \quad (2.142)$$

$$\Theta^T \mathbf{B} \Theta = \begin{bmatrix} \ddots & & \\ & b_r & \\ & & \ddots \end{bmatrix} \quad (2.143)$$

Some interesting considerations on the complex eigenvector  $\tilde{\Theta}$  of the original problems can be summarised substituting Eq. (2.141) in Eq. (2.143).

$$\tilde{\Theta}^T \mathbf{M} \tilde{\Theta} \tilde{\Lambda} + \tilde{\Lambda} \tilde{\Theta}^T \mathbf{M} \tilde{\Theta} + \tilde{\Theta}^T \mathbf{C} \tilde{\Theta} = \text{diag}(a_r) \quad (2.144)$$

$$\tilde{\Theta}^{*T} \mathbf{M} \tilde{\Theta} \tilde{\Lambda} + \tilde{\Lambda} \tilde{\Theta}^{*T} \mathbf{M} \tilde{\Theta} + \tilde{\Theta}^{*T} \mathbf{C} \tilde{\Theta} = \mathbf{0} \quad (2.145)$$

$$\tilde{\Lambda} \tilde{\Theta}^T \mathbf{M} \tilde{\Theta} \tilde{\Lambda} - \tilde{\Theta}^T \mathbf{K} \tilde{\Theta} = \text{diag}(b_r) \quad (2.146)$$

$$\tilde{\Lambda}^* \tilde{\Theta}^{*T} \mathbf{M} \tilde{\Theta} \tilde{\Lambda} - \tilde{\Theta}^{*T} \mathbf{K} \tilde{\Theta} = \mathbf{0} \quad (2.147)$$

Relationships analogous to Eq. (2.144)-(2.147) also hold for the complex conjugates pairs. These relationships show that  $\tilde{\Theta}$  cannot uncouple the original problem, because it is not able to diagonalise together  $\mathbf{M}$ ,  $\mathbf{C}$  and  $\mathbf{K}$  matrices. The eigenvectors are not energetically independent since the energy dissipated by one mode depends on the other modes.

## Eigenvector Normalisation

Eigenvector normalisation and sorting are necessary to define univocally the modal matrix  $\Theta$ . Several ways to sort and to normalise the mode shapes of the complex modal matrix  $\Theta$  exist. In this thesis the following choices are adopted.

The mode shapes are collected in the modal matrix in complex conjugated pairs. The eigenvector corresponding to positive imaginary part of the eigenvalues before the complex conjugated, in ascending values of the eigenvalues. The rigid body motion eigenvectors are the first, followed by the eigenvectors related to underdamped modes and finally overdamped modes.

The rigid body motion and overdamped modes are normalised at unitary modal constant  $a_r = 1$

$$\Psi_r = \frac{\Theta_r}{\sqrt{a_{0,r}}} \quad (2.148)$$

Underdamped modes are normalised to  $a_r = 2i\Im(s_r)$ :

$$\Psi_r = \frac{\Theta_r}{\sqrt{a_{0,r}}} \sqrt{2i\Im(s_r)} \quad (2.149)$$

where  $a_{0,r}$  is the modal constant related to  $\Theta_r$  and  $\Psi_r$  is the  $r^{th}$  normalised eigenvector. This normalisation minimises the imaginary part of the eigenvector, therefore most of the information are contained in the real part. Moreover, for proportional viscous damping system it is equivalent to the unitary modal mass normalisation. The result of this choice is a simplification of Eq. (2.142) and Eq. (2.143):

$$\Psi^T \mathbf{A} \Psi = \begin{bmatrix} \mathbf{I}_{rb \times rb} & & & \\ & \ddots & & \\ & & 2i\Im(s_r) & \\ & & & \ddots \\ & & & & \mathbf{I}_{o \times o} \end{bmatrix} \quad (2.150)$$

$$\Psi^T \mathbf{B} \Psi = \begin{bmatrix} \begin{bmatrix} \ddots & & \\ & -s_r & \\ & & \ddots \end{bmatrix}_{rb \times rb} & & \\ & -2i\Im(s_r)s_r & \\ & & \ddots \\ & & & \begin{bmatrix} \ddots & & \\ & -s_r & \\ & & \ddots \end{bmatrix}_{o \times o} \end{bmatrix} \quad (2.151)$$

where  $rb$  is the number of rigid body motion and  $o$  is the number of overdamped modes.

### Complex modal analysis

Modal analysis can be applied also in the case of non-proportional viscous damping to uncouple the equation of motion in first order form, given in Eq. (2.133). Considering an undamped and unforced system, given in Eq. (2.134), it is possible to apply the complex direct modal transformation:

$$\mathbf{y} = \Psi \boldsymbol{\eta} \quad (2.152)$$

where  $\Psi$  is the normalised complex modal matrix and  $\boldsymbol{\eta} \in \mathbb{R}^{2N \times 1}$  are the modal coordinates.

Substituting Eq. (2.152) in Eq. (2.87) and pre-multiplying by  $\Psi^T$  it is possible to obtain  $2N$  decoupled SDOF equations:

$$\dot{\eta}_r - s_r \eta_r = 0 \text{ with } r = 1, \dots, 2N \quad (2.153)$$

The effect of classical modal analysis on a nonproportional damped system are shown in Figure 2.21. The real eigenvector are not able to diagonalise the non-classical damping matrix.

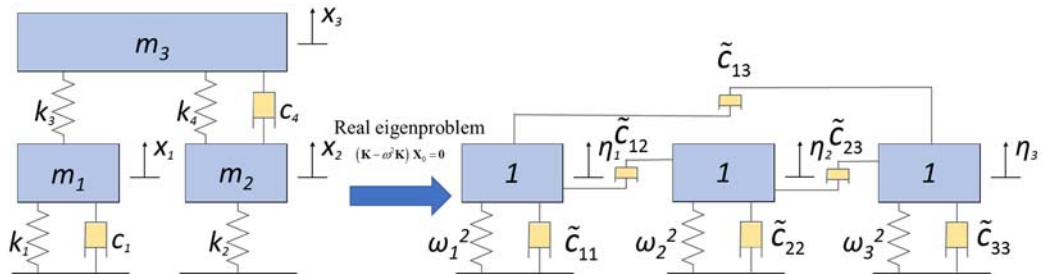


Figure 2.21 – Effects of real modal analysis on non-proportional damped system.

A representation of the uncoupling effect of complex modal analysis is given in Figure 2.22. The representation first representation is not a usual mechanical

representation, because the inertial element is no more visible, because it is hidden in the complex value of the stiffness. The oscillatory motion is given by the complex part of the stiffness, which has a positive real part in underdamped system. In overdamped system, the stiffness will be real and positive; therefore, the motion is monotonically decreasing to null displacement and velocity. The combination of complex conjugates poles gives again  $N$  uncoupled oscillatory system with modal mass, modal stiffness and modal damping.

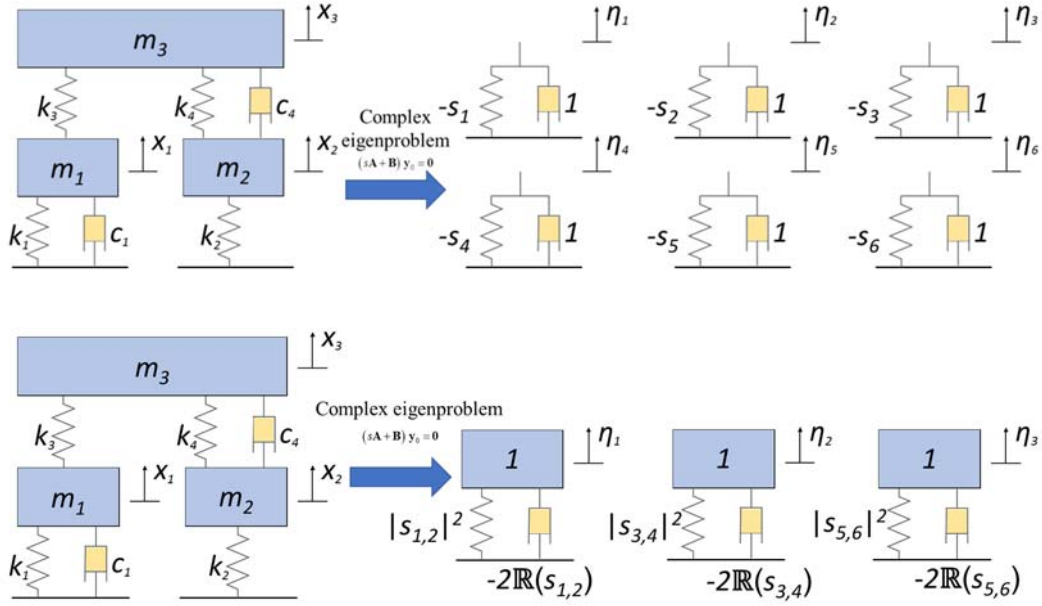


Figure 2.22 - Complex modal analysis uncoupling effect.

### Free response

The free response a MDOF non classical viscous damped system with a set of non-null initial conditions, given in Eq. (2.106), can be solved using again the direct modal transformation:

$$\mathbf{x} = [\mathbf{I}_{N \times N} \quad \mathbf{0}_{N \times N}] \mathbf{y} \quad (2.154)$$

$$\mathbf{x} = [\mathbf{I}_{N \times N} \quad \mathbf{0}_{N \times N}] \mathbf{\Psi} \boldsymbol{\eta} = [\mathbf{I}_{N \times N} \quad \mathbf{0}_{N \times N}] \sum_{r=1}^{2N} \mathbf{\Psi}_r \eta_r \quad (2.155)$$

The solutions  $\eta_r$  came from Eq. (2.153), they are oscillatory functions:

$$\eta_r = \eta_{r0} e^{s_r t} \quad (2.156)$$

The amplitude  $\eta_{r0}$  comes from the initial conditions:

$$\boldsymbol{\eta}_0 = \mathbf{\Psi}^{-1} \mathbf{y}_0 \quad (2.157)$$



$$\eta_{ro} = \frac{\Psi_r^T \mathbf{A} \mathbf{y}_0}{a_r} \quad (2.158)$$

The response of the example system in § 2.2.1 with an added localised damper on the first DOF,  $c_1 = 0.5$  Ns/m is shown in Figure 2.23.

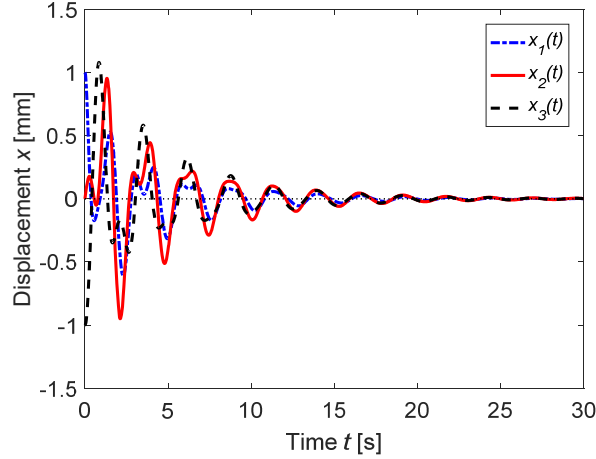


Figure 2.23 - Free response of a MDOF non-classical viscous damped system.

### Harmonic excitation

The equation of motion of a MDOF system forced with a harmonic excitation is given in Eq. (2.133). Using the complex direct modal transformation, given in Eq. (2.152), and pre-multiplying Eq. (2.133) by  $\Psi^T$

$$\Psi^T \mathbf{A} \Psi \dot{\boldsymbol{\eta}} + \Psi^T \mathbf{B} \Psi \boldsymbol{\eta} = \Psi^T \mathbf{F} e^{i\Omega t} \quad (2.159)$$

Eq. (2.159) represents a set of  $2N$  uncoupled equations in modal coordinates:

$$\dot{\eta}_r - s_r \eta_r = \Psi_r^T \mathbf{F}_0 e^{i\Omega t} \quad (2.160)$$

The solution of Eq. (2.160) will follow the excitation:

$$\eta_r = \eta_{0r} e^{i\Omega t} \quad (2.161)$$

$$\eta_{0r} = \frac{\Psi_r^T \mathbf{F}_0}{a_r (i\Omega - s_r)} \quad (2.162)$$

The solution of Eq. (2.133) in modal coordinated is harmonic and therefore

$$\mathbf{x}(t) = [\mathbf{I}_{N \times N} \quad \mathbf{0}_{N \times N}] \sum_{r=1}^{2N} \Psi_r \eta_{r0} e^{i\Omega t} \quad (2.163)$$

The receptance FRF  $\mathbf{H}$  of a MDOF system is defined in Eq. (2.115) and the response of the  $j^{th}$  DOF  $y_{j0}$  can be obtained as:

$$\mathbf{Y}_0 = \sum_{r=1}^{2N} \frac{\mathbf{\Psi}_r^T \mathbf{F}_0 \mathbf{\Psi}_r}{a_r(i\Omega - s_r)} \quad (2.164)$$

The receptance FRF  $\mathbf{H}_{j,k}$  results to be:

$$H_{j,k}(\Omega) = \sum_{r=1}^{2N} \frac{\Psi_{jr} \Psi_{kr}}{a_r(i\Omega - s_r)} \text{ with } 1 \leq j, k \leq N \quad (2.165)$$

and the complete receptance matrix  $\mathbf{H}$ :

$$\mathbf{H}(\Omega) = \sum_{r=1}^{2N} \frac{\mathbf{\Psi}_{1:N,r} \mathbf{\Psi}_{1:N,r}^T}{a_r(i\Omega - s_r)} \quad (2.166)$$

where  $\mathbf{H} \in \mathbb{C}^{N \times N}$ . It is interesting notice that if the response is measured in  $N+1 \leq j \leq 2N$ , it represents the velocity and therefore the computed FRF will be directly a mobility FRF. The receptance FRFs of the example system in § 2.2.3, with increasing values of  $c_1$ , are shown in Figure 2.24.

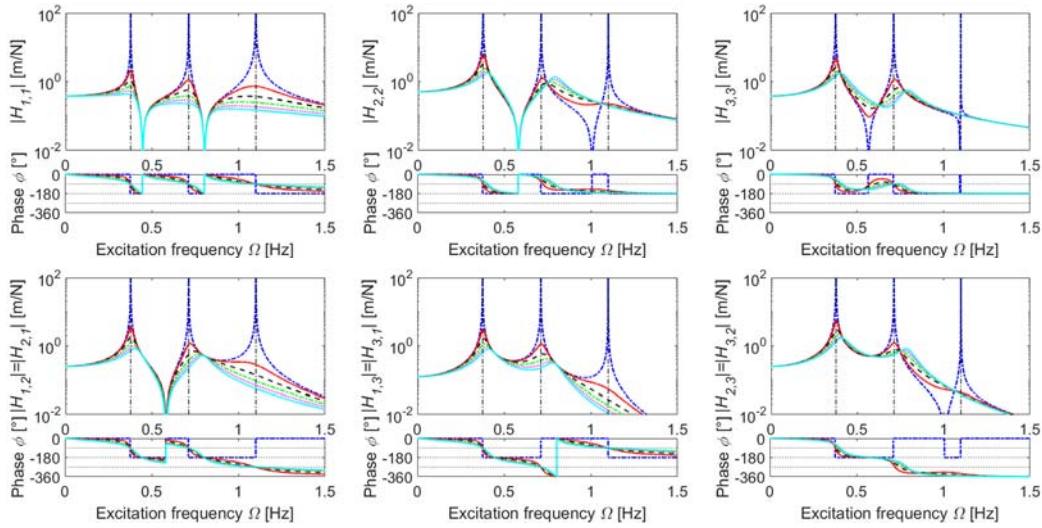


Figure 2.24 - Receptance matrix  $\mathbf{H}$  of 3 DOF non-classically damped system.

It is interesting to notice that the damped natural frequencies  $\omega_{d,r}$  of the non-classically damped system in Figure 2.24 can be higher than the natural frequency  $\omega_{n,r}$  of the undamped system, while for proportional damped system it is never the case. This phenomenon depends on the topology of the damping matrix and the mode separation. A good approximation of the  $i^{th}$  damped natural frequency  $\omega_{d,i}$  of the a non-proportional damped system can be obtained through second order perturbation analysis as [42]:

$$\omega_{d,r} = \omega_{n,r} \left[ 1 - \frac{\varepsilon^2}{2} \sum_{j=1, j \neq r}^N \frac{(\Phi_j^T \mathbf{C} \Phi_r)^2}{\omega_{n,r}^2 - \omega_{n,j}^2} - \frac{\varepsilon^2}{8\omega_{n,i}^2} (\Phi_r^T \mathbf{C} \Phi_r)^2 + o(\varepsilon^4) \right] \quad (2.167)$$

where  $\omega_{n,r}$  is the  $r^{th}$  natural frequency of the undamped system and  $\varepsilon$  is the perturbation. The damped natural frequency of the non-classically damped system  $\omega_{d,r}$  will be lower than the natural frequency of the undamped system  $\omega_{n,r}$  when:

$$\omega_{d,r} < \omega_{n,r} \text{ if } \sum_{j=1, j \neq r}^N \frac{(\Phi_j^T \mathbf{C} \Phi_r)^2}{\omega_{n,r}^2 - \omega_{n,j}^2} + \frac{(\Phi_r^T \mathbf{C} \Phi_r)^2}{4\omega_{n,r}^2} > 0 \quad (2.168)$$

If  $r = N$  Eq. (2.168) is always verified, therefore the damped natural frequency of the last mode of the damped system  $\omega_{d,N}$  is lower than the corresponding undamped system natural frequencies. If  $r = 1, \dots, N-1$  Eq. (2.168) could be not verified; in that case the damped natural frequencies of the non-proportionally damped system  $\omega_{d,r}$  will be higher than the corresponding natural frequency of the undamped system, hence also the natural frequency of the damped system will be higher.

### 2.2.4 Structural damping

The extension to  $N$  DOF of the structural damping leads to an equation of motion of the type:

$$\mathbf{M}\ddot{\mathbf{x}} + (\mathbf{K} + i\mathbf{D})\dot{\mathbf{x}} = \mathbf{f}_0 e^{i\Omega t} \quad (2.169)$$

Although the eigenproblem has not physical meaning, because the free behaviour of a structural damped system can't be studied, it is useful to compute eigenvalues and eigenvectors of the system to uncouple the equation of motion and simplify the study of the harmonic forced case.

If the structural matrix  $\mathbf{D}$  is proportional to mass  $\mathbf{M}$  and stiffness  $\mathbf{K}$  matrices, the modal matrix of the undamped problem  $\Phi$  diagonalise also the structural matrix  $\mathbf{D}$ . It is the same concept of proportional viscous damping.

When the structural damping is not proportional, it is not necessary to solve the problem in first order form. The solution is of the type:

$$\mathbf{X} = \mathbf{X}_0 e^{st} \quad (2.170)$$

Deriving two times Eq. (2.170) and substituting in Eq. (2.169)

$$(\tilde{s}^2 \mathbf{M} + \mathbf{K} + i\mathbf{D})\mathbf{X}_0 = \mathbf{0} \quad (2.171)$$

The eigenproblem in Eq. (2.171) gives  $N$  eigenvalues  $\tilde{s}_r \in \mathbb{C}$  and eigenvectors  $\tilde{\Psi}_r \in \mathbb{C}^{N \times 1}$ . Applying the direct modal transformation and pre-multiplying Eq. (2.169) by  $\tilde{\Psi}^T$ , a set of  $N$  uncoupled equations are found:

$$\tilde{m}_r \ddot{\eta}_r + (\tilde{k}_r + i\tilde{d}_r) \eta_r = \tilde{\Psi}^T \mathbf{f}_0 e^{i\Omega t} \quad (2.172)$$

where  $\tilde{m}_r, \tilde{k}_r, \tilde{d}_r \in \mathbb{C}$ . These coefficients are related by:

$$s_r = \frac{\tilde{k}_r + i\tilde{d}_r}{\tilde{m}_r} \quad (2.173)$$

Eq. (2.173) can be also written as:

$$s_r = \tilde{\omega}_r^2 (1 + i\beta_r) \quad (2.174)$$

where  $\tilde{\omega}_r \in \mathbb{R}$  and  $\tilde{\omega}_r \rightarrow \omega_r$  when  $\beta_r = \tilde{d}_r / (\tilde{\omega}_r \tilde{m}_r) \rightarrow 1$ .

Normalising the eigenvectors  $\tilde{\Psi}_r$  to unitary modal mass the receptance FRF is in this computed as:

$$\mathbf{H}(\Omega) = \sum_{r=1}^N \frac{\tilde{\Psi}_r \tilde{\Psi}_r^T}{s_r - \Omega^2} \quad (2.175)$$

The response of a MDOF structural damped system lost property of SDOF structural damped system, where the peak frequency  $\hat{f} = f_n$  is invariant with respect to the structural damping ratio  $\eta$ . In MDOF structural damped systems the peaks frequencies  $\hat{f}_{n,r}$  move increasing the damping ratio  $\eta$ . Generally, the peak frequency  $\hat{f}$  is lower than the respective undamped natural frequency  $f_n$ , however also in this case the natural frequency of the damped system can results higher with respect the undamped system. Performing the second order perturbation analysis of a structural damped system, a good approximation of the  $r^{th}$  damper natural frequency  $s_r$  is:

$$\omega_{d,r} = \omega_{n,r} \left[ 1 - \frac{\varepsilon^2}{2\omega_{n,r}^2} \left( \frac{(\Phi_r^T \mathbf{D} \Phi_r)^2}{4\omega_{n,r}^2} - \sum_{j=1, j \neq r}^N \frac{(\Phi_j^T \mathbf{D} \Phi_r)^2}{(\omega_{n,r}^2 - \omega_{n,j}^2)} \right) + o(\varepsilon^4) \right] \quad (2.176)$$

where  $\omega_{n,r}$  is the  $r^{th}$  natural frequency of the undamped system and  $\varepsilon$  is the perturbation. The damped natural frequency of the structural damped system  $\omega_{d,r}$  will be lower than the natural frequency of the undamped system  $\omega_{n,r}$  only when:

$$\omega_{d,r} < \omega_{n,r} \text{ if } 4\omega_{n,r}^2 \sum_{j=1, j \neq r}^N \frac{(\Phi_j^T \mathbf{D} \Phi_n)^2}{(\omega_{n,r}^2 - \omega_{n,j}^2)} < (\Phi_n^T \mathbf{D} \Phi_n)^2 \quad (2.177)$$

The same considerations already done for non-proportional viscous damped systems, holds also in the cases of non-proportional structural damped system.

The receptance FRF of the example system of § 2.2.1, with a localised structural damper acting of the first DOF is shown in Figure 2.25, for increasing values of the structural damping coefficient. The first and second damped peaks frequencies  $\hat{f}$  are higher than the related undamped natural frequencies  $\hat{f}_{n,r}$  because Eq. (2.177) does not hold in this case.

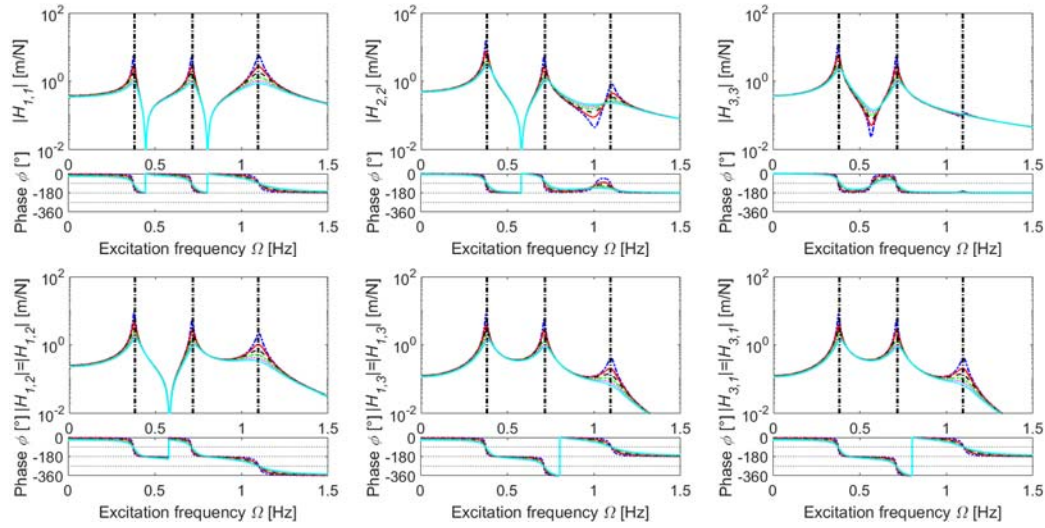


Figure 2.25 - Receptance matrix  $\mathbf{H}$  of a 3 DOF structural damped system.

## 2.3 Vibration control

The mechanical systems models, given in § 2.1 and § 2.2, describe the dynamic behaviour of mechanical systems. Correct values for mass damping and stiffness can be chosen when a specific response of the system is required, but it is not always the case that all the requirements can be achieved together and therefore the designer must make compromises to reconfigure the structure or to add additional components. This possibility is known as passive control, which depends only on fixed change in the physical system parameters. Passive vibration control can move some poles to the desired location, but also all the other poles of the system will be affected by the modification and could be moved in undesirable locations. Another possibility is active control of mechanical system, which uses external adjustable or active devices, the actuator, to provide a tool for shaping and controlling the system response. Active control requires an external energy source, while passive control does not. Active control can be performed using to different strategies. A simpler strategy is open loop control, which need only an

actuator to amplify/reduce the response of the system. The most used strategy is instead close-loop control which requires actuators and sensors to measure the system responses. It can change the dynamic response of the system by means of a control law, a relationship between the sensors measured quantities and the actual input to the system. The description of the control theory to the structural vibration is described in many text book, i.e. [34,36,43,44]. A brief overview of the close loop pole placement method for active control of structural vibration is given in the following paragraph.

### 2.3.1 Pole placement

One of the most common aims in vibration control is selective pole assignment, which means the possibility of moving a set of system poles in the desired locations. The general pole placement method in first order problem [45], using Achermann's formula [46], is difficult to be implemented in structural problem, because the matrices are often very large and the computation of all the eigenvalues and eigenvectors can be not performed accurately. Although a lot of research for automatic system control is presented in state-space formulation, the implementation of pole placement method is easier using the second order equation of motion of a mechanical system.

Close loop feedback control is performed providing an input to the system  $u(t) \in \mathbb{R}$  :

$$\mathbf{M}\ddot{\mathbf{x}} + \mathbf{C}\dot{\mathbf{x}} + \mathbf{K}\mathbf{x} = \mathbf{g}u(t) + \mathbf{f} \quad (2.178)$$

where  $\mathbf{g} \in \mathbb{R}^{N \times 1}$  is the input DOF selection vector.

The control force is a linear combination of position and velocity of the system and it can be written as:

$$u(t) = \mathbf{c}_p^T \mathbf{x} + \mathbf{c}_v^T \dot{\mathbf{x}} \quad (2.179)$$

where  $\mathbf{c}_p, \mathbf{c}_v \in \mathbb{R}^{N \times 1}$  are the position and velocity vector matrices. Eq. (2.179) is known as state feedback control law, because the input  $u(t)$  is proportional to the system states, both position and velocity. It can be seen also as a proportional derivative (PD) controller.

Substituting Eq. (2.179) in Eq. (2.178) the equation of motion of the close-loop control system can be found:

$$\mathbf{M}\ddot{\mathbf{x}} + (\mathbf{C} - \mathbf{g}\mathbf{c}_v^T)\dot{\mathbf{x}} + (\mathbf{K} - \mathbf{g}\mathbf{c}_p^T)\mathbf{x} = \mathbf{f} \quad (2.180)$$

The equation of motion is generally no more symmetric due to generally non-symmetric changes in the damping and stiffness matrix. Passive modifications are

always symmetric and affect all the poles of the system, while active control allow non-symmetric changes which let to selective assign pole to the system, without affecting the other poles, provided that the system is controllable, i.e.:

$$\text{rank}(s_i^2 \mathbf{M} + s_i \mathbf{C} + \mathbf{K} | \mathbf{g}) = N \quad 1 \leq i \leq 2N \quad (2.181)$$

More detail on controllability and observability of close loop mechanical system can be found in [47,48]. Although systems can be controlled to assign the desired dynamics, the stability of close loop systems becomes very important in close-loop system, because the feedback gains could destabilise a system which is originally stable.

The problem of pole and eigenvector assignment, which is called eigen-structure assignment, has been treated in many paper and textbooks, i.e. [49,50], it consist in find out the coefficients of the gain matrices to assign the desired poles. The pole placement method was formulated for mechanical system active control in [51], extended to continuous system in [52] and to gyroscopic system in [53].

The method can assign the desired location of a set of poles without affecting the others.

Let's suppose that the first  $m$  systems poles  $s_i$  should be reallocated to a prescribed set of desired poles  $s_{d,i}$ . Remembering the definition of the spectral matrix  $\mathbf{S}$  and the modal matrix  $\mathbf{\Psi}$  defined respectively is Eq. (2.139) and Eq. (2.148), it is possible to define a subset of the spectral matrix  $\mathbf{\Lambda}_1$  and modal matrix  $\mathbf{U}_1$  related to the poles which are wished to be changed:

$$\mathbf{\Lambda}_1 = \text{diag}([s_1, \dots, s_m]) \quad (2.182)$$

$$\mathbf{U}_1 = [\mathbf{\Psi}_1 \quad \dots \quad \mathbf{\Psi}_m] \quad (2.183)$$

The position  $\mathbf{c}_p$  and velocity  $\mathbf{c}_v$  feedback gain matrices are computed as:

$$\mathbf{c}_v = \mathbf{M} \mathbf{U}_1 \mathbf{\Lambda}_1 \mathbf{p} \quad (2.184)$$

$$\mathbf{c}_p = -\mathbf{K} \mathbf{U}_1 \mathbf{p} \quad (2.185)$$

where the vector  $\mathbf{p} \in \mathbb{R}^{m \times 1}$  is defined as:

$$p_i = \frac{1}{\mathbf{g}^T \mathbf{\Psi}_i} \frac{s_{d,i} - s_i}{s_i} \prod_{\substack{j=1 \\ j \neq i}}^m \frac{s_{d,j} - s_i}{s_j - s_i} \quad i = 1, \dots, m \quad (2.186)$$

The implementation of the control law in Eq. (2.179), with the position and velocity matrix chosen as in Eq. (2.184) and Eq. (2.185), guarantees the location of the desired set of poles, without affecting the other poles.

The system in § 2.2.3 with the same initial conditions is used to provide an example of active control pole placement. The system is non-classically damped with a lumped damper acting on the first mass  $c_1 = 0.06 \text{ N/(m/s)}$ . The open loop poles of the system are:

$$s_{1,2} = -0.022 \pm i2.364, s_{3,4} = -0.050 \pm i4.475, s_{5,6} = -0.228 \pm i6.899 \quad (2.187)$$

It is desired to move the first complex and conjugate couple of poles in the new location defined in Eq. (2.188), without changing the other poles and providing a single control input on the first degree of freedom, which means  $\mathbf{g} = [1 \ 0 \ 0]^T$ .

$$s_{d1,2} = -0.007 \pm i1.4; \quad \omega_{d,n1,2} = 0.22 \text{ Hz} \quad \zeta_{d1,2} = 0.005 \quad (2.188)$$

The feedback gain vector are computed using Eq. (2.184) and Eq. (2.185):

$$\mathbf{c}_p = [0.364 \ 1.246 \ 1.607]^T; \mathbf{c}_v = [0.003 \ 0.0030 \ 0.048]^T \quad (2.189)$$

The receptance FRF of the passive system and actively controlled close loop system are shown in Figure 2.26. The first peak is moved in the desired location, while the other peaks are not altered.

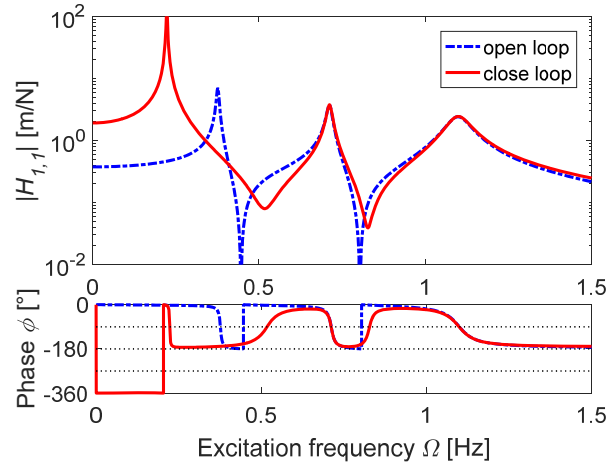


Figure 2.26 – Inertance FRF of the open and close loop system.

The poles of the close loop system result to be:

$$s_{1,2} = -0.007 \pm i1.4, s_{3,4} = -0.050 \pm i4.475, s_{5,6} = -0.228 \pm i6.899 \quad (2.190).$$

The time domain responses of the passive and controlled system are shown in Figure 2.27. The responses of the close loop start from the same initial conditions and then evolve with less damped because the desired pole is almost undamped.



The control force  $u(t)$ , necessary to control the system, computed using Eq. (2.179), shown in Figure 2.28.

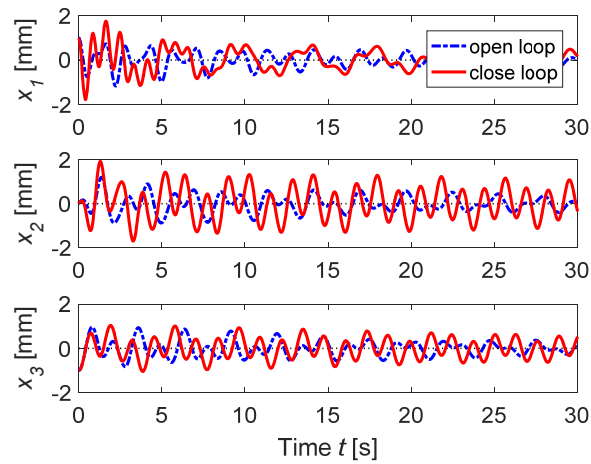


Figure 2.27 – Free response of open and controlled system.

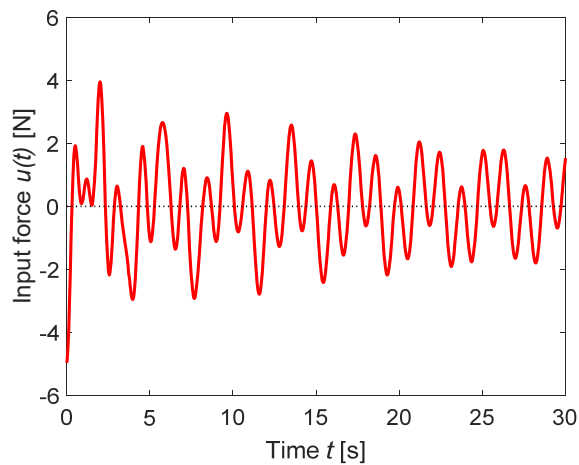


Figure 2.28 – Input force required for pole placement.

## 2.4 Conclusions

Classical models used to describe the dynamics and vibrational behavior mechanical systems were presented in this chapter. The complexity of the model depends on the systems and on the dynamics properties that is necessary to predict. Both SDOF and MDOF model are introduced, with particular focus on the effects of viscous and structural proportional and non-proportional damping. The usual effect of damping is to reduce vibration amplitude and peaks frequency. The last properties are not always true for non-proportional damped system, in which the damped natural frequency can also increase with respect to the undamped natural frequency. The result of first order perturbation analysis can predict when this happen using the undamped system properties and the non-proportional damping matrix layout.

Damping is generally used to reduce vibration amplitude. Damping distribution can be properly designed to obtain the desired behavior of the system using passive system modification. Not always all the requirements can be achieved using only passive modification and therefore active control strategies are necessary to achieve better result. Classical pole placements in MDOF linear mechanical system is presented. A closed form formulation to compute the proportional and derivative control gain of a close loop PD control is presented. The method can assign desired poles without changing the other poles of the system, which is a result impossible to obtain using only passive modifications.



## Chapter 3

### 3. Review of passive damping matrix identification and active vibration suppression methods

The identification of the model parameters to predict the behaviour of real systems is known as the inverse problem related to numerical - experimental correlation of systems dynamics behaviour. In § 2 the parameters of the presented models were given as known, however in real system not all the parameters are known, and the unknown ones should be identified to build up the system model. Also, the computation of the close loop control gains necessary to achieve desired system behaviour generally requires the structural matrix of the system, which should be identified.

While inertial and elastic properties of mechanical system are well understood and there are a lot of well-developed method to identify and model them, such as FE [54,55], dissipation properties remain obscure and tends to be modelled on the basis of ad hoc assumptions.

The exact identification, localisation and quantification of dissipation sources in mechanical system remain an unsolved problem. Better understanding the spatial distribution of dissipation sources is a desirable objective and potentially very useful design tool to improve the efficiency of many mechanical systems, both with passive modification or with active solutions.

Damping identifications methods based on measured FRF are presented in § 3.1, the importance of damping identification for system passive or active control is introduced in § 3.2 as a prelude for a brief review in § 3.3 of vibration suppression in linear and nonlinear system using active control methods.

### 3.1 FRF based damping matrix identification

Several different methods have been developed during the years for spatial damping matrix identification, but usually they have been validated by one-off application. The damping identification methods already presented in literature are based on several technique and physical properties. Large reviews of the most used methods can be find in [56–59].

Damping model identification methods can be subdivided into two main groups: identification of modal models or spatial models.

Modal models identification methods identify the modal property of the system, while spatial models identification methods are capable to identify the matrices of the system in physical coordinates. The identification of modal models or spatial models of a system depend on the identification purpose: the spatial model of a system provides the localisation and quantification of the dissipation sources, while usually are not able to represent high frequency system behaviour; modal models can provide good frequency domain models of the real system, but losing information on the dissipation distribution [60].

In this paragraph a review of the FRF based methods for direct non-proportional viscous and structural spatial models identification is presented. The word “direct” stands for identification from experimental measures without previous knowledge of the system, and “FRF based” stands for experimental measures in frequency domain. The methods can be subdivided into two different groups: 1) FRF methods, 2) modal parameters method.

The methods belonging to the first group identifies the damping matrix directly from the experimental frequency response matrix (FRM), while the ones belonging to the second group identify the spatial damping matrix from the previously identified modal properties of the system.

#### 3.1.1 Chen-Ju-Tsuei’s method

Chen, Ju and Tsuei presented in 1996 a method for estimate the mass  $\mathbf{M}$ , stiffness  $\mathbf{K}$  and non-classical viscous damping  $\mathbf{C}$  matrices in a mechanical system [61,62]. The method can identify the matrices directly from measured FRM. The non-classical viscous damping matrix  $\mathbf{C}$  is identified separately from mass  $\mathbf{M}$  and stiffness  $\mathbf{K}$  matrices. The identification procedure is based on the concept of normal FRM  $\mathbf{H}^N(\Omega) \in \mathbb{R}^{N \times N}$ , which is defined as the undamped FRM underlying the damped system [63,64].

The normal FRM  $\mathbf{H}^N(\Omega)$  is defined as in Eq. (3.1) and the transformation matrix  $\mathbf{G}(\Omega) \in \mathbb{R}^{N \times N}$  between damped FRM  $\mathbf{H}(\Omega) \in \mathbb{C}^{N \times N}$  and normal FRM  $\mathbf{H}^N(\Omega)$  is defined in Eq. (3.2).

$$\mathbf{H}^N(\Omega) = \Re(\mathbf{H}(\Omega)) + \Im(\mathbf{H}(\Omega))(\Re(\mathbf{H}(\Omega)))^{-1} \Im(\mathbf{H}(\Omega)) \quad (3.1)$$

$$\mathbf{G}(\Omega) = -\Im(\mathbf{H}(\Omega))(\Re(\mathbf{H}(\Omega)))^{-1} \quad (3.2)$$

The non-classical viscous damping matrix  $\mathbf{C} \in \mathbb{R}^{N \times N}$  is obtained with a least square approach from normal FRM  $\mathbf{H}^N(\Omega)$  and transformation matrix  $\mathbf{G}(\Omega)$ :

$$\mathbf{C} = \begin{bmatrix} \Omega_1 \mathbf{H}^N(\Omega_1) \\ \vdots \\ \Omega_K \mathbf{H}^N(\Omega_K) \end{bmatrix}^+ \begin{bmatrix} \mathbf{G}(\Omega_1) \\ \vdots \\ \mathbf{G}(\Omega_K) \end{bmatrix} \quad (3.3)$$

where  $K$  is the number of spectral lines considered in the identification.

More detail on this method can be find in § 4.2.

### 3.1.2 Lee-Kim's Method

Lee-Kim's method [65] identifies viscous  $\mathbf{C}$  and structural  $\mathbf{D}$  spatial damping matrices of a system directly from system experimental FRM. It is based on the definition of dynamic stiffness matrix (DSM)  $\mathbf{Z}(\Omega) \in \mathbb{C}^{N \times N}$ , it is the inverse of the FRM  $\mathbf{H}(\Omega)$ .

$$\mathbf{Z}(\Omega) = [\mathbf{H}(\Omega)]^{-1} = (-\Omega^2 \mathbf{M} + \mathbf{K}) + i(\Omega \mathbf{C} + \mathbf{D}) \quad (3.4)$$

where  $\mathbf{M}, \mathbf{K}, \mathbf{C}, \mathbf{D} \in \mathbb{R}^{N \times N}$  are respectively the mass, stiffness viscous damping and structural damping matrices and  $\Omega$  is the frequency of a spectral line. The damping matrices of the system are then related to the FRM:

$$\Im([\mathbf{H}(\Omega)]^{-1}) = \Omega \mathbf{C} + \mathbf{D} \quad (3.5)$$

Eq. (3.5) can be written in matrix form as:

$$[\Omega \mathbf{I} \quad \mathbf{I}] \begin{bmatrix} \mathbf{C} \\ \mathbf{D} \end{bmatrix} = \Im([\mathbf{H}(\Omega)]^{-1}) \quad (3.6)$$

The damping matrices  $\mathbf{C}$  and  $\mathbf{D}$  can be obtained in a least square sense inverting Eq. (3.6) for several spectral lines  $\Omega_i$  contained in the measured frequency range:

$$\begin{bmatrix} \mathbf{C} \\ \mathbf{D} \end{bmatrix} = \begin{bmatrix} \Omega_1 \mathbf{I} & \mathbf{I} \\ \vdots & \vdots \\ \Omega_i \mathbf{I} & \mathbf{I} \\ \vdots & \vdots \\ \Omega_K \mathbf{I} & \mathbf{I} \end{bmatrix}^+ \begin{bmatrix} \Im([\mathbf{H}(\Omega_1)]^{-1}) \\ \vdots \\ \Im([\mathbf{H}(\Omega_i)]^{-1}) \\ \vdots \\ \Im([\mathbf{H}(\Omega_K)]^{-1}) \end{bmatrix} \quad (3.7)$$

Eq. (3.7) implies that the viscous  $\mathbf{C}$  and structural  $\mathbf{D}$  damping matrices are constant with respect to the excitation frequencies  $\Omega_i$ . The choice of the spectral lines frequencies  $\Omega_i$  influences the solution.

### 3.1.3 Arora's Method

Arora proposes in 2009 [66,67] an identification method, based on modal updating, capable to identify non proportional structural damping matrices  $\mathbf{D}$  in mechanical system. In 2014 he proposes a direct spatial identification method [68,69] for structural damping in mechanical system based on the concept of normal FRM  $\mathbf{H}^N(\Omega)$  [63,64]. This method is the extension of Chen-Ju-Tseui's method § 3.1.1 to structural damping identification.

The structural damping matrix is obtained with a least square solution as:

$$\mathbf{D} = \begin{bmatrix} \Re(\mathbf{H}(\Omega_1)) \\ \vdots \\ \Re(\mathbf{H}(\Omega_K)) \end{bmatrix}^+ \begin{bmatrix} \Im(\mathbf{H}(\Omega_1))\mathbf{H}^N(\Omega_1) \\ \vdots \\ \Im(\mathbf{H}(\Omega_K))\mathbf{H}^N(\Omega_K) \end{bmatrix} \quad (3.8)$$

where  $K$  is the number of spectral lines used and  $\mathbf{H}^N(\Omega)$  the normal FRM defined in Eq. (3.1). More detail on this method are presented in § 4.2.

### 3.1.4 Instrumented variable method

This instrumented variable IV method was applied for the first time to structural dynamics parameters estimation by Fritzen [70]. It is based on the optimisation of a cost function, i.e. the error between the experimental FRM  $\mathbf{H}^{Exp}(\Omega) \in \mathbb{C}^{N \times N}$  and the numerical FRM evaluated from the identified system matrices. The method needs theoretically an infinite number of spectral lines, which is practically impossible in real applications. To overcome this problem a study of the most suitable regions where the spectral lines should be chosen is provided in [71]. The IV method was also extended to continuous frequency domain in [72].

The basic idea of the IV method consists in minimise the error  $\mathbf{E} \in \mathbb{C}^{N \times N}$ :

$$\mathbf{E} = \mathbf{H}^{Exp}(\Omega) \left( -\Omega^2 \mathbf{M} + i\Omega \mathbf{C} + \mathbf{K} \right)^{-1} - \mathbf{I} \quad (3.9)$$

Eq. (3.9) can be written separating real and imaginary part of Eq. (3.9):

$$\begin{bmatrix} -\Omega^2 \mathbf{H} & i\Omega \mathbf{H} & \mathbf{H} \end{bmatrix} \begin{bmatrix} \mathbf{M} \\ \mathbf{C} \\ \mathbf{K} \end{bmatrix} = \mathbf{I} + \mathbf{E} \quad (3.10)$$

The mass  $\mathbf{M}$ , stiffness  $\mathbf{K}$  and damping  $\mathbf{C}$  matrices can be evaluated from Eq. (3.10) with a least square approach, but the estimation will be affected from a non-negligible error due to the bias effect of the noise contained in the experimental FRM  $\mathbf{H}^{Exp}(\Omega)$ , details can be found in [70–72].

IV method proposes to solve the problem multiplying Eq. (3.10) by an instrumented variable  $\mathbf{W} \in \mathbb{C}^{N \times N}$ , which is uncorrelated with the error and has maximum correlation with the input data. These two properties are summarised as:

$$p \lim_{l \rightarrow \infty} \left( \frac{1}{l} \mathbf{W}^T \mathbf{E} \right) = 0, \quad p \lim_{l \rightarrow \infty} \left( \frac{1}{l} \mathbf{W}^T \begin{bmatrix} -\Omega^2 \mathbf{H} & i\Omega \mathbf{H} & \mathbf{H} \end{bmatrix} \right) \text{ not singular} \quad (3.11)$$

where  $p \lim$  is the probabilistic limit.

The estimation is now not affected by a bias due to the experimental noise. Pre-multiplying Eq. (3.10) by  $\mathbf{W}^T$  it becomes:

$$\begin{bmatrix} \mathbf{M} & \mathbf{C} & \mathbf{K} \end{bmatrix}^T = \left( \mathbf{W}^T \begin{bmatrix} -\Omega^2 \mathbf{H} & i\Omega \mathbf{H} & \mathbf{H} \end{bmatrix} \right)^{-1} \mathbf{W}^T \mathbf{I} \quad (3.12)$$

The choice of the instrumental variable  $\mathbf{W}$  is the open to the user. In [70] it is suggested to use a instrumented variable as the reconstructed FRM from the identified  $\mathbf{M}$ ,  $\mathbf{C}$  and  $\mathbf{K}$  matrices in an iterative procedure. The first guess for the instrumented variable can be constructed from the least square solution of Eq. (3.10), while for the next iteration it can be constructed from the structural matrices identified at precedent step. This method can be seen as an iterative version of the Lee-Kim method in § 3.1.2, but in this case it is necessary to identify mass  $\mathbf{M}$ , stiffness  $\mathbf{K}$  and damping  $\mathbf{C}$  matrices together.

### 3.1.5 Adhikari's method

Adhikari presented in 2001 a method [73] to identify non-classical viscous damping matrix  $\mathbf{C}$  starting from the measured FRM  $\mathbf{H}(\Omega)$ . The method is valid for system with light non-proportional damping because it is based on the results of perturbation theory for complex modes [24,74].



### 3. Review of passive damping matrix identification and active vibration suppression methods

---

The identification of the spatial damping matrix through this method requires the identification of the modal parameters of the system from experimental modal analysis (EMA): complex poles  $s_r$ , (natural frequency  $\omega_{n,r}$  and damping ratio  $\zeta_r$ ), and complex mode shapes  $\Psi_r$ .

The complex eigenvector  $\Psi_r$  of a non-proportional damping system is computed from the undamped system eigenvector  $\Phi_r$  using second order perturbation theory [74] as:

$$\Psi_r = \Phi_r + i \sum_{k=1, k \neq j}^N \frac{\omega_{n,j} \Phi_k^T \mathbf{C} \Phi_j}{(\omega_{n,j}^2 - \omega_{n,k}^2)} \Phi_k \quad (3.13)$$

where  $\Phi_r$  is the real eigenvector of the undamped or classically viscous damped system,  $\mathbf{C}$  is the non-proportional damping matrix and  $N$  the number of DOFs.

The experimental identified complex mode shape  $\Psi_r$  can be written as:

$$\Psi_r = \Re(\Psi_r) + i \Im(\Psi_r) \quad (3.14)$$

where  $\Re(\Psi_r) = \Phi_r$  and  $\Im(\Psi_r) = \mathbf{L}_r$ .

The imaginary part  $\mathbf{L}_r \in \mathbb{R}^{N \times 1}$  can be expressed as a linear combination of the real parts  $\Phi_r$ :

$$\mathbf{L}_r = \sum_{k=1}^R \tilde{B}_{kj} \Phi_k, \quad \tilde{B}_{kj} = \frac{\omega_{n,j} \Phi_k^T \mathbf{C} \Phi_j}{(\omega_{n,j}^2 - \omega_{n,k}^2)} \quad (3.15)$$

where  $R$  is the number of identified modes.

The error  $\varepsilon$  in the representation of imaginary part  $\mathbf{V}_r$  is:

$$\varepsilon = \mathbf{L}_r - \sum_{k=1}^R \tilde{B}_{kj} \Phi_r \quad (3.16)$$

The error  $\varepsilon$  should be minimised with an appropriate choice of the matrix  $\tilde{\mathbf{B}} \in \mathbb{R}^{N \times N}$ . It is proved in [73] that the  $\tilde{\mathbf{B}}$  matrix minimising the error is given by:

$$\tilde{\mathbf{B}} = (\Phi^T \Phi)^{-1} \Phi^T \mathbf{L} \quad (3.17)$$

where  $\mathbf{L} = \Im(\Psi)$  is the real modal matrix associated with the undamped or proportionally damped system. The non-proportional modal viscous damping matrix  $\tilde{\mathbf{C}} = \Phi^T \mathbf{C} \Phi$ , which is non-diagonal, can be computed from Eq. (3.15) as:

$$\begin{aligned}\tilde{C}_{kj} &= \Phi_k^T \mathbf{C} \Phi_j = \frac{\tilde{B}_{kj}(\omega_{n,j}^2 - \omega_{n,k}^2)}{\omega_{n,j}}, \quad k \neq j \\ \tilde{C}_{kj} &= \Phi_j^T \mathbf{C} \Phi_j = 2\Im(s_j)\end{aligned}\tag{3.18}$$

The spatial non-proportional viscous damping matrix is the computed as:

$$\mathbf{C} = (\Phi^+)^T \tilde{\mathbf{C}} \Phi^+ \tag{3.19}$$

where  $(\bullet)^+$  denote the pseudo-inverse matrix.

The identified spatial damping matrix is not mandatory symmetric, symmetry preserving method are also presented in [75]. The identification could result in a non-symmetric damping matrix  $\mathbf{C}$  when the FRM does not respect the Maxwell reciprocity theorem, this is due to errors in the measure or non-viscous damping mechanism in the system.

### 3.1.6 Phani-Woodhouse's method

Srikantha Phani and Woodhouse presented in [58] and experimentally validate in [76] a hybrid method for non-proportional viscous damping matrix  $\mathbf{C}$  identification. The method requires both experimental FRM  $\mathbf{H}(\Omega)$  and experimental identification of modal parameters: real modal matrix  $\Phi$ , spectral matrix  $\Lambda$  and damping ratios  $\zeta_r$ .

The method is called matrix perturbation method because it is based on the approximation of complex eigenvectors with a first-order perturbation theory starting from proportionally damped system eigenvectors [77].

The DSM of a MDOF mechanical system can be written as:

$$[\mathbf{H}(\Omega)]^{-1} = -\Omega^2 \mathbf{M} + i\Omega \mathbf{C} + \mathbf{K} \tag{3.20}$$

where  $\mathbf{H}(\Omega)$  can be obtained experimentally. Pre and post multiplying Eq. (3.20) by the real modal matrix  $\Phi$ , identified from the experimental FRM and unitary modal mass normalised and inverting:

$$\Phi^{-1} \mathbf{H}(\Omega) \Phi^{-T} = (-\Omega^2 \mathbf{I} + i\Omega \tilde{\mathbf{C}} + \Lambda)^{-1} \tag{3.21}$$

where  $\mathbf{I}$  is the identity matrix,  $\tilde{\mathbf{C}}$  is the non-diagonal modal damping matrix and  $\Lambda$  is the spectral matrix obtained from experimental identification of the natural frequencies.  $\tilde{\mathbf{C}}$  is not diagonal because it can't be diagonalised by the real modal matrix  $\Phi$ .

The viscous damping matrix in modal coordinates  $\tilde{\mathbf{C}}$  is the sum of a diagonal matrix  $\tilde{\mathbf{C}}_d \in \mathbb{C}^{N \times N}$  and a coupled matrix  $\tilde{\mathbf{C}}_o \in \mathbb{C}^{N \times N}$  ::

$$\tilde{\mathbf{C}} = \tilde{\mathbf{C}}_d + \tilde{\mathbf{C}}_o \quad (3.22)$$

The diagonal portion of the damping matrix  $\tilde{\mathbf{C}}_d$  is obtained from experimentally identified natural frequencies  $\omega_r$  and damping ratios  $\zeta_r$  as in Eq. (2.121). Defining the FRM in modal coordinates  $\mathbf{H}_m(\Omega)$ :

$$\mathbf{H}_m(\Omega) = -\Omega^2 \mathbf{I} + i\Omega \tilde{\mathbf{C}}_d + \mathbf{A} \quad (3.23)$$

Eq. (3.21) becomes:

$$\Phi^{-1} \mathbf{H}(\Omega) \Phi^{-T} = (\mathbf{A}(\Omega) + i\Omega \tilde{\mathbf{C}}_o)^{-1} \quad (3.24)$$

The inversion of Eq. (3.24) right hand side can be approximated to the leading order term in  $\tilde{\mathbf{C}}_o$ :

$$\Phi^{-1} \mathbf{H}(\Omega) \Phi^{-T} = (\mathbf{H}_m(\Omega) + i\Omega \tilde{\mathbf{C}}_o)^{-1} \approx [\mathbf{H}_m(\Omega)]^{-1} + i\Omega [\mathbf{H}_m(\Omega)]^{-1} \tilde{\mathbf{C}}_o [\mathbf{H}_m(\Omega)]^{-1} \quad (3.25)$$

The non-diagonal matrix  $\tilde{\mathbf{C}}_o$  can be evaluated from Eq. (3.25):

$$\tilde{\mathbf{C}}_o \approx \frac{\mathbf{H}_m(\Omega) - \mathbf{H}_m(\Omega) \Phi^{-1} \mathbf{H}(\Omega) \Phi^{-T} \mathbf{H}_m(\Omega)}{i\Omega} \quad (3.26)$$

Finally, the spatial non-proportional viscous damping matrix is obtained as:

$$\mathbf{C} = \Phi^{-T} \tilde{\mathbf{C}} \Phi^{-1} \quad (3.27)$$

Eq. (3.27) gives a frequency dependent viscous damping matrix if evaluated frequency by frequency or a least square solution if a set of Eq. (3.26) is used for damping matrix evaluation.

### 3.1.7 Lancaster's method

The method proposed by Lancaster in 1961 [78] lets to identifies mass  $\mathbf{M}$ , stiffness  $\mathbf{K}$  and non-classical damping  $\mathbf{C}$  matrices of a system from the identified system modal parameters poles  $s_j$  and complex eigenvectors  $\Psi_r$ .

The method is based on a normalisation of the complex eigenvector  $\Psi_r$  such that:

$$(\mathbf{M}s^2 + \mathbf{C}s + \mathbf{K})\hat{\Psi}_r = \mathbf{0} \quad (3.28)$$

where  $\hat{\Psi}_r$  is the normalised eigenvector.

The eigenvector normalisation required in Eq. (3.28) is proved [79] to be:

$$\hat{\Psi}_r^T (2\mathbf{M}s_r + \mathbf{C})\hat{\Psi}_r = 0 \quad (3.29)$$

The matrices of the system can be computed as:

$$\mathbf{M} = (\hat{\Psi}\mathbf{\Lambda}\hat{\Psi}^T + \hat{\Psi}^*\mathbf{\Lambda}^*\hat{\Psi}^H)^{-1} \quad (3.30)$$

$$\mathbf{K} = -(\hat{\Psi}\mathbf{\Lambda}^{-1}\hat{\Psi}^T + \hat{\Psi}^*\mathbf{\Lambda}^{*-1}\hat{\Psi}^H)^{-1} \quad (3.31)$$

$$\mathbf{C} = -\mathbf{M}(\hat{\Psi}\mathbf{\Lambda}^2\hat{\Psi}^T + \hat{\Psi}^*\mathbf{\Lambda}^{*2}\hat{\Psi}^H)\mathbf{M} \quad (3.32)$$

where  $\mathbf{\Lambda}$  and  $\hat{\Psi}$  are respectively the spectral matrix and the modal mass normalised as in Eq. (3.29),  $\bullet^*$  in the complex conjugated and  $\bullet^H$  is the Hermitian.

The method presupposes the normalisation of the experimental evaluated eigenvectors with respect to the mass  $\mathbf{M}$  and damping  $\mathbf{C}$  matrices, which are the object of the evaluation.

Pilkey proposes an iterative approach to circumvent this problem [80]. In his method also the mass matrix is given as known, it can be computed from FE codes or identified from experimental test using other methods. The iterative method starts from an initial guess of the damping matrix  $\mathbf{C}$  and it normalises the eigenvectors to satisfy Eq. (3.29). The damping matrix can be now computed using Eq. (3.32). The procedure can be repeated until the identified damping matrix  $\mathbf{C}$  converges.

Bajrić et al. [81] recently propose an improved Lancaster method to have an explicit solution, avoiding the iterative solution. The method is based on the first order equation of motion of viscous damped mechanical system. The method requires the mass matrix  $\mathbf{M}$  and the eigenvectors  $\tilde{\Theta}$  as defined in Eq. (2.141). The spatial damping matrix can be then identified as:

$$\mathbf{C} = \mathbf{M}(\tilde{\Theta}\mathbf{\Lambda}\tilde{\Theta}^{-1}\tilde{\Theta}^* - \tilde{\Theta}^*\mathbf{\Lambda}^2)(\tilde{\Theta}^*\mathbf{\Lambda}^* - \tilde{\Theta}\mathbf{\Lambda}\tilde{\Theta}^{-1}\tilde{\Theta}^*) \quad (3.33)$$

### 3.1.8 Okuma-Shi-Oho's method

Okuma, Shi and Oho presented in [60] an iterative method to identify spatial structural matrices of a mechanical system starting from system FRM  $\mathbf{H}(\Omega)$  and the set of measured point coordinates. The main aim of this method is to provide spatial matrices of the system: 1) with number of DOF higher with respect to the

### 3. Review of passive damping matrix identification and active vibration suppression methods

---

number of natural frequencies in the frequency range of interest and 2) capable to reproduce the system dynamics also in condition different with respect to the boundary condition used in the identification process. The method requires the modal analysis of the system in free-free boundary condition and the identification of experimental natural frequencies  $\omega_{n,r}$ , damping ratios  $\zeta_r$  and mode shapes  $\Phi_r$ , defines as target modal parameters. The identification of mass  $\mathbf{M}$  and stiffness  $\mathbf{K}$  matrices are required to identify non-proportional viscous damping matrix  $\mathbf{C}$ . The method is an iterative procedure. Physically connectivity are used to fix the zeros entries in the mass  $\mathbf{M}$  and stiffness  $\mathbf{K}$  matrices. The first guess of that matrices are obtained using Eq. (3.34) and Eq. (3.35), in which matrices are computed from the six rigid body motion of the system. The definition of the mass matrix of a rigid system  $\mathbf{M}_{rigid}$  is known:

$$\Phi_{1:6}^T \mathbf{M} \Phi_{1:6} = \mathbf{M}_{rigid} = \begin{bmatrix} m & & & & & sym \\ & m & & & & \\ & & m & & & \\ & -mz_g & my_g & I_{xx} & & \\ mz_g & & -mx_g & I_{yx} & I_{yy} & \\ -my_g & mx_g & & I_{zx} & I_{zy} & I_{zz} \end{bmatrix} \quad (3.34)$$

where  $\mathbf{M}$  is the spatial mass matrix to be identified,  $m$  is the translational mass of the system,  $(x_g, y_g, z_g)$  are the centre of gravity coordinates and  $I_{xx}, I_{yy}, I_{zz}, I_{xy}, I_{xz}, I_{yz}$  are the inertia around the reference system axis and the products of the moment of inertia.

The stress on the structure due to the rigid body motion are null for definition, therefore the stiffness matrix can be computed using:

$$\mathbf{K} \Phi_{1:6} = \mathbf{0} \quad (3.35)$$

where  $\mathbf{K}$  is the stiffness matrix to be identified.

The mass  $\mathbf{M}$  and stiffness  $\mathbf{K}$  matrices are improved to become respectively definite and semi-definite positive, using the sensitivity analysis of the matrices eigenvalues with respect to the matrices elements. Then the target modal properties are reached using the sensitivity analysis of the system eigenvalues and eigenvectors. The viscous damping matrix  $\mathbf{C}$  is identified starting from the stiffness matrix  $\mathbf{K}$  multiplied by a coefficient  $\alpha$ , which is obtained by a least square procedure with respect to the target damping ratio values. Finally, the resulting viscous damping matrix  $\mathbf{C}$  is formulated as:

$$\mathbf{C} = \mathbf{\Phi}^{-T} \begin{bmatrix} \ddots & & \\ & 2\zeta_r \omega_{n,r} & \\ & & \ddots \end{bmatrix} \mathbf{\Phi}^{-1} \quad (3.36)$$

resulting in a full non-proportional matrix.

### 3.1.9 Leuridian-Brown-Allemang's method

The method was presented in 1982 by Leuridian et al. [82]. The method aims to identify mass  $\mathbf{M}$ , stiffness  $\mathbf{K}$  and viscous damping  $\mathbf{C}$  matrices of a system from the frequency domain responses:

$$(-\Omega_i^2 \mathbf{M} + i\Omega_i \mathbf{C} + \mathbf{K}) \mathbf{x}_{i,j} = \mathbf{F}_{i,j} \quad (3.37)$$

where  $\mathbf{x}_{i,j}$  and  $\mathbf{F}_{i,j}$  are respectively the response and the force vectors at frequency  $\Omega_i$  in the measurement  $j$ . In Eq. (3.37) the parameters to be estimated occurs as element of the matrices. Eq. (3.37) is reorganised using constraints of symmetry, matrix bandwidth and known matrices element:

$$[\mathbf{CLS}]_{i,j} \mathbf{U} = [\mathbf{VLS}]_{i,j} \quad (3.38)$$

where  $[\mathbf{CLS}]$  is a complex matrix containing information on system responses, frequency and constraints,  $[\mathbf{VLS}]$  is complex vector containing information of the input force and known elements and  $\mathbf{U}$  is the vector of the unknown matrices elements.

Eq. (3.38) can be solved in a least square sense using a set of frequencies and a set of measurements:

$$[\mathbf{CLS}] \mathbf{U} = [\mathbf{VLS}] \quad (3.39)$$

where  $[\mathbf{CLS}]$  and  $[\mathbf{VLS}]$  include all the frequency and all the measures. The solution of Eq. (3.39) with a pseudo inverse of the right hand side makes the condition number of the problem the square of the  $[\mathbf{CLS}]$  matrix condition number. Hence, the solution of Eq. (3.39) is obtained though the Householder transformation:

$$[\mathbf{TC}] \mathbf{U} = [\mathbf{TV}] \quad (3.40)$$

where  $\mathbf{TC}$  is an upper triangular matrix with the same condition number of  $[\mathbf{CLS}]$

In this method the estimation is linear and does not imply single input data.

### 3.1.10 Link's method

The method proposed by Link in 1985 [83] is an extension of the ISSPA (Identification of structural System Parameters) [84,85]. It can identify the viscous damping matrix reduced to the measured DOFs  $\mathbf{C}_z$ .

The equation of motion in frequency domain is rearranged separating real and imaginary part of accelerations and excitation force and pre-multiplying by  $\mathbf{M}^{-1}$ :

$$\begin{aligned}\mathbf{A}\mathbf{K}^{*T} - \mathbf{\Omega}\mathbf{B}\mathbf{D}^{*T} + \mathbf{\Omega}^2\Re(\mathbf{P})\mathbf{M}^{-1} &= \mathbf{\Omega}^2\left(\Re(\ddot{\mathbf{U}}_b^T)\mathbf{T}^T + \mathbf{A}\right) = \mathbf{R}_A \\ \mathbf{B}\mathbf{K}^{*T} + \mathbf{\Omega}\mathbf{A}\mathbf{D}^{*T} + \mathbf{\Omega}^2\Im(\mathbf{P})\mathbf{M}^{-1} &= \mathbf{\Omega}^2\left(\Im(\ddot{\mathbf{U}}_b^T)\mathbf{T}^T + \mathbf{B}\right) = \mathbf{R}_B\end{aligned}\quad (3.41)$$

where  $\mathbf{T}$  is the geometric transformation matrix correlating the rigid body displacement of the structure with respect to the base excitation; the other matrices are defines as:

$$\mathbf{X} = \begin{bmatrix} \ddot{x}_1(\omega_1) & \cdots & \ddot{x}_1(\omega_m) \\ \vdots & & \vdots \\ \ddot{x}_p(\omega_1) & \cdots & \ddot{x}_p(\omega_m) \end{bmatrix}, \quad \begin{aligned} \mathbf{A}^T &= \Re(\mathbf{X}) \\ \mathbf{B}^T &= \Im(\mathbf{X}) \end{aligned}\quad (3.42)$$

$$\mathbf{K}^* = \mathbf{M}^{-1}\mathbf{K}, \quad \mathbf{C}^* = \mathbf{M}^{-1}\mathbf{C} \quad (3.43)$$

$$\mathbf{P} = \begin{bmatrix} f_1(\omega_1) & \cdots & f_p(\omega_1) \\ \vdots & & \vdots \\ f_1(\omega_m) & \cdots & f_p(\omega_m) \end{bmatrix}, \quad \ddot{\mathbf{U}}_b^T = \begin{bmatrix} \ddot{u}_{bx}(\omega_1) & \ddot{u}_{by}(\omega_1) & \ddot{u}_{bz}(\omega_1) \\ \vdots & \vdots & \vdots \\ \ddot{u}_{bx}(\omega_m) & \ddot{u}_{by}(\omega_m) & \ddot{u}_{bz}(\omega_m) \end{bmatrix} \quad (3.44)$$

The matrices  $\mathbf{K}^*$  and  $\mathbf{C}^*$  can be identified from Eq. (3.45)-(3.47), details in [83].

$$\mathbf{K}_z^{*T} = \mathbf{I}_z \mathbf{K}^{*T} = (\mathbf{Z}_a \mathbf{Z}_b + \mathbf{I})^{-1} (\mathbf{Z}_a \mathbf{Z}_c + \mathbf{Z}_d) \quad (3.45)$$

$$\mathbf{C}_{ez}^{*T} = \begin{bmatrix} \mathbf{I}_z \mathbf{C}^{*T} \\ \hat{\mathbf{M}}_z^{-1} \end{bmatrix} = (\mathbf{Z}_b \mathbf{Z}_a + \mathbf{I})^{-1} (\mathbf{Z}_b \mathbf{Z}_d - \mathbf{Z}_c) \quad (3.46)$$

$$\mathbf{Z}_a = \mathbf{B}^+ \mathbf{\Omega} \mathbf{A}_e, \quad \mathbf{Z}_b = \mathbf{B}_e^+ \mathbf{\Omega}^{-1} \mathbf{A}, \quad \mathbf{Z}_c = \mathbf{B}_e^+ \mathbf{\Omega}^{-1} \mathbf{R}_A, \quad \mathbf{Z}_d = \mathbf{B}^+ \mathbf{R}_B \quad (3.47)$$

where  $\mathbf{I}_z$  is the identity matrix of dimension equal to the measured DOFs,  $\mathbf{A}_e = [\mathbf{A} | -\mathbf{\Omega}\Re(\hat{\mathbf{P}})]$ ,  $\mathbf{B}_e = [\mathbf{B} | \mathbf{\Omega}\Im(\hat{\mathbf{P}})]$ ,  $\hat{\bullet}$  refers to only the measured DOFs and  $\bullet^+$  is the pseudo-inverse.

The left and right eigenproblem can be now solved to get left  $\mathbf{Y}$  and right  $\bar{\mathbf{X}}_z$  eigenvectors and natural frequencies  $\Omega_0$ :

$$\mathbf{K}_z^* \mathbf{Y} = \mathbf{Y} \Omega_0^2, \quad \mathbf{K}_z^{*T} \bar{\mathbf{X}}_z = \bar{\mathbf{X}}_z \Omega_0^2 \quad (3.48)$$

The left eigenvector  $\mathbf{Y}$  and the right  $\bar{\mathbf{X}}_z$  produces different modal masses matrix, respectively  $\mathbf{M}_g$  and  $\bar{\mathbf{M}}_g$ .

From the orthogonality condition of left and right eigenvector:

$$\mathbf{Y}^T \bar{\mathbf{X}}_z = \bar{\mathbf{M}}_g \quad (3.49)$$

$$\mathbf{Y}^T \mathbf{M} \mathbf{Y} = \mathbf{M}_g \quad (3.50)$$

The right eigenvector  $\bar{\mathbf{X}}_z$  can be normalised such that:

$$\mathbf{Y}^T \mathbf{M} \mathbf{Y} = \mathbf{Y}^T \alpha \bar{\mathbf{X}}_z = \mathbf{Y}^T \mathbf{X}_z \quad (3.51)$$

and the normalisation constant  $\alpha$  for each eigenvector can be found from:

$$\alpha_j = \left( \mathbf{a}_j^T \mathbf{a}_j \right)^{-1} \mathbf{a}_j^T \mathbf{Y}_j, \quad \mathbf{a}_j = \hat{\mathbf{M}}_z^{-1} \mathbf{X}_{z,j} \quad (3.52)$$

where  $\hat{\mathbf{M}}_z^{-1}$  comes from Eq. (3.46). The modal damping matrix  $\tilde{\mathbf{C}}$  is computed as:

$$\tilde{\mathbf{C}} = \mathbf{X}_z^T \mathbf{C} \mathbf{Y} \quad (3.53)$$

The modal damping matrix  $\tilde{\mathbf{C}}$  is in general non-diagonal, the relative spatial damping matrix  $\mathbf{C}_z$  reduced to the measured DOFs can be computed as:

$$\mathbf{C}_z = \mathbf{Y}^+ \tilde{\mathbf{C}}^{-1} \mathbf{Y} = \mathbf{X}_z \mathbf{C}_g^{-1} \mathbf{X}_z^T \quad (3.54)$$

In Eq. (3.54) it is no more necessary to compute the pseudo inverse of the left eigenvectors matrix, but using the relation in Eq. (3.51) the right eigenvector are directly used to identify the non-proportional damping matrix.

### 3.1.11 Minas-Inman's method

The method proposes by Minas and Inman in 1991 [86] is based on the previous knowledge of mass  $\mathbf{M}$  and stiffness  $\mathbf{K}$  from FE formulation, reduced to the experimentally measured DOFs.

The modal parameters poles  $s_r$ , natural frequencies  $\omega_{n,r}$ , damping ratios  $\zeta_r$  and mode shapes  $\Psi_r$  are experimentally identified from FRM  $\mathbf{H}(\Omega)$ .

The eigenproblem of the system can be written as:

$$\mathbf{C} \Psi_r = -\frac{1}{s_r} \left( s_r^2 \mathbf{M} + \mathbf{K} \right) \Psi_r = \mathbf{f}_r \quad (3.55)$$

where  $\mathbf{C}$  is the non-classical viscous damping matrix to be identified. Eq. (3.55) is valid for each experimentally identified mode.



The complex conjugate transpose of Eq. (3.55) is:

$$\Psi_r^* C = \mathbf{f}_r^* \quad (3.56)$$

Dividing real and imaginary part of Eq. (3.56) and rearranging it:

$$\begin{bmatrix} \Re(\Psi_r^*) \\ \Im(\Psi_r^*) \end{bmatrix} \mathbf{U} = \begin{bmatrix} \Re(\mathbf{f}_r^*) \\ \Im(\mathbf{f}_r^*) \end{bmatrix}, \quad \mathbf{G}_r \mathbf{U} = \mathbf{b}_r \quad (3.57)$$

where  $\mathbf{U}$  contains all the unknown element of the damping matrix  $\mathbf{C}$ , assumed symmetric.

Eq. (3.57) can be written for all the identified modes  $r=1, \dots, R$ , where  $R$  are the number of experimentally identified modes

$$\begin{bmatrix} \mathbf{G}_1 \\ \vdots \\ \mathbf{G}_R \end{bmatrix} \mathbf{U} = \begin{bmatrix} \mathbf{b}_1 \\ \vdots \\ \mathbf{b}_R \end{bmatrix} \quad (3.58)$$

and solved with a least square approach.

### 3.1.12 Local equation of motion method

Ablitzer et al. presented in 2014 [87] a spatial identification method for the structural damping ratio  $\eta$  of simple geometry structures. It is based on the knowledge of the analytical formulation of the equation of motion in continuous domain. The method was developed for thin plate in [87] and extended for beams in [57]. The method is proved [57] to works quite well with respect to the all others method but it is useful only for very simple structures, in which the continuous equation of motion can be formulate in close form.

The equation of motion of an isotropic thin plate in the harmonic regime is:

$$D \left( \frac{\partial^4 w(x,y)}{\partial x^4} + 2 \frac{\partial^4 w(x,y)}{\partial x^2 \partial y^2} + \frac{\partial^4 w(x,y)}{\partial y^4} \right) - \rho h \Omega^2 w(x,y) = f(x,y) \quad (3.59)$$

where  $D$  is the flexural stiffness,  $\rho$  the density,  $h$  the thickness,  $\Omega$  the excitation angular frequency,  $w(x,y)$  the transverse displacement and  $f(x,y)$  the excitation force per unit of area.

The flexural stiffness is defined as

$$D = \frac{E(1+i\eta)h^3}{12(1-\nu^2)} \quad (3.60)$$

where  $E$  is the Young modulus,  $\eta$  is the structural damping ratio and  $\nu$  the Poisson ratio.

In a point  $(x, y)$  where no excitation is applied Eq. (3.59) becomes:

$$D \left( \frac{\partial^4 w(x, y)}{\partial x^4} + 2 \frac{\partial^4 w(x, y)}{\partial x^2 \partial y^2} + \frac{\partial^4 w(x, y)}{\partial y^4} \right) - \rho h \Omega^2 w(x, y) = 0 \quad (3.61)$$

$$(3.62)$$

The properties in a general point  $(x_0, y_0)$  of the plate space can be computed from Eq. (3.61) :

$$\left( \frac{D}{\rho h} \right)_{x_0, y_0} = -\Omega^2 \frac{w(x_0, y_0)}{\nabla^4 w(x_0, y_0)} \quad (3.63)$$

which is a complex number. The term  $\nabla^4 w(x_0, y_0)$  is the numerical approximation of the differential in Eq. (3.61), using discrete steps  $\Delta x$  and  $\Delta y$ .

The properties can be computed point by point. The structural damping ratio and Young modulus in a generic point  $(x_0, y_0)$  can be evaluated from Eq. (3.61) and Eq. (3.60) as:

$$\eta_{x_0, y_0} = \Im \left( \frac{D}{\rho h} \right)_{x_0, y_0} (\rho h)_{x_0, y_0} \frac{12(1-\nu^2)}{E h^3} \quad (3.64)$$

$$E_{x_0, y_0} = \Re \left( \frac{D}{\rho h} \right)_{x_0, y_0} (\rho h)_{x_0, y_0} \frac{12(1-\nu^2)}{h^3} \quad (3.65)$$

Brumat et al. [57] extended the method to beams, identifying structural damping ratio  $\eta$ , Young modulus  $E$  and viscous damping coefficient  $c_{x_0}$

$$\eta_{x_0} = \frac{\varphi A \Omega^2}{E_{x_0} I} \Im \left( \frac{w_{x_0}}{\nabla^4 w(x_0)} \right) \quad (3.66)$$

$$E_{x_0} = \frac{\varphi A \Omega^2}{I} \Re \left( \frac{w_{x_0}}{\nabla^4 w(x_0)} \right) \quad (3.67)$$

$$\gamma_{x_0} = \frac{E_{x_0} I}{\Omega} \Im \left( \frac{w_{x_0}}{\nabla^4 w(x_0)} \right) \quad (3.68)$$

where  $\gamma_{x_0}$  is the damping per unit of length in the location  $x_0$ . The discrete viscous damping coefficient can be obtained as:

$$c_{x_0} = \gamma_{x_0} \Delta x \quad (3.69)$$

### 3.1.13 Other methods

Several other methods can be found in literature. Prandina et al. [88,89] present a spatial damping identification method based on energetic approach. Roamer and Mook [90] identify the system matrices from noise time domain data. Beliveau [91] proposed a method to identify structural matrices from modal information using a Bayesian approach. Boltezar and Slavic proposes [92–94] an identification method of damping based on Wavelet transform. Dalenbring [95] estimates structural damping functions and its parameters from modal models of the system and experimental FRFs. Ibrahim [96] proposes a method to identify non proportional viscous damping matrix from modal properties and a mathematical model of the system to be updated. Mondal et al. [97] propose a method for non-proportional viscous damping matrix identification using a gradient based FE modal updating. Several other method to identify spatial damping matrices using model updating have been proposed by Friswell [98], Ewins et al. [99], Imregun [100,101] and Pradhan and Modak [102].

## 3.2 Damping identification for vibration design

Damping represents a mathematical tool to model energy dissipation in the systems, hence it is commonly exploited to design the dynamic behaviour of systems. In fact, the vibrational response of mechanical systems to dynamic excitation is governed by damping, as discussed in § 2.1.2. A system can oscillate for long time or just for a small transitory depending on the amount of damping. In most of engineering applications it is desired to suppressing or attenuate as much as possible vibrations. Damping matrix identification can be useful to design and add optimised damping layouts in passive systems. The additional damping can be designed to have desired damping ratio values  $\zeta_{d,i}$ .

Damping ratios  $\zeta_i$  of MDOF proportional viscous damping systems can be defined as [34]:

$$\zeta_i = \frac{\lambda_i(\mathbf{C}_m)}{2\omega_{n,i}} \quad (3.70)$$

where  $\mathbf{C}_m$  is the mass normalised damping matrix of the system Eq. (3.71),  $\lambda_i(\mathbf{C}_m)$  represent the  $i^{th}$  eigenvalues of the mass normalised proportional viscous damping matrix  $\mathbf{C}$  and  $\omega_{n,i}$  is the  $i^{th}$  undamped natural frequency of the system.

$$\mathbf{C}_m = \mathbf{M}^{-1/2} \mathbf{C} \mathbf{M}^{-1/2} \quad (3.71)$$

Damping ratio  $\zeta_i$  directly gives an indication on the system responses evolution of the system, i.e. oscillatory or not if the system is respectively underdamped or overdamped.

Eq. (3.70) is no more valid when non-classical damped system are considered. The extension of Eq. (3.70) to non-classical damped system, i.e. system in which does not hold Eq. (2.119), was presented in [103]. Non-classical damping matrix is not diagonalised by the eigenvector of the undamped system and therefore it is not possible to directly predict the system evolution. In these cases, the non-diagonal damping ratio matrix  $\bar{\mathbf{Z}}$  can be defined as:

$$\bar{\mathbf{Z}} = \mathbf{C}_{cr}^{-1/2} \mathbf{C}_m \mathbf{C}_{cr}^{-1/2} \quad (3.72)$$

where  $\mathbf{C}_{cr}$  is the critical damping ratio matrix defined as:

$$\mathbf{C}_{cr} = 2\mathbf{M}^{-1/2} \mathbf{K} \mathbf{M}^{-1/2} \quad (3.73)$$

The eigenvalues  $\zeta^*$  of the damping ratio matrix  $\bar{\mathbf{Z}}$  are not the damping ratio of the system, however they can be used as indices to predict the system behaviour, as for viscous damping system.

It would be useful a design technique to define the damping matrix so that all or a set of poles would possess the desired damping ratio, starting from the damping ratio matrix  $\bar{\mathbf{Z}}$  and back to the damping matrix  $\mathbf{C}$ . However, since generally  $\mathbf{C}\mathbf{M}^{-1}\mathbf{K}$  is not symmetric, eigenvalues  $\zeta^*$  do not represent the damping ratio of the poles, and therefore is not always possible to predict the desired passive damping matrix. This is the reason why active vibration control becomes necessary in the design the system behaviour. Pole placement already introduced in § 2.3.1 is one of the methods useful for linear system. A review of active control techniques for vibrations suppression in linear and nonlinear system are presented in the next chapters.

### 3.3 Vibration suppression by active control

The growing demand for increased performance of mechanical and aerospace systems with reduced weight and fewer emissions leads to research initiatives that aim to exploit the characteristics of nonlinear systems. While the control of linear systems is well understood, most engineering systems behave nonlinearly, at least to some degree, and require the application of a nonlinear controller if the system is to behave according to design requirements. Non-smooth nonlinearities such as bi-linearity and free-play are commonplace in joints and connections, but difficult to treat because of the abrupt changes in dynamic behaviour that occur as parts come into contact and separate.

Vibration of mechanical system can be controlled to behave as desired using passive modification, which are always symmetric system, or using active control strategies which allow to obtain not self-adjoint system. The desired control law introduced in § 2.3, can be designed according to any design rule, therefore it can act also non-symmetrically. Usually in mechanical system the input is a force and the relative control law is design as a linear combination of the states to maintain the linearity of the system. Automatic control theory [104] states that the dynamic of controllable systems can be regulated assigning the poles of the system and using a single input force. The basic algorithms for pole assignment in first order systems are given in [105,106]. The desired dynamics can be also assigned using multiple input to the system [107] which ensure robustness of the controller with respect to the system parameters [108]. A closed-form solution for the partial pole in linear vibrational system was derived in [51], the solution is presented in § 2.3. The control problem is slightly more complicated when both poles and eigenvectors should be assigned, i.e. eigensystem assignment [49,109–113]. Control laws to assign both poles and zeros to a transfer function were presented in [114,115]. Pole placement for damped vibration was developed in [116]. Eigensystem assignment methods were also developed considering vibration confinement [117], state tracking control [118] and model updating [119].

Pole placement by receptance method for mechanical system was developed in [120,121]. Receptance method is a frequency domain method which let to control a system without the necessity of system matrices, contrary to all the methods presented before which requires the structural matrices of the system. A robust eigenvalues assignment method by receptance method was presented in [122]. Receptance method was applied for poles assignment [123–125]. Method of receptance was also applied for the control of nonlinear [126] systems, while methods for the control of nonlinear system in literature are usually developed in time domain: sliding mode control, backstepping and feedback linearisation [127–129],

This paragraph focuses pole placement by method of receptance in linear system, state space feedback linearisation in non-linear system and finally a receptance based feedback linearisation method, which are the base of the active control strategies applied in § 11 and § 12.

#### **3.3.1 Method of receptances**

The method of receptances was introduced by Mottershead and Ram in [120] for single input system and extended to MIMO system in [121]. It is an active control strategy for linear systems. The method of receptance has several advantages: it is not necessary to evaluate or to know the structural  $\mathbf{M}$ ,  $\mathbf{C}$ ,  $\mathbf{K}$  matrices, there: is no requirement for model reduction or for the use of an observer to determine unmeasured state variables and it is not necessary to place a

sensor (or an actuator) at every degree of freedom of the system. The number of sensors is determined precisely by the number of pairs of complex-conjugate poles to be exactly assigned and, in principle, all the poles of the system can be assigned using a single actuator. The pole placement using a single actuator is obtained by receptance method exploiting a rank-one modification based on Sherman-Morrison formula [130]. Being a rank-one modification can't be used in MIMO control.

In this chapter the theory of method of receptance for single and multiple input control is introduced.

### Single input control

The quadratic eigenvalues problem concerning the open loop system in Eq. (2.124) is:

$$(s_i^2 \mathbf{M} + s_i \mathbf{C} + \mathbf{K}) \mathbf{\Psi}_i = \mathbf{0} \quad i = 1, \dots, 2N \quad (3.74)$$

while the eigenproblem associated with a PD close loop control in Eq. (2.178) becomes:

$$(s_{d,i}^2 \mathbf{M} + s_{d,i} \mathbf{C} + \mathbf{K}) \mathbf{\Psi}_{cl,i} = \mathbf{g} (s_{d,i} \mathbf{c}_v^T + \mathbf{c}_p^T) \mathbf{\Psi}_{cl,i} \quad (3.75)$$

where  $s_{d,i}$  is  $i^{th}$  desired pole,  $\mathbf{\Psi}_{cl,i}$  is the  $i^{th}$  close loop eigenvector and  $\mathbf{c}_p$  and  $\mathbf{c}_v$  are respectively the velocity and displacement gain vector of the PD control, already introduced in Eq. (2.179).

Assuming a partial pole assignment of the first  $p$  poles, distinct from the open loop pole of the system without changing the remaining poles:

$$\begin{aligned} s_{d,i} &= s_d \\ \mathbf{\Psi}_{cl,i} &= \mathbf{\Psi}_i \end{aligned} \quad i = p+1, \dots, 2N \quad (3.76)$$

and substituting Eq. (3.76) in Eq. (3.75) and comparing with Eq. (3.74), it results:

$$\mathbf{g} (s_i \mathbf{c}_v^T + \mathbf{c}_p^T) \mathbf{\Psi}_i = \mathbf{0} \quad i = p+1, \dots, 2N \quad (3.77)$$

and since the selection vector  $\mathbf{g} \neq \mathbf{0}$ :

$$(s_i \mathbf{c}_v^T + \mathbf{c}_p^T) \mathbf{\Psi}_i = \mathbf{0} \quad i = p+1, \dots, 2N \quad (3.78)$$

Eq. (3.78) in matrix form becomes:

$$\begin{bmatrix} s_{p+1} \Psi_{p+1}^T & \Psi_{p+1}^T \\ \vdots & \vdots \\ s_{2N} \Psi_{p+1}^T & \Psi_{p+1}^T \end{bmatrix} \begin{bmatrix} \mathbf{c}_v \\ \mathbf{c}_p \end{bmatrix} = \mathbf{0} \quad (3.79)$$

or in compact form:

$$\mathbf{Q} \begin{bmatrix} \mathbf{c}_v \\ \mathbf{c}_p \end{bmatrix} = \mathbf{0} \quad (3.80)$$

The first  $p$  equations of Eq. (3.75) give:

$$\Psi_{cl,i} = (s_{d,i}^2 \mathbf{M} + s_{d,i} \mathbf{C} + \mathbf{K})^{-1} \mathbf{g} (s_{d,i} \mathbf{c}_v^T + \mathbf{c}_p^T) \Psi_{cl,i} \quad (3.81)$$

where the dynamic stiffness matrix  $\mathbf{Z}(s_{d,i}) = (s_{d,i}^2 \mathbf{M} + s_{d,i} \mathbf{C} + \mathbf{K})$  is invertible since the desired poles  $s_{d,i}$  are distinct from the close loop pole  $s_d$ .

Defining the vector  $\mathbf{r}_s \in \mathbb{C}^{N \times 1}$  as:

$$\mathbf{r}_s = \mathbf{H}(s) \mathbf{g} \quad (3.82)$$

Eq. (3.81) becomes:

$$\Psi_{cl,i} = \mathbf{r}(s_{d,i}) (s_{d,i} \mathbf{c}_v^T + \mathbf{c}_p^T) \Psi_{cl,i} \quad i=1, \dots, p \quad (3.83)$$

Since the eigenvectors can be scaled arbitrary, it is possible to choose a proper scaling of the close loop eigenvectors  $\Psi_{cl,i}$  so that:

$$(s_{d,i} \mathbf{c}_v^T + \mathbf{c}_p^T) \Psi_{cl,i} = 1 \quad i=1, \dots, p \quad (3.84)$$

and substituting Eq. (3.84) in Eq. (3.83):

$$\Psi_{cl,i} = \mathbf{r}(s_{d,i}) \quad i=1, \dots, p \quad (3.85)$$

and Eq. (3.85) back again in Eq. (3.84):

$$(s_{d,i} \mathbf{c}_v^T + \mathbf{c}_p^T) \mathbf{r}(s_{d,i}) = 1 \quad i=1, \dots, p \quad (3.86)$$

Eq. (3.86) in matrix form becomes:

$$\begin{bmatrix} s_1 \mathbf{r}_1^T & \mathbf{r}_p^T \\ \vdots & \vdots \\ s_p \mathbf{r}_p^T & \mathbf{r}_p^T \end{bmatrix} \begin{bmatrix} \mathbf{c}_v \\ \mathbf{c}_p \end{bmatrix} = \mathbf{e} \quad (3.87)$$

where  $\mathbf{e} \in \mathbb{R}^{p \times 1}$  is a vector full of ones. Eq. (3.87) in compact form becomes:

$$\mathbf{P} \begin{bmatrix} \mathbf{c}_v \\ \mathbf{c}_p \end{bmatrix} = \mathbf{0} \quad (3.88)$$

Collecting together the  $p$  equations deriving from the assigned poles in Eq. (3.88) and the  $2N - p$  equations deriving from the unchanged poles in Eq. (3.80), the position  $\mathbf{c}_p$  and derivative  $\mathbf{c}_v$  vector for the pole placement can be computed:

$$\begin{bmatrix} \mathbf{P} \\ \mathbf{Q} \end{bmatrix} \begin{Bmatrix} \mathbf{c}_v \\ \mathbf{c}_p \end{Bmatrix} = \begin{Bmatrix} \mathbf{e} \\ \mathbf{0} \end{Bmatrix} \quad (3.89)$$

Using this method, it is no more necessary to evaluate the system matrix to derive the proportional and derivative gain vector for active pole placement.

### Multi input control

The method of receptances can be extended to the case of multiple input control, therefore when more actuators act together on the structure.

The MIMO close loop eigenproblem result to be:

$$(s_{d,i}^2 \mathbf{M} + s_{d,i} \mathbf{C} + \mathbf{K}) \boldsymbol{\Psi}_{cl,i} = \mathbf{G} (s_{d,i} \mathbf{C}_v^T + \mathbf{C}_p^T) \boldsymbol{\Psi}_{cl,i} \quad (3.90)$$

where  $\mathbf{G} \in \mathbb{R}^{N \times M}$  is the selection matrix,  $M$  is the number of actuators and  $\mathbf{C}_v^T, \mathbf{C}_p^T \in \mathbb{R}^{N \times M}$  are the gain matrices for PD control, defined as:

$$\mathbf{G} = [\mathbf{g}_1 \quad \cdots \quad \mathbf{g}_M], \mathbf{C}_v = [\mathbf{c}_{v,1} \quad \cdots \quad \mathbf{c}_{v,M}], \mathbf{C}_p = [\mathbf{c}_{p,1} \quad \cdots \quad \mathbf{c}_{p,M}] \quad (3.91)$$

The MIMO eigenproblem in Eq. (3.90) can be written as:

$$(s_{d,i}^2 \mathbf{M} + s_{d,i} \mathbf{C} + \mathbf{K}) \boldsymbol{\Psi}_{cl,i} = [\mathbf{g}_1 (s_{d,i} \mathbf{c}_{v,1}^T + \mathbf{c}_{p,1}^T) + \cdots + \mathbf{g}_M (s_{d,i} \mathbf{c}_{v,M}^T + \mathbf{c}_{p,M}^T)] \boldsymbol{\Psi}_{cl,i} \quad (3.92)$$

For the  $p$  pole to assign Eq. (3.92) becomes:

$$\boldsymbol{\Psi}_{cl,i} = \mathbf{H}(s_{d,i}) [\mathbf{g}_1 (s_{d,i} \mathbf{c}_{v,1}^T + \mathbf{c}_{p,1}^T) + \cdots + \mathbf{g}_M (s_{d,i} \mathbf{c}_{v,M}^T + \mathbf{c}_{p,M}^T)] \boldsymbol{\Psi}_{cl,i} \quad (3.93)$$



and denoting:

$$\mathbf{r}_i(s_{d,j}) = \mathbf{H}(s_{d,j}) \mathbf{g}_i \quad (3.94)$$

$$\alpha_i(s_{d,j}) = (s_{d,j} \mathbf{c}_{v,i}^T + \mathbf{c}_{p,i}^T) \mathbf{\Psi}_{cl,j} \quad \begin{matrix} i = 1, \dots, M \\ j = 1, \dots, p \end{matrix} \quad (3.95)$$

Eq. (3.93) can be written as:

$$\mathbf{\Psi}_{cl,i} = \alpha_1(s_{d,i}) \mathbf{r}_1(s_{d,i}) + \alpha_2(s_{d,i}) \mathbf{r}_2(s_{d,i}) + \dots + \alpha_M(s_{d,i}) \mathbf{r}_M(s_{d,i}) \quad (3.96)$$

Recasting Eq. (3.95) in matrix form it becomes:

$$\begin{bmatrix} s_{d,j} \mathbf{\Psi}_{cl,j}^T & & & \mathbf{\Psi}_{cl,j}^T & & \\ & \ddots & & & \ddots & \\ & & s_{d,j} \mathbf{\Psi}_{cl,j}^T & & & \mathbf{\Psi}_{cl,j}^T \end{bmatrix} \begin{Bmatrix} \mathbf{c}_{v,1} \\ \vdots \\ \mathbf{c}_{v,M} \\ \mathbf{c}_{p,1} \\ \vdots \\ \mathbf{c}_{p,M} \end{Bmatrix} = \begin{Bmatrix} \alpha_1(s_{d,j}) \\ \vdots \\ \alpha_m(s_{d,j}) \end{Bmatrix} \quad (3.97)$$

or in compact form:

$$\mathbf{P}_j \mathbf{y} = \mathbf{a}_j \quad j = p+1, \dots, 2N \quad (3.98)$$

For the unchanged  $2N - p$  poles, generalising the single input case it results:

$$\left[ \mathbf{b}_1 (s_i \mathbf{c}_{v,1}^T + \mathbf{c}_{p,1}^T) + \dots + \mathbf{b}_M (s_i \mathbf{c}_{v,M}^T + \mathbf{c}_{p,M}^T) \right] \mathbf{\Psi}_i = \mathbf{0} \quad i = p+1, \dots, 2N \quad (3.99)$$

and in matrix form:

$$\begin{bmatrix} s_i \mathbf{\Psi}_M^T & & & \mathbf{\Psi}_M^T & & \\ & \ddots & & & \ddots & \\ & & s_i \mathbf{\Psi}_M^T & & & \mathbf{\Psi}_M^T \end{bmatrix} \begin{Bmatrix} \mathbf{c}_{v,1} \\ \vdots \\ \mathbf{c}_{v,M} \\ \mathbf{c}_{p,1} \\ \vdots \\ \mathbf{c}_{p,M} \end{Bmatrix} = \mathbf{0} \quad (3.100)$$

or in compact form as:

$$\mathbf{Q}_j \mathbf{y} = \mathbf{0} \quad j = p+1, \dots, 2N \quad (3.101)$$

For complete the pole placement by the method of receptance the procedure consist in choose arbitrarily  $\alpha_j(s_{d,i})$   $i=1,\dots,p$   $j=1,\dots,M$  and compute  $\Psi_{cl,i}$  using Eq. (3.96) and then compute the PD control gain matrices  $C_p$  and  $C_v$  using both the relations related to the assigned poles Eq. (3.98) and unchanged poles Eq. (3.101):

$$\begin{bmatrix} \mathbf{P}_1 \\ \vdots \\ \mathbf{P}_p \\ \mathbf{Q}_{p+1} \\ \vdots \\ \mathbf{Q}_{2N} \end{bmatrix} \begin{bmatrix} \mathbf{c}_{v,1} \\ \vdots \\ \mathbf{c}_{v,M} \\ \mathbf{c}_{p,1} \\ \vdots \\ \mathbf{c}_{p,M} \end{bmatrix} = \begin{bmatrix} \mathbf{a}_1 \\ \vdots \\ \mathbf{a}_p \\ \mathbf{0} \\ \vdots \\ \mathbf{0} \end{bmatrix} \quad (3.102)$$

### 3.3.2 State space feedback linearisation

Standard input-output feedback linearisation relates to smooth nonlinearities in the system or in the input, which means that there are no non-differentiable points in the nonlinear characteristic.

The method has found application in numerous engineering fields including the following: robotics, to control the trajectory and the body posture of a mobile robot [131–134]; electric motors, to stabilise the position and velocity of the rotor and to control the voltage [135–141]; in fuel cells, to control the pressure of hydrogen and oxygen [142]; and in actuation systems with valve nonlinearities [143,144]. In aerospace engineering the technique is used to control drones [145–147] and to suppress wing flutter [148,149]. In [150] wing flutter was experimentally suppressed using feedback linearisation with a model including a real-time aeroelastic states estimation.

More recently, in [151] feedback linearisation was experimentally applied to achieve precise beam-tip position control in a nonlinear two DOFs flexible-beam sensor. A similar position control application was presented in [152], where feedback linearisation is applied to ensure accurate path following of a space manipulator in the presence of joint flexibilities, which also had the effect of mitigating vibrations transmitted to the spacecraft supporting the manipulator.

Although feedback linearisation is a well-known technique in the control community, it is not widely applied in vibration problems. It has the advantage of transform a nonlinear system model in the equivalent linear system, thereby enabling the avoidance of the complicated mathematics associated with nonlinear problems.

Feedback linearisation can be applied in two different ways: the “input-state linearisation”, where the full state equation is linearised and “input-output linearisation”, where the emphasis is on linearising the input-output map even if the state equation is only partially linearised.

This paragraph is focused on the input-output linearisation theory, which is numerically and experimentally implemented in § 11.

Usually in the control textbook the method is approached from a first-order equation of motion of the system [127,128], and repeated differentiations of the state using the Lie-algebra notation [153] are needed.

The classic theory of feedback in second order form was simplified from Jiffri et al. in [148] in the cases of application to nonlinear structural or aero-elastic vibration nonlinear problem, showing that the Lie-algebra is not necessary in the case of structural systems. The same theory can be found in first order form in [154].

Feedback linearisation theory is briefly introduced in the following, both using first and second order form.

The equation of motion of elasto-mechanical or aeroelastic nonlinear systems in second order form can be written as:

$$\mathbf{M}\ddot{\mathbf{x}} + \mathbf{C}\dot{\mathbf{x}} + \mathbf{K}\mathbf{x} + \mathbf{f}_{nl}(\mathbf{x}, \dot{\mathbf{x}}) = \mathbf{B}\mathbf{u}(t) \quad (3.103)$$

where  $\mathbf{M}, \mathbf{C}, \mathbf{K} \in \mathbb{R}^{N \times N}$  are respectively the mass, stiffness and viscous damping matrices,  $\mathbf{x}, \dot{\mathbf{x}}, \ddot{\mathbf{x}} \in \mathbb{R}^{N \times 1}$  are the displacements, velocity and acceleration vectors,  $\mathbf{f}_{nl}(\mathbf{x}, \dot{\mathbf{x}}) \in \mathbb{R}^{N \times 1}$  is the nonlinear force depending on displacements  $\mathbf{x}$  and velocity  $\dot{\mathbf{x}}$ ,  $\mathbf{u}(t) \in \mathbb{R}^{M \times 1}$  is the vector of physical input applied to the nonlinear system and  $\mathbf{B} \in \mathbb{R}^{N \times M}$  is a selector matrix to localise the application DOFs of the  $M$  inputs.  $N$  is the number of DOFs of the system (or the number of measured DOF, i.e. the number of sensors) and  $M$  is the number of actuators.

Feedback linearisation is an exact method; it let to cancel the whole open loop dynamic and it results in a set of independent linear SDOF systems.

Eq. (3.103) can be written as:

$$\ddot{\mathbf{x}} = \mathbf{f}(\mathbf{x}, \dot{\mathbf{x}}) + \mathbf{G}\mathbf{u}(t) \quad (3.104)$$

where  $\mathbf{f}(\mathbf{x}, \dot{\mathbf{x}}) \in \mathbb{R}^{N \times 1}$  and  $\mathbf{G} \in \mathbb{R}^{N \times M}$  are:

$$\mathbf{f}(\mathbf{x}, \dot{\mathbf{x}}) = \mathbf{\Psi}\mathbf{x} + \mathbf{\Phi}\dot{\mathbf{x}} + \mathbf{\Omega}\mathbf{f}_{nl}, \quad \mathbf{\Psi} = -\mathbf{M}^{-1}\mathbf{K}, \quad \mathbf{\Phi} = -\mathbf{M}^{-1}\mathbf{C}, \quad \mathbf{\Omega} = -\mathbf{M}^{-1} \quad (3.105)$$

$$\mathbf{\Psi}, \mathbf{\Phi}, \mathbf{\Omega} \in \mathbb{R}^{N \times N} \quad (3.106)$$

$$\mathbf{G} = -\mathbf{M}^{-1}\mathbf{B}$$

The equation of motion Eq. (3.103) in first order formulation becomes:

$$\dot{\mathbf{v}} = \underline{\mathbf{f}}(\mathbf{v}) + \underline{\mathbf{G}}\mathbf{u}(t) \quad (3.107)$$

where  $\mathbf{v}, \dot{\mathbf{v}} \in \mathbb{R}^{2N \times 1}$ ,  $\underline{\mathbf{f}}(\mathbf{v}) \in \mathbb{R}^{2N \times 1}$  and  $\underline{\mathbf{G}} \in \mathbb{R}^{2N \times M}$  are defined as:

$$\mathbf{v} = \begin{Bmatrix} \mathbf{x} \\ \dot{\mathbf{x}} \end{Bmatrix} \quad (3.108)$$

$$\underline{\mathbf{f}}(\mathbf{v}) = \begin{Bmatrix} [\mathbf{0} \quad \mathbf{I}] \mathbf{v} \\ [\boldsymbol{\Psi} \quad \boldsymbol{\Phi}] \mathbf{v} + \boldsymbol{\Omega} \mathbf{f}_{nl} \end{Bmatrix} \quad (3.109)$$

$$\underline{\mathbf{G}} = \begin{bmatrix} \mathbf{0} \\ \mathbf{G} \end{bmatrix} \quad (3.110)$$

The physical input  $\mathbf{u}(t)$  is designed to neutralize the effect of the nonlinearity. This can be achieved in full or partially: in the first case is called complete input-output feedback linearisation, the second case is known as partial input-output feedback linearisation.

### Complete input-output linearisation

The complete input-output feedback linearisation lets to linearise globally the system. It is possible only if the number of sensors and actuators is the same of the system dimension,  $N = M$ .

The aim is to provide a physical input to the system  $\mathbf{u}(t)$  so that the complete open-loop dynamics or only the nonlinearity is cancelled out and replaced by the desired dynamics.

### Second order form

The physical input  $\mathbf{u}(t)$  is chosen so that it cancels out the nonlinearity:

$$\mathbf{u}(t) = \mathbf{G}^{-1} [\bar{\mathbf{u}}(t) - \mathbf{f}(\mathbf{x}, \dot{\mathbf{x}})] \quad (3.111)$$

where  $\bar{\mathbf{u}}(t) \in \mathbb{R}^{(M=N) \times 1}$  is the virtual input.

Substituting Eq. (3.111) in Eq. (3.104) the nonlinearity is removed from the system and also the linear open loop dynamic is cancelled:

$$\begin{pmatrix} \ddot{x}_1 \\ \ddot{x}_2 \\ \vdots \\ \ddot{x}_N \end{pmatrix} = \begin{pmatrix} \bar{u}_1 \\ \bar{u}_2 \\ \vdots \\ \bar{u}_N \end{pmatrix} \quad (3.112)$$

The result is a linearised system of independent, second-order, SDOF equations. This is a special case in which the original coordinates  $\mathbf{x}$  and the linearised one  $\mathbf{z}$  are the same:  $\mathbf{x} = \mathbf{z}$ .

The choice of the artificial input  $\bar{\mathbf{u}}(t)$  depends upon the control objective. For example, the assignment of a pair of complex conjugate poles in each of the SDOF system in Eq. (3.112) to avoid resonance (Pole Placement [155]).

Whatever the control objective is, it will be result in the determination of the gains defined in terms of negative feedback as:

$$\begin{aligned}\bar{u}_1(t) &= -[\varsigma_1 \quad \nu_1] \{x_1 \quad \dot{x}_1\}^T \\ &\vdots \\ \bar{u}_N(t) &= -[\varsigma_N \quad \nu_N] \{x_N \quad \dot{x}_N\}^T\end{aligned}\quad (3.113)$$

where  $\varsigma_i$  and  $\nu_i$   $1 < i < M = N$  are control gains.

If the physical input  $\mathbf{u}(t)$  is chosen so that only the nonlinearity (not the entire open loop dynamics) is cancelled out, then Eq. (3.111) would be replaced by:

$$\mathbf{u}(t) = \mathbf{G}^{-1} (\bar{\mathbf{u}}(t) - \mathbf{\Omega} \mathbf{f}_{nl}) \quad (3.114)$$

and the linearised system would remain coupled:

$$\begin{Bmatrix} \bar{u}_1 \\ \bar{u}_2 \\ \vdots \\ \bar{u}_N \end{Bmatrix} = - \begin{bmatrix} \varsigma_{11} & \nu_{11} & \varsigma_{12} & \nu_{12} & \cdots & \varsigma_{1N} & \nu_{1N} \\ \varsigma_{21} & \nu_{21} & \varsigma_{22} & \nu_{22} & \cdots & \varsigma_{2N} & \nu_{2N} \\ \vdots & \vdots & \vdots & \vdots & \ddots & \vdots & \vdots \\ \varsigma_{N1} & \nu_{N1} & \varsigma_{N2} & \nu_{N2} & \cdots & \varsigma_{NN} & \nu_{NN} \end{bmatrix} \begin{Bmatrix} x_1 \\ \dot{x}_1 \\ x_2 \\ \dot{x}_2 \\ \vdots \\ x_N \\ \dot{x}_N \end{Bmatrix} \quad (3.115)$$

where  $\varsigma_{i,j}$  and  $\nu_{i,j}$   $1 < i, j < M = N$  are control gains. There are a greater number of control gains in Eq. (3.115) than in Eq. (3.113), which means that there is more control flexibility. The great number of gains might be used, for example, to assign the poles and eigenvectors.

### First order form

In first order formulation the complete input-output feedback linearisation is performed choosing the displacement as output variables:

$$\mathbf{y} = [\mathbf{I} \quad \mathbf{0}] \mathbf{v} \quad (3.116)$$

When the complete dynamics of the system is cancelled out, as in Eq. (3.111), the  $j^{th}$   $1 \leq j \leq N$  linearised system in first order formulation results in:

$$\chi_{2j-1} = y_j = x_j = v_j \quad (3.117)$$

$$\dot{\chi}_{2j} = \dot{y}_j = \dot{x}_j = \dot{v}_j = v_{j+N}$$

$$\begin{Bmatrix} \dot{\chi}_{2j-1} \\ \dot{\chi}_{2j} \end{Bmatrix} = \begin{bmatrix} 0 & 1 \\ 0 & 0 \end{bmatrix} \begin{Bmatrix} \chi_{2j-1} \\ \chi_{2j} \end{Bmatrix} + \begin{bmatrix} 0 \\ 1 \end{bmatrix} \bar{u}_j(t) \quad (3.118)$$

$$\bar{u}_j(t) = -[\varsigma_j \quad v_j] \begin{Bmatrix} \chi_j \\ \chi_{j+1} \end{Bmatrix}^T \quad (3.119)$$

where  $\varsigma_i$  and  $v_i$   $1 < i < M = N$  are the same control gains of Eq. (3.113) and  $\chi$  is the vector of linearised coordinates. The complete linearised system result in:

$$\dot{\chi} = \mathbf{A}\chi + \mathbf{B}\bar{\mathbf{u}}(t) \quad (3.120)$$

where

$$\mathbf{A}(2j-1, 2j) = 1, 1 \leq j \leq N \text{ all the other entries } 0 \quad (3.121)$$

$$\mathbf{B}(2j, j) = 1, 1 \leq j \leq N \text{ all the other entries } 0 \quad (3.122)$$

$$\mathbf{u}(t) = \mathbf{G}(\bar{\mathbf{u}}(t) - \mathbf{f}_{N+1:2N}) \quad (3.123)$$

The transformation matrix  $\mathbf{T}$  which maps the linearised coordinates  $\chi$  in the original one  $\mathbf{v}$  is:

$$\chi = \mathbf{T}\mathbf{v}, \mathbf{T}(2j-1, j) = \mathbf{T}(2j, j+N) = 1, 1 \leq j \leq N \text{ all the other entries } 0 \quad (3.124)$$

The relation between the linearised coordinate in second order form  $\mathbf{z}$  and in first order form  $\chi$ , is given by:

$$z_j = \chi_{2j-1} \text{ with } 1 \leq j \leq N \quad (3.125)$$

### Partial input-output linearisation

Partial input-output feedback linearisation linearise only some DOFs of a system, therefore there is a part which remains nonlinear. The number of actuators  $M$  is fewer than the number of DOFs  $N$ ,  $M < N$ .

### Second order form

Eq. (3.104) can be rewritten as:

$$\begin{Bmatrix} \ddot{x}_1 \\ \vdots \\ \ddot{x}_M \\ \ddot{x}_{M+1} \\ \vdots \\ \ddot{x}_N \end{Bmatrix} = \begin{Bmatrix} f_1(x, \dot{x}) \\ \vdots \\ f_M(x, \dot{x}) \\ f_{M+1}(x, \dot{x}) \\ \vdots \\ f_N(x, \dot{x}) \end{Bmatrix} + \begin{bmatrix} g_{1,1} & \cdots & g_{1,M} \\ \vdots & & \vdots \\ g_{M,1} & \cdots & g_{M,M} \\ g_{M+1,1} & \cdots & g_{M+1,M} \\ \vdots & & \vdots \\ g_{N,1} & \cdots & g_{N,M} \end{bmatrix} \begin{Bmatrix} u_1(t) \\ \vdots \\ u_M(t) \end{Bmatrix} \quad (3.126)$$

or in compact form

$$\begin{Bmatrix} \ddot{\mathbf{x}}_M \\ \ddot{\mathbf{x}}_{M-N} \end{Bmatrix} = \begin{Bmatrix} \mathbf{f}_M(\mathbf{x}, \dot{\mathbf{x}}) \\ \mathbf{f}_{M-N}(\mathbf{x}, \dot{\mathbf{x}}) \end{Bmatrix} + \begin{bmatrix} \mathbf{G}_M \\ \mathbf{G}_{M-N} \end{bmatrix} \mathbf{u}(t) \quad (3.127)$$

where in this case  $\mathbf{G} \in \mathbb{R}^{N \times M}$ . The coordinate transformation  $\mathbf{T}$  which maps the nonlinear system from the original coordinate set  $\mathbf{x}$  into the new linearised coordinates  $\mathbf{z}$  may be expressed as:

$$\{z_1 \ z_2 \ \cdots \ z_M\}^T = \{x_1 \ x_2 \ \cdots \ x_M\}^T \quad (3.128)$$

which is the same of the complete input-output feedback linearisation, with the exception that it is valid for only  $M$  DOFs, because there are only  $M < N$  actuators.

The bottom portion of the Eq. (3.126) is defined as internal dynamics.

Further  $N - M$   $\mathbf{z}$  coordinates are needed. These are chosen as coefficients of the orthonormal basis of the null space of  $\mathbf{G}^T$  so that:

$$\{x_1 \ \cdots \ x_N\}^T = \mathbf{V} \{z_{M+1} \ \cdots \ z_N\}^T \quad (3.129)$$

where  $\mathbf{V} \in \mathbb{R}^{N \times (N-M)}$  is the transformation matrix and satisfy the following properties:

$$\mathbf{V}^T \mathbf{V} = \mathbf{I}_{(N-M) \times (N-M)}, \mathbf{V}^T \mathbf{G} = \mathbf{0} \quad (3.130)$$

Finally the transformation matrix  $\mathbf{T}$  which maps the nonlinear system from the original coordinate set  $\mathbf{x}$  into the new linearised coordinates  $\mathbf{z}$  may be expressed as:

$$\mathbf{z} = \begin{bmatrix} \mathbf{I} & \mathbf{0} \\ \mathbf{V}^T & \end{bmatrix} \mathbf{x} \quad (3.131)$$

where  $\mathbf{I} \in \mathbb{R}^{M \times M}$  is an identity matrix and  $\mathbf{0} \in \mathbb{R}^{M \times (N-M)}$  is a zero matrix.

The actual input  $\mathbf{u}(t)$  which eliminates the nonlinearity can be expressed as:

$$\mathbf{u}(t) = \mathbf{G}_M^{-1} [\bar{\mathbf{u}}(t) - \mathbf{f}_M(\mathbf{x}, \dot{\mathbf{x}})] \quad (3.132)$$

The substitution of Eq. (3.132) into the upper portion of Eq. (3.127) leads to  $M$  independent linear second-order systems:

$$\begin{Bmatrix} \ddot{z}_1 \\ \ddot{z}_2 \\ \vdots \\ \ddot{z}_M \end{Bmatrix} = \begin{Bmatrix} \ddot{x}_1 \\ \ddot{x}_2 \\ \vdots \\ \ddot{x}_M \end{Bmatrix} = \begin{Bmatrix} \bar{u}_1(t) \\ \bar{u}_2(t) \\ \vdots \\ \bar{u}_M(t) \end{Bmatrix} \quad (3.133)$$

The artificial input  $\bar{\mathbf{u}}(t)$  can be computed as in Eq. (3.113), but only for the  $N - M$  first  $M$  coordinates.

The remaining coordinated can be computed from Eq. (3.129):

$$\{\ddot{z}_{M+1} \quad \cdots \quad \ddot{z}_N\}^T = \mathbf{V}^T \{\ddot{x}_1 \quad \ddot{x}_M\}^T \quad (3.134)$$

Now substituting Eq. (3.127) in Eq. (3.134):

$$\begin{Bmatrix} \ddot{z}_{M+1} \\ \vdots \\ \ddot{z}_N \end{Bmatrix} = \mathbf{V}^T \begin{Bmatrix} f_1(\mathbf{z}, \dot{\mathbf{z}}) \\ \vdots \\ f_N(\mathbf{z}, \dot{\mathbf{z}}) \end{Bmatrix} + \mathbf{V}^T \mathbf{G} \begin{Bmatrix} u_1 \\ \vdots \\ u_M \end{Bmatrix} \quad (3.135)$$

and remembering the proprieties of the matrix  $\mathbf{V}$  in Eq. (3.130):

$$\begin{Bmatrix} \ddot{z}_{M+1} \\ \vdots \\ \ddot{z}_N \end{Bmatrix} = \mathbf{V}^T \begin{Bmatrix} f_1(\mathbf{z}, \dot{\mathbf{z}}) \\ \vdots \\ f_N(\mathbf{z}, \dot{\mathbf{z}}) \end{Bmatrix} \quad (3.136)$$

Eq. (3.136) ensures uncontrollability of the nonlinear internal dynamics.

The stability on the system is determined by the zero dynamics, obtained by setting to zero in Eq. (3.136) the external coordinates  $(z_1 \quad \cdots \quad z_M)$  of the partially linearised system in Eq. (3.133).

The stability of the zero dynamics is a necessary condition to apply the partial feedback linearisation; when the zero dynamics, generally nonlinear, are found to be globally stable, then the desired control behaviour is unaffected by the nonlinearity confined to the internal dynamics.

### First order form

The same procedure can be applied in first-order form, when  $M < N$ . Only  $2M$  states of the first order system are linearised. The remaining  $2(M - N)$  states constitute the so-called internal dynamics, which is uncontrollable.



Partial feedback linearisation is stable only if the internal dynamics is stable, this can be checked by studying the stability of the zero dynamics, which is the internal dynamics where all the controllable states are set to zero [127].

The transformation matrix of the partially linearised states  $\mathbf{T}_{pl} \in \mathbb{R}^{2M \times 2N}$  is obtained as in the complete input-output feedback linearisation, Eq. (3.124), for the first  $2M$  states. The global transformation matrix  $\mathbf{T}$  must be non-singular, thus the internal dynamics coordinates is orthogonal to  $\underline{\mathbf{G}}$ .

$$\chi = \mathbf{T}\mathbf{v} \quad (3.137)$$

The latter conditions are satisfied by a transformation matrix  $\mathbf{T}$  having the following structure:

$$\mathbf{T} = \begin{bmatrix} \mathbf{T}_{pl} \\ \mathbf{0} \quad \mathbf{I} \quad \mathbf{0} \\ \mathbf{0} \quad \ker(\mathbf{G}) \end{bmatrix} \quad (3.138)$$

where the null  $\mathbf{0}$  and identity  $\mathbf{I}$  matrices are of appropriate dimensions and  $\ker(\mathbf{G}) \in \mathbb{R}^{(N-M) \times N}$  is the null space of matrix  $\mathbf{G}$  defined as:

$$\mathbf{G} \ker(\mathbf{G}) = \mathbf{0} \quad (3.139)$$

The relation between the linearised coordinates in first  $\chi$  and second order form  $\mathbf{z}$  partial input-output feedback linearisation is the same presented in Eq. (3.125) for the linearised coordinates.

### 3.3.3 Feedback linearisation via method of receptances

The classical feedback linearisation method, already described in § 3.3.2, requires the numerical model of the system. It is generally applicable to under-actuated systems and, by an application of a linear transformation, the system is separated into two parts. An artificial input is applied to the first part that renders it linear and enables classical linear control methods, such as pole placement, to be applied. The second part generally remains nonlinear and is rendered uncontrollable by the transformation. The stability of the second part is guaranteed when the zero dynamics are stable. The dynamics of the second part with the controlled coordinates set to zero and subject to arbitrary disturbance.

The method of receptances, presented in § 3.3.1 is an active control method that makes use of measurements acquired directly from the test structure and therefore eliminates the necessity of evaluating the system mass  $\mathbf{M}$ , damping  $\mathbf{C}$  and stiffness  $\mathbf{K}$  matrices.

The theory of feedback linearisation by the receptance method was recently presented in [156], and it is here briefly summarised for purposes of completeness.

Considering the equation of motion of a nonlinear system as in Eq. (11.11), it can be written in Laplace domain ‘ $s$ ’ as:

$$[\mathbf{Z}(s)]\mathbf{x}(s) + \mathbf{F}_{nl}(\mathbf{X}, s) = \mathbf{B}\mathbf{u}(s) \quad (3.140)$$

where  $\mathbf{Z}(s) \in \mathbb{C}^{N \times N}$  is the DSM of the underlying linear system,  $\mathbf{F}_{nl}(\mathbf{X}, s) \in \mathbb{C}^{N \times 1}$  is the sinusoidal input DF approximation [157] of the nonlinearity undergoing limit cycle oscillation of amplitude  $\mathbf{X}$ ,  $\mathbf{B} \in \mathbb{R}^{N \times M}$  is the force distribution matrix and  $\mathbf{u}(s) \in \mathbb{C}^{M \times 1}$  is the vector of input.  $N$  is the number of DOFs and  $M$  is the number of actuators.

Eq. (3.140) can be re-written in compact form as:

$$\mathbf{Z}_{nl}(\mathbf{X}, s)\mathbf{x}(s) = \mathbf{B}\mathbf{u}(s) \quad (3.141)$$

where  $\mathbf{Z}_{nl}(\mathbf{X}, s) \in \mathbb{C}^{N \times N}$  is the nonlinear DSM under limit cycle oscillation of amplitude  $\mathbf{X}$ .

Finally, the problem can be written using the receptances formulation as:

$$\mathbf{x}(s) = \mathbf{H}_{nl}(\mathbf{X}, s)\mathbf{B}\mathbf{u}(s) \quad (3.142)$$

where  $\mathbf{H}_{nl}(\mathbf{X}, s) \in \mathbb{C}^{N \times N}$  is the nonlinear FRM at constant amplitude of oscillation across the nonlinearity and it is defined as:

$$\mathbf{Z}_{nl}(\mathbf{X}, s) = [\mathbf{H}_{nl}(\mathbf{X}, s)]^{-1} \quad (3.143)$$

The outputs  $\mathbf{y} \in \mathbb{R}^{M \times 1}$  of the partial input-output feedback linearisation are chosen as  $M$  displacement states:

$$\mathbf{y} = \mathbf{x}_1 \quad (3.144)$$

where  $\mathbf{x}_1 \in \mathbb{R}^{M \times 1}$  is the first part of the displacement vector  $\mathbf{x}$ :

$$\mathbf{x} = [\mathbf{x}_1 \quad \mathbf{x}_2]^T \quad (3.145)$$

The system in Eq. (3.140) can be partially linearised using a transformation matrix  $\mathbf{T}$  between the linearised  $\mathbf{z}$  coordinates and nonlinear one  $\mathbf{x}$  and an input vector  $\mathbf{u}(t)$  appropriate to cancel out the open loop dynamics and assigned the desired dynamics.

$$\mathbf{z} = \mathbf{T}\mathbf{x} \quad (3.146)$$

The transformation matrix  $\mathbf{T}$  is defined with the purpose of separating the system into two parts, controllable and uncontrollable, known as normal form.

$$\mathbf{T} = \begin{bmatrix} \mathbf{I} & \mathbf{0} \\ \mathbf{V}^T & \end{bmatrix} \quad (3.147)$$

where  $\mathbf{I}$  is the identity matrix of dimension  $M$ ,  $\mathbf{0} \in \mathbb{R}^{(N-M) \times N}$  is the null matrix and  $\mathbf{V} \in \mathbb{R}^{N \times M}$  is a matrix following the properties:

$$\mathbf{V}^T \mathbf{B} = \mathbf{0}, \quad \mathbf{V}^T \mathbf{V} = \mathbf{I} \quad (3.148)$$

Substituting Eq. (3.142) in Eq. (3.146) the system can be written in linearised coordinates  $\mathbf{z}$  as:

$$\mathbf{z}(s) = \mathbf{T}\mathbf{x}(s) = (\mathbf{T}\mathbf{H}_{nl}(\mathbf{X}, s)\mathbf{T}^{-1})\mathbf{T}\mathbf{B}\mathbf{u}(s) \quad (3.149)$$

$$\tilde{\mathbf{H}}_{nl}(\mathbf{Z}_0, s) = \mathbf{T}\mathbf{H}_{nl}(\mathbf{X}, s)\mathbf{T}^{-1} \quad (3.150)$$

where  $\tilde{\mathbf{H}}_{nl}(\mathbf{Z}_0, s) \in \mathbb{C}^{N \times N}$  is the nonlinear FRM and  $\mathbf{Z}_0 = \mathbf{T}\mathbf{X}$  is the amplitude of oscillation of limit cycle in the new set of coordinates  $\mathbf{z}$ . The force distribution matrix  $\mathbf{B}$  can be written as:

$$\mathbf{B} = \begin{bmatrix} \mathbf{B}_1 \\ \mathbf{B}_2 \end{bmatrix} \quad (3.151)$$

where  $\mathbf{B}_1 \in \mathbb{R}^{M \times 1}$  and  $\mathbf{B}_2 \in \mathbb{R}^{(N-M) \times 1}$  are respectively the upper and lower portion of the distribution matrix  $\mathbf{B}$ .

Remembering the definition of the transformation matrix  $\mathbf{T}$  in Eq. (3.147) and the properties of the matrix  $\mathbf{V}$  in Eq. (3.148), Eq. (3.149) can be re-written as:

$$\mathbf{z}(s) = \tilde{\mathbf{H}}_{nl}(\mathbf{Z}_0, s) \begin{bmatrix} \mathbf{B}_1 \mathbf{u}(s) \\ \mathbf{0} \end{bmatrix} \quad (3.152)$$

and using partitioning consistent with that in Eq. (3.145) and Eq. (3.151):

$$\begin{bmatrix} \mathbf{z}_1(s) \\ \mathbf{z}_2(s) \end{bmatrix} = \begin{bmatrix} (\tilde{\mathbf{H}}_{nl}(\mathbf{Z}_0, s))_{11} & (\tilde{\mathbf{H}}_{nl}(\mathbf{Z}_0, s))_{12} \\ (\tilde{\mathbf{H}}_{nl}(\mathbf{Z}_0, s))_{21} & (\tilde{\mathbf{H}}_{nl}(\mathbf{Z}_0, s))_{22} \end{bmatrix} \begin{bmatrix} \mathbf{B}_1 \mathbf{u}(s) \\ \mathbf{0} \end{bmatrix} \quad (3.153)$$

Inverting Eq. (3.153) leads to,

$$\begin{bmatrix} \mathbf{B}_1 \mathbf{u}(s) \\ \mathbf{0} \end{bmatrix} = \begin{bmatrix} \left( \left( \tilde{\mathbf{H}}_{nl}(\mathbf{Z}_0, s) \right)^{-1} \right)_{11} & \left( \left( \tilde{\mathbf{H}}_{nl}(\mathbf{Z}_0, s) \right)^{-1} \right)_{12} \\ \left( \left( \tilde{\mathbf{H}}_{nl}(\mathbf{Z}_0, s) \right)^{-1} \right)_{21} & \left( \left( \tilde{\mathbf{H}}_{nl}(\mathbf{Z}_0, s) \right)^{-1} \right)_{22} \end{bmatrix} \begin{bmatrix} \mathbf{z}_1(s) \\ \mathbf{z}_2(s) \end{bmatrix} \quad (3.154)$$

If the control input is chosen as:

$$\mathbf{u}(s) = \mathbf{B}_1^{-1} \left[ \tilde{\mathbf{u}}(s) + \left( \left( \tilde{\mathbf{H}}_{nl}(\mathbf{Z}_0, s) \right)^{-1} \right)_{11} \mathbf{z}_1(s) + \left( \left( \tilde{\mathbf{H}}_{nl}(\mathbf{Z}_0, s) \right)^{-1} \right)_{12} \mathbf{z}_2(s) - \text{diag}(s^2) \mathbf{z}_1(s) \right] \quad (3.155)$$

the first row of Eq. (3.154) is linearised and may be written as:

$$\text{diag}(s^2) \mathbf{z}_1(s) = \bar{\mathbf{u}}(s) \quad (3.156)$$

where  $\bar{\mathbf{u}}(s) \in \mathbb{C}^{M \times 1}$  is the artificial input to the system, required to assign the desired dynamics.

It should be noted that Eq. (3.155) must be implemented in the time domain, which requires the form of the nonlinearity to be known, either explicitly or by inversion of a DF, which can be analytical or derivate by a series of slow-sweep amplitude-controlled sine-excitation tests.

Desired pole  $\mu_{i,d}$   $1 \leq i \leq M$  can be assigned using the method of receptances:

$$\bar{\mathbf{u}}(s) = -\left( s\mathbf{F}^T(\mu_{i,d}) + \mathbf{G}^T(\mu_{i,d}) \right) \mathbf{z}_1(s) \quad (3.157)$$

where  $\mathbf{F} \in \mathbb{R}^{M \times M}$  and  $\mathbf{G} \in \mathbb{R}^{M \times M}$  are control gains defined in [120] as:

$$\mathbf{F}(\mu_{i,d}) = \text{diag}\left(-(\mu_{i,d} + \mu_{i,d}^*)\right) = \text{diag}\left(2\zeta_{i,d}\omega_{n_{i,d}}\right) \quad (3.158)$$

$$\mathbf{G}(\mu_{i,d}) = \text{diag}\left(\Re(\mu_{i,d}\mu_{i,d}^*)\right) = \text{diag}\left(\omega_{n_{i,d}}^2\right) \quad (3.159)$$

Substituting Eq. (3.157) in Eq. (3.156), the dynamics of the controlled part becomes:

$$(s^2\mathbf{I} + s\mathbf{F}^T + \mathbf{G}^T) \mathbf{z}_1(s) = \mathbf{0} \quad (3.160)$$

which represents a set of  $M$  uncoupled and linear SDOF systems, with the desired poles  $\mu_{i,d}$ .

### Stability of the zero dynamics

For the close-loop system to be stable, not only must the poles of the controllable part be stable, but also the so-called zero dynamics  $\mathbf{z}_{zd}$  must be

stable. The zero dynamics  $\mathbf{z}_{zd}$  represent the dynamic behaviour of the of the uncontrollable portion of the system  $\mathbf{z}_2$  (known as the internal dynamics  $\mathbf{z}_{in}$ ) when the controlled DOFs  $\mathbf{z}_1$  are set to zero.

Classical feedback linearisation requires checking the stability of all the equilibrium point of the zero dynamics  $\mathbf{z}_{zd}$ , which is in general nonlinear. This can be mathematically difficult and even more if the nonlinearity is non-smooth, as shown in § 11.4.2.

The stability of the zero dynamics can alternatively be verified using the receptance method with a DF approach [157], either using an analytical DF or by carrying out a series of slow-sweep amplitude-controlled sine-excitation tests.

The alternative method to study the zero dynamic was presented [156].

Considering the system equation in the form of Eq. (3.153), the zero dynamics is found by setting to zero the controlled DOFs  $\mathbf{z}_1$ . A disturb  $\tilde{\delta}$  on the uncontrolled DOFs  $\mathbf{z}_2$  must not destabilise the system if the zero dynamics is stable:

$$\begin{bmatrix} \mathbf{0} \\ \mathbf{z}_2(s) \end{bmatrix} = \begin{bmatrix} (\tilde{\mathbf{H}}_{nl}(\mathbf{Z}_0, s))_{11} & (\tilde{\mathbf{H}}_{nl}(\mathbf{Z}_0, s))_{12} \\ (\tilde{\mathbf{H}}_{nl}(\mathbf{Z}_0, s))_{21} & (\tilde{\mathbf{H}}_{nl}(\mathbf{Z}_0, s))_{22} \end{bmatrix} \begin{bmatrix} \mathbf{B}_1 \mathbf{u}(s) \\ \tilde{\delta} \end{bmatrix} \quad (3.161)$$

Substituting the first row of Eq. (3.161) in its second row and considering that the matrix  $\mathbf{B}_1$  is invertible when  $\mathbf{T}$  is invertible, proof. in [156], (i.e. feedback linearisation can be applied) the transfer function between the zero dynamics  $\mathbf{z}_{zd}$  and the disturb  $\tilde{\delta}$  becomes:

$$\mathbf{z}_{zd} = \mathbf{z}_{in}|_{\mathbf{z}_1=0} = \mathbf{z}_2|_{\mathbf{z}_1=0} = \left[ (\tilde{\mathbf{H}}_{nl}(\mathbf{Z}_0, s))_{22} - (\tilde{\mathbf{H}}_{nl}(\mathbf{Z}_0, s))_{21} (\tilde{\mathbf{H}}_{nl}(\mathbf{Z}_0, s))_{11}^{-1} (\tilde{\mathbf{H}}_{nl}(\mathbf{Z}_0, s))_{12} \right] \tilde{\delta} \quad (3.162)$$

The poles of the transfer function in Eq. (3.162) must be stable for the range of all amplitudes  $\mathbf{Z}_0$  of vibrations of the system, i.e. negative real part, to guarantee a stable zero dynamics  $\mathbf{z}_{zd}$ , which is required for the application of the feedback linearisation method.

The test of the stability does not require any more complex math, because the transfer function can be assembled from  $\tilde{\mathbf{H}}_{nl}(\mathbf{Z}_0, s)$ , which can be computed using Eq. (3.150).  $\tilde{\mathbf{H}}_{nl}(\mathbf{X}, s)$  is the combination of the linear receptance matrix  $\mathbf{H}(s)$  and the DF approximation of the nonlinear force  $\mathbf{F}_{nl}(\mathbf{X}, s)$  is obtained from several slow-sweep at different amplitude  $\mathbf{X}$ , using Sherman–Morrison formula [130,158]. The nonlinear force  $\mathbf{F}_{nl}(\mathbf{X}, s)$  can be known analytically or using inverse DF approach [159,160].

### 3.4 Conclusions

The identification of the system model is very important for both predict the response of the passive system and implement active control strategy to change its behaviour. Several robust identification methods for mass and stiffness matrices are established, while the damping matrix is usually modelled as an equivalent matrix which dissipate the same amount of energy. Several methods for the identification of spatial distribution of damping from experimental frequency domain measures were presented. These methods can be collected into two groups: 1) spatial damping identification from system FRF and 2) spatial damping identification from modal properties. The identified damping matrix are usually equivalent damping matrix and do not consider the physics of the system.

The Che-Ju-Tsuei method is one of the most promising method [76] and it is the base on the novel damping identification method presented in § 4.

The identified of the damping matrix of the system can be used together with mass matrix to compute the system damping ratio and understand the vibrational behaviour of the system. Passive damping matrix can be designed in some cases to obtain the desired vibrational behaviour and suppress vibration. When vibration suppression can not be achieved with passive solution or more stringent requirements must be met active control strategies can be used.

The state space feedback linearisation and method of receptance are presented for pole placement respectively in nonlinear and linear system. The first strategy requires the nonlinear model of the plant, while the second one require only the system open loop behaviour.

The combination of method of receptance and feedback linearisation is presented, it let to linearise a nonlinear system without the requirements for structural matrices.



# Chapter 4

## 4. Stabilised Layers Method

The Stabilised Layers Method (SLM) is the novel direct spatial damping matrices identification method proposed in this work. The method lets to identify spatial non-classical viscous  $\mathbf{C}$  and structural  $\mathbf{D}$  damping matrices directly from experimental frequency domain data. The damping matrices identification is performed without any previous knowledge of the system matrices and does not imply any knowledge or simultaneous identification of the mass  $\mathbf{M}$  and stiffness  $\mathbf{K}$  matrices.

The method belongs to inverse receptance methods and it uses a constrained least square solution approach; therefore, the identified matrices should be constant with respect to frequency. Theoretical formulation and application of the SLM are also presented in [161,162].

The method names meaning is linked to how it works: the procedure requires the knowledge of the geometry of the system to be identified, i.e. the connectivity between the experimentally measured nodes. In fact, the damping matrices are identified considering the dissipation of each physical connection, called “Layer”. The stabilisation is referred to the robustness of the identified damping matrix against changes in the spectral lines used in the least square approach.

This chapter is organised as follow: in § 4.1 the damping matrix through Layers method is presented, in § 4.2 the damping identification method is described in detail and finally in § 4.3 the stabilisation diagram is discussed.

### 4.1 Layers formulation for damping matrices

The Layers Method is a strategy to write the damping matrices. It consists in representing a matrix as the sum of a finite number of simpler matrices called “Layer”, with the same dimension of the global matrix. Each Layer represents a unique element of the structure.



This kind of approach has been mainly used for modal updating of structural dynamics problems discretised with FE method and in the classical matrix building definition. In FE model updating two type of strategies are usually adopted to tune the FE model on the basis of experimental data [99–101,163,164]. The first strategy each element of the damping matrix is corrected though a delta to be added to the original element value. In the second strategy each element is correct using a *p-value*, which is a multiplication coefficient of the original layer. In modal updating however an initial matrix to be updated is required.

A “Layer”-like concept is used in [60] for the identification mass  $\mathbf{M}$  and stiffness  $\mathbf{K}$  matrices: the “physical connectivity” between DOFs are used to imposed some constraints to the identification.

In the present work the “Layers Method” is introduced to write down the dissipative matrices in a structural system, including both non-classical viscous  $\mathbf{C} \in \mathbb{R}^{N \times N}$  and structural  $\mathbf{D} \in \mathbb{R}^{N \times N}$  damping matrices.  $N$  is the number of active DOFs of the system.

The viscous  $\mathbf{C}$  and structural  $\mathbf{D}$  damping matrices are written, just like in FE matrix building process, as the superposition of all the Layers:

$$\mathbf{C} = \sum_{j=1}^{NL} \mathbf{C}_j, \quad \mathbf{D} = \sum_{j=1}^{NL} \mathbf{D}_j \quad (4.1)$$

where  $\mathbf{C}_j \in \mathbb{R}^{N \times N}$  and  $\mathbf{D}_j \in \mathbb{R}^{N \times N}$  are the  $j^{th}$  layers of the two matrices and  $NL$  is the total number of layers. The number of layers  $NL$  and the structure of each Layer are defined by topology of the physical connectivity of the structure to be identified.

Three fundamental conditions can be easily imposed on the damping matrices written as in Eq. (4.1): to be stable, to comply with physical constraints and to be symmetric.

Usually mechanical systems are stable; hence the damping matrices should be locally and globally stable. This means that each layer must be stable or, mathematically, semi-positive definite.

Dissipations can involve only DOFs physically linked, this means that only Layers involving DOFs with a physical connectivity in the real structure or connected to the ground should be used as Layers in Eq. (4.1). The geometry and topology of the structure must be known, where the word “topology” refers to the connectivity existing between DOFs.

Finally, in classical linear systems the matrices are symmetric, thus each Layer must be symmetric.

The result is a general non-proportional viscous  $\mathbf{C}$  and/or structural  $\mathbf{D}$  damping matrices respecting physical and topological constraints.

The Layers  $\mathbf{C}_j$  or  $\mathbf{D}_j$  represent the elementary damping matrix  $\mathbf{C}_{el,j}$  expanded to the global dimension  $N$  of the full system.

$$\mathbf{C}_j = c_j \mathbf{T}_j^T \mathbf{C}_{el,j} \mathbf{T}_j, \quad \mathbf{D}_j = d_j \mathbf{T}_j^T \mathbf{C}_{el,j} \mathbf{T}_j \quad (4.2)$$

where  $c_j, d_j \geq 0$  are the viscous or structural coefficient damping value,  $\mathbf{T}_j$  is the localisation matrix containing the information about the topology of the  $j^{th}$  Layer and  $\mathbf{C}_{el,j}$  is the elementary matrix of the  $j^{th}$  damping element.

The elementary matrix  $\mathbf{C}_{el,j}$  can represents a relative damping element or an absolute damping element, Figure 4.1. It is the same matrix for both viscous and structural damping. A relative damper represents the dissipation between two system DOFs, while an absolute damper acts between the ground (not considered in the system) and one single system DOF.

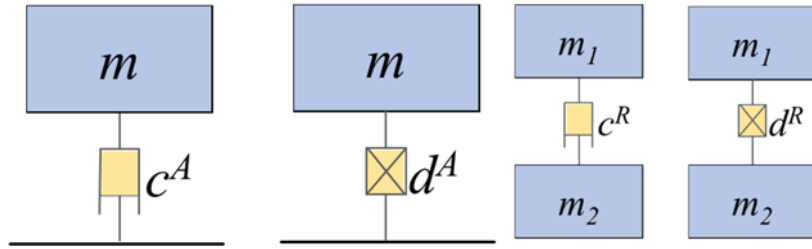


Figure 4.1 - Absolute (left) and relative (right) dampers.

The elementary matrices for relative  $\mathbf{C}_{el}^R \in \mathbb{R}^{2 \times 2}$  and absolute  $\mathbf{C}_{el}^A \in \mathbb{R}^{1 \times 1}$  dampers may be expressed as,

$$\mathbf{C}_{el}^R = \begin{bmatrix} +1 & -1 \\ -1 & +1 \end{bmatrix}, \quad \mathbf{C}_{el}^A = 1 \quad (4.3)$$

The absolute elementary element  $\mathbf{C}_{el}^A$  is obtained from the relative elementary matrix  $\mathbf{C}_{el}^R$  cancelling out the row and the column related to the fixed point, which is not part of the system.

The localisation matrix  $\mathbf{T}_j^A$  for the  $j^{th}$  absolute damper at the  $m^{th}$  DOF is defined as:

$$\mathbf{T}_j^A \in \mathbb{R}^{1 \times N} \quad \begin{cases} \{\mathbf{T}_j^A\}_i = 0; & i = 1, \dots, m-1, m+1, \dots, N \\ \{\mathbf{T}_j^A\}_m = 1 \end{cases} \quad (4.4)$$

The localisation matrix  $\mathbf{T}_j$  for the  $j^{th}$  relative damper connected between the  $m^{th}$  and  $\ell^{th}$  DOFs is given by,

$$\mathbf{T}_j^R \in \mathbb{R}^{2 \times N} \quad \begin{cases} [\mathbf{T}_j^R]_{i,k} = 0; & \begin{cases} i = 1; & k = 1, \dots, m-1, m+1, \dots, N \\ i = 2; & k = 1, \dots, \ell-1, \ell+1, \dots, N \end{cases} \\ [\mathbf{T}_j^R]_{1,m} = [\mathbf{T}_j^R]_{2,\ell} = 1 \end{cases} \quad (4.5)$$

#### 4. Stabilised Layers Method

The process of matrix building starts from elementary matrix  $\mathbf{C}_{el,j}$  of the  $j^{th}$  damping element, multiplied by its damping coefficient  $c_j$  or  $d_j$ , then the local damper is expended to the global system dimensions through the localisation matrix  $\mathbf{T}_j^A$  or  $\mathbf{T}_j^R$ , which requires the topological information of the damping element. The product of damping coefficient and elementary matrix expanded to the global system dimension is a Layer  $\mathbf{C}_j$  or  $\mathbf{D}_j$ . Finally, the global matrix is the sum of all the  $NL$  layers. Figure 4.2 is a schematic of the Layers Method: the  $j^{th}$  damping element is represented in its local reference system as an elementary matrix multiplied by the coefficient, then it is expanded to the system global dimensions in a Layer. Finally, the global matrix is the sum of the Layers.

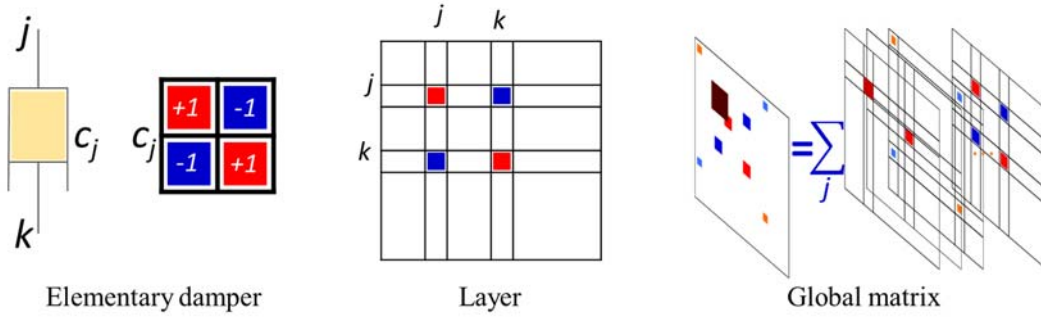


Figure 4.2 - Matrix building process by Layers Method.

The global viscous and structural damping matrices can be now written as:

$$\mathbf{C} = \sum_{j=1}^{NL} \mathbf{C}_j = \sum_{p=1}^{NA^*} c_p (\mathbf{T}_p^A)^T \mathbf{C}_{el}^A \mathbf{T}_p^A + \sum_{q=1}^{NR^*} c_q (\mathbf{T}_q^R)^T \mathbf{C}_{el}^R \mathbf{T}_q^R \quad (4.6)$$

$$\mathbf{D} = \sum_{j=1}^{NL} \mathbf{D}_j = \sum_{p=1}^{NA^*} d_p (\mathbf{T}_p^A)^T \mathbf{C}_{el}^A \mathbf{T}_p^A + \sum_{q=1}^{NR^*} d_q (\mathbf{T}_q^R)^T \mathbf{C}_{el}^R \mathbf{T}_q^R \quad (4.7)$$

where  $NA^*$  and  $NR^*$  are the number of absolute and relative layers. The total number of layers is given by  $NL = NA^* + NR^*$ .

The formulations in Eq. (4.6) and Eq. (4.7) impose topological constraints to the damping matrices. Another type of constraint can be considered when nominally equivalent damping element are present in the structure. Allowing for multiple dampers (absolute and relative) with the same damping coefficients  $c$  or  $d$  and re-writing Eq. (4.6) and Eq. (4.7), the non-proportional viscous  $\mathbf{C}$  and structural  $\mathbf{D}$  damping matrices may be written as:

$$\mathbf{C} = \sum_{j=1}^{NL} \mathbf{C}_j = \sum_{p=1}^{NA} \sum_{t=1}^{N_p} c_p (\mathbf{T}_{p,t}^A)^T \mathbf{C}_{el}^A \mathbf{T}_{p,t}^A + \sum_{q=1}^{NR} \sum_{z=1}^{N_q} c_q (\mathbf{T}_{q,z}^R)^T \mathbf{C}_{el}^R \mathbf{T}_{q,z}^R \quad (4.8)$$

$$\mathbf{D} = \sum_{j=1}^{NL} \mathbf{D}_j = \sum_{p=1}^{NA} \sum_{t=1}^{N_p} d_p (\mathbf{T}_{p,t}^A)^T \mathbf{C}_{el}^A \mathbf{T}_{p,t}^A + \sum_{q=1}^{NR} \sum_{z=1}^{N_q} d_q (\mathbf{T}_{q,z}^R)^T \mathbf{C}_{el}^R \mathbf{T}_{q,z}^R \quad (4.9)$$

where  $NA$  and  $NR$  denote respectively the number of distinct absolute and relative damping coefficients. The number of repetitions of absolute and relative dampers having the same damping coefficient (i.e.  $c_p$  and  $c_q$  or  $d_p$  and  $d_q$  respectively) are denoted by  $N_p$  and  $N_q$ . The number of coefficients to be estimated  $NA + NR$  is fewer than the total number of dampers present. The relation between the number of absolute  $NA$  and relative  $NR$  coefficients and the total number of layers  $NL$  is:

$$NL = \sum_{p=1}^{NA} N_p + \sum_{q=1}^{NR} N_q \quad (4.10)$$

All the viscous  $c$  and structural damping  $d$  coefficients can be collected in a single vector  $\mathbf{u} \in \mathbb{R}_+^{2(NA+NR) \times 1}$ , defined in Eq. (4.11):

$$\mathbf{u} = \{\mathbf{c}_A^T \quad \mathbf{c}_R^T \quad \mathbf{d}_A^T \quad \mathbf{d}_R^T\}^T \quad (4.11)$$

where  $\mathbf{c}_A \in \mathbb{R}_+^{NA \times 1}$ ,  $\mathbf{c}_R \in \mathbb{R}_+^{NR \times 1}$ ,  $\mathbf{d}_A \in \mathbb{R}_+^{NA \times 1}$  and  $\mathbf{d}_R \in \mathbb{R}_+^{NR \times 1}$  are four column vectors containing respectively the absolute and relative viscous and structural damper coefficients. Substituting Eq. (4.11) in Eq. (4.8) and in Eq. (4.9) the viscous  $\mathbf{C}$  and structural  $\mathbf{D}$  damping matrices may be written as:

$$\mathbf{C} = \sum_{j=1}^{NL} \mathbf{C}_j = \sum_{p=1}^{NA} u_p \sum_{t=1}^{N_p} (\mathbf{T}_{p,t}^A)^T C_{el}^A \mathbf{T}_{p,t}^A + \sum_{q=1+NA}^{NA+NR} u_q \sum_{z=1}^{N_q} (\mathbf{T}_{q,z}^R)^T C_{el}^R \mathbf{T}_{q,z}^R \quad (4.12)$$

$$\mathbf{D} = \sum_{j=1}^{NL} \mathbf{D}_j = \sum_{p=NA+NR+1}^{2NA+NR} u_p \sum_{t=1}^{N_p} (\mathbf{T}_{p,t}^A)^T C_{el}^A \mathbf{T}_{p,t}^A + \sum_{q=1+2NA+NR}^{2(NA+NR)} u_q \sum_{z=1}^{N_q} (\mathbf{T}_{q,z}^R)^T C_{el}^R \mathbf{T}_{q,z}^R \quad (4.13)$$

where  $u_p$  and  $u_q$  are respectively the  $p^{th}$  and  $q^{th}$  components of the coefficients vector  $\mathbf{u}$ .

The inner sums in Eq. (4.12) and Eq. (4.13) depend only on the system topology, i.e. on the type of dampers and their location. Each of these inner sums can be defined as a pattern  $\mathbf{P}_j$ , representing the distribution of the  $j^{th}$  damping element in the considered structure. The absolute  $\mathbf{P}_p^A$   $p^{th}$  pattern and the relative  $\mathbf{P}_q^R$   $q^{th}$  pattern, that are the distribution of the  $u_p$  and  $u_q$  coefficients in Eq. (4.12) and Eq. (4.13) are defined as:

$$\mathbf{P}_p^A = \sum_{t=1}^{N_p} (\mathbf{T}_{p,t}^A)^T C_{el}^A \mathbf{T}_{p,t}^A, \quad \mathbf{P}_q^R = \sum_{u=1}^{N_q} (\mathbf{T}_{q,u}^R)^T C_{el}^R \mathbf{T}_{q,u}^R \quad (4.14)$$

Eq. (4.12) and Eq. (4.13) may be re-arranged in the form:

$$\mathbf{C} = \begin{bmatrix} \mathbf{P}_1^A & \cdots & \mathbf{P}_{NA}^A & \mathbf{P}_1^R & \cdots & \mathbf{P}_{NR}^R \end{bmatrix} \begin{bmatrix} u_1 \mathbf{I} \\ \vdots \\ u_{NA} \mathbf{I} \\ u_{NA+1} \mathbf{I} \\ \vdots \\ u_{NA+NR} \mathbf{I} \end{bmatrix} \quad (4.15)$$

$$\mathbf{D} = \begin{bmatrix} \mathbf{P}_1^A & \cdots & \mathbf{P}_{NA}^A & \mathbf{P}_1^R & \cdots & \mathbf{P}_{NR}^R \end{bmatrix} \begin{bmatrix} u_{1+NA+NR} \mathbf{I} \\ \vdots \\ u_{2NA+NR} \mathbf{I} \\ u_{2NA+NR+1} \mathbf{I} \\ \vdots \\ u_{2(NA+NR)} \mathbf{I} \end{bmatrix} \quad (4.16)$$

where  $\mathbf{I}$  is the identity matrix of dimension  $N$ . Defining matrix  $\bar{\mathbf{P}} \in \mathbb{R}^{N \times N(NA+NR)}$ :

$$\bar{\mathbf{P}} = \begin{bmatrix} \mathbf{P}_1^A & \cdots & \mathbf{P}_{NA}^A & \mathbf{P}_1^R & \cdots & \mathbf{P}_{NR}^R \end{bmatrix} \quad (4.17)$$

Eq. (4.18) and Eq. (4.19) can be re-arranged in a more compact form as:

$$\mathbf{C} = \bar{\mathbf{P}} \begin{bmatrix} u_1 \mathbf{I} & \cdots & u_{NA} \mathbf{I} & u_{NA+1} \mathbf{I} & \cdots & u_{NA+NR} \mathbf{I} \end{bmatrix}^T \quad (4.18)$$

$$\mathbf{D} = \bar{\mathbf{P}} \begin{bmatrix} u_{1+NA+NR} \mathbf{I} & \cdots & u_{2NA+NR} \mathbf{I} & u_{2NA+NR+1} \mathbf{I} & \cdots & u_{2(NA+NR)} \mathbf{I} \end{bmatrix}^T \quad (4.19)$$

The Layers Method is very flexible and can be combined with several identification methods to ensure physical results. It could be easily implemented in Chen-Ju-Tsuei's method § 3.1.1, Lee-Kim's method § 3.1.2, Arora's method § 3.1.3, Leuridan-Brown-Allemang's method § 3.1.9 and Minas-Inman's method § 3.1.11.

The Layers formulation may be applied also to the methods requiring the modal identification from experimental FRM such as Adhikari's § 3.1.5 and Phani-Woodhouse's § 3.1.6 methods.

Extending the Layers approach to also mass  $\mathbf{M}$  and stiffness  $\mathbf{K}$  matrix, it could be applied also to IV method § 3.1.4.

The stability of the elementary matrices is guaranteed by the condition  $c_j, d_j \geq 0$ , the topological coherence of the damping matrices is ensured using Layers involving only physically linked DOFs, and finally the symmetry of the resulting damping matrix is guaranteed by the symmetry of elementary matrices.

#### 4.1.1 Layers selection

The selection of the Layers is a very important step for the creation of viscous  $\mathbf{C}$  and structural  $\mathbf{D}$  damping matrices. The Layers are selected starting from the

system geometry of the experimental measured nodes. These nodes have six DOFs: three translations and three rotations that in general can't be measured. Only the active DOFs should be considered.

The Layers are selected based on the physical connectivity between DOFs in the structure. There is no necessity of pre-knowledge of the dampers connectivity. A Layer for each connection is used to represent the damping matrix, even if there is no damper between to physically connected node. In that case the damping coefficient  $c_j$  or  $d_j$  representing those layers is set to zero, or better in the identification process will results null.

An example is used to clarify this concept: a 4 DOFs system is schematised in Figure 4.3.

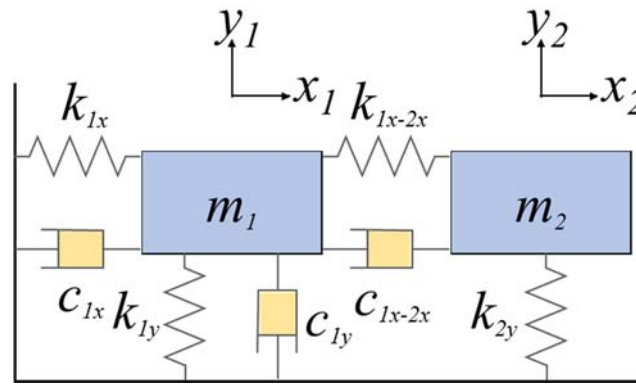


Figure 4.3 - Schematic of an example 4 DOFs system.

The system is made by two masses, with two translational DOFs for each mass. The first mass is linked to the ground in both the active DOFs and with the second mass in  $x$  direction; the second mass is linked with the ground only along  $y$  and with the first mass along  $x$ .

The Layers to be selected in this example are divided in absolute and relative dampers. The absolute dampers are: the physical connection between the ground and the first mass, with damping coefficient  $c_{1x}$  and  $c_{1y}$ ; the existing physical connection between the ground and the second mass, with coefficient  $c_{2y} = 0$ . Even if the damper  $c_{2y}$  is not present in the schematic, a Layer must be selected for that physical connectivity, because in real system there is no pre-knowledge of the dampers distribution. Finally, the relative damper linking the two masses along  $x$  is selected as relative layer.

In this case  $NL=4$ , therefore four layers are used to represent the system viscous matrix  $C$ , given by the system topology.

## 4.2 Direct spatial damping identification

In this context the Layers Method is combined with the work of Chen et al. [61], briefly described in § 3.1.1. The method lets to identify the non-proportional viscous  $\mathbf{C}$  damping matrix of the system directly from the experimentally measured FRM of the system. Arora in [68,69] identifies only the structural damping matrix  $\mathbf{D}$ , using the same approach. In both the works, [61,68,69] the matrices are identified without any stability or topological constraints. Only the symmetry of the matrix is guaranteed. The two methodologies are here unified to identify together viscous  $\mathbf{C}$  and structural  $\mathbf{D}$  damping matrices of a system.

The dynamic matrix equation of motion of a system including both viscous  $\mathbf{C}$  and structural  $\mathbf{D}$  damping matrices is:

$$\mathbf{M} \ddot{\mathbf{x}} + \mathbf{C} \dot{\mathbf{x}} + (\mathbf{K} + i\mathbf{D}) \mathbf{x} = \mathbf{f}(t) \quad (4.20)$$

where the DOFs of the system are  $N$ , and the boundary conditions and the relative kinematic relations have been applied.  $\mathbf{M}$ ,  $\mathbf{C}$ ,  $\mathbf{K}$  and  $\mathbf{D}$  are respectively the mass, viscous damping, stiffness and structural damping matrices of the system.

The damping matrices are in general non-proportional.  $\mathbf{x}$ ,  $\dot{\mathbf{x}}$  and  $\ddot{\mathbf{x}}$  are respectively the displacement, velocity and acceleration vectors and  $\mathbf{f}(t)$  is the vector of the generalised external forces acting on the system.

Eq. (4.20) can be written in frequency domain as:

$$\left[ (\mathbf{K} - \Omega^2 \mathbf{M}) + i(\Omega \mathbf{C} + \mathbf{D}) \right] \mathbf{X}(\Omega) = \mathbf{F}(\Omega) \quad (4.21)$$

The matrix multiplying the amplitudes in Eq. (4.21) left hand side (l.h.s.) is the complex DSM  $(\mathbf{H}(\Omega))^{-1} \in \mathbb{C}^{N \times N}$ :

$$(\mathbf{H}(\Omega))^{-1} = (\mathbf{K} - \Omega^2 \mathbf{M}) + i(\Omega \mathbf{C} + \mathbf{D}) \quad (4.22)$$

where  $\mathbf{H}(\Omega) \in \mathbb{C}^{N \times N}$  is the frequency dependent complex FRM. This matrix can be directly measured from experimental frequency domain tests, such as impact test, sweep tests or response to random excitation.

Eq. (4.22) can be divided in its imaginary and real part:

$$\Im \left( (\mathbf{H}(\Omega))^{-1} \right) = \Omega \mathbf{C} + \mathbf{D} \quad (4.23)$$

$$\Re \left( (\mathbf{H}(\Omega))^{-1} \right) = \mathbf{K} - \Omega^2 \mathbf{M} \quad (4.24)$$

The real part, given in Eq. (4.24), is related to only elastic and inertial properties of the system; while the imaginary part, given in Eq. (4.23), is related

to the dissipation properties of the system, i.e. viscous  $\mathbf{C}$  and structural  $\mathbf{D}$  damping matrices.

In the Chen-Ju-Tsuei method [61] the viscous damping matrix is identified introducing the normal FRM  $\mathbf{H}^N(\Omega) \in \mathbb{R}^{N \times N}$ , which is the FRM of the undamped system.

The equation of motion in the frequency domain, given in Eq. (4.21), can be rewritten using the normal DSM of the undamped system  $(\mathbf{H}^N(\Omega))^{-1}$ :

$$(\mathbf{H}^N(\Omega))^{-1} = \mathbf{K} - \Omega^2 \mathbf{M} \quad (4.25)$$

$$(\mathbf{H}^N(\Omega))^{-1} \mathbf{X}(\Omega) + i(\Omega \mathbf{C} + \mathbf{D}) \mathbf{X}(\Omega) = \mathbf{F}(\Omega) \quad (4.26)$$

Pre-multiplying Eq. (4.26) by  $\mathbf{H}^N(\Omega)$  yields:

$$[\mathbf{I} + i\mathbf{H}^N(\Omega)(\Omega \mathbf{C} + \mathbf{D})] \mathbf{X}(\Omega) = \mathbf{H}^N(\Omega) \mathbf{F}(\Omega) \quad (4.27)$$

and solving for the amplitude vector  $\mathbf{X}(\Omega)$ :

$$\mathbf{X}(\Omega) = (\mathbf{I} + i\mathbf{G}(\Omega))^{-1} \mathbf{H}^N(\Omega) \mathbf{F}(\Omega) \quad (4.28)$$

where the  $\mathbf{G}(\Omega) \in \mathbb{R}^{N \times N}$  is defined as:

$$\mathbf{G}(\Omega) = \mathbf{H}^N(\Omega)(\Omega \mathbf{C} + \mathbf{D}) \quad (4.29)$$

Comparing Eq. (4.21) and Eq. (4.28) the relationship between the complex FRM  $\mathbf{H}(\Omega)$  and the normal FRM  $\mathbf{H}^N(\Omega)$  is given by:

$$\mathbf{H}^N(\Omega) = (\mathbf{I} + i\mathbf{G}(\Omega)) \mathbf{H}(\Omega) \quad (4.30)$$

The complex FRM  $\mathbf{H}(\Omega)$  can be written as:

$$\mathbf{H}(\Omega) = \Re(\mathbf{H}(\Omega)) + i\Im(\mathbf{H}(\Omega)) = \mathbf{H}_R(\Omega) + i\mathbf{H}_I(\Omega) \quad (4.31)$$

Eq. (4.30) can be subdivided in its real and imaginary parts:

$$\Re(\mathbf{H}^N(\Omega)) = \mathbf{H}_R(\Omega) - \mathbf{G}(\Omega) \mathbf{H}_I(\Omega) \quad (4.32)$$

$$\Im(\mathbf{H}^N(\Omega)) = \mathbf{H}_I(\Omega) + \mathbf{G}(\Omega) \mathbf{H}_R(\Omega) = \mathbf{0} \quad (4.33)$$



Since the normal receptance matrix  $\mathbf{H}^N(\Omega)$  is a real matrix, the transformation matrix  $\mathbf{G}(\Omega)$  has to eliminate the imaginary part in the right hand side (r.h.s.) of Eq. (4.30) and can be computed from Eq. (4.33).

$$\mathbf{G}(\Omega) = -\mathbf{H}_I^C(\Omega)(\mathbf{H}_R(\Omega))^{-1} \quad (4.34)$$

$\mathbf{G}(\Omega)$  can be computed directly from the measured complex FRM  $\mathbf{H}(\Omega)$  and together with Eq. (4.30) define the transformation matrix between the normal FRM  $\mathbf{H}^N(\Omega)$  of the undamped system and the complex one  $\mathbf{H}(\Omega)$  of the damped system.

Substituting Eq. (4.34) in Eq. (4.30) yields to the relationship between the normal FRM  $\mathbf{H}^N(\Omega)$  and the complex FRM  $\mathbf{H}(\Omega)$ :

$$\mathbf{H}^N(\Omega) = \mathbf{H}_R(\Omega) + \mathbf{H}_I(\Omega)(\mathbf{H}_R(\Omega))^{-1}\mathbf{H}_I(\Omega) \quad (4.35)$$

The viscous  $\mathbf{C}$  and structural  $\mathbf{D}$  damping matrices can be estimated from Eq. (4.29) as:

$$\begin{bmatrix} \Omega \mathbf{H}^N(\Omega) & \mathbf{H}^N(\Omega) \end{bmatrix} \begin{bmatrix} \mathbf{C} \\ \mathbf{D} \end{bmatrix} = \mathbf{G}(\Omega) \quad (4.36)$$

where  $\mathbf{H}^N(\Omega)$  and  $\mathbf{G}(\Omega)$  are defined respectively in Eq. (4.35) and Eq. (4.34).

In real applications using experimental measurements, the evaluation of viscous  $\mathbf{C}$  and structural  $\mathbf{D}$  damping matrices requires the computation of the normal FRM  $\mathbf{H}^N(\Omega)$  at several arbitrarily chosen excitation frequencies. This results in an overdetermined system in Eq. (4.37), to estimate viscous  $\mathbf{C}$  and structural  $\mathbf{D}$  damping matrices, which are supposed constant with respect to frequency.

$$\begin{bmatrix} \Omega_1 \mathbf{H}^N(\Omega_1) & \mathbf{H}^N(\Omega_1) \\ \Omega_2 \mathbf{H}^N(\Omega_2) & \mathbf{H}^N(\Omega_2) \\ \vdots & \vdots \\ \Omega_K \mathbf{H}^N(\Omega_K) & \mathbf{H}^N(\Omega_K) \end{bmatrix} \begin{bmatrix} \mathbf{C} \\ \mathbf{D} \end{bmatrix} = \begin{bmatrix} \mathbf{G}(\Omega_1) \\ \mathbf{G}(\Omega_2) \\ \vdots \\ \mathbf{G}(\Omega_K) \end{bmatrix} \quad (4.37)$$

Eq. (4.37) can be written in compact form as:

$$\mathbf{V} \begin{bmatrix} \mathbf{C} \\ \mathbf{D} \end{bmatrix} = \mathbf{Q} \quad (4.38)$$

where  $\mathbf{V} \in \mathbb{R}^{KN \times 2N}$  and  $\mathbf{Q} \in \mathbb{R}^{KN \times N}$  are:

$$\mathbf{V} = \begin{bmatrix} \Omega_1 \mathbf{H}^N(\Omega_1) & \mathbf{H}^N(\Omega_1) \\ \Omega_2 \mathbf{H}^N(\Omega_2) & \mathbf{H}^N(\Omega_2) \\ \vdots & \vdots \\ \Omega_K \mathbf{H}^N(\Omega_K) & \mathbf{H}^N(\Omega_K) \end{bmatrix} \quad (4.39)$$

$$\mathbf{Q} = \begin{bmatrix} \mathbf{G}(\Omega_1)^T & \mathbf{G}(\Omega_2)^T & \cdots & \mathbf{G}(\Omega_K)^T \end{bmatrix}^T \quad (4.40)$$

The solution of Eq. (4.38) does not take into account the physical properties of the system. The viscous  $\mathbf{C}$  and structural  $\mathbf{D}$  damping matrices of the system can present negative values on the diagonal element and positive element out of diagonal, which means unstable damper in the structure. Furthermore, the identified matrices most probably are full matrices. They do not consider the known physical connectivity. The solution of Eq. (4.38) without any constraints is the minimum norm solution among the infinite energetic equivalent possible solutions. It the identified damping matrices dissipate the same amount of energy of the actual damping distribution, but they are not the closest to the actual topologically.

#### 4.2.1 Damping matrices identification via Layers Method

The physical connectivity of the structure are generally known from the real test bench, therefore they can be exploited to obtain the viscous  $\mathbf{C}$  and structural  $\mathbf{D}$  damping matrices most close to the real dissipation distribution in the structure.

The topological and engineering conditions should be imposed as constraints to the inversion problem. The Layers Method lets to impose directly the correct system topology, the stability and the symmetry of the damping matrices.

The viscous  $\mathbf{C}$  and structural  $\mathbf{D}$  damping matrices can be written as in Eq. (4.18) and Eq. (4.19), where the damping coefficients vector  $\mathbf{u}$  becomes the vector of the unknowns.

The viscous  $\mathbf{C}$  and structural  $\mathbf{D}$  damping matrices written by the Layers Method, given in Eq. (4.18) and in Eq. (4.19), are substituted in Eq. (4.38):

$$\mathbf{V} \tilde{\mathbf{P}} \begin{bmatrix} [u_1 \mathbf{I} \quad \cdots \quad u_{N_A} \mathbf{I} \quad u_{N_A+1} \mathbf{I} \quad \cdots \quad u_{N_A+NR} \mathbf{I}]^T \\ [u_{1+N_A+NR} \mathbf{I} \quad \cdots \quad u_{2N_A+NR} \mathbf{I} \quad u_{2N_A+NR+1} \mathbf{I} \quad \cdots \quad u_{2(N_A+NR)} \mathbf{I}]^T \end{bmatrix} = \mathbf{Q} \quad (4.41)$$

where  $\tilde{\mathbf{P}} \in \mathbb{R}^{2N \times 2N(N_A+NR)}$  is defined as:

$$\tilde{\mathbf{P}} = \begin{bmatrix} \bar{\mathbf{P}} \\ \mathbf{P} \end{bmatrix} \quad (4.42)$$

Eq. (4.42) can be re-arrangement to make explicit the vector of unknown damping coefficients  $\mathbf{u}$  :

$$\begin{bmatrix} \mathbf{V}\tilde{\mathbf{P}}\mathbf{Z}_1 \\ \vdots \\ \mathbf{V}\tilde{\mathbf{P}}\mathbf{Z}_n \end{bmatrix} \mathbf{u} = \begin{bmatrix} \mathbf{Q}\mathbf{W}_1 \\ \vdots \\ \mathbf{Q}\mathbf{W}_n \end{bmatrix} \quad (4.43)$$

where  $\mathbf{Z}_i \in \mathbb{R}^{2N(NA+NR) \times 2(NA+NR)}$  and  $\mathbf{W}_i \in \mathbb{R}^{N \times 1}$  with  $i = 1, 2, \dots, N$  are defined as:

$$\mathbf{Z}_i = \mathbf{0} \text{ and } (\mathbf{Z}_i)_{(y-1)N+i,y} = 1 \text{ with } y = 1, 2, \dots, 2(NA + NR) \quad (4.44)$$

$$\mathbf{W}_i = \mathbf{0} \text{ and } (\mathbf{W}_i)_{i,1} = 1 \quad (4.45)$$

Eq. (4.43) can be written in compact form as:

$$\bar{\mathbf{V}}\mathbf{u} = \bar{\mathbf{Q}} \quad (4.46)$$

where  $\bar{\mathbf{V}} \in \mathbb{R}^{N^2K \times 2(NA+NR)}$  and  $\bar{\mathbf{Q}} \in \mathbb{R}^{N^2K \times 1}$  are:

$$\bar{\mathbf{V}} = \begin{bmatrix} \mathbf{V}\tilde{\mathbf{P}}\mathbf{Z}_1 \\ \vdots \\ \mathbf{V}\tilde{\mathbf{P}}\mathbf{Z}_n \end{bmatrix} \quad (4.47)$$

$$\bar{\mathbf{Q}} = \begin{bmatrix} \mathbf{Q}\mathbf{W}_1 \\ \vdots \\ \mathbf{Q}\mathbf{W}_n \end{bmatrix} \quad (4.48)$$

Eq. (4.43) is generally an overdetermined problem; this means that the matrix  $\bar{\mathbf{V}}$  has more rows than columns, i.e.  $N^2K > 2(NA + NR)$ . Therefore the solution of Eq. (4.46) requires a pseudo inverse of the l.h.s. matrix of Eq. (4.46) as:

$$(\bar{\mathbf{V}}^T \bar{\mathbf{V}})\mathbf{u} = \bar{\mathbf{V}}^T \bar{\mathbf{Q}} \quad (4.49)$$

The matrix  $\bar{\mathbf{V}}$  is ill conditioned and the solution of Eq. (4.46) through Eq. (4.49) is even more ill conditioned, since the condition number of  $(\bar{\mathbf{V}}^T \bar{\mathbf{V}})$  is the square of the condition number of  $\bar{\mathbf{V}}$  [82]. A better way to solve Eq. (4.46) is to use a Householder transformation [165], which result is the same condition number of the original problem. A transformation matrix  $\mathbf{T}$  is applied to both side of Eq. (4.46) so that the product  $\mathbf{T}\bar{\mathbf{V}}$  is an upper triangular matrix and has the same condition number of  $\bar{\mathbf{V}}$ .

$$\mathbf{T}\bar{\mathbf{V}}\mathbf{u} = \mathbf{T}\bar{\mathbf{Q}} \quad (4.50)$$

From a practical point of view this means to perform the QR decomposition using Householder reflection [130] of the matrix  $\bar{\mathbf{V}}$ .

$$\bar{\mathbf{V}} = \mathbf{Q}^* \mathbf{R}^* \quad (4.51)$$

where  $\mathbf{R}^* \in \mathbb{R}^{N^2 K \times 2(NA+NR)}$  is an upper triangular matrix and  $\mathbf{Q}^* \in \mathbb{R}^{N^2 K \times N^2 K}$  is a unitary and orthogonal matrix:

$$(\mathbf{Q}^*)^{-1} = (\mathbf{Q}^*)^T \quad (4.52)$$

The transformation matrix  $\mathbf{T}$  so that  $\mathbf{T}\bar{\mathbf{V}}$  is an upper triangular matrix is no more necessary. Substituting Eq. (4.51) in Eq. (4.50) and using the property in Eq. (4.52) the linear problem becomes:

$$\mathbf{R}^* \mathbf{u} = (\mathbf{T} \mathbf{Q}^*)^{-1} \mathbf{T} \bar{\mathbf{Q}} \quad (4.53)$$

$$\mathbf{R}^* \mathbf{u} = (\mathbf{Q}^*)^T \bar{\mathbf{Q}} \quad (4.54)$$

The identification of the damping coefficients for each pattern, therefore for each Layer, may then be cast as an optimisation problem, subject to the constraint that  $u_j \geq 0$ :

$$\mathbf{R}^* \mathbf{u} = (\mathbf{Q}^*)^T \bar{\mathbf{Q}} \text{ with } \mathbf{u} > \mathbf{0} \quad (4.55)$$

The problem can be solved using a classical constrained optimisation

$$\min_{\mathbf{u}} \left( \left\| \mathbf{R}^* \mathbf{u} - (\mathbf{Q}^*)^T \bar{\mathbf{Q}} \right\| \right) \text{ with } \mathbf{u} > \mathbf{0} \quad (4.56)$$

using the algorithm described by Lawson and Hanson [166].

Another classical approach to solve Eq. (4.55) is to treat this constrained system as the input to the first phase of the classical two phase simplex method for linear programming [167], normalising the linear system so that  $(\mathbf{Q}^*)^T \bar{\mathbf{Q}}$  is non negative.

Let introduce a new artificial variable  $\mathbf{w} \in \mathbb{R}^{2(NA+NR) \times 1}$  and apply the simplex method to the linear programming problem:

$$\min \left( \sum_i w_i \right) \text{ subject to } \mathbf{R}^* \mathbf{u} + \mathbf{I} \mathbf{w} = (\mathbf{Q}^*)^T \bar{\mathbf{Q}}, \mathbf{u} \geq \mathbf{0}, \mathbf{w} \geq \mathbf{0} \quad (4.57)$$

where  $\mathbf{I}$  is the identity matrix of dimension  $2(NA+NR)$ .

The theory of linear programming ensures that the simplex method will converge in finite time to an optimal solution respecting the constraints. Either all the entry of  $\mathbf{w}$  are equal to zero, then  $\mathbf{u}$  is the non-negative solution, or else  $\mathbf{w}$  has at least a positive entry in which case there is not non-negative optimal solution  $\mathbf{u}$ . This latter should be not the case of the problem in Eq. (4.55) because this can happen only if there are local unstable dampers in the real system. All the details and proofs of the precedent consideration can be found in [167].

### 4.2.2 Considerations on unknowns number

The proposed approach reduces significantly the number of unknowns with respect to the classical Chen-Ju-Tsuei method. In fact, for each considered Layer it is necessary to compute only one unknown, instead of identifying three different damping coefficients for each elementary matrix of each pattern (two elements on the diagonal and one out-of-diagonal element), guaranteeing only the symmetry.

Let's considering the viscous damping matrix of a single physical connectivity between two DOFs:

$$\mathbf{C} = \begin{bmatrix} c_{11} & c_{12} \\ c_{21} & c_{22} \end{bmatrix} \quad (4.58)$$

The classical Chen-Ju-Tsuei method identifies four unknowns without any physical constraint between them. The symmetry preserving version of the method identifies three unknowns, imposing  $c_{12} = c_{21}$ . However, there is no guarantee that the viscous damping matrix  $\mathbf{C}$  will result positive definite and it is even more difficult that  $c_{11} = c_{22} = -c_{12} = -c_{21}$ .

The identification via Layers Method identifies only a single unknown, i.e. the damping coefficient which multiply the elementary matrix. The viscous damping matrix  $\mathbf{C}$  will be symmetric, definite positive and respect the physics of a damper connectivity.

In general, given a  $N$  DOFs system with viscous and structural damping the number of unknowns to identify is given in Table 4.1

Table 4.1 - Identification unknowns number.

	Chen-Ju-Tsuei	Symmetric Chen-Ju-Tsuei	Layers method
# unknowns	$2N^2$	$N(N+1)$	$2(NA + NR)$

Let's considering the worst case: a  $N$  DOFs system with viscous and structural damping in which all the connectivity are different, all the DOFs are linked to the ground and each DOFs is connected with all the remaining DOFs, that means full damping matrices and it is not usually the case.

The number of absolute dampers is equal to the number of different physical connectivity with the ground, in this case

$$NA = N \quad (4.59)$$

The number of relative dampers is the number of physical connectivity between two different DOFs, in this case:

$$NR = \sum_{i=1}^N (N-i) = \frac{N}{2}(N-1) \quad (4.60)$$

The Layers Method considers always a number of unknowns less or equal than the Chen-Ju-Tsuei method the symmetry preserving version, also in the worst case:

$$2\left(N + \frac{N}{2}(N-1)\right) < 2N^2 \quad (4.61)$$

$$2\left(N + \frac{N}{2}(N-1)\right) = N(N+1) \quad (4.62)$$

In general the damping matrices **C** and **D** are  $n$ -diagonal matrices, hence in general  $2(NA + NR) \ll 2N^2$ , the number of unknowns to be identified with the Layers Method is much less than in the original method.

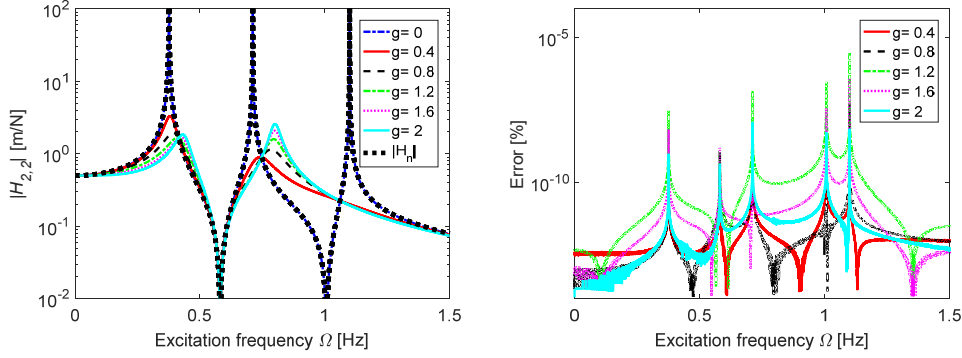
### 4.2.3 Considerations on the normal FRM

The normal FRM  $\mathbf{H}^N(\Omega)$  is defined as the FRM of the underlying undamped system, it can be computed using Eq. (4.35). The normal FRM  $\mathbf{H}^N(\Omega)$  extracted from the example system in § 2.2.3 are compared to the FRM of the undamped version of the same system.

The FRM  $\mathbf{H}(\Omega)$  is synthesised from the modal properties numerically computed using the system matrices. The comparison is performed for different dissipation levels of the non-classical damping matrix, changing the gain  $g$ :

$$\mathbf{C} = g \begin{bmatrix} 1 & 0 & 0 \\ 0 & 0 & 0 \\ 0 & 0 & 0 \end{bmatrix} \quad (4.63)$$

The results are shown in Figure 4.4.


 Figure 4.4 - Normal FRF changing  $g$  :normal FRF (left) and error (right).

In Figure 4.4 (left) the normal FRF are computed for each value of the gain  $g$ . When the gain  $g = 0$  the FRF represent the undamped system FRF, blue dashed-dot line in Figure 4.4 (left). Increasing the gain  $g$  the extracted normal FRF is perfectly overlapped with the undamped system FRF.

The second peak of the FRF decreases its amplitude until a certain value and then starts again to increase the amplitude around a higher frequency. The system seems to become stiffer. Although in that case the closest undamped system could be a 2 DOFs system around the higher frequencies, the estimation of  $\mathbf{H}^N(\Omega)$ , Eq. (4.35) correctly identifies the undamped system FRF.

The error between the estimated normal FRF using Eq. (4.35) and the undamped system FRF are computed as:

$$Err_{\%}(\Omega) = \frac{|H_{c=0}(\Omega)| - |H^N(\Omega)|}{|H_{c=0}(\Omega)|} \quad (4.64)$$

The errors between estimated normal FRF and the undamped system FRF, Figure 4.4 (left), are negligible in all the frequency range. However, the error becomes higher at resonances and anti-resonances frequencies.

### 4.3 Solution regularization and stability

The identification, localisation and quantification of viscous  $\mathbf{C}$  and structural  $\mathbf{D}$  damping matrices using normal FRM  $\mathbf{H}^N(\Omega)$  and Layers Method is performed through Eq. (4.56). There are two aspects of the solution of the layered damping matrices coefficients in Eq. (4.56), namely that a solution  $\mathbf{u}$  should exist and that it should be a stable solution. Eq. (4.46) involves matrices  $\bar{\mathbf{V}}$  and  $\bar{\mathbf{Q}}$ , which depend of the choice of the  $K$  spectral lines  $\omega_i$ , used in Eq. (4.39) and Eq. (4.40). In § 4.2 there is no reference to how many, i.e.  $K$ , and where the spectral lines  $\Omega_i$  are located. Considering the example three DOFs system, a damped FRF and the related normal FRF are shown Figure 4.5.

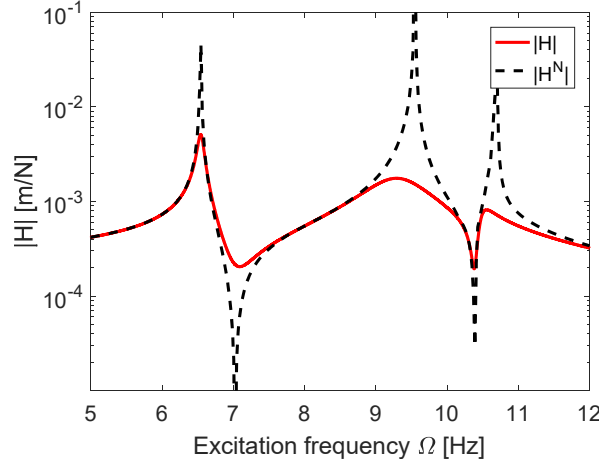


Figure 4.5 - Normal and damped FRF.

It is well-known that the FRF is affected by damping only in the frequency ranges around the natural frequencies peaks. Therefore, the spectral lines  $\omega_i$  should be located around the peaks of the damped FRF, because it is reasonable very difficult to identify the damping matrices in a region far from FRF peaks, where damped and undamped FRF are almost the same.

The approach described in § 4.2.1 is therefore implemented within a band consisting of  $\tilde{k}$  equally-spaced spectral lines around the measured (damped) FRM  $\mathbf{H}(\Omega)$  peaks and arranged symmetrically. The total number of spectral lines in Eq. (4.46) is  $K = R\tilde{k}$ , where  $R$  is the number of modes taken into account in the identification.

The exact location of the spectral lines  $\Omega_i$  depends on the chosen frequency band  $\Delta f_i$  around each peak. The frequency band  $\Delta f_i$  is normalised with respect to a range  $r_{\%}$ , which is a percentage of the  $i^{th}$  peak frequency  $\hat{f}_i$ , it is given by:

$$\Delta f_i = \frac{r_{\%} \hat{f}_i}{100} = \frac{r_{\%} \hat{\Omega}_i}{200\pi} \quad (4.65)$$

When only a spectral line  $\Omega_i$  is used, it is the spectral line corresponding to the peak  $\Omega_i = \hat{\omega}_i$  of each mode. The frequency interval  $\delta f_k$  between consecutive lines inside each range  $\Delta f_i$  may then be written as:

$$\delta f_k = \frac{\Delta f_i}{\tilde{k} - 1} \text{ with } \tilde{k} > 1 \quad (4.66)$$

A qualitative example of the frequency intervals  $\Delta f$  and the spread of the spectral line within the intervals are shown in Figure 4.6.



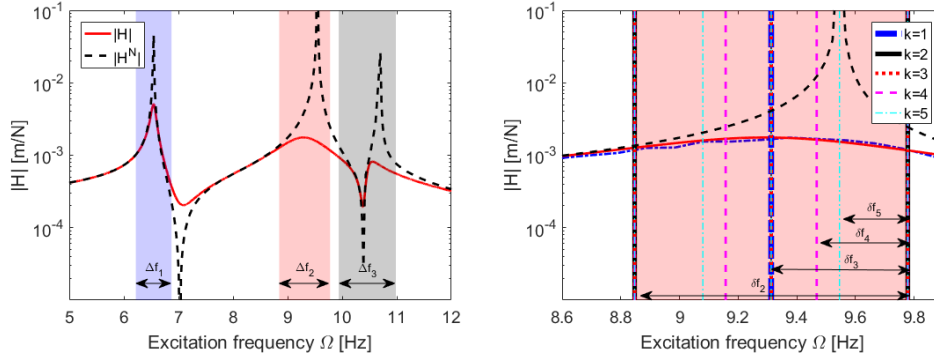


Figure 4.6 - Frequency range (left) and spectral lines changing  $\tilde{k}$  (right).

In the example three frequency intervals are shown ( $\Delta f_1, \Delta f_2$  and  $\Delta f_3$ ) corresponding to three damped natural frequencies. The range  $r_\%$  and the difference between damped system peak frequency  $\hat{f}_i$  and undamped natural frequency  $f_{n,i}$  are intentionally emphasised for clarity.

Parallel computing [168] can be used to compute the solution  $\mathbf{u}(r_\%, \tilde{k})$  because the computation are independent for each  $(r_\%, \tilde{k})$  couple. In this way it is possible to speed up the identification process.

### 4.3.1 Stability test and optimal solution

The range  $r_\%$  and number of spectral lines  $\tilde{k}$  are two independent variables, they can be chosen independently and arbitrarily. A grid of  $(r_\%, \tilde{k})$  points can be used to test the stability of solutions. A stabilisation diagram is produced to test the divergence of damping coefficient solution vector  $\mathbf{u}$ . If the solution  $\mathbf{u}$  is physical and correct, it will not change even if a slightly different number of spectral lines  $\tilde{k}$  or range  $r_\%$  is used for the identification.

A stabilisation diagram can be built for each of the damping coefficient  $u_i$ , thus a total of  $2(NA + NR)$  stabilisation diagrams are obtained.

The coefficient  $u_i$  obtained for a couple  $(r_\%, \tilde{k})$ , called  $u_i(r_\%, \tilde{k})$ , is compared to those solutions  $u_i$  obtained at the eight  $(r_\%, \tilde{k})$  points surrounding the  $(r_\%, \tilde{k})$ . If the variation of the considered point with respect to all it neighbours is less than a tolerance  $\varepsilon$ , then the solution  $u_i$  obtained at the point  $(r_\%, \tilde{k})$  is deemed to be stable. A stability Boolean matrix  $\mathbf{S}_i \in \{0, 1\}^{\tilde{k} \times r}$  can be built for the Layer solution  $u_i$  defined as:

$$\mathbf{S}_i(r_{\%}, \tilde{k}) = 1 \text{ when } \frac{|u_i(r_{\%}, \tilde{k}) - u_i(r_{\%} + j, \tilde{k} + t)|}{u_i(r_{\%}, \tilde{k})} < \varepsilon \quad -1 \leq \forall(j, t) \in \mathbb{Z} \leq +1 \quad (4.67)$$

where  $\varepsilon$  is a reasonable small threshold.

A global stabilisation diagram  $\bar{\mathbf{S}}$  can be obtained by the Boolean “AND” operator for the complete set of  $2(NA + NR)$  stabilisation diagrams  $\mathbf{S}_i$ , such that:

$$\bar{\mathbf{S}} = \bigcap_{i=1}^{2(NA+NR)} \mathbf{S}_i \quad (4.68)$$

Commonly an area of stability is obtained, represented by all the couples  $(r_{\%}, \tilde{k})$  where  $\bar{\mathbf{S}}$  is true. The identified damping coefficient values  $\mathbf{u}(r_{\%}, \tilde{k})$  are quite similar for all the stable  $(r_{\%}, \tilde{k})$  couples. All the stable identified solutions  $\mathbf{u}(r_{\%}, \tilde{k})$  are eligible as correct solution. Among all that solution the optimal solution  $\mathbf{u}^*$  is the points  $(r_{\%}^*, \tilde{k}^*)$  that guarantee the smallest normalised residuum  $E_{\%}$  of the optimisation problem defined in Eq. (4.56). The normalised residuum  $E_{\%}$  is defined as:

$$E_{\%}(r_{\%}, \tilde{k}) = 100 \sqrt{\frac{\sum_i (\mathbf{T}\bar{\mathbf{V}}\mathbf{u} - \mathbf{T}\bar{\mathbf{Q}})_i^2}{\sum_i \bar{\mathbf{Q}}_i^2}} \bigg|_{(r_{\%}, \tilde{k})} \quad (4.69)$$

where the sum symbols stand for sum of the column vector.

An error map  $\mathbf{E}$  can be built for each identified unknown vector  $\mathbf{u}(r_{\%}, \tilde{k})$  showing the normalised residuum.

The optimal solution  $\mathbf{u}^*$  can be defined as:

$$\mathbf{u}^* = \mathbf{u}(r_{\%}^*, \tilde{k}^*) \text{ and } \left[ E_{\%}(r_{\%}^*, \tilde{k}^*) = \min(\mathbf{E}) \right] \cap \left[ \bar{\mathbf{S}}_{(r_{\%}^*, \tilde{k}^*)} = 1 \right] \quad (4.70)$$

### 4.3.2 Considerations on the range span

The damping identification from Eq. (4.38) is based upon the normal FRM  $\mathbf{H}^N(\Omega)$ , which becomes infinite when  $\Omega = \omega_{n,i}$ , where  $\omega_{n,i}$  is the  $i^{\text{th}}$  resonance frequency of the undamped system or normal FRM  $\mathbf{H}^N(\Omega)$ . It is the case of  $\tilde{k} = 5$  in Figure 4.6 (right): a spectral line is exactly the resonance of the undamped system, hence the values of  $\mathbf{H}^N(\Omega = \omega_{n,2})$  will be infinite in that point, or at least very high.

Figure 4.7 shows as discrete points those  $(r_{\%}, \tilde{k})$  pairs that makes the matrix  $\bar{\mathbf{V}}$  to become ill conditioned or in the worst case singular. When these points are connected by the dash-dotted lines shown in Figure 4.7, it is seen that each line becomes an asymptote to one of three vertical lines, one for each of the three undamped natural frequencies of the example system.

The undamped natural frequency will generally differ than the peak of the damped receptance and therefore it is possible that the upper limit of the range  $\Delta f_i$  (i.e. the  $k^{th}$  spectral line) corresponds exactly with an undamped natural frequency. In this case  $\mathbf{H}^N(\omega_{n,k})$  becomes infinite and the matrix  $\bar{\mathbf{V}}$  is singular. Since, for the same range  $r_{\%}$ , irrespective of the number of spectral lines, the  $\tilde{k}^{th}$  line always defines the upper limit of the range, it is apparent that the coincidence of the range upper limit with an undamped natural frequency defines the three vertical lines in Figure 4.7. The points to the right occur when  $\omega_{n,i}$  is included within the  $i^{th}$  range.

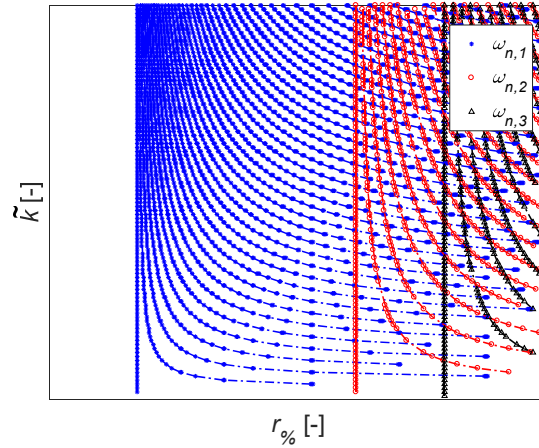


Figure 4.7 - Singularity diagram in terms of  $(r_{\%}, \tilde{k})$ .

The ranges that just locate the vertical lines, the asymptotes in Figure 4.7, may be expressed as:

$$r_{\%asympote,i} = 100 \frac{2|\omega_{n,i} - \hat{\omega}_i|}{\hat{\omega}_i} \quad \text{with } i = 1, \dots, R \quad (4.71)$$

The  $r_{\%asympote}$  gives a hint on the frequency range  $r_{\%}$  necessary to find a physical solution of Eq. (4.56). Considering a usual non-proportionally damped system, where the peaks  $\hat{\omega}_i$  of the damped FRM  $\mathbf{H}(\Omega)$  moves left with respect to the undamped peaks  $\omega_{n,i}$ . If the range  $r_{\%} < \min(r_{\%asympote,i})$  then all the spectral lines are selected on the left of the normal FRM  $\mathbf{H}^N(\Omega)$  peaks, therefore for each

peak all the spectral lines have the same sign. The optimisation problem does not have enough information to find a correct and stable solution. Therefore the range should be at least  $r_{\%} > \min(r_{\%asympote,i})$  so that positive and negative spectral lines are used in the optimisation problem in Eq. (4.56). Good results are generally found inside the range between the first two asymptotes.

## 4.4 Conclusions

The SLM is the novel damping matrices identification method presented in this chapter, it can identify the viscous and structural matrices of a MDOF mechanical system using the system receptance matrix and the topology of the system. The viscous and structural damping matrix are written as the sum of several layers. Each Layer represent the dissipation of a connection between two system DOFs. A Layer is considered in the damping matrices building only if exists a physical connectivity between the two DOFs. This way to rewrite the damping matrix is combined with a damping identification method in frequency domain. The original method was able to find out an equivalent damping matrix, without consider several properties of physical system: positive definiteness of the identified damping matrix was not guaranteed and physical connectivity were not considered. The damping matrix identified using the SLM is the closest to the real dissipation distribution in the real system, because it considers the physical connectivity in the structure. Moreover, it ensures symmetry and positive definition of the identified matrix. At the same time the SLM massively reduces the number of unknowns with respect to the original damping identification method. The identification is affected by the number and the location of the spectral lines used in the matrix identification process. A regularisation and stabilisation method for the identification was developed. The damping matrix should be identified using spectral lines located close to the system resonances, because damping affects visibly the system FRF in that regions. The identification far from the system resonance is not reliable because damped and undamped FRF are almost the same far for the resonances. The stabilisation method developed in the SLM exploits another physical property of linear system: the damping matrix can not change if it is identified using a defined amount of spectral lines in a defined location or a slightly different set of spectral lines. The identification is therefore performed several times changing location and amount of spectral lines. The identified damping matrix is chosen among the stable solution, i.e. the solution that do not change changing identification parameters, as the one with the lowest normalised inversion error.



## Chapter 5

### 5. Enhancing methods for direct identification

The accuracy of direct identification of system viscous  $\mathbf{C}$  and structural  $\mathbf{D}$  damping matrices depends on the experimental measured data. The SLM presented in § 4 lets to identify the system matrix to global dimension  $N$ , but requires the complete FRM  $\mathbf{H}(\Omega)$  of the same dimension.

In real application there are three main problems affecting experimental FRM  $\mathbf{H}^{Exp}(\Omega)$ , namely: incompleteness, noise and frequency resolution.

Incompleteness can be defined as impossibility to measure the complete FRM: usually the experimentally measured FRM  $\mathbf{H}^{Exp}(\Omega)$  is a rectangular matrix.  $\mathbf{H}^{Exp}(\Omega) \in \mathbb{C}^{I \times O}$  where  $I$  is the number of excited DOFs (input) and  $O$  is the number of measured DOFs (output). The standard techniques used for mechanical system testing are roving hammer, roving accelerometers or shaker test [35]. In hammer test the structure is excited in  $I$  DOFs and the response is measured in  $O$  DOFs:  $I \gg O$  in roving hammer and  $O \gg I$  in roving accelerometers.

In shaker tests usually the response of several DOFs is measured and few points are excited, i.e.  $O \gg I$ . In both techniques some of the input  $I$  and output  $O$  DOFs can be in common. However, the measured  $\mathbf{H}^{Exp}(\Omega)$  will be incomplete.

The measured FRM  $\mathbf{H}^{Exp}(\Omega)$  is also affected by noise, in both input force and measured responses. Therefore  $\mathbf{H}^{Exp}(\Omega)$  is not smooth as in numerical examples, the results of the identification will be affected by the random noise in the spectral lines used in the identification.

Finally, amplitude and phase of the measured FRM  $\mathbf{H}^{Exp}(\Omega)$  are obtained at discrete spectral lines, with a constant frequency resolution. This means it is not possible to change arbitrary the couple  $(r_0, \tilde{k})$ , introduced in § 4.3, to check the

stability of the solution with respect to spectral lines number  $\tilde{k}$  and frequency ranges  $r_{\%}$ .

In this chapter some methods to overcome the influence of incompleteness, noise and discrete frequency resolution are presented.

In § 5.1 the standard method to solve the three main issues when  $\max(I, O) = N$  is presented, in § 5.2 a method to expand incomplete set of data to the global dimension  $N$  is presented when  $\max(I, O) < N$ . Finally, in § 5.3 the properness condition for complex eigenvector is introduced as a tool to improve system identification. These methods can be applied in combination or stand-alone.

## 5.1 Synthesis of FRM from modal parameters

The synthesis of the FRM consists in reproducing the measured FRF through the modal model identified from EMA.

When  $\max(I, O) = N$  and the system is linear it is possible to obtain the complete FRM  $\mathbf{H}(\Omega)$  by synthesising the missing experimental FRF as:

$$\mathbf{H}_{syn}(\Omega) = \sum_{r=1}^{2N} \frac{\mathbf{\Psi}_{1:N,r} \mathbf{\Psi}_{1:N,r}^T}{a_r (i\Omega - s_r)} \quad (5.1)$$

where  $\mathbf{\Psi}$ ,  $a_r$  and  $s_r$  are respectively the complex modal matrix, the modal constant and the pole of the  $r^{th}$  eigenvector identified from EMA.

Using the Maxwell-Betty reciprocity theorem [169,170] the measured  $I$  DOFs or excited  $O$  DOFs can be switched to have the  $\max(I, O)$  as measured responses, so that  $\mathbf{\Psi} \in \mathbb{C}^{N \times \min(I, O)}$  and the synthesised FRM  $\mathbf{H}_{syn}(\Omega) \in \mathbb{C}^{N \times N}$ . The synthesised  $\mathbf{H}_{syn}(\Omega)$  has several advantages for the identification:

- 1) the receptance matrix is complete to dimension  $N$  and therefore the global viscous  $\mathbf{C}$  or structural  $\mathbf{D}$  damping matrices;
- 2) the noise effect is attenuated because a modal model is fitted though the experimental curves smoothing the noise effect;
- 3) the response FRM  $\mathbf{H}_{syn}(\Omega)$  can be computed at whatever spectral line  $\Omega$  in a continuous domain; the stabilization procedure, § 4.3 can be now followed using all the necessary couples  $(r_{\%}, \tilde{k})$ .

The identified modal model and the fitted FRM  $\mathbf{H}_{syn}(\Omega)$  should be as close as possible to the experimental FRM  $\mathbf{H}^{Exp}(\Omega)$  to obtain a good identification of the mechanical system under analysis.

An example of FRF synthesis is shown in Figure 5.1. The experimental FRF is computed only at defined frequencies (blue stars), depending of the acquisition parameters; moreover, it is affected by the uncontrollable noise. The synthesised FRF (red curve) perfectly overlap the experimental FRF, fitting the experimental data through a second order model, given in Eq. (5.1), and mitigating the noise effects.

Few spectral lines are acquired around each FRF peak; therefore, the stabilisation procedure, presented in § 4.3 becomes not useful. Instead using the synthesised FRM  $\mathbf{H}_{syn}(\Omega)$  for the identification process, an infinite number of spectral lines in a small range around each natural frequency peak can be potentially considered.

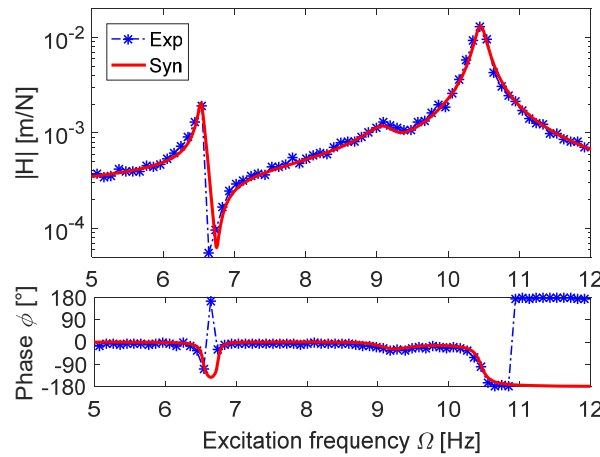


Figure 5.1 - Synthesised and experimental FRF.

### 5.1.1 Modal models identification

Several techniques exist for identification of the modal parameters used in Eq. (5.1), a complete list can be found in [171]. The most used are: least squares complex exponential (LSCE) [35,172], Least-squares rational function estimation method (LSRF) [173] and Least-Squares Complex Frequency-domain (LSCF) [174].

The methods used for fitting all the experimental data in this work are the polyreference least-squares complex frequency-domain method (pLSCF) [175] and maximum likelihood modal parameter identification (ML-MM) [176], both implemented in Siemens LMS Test.Lab.

The pLSCF method, also called PolyMAX, is a poly-reference version of the LSCF method, which make use of the so-called right matrix-fraction model. This method uses all the available FRF together to identify the modal parameters. PolyMAX is subdivided into two phases. In the first phase a clear poles stabilisation diagram is obtained, containing natural frequency, damping ratio and participation factor. In the second step is used to find the mode shapes are



identified using a least-square approach. With respect to the classical LSCF method it can identify also closely spaced modes.

The results of the identification using PolyMAX are quite satisfactory in many cases, except when very high damped systems are studied. In that cases the ML-MM method is much powerful in identify the modal parameters.

The ML-MM method satisfies the physical property of linear non-gyroscopic, non-circulatory, and passive mechanical systems, which are Maxwell-Betti reciprocity theorem [169] and identification of real normal modes. The modal parameters are identified by fitting directly the modal model to the measured frequency-domain data in a maximum likelihood sense. The method consists in an iterative procedure: an initial guess of the natural frequency and participation factor is obtained from pLSCF and then fitted in the FRM  $\mathbf{H}^{Exp}(\Omega)$  to estimate mode shapes, their scaling factor and lower and upper residual matrix. The poles and participation factor are optimised considering the reciprocity constraint. The last two points are repeated until converge criteria for the cost function are satisfied. The cost function to be minimized is the sum of the squared absolute value of the weighted-error between the model  $\mathbf{H}^{syn}(\Omega)$  and the measured FRM  $\mathbf{H}^{Exp}(\Omega)$ . In Figure 5.2 the synthesised FRF of a high damped system is shown. When the systems are high damped, the modal parameters identification is more difficult.

It is evident that in these cases the first attempt to modal parameters identification given by pLSCF method is not enough accurate (red curve), instead few iterations using the ML-MM method (black dashed-dot curve) are necessary to produce improved results.

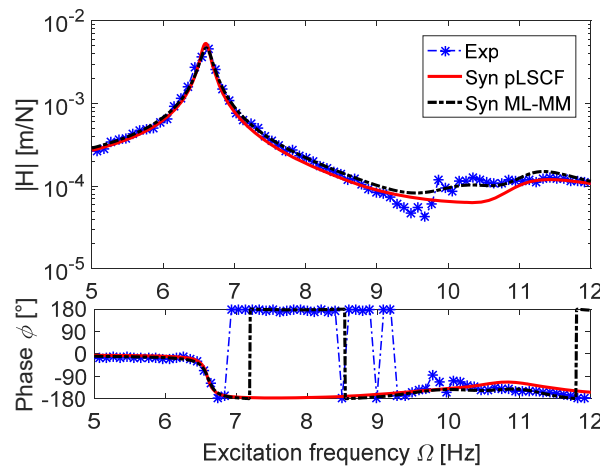


Figure 5.2 - Synthesised FRF using pLSCF and ML-MM.

## 5.2 Mode shapes expansion and smoothing

In § 5.1 it is discussed how to complete the modal matrix when  $\max(I, O) = N$ . However, if the  $\max(I, O) < N$  then the synthesised FRM  $\mathbf{H}_{syn}(\Omega) \in \mathbb{C}^{\max(I, O) \times \max(I, O)}$  is still incomplete.

In this last case the experimentally extracted modal matrix is both spatially and modal incomplete. The modal incompleteness, i.e. modal truncation, depends on the frequency range of interest for the identification; while the spatial incompleteness is usually related to the possibility of exciting only some DOFs and in limited directions due to encumbrance problems or physical impossibility to excite all the directions. The experimental measured DOFs are however affected by measurement noise.

A method to mitigate these issues is presented in this paragraph, it consists in expanding and smoothing the identified modal matrix  $\Psi \in \mathbb{C}^{\max(I, O) \times R}$  to a complete modal matrix  $\Psi_e \in \mathbb{C}^{N \times R}$ , where  $R$  is the number of identified modes.

A master-slave network relationship can be hypothesised between the nodes physically linked considering the real topology of the system, that are the same physical connectivity used in the Layers Method. The method is based on the topology of the model, because only nodes connected by links have influences one on the others: nodes geometrically very close but not linked will have no influence each other.

Each node of the geometrical model is considered as slave of all the other nodes linked to it, i.e. which present a physical connectivity. The importance of each master is weighed through a coefficient  $\alpha_j$  related to a physical parameter (for example the normalised distance between the nodes). The spatial noise is at least attenuated and the values of the DOFs not excited can be estimated considering the measured value of the linked nodes. The method can be used for global mode shapes, because it attenuates local motion.

For a defined node  $U$ , the response value in each direction  $d$  can be computed as:

$$U_{new,d} = \frac{1}{n+1} \sum_{j=1}^n \frac{U_d + \alpha_j U_{j,d}}{1 + \alpha_j} \quad (5.2)$$

where  $n$  is the number of physical connectivity starting from node  $U$ ,  $U_d$  is the displacement of the node  $U$  in direction  $d$ ,  $\alpha_j$  is the weight coefficient and  $U_{j,d}$  is the displacement in direction  $d$  of the  $j^{th}$  node physically connected to  $U$ . Fixed DOFs are not considered slaves of other DOFs, because their displacement is imposed by the boundary condition.

The method can be applied iteratively; each iteration further smooths the data. The number of iterations required must be judged visually and it depends on the

quality of the test data. Some experimentation may be required to find good results. The best smoothing results are obtained for dense experimental meshes and when  $n$  is at least 2.

When smoothing test data, the eigenvectors lose the normalisation with respect to  $a_r$  because they are recast; therefore it is necessary to find out the new modal constant  $a_{r,new}$  for each eigenvector.

The FRM  $\mathbf{H}_{syn}(\Omega)$  of a non-proportionally damped system can be computed using Eq. (5.1). It is necessary to compute the new modal constant  $a_{r,new}$  so that the energy of the  $r^{th}$  mode shape  $\Psi_r$ , considering the original number of DOFs, is the same before and after the expansion process. The energy of a mode shape is directly proportional to the area under the curve representing the sum of all the FRFs of that mode shape. The new modal constant  $a_{r,new}$  can be evaluated considering that the sum of all the FRFs computed for a specific eigenvector  $\Psi_r$ , must be the same before and after the expansion and filtering process. Hence, the new modal constant results  $a_{r,new}$ :

$$a_{r,new} = a_r \frac{\sum_{j=1}^{2N} \sum_{k=1}^{2N} |\mathbf{H}_{syn_{j,k}}^{\Psi_r}(\omega_d)|}{\sum_{j=1}^{2N} \sum_{k=1}^{2N} |\mathbf{H}_{syn_{j,k}}^{\Psi_{e,r}}(\omega_d)|} \quad (5.3)$$

where  $\mathbf{H}_{syn_{j,k}}^{\Psi_r}(\omega_d)$  is the FRF obtained using Eq. (5.1) computed at the damped natural frequency  $\omega_d$ , using the single  $r^{th}$  eigenvector and original modal constant  $a_r$ ;  $\mathbf{H}_{syn_{j,k}}^{\Psi_{e,r}}(\omega_d)$  is the FRF obtained considering only the smoothed  $r^{th}$  mode shapes and the original modal constant  $a_r$  at the damped natural frequency  $\omega_d$ . Indexes  $j$  and  $k$  refer only to the nodes experimentally excited, i.e.  $j, k = 1, \dots, \max(I, O)$ .

An example of the expansion and smoothing method on an incomplete mode of a complex structure, i.e. a suspended car chassis, is shown in Figure 5.3.

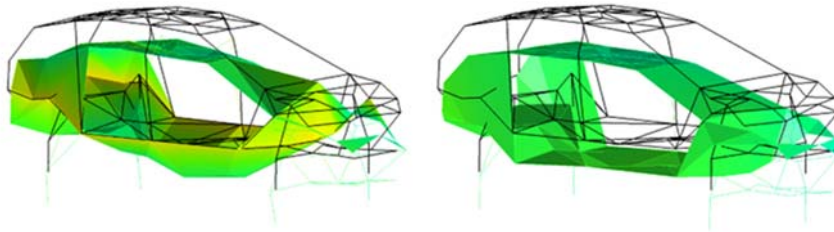


Figure 5.3 - Incomplete mode shapes (left) and expanded mode shape (right).

The original mode shape Figure 5.3 (left) is incomplete, because some DOFs are not measured; only the measured DOFs are extracted from EMA in the eigenvector, therefore the components of the non-measured DOFs are not

identified and the eigenvector is incomplete. The expanded eigenvector Figure 5.3 (right) has the same shape information and it is complete.

The effects of the expansion process on the mode energy are presented in Figure 5.4, where the sum of all the FRF is shown. The area under the original sum FRF (blue curve) is proportional to the energy associated with that mode shape considering the tested nodes. The expanded mode shape under-estimated this energy (red dashed-dot curve) when the original modal constant  $a_r$  is used. The FRF synthesised with the adjusted modal constant  $a_{r,new}$  from Eq. (5.3) (black dotted curve), perfectly overlap the original FRF, therefore both the total amount of energy and its distribution over frequency are correct.

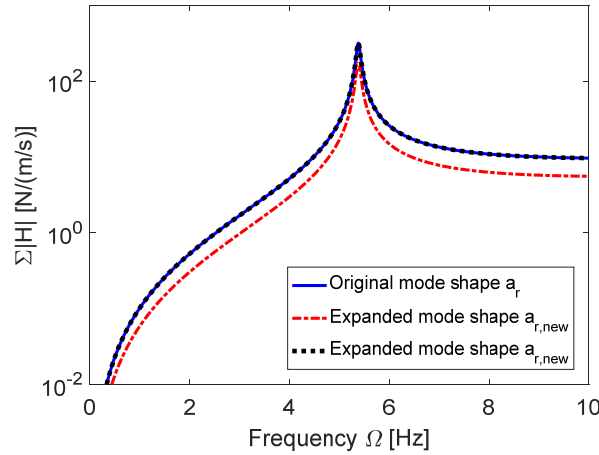


Figure 5.4 - Effects of mode shape expansion and filtering on FRF.

### 5.3 Properness condition for complex modes

The equation of motion a MDOF viscous damped system, given in Eq. (2.118), can be written in first order form as:

$$\mathbf{A}\dot{\mathbf{y}} + \mathbf{B}\mathbf{y} = \mathbf{F}(t) \quad (5.4)$$

$$\mathbf{A} = \begin{bmatrix} \mathbf{C} & \mathbf{M} \\ \mathbf{M} & \mathbf{0} \end{bmatrix}, \quad \mathbf{B} = \begin{bmatrix} -\mathbf{K} & \mathbf{0} \\ \mathbf{0} & \mathbf{M} \end{bmatrix}, \quad \mathbf{F} = \begin{bmatrix} \mathbf{f}(t) \\ \mathbf{0} \end{bmatrix}, \quad \mathbf{y}(t) = \begin{bmatrix} \mathbf{x}(t) \\ \dot{\mathbf{x}}(t) \end{bmatrix} \quad (5.5)$$

and the modal matrix  $\mathbf{\Theta} = \begin{bmatrix} \tilde{\mathbf{\Theta}} \\ \tilde{\mathbf{\Theta}}\mathbf{\Lambda} \end{bmatrix}$  is normalised so that  $\mathbf{\Theta}^T \mathbf{A} \mathbf{\Theta} = \mathbf{I}$  and  $\mathbf{\Theta}^T \mathbf{B} \mathbf{\Theta} = \mathbf{S}$ .

The inverse of the matrix  $\mathbf{B}$  can be computed inverting the orthogonality condition, Eq. (2.151):

$$\mathbf{B}^{-1} = \mathbf{\Theta} \mathbf{\Lambda}^{-1} \mathbf{\Theta}^T = \begin{bmatrix} \tilde{\mathbf{\Theta}} \mathbf{\Lambda}^{-1} \tilde{\mathbf{\Theta}}^T & \tilde{\mathbf{\Theta}} \tilde{\mathbf{\Theta}}^T \\ \tilde{\mathbf{\Theta}} \tilde{\mathbf{\Theta}}^T & \tilde{\mathbf{\Theta}} \mathbf{\Lambda} \tilde{\mathbf{\Theta}}^T \end{bmatrix} \quad (5.6)$$

or inverting its definition, Eq. (5.5):

$$\mathbf{B}^{-1} = \begin{bmatrix} -\mathbf{K}^{-1} & \mathbf{0} \\ \mathbf{0} & \mathbf{M}^{-1} \end{bmatrix} \quad (5.7)$$

Eq. (5.6) and (5.7) represent the same quantity, therefore:

$$\begin{bmatrix} -\mathbf{K}^{-1} & \mathbf{0} \\ \mathbf{0} & \mathbf{M}^{-1} \end{bmatrix} = \begin{bmatrix} \tilde{\mathbf{\Theta}} \mathbf{\Lambda}^{-1} \tilde{\mathbf{\Theta}}^T & \tilde{\mathbf{\Theta}} \tilde{\mathbf{\Theta}}^T \\ \tilde{\mathbf{\Theta}} \tilde{\mathbf{\Theta}}^T & \tilde{\mathbf{\Theta}} \mathbf{\Lambda} \tilde{\mathbf{\Theta}}^T \end{bmatrix} \quad (5.8)$$

All the block matrix terms in Eq. (5.8) should be equal:

$$\mathbf{K} = -\tilde{\mathbf{\Theta}}^{-T} \mathbf{\Lambda} \tilde{\mathbf{\Theta}}^{-1} \quad (5.9)$$

$$\mathbf{M} = \tilde{\mathbf{\Theta}}^{-T} \mathbf{\Lambda} \tilde{\mathbf{\Theta}}^{-1} \quad (5.10)$$

$$\tilde{\mathbf{\Theta}} \tilde{\mathbf{\Theta}}^T = \mathbf{0} \quad (5.11)$$

Eq. (5.11) identifies the so called proper condition [177], it means that the modal matrix  $\tilde{\mathbf{\Theta}}$  contains eigenvector associated to a second order model of the form in Eq. (2.118). This condition should be satisfied if the identified is enough accurate, but due to not good identified, improper scaling or inaccuracy Eq. (5.11) could be not satisfied.

Although the error of the mode shapes identified using the pLSCF and ML-MM methods (§ 5.1.1) with respect to Eq. (5.11) is usually moderated, the identified modal matrix can be improved to make it satisfying Eq. (5.11).

Proper condition is even more powerful if applied to expanded mode shapes § 5.2, which have larger errors with respect to Eq. (5.11).

The method is an optimisation procedure presented in [177,178] to find the proper modal matrix  $\hat{\mathbf{\Theta}}$  most close to the identified one  $\tilde{\mathbf{\Theta}}$  so that Eq. (5.11) is satisfied:

$$\min_{\hat{\mathbf{\Theta}}} \|\hat{\mathbf{\Theta}} - \tilde{\mathbf{\Theta}}\| \cap \hat{\mathbf{\Theta}} \hat{\mathbf{\Theta}}^T = \mathbf{0} \quad (5.12)$$

In [178] the proper modal matrix  $\hat{\mathbf{\Theta}}$  for structural problem is proved to be:

$$\hat{\mathbf{\Theta}} = (\mathbf{I} - \delta \delta^*) (\tilde{\mathbf{\Theta}} - \tilde{\mathbf{\Theta}}^*) \quad (5.13)$$

where  $\delta$  is the Langrage Multiplier matrix obtained by solving the Riccati's equation:

$$\tilde{\mathbf{\Theta}} \tilde{\mathbf{\Theta}}^T - \delta \tilde{\mathbf{\Theta}}^* \tilde{\mathbf{\Theta}}^T - \tilde{\mathbf{\Theta}} \tilde{\mathbf{\Theta}}^* \delta + \delta \tilde{\mathbf{\Theta}}^* \tilde{\mathbf{\Theta}}^* \delta = \mathbf{0} \quad (5.14)$$

where  $(\bullet)^*$  denoted the complex conjugate.

The effect of the proper condition application or slightly visible on synthesised FRF, the effect is much more important for the semi-positive

definition of stiffness matrix  $\mathbf{K}$  and positive definition of mass matrix  $\mathbf{M}$  computed using respectively Eq. (5.9) and Eq. (5.10). The differences between the synthesised FRF without (red curve) and proper FRF (black dashed-dot curve) proper condition is shown in Figure 5.5.

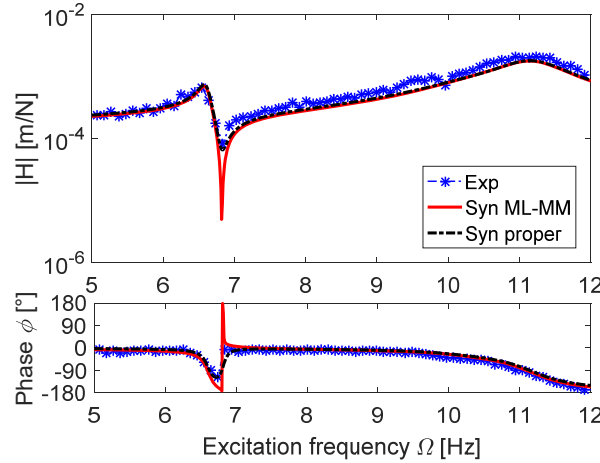


Figure 5.5 - Synthesised FRF imposing proper condition.

Formulation to obtain the proper modal matrix for more complex problems, such as combined problems and non-symmetric system, can be found in [179,180].

## 5.4 Conclusion

This chapter presented some method useful to the implementation of the SLM. The SLM, in the stabilisation phase, requires the identification of the system matrix several times changing the location and amount of spectral lines. This is not feasible with experimental data which are usually acquired at fixed frequency resolution. The experimental frequency resolution is generally not enough small to provide a good amount of spectral lines around the FRF peaks. The solution is to use the synthesised FRF in the stabilised layer method. The use of synthesised FRFs has two main advantages: 1) all the necessary spectral lines can be computed without any limitation due to the experimental frequency resolution, 2) the effect of noise is filtered out and therefore the identification is no more affected by noise in input and output. The synthesis of experimental FRF can be obtained from the identified modal parameters which can be identified with classical or more advanced method. i.e. PolyMAX and ML-MM were introduced, which improve the synthesis results.

Another problem affecting the damping matrix identification via SLM is the generally incompleteness of the receptance matrix. Not all the DOFs can be usually measured and the identified damping matrix will be limited to the measured DOFs. An iteratively expand the he measured mode shapes to the global set of DOF was presented. It let to compute the complete synthesised receptance

matrix from incomplete measured receptance matrix, and therefore to identify the global damping matrix.

Finally, the proper condition is introduced. It is an analytical method to improve the synthesis from identified or expanded eigenvectors. It improves the mode shapes to consider the physical properties of the system, i.e. mode shapes should be related to a second order model. The identification of physical damping matrix from a physical modal model results more reliable and easier.

# Chapter 6

## 6. Test-rig for spatial damping matrix identification and nonlinear vibration control

This chapter presents a three DOFs test-rig designed to perform both direct spatial damping matrix identification and nonlinear active control, assigning the desired vibration behaviour to the system. The test-rig here introduced will be used in different applications in next chapters.

The basic linear configuration of the test-rig is described in § 6.1. The damped configurations of the test-rig are introduced in § 6.2 and the non-smooth nonlinear configuration in § 6.3.

### 6.1 The three DOFs test-rig lumped parameters test-rig

The base of the test-rig is a linear three DOFs lumped mass-damper-spring system with plate-like springs, shown in Figure 6.1. Each mass is connected to the ground through a “ground spring” and linked with its nearest neighbor through a “coupling spring”. The system possesses only translational DOFs, one for each mass, which are numbered 1-2-3 from left to right in Figure 6.1.

Each of the three “ground springs” is made by a couple of parallel plate springs. This design introduced a low stiffness in the horizontal direction and locks the rotational DOFs of the masses in the plane of the picture. The stiffness of the springs in the other directions is orders of magnitude higher and the related DOFs can be considered fixed or at least with very high constraints stiffness.

The “Coupling spring” are composed by a two plate-like spring linked by a rigid element on the top. The springs can be considered almost massless, because the weight of the rigid plates is negligible with respect to the three main masses.



The two additional modes related to the two rigid links are far from the frequency range of the three heavier masses.

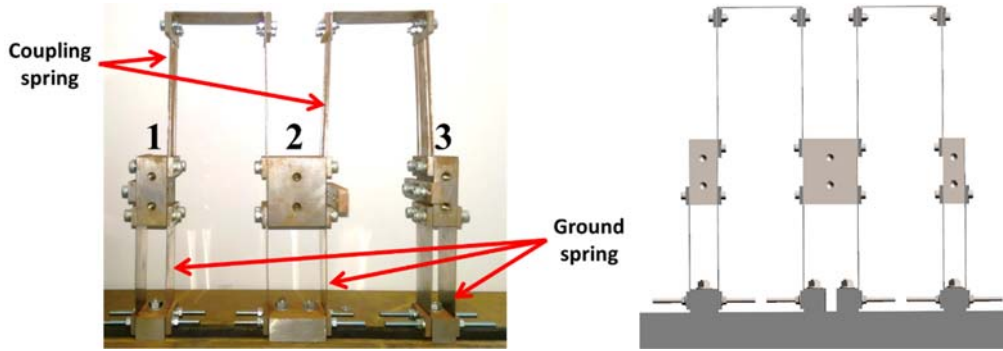


Figure 6.1 - Three DOFs lumped parameters test-rig (left) and CAD model (right).

The linear configuration of the test rig is parametric, in fact the stiffness of the “coupling springs” can be set changing the position of the rigid link. The rigid link can be moved inside two slots obtained in each of the thin plate. In particular, the lowest stiffness of the coupling spring is achieved when the rigid link is the upper position, while it becomes almost rigid when the rigid link is mounted in the lower position.

The nominal weight of the three masses are respectively  $m_1 = 1.3297$  kg ,  $m_2 = 2.4234$  kg ,  $m_3 = 0.9065$  kg .

The spring stiffnesses are computed using Euler-Bernoulli beam model and appropriate boundary conditions. The ground spring stiffness is computed as the equivalent stiffness of two plate spring in parallel. Each of the two spring is fixed at the bottom end and with only the translation DOF free to move at the top end, the nominal stiffness of the global ground springs result to be  $\tilde{k}_g = 3617.4$  N/m .

The “coupling springs” are two Euler-Bernoulli springs linked by a rigid element and with only horizontal translations allowed in the two ends. The stiffness of the “coupling spring” in the nominal configuration, given in Figure 6.1, result to be  $\tilde{k}_g = 1735.5$  N/m .

The base configuration of the system is almost undamped, only small amount of viscous damping due to the low dissipation of the material is present.

## 6.2 Test-rig damped configuration

The damped configuration of the test-rig presented in Figure 6.1 is obtained adding viscous damping to the system through two air dashpots, model 2K S 160 A 2.0 NF [181]. The damped configuration of the lumped parameters test rig is shown in Figure 6.2.

A dashpot is placed between the first and second DOFs, it is a relative damper and its viscous damping coefficient is  $c_{12}$ . The other dashpot is an absolute damper acting on the third DOF, its viscous damping coefficient is  $c_3$ .

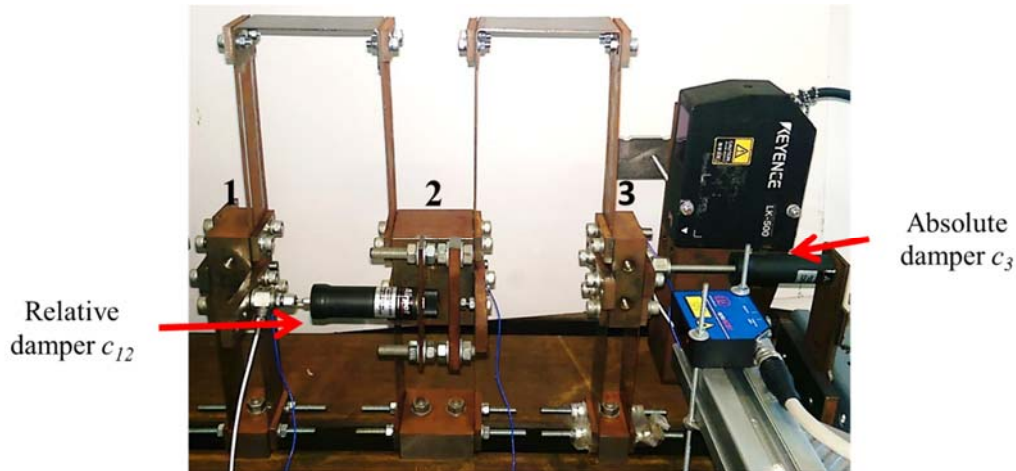


Figure 6.2 - Three DOFs damping configurable test-rig.

The test-rig is configurable because the dashpots can be activated arbitrary and the viscous damping coefficients  $c_{12}$  and  $c_3$  can be easily changed, Figure 6.3.

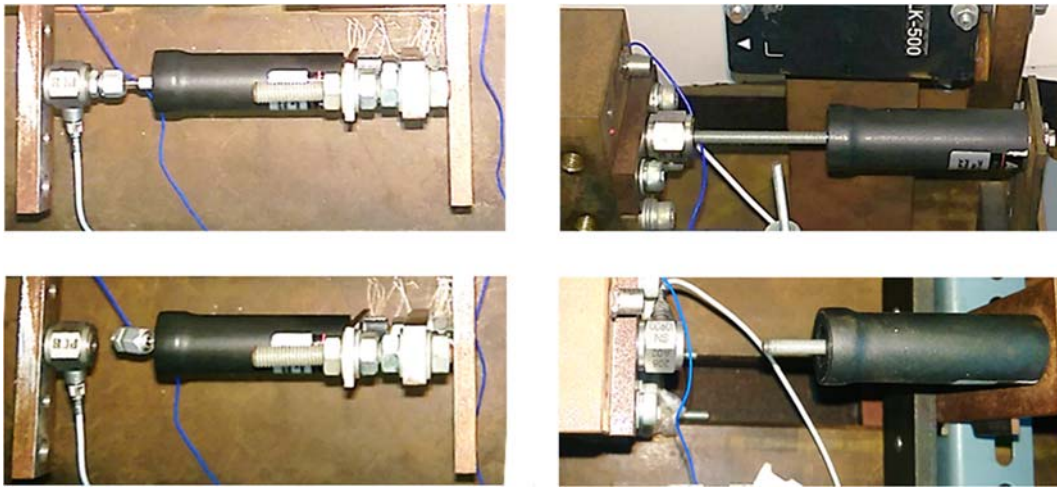


Figure 6.3 - Dampers activated (top) and excluded (bottom):  
relative damper  $c_{12}$  (left) and absolute damper  $c_3$  (right).

Activated dashpots, i.e. with fixed ends, are shown in Figure 6.3 (top), in this configuration they dissipate energy from the system. When the dashpots are disconnected, Figure 6.3 (bottom), the absolute damper  $c_3$  is not part of the system, while the relative damper  $c_{12}$  simply becomes an addition mass attached to the second DOF. The dashpots damping coefficients values are continuously adjustable. Four different levels of damping were chosen for the relative damper  $c_{12}$ , while the absolute damper  $c_3$  was maintained constant at a moderately high

## 6. Test-rig for spatial damping matrix identification and nonlinear vibration control

level of dissipation. In total ten configurations of the test-rig, differing for levels and damping distribution, were tested. The configurations are reported in Table 6.1.

Table 6.1 - Identified test-rig configurations.

Configuration	Description
undamped	Dashpots deactivated
D3	Absolute dashpot active
D12 L1	Relative dashpot active, dissipation level L1
D12 L2	Relative dashpot active, dissipation level L2
D12 L3	Relative dashpot active, dissipation level L4
D12 L4	Relative dashpot active, dissipation level L4
D3 & D12 L1	Absolute and relative dashpots active, relative diss. level L1
D3 & D12 L2	Absolute and relative dashpots active, relative diss. level L2
D3 & D12 L3	Absolute and relative dashpots active, relative diss. level L3
D3 & D12 L4	Absolute and relative dashpots active, relative diss. level L4

The reference damping values in each configuration were obtained by testing the damper separately, away from the test-rig. The dampers were tested, fixed at one end with a known mass attached to the other, as shown in Figure 6.4 (left). The time necessary to travel a known stroke  $h$  of the damper was measured and the damping value computed from a mass-damper model. The test was repeated for both damper extension and retraction, as in the scheme of Figure 6.4 (left).

The damping values computed from the mass-damper model are reported in Figure 6.4 (right). The damping coefficients differences between extension and retraction is mainly due to time measurement accuracy and friction in the retraction tests. The mean values between extension and compression were considered as reference damping values, reported in Table 6.2, and although nonlinear effects might be present to some degree they were not considered in the present study.

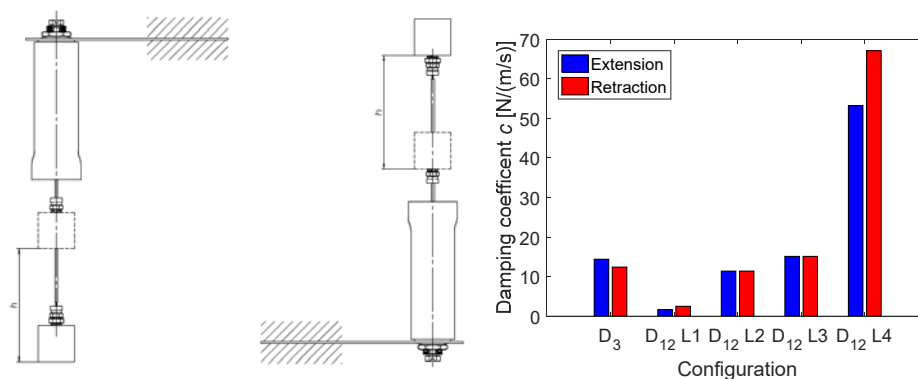


Figure 6.4 - Schematic of the dampers test setup: extension - retraction (left), expected damping coefficients values (right).

Table 6.2 - Reference damping coefficients.

Damper	Values [N/(m/s)]
D12 L1, $c_{1,2}$	13.39
D12 L2, $c_{1,2}$	2.05
D12 L3, $c_{1,2}$	11.41
D12 L4, $c_{1,2}$	15.13
D3, $c_3$	60.12

### 6.3 Test-rig non-smooth nonlinear configuration

The non-smooth nonlinear experimental test-rig is shown in Figure 6.5. It consists of the linear test rig, shown in Figure 6.1, with an additional non-smooth piecewise spring located at the third DOF. The non-smooth nonlinear test rig is configurable, because the nonlinearity can be added to each of the three DOFs, in fact the nonlinearity can be moved in the other two DOFs or more than one nonlinearity can be added. For example the nonlinearity was located across the first DOF in [182]. The non-smooth piecewise nonlinearity is achieved by means of two additional springs, which we will call setting springs, mounted either side of the third mass. Each setting spring include a slider, which is the contact point with one of the ground springs. The slider is separated from a grounding spring by a continuously adjustable gap,  $g_1$  on the left and  $g_2$  on the right.

The result is a non-smooth nonlinear hardening spring characteristic due to the different values of stiffness, shown in Figure 6.6, when the gaps are open or closed. The nonlinear effect can be modified by changing the length of the setting spring  $l_2$  (i.e. vertical contact location).

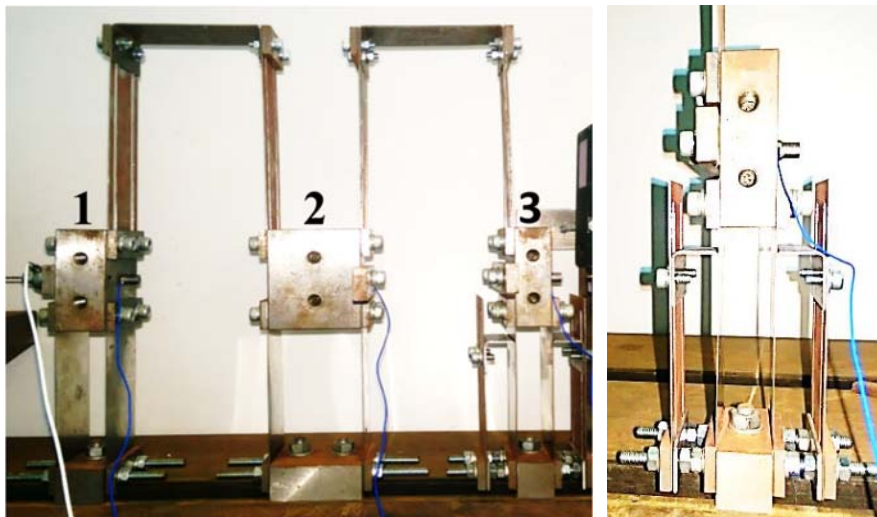


Figure 6.5 - Non-smooth nonlinear test-rig(left), nonlinear spring (right).

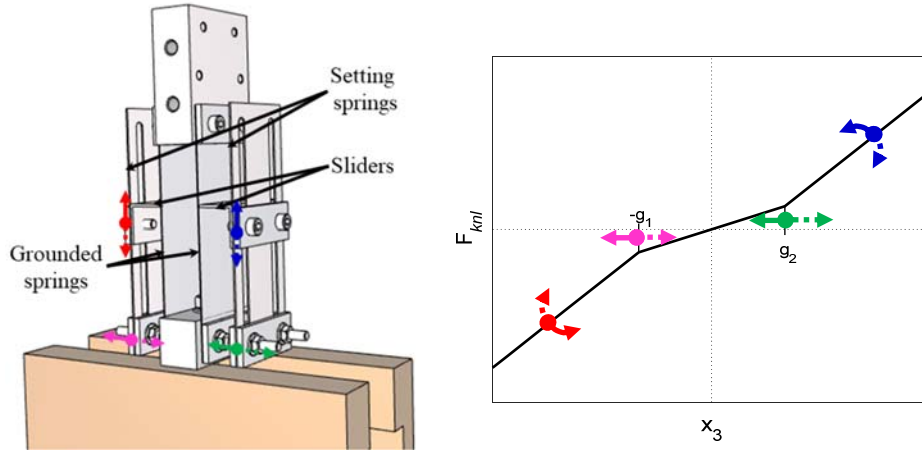


Figure 6.6 - Nonlinear spring: model (left) and characteristic (right).

The effects of changes in the nonlinear spring configuration on the spring characteristic are qualitatively shown in Figure 6.6 (left). The vertical position of the sliders affects the stiffness of the close gap region, while the gap value locates the switching points between the close gap and open gap working conditions.

The non-smooth nonlinear spring could be also set in a non-symmetric configuration in both stiffness of the two close gaps regions and gap values.

The settings chosen for the experiments carried out in the following chapters are  $g_1 = g_2 = 0.035$  mm and  $l_2 = 81.6$  mm.

## 6.4 Conclusions

A three DOF lumped parameters system is presented in this chapter. Its damped and nonlinear configurations are introduced. The damped configuration can be adjusted to change both the distribution and the amount of damping in the structure. The viscous damping coefficients of the air dashpot at different levels of dissipation are presented and will be used as reference values.

The nonlinear configuration is adjustable both in the location and characteristic of the non-smooth nonlinearity.

The test-rig will be used in § 7 for validate the SLM method presented in § 4 using some of the enhancing methods given in § 5. It is also used in § 11 and § 12 for the experimental application of state space and receptance based feedback linearisation for active control of the nonlinear non-smooth version of the test rig.

# Chapter 7

## 7. Experimental direct damping identification in a lumped parameters system

The SLM and the considerations on treatment of experimental data, presented respectively § 4 and § 5, are in this chapter applied to identify the viscous dissipation in the damped configuration of three DOFs test-rig presented in § 6.2. The test-rig present non-classical viscous damping and it is configurable as regards both damping amount and distribution.

The application of the SLM methodology to a simple mechanical system is necessary for its validation. In the example presented in the next paragraphs. The results of the identification are compared to the reference topology and reference damping coefficient values.

The SLM is simplified to only viscous damping matrix identification in § 7.1. The experimental setup used for testing the structure are described in § 7.2. The SLM is applied in § 7.3 for the identification of ten different damping layout of the test-rig, presented in § 6.2. Finally, in § 7.4 considerations on the robustness and coherence of the identified results are shown.

A summary of the work presented in this paragraph can be found in [161].

### 7.1 SLM for viscous damped system

The SLM presented in § 4 identifies both viscous  $\mathbf{C}$  and structural  $\mathbf{D}$  damping together. In this case, the system is only viscous damped; therefore, the SLM is simplified and adapted to the identification of only viscous damped matrix  $\mathbf{C}$ . The unknowns vector  $\mathbf{u}$  in Eq. (4.11), becomes:

$$\mathbf{u} = \left\{ \mathbf{c}_A^T \quad \mathbf{c}_R^T \right\}^T \quad (7.1)$$

hence only  $NA + NR$  unknowns should be identified: the absolute and relative viscous damping coefficients.

The identification of the non-classical viscous damping matrix  $\mathbf{C}$  simplifying Eq. (4.37), into

$$\begin{bmatrix} \Omega_1 \mathbf{H}^N(\Omega_1) \\ \Omega_2 \mathbf{H}^N(\Omega_2) \\ \vdots \\ \Omega_K \mathbf{H}^N(\Omega_K) \end{bmatrix} \mathbf{C} = \begin{bmatrix} \mathbf{G}(\Omega_1) \\ \mathbf{G}(\Omega_2) \\ \vdots \\ \mathbf{G}(\Omega_K) \end{bmatrix} \quad (7.2)$$

Substituting the definition of viscous damping matrix  $\mathbf{C}$ , given in Eq. (4.15), in Eq. (7.2), it is possible to obtain the simplified version of Eq. (4.41):

$$\mathbf{VP} \begin{bmatrix} u_1 \mathbf{I} & \cdots & u_{NA} \mathbf{I} & u_{NA+1} \mathbf{I} & \cdots & u_{NA+NR} \mathbf{I} \end{bmatrix}^T = \mathbf{Q} \quad (7.3)$$

Finally Eq. (7.3) becomes:

$$\begin{bmatrix} \mathbf{VPZ}_1 \\ \vdots \\ \mathbf{VPZ}_n \end{bmatrix} \mathbf{u} = \begin{bmatrix} \mathbf{QW}_1 \\ \vdots \\ \mathbf{QW}_n \end{bmatrix} \quad (7.4)$$

where  $\mathbf{Z}_i$  and  $\mathbf{W}_i$  defined in Eq. (4.44) and Eq. (4.45).  $\mathbf{Z}_i$  is adapted to the  $NA + NR$  unknowns:

$$\mathbf{Z}_i = \mathbf{0} \text{ and } (\mathbf{Z}_i)_{(y-1)N+i,y} = 1 \text{ with } y = 1, 2, \dots, (NA + NR) \quad (7.5)$$

Eq. (7.4) can be written in compact form as:

$$\bar{\mathbf{V}} \mathbf{u} = \bar{\mathbf{Q}} \quad (7.6)$$

and solved for  $\mathbf{u} > 0$ , with the same procedure already presented for the solution of Eq. (4.46). The stabilisation procedure to identify the solution  $\mathbf{u}^*$ , presented in § 4.3, is then applied on the  $NA + NR$  unknowns.

## 7.2 Experimental setup

Experimental roving-hammer modal analysis was carried out on the test-rig presented in § 6.2, using LMS SCADAS III and Siemens LMS Test.Lab. The FRFs in term of displacement were obtained by averaging the FRFs obtained from five separate impacts for each DOF, using a PCB 086C03 instrumented hammer. System responses were measured with three displacement laser sensors



(Keyence LK-500 and LK-G402 and Micro-Epsilon OptoNCDT 1402-100), one for each system DOF as shown in Figure 7.1. The system was completely monitored also in terms of accelerations with three mono-axial accelerometers K-Shear 8728A500 and damping forces produced by the dampers, measured using load cell PCB 208C02 attached at one end of the damper. However, acceleration and damping forces are not necessary for damping matrix identification using SLM, hence these measurements were not used in the identification process.

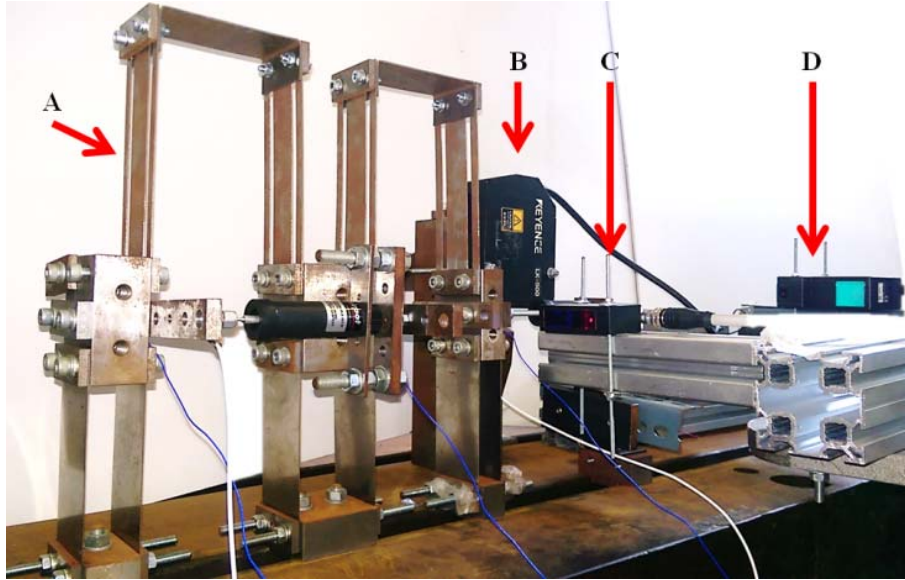


Figure 7.1 - Experimental laboratory setup: A - test rig; B - laser displacement DOF 1; C - laser displacement DOF 2; D - laser displacement DOF 3.

### 7.3 Experimental viscous damping identification

The SLM described § 4 and simplified to only viscous damping identification in § 7.3 is applied for the localisation and quantification of the viscous damping matrix  $\mathbf{C}$  of the three DOFs lumped parameters system. In this case the global dimension of the system is  $N = 3$ .

The identification is based on the complete measured FRM  $\mathbf{H}^{Exp}(\Omega) \in \mathbb{C}^{3 \times 3}$  of the ten configurations described in Table 6.1.

Tests carried out on the individual dampers in isolation, described in § 6.2 allows the validation of the identified damping matrix terms at different levels of dissipation and with different damping distribution. The identification results in different configurations should be coherent among the configurations and in agreement with the expected values.

The receptances used for the identification method were synthesised from the experimental complex modal parameters, using Eq. (5.1). The complex eigenvalues, mode shapes and modal constant are estimated by identification using the pLSFC algorithm [175] (§ 5.1.1), and when necessary optimised using



ML-MM [176] (§ 5.1.1) and proper conditions [177,178] (§ 5.3) to obtain a good synthesis of the receptance FRM  $\mathbf{H}_{syn}(\Omega)$ .

The assumption of a only viscous damping dissipations is considered to be justified for the following reasons: 1) from a physical point of view only viscous damping is present in the form of air-dashpots; 2) from an analytical point of view, the entire set of configurations presents a low non-viscosity index  $\gamma_3$  (Adhikari and Woodhouse [25]). The non-viscosity  $\gamma_3$  index is applicable only when all the mode shapes of the system are available, as is the case for the analysed lumped system, and should result zero for perfect viscously damped systems. Non-viscosity index  $\gamma_3$  of the ten configurations appear to be very low, i.e. almost perfectly viscous damped system. The non-viscosity indices  $\gamma_3$  for each configuration are reported in Table 7.1.

Table 7.1 - Non-viscosity index of the test-rig configurations.

Configuration	Non-viscosity $\gamma_3$	Configuration	Non-viscosity $\gamma_3$
undamped	0.0049	D3	0.0023
D12 L1	0.0028	D3 & D12 L1	0.0071
D12 L2	0.0025	D3 & D12 L2	0.0023
D12 L3	0.0058	D3 & D12 L3	0.0026
D12 L4	0.0046	D3 & D12 L4	0.0018

The selection of the Layers is required to apply SLM. In this case, assuming no prior knowledge of the damper locations, 5 layers must be chosen: three absolute damping layers  $c_1$ ,  $c_2$  and  $c_3$ , representing the absolute damping arising from the physical connectivity of the three masses with the ground, and two relative dampers  $c_{1,2}$  and  $c_{2,3}$  arising from the physical connectivity between the DOFs 1 and 2 and DOFs 2 and 3. The system topology does not include any physical connection between DOFs 1 and 3, therefore that layer is not considered.

In the stabilisation phase, the value of the tolerance  $\varepsilon$ , used in Eq. (4.67), is set to 1% of the identified damping value,  $\varepsilon = 0.01$ . In the following sections the SLM is applied to the ten configurations of the system.

### 7.3.1 Undamped configuration

The undamped configuration of the three DOFs system do not include both the relative dampers  $c_{12}$  and absolute damper  $c_3$ , which are deactivated. The test-rig present only small viscous damping, which is always present in real structure. The synthesised FRM  $\mathbf{H}_{syn}(\Omega)$  is in very good agreement with the experimental FRM  $\mathbf{H}^{Exp}(\Omega)$ , as shown in Figure 7.2. The system is almost undamped, with very sharp resonance peaks.

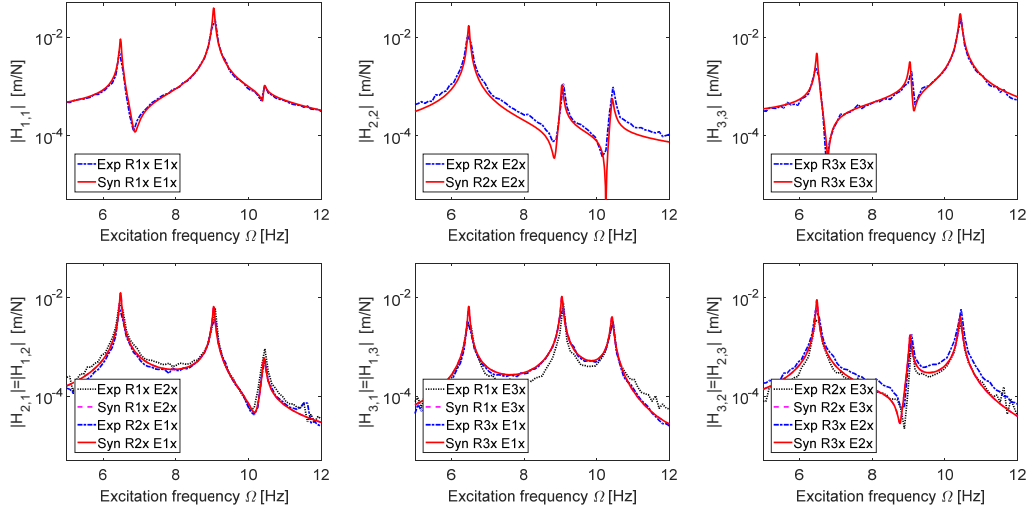
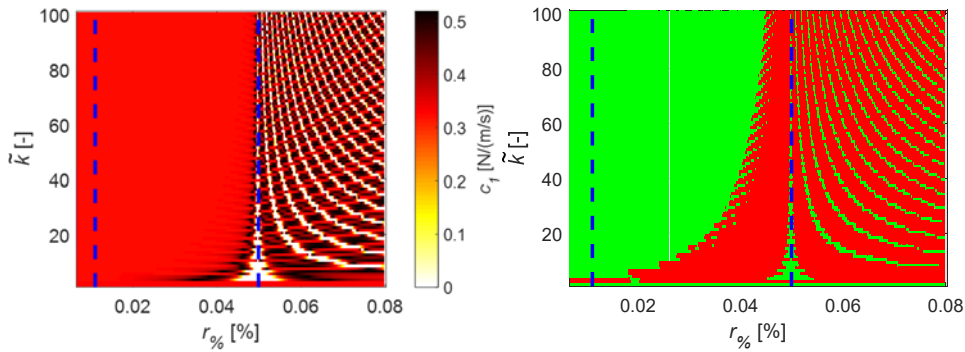


Figure 7.2 - Experimental and synthesised FRM of the conf. undamped.

The vertical asymptote ranges values  $r_{\%}$ , computed using Eq. (4.71), were found to be  $r_{\% \text{ asymptote}} = 0.028, 0.0585, 0.2658 \%$ . The identified damping coefficients of the five layers and their regions of stability are mapped onto the  $(r_{\%}, \tilde{k})$  plane in Figure 7.3-Figure 7.7. The expected asymptotes are highlighted in blue dashed vertical lines and the stabilisation diagrams show stable (green) and unstable (red) regions of the  $(r_{\%}, \tilde{k})$  plane. The damping coefficient  $c_1$  of the absolute damper acting of the first mass is identified in Figure 7.3. It is very low, although it is the highest identified damping value in this configuration. It is stable within frequency ranges between the first and the second asymptotes, close to the first vertical asymptote on the right. The absolute dampers acting on the second and third DOFs are shown in Figure 7.4 and in Figure 7.4. They are stable onto the entire  $(r_{\%}, \tilde{k})$  plane and almost null. The coefficient  $c_{1,2}$  of the first relative damper, shown in Figure 7.6, is very low and stable between the first two asymptotes. The relative damper  $c_{2,3}$  between the second and the third DOFs, shown in Figure 7.7, is zero. The identified damping values result very low.


 Figure 7.3 - Damping coefficient  $c_1$ : quantification (left) , stability (right).

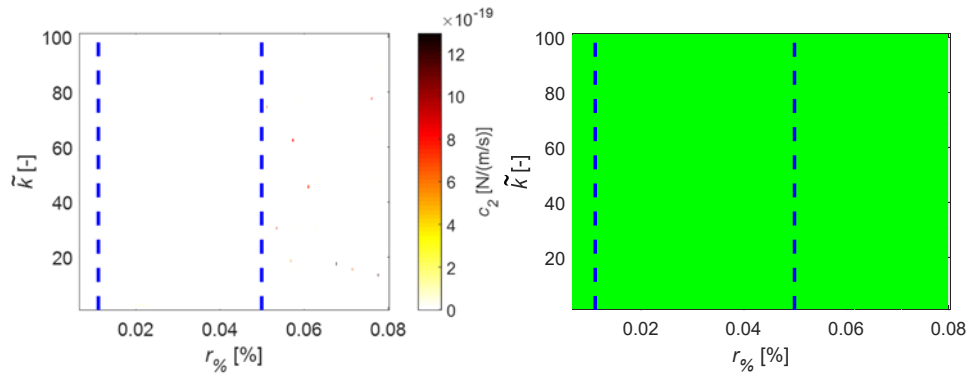


Figure 7.4 - Damping coefficient  $c_2$ : quantification (left) , stability (right).

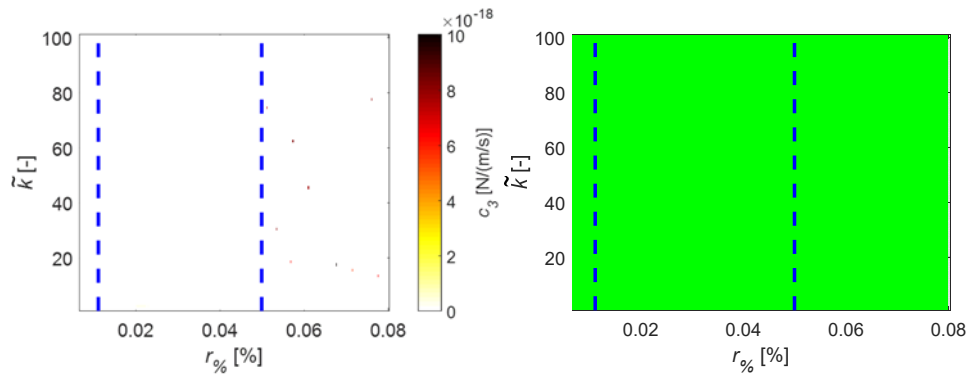


Figure 7.5 - Damping coefficient  $c_3$ : quantification (left) , stability (right).

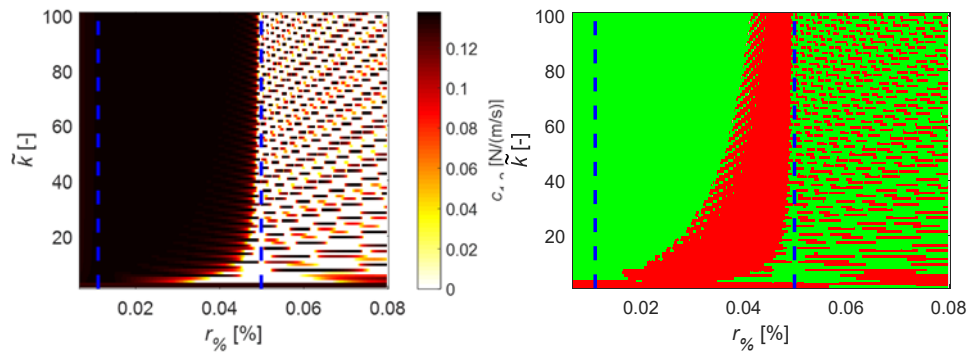


Figure 7.6 - Damping coefficient  $c_{1,2}$ : quantification (left) , stability (right).

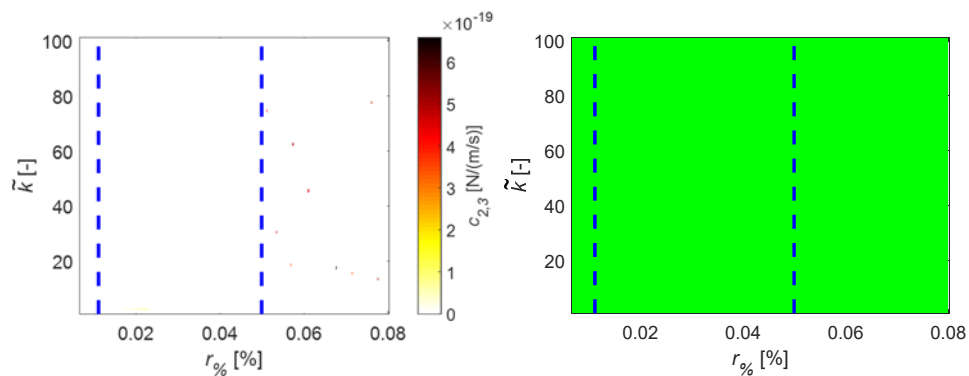


Figure 7.7 - Damping coefficient  $c_{2,3}$ : quantification (left) , stability (right).

The optimal identified solution  $\mathbf{u}^*$  can be selected looking for  $(r_{\%}^*, \tilde{k}^*)$  satisfying Eq. (4.70). The global stabilisation diagram  $\bar{\mathbf{S}}$ , computed as in Eq. (4.68), and the error map  $\mathbf{E}$ , computed using Eq. (4.69), are shown in Figure 7.8. The identification is globally stable in a region close to the first asymptote, in the same region also the normalised residuum  $E_{\%}$  reaches a minimum value.

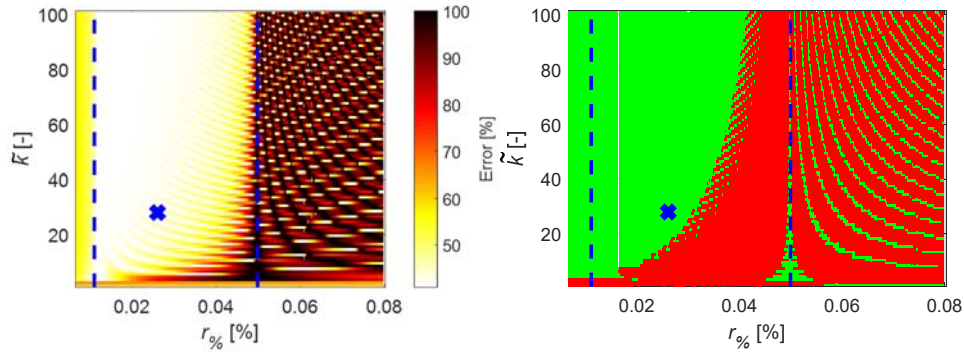


Figure 7.8 - Normalised residuum (left) and global stability diagram (right).

The optimal identification couple  $(r_{\%}^*, \tilde{k}^*)$  is the one with minimum residuum at  $(r_{\%}^*, \tilde{k}^*) = (0.0261\%, 28)$  and present an inversion error  $E_{\%}^* = 40.92\%$ , corresponding to the blue cross in Figure 7.8. The inversion error is high because it is normalised with respect to a very low value, related to the almost undamped configuration analysed.

The identified damping matrix is shown in Figure 7.9. The damping coefficient values of the five layers are reported in Table 7.2. The viscous damping matrix is almost empty.

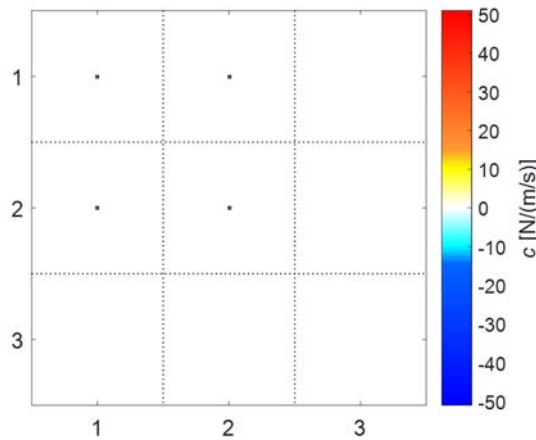


Figure 7.9 - Identified viscous damping matrix of the conf. undamped.

Table 7.2 - Identified damping coefficients values of undamped configuration.

Damper	Values [N/(m/s)]
$c_1$	0.3193
$c_2$	0.0000
$c_3$	0.0000
$c_{1,2}$	0.1379
$c_{2,3}$	0.0000

### 7.3.2 Configuration D3

The configuration D3 of the three DOFs system consist in the undamped configuration with the absolute viscous damper  $c_3$  acting on the test-rig and the relative damper  $c_{12}$  is deactivated. The system synthesised FRM  $\mathbf{H}_{syn}(\Omega)$  is in very good agreement with the experimental FRM  $\mathbf{H}^{Exp}(\Omega)$ , as shown in Figure 7.10. The damping effects are clearly visible on the third peaks of the FRM. The vertical asymptote ranges values  $r_{\%}$ , computed using Eq. (4.71), were found to be  $r_{\%asympote} = 0.089, 0.2092, 1.2568 \%$ . The identified damping coefficients of the five layers and their regions of stability are mapped onto the  $(r_{\%}, \tilde{k})$  plane in Figure 7.11 - Figure 7.15. The expected asymptotes are highlighted in blue dashed vertical lines and the stabilisation diagrams show stable (green) and unstable (red) regions of  $(r_{\%}, \tilde{k})$  plane. The quantification of damping coefficient  $c_1$ , i.e. the absolute damper acting of the first mass is shown in Figure 7.35. It is quite low and like the quantification already presented in the undamped configuration § 7.3.1. It is stable within frequency ranges between the first and the second asymptotes, close to the first vertical asymptote on the right.

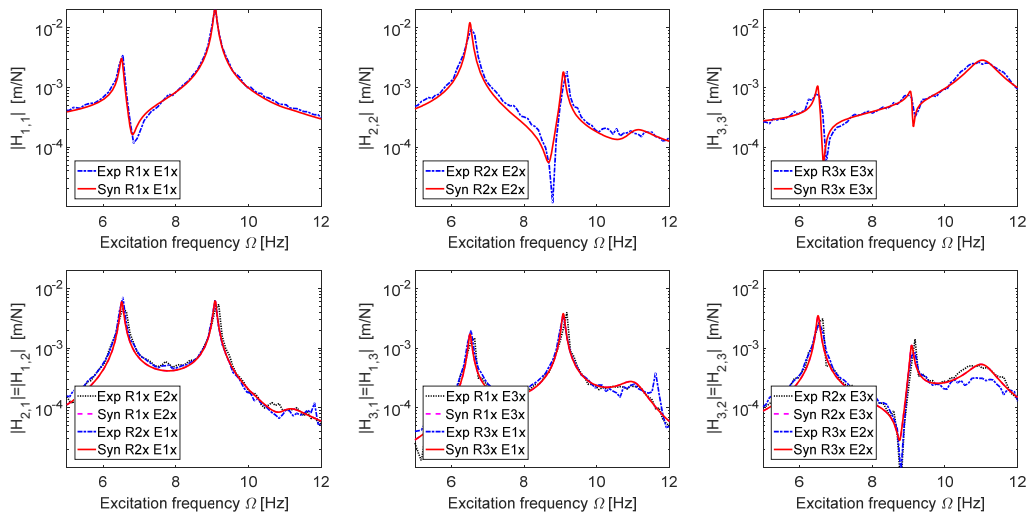


Figure 7.10 - Experimental and synthesised FRM of the configuration D3.

The absolute damping viscous coefficient  $c_2$  is shown onto the  $(r_{\%}, \tilde{k})$  plane in Figure 7.12. It is stable within frequency ranges between the first and the second asymptotes. The identified value is low but no more null, as in the undamped configuration. The viscous damping  $c_3$  is shown in Figure 7.13. It is stable in the frequency range between the first two asymptotes. The stable value is very high, as expected, and in good agreement with the reference value. The relative viscous damping coefficients  $c_{1,2}$  and  $c_{2,3}$  are shown in Figure 7.14 and Figure 7.15. They are stable onto the entire  $(r_{\%}, \tilde{k})$  plane and very low. Their quantification is comparable with the undamped identification. Only the quantification of absolute viscous damping coefficient  $c_3$  acting of the third DOF presents a high value, as expected from the topology of the configuration D3.

The optimal identified solution  $\mathbf{u}^*$  can be selected looking for  $(r_{\%}^*, \tilde{k}^*)$  satisfying Eq. (4.70). The global stabilisation diagram  $\bar{\mathbf{S}}$ , computed as in Eq. (4.68), and the error map  $\mathbf{E}$ , computed using Eq. (4.69), are shown in Figure 7.16. The identification is globally stable in a region close to the first asymptote, in the same region also the normalised residuum  $E_{\%}$  reaches a minimum value. The optimal identification couple  $(r_{\%}^*, \tilde{k}^*)$  is  $(r_{\%}^*, \tilde{k}^*) = (0.16\%, 97)$  and inversion error  $E_{\%}^* = 0.012\%$ , blue cross in Figure 7.16.

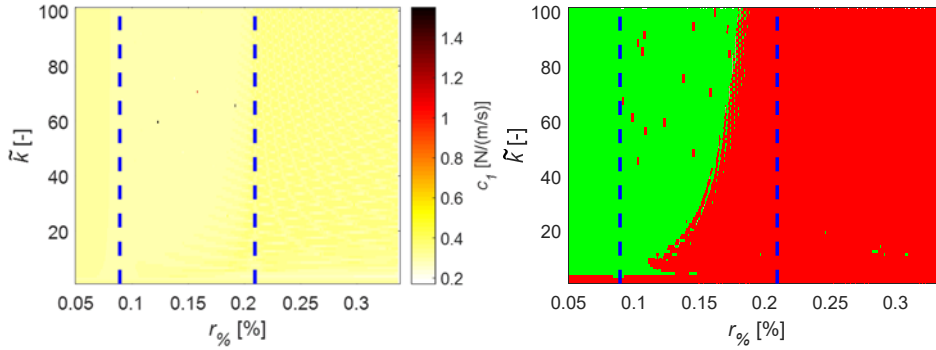


Figure 7.11 - Damping coefficient  $c_1$  : quantification (left) , stability (right).

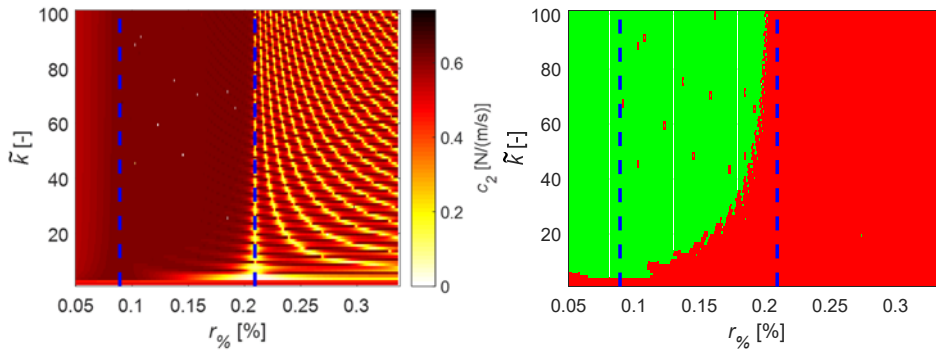


Figure 7.12 - Damping coefficient  $c_2$  : quantification (left) , stability (right).

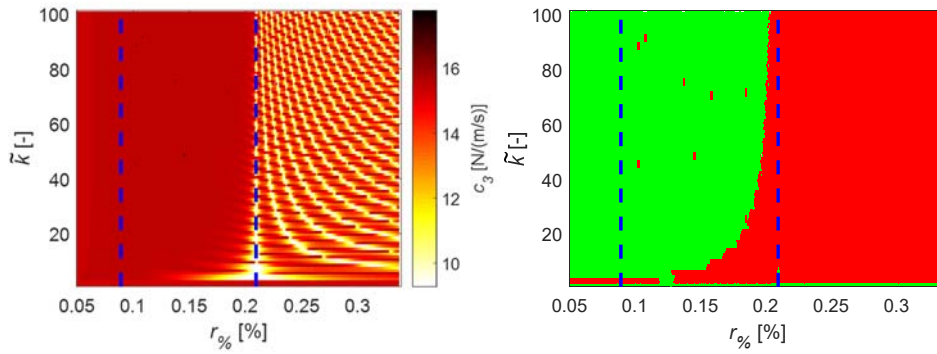


Figure 7.13 - Damping coefficient  $c_3$ : quantification (left) , stability (right).

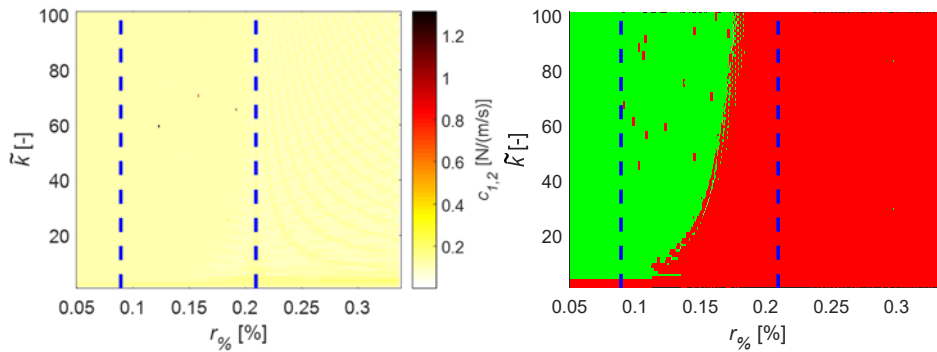


Figure 7.14 - Damping coefficient  $c_{1,2}$ : quantification (left) , stability (right).

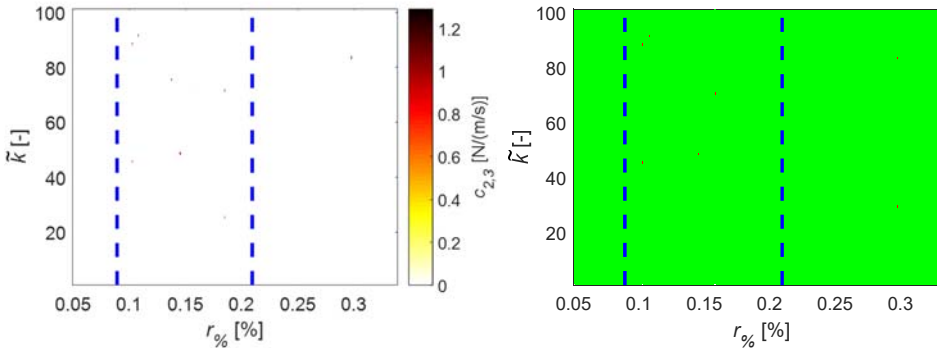


Figure 7.15 - Damping coefficient  $c_{2,3}$ : quantification (left) , stability (right).

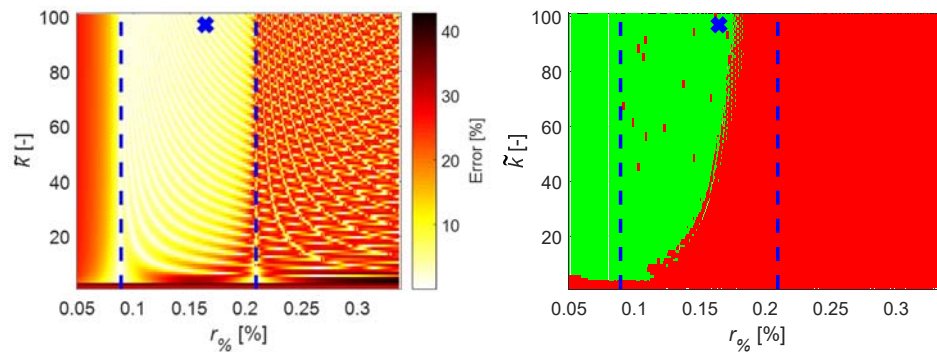


Figure 7.16 - Normalised residuum (left) and global stability diagram (right).

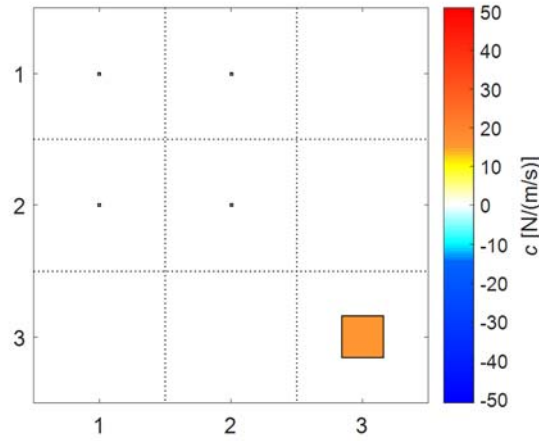


Figure 7.17 - Identified viscous damping matrix of the configuration D3.

The identified damping matrix is shown in Figure 7.17. The identified damping coefficient values of the five layers are reported in Table 7.3. The identified viscous damping matrix shows a localised damper acting on the third DOF, as expected. The damping coefficient value  $c_3$  is very close to the reference value.

Table 7.3 - Identified damping coefficients values of the configuration D3.

Damper	Values [N/(m/s)]
$c_1$	0.2901
$c_2$	0.6149
$c_3$	15.4703
$c_{1,2}$	0.1136
$c_{2,3}$	0.0000

### 7.3.3 Configuration D12 L1

The configuration D12 L1 of the three DOFs system presents only the relative viscous damper  $c_{1,2}$  acting on the system, while the absolute damper is deactivated. The system synthesised FRM  $\mathbf{H}_{syn}(\Omega)$  agrees very well with the experimental FRM  $\mathbf{H}^{Exp}(\Omega)$ , as shown in Figure 7.18. The damping effects are visible on the second peaks of the FRM, which shows a higher level of damping than the other peaks.

The vertical asymptote ranges values  $r_{\%}$ , computed using Eq. (4.71), were found to be  $r_{\%asymptote} = 0.0398, 0.1491, 0.1875 \%$ .



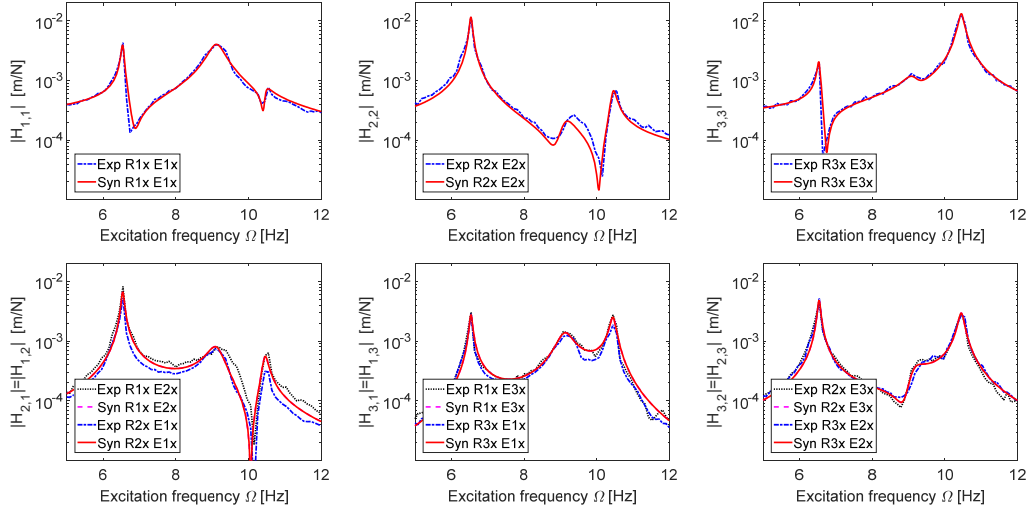
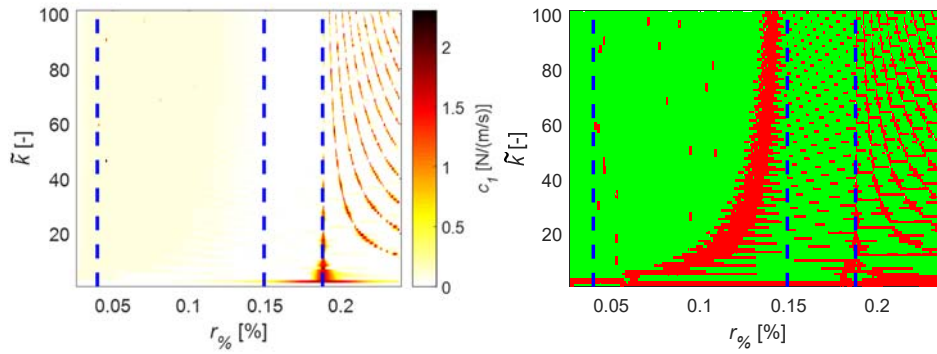
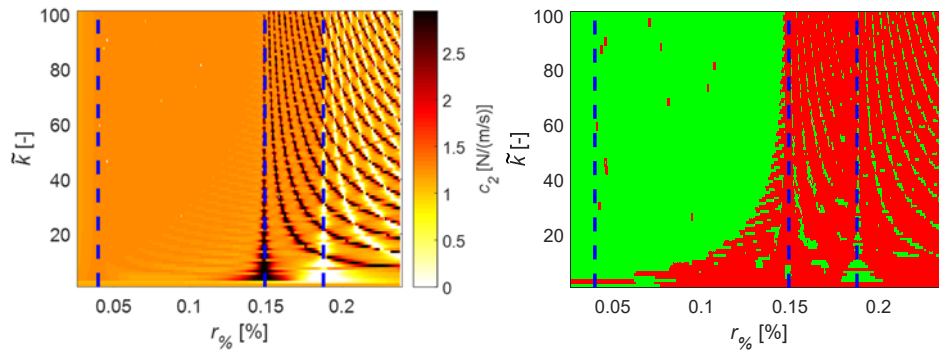
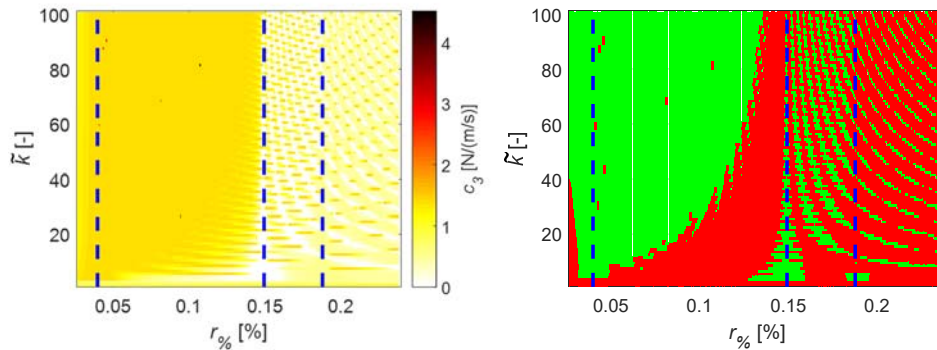
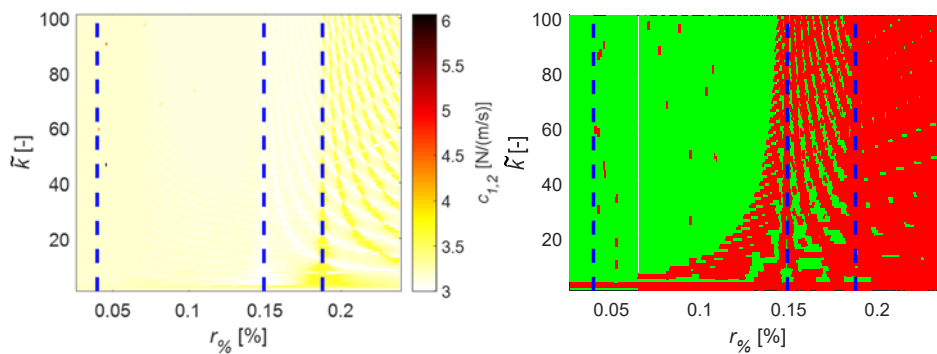


Figure 7.18 - Experimental and synthesised FRM of the conf. D12 L1.

The identified damping coefficients of the five layers and their regions of stability are mapped onto the  $(r_{\%}, \tilde{k})$  plane in Figure 7.19 - Figure 7.23. The expected asymptotes are highlighted in blue dashed vertical lines and the stabilisation diagrams show stable (green) and unstable (red) regions of  $(r_{\%}, \tilde{k})$  plane. The damping coefficient  $c_1$  of the absolute damper acting of the first mass is quantified in Figure 7.19. It is shown to be quite low and comparable with identification of the undamped and D3 configurations in § 7.3.1 and § 7.3.2. It is stable within frequency ranges between the first and the second asymptotes. The absolute damping viscous coefficients  $c_2$  and  $c_3$  are shown onto the  $(r_{\%}, \tilde{k})$  plane in Figure 7.20 and Figure 7.21. They are stable within frequency ranges between the first and the second asymptotes. The identified values are  $\approx 1 \text{ N/(m/s)}$ , they are higher with respect to the previous configurations, probably to the influence of the relative damper. The relative viscous damping coefficient  $c_{1,2}$  is shown in Figure 7.21. It is stable between the first to asymptotes, and its value is higher than in the previous configurations, as expected. The relative dampers  $c_{2,3}$  acting between the second and third DOFs is null and stable onto the entire  $(r_{\%}, \tilde{k})$  plane. The relative damped  $c_{1,2}$  is the main source of dissipation in this configuration, although also the identified absolute dampers acting on the second and third DOFs are not null.


 Figure 7.19 - Damping coefficient  $c_1$  : quantification (left) , stability (right).

 Figure 7.20 - Damping coefficient  $c_2$  : quantification (left) , stability (right).

 Figure 7.21 - Damping coefficient  $c_3$  : quantification (left) , stability (right).

 Figure 7.22 - Damping coefficient  $c_{1,2}$  : quantification (left) , stability (right).

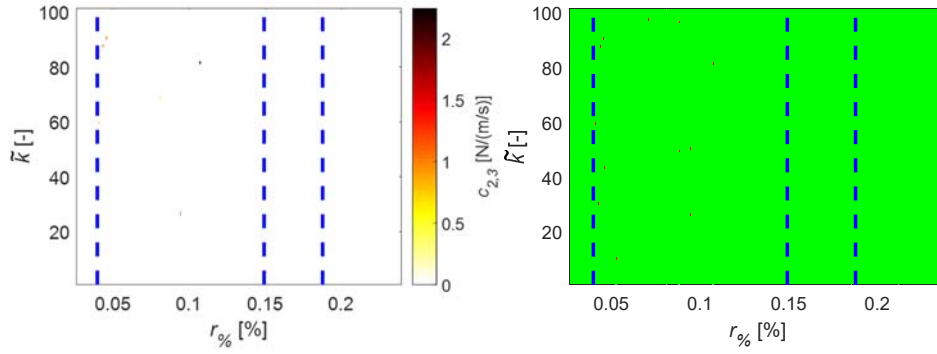


Figure 7.23 - Damping coefficient  $c_{2,3}$  : quantification (left) , stability (right).

The optimal identified solution  $\mathbf{u}^*$  can be selected looking for  $(r_{\%}^*, \tilde{k}^*)$  satisfying Eq. (4.70). The global stabilisation diagram  $\bar{\mathbf{S}}$ , computed as in Eq. (4.68), and the error map  $\mathbf{E}$ , computed using Eq. (4.69), are shown in Figure 7.24. The identification is globally stable in a region close to the first asymptote, in the same region also the normalised residuum  $E_{\%}$  reaches a minimum value. The optimal identification couple  $(r_{\%}^*, \tilde{k}^*)$  is the one with minimum residuum at  $(r_{\%}^*, \tilde{k}^*) = (0.04\%, 84)$  and inversion error  $E_{\%}^* = 0.004\%$ , blue cross in Figure 7.24.

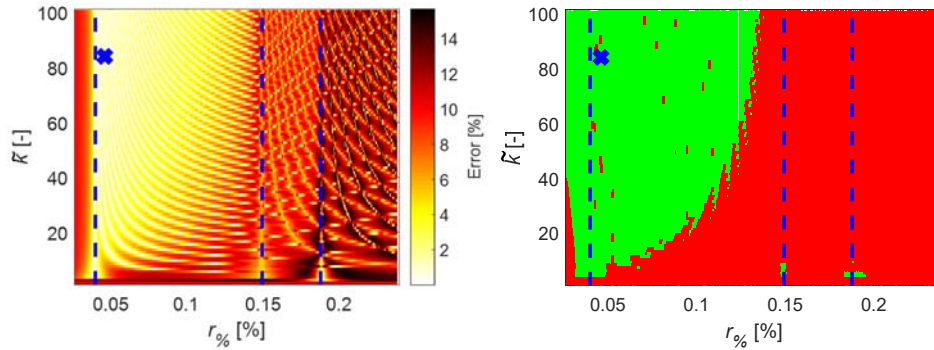


Figure 7.24 - Normalised residuum (left) and global stability diagram (right).

The identified damping matrix is shown in Figure 7.25. The damping coefficient values of the five layers are reported in Table 7.4.

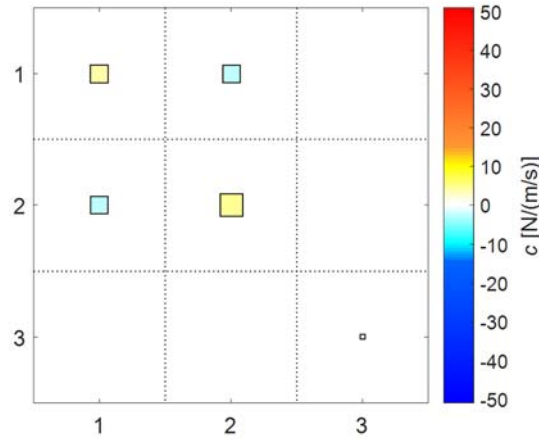


Figure 7.25 - Identified viscous damping matrix of the configuration D12 L1.

Table 7.4 - Identified damping coefficients values of the conf. D12 L1.

Damper	Values [N/(m/s)]
$c_1$	0.0849
$c_2$	1.2629
$c_3$	1.3715
$c_{1,2}$	3.1300
$c_{2,3}$	0.0000

The identified viscous damping matrix shows an evident relative damper between the first two DOFs, as expected; quite small absolute dampers on the second and third DOF are also identified. The quantification of the relative damping coefficient  $c_{12}$  is very close to the reference value.

#### 7.3.4 Configuration D12 L2

The configuration D12 L2 of the three DOFs system is topologically the same of the D12 L1, discussed in § 7.3.3. The only difference is the dissipation level of the relative damper, which is set to level L2 in this configuration. The absolute damper is deactivated. The system synthesised FRM  $\mathbf{H}_{syn}(\Omega)$  is in very good agreement with the experimental FRM  $\mathbf{H}^{Exp}(\Omega)$ , as shown in Figure 7.26. The damping effects are clearly visible on the second peaks of the FRM, which show a higher level of damping then in configuration D12 L1.

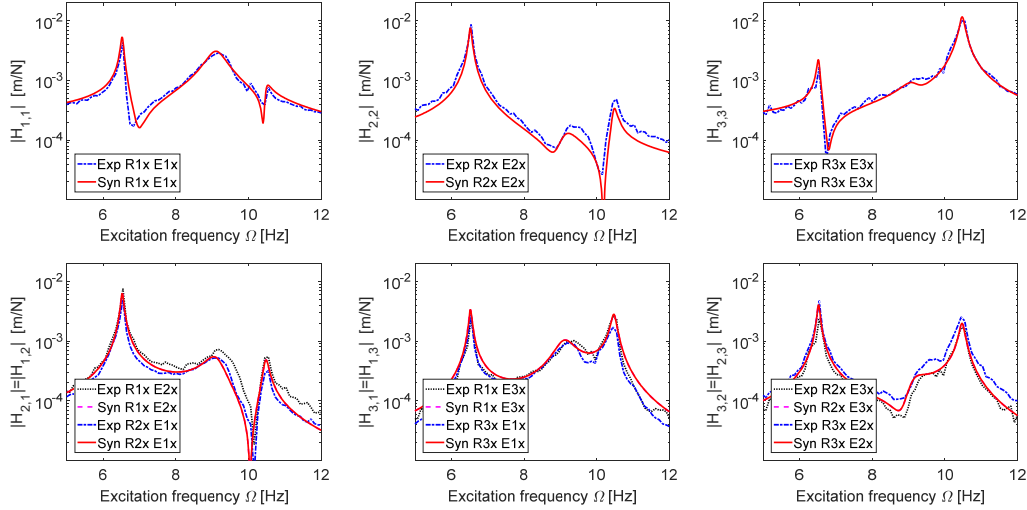


Figure 7.26 - Experimental and synthesised FRM of the conf. D12 L2.

The vertical asymptote ranges values  $r_{\%}$ , computed using Eq. (4.71), were found to be  $r_{\% \text{ asymptote}} = 0.0766, 0.2042, 0.2825 \%$ .

The identified damping coefficients of the five layers and their regions of stability are mapped onto the  $(r_{\%}, \tilde{k})$  plane in Figure 7.27 - Figure 7.31.

The expected asymptotes are highlighted in blue dashed vertical lines and the stabilisation diagrams show stable (green) and unstable (red) regions of the  $(r_{\%}, \tilde{k})$  plane.

The damping coefficient  $c_1$ , the absolute damper acting of the first mass is quantified in Figure 7.27. It results null. The quantification of  $c_1$  is lower than the identification already presented for the other configurations. It is stable onto the entire plane  $(r_{\%}, \tilde{k})$ . The absolute damping viscous coefficients  $c_2$ , shown in Figure 7.28, is coherent with the values already identified in the configuration D12 L1, discussed in § 7.3.3, and stable in the range between the first two asymptotes. The absolute damper  $c_3$ , shown in Figure 7.29, result to be null in the stable region between the first and the second asymptotes. The relative viscous damping coefficient  $c_{1,2}$  is shown in Figure 7.30. It is stable between the first to asymptotes, and its value is higher than in the previous configurations, as expected. The relative damper  $c_{2,3}$ , shown in Figure 7.31, acting between the second and third DOFs is low, but not zero. It is stable in the region between the first two asymptotes, close to the first one. The relative damped  $c_{1,2}$  is the main source of dissipation in this configuration.

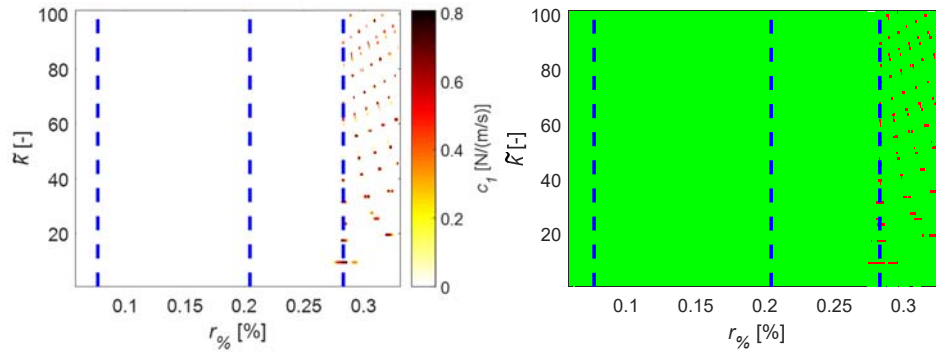


Figure 7.27 - Damping coefficient  $c_1$  : quantification (left) , stability (right).

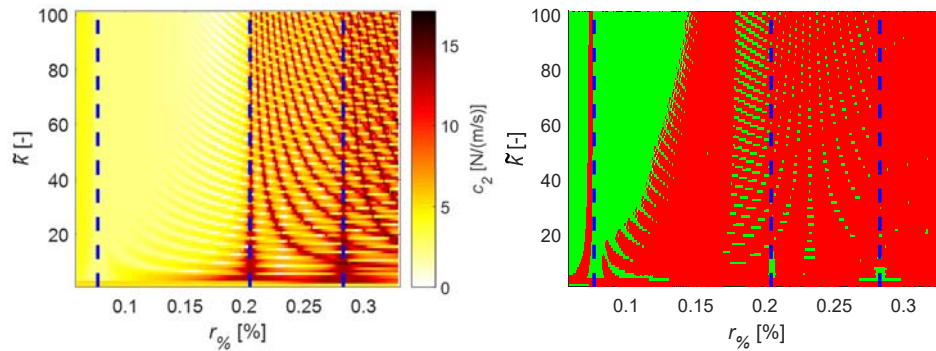


Figure 7.28 - Damping coefficient  $c_2$  : quantification (left) , stability (right).

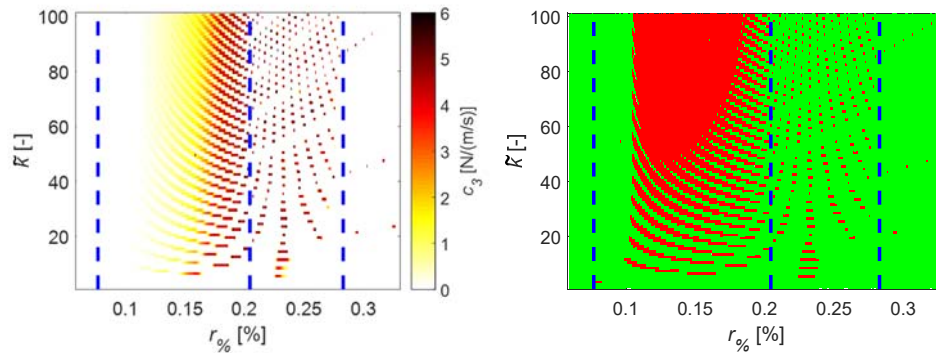


Figure 7.29 - Damping coefficient  $c_3$  : quantification (left) , stability (right).

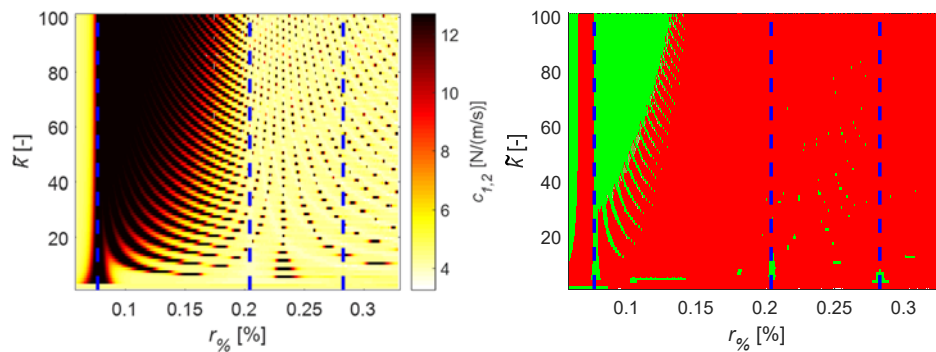


Figure 7.30 - Damping coefficient  $c_{1,2}$  : quantification (left) , stability (right).

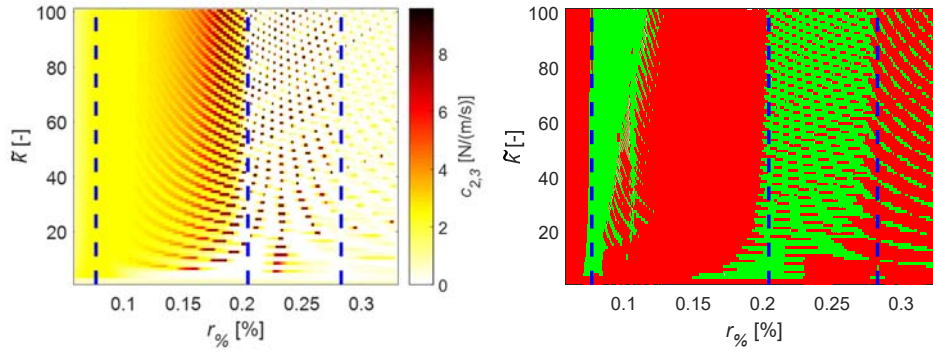


Figure 7.31 - Damping coefficient  $c_{2,3}$  : quantification (left) , stability (right).

The optimal identified solution  $\mathbf{u}^*$  can be selected looking for  $(r_{\%}^*, \tilde{k}^*)$  satisfying Eq. (4.70). The global stabilisation diagram  $\bar{\mathbf{S}}$ , computed as in Eq. (4.68), and the error map  $\mathbf{E}$ , computed using Eq. (4.69), are shown in Figure 7.32. The identification is globally stable in a region close to the first asymptote, in the same region also the normalised residuum  $E_{\%}$  reaches a minimum value. The optimal identification couple  $(r_{\%}^*, \tilde{k}^*)$  is the one with minimum residuum at  $(r_{\%}^*, \tilde{k}^*) = (0.1025\%, 59)$  and  $E_{\%}^* = 0.097\%$ , blue cross in Figure 7.32.

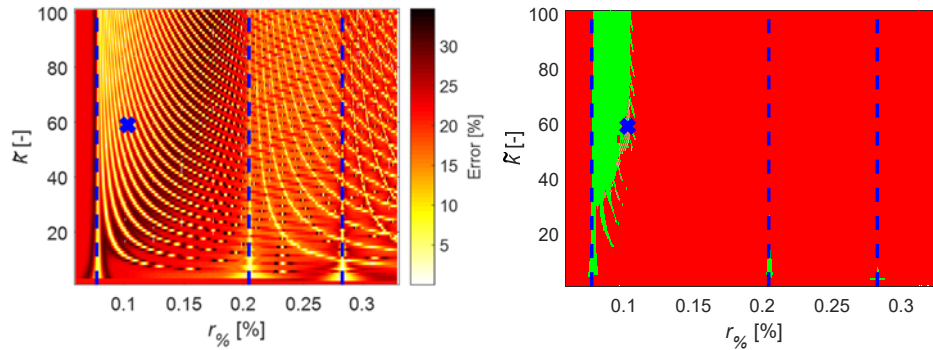


Figure 7.32 - Normalised residuum (left) and global stability diagram (right).

The identified damping matrix is shown in Figure 7.33. The damping coefficient values of the five layers are reported in Table 7.5. The identified viscous damping matrix shows an evident dissipation in the relative damper  $c_{12}$  between the first two DOFs, as expected; quite small relative damper acting between the second and the third DOFs is also identified. The quantification on the relative  $c_{1,2}$  damper at level L2 is very close to the reference value.



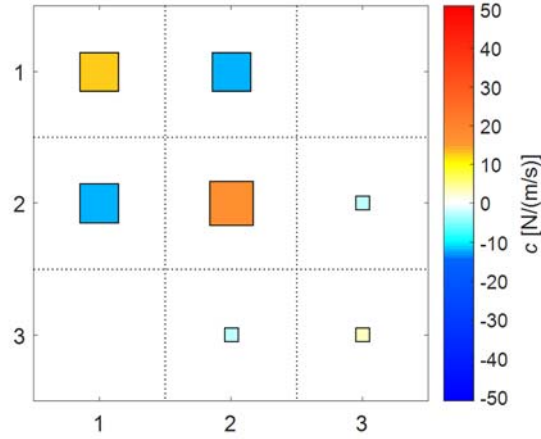


Figure 7.33 - Identified viscous damping matrix of the configuration D12 L2.

Table 7.5 - Identified damping coefficients values of the conf. D12 L2.

Damper	Values [N/(m/s)]
$c_1$	0.0000
$c_2$	2.3071
$c_3$	0.0000
$c_{1,2}$	12.5603
$c_{2,3}$	2.4538

### 7.3.5 Configuration D12 L3

The configuration D12 L3 includes the relative dampers at dissipation level L3, while the absolute damper D3 is deactivated. The system synthesised FRM  $\mathbf{H}_{syn}(\Omega)$  is in very good agreement with the experimental FRM  $\mathbf{H}^{Exp}(\Omega)$ , as shown in Figure 7.34. The second mode shape is quite damped.

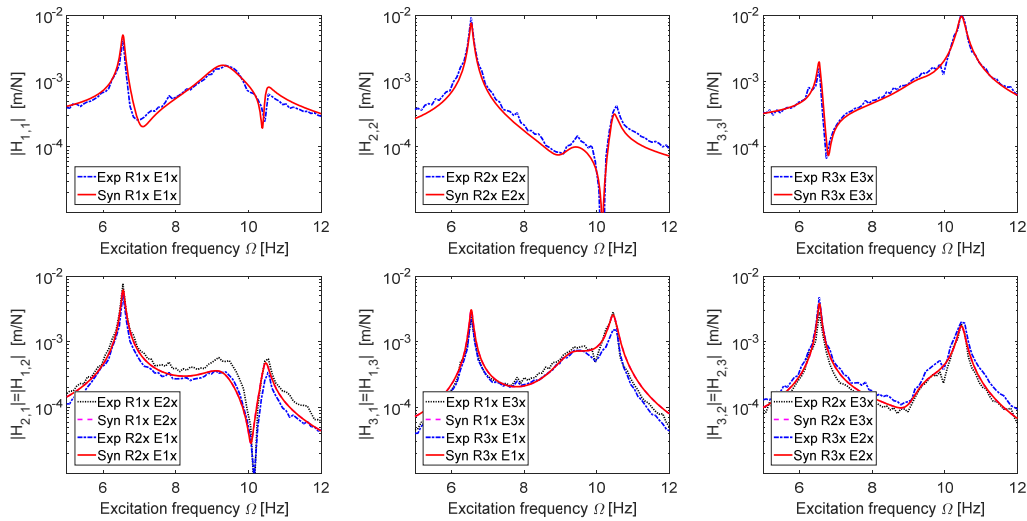


Figure 7.34 - Experimental and synthesised FRM of the conf. D12 L3.



## 7. Experimental direct damping identification in a lumped parameters system

The vertical asymptote ranges values  $r_{\%}$ , computed using Eq. (4.71), were found to be  $r_{\%asymptote} = 0.1617, 0.4919, 0.6419 \%$ . The identified damping coefficients of the five layers and their regions of stability are mapped onto the  $(r_{\%}, \tilde{k})$  plane in Figure 7.35 - Figure 7.39. The expected asymptotes are highlighted in blue dashed vertical lines and the stabilisation diagrams show stable and unstable regions.

The damping coefficient  $c_1$  of the absolute damper acting of the first mass is quantified in Figure 7.35. It results stable and very low (close to zero) onto the entire  $(r_{\%}, \tilde{k})$  plane. This is an expected result because there is no physical absolute damper acting on the first mass. The absolute damper acting on the second DOF  $c_2$  is shown in Figure 7.36. In this case the identified values are stable within frequency ranges between the first and the second asymptotes, close to the first vertical asymptote on the right. The identified value is low but not zero. The same consideration is valid for the damping coefficient value related to the absolute damper acting on the third DOF, shown in Figure 7.37.

The damping coefficient value  $c_{1,2}$  for the first relative damper, shown in Figure 7.38, is well identified and stable between the first two asymptotes, whereas elsewhere in the diagram damping values are not stable and very different from the expected one. The relative damper coefficient  $c_{2,3}$  between the second and the third DOFs, shown in Figure 7.39, is low and stable in the region between the first two asymptotes. All the identified damping values were found to be similar to the expected values in the stable regions.

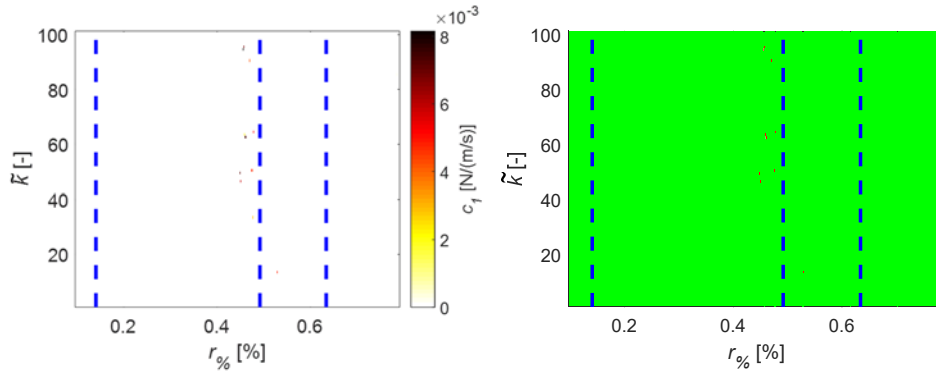


Figure 7.35 - Damping coefficient  $c_1$  : quantification (left) , stability (right).

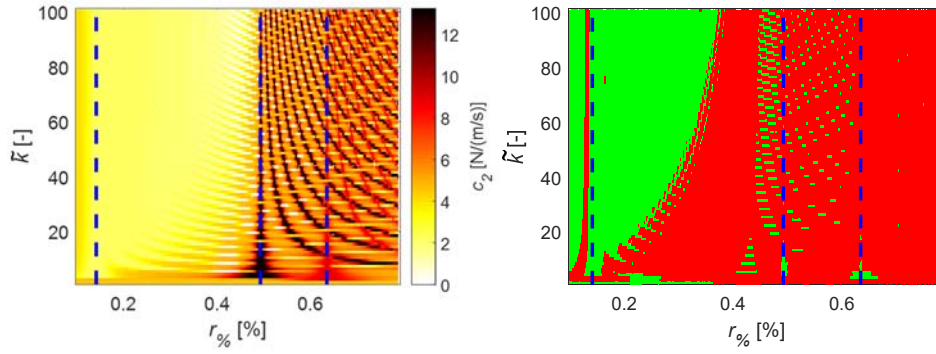


Figure 7.36 - Damping coefficient  $c_2$  : quantification (left) , stability (right).

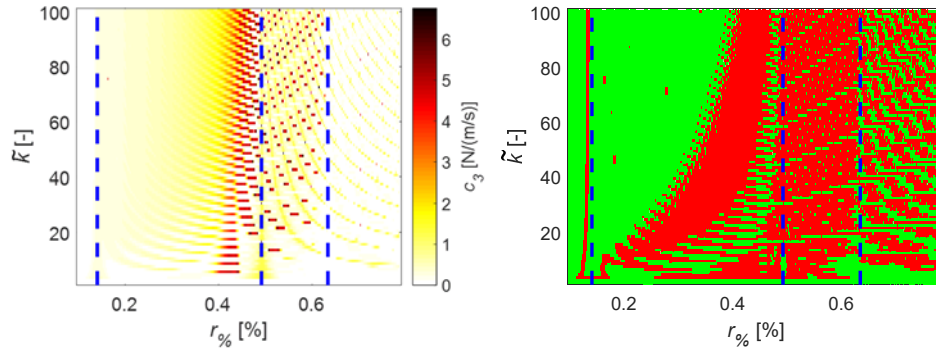


Figure 7.37 - Damping coefficient  $c_3$  : quantification (left) , stability (right).

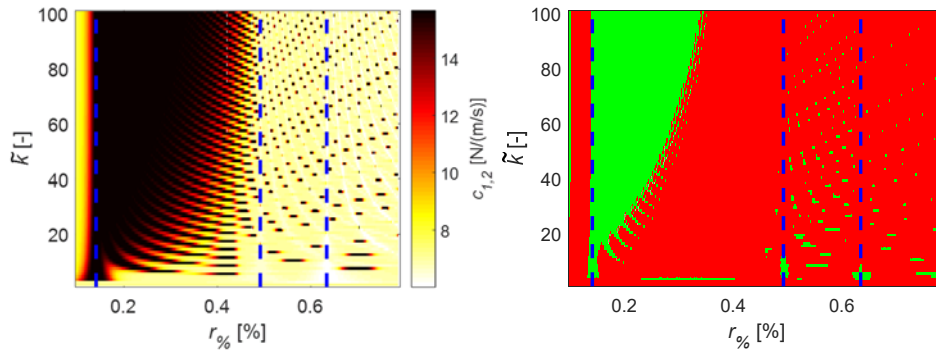


Figure 7.38 - Damping coefficient  $c_{1,2}$  : quantification (left) , stability (right).

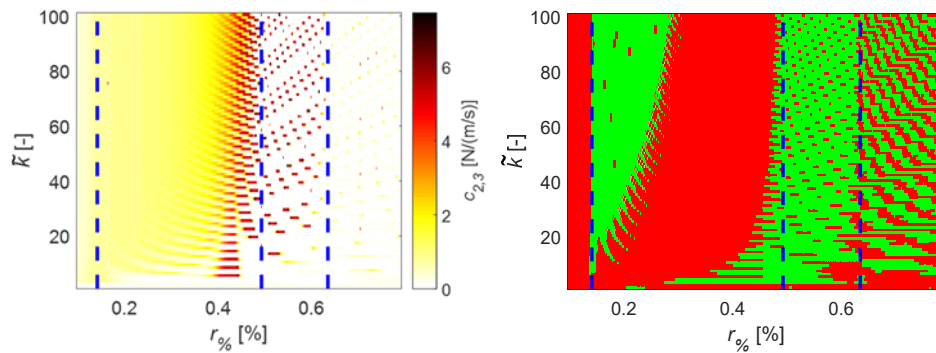


Figure 7.39 - Damping coefficient  $c_{2,3}$  : quantification (left) , stability (right).

## 7. Experimental direct damping identification in a lumped parameters system

The optimal identified solution  $\mathbf{u}^*$  can be selected looking for  $(r_{\%}^*, \tilde{k}^*)$  satisfying Eq. (4.70). The global stabilisation diagram  $\bar{\mathbf{S}}$ , computed as in Eq. (4.68), and the error map  $\mathbf{E}$ , computed using Eq. (4.69), are shown in Figure 7.40. The identification is globally stable in a region close to the first asymptote, in the same region also the normalised residuum  $E_{\%}$  reaches a minimum value.

The optimal identification couple  $(r_{\%}^*, \tilde{k}^*)$  is the one with minimum residuum at  $(r_{\%}^*, \tilde{k}^*) = (55, 0.1731\%)$  and presents an extremely low inversion error  $E_{\%}^* = 0.043\%$ , corresponding to the blue cross in Figure 7.40.

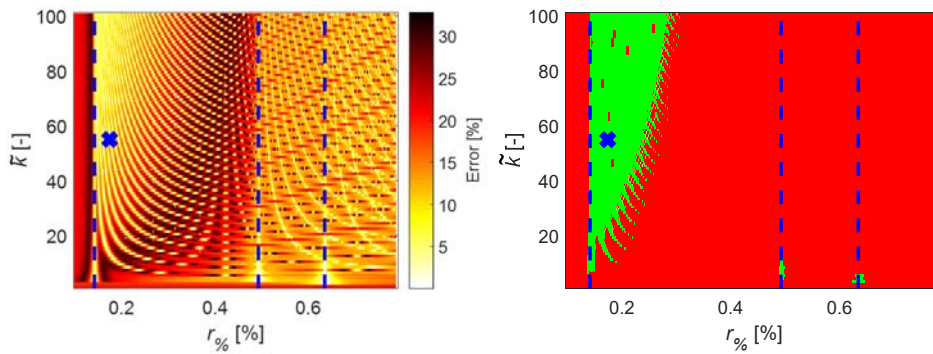


Figure 7.40 - Normalised residuum (left) and global stability diagram (right).

The identified damping matrix is shown in Figure 7.41. The damping coefficient values of the five layers are reported in Table 7.6. The spatial distribution of the damping is perfectly identified and the damping values are in very good agreement with the expected ones.

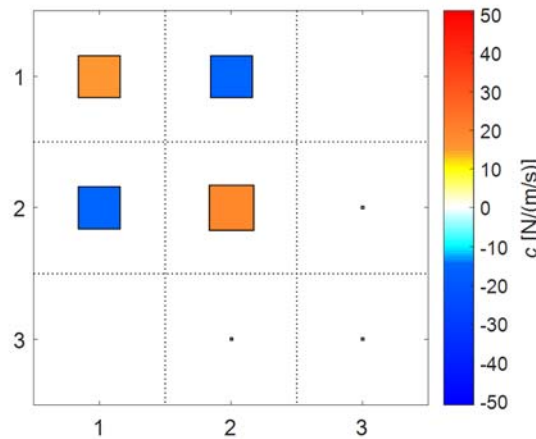


Figure 7.41 - Identified viscous damping matrix of the configuration D12 L3.

Table 7.6 - Identified damping coefficients values of the conf. D12 L3.

Damper	Values [N/(m/s)]
$c_1$	0.0000
$c_2$	2.1946
$c_3$	0.2879
$c_{1,2}$	15.5820
$c_{2,3}$	0.8241

### 7.3.6 Configuration D12 L4

The configuration D12 L4 of the system consist in the test-rig with the relative damper at dissipation level L4 activated and the absolute damper D3 deactivated. The system synthesised FRM  $\mathbf{H}_{syn}(\Omega)$  is in agreement with the experimental FRM  $\mathbf{H}^{Exp}(\Omega)$ , as shown in Figure 7.42. The second mode shape is quite damped, even more than in the other configurations D12. The system is high damped, and the modal identification method shows difficulties in identifying the correct modal parameters.

The vertical asymptote ranges values  $r_{\%}$ , computed using Eq. (4.71), were found to be  $r_{\%asympote} = 0.0610, 1.7635, 1.8403 \%$ . The identified damping coefficients of the five layers and their regions of stability are mapped onto the  $(r_{\%}, \tilde{k})$  plane in Figure 7.43 - Figure 7.47. The expected asymptotes are highlighted in blue dashed vertical lines and the stabilisation diagrams show stable (green) and unstable (red) regions of  $(r_{\%}, \tilde{k})$  plane. The damping coefficient  $c_1$  of the absolute damper acting of the first mass is identified in Figure 7.43.

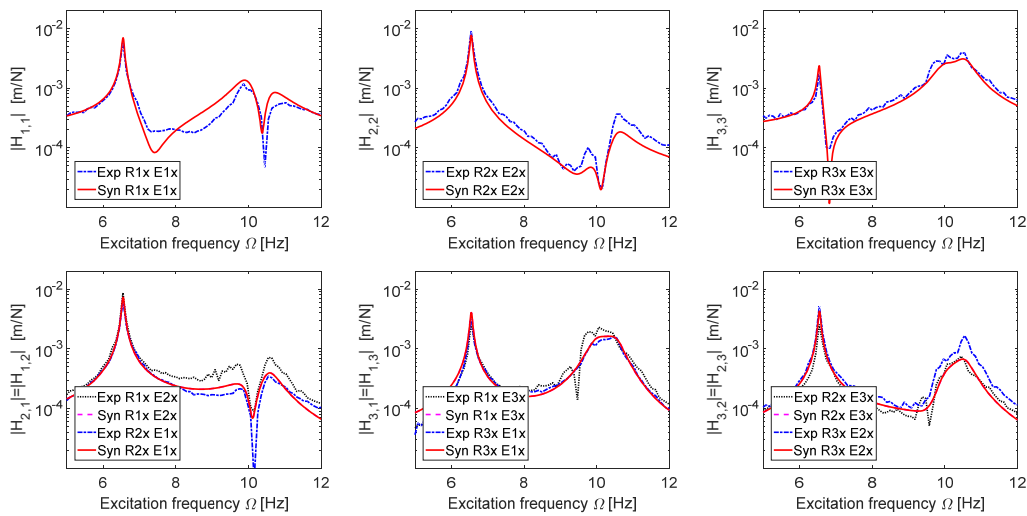


Figure 7.42 - Experimental and synthesised FRM of the conf. D12 L4.

It is zero and stable onto the entire plane  $(r_0, \tilde{k})$ . The absolute dampers acting on the second and third DOFs are shown in Figure 7.44 and in Figure 7.45. The identified values are stable within frequency ranges between the first and the second asymptotes, close to the first vertical asymptote on the right. The identified values are low with respect to the other sources of damping, but non-zero.

The damping coefficient value  $c_{1,2}$  of the first relative damper in, shown in Figure 7.46, is stable between the first two asymptotes, whereas elsewhere in the diagram damping values are not stable and very different from the expected one. Its quantification is higher than the other D12 configurations, in accordance with the reference value for the relative damper set at dissipation level L4. The relative damper coefficient  $c_{2,3}$  acting between the second and the third DOFs, shown in Figure 7.47, is zero and stable in almost the entire  $(r_0, \tilde{k})$  plane. The identified damping values were found to be similar to the expected values in the stable regions. Most of the dissipations are due to the relative damper acting between the first and second DOFs, as expected from the system topology.

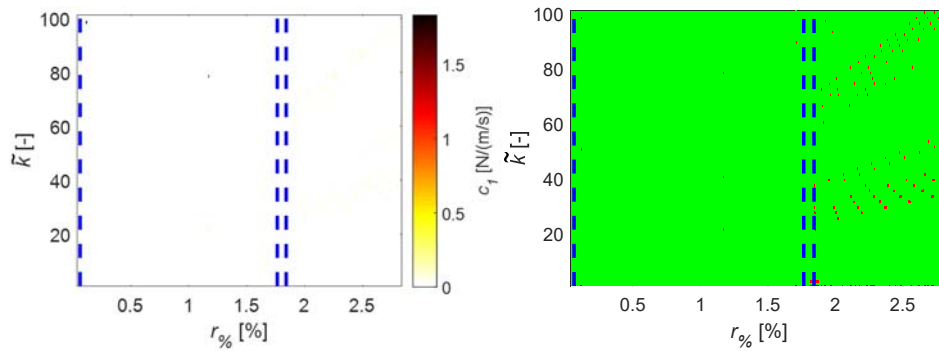


Figure 7.43 - Damping coefficient  $c_1$  : quantification (left) , stability (right).

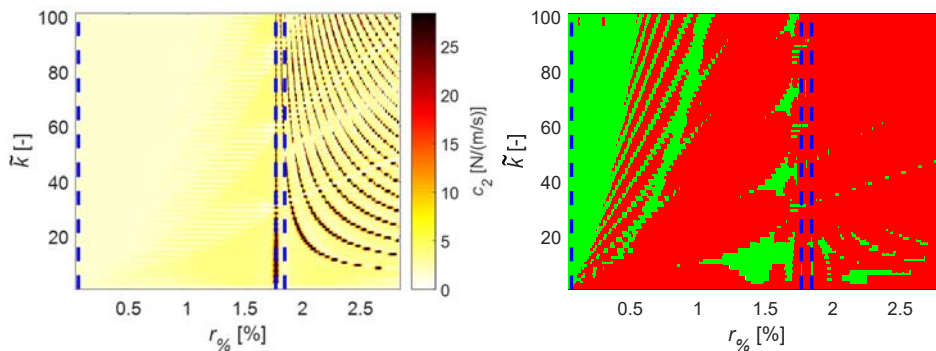
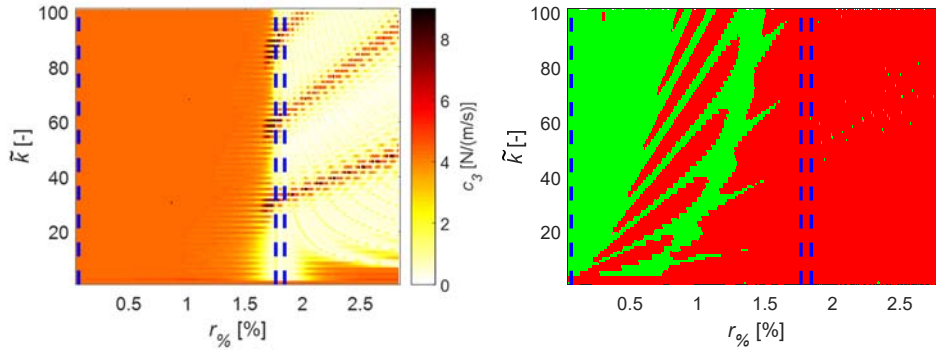
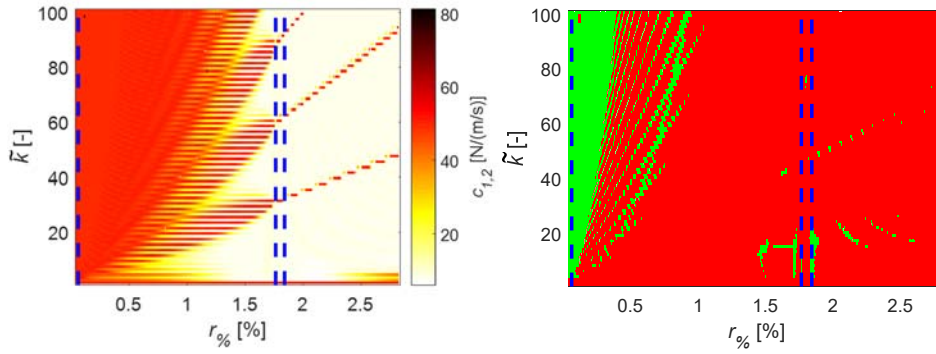
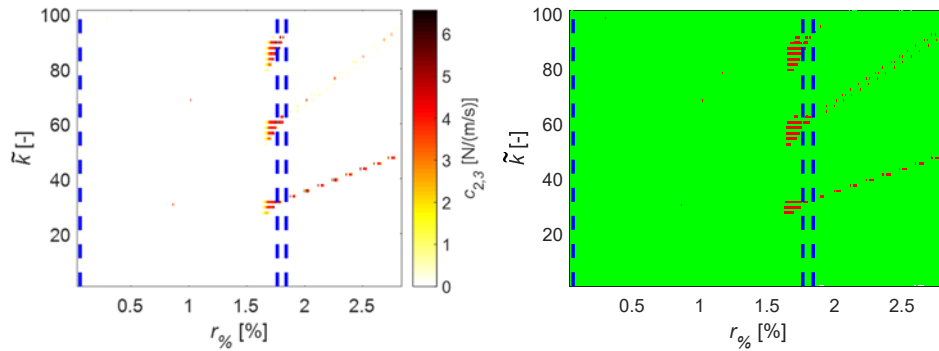


Figure 7.44 - Damping coefficient  $c_2$  : quantification (left) , stability (right).


 Figure 7.45 - Damping coefficient  $c_3$ : quantification (left), stability (right).

 Figure 7.46 - Damping coefficient  $c_{1,2}$ : quantification (left), stability (right).

 Figure 7.47 - Damping coefficient  $c_{2,3}$ : quantification (left), stability (right).

The optimal identified solution  $\mathbf{u}^*$  can be selected looking for  $(r_{\%}^*, \tilde{k}^*)$  satisfying Eq. (4.70). The global stabilisation diagram  $\bar{\mathbf{S}}$ , computed as in Eq. (4.68), and the error map  $\mathbf{E}$ , computed using Eq. (4.69), are shown in Figure 7.48. The identification is globally stable in a region close to the first asymptote, in the same region also the normalised residuum  $E_{\%}$  reaches a minimum value. The optimal solution  $\mathbf{u}^*$  is at  $(r_{\%}^*, \tilde{k}^*) = (70, 0.0995\%)$  and inversion error  $E_{\%}^* = 0.0484\%$ , blue cross in Figure 7.48.

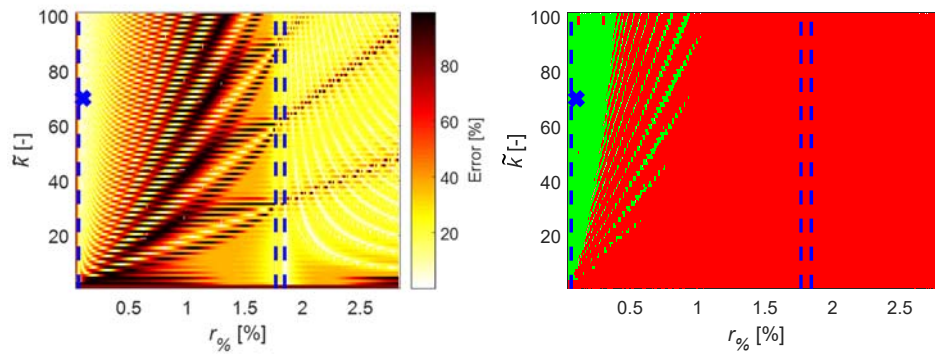


Figure 7.48 - Normalised residuum (left) and global stability diagram (right).

The identified damping matrix is shown in Figure 7.49. The damping coefficient values of the five layers are reported in Table 7.7. The spatial distribution of the damping is well identified and the damping values are in very good agreement with the expected ones. A small unexpected absolute damping coefficient acting on the third DOF is identified, probably due to the high damping level of the relative damper.

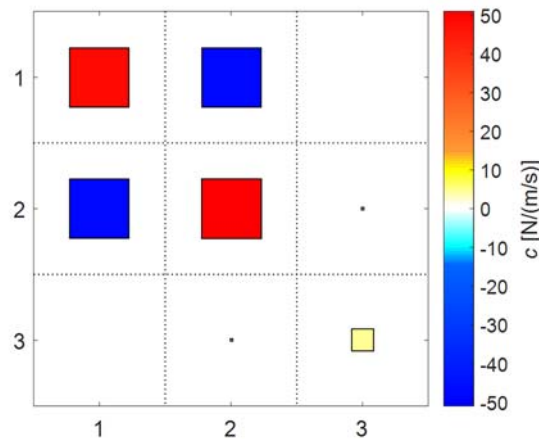


Figure 7.49 - Identified viscous damping matrix of the configuration D12 L4.

Table 7.7 - Identified damping coefficients values of the conf. D12 L4.

Damper	Values [N/(m/s)]
$c_1$	0.0000
$c_2$	1.7335
$c_3$	4.2336
$c_{1,2}$	48.9464
$c_{2,3}$	0.0000



### 7.3.7 Configuration D3 & D12 L1

The configuration D3 & D12 L1 of the system includes both the relative dampers at dissipation level L1 and the absolute dampers. The system synthesised FRM  $\mathbf{H}_{syn}(\Omega)$  is in agreement with the experimental FRM  $\mathbf{H}^{Exp}(\Omega)$ , as shown in Figure 7.50. The second and third peaks are quite damped.

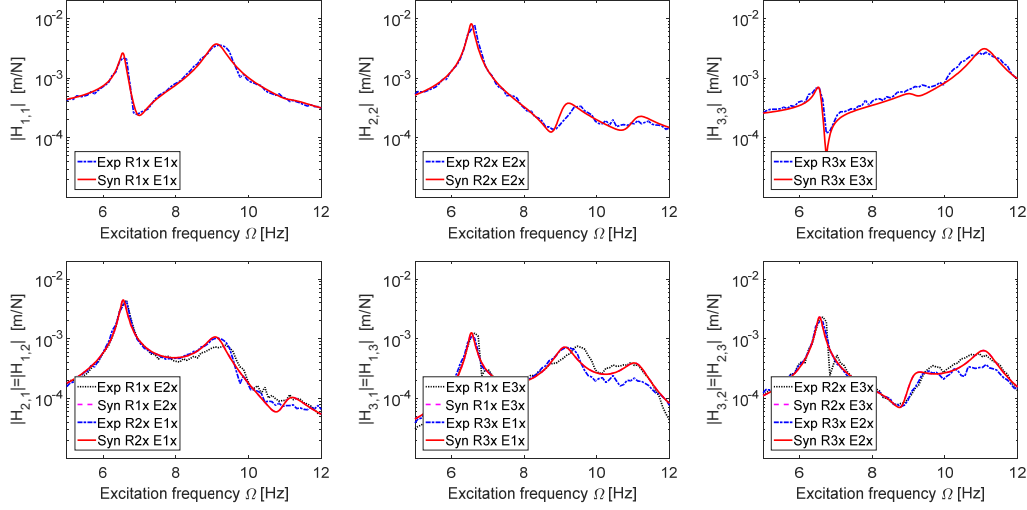


Figure 7.50 - Experimental and synthesised FRM of the conf. D3 & D12 L1.

The vertical asymptote ranges values  $r_{\%}$ , computed using Eq. (4.71), were found to be  $r_{\%asympote} = 0.4092, 0.6995, 1.1194 \%$ .

The identified damping coefficients of the five layers and their regions of stability are mapped onto the  $(r_{\%}, \tilde{k})$  plane in Figure 7.51 - Figure 7.55.

The expected asymptotes are highlighted in blue dashed vertical lines and the stabilisation diagrams show stable (green) and unstable (red) regions of  $(r_{\%}, \tilde{k})$  plane.

The damping coefficient  $c_1$  of the absolute damper acting of the first mass is identified in Figure 7.51. It is very low, close to zero, and stable in the range between the first two asymptotes. The absolute dampers  $c_2$  acting on the second DOFs is shown in Figure 7.52. The identified damping value is small and stable between the first two asymptotes. The absolute damper acting of the third DOF is shown in Figure 7.53. The identified values are high with respect all the others and stable between the first two asymptotes.

The damping coefficient value  $c_{1,2}$  for the first relative damper in, shown in Figure 7.54, is stable between the first two asymptotes, whereas elsewhere in the diagram damping values are not stable. Its quantification is very similar to the configuration D12 § 7.3.3 and in accordance with the reference value for the relative damper set at dissipation level L1. The relative damper coefficient  $c_{2,3}$



between the second and the third DOFs, shown in Figure 7.55, is zero and stable in the entire  $(r_{\%}, \tilde{k})$  plane.

The identified damping values were found to be similar to the expected values in the stable regions. Most of the dissipation is due to the relative damper acting between the first and second DOFs and absolute damped on acting the third DOF, as expected from the system topology of this configuration.

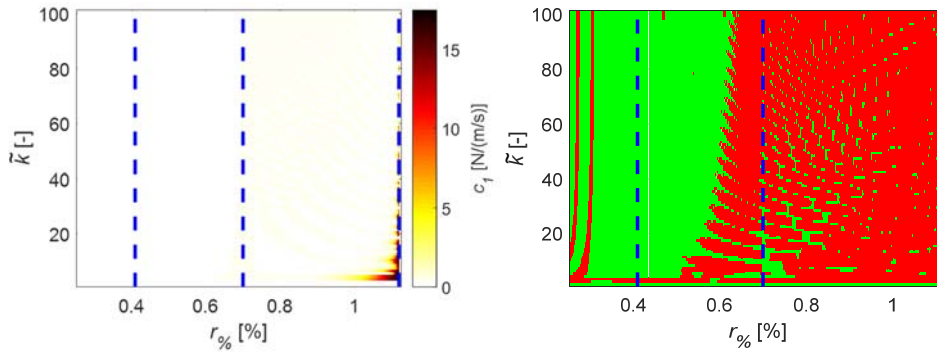


Figure 7.51 - Damping coefficient  $c_1$  : quantification (left) , stability (right).

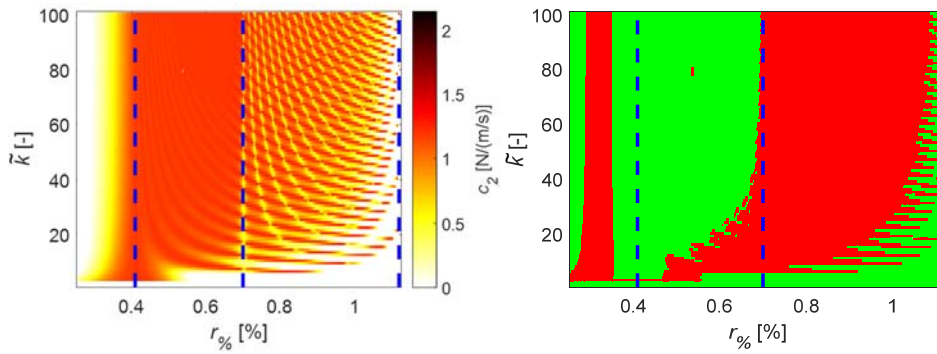


Figure 7.52 - Damping coefficient  $c_2$  : quantification (left) , stability (right).

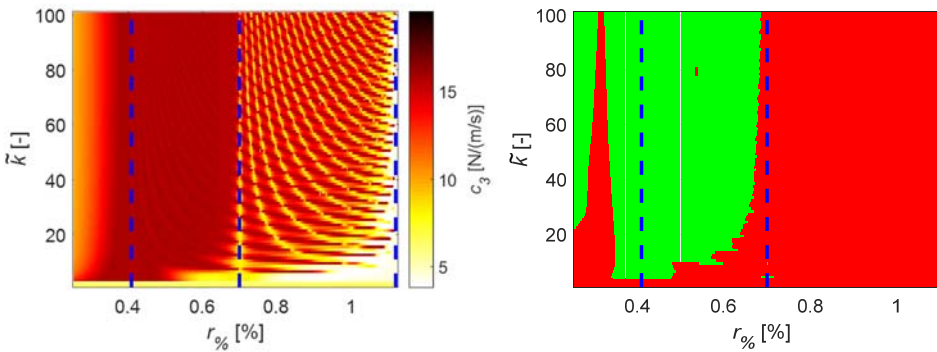
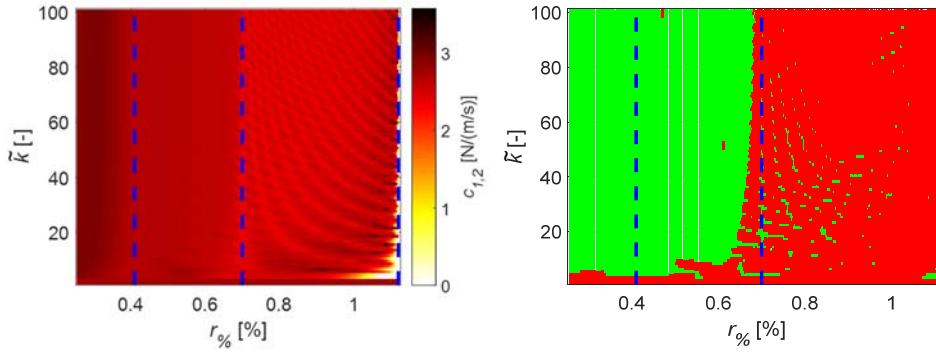
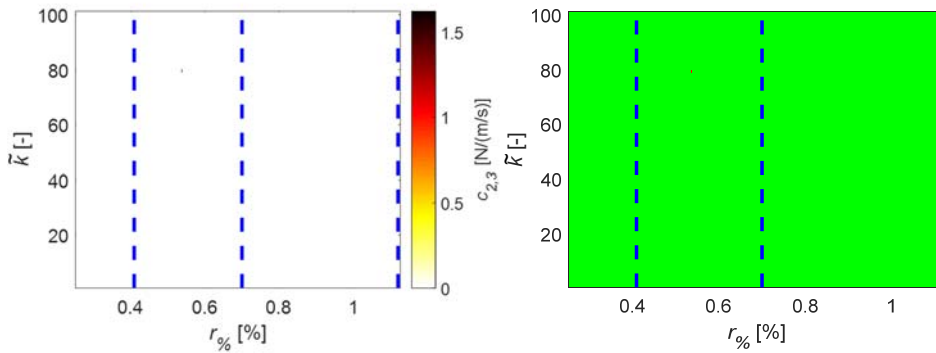


Figure 7.53 - Damping coefficient  $c_3$  : quantification (left) , stability (right).


 Figure 7.54 - Damping coefficient  $c_{1,2}$  : quantification (left) , stability (right).

 Figure 7.55 - Damping coefficient  $c_{2,3}$  : quantification (left) , stability (right).

The optimal identified solution  $\mathbf{u}^*$  can be selected looking for  $(r_{\%}^*, \tilde{k}^*)$  satisfying Eq. (4.70). The global stabilisation diagram  $\bar{\mathbf{S}}$ , computed as in Eq. (4.68), and the error map  $\mathbf{E}$ , computed using Eq. (4.69), are shown in Figure 7.56. The identification is globally stable in a region close to the first asymptote, in the same region also the normalised residuum  $E_{\%}$  reaches a minimum value.

The optimal solution  $\mathbf{u}^*$  is found at  $(r_{\%}^*, \tilde{k}^*) = (78, 0.5034\%)$  and inversion error  $E_{\%}^* = 0.0212\%$ , blue cross in Figure 7.56.

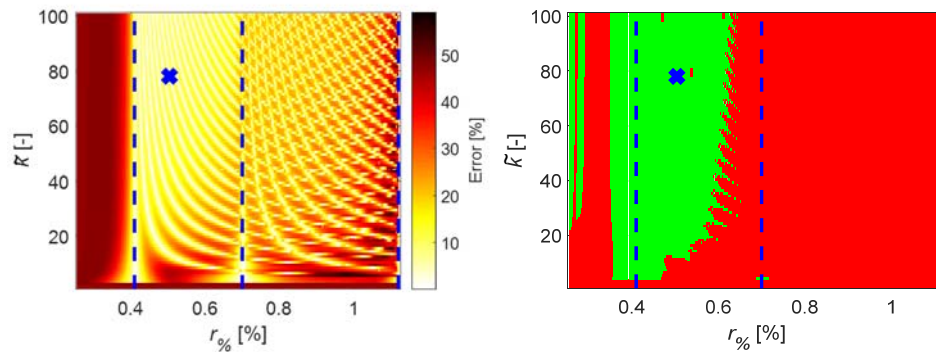


Figure 7.56 - Normalised residuum (left) and global stability diagram (right).

The identified damping matrix is shown in Figure 7.57. The damping coefficient values of the five layers are reported in Table 7.8. The spatial distribution of the damping is well identified and the damping values are in very good agreement with the expected ones.

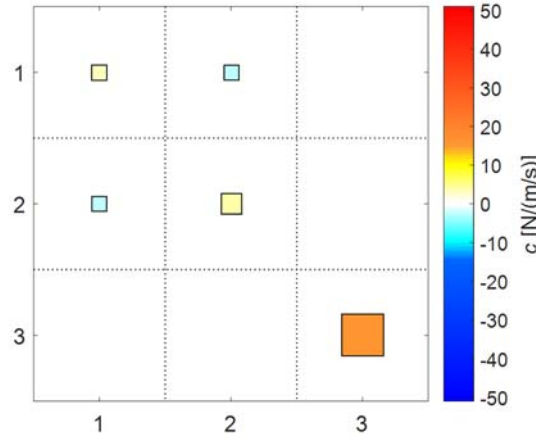


Figure 7.57 - Identified viscous damping matrix of the config. D3 & D12 L1.

Table 7.8 - Identified damping coefficients values of the conf. D3 & D12 L1.

Damper	Values [N/(m/s)]
$c_1$	0.0640
$c_2$	1.1805
$c_3$	15.5931
$c_{1,2}$	2.6446
$c_{2,3}$	0.0000

### 7.3.8 Configuration D3 & D12 L2

In the configuration D3 & D12 L2 the system includes both the relative dampers at dissipation level L2 and the absolute dampers. The system synthesised FRM  $\mathbf{H}_{syn}(\Omega)$  is in agreement with the experimental FRM  $\mathbf{H}^{Exp}(\Omega)$ , as shown in Figure 7.58. The second and third peaks are quite damped.

The vertical asymptote ranges values  $r_{\%}$ , computed using Eq. (4.71), were found to be  $r_{\%asymptote} = 0.3667, 0.7582, 1.1933 \%$ . The identified damping coefficients of the five layers and their regions of stability are mapped onto the  $(r_{\%}, \tilde{k})$  plane in Figure 7.59 - Figure 7.63. The expected asymptotes are highlighted in blue dashed vertical lines and the stabilisation diagrams show stable (green) and unstable (red) regions of  $(r_{\%}, \tilde{k})$  plane. The damping coefficient  $c_1$  of the absolute damper acting of the first mass is identified in Figure 7.59. It

results zero and stable in almost the entire  $(r_0, \tilde{k})$  plane. The absolute dampers  $c_2$  acting on the second DOFs is shown in Figure 7.60. The identified damping value is small and stable between the first two asymptotes. In Figure 7.61 the absolute damper acting of the third DOF is shown. The identified values are high with respect all the others and stable between the first two asymptotes.

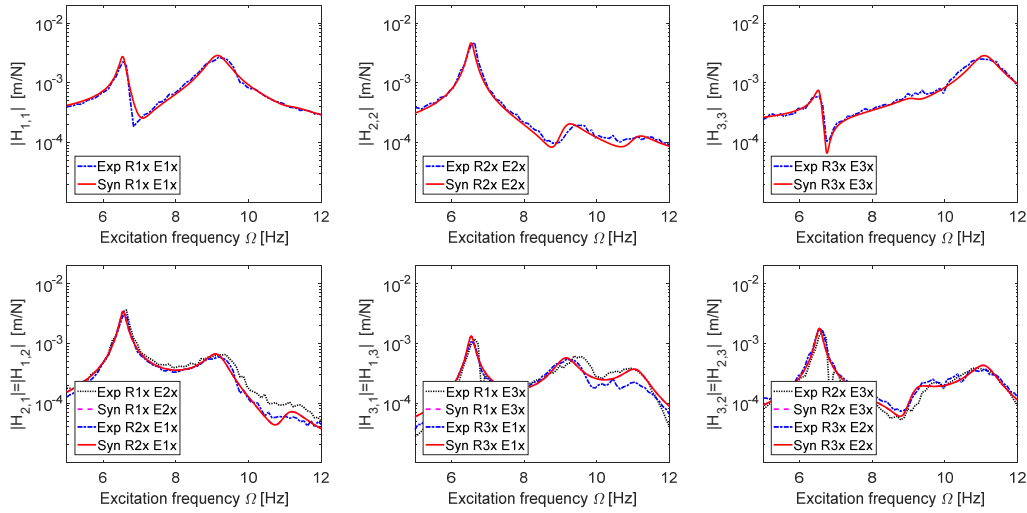


Figure 7.58 - Experimental and synthesised FRM of the conf. D3 & D12 L2.

The damping coefficient value  $c_{1,2}$  for the first relative damper, shown in Figure 7.62, is stable between the first two asymptotes, whereas elsewhere in the diagram damping values are not stable. Its quantification is very similar to the configurations D12 L1, discussed in § 7.3.3, and D12 Lx & D3 configurations. The identified damping coefficient value is in accordance with the reference value for the relative damper set at dissipation level L2. The relative damper  $c_{2,3}$  between the second and the third DOFs, shown in Figure 7.63, is zero and stable in the range between the first two asymptotes. The identified damping values were found to be similar to the expected values in the stable regions. Most of the dissipation are due to the relative damper acting between the first and second DOFs and absolute damped on acting the third DOF, as expected.

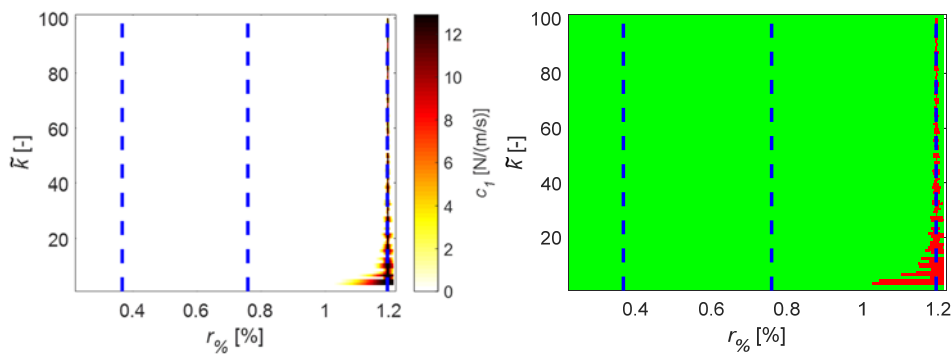


Figure 7.59 - Damping coefficient  $c_1$  : quantification (left) , stability (right).

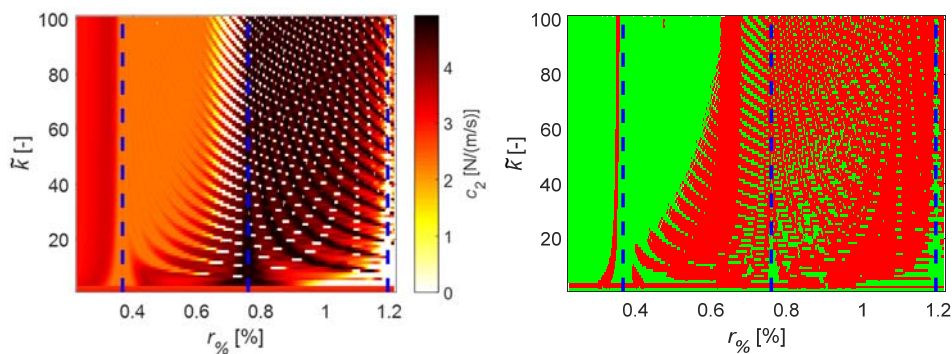


Figure 7.60 - Damping coefficient  $c_2$  : quantification (left) , stability (right).

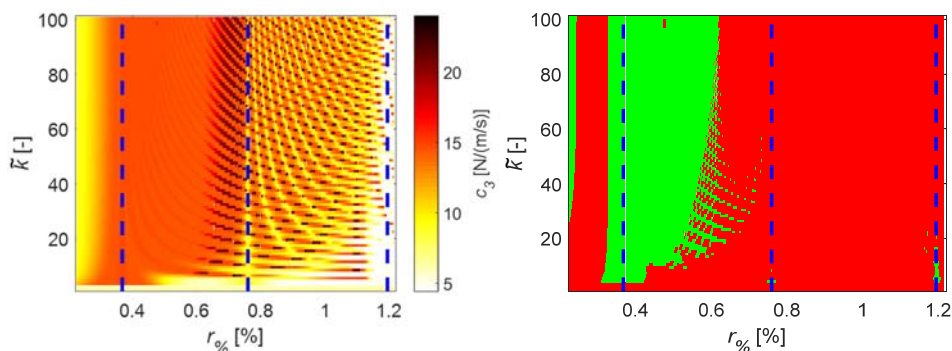


Figure 7.61 - Damping coefficient  $c_3$  : quantification (left) , stability (right).

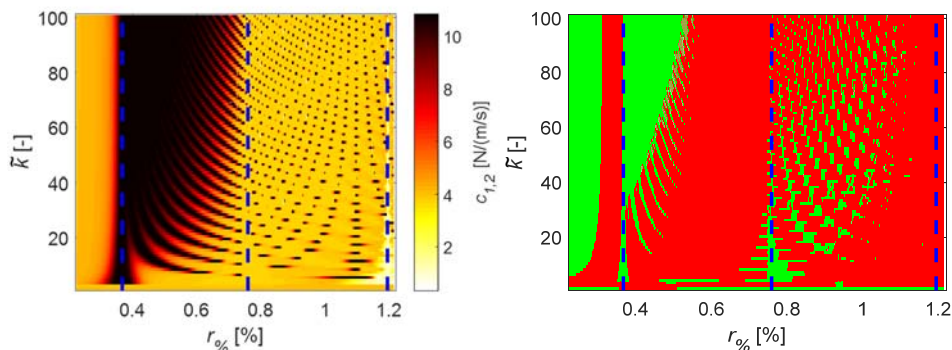


Figure 7.62 - Damping coefficient  $c_{1,2}$  : quantification (left) , stability (right).

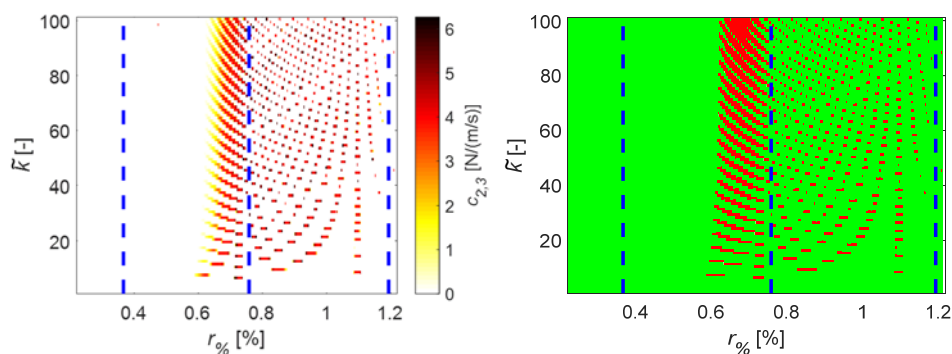


Figure 7.63 - Damping coefficient  $c_{2,3}$  : quantification (left) , stability (right).

The optimal identified solution  $\mathbf{u}^*$  can be selected looking for  $(r_{\%}^*, \tilde{k}^*)$  satisfying Eq. (4.70). The global stabilisation diagram  $\bar{\mathbf{S}}$ , computed as in Eq. (4.68), and the error map  $\mathbf{E}$ , computed using Eq. (4.69), are shown in Figure 7.64. The identification is globally stable in a region close to the first asymptote, in the same region also the normalised residuum  $E_{\%}$  reaches a minimum value.

The optimal identification couple  $(r_{\%}^*, \tilde{k}^*)$  is the one with minimum residuum at  $(r_{\%}^*, \tilde{k}^*) = (85, 0.4663\%)$  and  $E^* = 0.0141\%$ , blue cross in Figure 7.56.

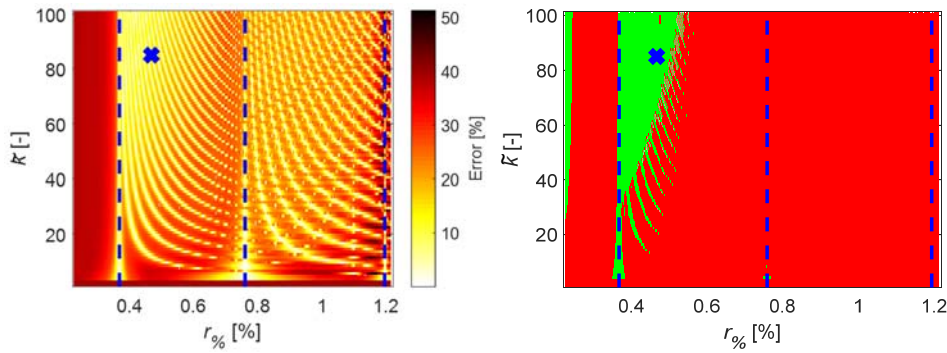


Figure 7.64 - Normalised residuum (left) and global stability diagram (right).

The identified damping matrix is shown in Figure 7.65. The damping coefficient values of the five layers are reported in Table 7.9. The spatial distribution of the damping is well identified and the damping values are in very good agreement with the expected ones.

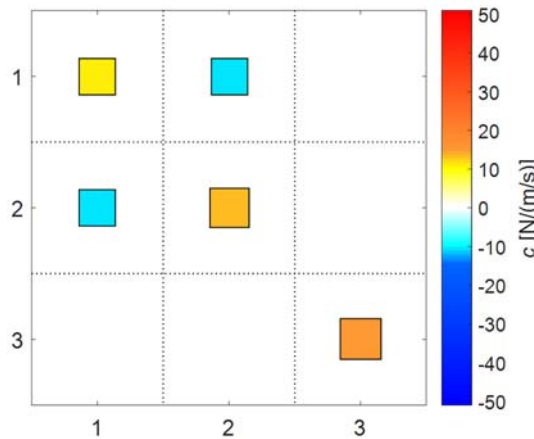


Figure 7.65 - Identified viscous damping matrix of the config. D3 & D12 L2.

Table 7.9 - Identified damping coefficients values of the conf. D3 &amp; D12 L2.

Damper	Values [N/(m/s)]
$c_1$	0.0000
$c_2$	2.3105
$c_3$	14.5662
$c_{1,2}$	10.8297
$c_{2,3}$	0.0000

### 7.3.9 Configuration D3 & D12 L3

The configuration D3 & D12 L3 of the system includes both the relative dampers at dissipation level L3 and the absolute dampers. The system synthesised FRM  $\mathbf{H}_{syn}(\Omega)$  is in agreement with the experimental FRM  $\mathbf{H}^{Exp}(\Omega)$ , as shown in Figure 7.66. The second and third peaks are quite damped.

The vertical asymptote ranges values  $r_0$ , computed using Eq. (4.71), were found to be  $r_{\%asymptote} = 0.8516, 2.3685, 2.5097\%$ . The identified damping coefficients of the five layers and their regions of stability are mapped onto the  $(r_0, \tilde{k})$  plane in Figure 7.67 - Figure 7.71. The expected asymptotes are highlighted in blue dashed vertical lines and the stabilisation diagrams show stable (green) and unstable (red) regions of  $(r_0, \tilde{k})$  plane. The damping coefficient  $c_1$  of the absolute damper acting of the first mass is identified in Figure 7.67. It is zero and stable in the range between the first two asymptotes.

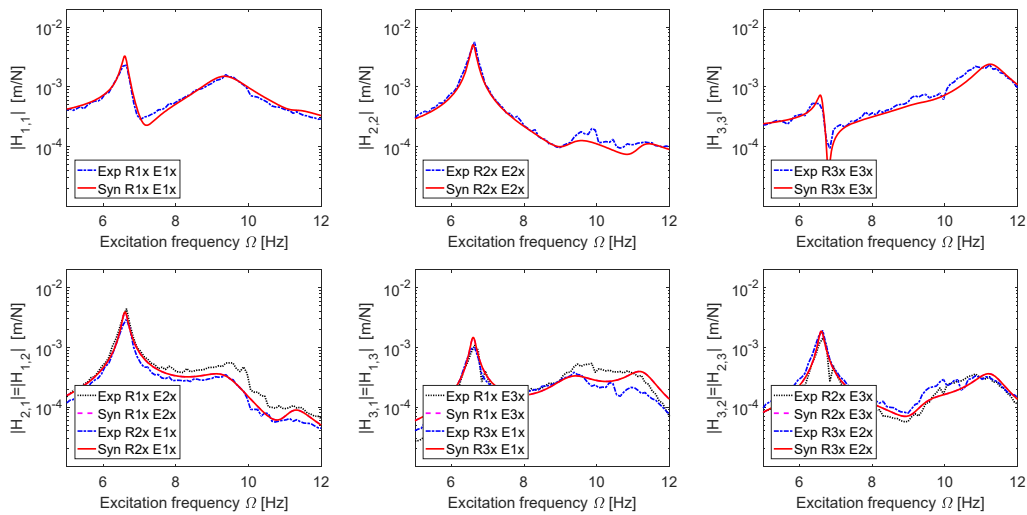


Figure 7.66 - Experimental and synthesised FRM of the conf. D3 &amp; D12 L3.

The absolute dampers  $c_2$  acting on the second DOFs is shown in Figure 7.68. The identified damping value is small and stable between the first two asymptotes. The absolute damper acting of the third DOF is shown in Figure 7.69.



The identified value is comparable to the  $c_3$  identified values of all the other configurations with damper D3 activated. The damping coefficient value  $c_{1,2}$  for the first relative damper, shown in Figure 7.70, is stable between the first two asymptotes, whereas elsewhere in the diagram damping values are not stable. The relative damper coefficient  $c_{2,3}$  between the second and the third DOFs, shown in Figure 7.71, is zero and stable in the entire  $(r_\%, \tilde{k})$  plane. The identified damping values were found to be similar to the expected values in the stable regions. Most of the dissipations are due to the relative damper acting between the first and second DOFs and absolute damped on acting the third DOF, as expected.

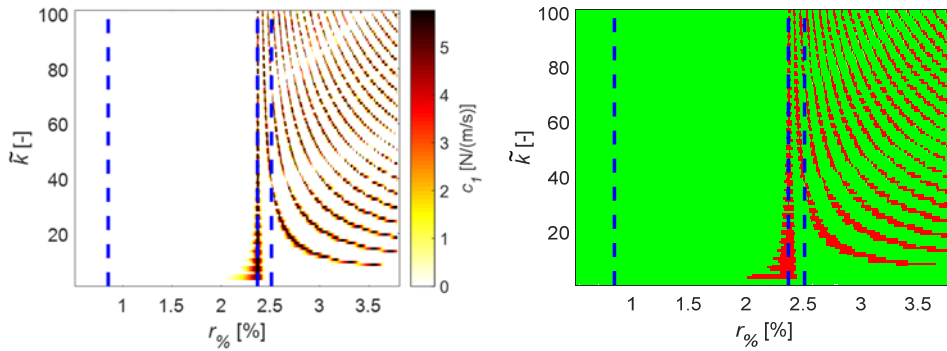


Figure 7.67 - Damping coefficient  $c_1$  : quantification (left) , stability (right).

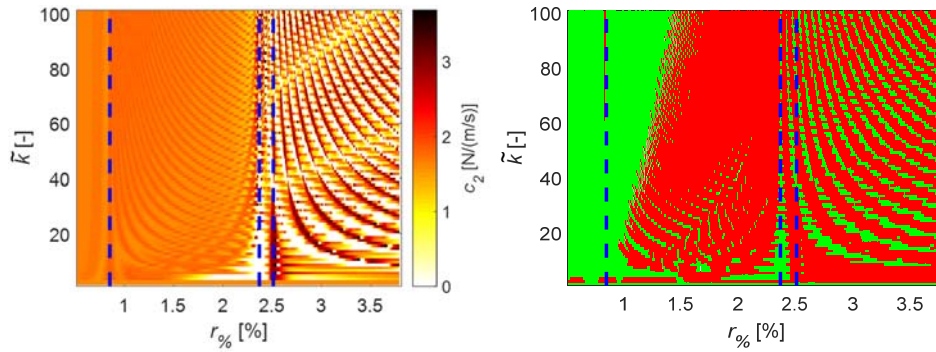


Figure 7.68 - Damping coefficient  $c_2$  : quantification (left) , stability (right).

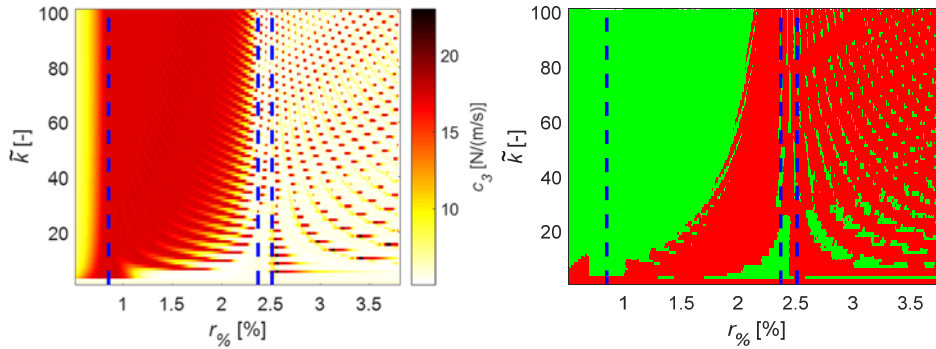


Figure 7.69 - Damping coefficient  $c_3$  : quantification (left) , stability (right).



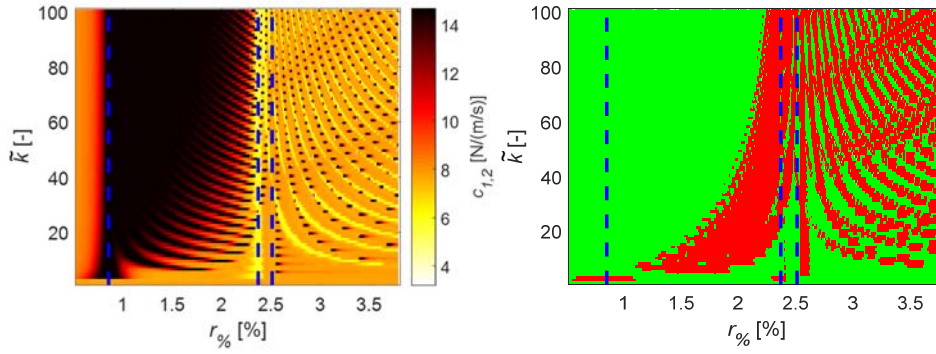


Figure 7.70 - Damping coefficient  $c_{1,2}$  : quantification (left) , stability (right).

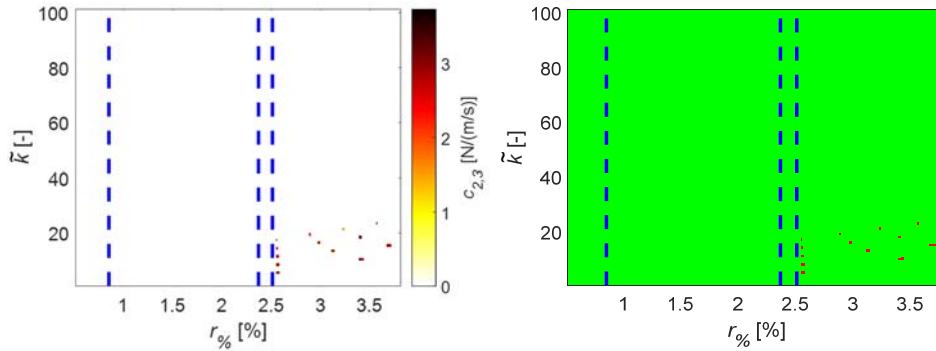


Figure 7.71 - Damping coefficient  $c_{2,3}$  : quantification (left) , stability (right).

The optimal identified solution  $\mathbf{u}^*$  can be selected looking for  $(r_{\%}^*, \tilde{k}^*)$  satisfying Eq. (4.70). The global stabilisation diagram  $\bar{\mathbf{S}}$ , computed as in Eq. (4.68), and the error map  $\mathbf{E}$ , computed using Eq. (4.69), are shown in Figure 7.72. The identification is globally stable in a region close to the first asymptote, in the same region also the normalised residuum  $E_{\%}$  reaches a minimum value.

The solution  $\mathbf{u}^*$  is the one with minimum residuum at  $(r_{\%}^*, \tilde{k}^*) = (90, 0.9138\%)$  and inversion error  $E_{\%}^* = 0.0272\%$  , blue cross in Figure 7.72.

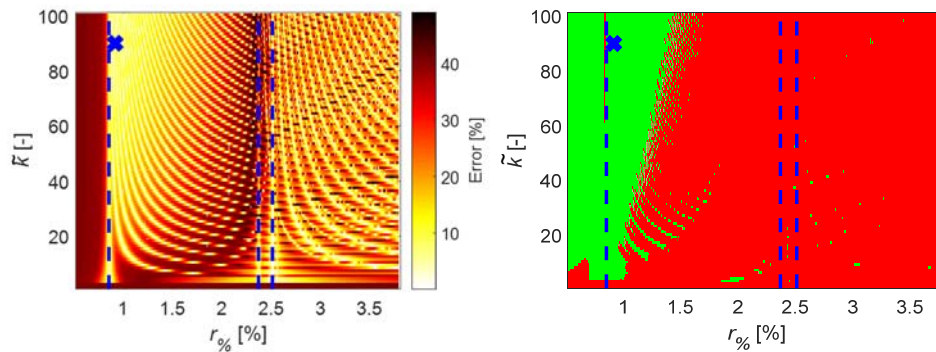


Figure 7.72 - Normalised residuum (left) and global stability diagram (right).

The identified damping matrix is shown in Figure 7.73. The damping coefficient values of the five layers are reported in Table 7.10. The spatial distribution of the damping is well identified and the damping values are in very good agreement with the expected ones.

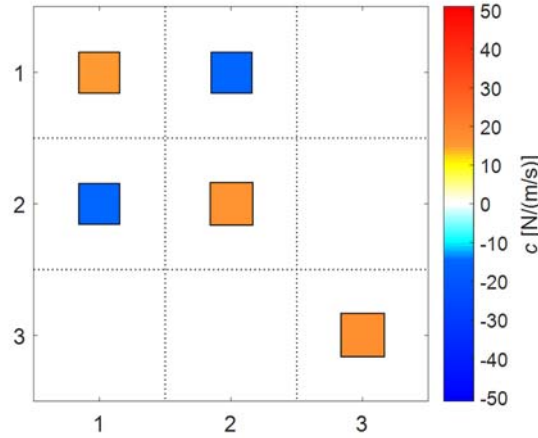


Figure 7.73 - Identified viscous damping matrix of the config. D3 & D12 L3.

Table 7.10 - Identified damping coefficients values of the conf. D3 & D12 L3.

Damper	Values [N/(m/s)]
$c_1$	0.0000
$c_2$	1.8081
$c_3$	17.3419
$c_{1,2}$	14.6215
$c_{2,3}$	0.0000

### 7.3.10 Configuration D3 & D12 L4

The configuration D3 & D12 L4 of the system includes both the relative dampers at dissipation level L4 and the absolute dampers. The system synthesised FRM  $\mathbf{H}_{syn}(\Omega)$  is in agreement with the experimental FRM  $\mathbf{H}^{Exp}(\Omega)$ , as shown in Figure 7.74. The second and third peaks are very high damped.

The vertical asymptote ranges values  $r_{\%}$ , computed using Eq. (4.71), were found to be  $r_{\%asymptote} = 0.6621, 2.7120, 6.2345 \%$ . The identified damping coefficients of the five layers and their regions of stability are mapped onto the  $(r_{\%}, \tilde{k})$  plane in Figure 7.75 - Figure 7.78. The expected asymptotes are highlighted in blue dashed vertical lines and the stabilisation diagrams show stable (green) and unstable (red) regions of  $(r_{\%}, \tilde{k})$  plane.

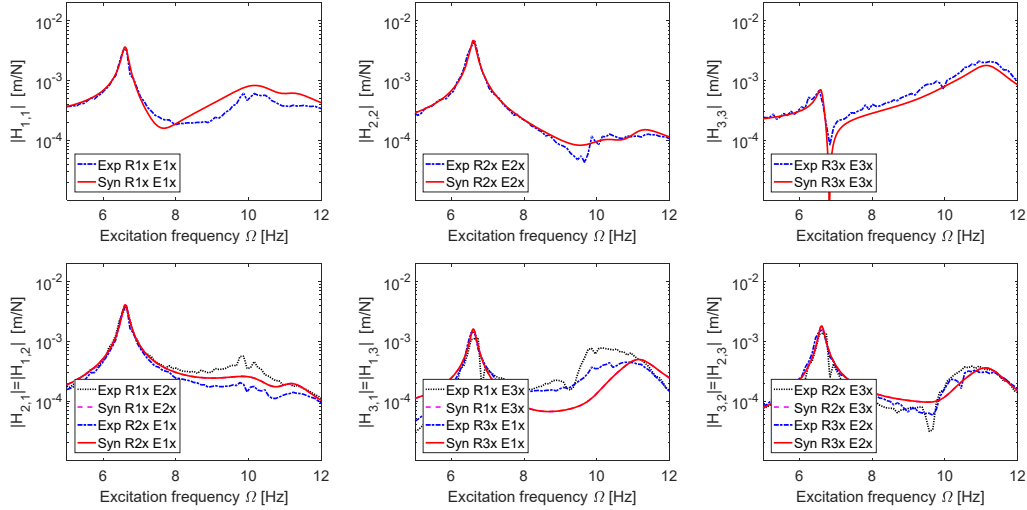
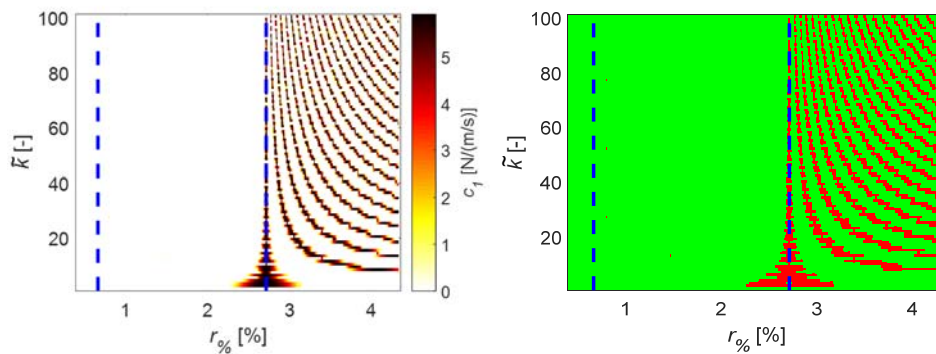


Figure 7.74 - Experimental and synthesised FRM of the conf. D3 &amp; D12 L4.

The damping coefficient  $c_1$  of the absolute damper acting of the first mass is identified in Figure 7.75. It is zero and stable in the range between the first two asymptotes. The absolute dampers  $c_2$  acting on the second DOFs is shown in Figure 7.76. The identified damping value is small and stable between the first two asymptotes. The absolute damper acting of the third DOF is shown in Figure 7.77. The identified value is slightly higher than the  $c_3$  identified values in all the other configurations with damper D3 activated. The damping coefficient value  $c_{1,2}$  for the first relative damper, shown in Figure 7.78, is stable between the first two asymptotes, elsewhere damping values are not stable. Its quantification is very similar to the D12 L4 configuration and it is in accordance with the reference value for the relative damper set at dissipation level L4. The relative damper coefficient  $c_{2,3}$  between the second and the third DOFs, shown in Figure 7.79, is zero and stable in the  $(r_{\%}, \tilde{k})$  plane. The identified damping values were found to be similar to the expected values in the stable regions. Most of the dissipations are due to the relative damper acting between the first and second DOFs and absolute damped on acting the third DOF, as expected.


 Figure 7.75 - Damping coefficient  $c_1$  : quantification (left) , stability (right).

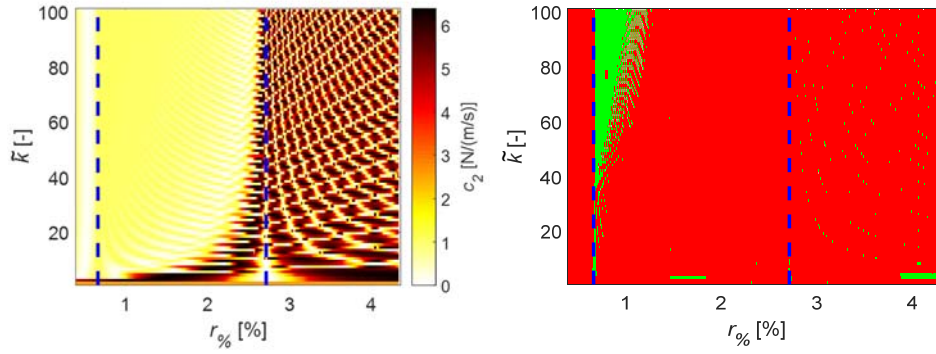


Figure 7.76 - Damping coefficient  $c_2$  : quantification (left) , stability (right).

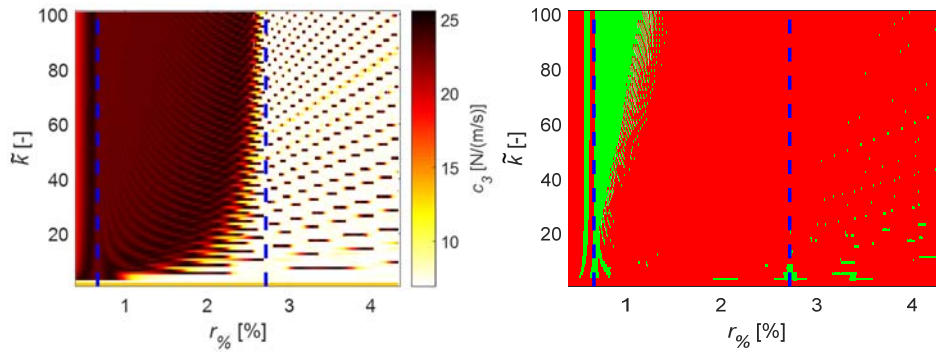


Figure 7.77 - Damping coefficient  $c_3$  : quantification (left) , stability (right).

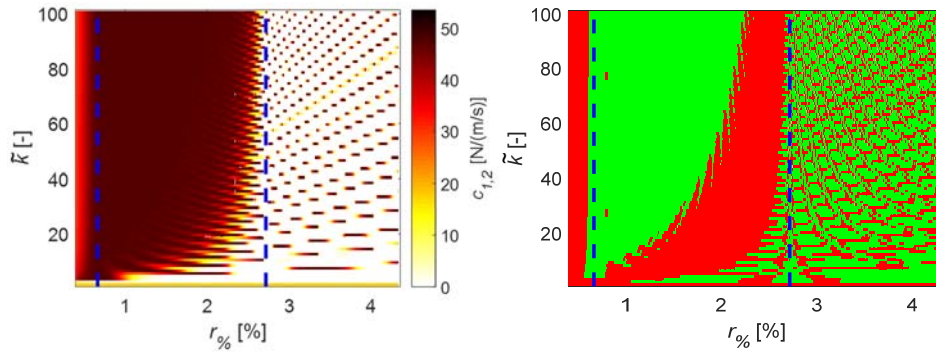


Figure 7.78 - Damping coefficient  $c_{1,2}$  : quantification (left) , stability (right).

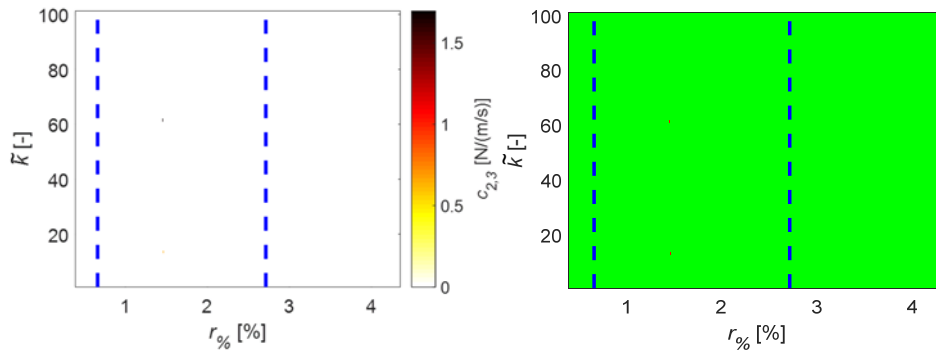


Figure 7.79 - Damping coefficient  $c_{2,3}$  : quantification (left) , stability (right).

## 7. Experimental direct damping identification in a lumped parameters system

The optimal identified solution  $\mathbf{u}^*$  can be selected looking for  $(r_{\%}^*, \tilde{k}^*)$  satisfying Eq. (4.70). The global stabilisation diagram  $\bar{\mathbf{S}}$ , computed as in Eq. (4.68), and the error map  $\mathbf{E}$ , computed using Eq. (4.69), are shown in Figure 7.80. The identification is globally stable in a region close to the first asymptote, in the same region also the normalised residuum  $E_{\%}$  reaches a minimum value.

The optimal identification couple  $(r_{\%}^*, \tilde{k}^*)$  is the one with minimum residuum at  $(r_{\%}^*, \tilde{k}^*) = (81, 0.8887\%)$  and  $E_{\%}^* = 0.0417\%$ , blue cross in Figure 7.80.

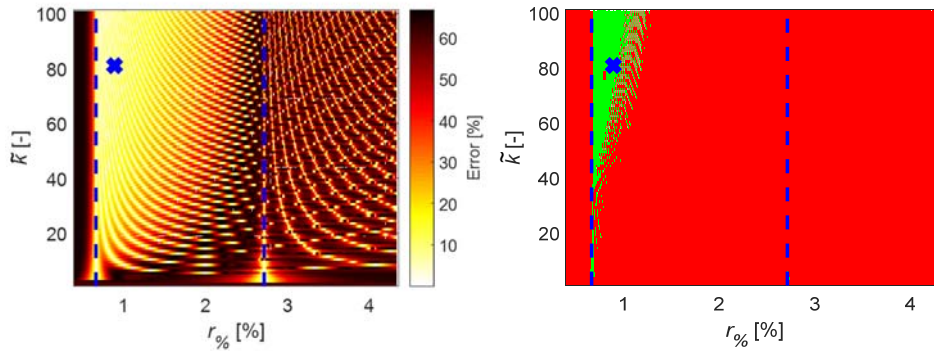


Figure 7.80 - Normalised residuum (left) and global stability diagram (right).

The identified damping matrix is shown in Figure 7.81. The damping coefficient values of the five layers are reported in Table 7.11. The spatial distribution of the damping is well identified and the damping values are in very good agreement with the expected ones.

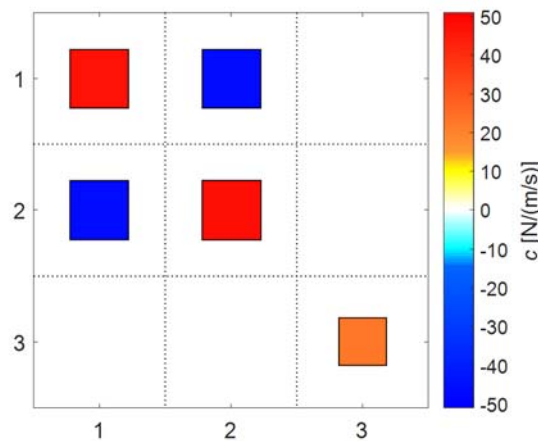


Figure 7.81 - Identified viscous damping matrix of the config. D3 & D12 L4.

Table 7.11 - Identified damping coefficients values of the conf. D3 &amp; D12 L4.

Damper	Values [N/(m/s)]
$c_1$	0.0000
$c_2$	1.0556
$c_3$	22.7597
$c_{1,2}$	46.7817
$c_{2,3}$	0.0000

## 7.4 Identification comparison

The SLM process identification was carried out for all the ten configurations of the parametric system under analysis. The identified values of the absolute dampers  $c_3$  is expected to be almost the same in all the configurations in which it is active; the relative damper viscous damping coefficient  $c_{12}$  is expected to be the same in the twin configurations in which it is set to the same dissipation level.

The experimental FRM  $\mathbf{H}^{Exp}(\Omega)$  and the synthesised FRM  $\mathbf{H}_{syn}(\Omega)$  are shown in Figure 7.82 and Figure 7.83. The normal FRM  $\mathbf{H}^N(\Omega)$ , extracted from the synthesised one using Eq. (4.35), are shown in Figure 7.84 and Figure 7.85. The FRMs can be divided into two families: the first family aligned with the undamped configuration, and a second family aligned with the configuration D3. This last family presents a higher frequency of the third mode shape, due to the small elastic effect of the air dashpots, given by the air compressibility. The normal FRMs  $\mathbf{H}^N(\Omega)$ , being the FRF of the undamped system underlying the damped one, should be the same for all the configuration, if the air dashpots introduce only damping in the test-rig.

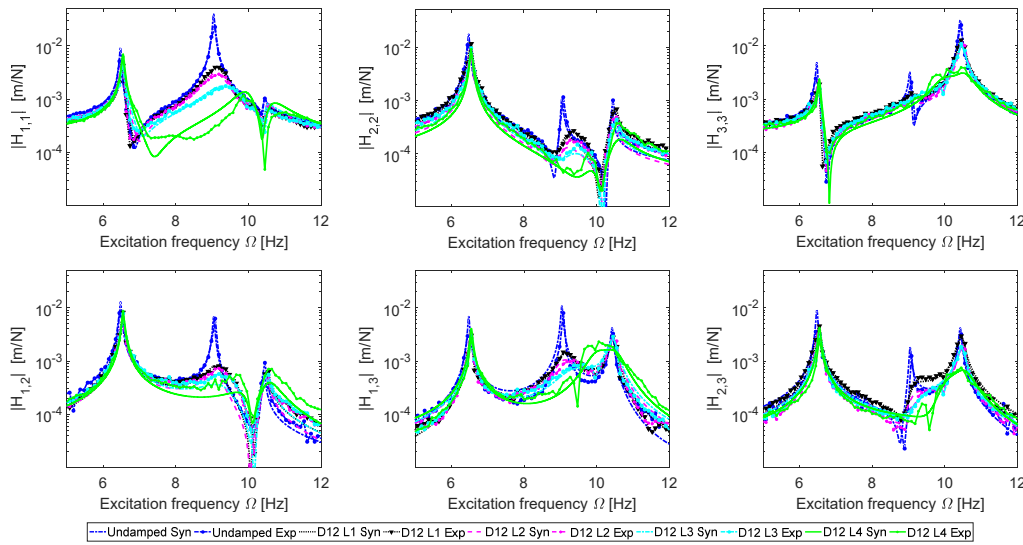


Figure 7.82 - FRM of configurations undamped and D12 Lx.

## 7. Experimental direct damping identification in a lumped parameters system

The normal FRMs  $\mathbf{H}^N(\Omega)$  are almost the same for the two families of data, but the natural frequencies slightly increase with damping, due to the small elastic effect of air compression. This effect is clearly visible for the D12 L4 and D3 & D12 L4 configuration, in which the dissipation level is set at a very high value and therefore the added stiffness increases. In the last case the second normal mode shape has a higher natural frequency, consistent between the configurations D12 L4 and D3 & D12 L4.

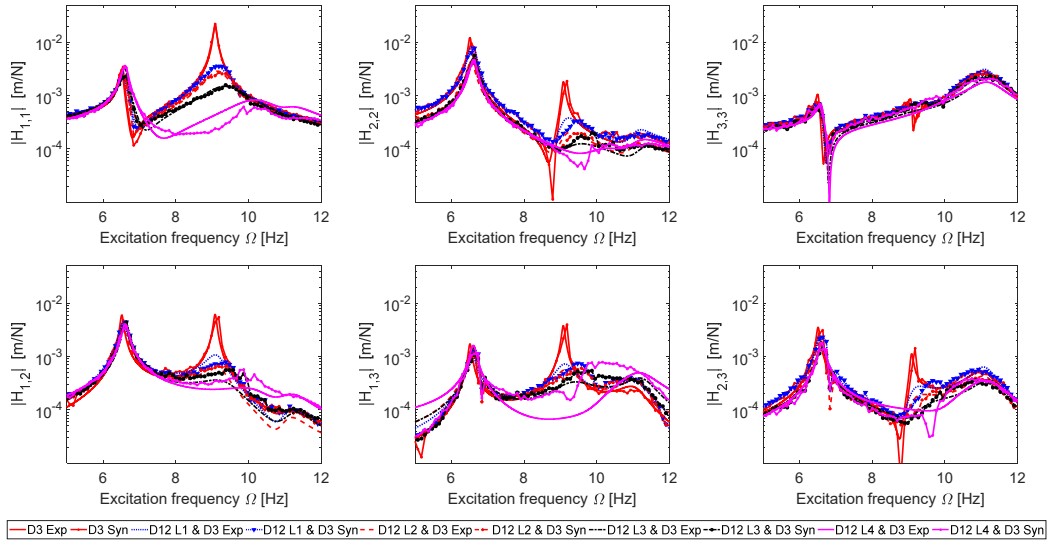


Figure 7.83 - FRM of configurations D3 and D3 & D12 Lx.

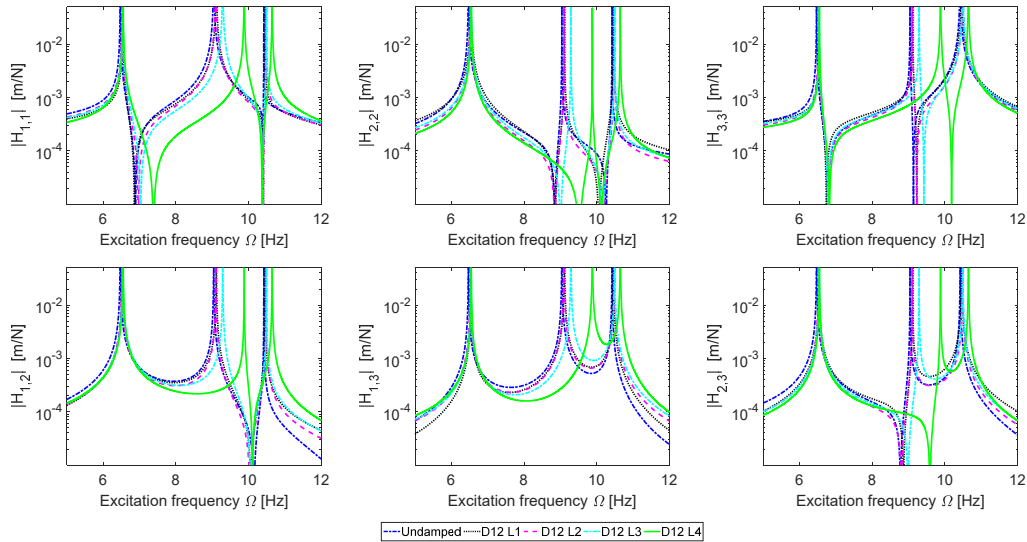


Figure 7.84 - Normal FRM of configurations undamped and D12 Lx.



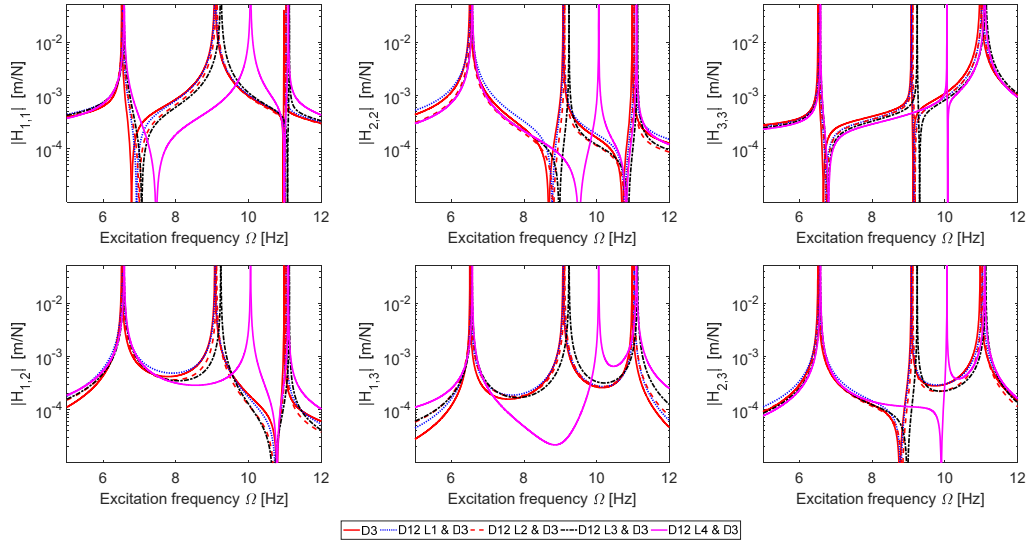


Figure 7.85 - Normal FRM of configurations D3 and D3 &amp; D12 Lx.

The identified damping matrices of all the ten configurations are shown in Figure 7.86, where the sizes of the coloured squares are proportional to the logarithm of the corresponding damping matrix term. The first row includes all the configurations with the absolute dampers active and with increasing dissipation levels for the relative damper. In the second row the relative damper only is present.

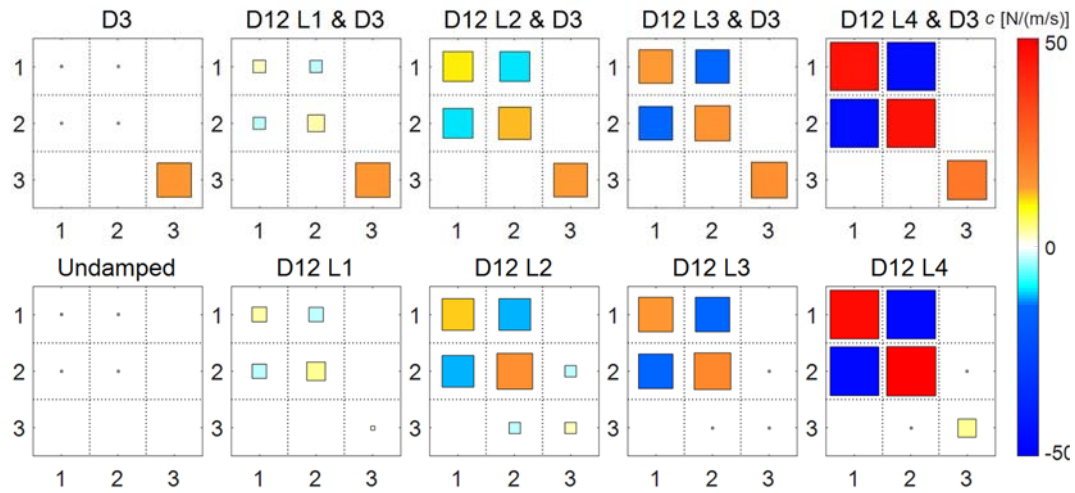


Figure 7.86 - Identified viscous damping matrices

The comparison of the results between the configurations shows consistent results. The identified absolute viscous damping coefficient value is almost the same in the entire set of configurations in which it is present. The identified relative damping coefficient increase as expected with the increasing levels of damping set on the air dashpot. Moreover, in those configurations in which the relative damper is set at the same level, the identified damping matrix terms are almost the same.



## 7. Experimental direct damping identification in a lumped parameters system

The normalised residuum error  $E_{\%}$  is very low in all the configurations, the maximum error is  $E_{\%} = 0.116\%$  in the configuration D12 L4. The only exception being the undamped configuration in which the error result is very high. This is because the method is trying to identify a damping matrix in an almost undamped structure and is an unrepresentative result. Although dissipation is predominantly due the air dashpots, the internal damping of the structure is also identified, i.e. damping between the second and third DOFs or small amount of absolute damping on each DOF.

The identified air dashpots viscous damping coefficients are found to be in very good agreement with expected values, presented in § 6.2. The comparison is shown in Figure 7.87. The expected trend is perfectly identified, only the air dashpot D12 at dissipation level L4 presents a significantly greater difference. This discrepancy is due to the overestimation of the expected value in dissipation level L4 during the separate air dashpot testing, where Figure 6.4 shows a difference between estimated values depending upon the direction of motion.

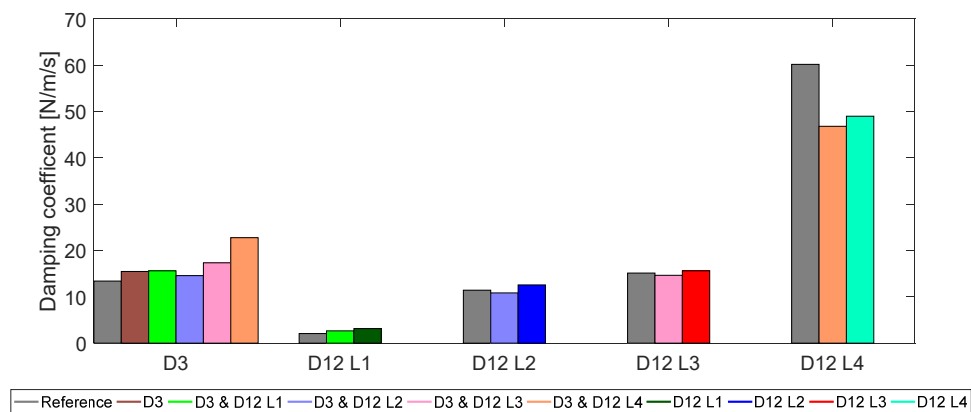


Figure 7.87 - Expected and identified dashpot viscous damping coefficients.

The identified damping coefficients of the ten configurations are summarised in Table 7.12, where also the viscous damping coefficients of the Layers not involving air dashpots can be compared. The viscous damping coefficient  $c_1$  of the layer representing the absolute damper acting of the first DOF is identified to be zero in almost all the configurations. The exceptions are: the two configuration in which the relative damper D12 is set to dissipation level L1, in which the identified viscous damping value is really small  $\approx 0.07 \text{ Nm/s}$ , and the undamped and D3 configuration, in which the identified value is  $\approx 0.3 \text{ Nm/s}$ . The viscous damping coefficient  $c_2$  of the layer representing the absolute damper acting of the second DOF is identified to be  $0.6 < c_2 < 2.3 \text{ Ns/m}$ , with an increasing trend when the dissipation level of the D12 air dashpot increases. The identified values are quite close between the twin configurations D12 Lx and D3 & D12 Lx. The viscous damping coefficient  $c_3$  of the layer representing the absolute damper

acting of the second DOF is identified to be zero or very low when it is deactivated, while close to the reference value when it is activated. An exception is the configurations D12 L4 and D3 & D12 L4 where it is respectively identified to be respectively  $\approx 4 \text{ N/(m/s)}$  and  $\approx 5 \text{ N/(m/s)}$  more than the reference values. This is probably because of the very high level of dissipation of the D12 air dashpot. The viscous damping coefficient  $c_{1,2}$  of the layer representing the relative damper acting between the first and second DOFs changes in accordance to the dissipation level Lx of the air dashpot. When the D12 is deactivated, in undamped and D3 configurations,  $c_{1,2}$  results  $\approx 0.1 \text{ Ns/m}$ . The viscous damping coefficient  $c_{2,3}$  of the layer representing the relative damper acting between the second and third DOFs is identified to be always zero, the only exceptions are configurations D12 L2 and D12 L3 where it is low.

Table 7.12 - Identified damping coefficients comparison.

<b>Damper</b>	<b>undamped</b>	<b>D12 L1</b>	<b>D12 L2</b>	<b>D12 L3</b>	<b>D12 L4</b>
$c_1$	0.3193	0.0849	0.0000	0.0000	0.0000
$c_2$	0.0000	1.2629	2.3071	2.1946	1.7335
$c_3$	0.0000	1.3715	0.0000	0.2879	4.2336
$c_{1,2}$	0.1379	3.1300	12.5603	15.5820	48.9464
$c_{2,3}$	0.0000	0.0000	2.4538	0.8241	0.0000
<b>Damper</b>	<b>D3</b>	<b>D3 &amp; D12 L1</b>	<b>D3 &amp; D12 L2</b>	<b>D3 &amp; D12 L3</b>	<b>D3 &amp; D12 L4</b>
$c_1$	0.2901	0.0640	0.0000	0.0000	0.0000
$c_2$	0.6149	1.1805	2.3105	1.8081	1.0556
$c_3$	15.4703	15.5931	14.5662	17.3419	22.7597
$c_{1,2}$	0.1136	2.6446	10.8297	14.6215	46.7817
$c_{2,3}$	0.0000	0.0000	0.0000	0.0000	0.0000

## 7.5 Conclusions

The SLM was applied for the identification of ten different configuration of the damped three DOFs system. The configurations differ for distribution and amount of dissipations. In particular a relative air dashpot damper between the first and second DOF could be activated at 4 different dissipation level and an absolute damper on the third DOF could be activated at a fixed dissipation level.

The SLM was able to identify the correct damping distribution in all the configurations. The inversion error is very low in all the cases, except the undamped configuration. The global stabilisation diagrams show a stable region in the range between the first to asymptotes, as predicted in § 4.3.2.

## 7. Experimental direct damping identification in a lumped parameters system

---

The identified damping values are coherent among similar configurations for both the air dashpot damping coefficients and the small damping coefficients of the structure in the other DOFs.

The air dashpots are very well identified and also the quantification is in good agreement with the expected damping coefficient of § 6.2. This experimental campaign validates the SLM.

## Chapter 8

# 8. Experimental direct spatial damping identification of a car chassis

In this chapter, the SLM is applied for the identification of the damping matrices of an industrial application: a BIW car chassis including the suspension system. The effects of the shock absorbers on the modal properties and damping matrices of the chassis are investigated. The four shock absorbers act as localised viscous dampers; therefore, the global system results non-proportionally damped. The SLM is here applied to evaluate the changes induced by localised dissipations on damping matrices and modal behaviour.

The effects of non-proportional damping on a real system are here analysed from an experimental point of view. The work focuses on: 1) the influence of localised dampers on the modal properties of the first chassis global modes and 2) the localisation, identification and quantification of the energy dissipation sources, looking for equivalent non-proportional viscous and/or structural damping matrices.

The chapter is organised as follows: the automotive chassis and the experimental setups are described in § 8.1. In § 8.2 the experimental modal properties identified for three different configurations are presented; experimental results are then compared in § 8.4 to evaluate the shock absorbers effects on the system modal properties. In § 8.5 the SLM is applied to the experimental BIW data and the resulting viscous and structural matrix are discussed.

The work presented in this chapter is summarised in [162,183].

### 8.1 BIW car chassis

The system under investigation is the BIW of a D segment car, including its suspension system, shown in Figure 8.1. The vehicle is equipped with independent MacPherson front suspensions and independent multi-link rear suspensions. The car floor is covered with a viscoelastic material to damp the floor vibrations, therefore local modes of the floor are not expected. The frame includes a glass sunroof, composed of two panels.

The chassis is tested in three configurations to include or exclude the shock absorbers effects on the dynamic behaviour and to understand how the shock absorbers affect the dynamic behaviour of the first global flexible modes.



Figure 8.1 - Experimental setups configurations: MK (left) and MCK (right).

In the first configuration the chassis is suspended by means of an overhead crane (Figure 8.1, left). In this configuration, the shock absorbers have no influence on the car chassis since the wheels are not touching the ground. For this reason, it will be called “MK configuration” hereafter. The structure is hanged with four flat woven webbing slings fixed in four points: two on the front cross member and in other two on the rear part of the chassis in correspondence of the taillights, as shown in Figure 8.2. In this configuration, each suspension is at its bottom stroke and the shock absorbers with the wheels can be considered simply as hanging masses respect to the chassis, free to oscillate as a multi-body system. The effects of the localised dampers should be lowest in this configuration. The frame in MK configuration may be modelled as a proportionally damped system, although some effects due to the chassis internal damping (steel and viscoelastic materials) and hanging slings are present.

The other configuration includes the shock absorbers effects: the car chassis is tested in the standard position, i.e., with the four wheels on the floor (Fig. 1, right) so that the suspensions are in their working position. The system is analysed with two different tires pressures, nominal pressure 2.4 bar and reduced pressure 1.2 bar, to investigate the inflating pressure influence on the global modes. These configurations will be called “MCK 2.4” and “MCK 1.2”, respectively.



Figure 8.2 - Hanging points: front and rear, right and left (left to right).

Roving hammer modal tests were performed on the three configurations, using an 8-channel LMS SCADAS Mobile. The impact points selection is based on MoGeSeC methodology [184]. This methodology selects the best points for experimental analysis weighting modal and geometrical factors, to have the best description of the modal parameters. Some other points were added to complete the chassis geometry. In total, 95 points were selected: 88 points are located on the chassis and 2 points on each wheel, one in correspondence of the rotation axis and the other in the centre of the tire contact patch. The chassis geometry is sketched using the selected nodes linked by lines, which represent the physical connectivity, and triangular surfaces (Figure 8.3).

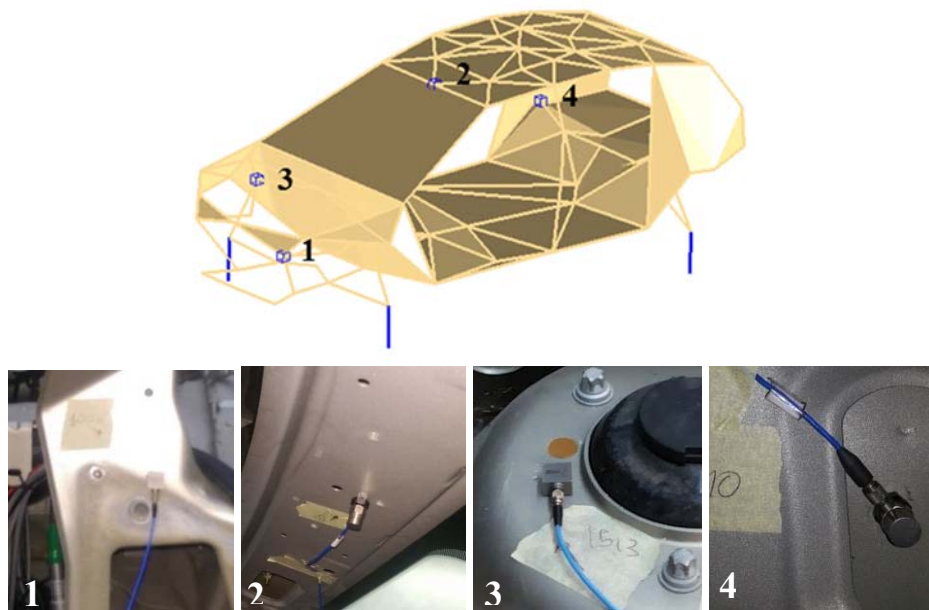


Figure 8.3 - Test grid (top) and accelerometers location (bottom).

Two tri-axial PCB 339A32 and two mono-axial PCB 352C33 accelerometers are used to measure the responses of the system, located as Figure 8.3. All the selected points were excited in the MK configuration, when feasible in more than one direction. In total 142 DOFs were excited, thus 994 FRFs were computed. In the MCK configurations, the contact points between floor and tires cannot be

excited and are considered constrained; thus 138 DOFs were excited and 966 FRFs were measured for each of the two MCK configurations. For each point, the results are obtained averaging five repetitions. The acquisition time duration is 2.56 s, a force-exponential window is applied to the input signal while an exponential window is applied to the response signals; these are the typical settings for hammer tests. The frequency bandwidth is 1600 Hz and 4096 spectral lines are used; the resulting FRF resolution frequency is 0.39 Hz. The FRFs are computed using  $H_1$  estimator.

### 8.1.1 Hammer tip choice

The hammer tip choice is not trivial in this application: the tip must be quite soft to give good excitation in the low frequency range and at the same time stiff enough to provide the same excitation level for all the frequencies. Furthermore, the tip must be capable of properly exciting all the different materials and component of the car chassis.

Four different hammer tips are available: super soft, soft, medium and hard.

The selection of the tip is based FRF cleanness and the power spectral density (PSD) of the impact. The PSD is useful to check the ability to excite frequency range of interest.

The FRFs and the PSDs of the input impact are shown in Figure 8.4.

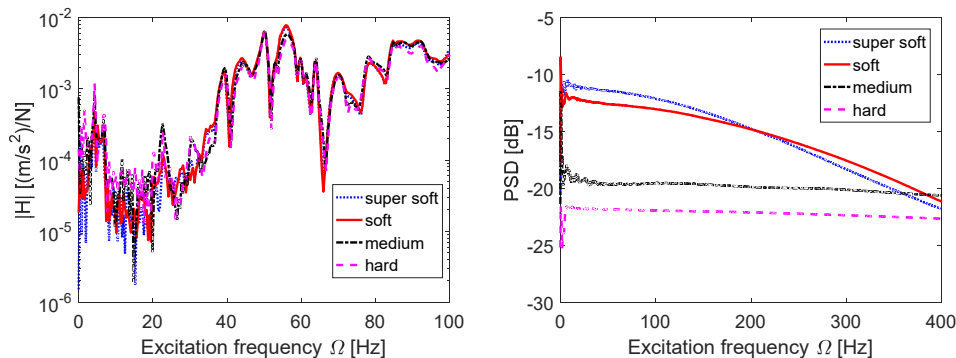


Figure 8.4 - FRF (left) and PSD (right) with different hammer tips.

The FRFs obtained with the different tips are quite similar, with some differences in peaks amplitude: the highest peaks are obtained with soft point.

The input PSD behaviours are very different, as expected. The hard and medium point excite the system with low energy up to 400 Hz, while the other tips are capable of properly excite the system up to 50 Hz, but with much more energy. Because the frequency range of interest focus on the first 40 Hz, the soft tip (rubber) was selected. It has a flatter PSD than the super soft at low frequencies. The rubber tip gives the best compromise between all the requirements.

## 8.2 Shock absorbers effects on chassis dynamic behaviour

The dynamic behaviour of automotive chassis has been widely studied [185–187], but there are no references to the effects of the suspension system on the frame modal behaviour, neither to its dissipations identification. More in general direct spatial damping identification applications to real complex structure are rarely available in literature. In [188] a numerical study of the performance of structural nonlinear suspension system on vehicle dynamics is presented, but the chassis flexibility is not taken into account. The effects of the suspension system on the flexible modes of the BIW are here analysed through EMA. The complex modal parameters - natural frequencies  $f_{n,i}$ , damping ratios  $\zeta_i$  and mode shapes  $\Psi_i$  - in the frequency range between 0 - 40 Hz were extracted from the experimental data using PolyMAX algorithm [175]. Complex modal parameters were extracted for the MK and the two MCK configurations. The modal shapes have  $N=142$  physical coordinates in the MK configuration, corresponding to the number of excited DOFs  $I$ . In MCK configurations  $N=138$ , because the four point of the contact patch are on the ground, therefore they act as four boundary conditions. The modal behaviour of the three configurations is presented in § 8.2.1, § 0 and § 8.2.3, together with the Auto-MACX matrices, necessary to better understand the coupling between local and global mode shapes.

The modal assurance criterion for complex eigenvector, called MACX, is the modal assurance criterion (MAC) extended to complex eigenvectors [189]. The correlation between two complex eigenvectors  $\Psi_p$  and  $\Psi_q$  is computed as:

$$MACX(\Psi_p, \Psi_q) = \frac{(|\Psi_p^* \Psi_q| + |\Psi_p^T \Psi_q|)^2}{(\Psi_p^* \Psi_p + |\Psi_p^T \Psi_p|)(\Psi_q^* \Psi_q + |\Psi_q^T \Psi_q|)} \quad (8.1)$$

The MACX matrices, Figure 8.5, Figure 8.6

Figure 8.6 and Figure 8.7, are presented with the mode shapes spaced proportionally to the natural frequencies to better understand the frequency distance between the modes. The Auto-MACX matrices are obtained from Eq. (8.1) when  $p = q$ , thus  $\Psi_p = \Psi_q$ , i.e. the same configuration is used.

### 8.2.1 Configuration MK

In the suspended configuration, the modal density is high: 34 modes are identified in the first 40 Hz. The mode shapes are reported in Table 8.1. The Auto-MACX matrix, Figure 8.5, presents four clear clusters of mode shapes: the rigid body motions, the torsional modes, the vertical bending modes and the horizontal bending modes, in frequency ascendant order. EMA was not able to detect the first rigid body motions even if the FRFs present clear rigid body motion peaks.



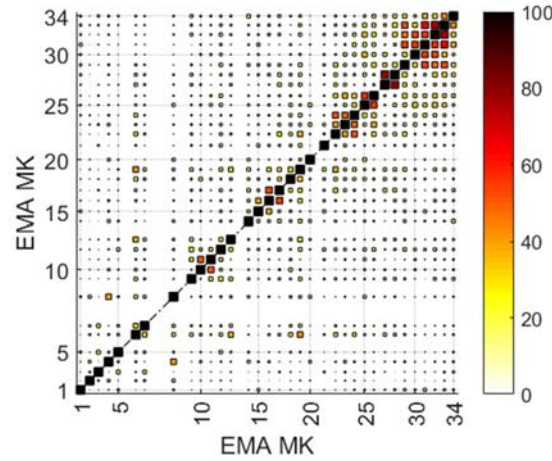
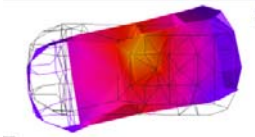

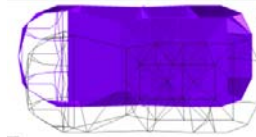

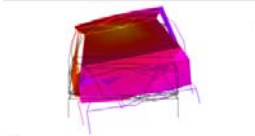
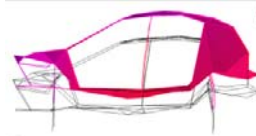
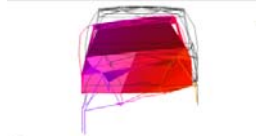









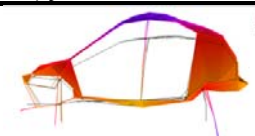


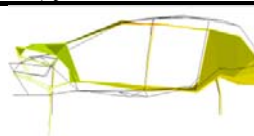
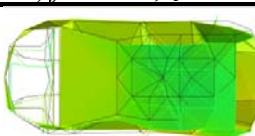
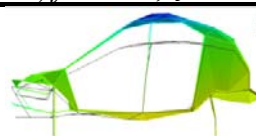
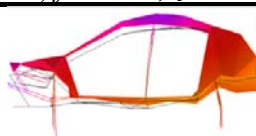

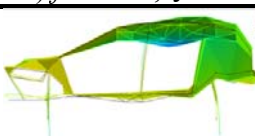
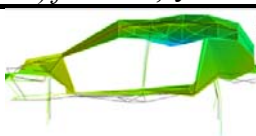
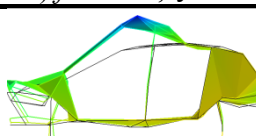


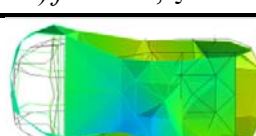
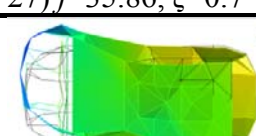

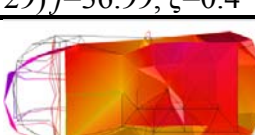
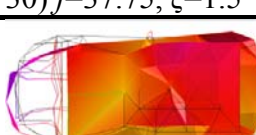


Figure 8.5 - Configuration MK Auto-MACX matrix.

The rigid body motions are therefore obtained exploiting the pendulum effect of the suspended chassis [190]. The chassis can oscillate in four different DOFs: x-translation, y-translation, rotation respect to x-axis and y-axis. For each type of excitation, the oscillation response period was measured. The repeatability of the tests is very high, with a relative repeatability error of 0.5 % on the measured period of oscillation. The natural frequency  $f_{n,i}$  results to be the inverse of the oscillation period and the damping ratio  $\zeta_i$  was computed using the logarithmic decrement method, from the starting amplitude up to one-half of the amplitude initial value. The rigid body motions are modes 1 to 6 in Table 8.1. Some suspension modes are detected (7, 8, and 13), they are multi-body modes: the wheels move almost independently respect to the chassis, which acts like a rigid body. The first global flexible mode is torsion: four torsional modes are detected (modes 9-12), coupled with vertical and horizontal wheel modes. Two of the torsional modes present higher damping ratio because of relative motion between wheels and chassis, while the other two have lower damping ratio, because the wheels are simply dragged by the chassis global torsional mode. Vertical bending modes are then identified (modes 14-16 and 19): these modes are differently coupled with wheels and sunroof modes. Two of the bending modes have high damping and other two low damping, similarly to torsional modes. It can result difficult to graphically distinguish torsional and vertical bending mode shapes, due to the tri-dimensional nature of the structure, but they have different modal behaviour: the BIW left and right sides move out of phase in torsion, while they are in phase in vertical bending. A y-translation mode of the roof is detected (mode 21). Three pairs of roof modes with participation of wheel modes are identified: a pair of roof mode (1,1) (modes 17-18), a pair of mode (1,2) (modes 25-26) and a pair of mode (2,1) (modes 27-28). For each pair in which the wheels participate, the damping is clearly higher. The front cross member vertical bending mode shapes are detected (mode 20 and 22-24) coupled with both wheel and roof modes.

Table 8.1 - Configuration MK EMA identified modes:  $f_{n,i}$  [Hz],  $\zeta_i$  [%].

 1) $f=0$ , $\zeta=0$	 2) $f=0.22$ , $\zeta=2.1$	 3) $f=0.23$ , $\zeta=2.1$	 4) $f=0.93$ , $\zeta=2.7$
 5) $f=1.36$ , $\zeta=1.4$	 6) $f=5.38$ , $\zeta=0.7$	 7) $f=5.45$ , $\zeta=0.9$	 8) $f=14.69$ , $\zeta=0.9$
 9) $f=18.87$ , $\zeta=2.3$	 10) $f=19.12$ , $\zeta=0.6$	 11) $f=19.82$ , $\zeta=2.0$	 12) $f=20.41$ , $\zeta=0.6$
 13) $f=21.01$ , $\zeta=0.5$	 14) $f=25.14$ , $\zeta=2.0$	 15) $f=25.63$ , $\zeta=2.2$	 16) $f=26.54$ , $\zeta=0.7$
 17) $f=27.33$ , $\zeta=0.9$	 18) $f=28.46$ , $\zeta=1.4$	 19) $f=28.86$ , $\zeta=1.5$	 20) $f=29.42$ , $\zeta=1.1$
 21) $f=31.91$ , $\zeta=1.7$	 22) $f=33.14$ , $\zeta=1.7$	 23) $f=33.50$ , $\zeta=2.1$	 24) $f=33.80$ , $\zeta=0.6$
 25) $f=34.54$ , $\zeta=2.5$	 26) $f=34.80$ , $\zeta=0.6$	 27) $f=35.86$ , $\zeta=0.7$	 28) $f=36.45$ , $\zeta=0.8$
 29) $f=36.99$ , $\zeta=0.4$	 30) $f=37.75$ , $\zeta=1.5$	 31) $f=38.30$ , $\zeta=1.9$	 32) $f=38.91$ , $\zeta=1.6$
 33) $f=39.28$ , $\zeta=1.0$	 34) $f=39.44$ , $\zeta=3.6$		

Finally, 6 mixed horizontal bending modes are found: a pair of horizontal bending and front cross member torsional modes (modes 29-31), a pair of horizontal bending and roof (2,1) modes (modes 30 and 32) and a pair of horizontal bending and front cross member vertical bending modes (33 and 34). For each pair of global horizontal bending coupled front cross member modes, one mode has clearly higher damping; for the other pair (coupling with roof mode), damping is almost the same.

### 8.2.2 Configuration MCK 1.2 bar

In the configurations MCK, the chassis global modes are expected to be influenced by shock absorbers. The identified mode shapes are completed by adding null displacements in the nodes corresponding to the boundary conditions.

The modal density of the MCK 1.2 bar configuration is lower than for the MK configuration: only 21 modes are detected in the first 40 Hz, Table 8.2. The Auto-MAC matrix Figure 8.6 shows again four clusters of modes: multibody modes, torsional modes, vertical bending and horizontal bending modes.

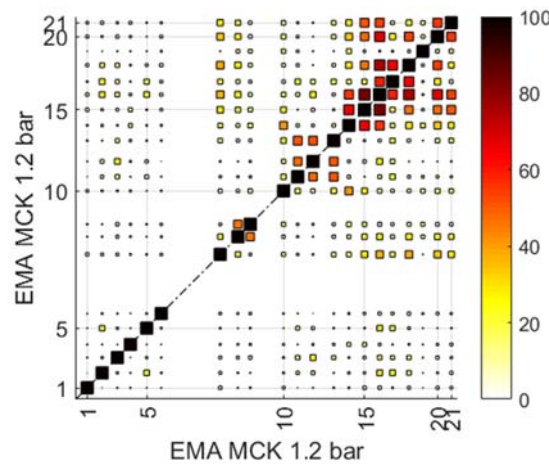


Figure 8.6 - Configuration MCK 1.2 bar Auto-MACX matrix.

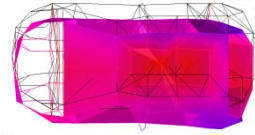

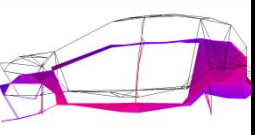
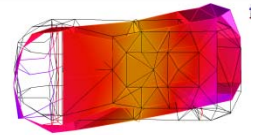

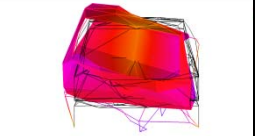

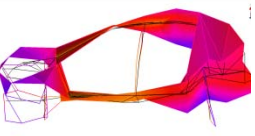

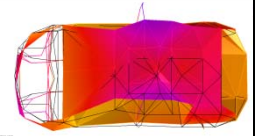

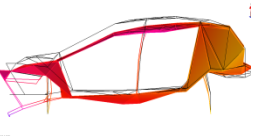
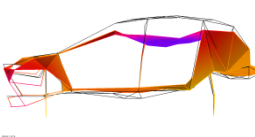
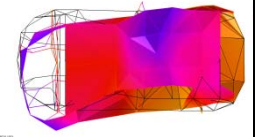
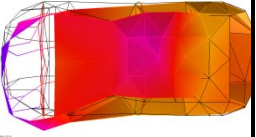
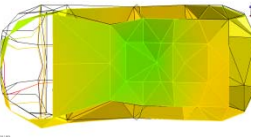

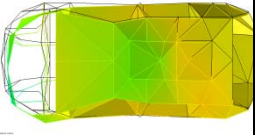
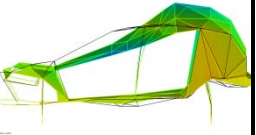
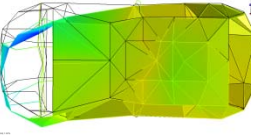
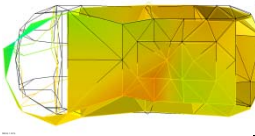
Six multi-body mode shapes (1-6) are detected, i.e. the chassis motions with respect to the wheels. The first global flexible modes detected are the three torsions, coupled with different behaviour of the wheels. A single y-vibration roof mode is detected (mode 10).

Four vertical bending modes are detected, coupled with different roof modes: global vertical bending, roof mode (1,1) and wheel pitch (mode 11), global vertical bending and wheel pitch (mode 12), global vertical bending and roof mode (1,1) (mode 13) and global vertical bending, roof mode (1,1) and wheel roll (mode 17).

Six global horizontal bending modes are found: a pair of horizontal bending mixed with front cross member vertical bending and roof mode (1,1) (modes 14 and 18), a pair of mixed ones with front cross member torsional mode and roof

mode (1,1) (modes 15 and 16) and a pair of global bending modes in horizontal plane and roof mode (2,1) (modes 20 and 21). As expected, damping is higher when the shock absorbers are working. Finally, (2,1) roof mode is detected (mode 19).

Table 8.2 - Conf. MCK 1.2 bar EMA identified modes:  $f_{n,i}$  [Hz],  $\zeta_i$  [%].

 1) $f=3.37$ , $\zeta=1.7$	 2) $f=4.18$ , $\zeta=2.2$	 3) $f=5.10$ , $\zeta=2.4$	 4) $f=5.38$ , $\zeta=2.2$
 5) $f=6.60$ , $\zeta=5.0$	 6) $f=7.32$ , $\zeta=2.6$	 7) $f=21.16$ , $\zeta=1.6$	 8) $f=22.80$ , $\zeta=1.4$
 9) $f=22.87$ , $\zeta=1.2$	 10) $f=29.11$ , $\zeta=2.0$	 11) $f=29.71$ , $\zeta=2.1$	 12) $f=30.64$ , $\zeta=1.4$
 13) $f=33.19$ , $\zeta=1.5$	 14) $f=34.07$ , $\zeta=2.1$	 15) $f=35.10$ , $\zeta=1.5$	 16) $f=36.01$ , $\zeta=2.0$
 17) $f=36.22$ , $\zeta=0.8$	 18) $f=37.48$ , $\zeta=0.1$	 19) $f=38.01$ , $\zeta=2.0$	 20) $f=38.74$ , $\zeta=1.3$
 21) $f=39.23$ , $\zeta=1.0$			

### 8.2.3 Configuration MCK 2.4 bar

The experimental setup of this configuration is identical to the v MCK 1.2 bar; only tire pressure is different. The expected damping should be lower with respect to the MCK 1.2 bar because tires damping decreases when pressure increases. In the configuration MCK 2.4 bar, 24 modes are identified in the frequencies range 0 - 40 Hz, Table 8.3. The Auto-MAC matrix is almost totally diagonal, Figure 8.7.



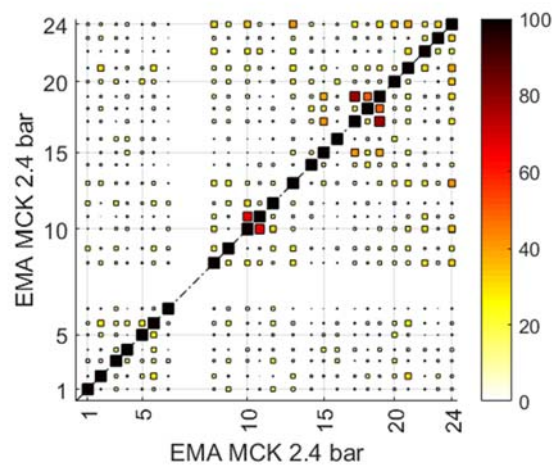
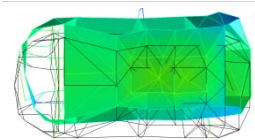
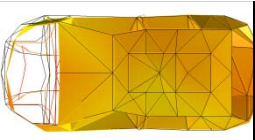
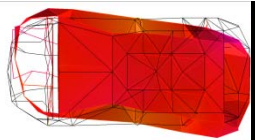
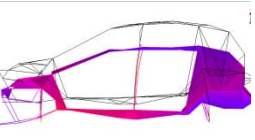
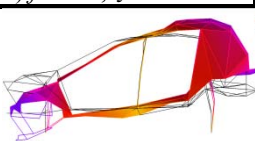
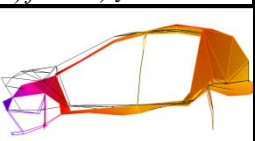
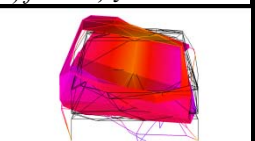
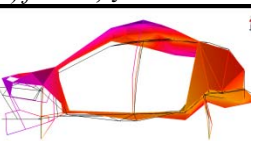
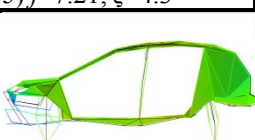
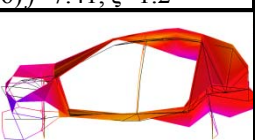
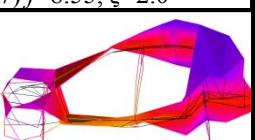

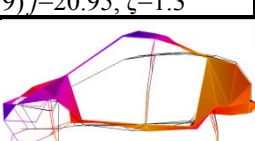
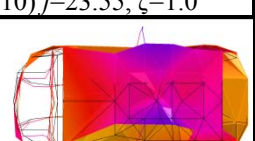
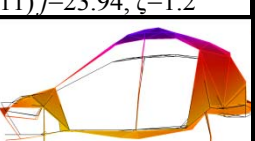
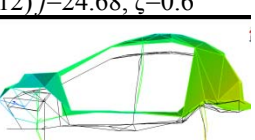
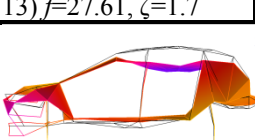
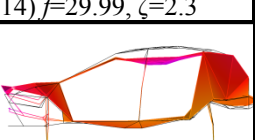
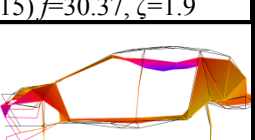
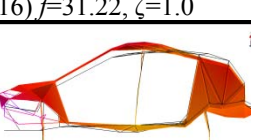
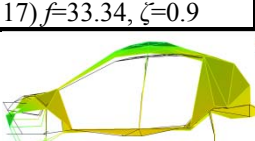
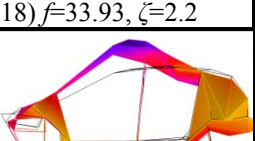
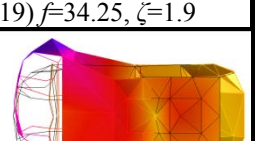
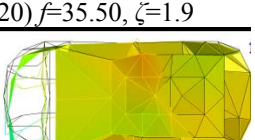


Figure 8.7 - Configuration MCK 2.4 bar Auto-MACX matrix.

Table 8.3 - Conf. MCK 1.2 bar EMA identified modes:  $f_{n,i}$  [Hz],  $\zeta_i$  [%].

 1) $f=3.91$ , $\zeta=1.6$	 2) $f=4.54$ , $\zeta=1.8$	 3) $f=5.93$ , $\zeta=2.1$	 4) $f=5.96$ , $\zeta=2.1$
 5) $f=7.21$ , $\zeta=4.3$	 6) $f=7.41$ , $\zeta=1.2$	 7) $f=8.55$ , $\zeta=2.0$	 8) $f=19.84$ , $\zeta=0.24$
 9) $f=20.95$ , $\zeta=1.3$	 10) $f=23.55$ , $\zeta=1.0$	 11) $f=23.94$ , $\zeta=1.2$	 12) $f=24.68$ , $\zeta=0.6$
 13) $f=27.61$ , $\zeta=1.7$	 14) $f=29.99$ , $\zeta=2.3$	 15) $f=30.37$ , $\zeta=1.9$	 16) $f=31.22$ , $\zeta=1.0$
 17) $f=33.34$ , $\zeta=0.9$	 18) $f=33.93$ , $\zeta=2.2$	 19) $f=34.25$ , $\zeta=1.9$	 20) $f=35.50$ , $\zeta=1.9$
 21) $f=36.33$ , $\zeta=1.1$	 22) $f=38.2$ , $\zeta=1.8$	 23) $f=38.89$ , $\zeta=1.8$	 24) $f=39.80$ , $\zeta=0.1$

The clusters of modes are less clear with respect to the other configurations, but still visible. The first six modes are multi-body quasi-rigid motion mode shapes. Modes 8 and 9 are roof modes with different behaviour of the chassis with respect to the wheels.

Three torsional modes are identified (modes 10, 11 and 12): two global torsional modes in quadrature/phase with respect to the wheels (mode 10 and 12) and a global torsional mode (mode 11). The damping of the global torsional mode in phase with the wheel displacements is lower. Only one global vertical bending is detected (mode 21).

Two torsional modes of the front cross member mixed with in phase/quadrature roof mode (1,1) are detected (mode 13 and 17). A y-vibration (mode 14), a (1,1) roof mode (mode 15) and a multi-body pitch mode (mode 16) are identified. A front cross member vertical bending mode mixed with in quadrature roof mode (1,1) (mode 18) and in quadrature roof mode (2,1) (mode 20) are identified.

Finally, four global horizontal bending modes are identified: modes 18, 22 and a pair of global horizontal bending modes (mode 23 and 24) with very different damping ratios.

### 8.3 Experimental mode shapes expansion and filtering

The tested BIW car chassis is very large and the excitation level is low with respect to the structure; furthermore, the frequencies under investigation are low, thus the identified eigenvectors are affected by both time and spatial noise. The system was excited in  $I=142$  DOFs, and the response of the system measured in  $O=7$  DOFs, while the global system dimension considering the 95 selected point results to be  $N=285$  DOFs. The FRM is incomplete and the expansion and smoothing process described in § 5.2 should be applied to obtain the complete FRM  $\mathbf{H}(\Omega)$  and attenuate the noise effect. The method implies also a spatial smoothing of the identified mode shapes, which allows a better comparison and matching of the three different configurations. The process was applied iteratively, using  $\alpha_i=1$ . The master-slave net, created between physically connected nodes, is represented by the lines in Figure 8.3 (top). The DOFs of the eigenvectors increase at each iteration, as reported in Table 8.4.

Table 8.4 - Expanded eigenvectors number of DOFs of the at each iteration.

Iteration	0	1	2	3	4	5
DOFs	142	243	269	281	285	285

Four iterations are necessary to complete the 285 DOFs of the eigenvectors: the eigenvector obtained after four iterations are enough smooth without hiding any motion. Increasing the iteration number would lead to a stiffer structure.

The MACX matrices between experimental identified and expanded mode shapes are shown in Figure 8.8, Figure 8.9 and Figure 8.10.

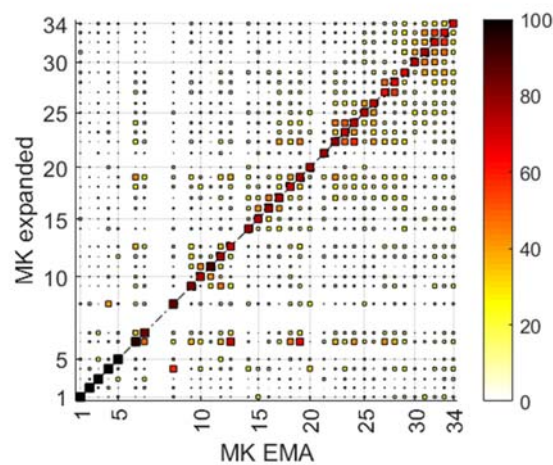


Figure 8.8 - MACX identified and expanded modes, conf. MK.

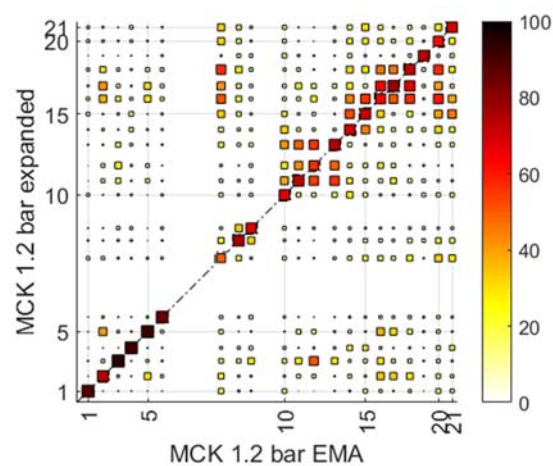


Figure 8.9 - MACX identified and expanded modes, conf. MCK 1.2 bar.

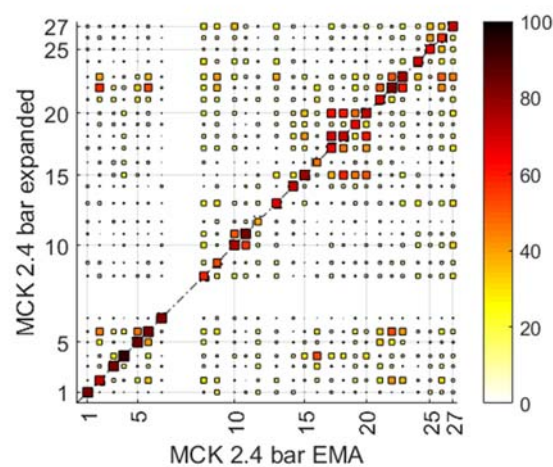


Figure 8.10 - MACX identified and expanded modes, conf. MCK 2.4 bar.

The MACX diagonal presents high values for the three configurations. The differences in the eigenvectors are due to noise filtering and topological master-slave network relationship. Although the eigenvectors are slightly different, the method works properly because it does not change the nature of each mode (high MACX values), rather highlights it and attenuates the noise effect while expanding the eigenvector sets to the global system dimension  $N = 285$ .

## 8.4 Shock absorber effects on global flexible modes

The study of the shock absorbers effects on the global chassis flexible modes is based on the hypothesis that the mode shapes do not change too much within the three configurations: the correlation between the three configurations was studied to follow the modal properties changes of each mode. The three set of modes must be matched to analyse the effects of localised damping. The best indicator of modes similarities is again the MACX criterion, given in Eq. (8.1).

The MACX matrices between different configurations, computed on the expanded and filtered sets of eigenvectors are reported in Figure 8.11, Figure 8.12 and Figure 8.13. The eigenvector sets are spaced respect to the natural frequency to highlight differences in resonance frequencies. The thick dot-dashed black line represents the iso-frequency line.

The matching between the eigenvectors is performed choosing the best combination to maximise the mean MACX value and the correspondence between the three configurations. The matching of modes shapes involves three configurations, therefore the MACX, defined in Eq. (8.1), is not enough for a correct matching. A specific index is defined to measure the correlation between a triplet of modes; it is called MACX3 and defined as:

$$MACX3 = \sqrt[3]{MACX_{MK-MCK1.2} MACX_{MK-MCK2.4} MACX_{MCK1.2-MCK2.4}} \quad (8.2)$$

The MACX3 index is the geometric mean of the three MACX indices, and because  $MACX \leq 1$  it results to be:

$$\begin{aligned} MACX3 &\geq \min(MACX_{MK-MCK1.2}, MACX_{MK-MCK2.4}, MACX_{MCK1.2-MCK2.4}) \geq 0 \\ MACX3 &\leq \max(MACX_{MK-MCK1.2}, MACX_{MK-MCK2.4}, MACX_{MCK1.2-MCK2.4}) \leq 1 \end{aligned} \quad (8.3)$$

Considering the three modal matrices  $\Psi_{MK}$ ,  $\Psi_{MCK1.2}$ ,  $\Psi_{MCK2.4}$  and a high MACX3, if the correlations between  $(\Psi_{MK,i}, \Psi_{MCK1.2,k})$  and  $(\Psi_{MK,i}, \Psi_{MCK2.4,t})$  are good, then also the correlation between  $(\Psi_{MCK1.2,k}, \Psi_{MCK2.4,t})$  results to be good.



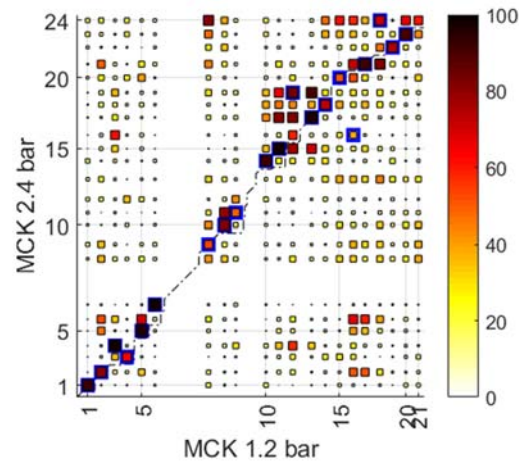


Figure 8.11 - MACX between configurations MCK 1.2 bar and MCK 2.4 bar.

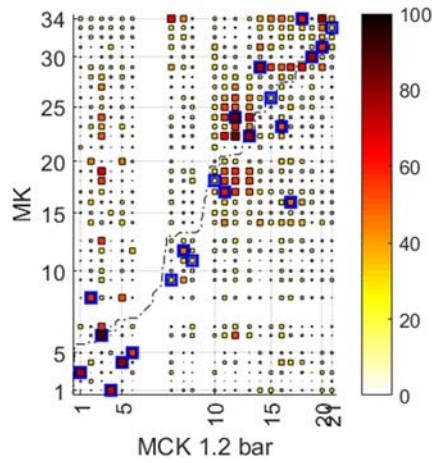


Figure 8.12 - MACX between configurations MCK 1.2 bar and MK.

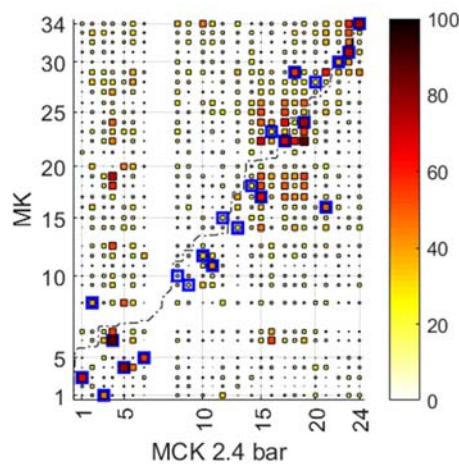



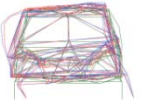

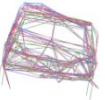



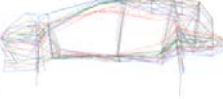







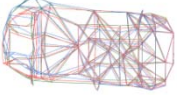
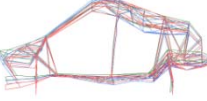


Figure 8.13 - MACX between configurations MCK 2.4 bar and MK.

Matched modes are highlighted in blue rectangles in Figure 8.11, Figure 8.12 and Figure 8.13. The comparison between the two MCK configurations, shown ,

Figure 8.11, is quite diagonal and couples of matched modes are clearly visible, while the comparison between MCK and MK configurations, shown in Figure 8.12 and in Figure 8.13, are not extremely clear. The matching of the first modes is quite distant with respect to the diagonal, because rigid body motion and multibody motion are very similar, but they are far in frequencies. Almost all the other matched modes are close to the main diagonal and the iso-frequency line. Nineteen triplets of modes shapes are correlated among the three configurations. The matched modes are reported in Table 8.5.

The triplets of matched mode shapes are quite similar, although for few matched triplets the MACX3 is not extremely high. The shock absorbers effects can be studied through the comparison of three parameters: natural frequency  $f_n$  shown in Figure 8.14, damping ratio  $\zeta$  shown in Figure 8.15 and Modal Phase Collinearity (MPC) [191] shown in Figure 8.16. MPC is an indicator of the degree of complexity of a mode evaluating the linear functional relationship between the real and the imaginary parts of the mode shape vector. This index should be high ( $> 90\%$ ) for real normal modes. A low MPC index indicates a rather complex mode, due either to local damping elements in the tested structure or to errors in the data measurements or to mistakes in the analysis procedure [191]. The natural frequency and damping ratio are directly extracted from the experimental results, while MPC values are computed from the unscaled complex mode shapes.

Table 8.5 - Triplets of matched modes:  
MK (green)-MCK 1.2 bar (blue)-MCK 2.4 bar (red)-MACX3.

 1-4-3-58.95%	 3-1-1-77.28%	 4-5-5-82.98%	 5-6-7-66.80%
 6-3-4-91.36%	 8-2-2-56.93%	 9-7-9-31.16%	 11-9-11-40.47%
 12-8-10-46.22%	 16-17-21-60.86%	 17-11-15-72.20%	 18-10-14-42.48%
 22-13-17-80.19%	 23-16-16-39.26%	 24-12-19-81.60%	 29-14-18-68.30%
 30-19-22-61.63%	 31-20-23-71.04%	 34-18-24-69.49%	

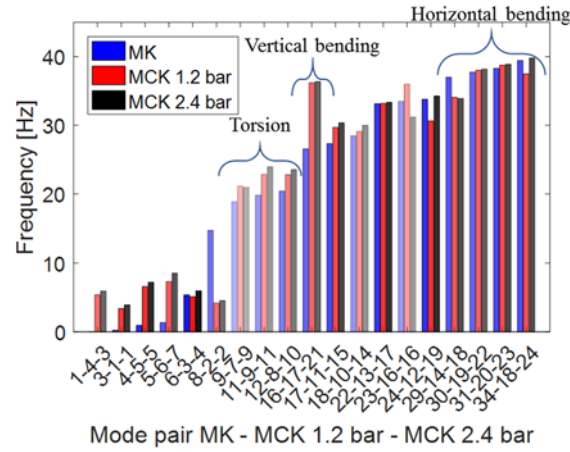


Figure 8.14 - Natural frequency comparison of the triplet of matched modes.

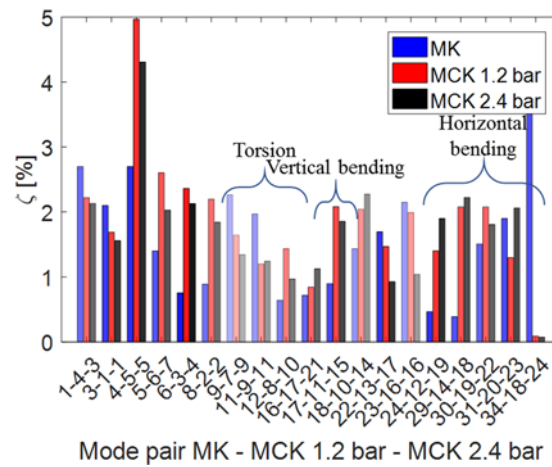


Figure 8.15 - Damping ratio comparison of the triplet of matched modes.

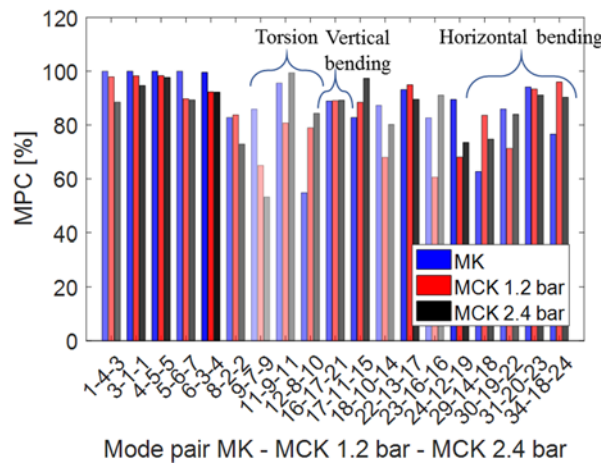


Figure 8.16 - MPC comparison of the triplet of matched modes.

The first global flexible mode is torsion: three triplets of torsional modes are correlated: 9-7-9, 11-9-10 and 12-8-10. The natural frequency  $f_n$  of the torsional modes in the MCK configurations is about 3 Hz higher; it is even higher in the MCK 2.4 bar configuration. The third triplet shows an increment of damping, as

expected. The two triplets corresponding to the higher damped torsional modes of MK configuration result less damped in the MCK configurations: this is not an expected result, the reason being the bands used to suspend the chassis. The slings must be attached near the engine elastic mounts for equilibrium and safety reasons, thus they are responsible for the higher damping in the torsional modes. The MCK configurations, instead, show a lower damping ratio with an increment of the pressure, which reduces the tires damping. For the first triplet of torsional mode the MPC index gives a clear idea of the complexity of the mode shapes due to the suspensions.

Triplet 16-17-21 is the only vertical bending correlated between the three configurations; damping increases in the MCK configurations. The natural frequency increases (about 10 Hz) between MK and MCK, due to the different boundary conditions. The MPC is quite high and constant between the configurations.

Triplets 29-17-18, 30-19-22, 31-20-23 and 34-18-24 are horizontal bending modes with participation of the roof. The natural frequencies are almost constant, slightly higher in the MCK configurations. This is because the shock absorbers have almost no influence in the horizontal plane. For the first three triplets, the damping increases in MCK with respect to MK configuration, while the last triplet presents high damping in MK configuration and low damping in MCK ones. Probably this matching is not realistic because the corresponding modes are over 40 Hz. No evidences are present in the MPC values.

Focusing only on the effects of the shock absorbers on the chassis global mode shapes, an example of the frequency domain change is shown in Figure 8.17. Only one natural frequency is reported for each cluster of global mode.

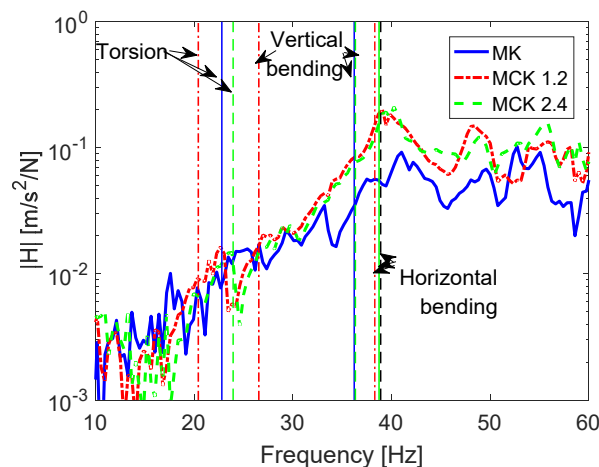


Figure 8.17 - Experimental FRF comparison between the three setups.

## 8.5 Damping matrices identification

Viscous  $\mathbf{C}$  and structural  $\mathbf{D}$  damping matrices of the BIW car chassis are identified using the SLM presented in § 4. The identification is performed in the three configurations of the system: MK, MCK 1.2 bar and MCK 2.4 bar.

The SLM needs the choices of the Layers to build up the damping matrices, as discussed in § 4.1, and the complete FRM  $\mathbf{H}(\Omega)$ . The Layers selection is discussed in § 8.5.1. Considerations on the extraction of the normal FRM  $\mathbf{H}^N(\Omega)$  in industrial system with a lot of DOFs are presented in § 8.5.2. The identified spatial damping matrices of the three configurations are presented in § 8.5.3. The identified viscous damping of the shock absorber is compared to reference values in § 8.5.4.

The complete synthesised FRM  $\mathbf{H}_{syn}(\Omega) \in \mathbb{C}^{285 \times 285}$ , computed with Eq. (5.1), using the expanded eigenvectors, were discussed in § 0.

### 8.5.1 Layers selection

The Layers are the physical connectivity between DOFs, which are represented by the lines between nodes in Figure 8.3, (top) in this application.

In this case, it is useful to group the Layers in pattern  $\mathbf{P}_j$ , as in Eq. (4.14), collecting all the layers with the same dissipation properties. The patterns are built based on the BIW components: e.g. all the layers laying on the glass should have the same damping properties; the two front shock absorbers are nominally the same, as the two rear shock absorbers, etc. All the used patterns  $\mathbf{P}_j$  with the number of Layers  $N_j$  involved are reported in Table 8.6.

For each link, six different layers are used to consider the 3D behaviour. For each link the unknown damping coefficients are  $c_{xx}$ ,  $c_{yy}$ ,  $c_{zz}$ ,  $c_{xy}$ ,  $c_{xz}$  and  $c_{yz}$ : where the subscripts refer to the global reference system.

Three different absolute dampers, acting of the three directions, are used to identify the several local absolute damping sources, spread in the BIW.

The same Layers are used for both viscous  $\mathbf{C}$  and structural  $\mathbf{D}$  damping matrices. The number of the unknowns damping coefficients, i.e. the dimension of the unknowns vector  $\mathbf{u}$ , given in Eq. (4.11), results to be:

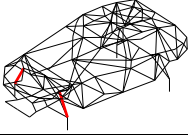
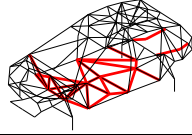
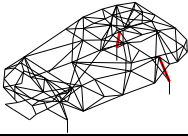
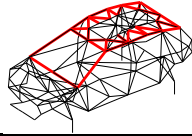
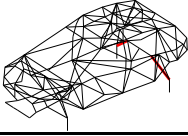
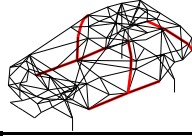
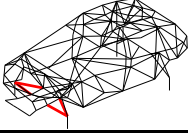
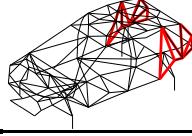
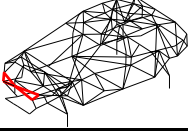
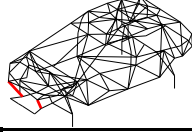
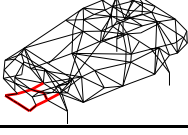
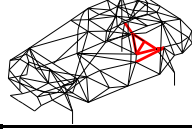
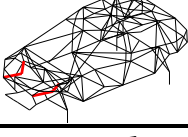
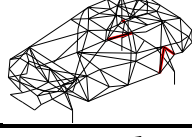
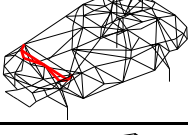
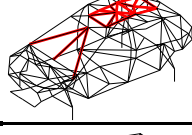
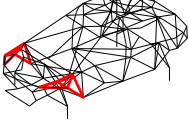
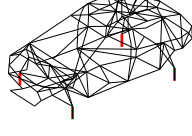
$$2(N_A + N_R) = 786 \quad (8.4)$$

According to Eq. (4.10) the number of Layers  $N_L$  corresponds to the number of elementary dampers result to be:

$$N_L = \sum_{p=1}^{N_A} N_p + \sum_{q=1}^{N_R} N_q = 285 + 1818 = 2103 \quad (8.5)$$

for each of the two damping matrices (viscous  $\mathbf{C}$  and structural  $\mathbf{D}$ ).

Table 8.6 - Patterns and Layers for damping matrices building.

Pattern	$N_j$	Description	Pattern	$N_j$	Description
Front shock absorbers	2 x 6		Floor with viscous elastic material	30 x 6	
Rear shock absorber dashpots	2 x 6		Glass seals	38 x 6	
Rear shock absorbers springs	2 x 6		Boot seals	14 x 6	
Lower control arms	4 x 6		Back car body	20 x 6	
Front sill	6 x 6		Engine elastic mountings	2 x 6	
Front cross member	11 x 6		Luggage compartment panel	9 x 6	
Lower frame	4 x 6		Filling up material	4 x 6	
Engine	8 x 6		Glass	26 x 6	
Engine compartment panel	16 x 6		Tires	4 x 6	

### 8.5.2 Consideration on normal FRM extraction

The extraction of the normal FRM  $\mathbf{H}^N(\Omega)$  is performed using Eq. (4.35), which involves the inversion of measured or synthesised FRM  $\Re(\mathbf{H}(\Omega))$ . The extraction of the normal FRM  $\mathbf{H}^N(\Omega)$  is not a huge problem for small systems, as shown in the three DOFs lumped parameter system in § 7.4; however the



inversion of  $\Re(\mathbf{H}(\Omega))$  should be carefully handled when the numbers of DOFs increase.

When the  $\Re(\mathbf{H}(\Omega))$  is huge it could become very ill conditioned and the inversion is no more reliable. This aspect is even more important when the mode shapes expansion and filtering process, § 5.2, is used to obtain the complete FRM, since the effect of Eq. (5.2) makes the different rows of the modal matrix somehow linear dependent.

The sum of all the FRF of normal FRM  $\mathbf{H}^N(\Omega)$  computed using Eq. (4.35) in the configuration MK is shown in Figure 8.18.

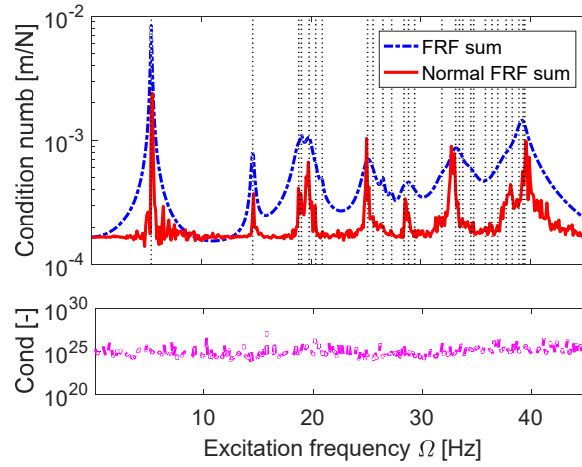


Figure 8.18 - Normal FRM with classical inversion.

The extracted normal FRM  $\mathbf{H}^N(\Omega)$  is clearly unstable and the condition number is very high; the matrix  $\Re(\mathbf{H}(\Omega))$  could have zero or close to zero eigenvalues, due to which the matrix becomes singular:  $\Re(\mathbf{H}^C(\Omega))$  is ill conditioned and the inversion is not reliable. The use of this normal FRM  $\mathbf{H}^N(\Omega)$  in the identification process will lead to completely wrong results.

The solution of this problem is the Marquardt-Levenberg inversion method [192,193]. It consists in adding a small value  $p$  to the diagonal of the matrix  $\Re(\mathbf{H}^C(\Omega))$  to be inverted. This procedure is known as damping the inversion and the small value to be added  $p$  is called Marquardt-Levenberg coefficient. Adding a small damping coefficient to the diagonal elements makes it stable. Bigger is the value of  $p$ , bigger is the damping, the matrix inversion is more stable, but the solution is further away from true solution. Smaller is the value of  $p$ , smaller is the damping, closer is the inverted matrix to true inverted matrix but it might become unstable.

$$\left[\Re(\mathbf{H}(\Omega))\right]^{-1} \approx \left[\Re(\mathbf{H}(\Omega)) + p(\Omega)\mathbf{I}\right]^{-1} \quad (8.6)$$

where  $\mathbf{I}$  is the identity matrix of coherent dimension.

The Marquardt-Levenberg coefficient is a function of the excitation frequency  $p(\Omega)$ , since it must be chosen for each spectral line. An adaptive technique is implemented to find out the best Marquardt-Levenberg coefficient  $p$ . The inversion for each spectral line starting from a very low value of  $p$ . The  $p$  value is increased until the discrepancies between the two last inverted matrix is below a threshold, so that the inversion becomes stable and the smallest  $p$  is used. The inverted matrix is therefore the closest to the true inverse matrix.

The sum of all the FRF of normal FRM  $\mathbf{H}^N(\Omega)$  computed using Eq. (4.35) and Eq. (8.6) in the configuration MK is shown in Figure 8.19.

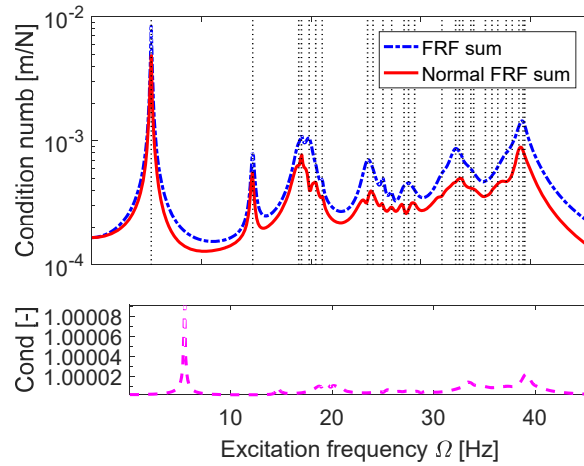


Figure 8.19 - Normal FRM using Marquardt-Levenberg inversion.

The extracted normal FRM  $\mathbf{H}^N(\Omega)$  is now reliable, although it is a little bit damped due to the damped inversion. The condition number of the matrix is now very low, and a good inversion can be performed.

### 8.5.3 Spatial matrix identification results

The viscous  $\mathbf{C}$  and structural  $\mathbf{D}$  damping matrices of the system in the three configurations were identified using the SLM.

Due to the complexity of the system is not possible to perform the full procedure of the SLM, which imply the damping identification of the system onto the  $(r_0, \tilde{k})$  plane. The computational cost of a complete identification is too high.

To avoid this problem the identification was performed in a couple  $(r_0, \tilde{k})$ , which is expected to be stable. The experience of the identification of the lumped system performed in § 7, and the consideration on the stability of the solution presented



in § 4.3.2, suggest that a good location onto the  $(r_{\%}, \tilde{k})$  plane is a value of  $r_{\%}$  between the first two vertical asymptotes range values (close to the first asymptote) and a number of spectral lines for each considered mode moderately high. The arbitrary choice of the  $(r_{\%}, \tilde{k})$  couple does not guarantee that the solution is the optimal solution  $\mathbf{u}^*$  of Eq. (4.70), neither that the inversion error  $E_{\%}$ , given in Eq. (4.69), is the minimum one; however the identified solution  $\mathbf{u}$  will be very similar to the optimal one because it should lie in the stability area. This is a compromise between available hardware and optimality of the solution.

The identified damping matrices of the BIW chassis in the three configurations are shown in Figure 8.20, Figure 8.21 and Figure 8.22. The six identified damping coefficients for each relative physical connection and the absolute dampers acting on each node in the three directions are shown grouped with respect to the directions. The thickness of the line (relative dampers) or of the squares (absolute dampers) is proportional to the identified damping coefficient.

### Configuration MK

The configuration MK previously discussed § 8.2.1, presents 34 mode shapes, six of them are rigid body motion. The rigid body motion activates the absolute dampers, i.e. the slings used to suspend the car chassis, but not all the relative dampers because the system acts as a rigid body. Therefore, the rigid body motions are not included in the computation of the synthesised FRM  $\mathbf{H}_{syn}(\Omega)$ , Eq. (5.1).

One asymptote for each considered mode will be present onto the  $(r_{\%}, \tilde{k})$  plane. The 28 range values, computed using Eq. (4.71). The five smallest range values at which the asymptotes are located are:

$$r_{\%asympotes} = \{0.0680, 0.1046, 0.3055, 0.4216, 0.7029\}\% \quad (8.7)$$

The solution is computed at a range value  $r_{\%}$  located at 1/6 of the range intervals between the first two asymptotes, using a number of spectral lines  $\tilde{k}$  that is not too high to reduce the matrices dimensions:

$$(r_{\%}, \tilde{k}) = (0.0741\%, 20) \quad (8.8)$$

The identified damping matrices are mapped in Figure 8.20. The damping identification of MK configuration, Figure 8.20, shows some patterns, which clearly dissipates energy. The viscous damping of the seals between the chassis and the sunroof in  $x$ - $x$  direction is localised and identified. These seals show also a structural term in the  $x$ - $z$  direction. The damping of the glass is also identified: the

glass presents viscous damping in  $x$ - $z$  direction and structural damping in  $x$ - $y$  direction. No viscous damping effects are identified in  $y$ - $y$  and  $x$ - $y$  direction. The viscous damping of the seals between the chassis, doors, boot and bonnet is highlighted in  $x$ - $z$  direction. The structural damping effects of the dissipative material covering the chassis floor is identified in  $x$ - $x$  and  $y$ - $z$  directions. Finally, in  $z$ - $z$  direction different expected damping effects are identified: shock absorbers viscous damping, tire viscous damping and structural damping of the suspension lower arms. The engine mounts dissipation effect is localised and evident only in this configuration: this because the way in which the BIW is hung makes these components dissipating a lot of energy and explain why the torsional mode for the MK configuration are quite damped, which was a not expected result.

The absolute dampers show high localised dissipative effects in sunroof  $x$ - $x$  direction due to the opening/closing device and the effect of the elastic bands on the fixing points.

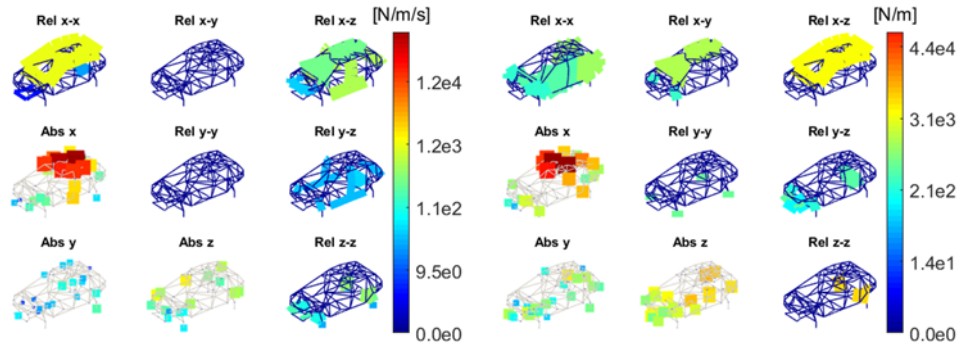


Figure 8.20 - Identified damping matrices of conf. MK: viscous (left), structural (right).

### Configuration MCK 1.2 bar

The MCK 1.2 bar configuration, previously discussed in § 0, presents 21 mode shapes, six of them are rigid multi-body motion. The multi-rigid body motion activates the dampers acting between different bodies, i.e. the shock absorbers and tires. Differently from the rigid body motion, these mode shapes are considered in the computation of the synthesised FRM  $\mathbf{H}_{syn}(\Omega)$ , Eq. (5.1).

One asymptote for each considered mode will be present onto the  $(r_{\%}, \tilde{k})$  plane, hence 21 asymptotes range values are computed using Eq. (4.71). The five smallest range values at which the asymptotes are located are:

$$r_{\%asympotes} = \{0.0510, 0.0875, 0.7019, 1.2131, 2.8688\}\% \quad (8.9)$$

The solution is computed at a range value  $r_{\%}$  located at 1/6 of the range intervals between the first two asymptotes, using a number of spectral lines  $\tilde{k}$  that is not too high to reduce the matrices dimensions:

$$(r_{\%}, \tilde{k}) = (0.1381\%, 20) \quad (8.10)$$

The identified damping matrices are mapped in Figure 8.21.

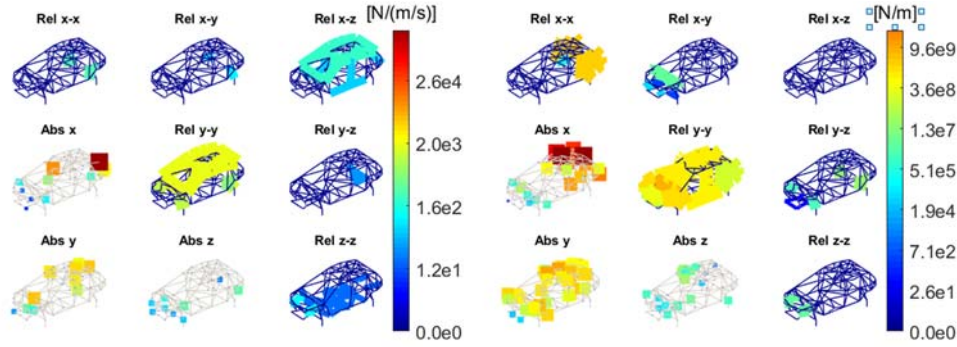


Figure 8.21 - Identified damping matrices of conf. MCK 1.2 bar: viscous (left), structural (right).

The identification performed on the configuration MCK 1.2 bar identified approximately the same sources of dissipation already identified in MK configuration, presented in the previous paragraph. Structural damping is identified on the several steel plates of the chassis, while viscous damping is found in correspondence of the seals between chassis and sunroof, boots and dissipative material on the floor. Also, for this configuration, damping due to the shock absorbers is well localised in  $z$ - $z$  direction. Damping values are higher with respect to the MK configuration and the absolute dampers show strong local dissipative effects for the sunroof.

### Configuration MCK 2.4 bar

The configuration MCK 2.3 bar, previously discussed in § 8.2.3, presents 24 mode shapes, six of them are rigid multi-body motion. As for the configuration MCK 1.2 bar, the multi-rigid body motions are considered in the computation of the synthesised FRM  $\mathbf{H}_{syn}(\Omega)$ , given in Eq. (5.1).

One asymptote for each considered mode will be present onto the  $(r_{\%}, \tilde{k})$  plane. The 24 asymptotes range values are computed using Eq. (4.71). The five smallest range values at which the asymptotes are located are:

$$r_{\%asymptotes} = \{0.2011, 0.2752, 0.3024, 0.3242, 0.3397\} \% \quad (8.11)$$

The solution is computed at a range value  $r_{\%}$  located at 1/6 of the range intervals between the first two asymptotes, using a number of spectral lines  $\tilde{k}$  that is not too high to reduce the matrices dimensions:

$$(r_{\%}, \tilde{k}) = (0.2797\%, 20) \quad (8.12)$$

The identified damping matrices are mapped in Figure 8.22.

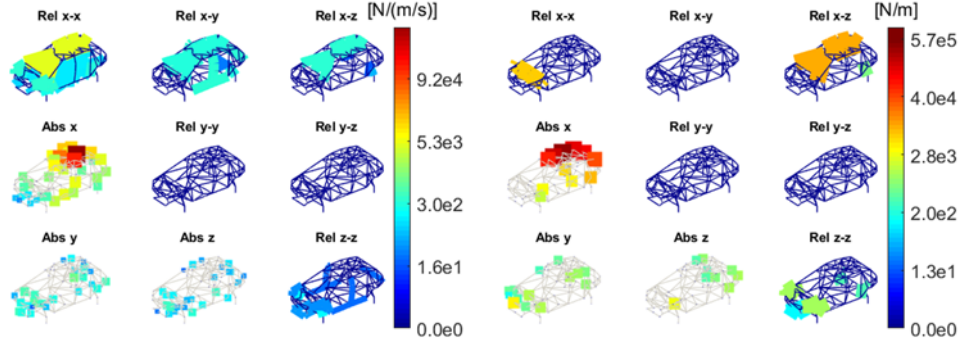


Figure 8.22 - Identified damping matrices of conf. MCK 2.4 bar: viscous (left), structural (right).

In the configuration MCK 2.4 bar the strongest localised dissipative sources are seals, glass and viscous material on the chassis floor. As in the other cases, the shock absorbers are identified in the vertical direction, with quantification higher with respect to the MK configuration.

#### 8.5.4 Quantification of the front shock absorber viscous damping

The identified values of viscous damping coefficient of the shock absorber can be easily compared with the reference values found in the literature. A classical shock absorber is usually modelled as a viscous damper; with piecewise nonlinear characteristics. The damping values in extension and compression are different and damping value is higher for low velocities [194,195].

The SLM linearises the behaviour of the shock absorbers; the impact test modal analysis averaged on five repetitions for each point, the expansion process on the experimental linearised data and the linear “Layer model” adopted for the identification are consistent hypothesis.

A comparison between the results found in this analysis and the reference values is reported in Figure 8.23.

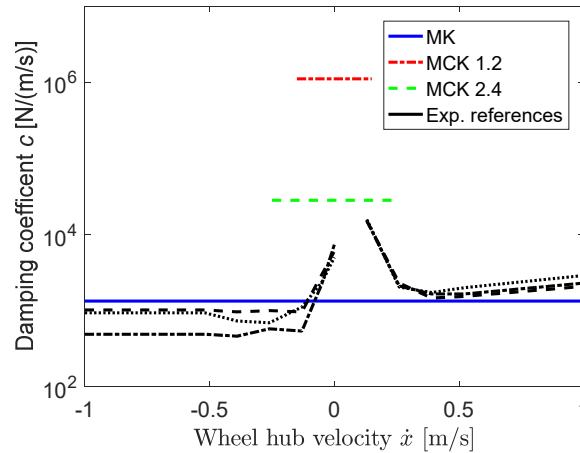


Figure 8.23 - Front shock absorbers viscous damping coefficient.

The reference values are experimental data acquired during the characterisation of three different shock absorbers provided by an industrial partner.

The damping values in Figure 8.23 are the identified linearisation of the viscous damping coefficient values in the velocity range of vibration.

In the MK configuration, when the wheels are free to move, the identified viscous damping coefficient is perfectly aligned with the linearised values of the actual shock absorbers damping. This confirms the validity of the direct identification from experimental FRM opportunely constrained with the topological evidence and through the SLM, even if the analysed system is a huge industrial test case. In the MCK 1.2 bar configuration, the identified values are almost three orders of magnitude higher; two different reasons can justify this discrepancy:

- when the tires pressure is low, the damping coefficient of the tire is very high and the stiffness lower; the identification could be influenced by the damping of the tires;
- when the system is on the floor, it is excited with the same level of force of the MK configuration, so the velocity is much lower and for low velocity the reference damping result to be larger.

In the configuration MCK 2.4 bar the identified values are lower with respect to the MCK 1.2 bar and higher with respect to the configuration MK, thus confirming the hypothesis of the influence of tire damping due to the pressure changes: at nominal pressure the tire damping is lower and the stiffness higher. The value is higher than the references since the small velocity experienced by the system excited with the hammer in the configurations on the floor.

## 8.6 Conclusions

The modal analysis of a BIW chassis was performed in this chapter to analyse the effects of the suspension system on the first global modes. The EMA was performed in three different configurations of the BIW: suspended to minimise the suspension effect and on the floor with two different tires pressure.

The effects of the suspension system are clear for the vertical bending and for the torsional modes.

The SLM was applied for the identification of the global viscous and structural damping matrices of the chassis in the three configurations. The expansion and filtering process described in § 5.2 was applied to obtain the complete receptance matrix of the system. The receptance matrix is quite huge and ill conditioned, thus the inversion requires for the computation of the normal receptance make it quite unstable. A solution to this problem was presented in § 8.5.2, it consists in a damped inversion so that the inverse matrix in the stable inverse matrix closest to the real inverse.

Due to the big amount of data the stabilisation process was difficult to be performed due to high computational cost. Therefore, the damping matrices were identified in a region of the stability diagram between the first two asymptotes, although it is not the best solution it should be quite close to the best solution.

The identified damping matrix are quite realistic and highlight all the dissipation sources of the structure.

The viscous damping coefficient of the front shock absorber was compared with reference value. The real behaviour of the shock absorber is piecewise linear, the identified damping value is in very good agreement with the reference one, although the identification process linearises the result.



## Chapter 9

# 9. Stabilised Layers Method for nonlinear damping identification

In this chapter the SLM presented in § 4 is extended to nonlinear damping identification of systems with a localised damping nonlinearity. Linear viscous or structural damping are the simplest representation of dissipative phenomena in mechanical system, but often this simplification is not enough to model in a proper way the damping forces.

The identification is performed in frequency domain, as for the linear case. The nonlinear problem is presented in § 9.1. Describing function (DF) approximation with constant amplitude of oscillation is performed to obtain the frequency domain damping force § 9.2. The frequency domain nonlinear damping force is written using Layers § 9.2.1 and the SLM is extended to identify the coefficients of the nonlinearity in § 9.2.2. Finally, the extended SLM is applied for the identification of the linear and nonlinear dissipations of a numerically generated example in § 9.3.

The extension of the stabilised Layers Method to nonlinear damping force identification is presented in [196].

### 9.1 Nonlinearly damped system

The general equation of motion of MDOF mechanical system with nonlinear amplitude dependent damping  $\mathbf{f}_{c,nl}(\mathbf{x}, \dot{\mathbf{x}}) \in \mathbb{R}^{N \times 1}$  can be written as in Eq. (1):

$$\mathbf{M} \ddot{\mathbf{x}} + \mathbf{C} \dot{\mathbf{x}} + (\mathbf{K} + i\mathbf{D}) \mathbf{x} + \mathbf{f}_{c,nl}(\mathbf{x}, \dot{\mathbf{x}}) = \mathbf{f}(t) \quad (9.1)$$

This is the generalisation of Eq. (4.20) to a system with an amplitude dependent damping nonlinearity.



While stiffness nonlinearity gives peculiar system behaviour like jumps, limit cycle oscillations, internal resonances, etc. [197], damping nonlinearity is not easy to detect from standard dynamics since it just change the amplitude of oscillation of the system with respect to the linear one, since an equivalent linear viscous damping matrix  $\mathbf{C}_{eq}$  always exists [198], which is able to model the nonlinear system at a constant level of oscillation.

This chapter focus on systems where the nonlinear force is localised on the structure. The nonlinearity acts on a single  $m^{th}$  DOF (absolute nonlinear damper) or between two  $m^{th}$  and  $l^{th}$  DOFs (relative nonlinear damper), thus Eq. (9.1) can be simplified in:

$$\mathbf{M} \ddot{\mathbf{x}} + \mathbf{C} \dot{\mathbf{x}} + (\mathbf{K} + i\mathbf{D}) \mathbf{x} + \mathbf{g}f_{C,nl} = \mathbf{f}(t) \quad (9.2)$$

where  $\mathbf{g} \in \mathbb{R}^{N \times 1}$  is a column selection vector:

$$\mathbf{g} = \mathbf{0} \quad \begin{cases} g_m = 1 & \text{absolute nonlinear damper} \\ g_m = 1, g_l = -1 & \text{relative nonlinear damper} \end{cases} \quad (9.3)$$

Amplitude dependent damping forces  $f_{C,nl}$  can be usually well fitted by a polynomial function in amplitude:

$$f_{C,nl}(x, \dot{x}) = (c_{nl,0} + c_{nl,1}|x| + c_{nl,2}x^2 + c_{nl,3}|x^3| + \dots c_{nl,t}x^T) \dot{x} \quad (9.4)$$

where  $c_{nl,i}$  are the coefficients of the polynomial of order  $T$ .  $T$  is the polynomial order necessary to fit well the nonlinear damping function. The moduli on the odd terms of the amplitude dependent polynomial are required to guarantee an only dissipative force.

## 9.2 Nonlinear damping identification

The aim of the identification is to identify the spatial linear non-proportional viscous  $\mathbf{C}$  and structural  $\mathbf{D}$  damping matrices as in § 4, together with the quantification of  $c_{nl,i}$  unknown coefficients that model the nonlinear damping force  $f_{C,nl}(x, \dot{x})$ .

The identification of the nonlinear coefficients could be very difficult under arbitrary motion around the nonlinearity, while it is easier to identify these coefficients under sinusoidal amplitude-controlled oscillation across the nonlinearity. The coefficients  $c_{nl,i}$  identified under controlled oscillation, are then valid to be used in the nonlinear time domain damping force model under uncontrolled oscillation.

The identification method presented in § 4.2 is here extended to identify the coefficients of the nonlinear damping force.

Eq. (9.2) can be written in frequency domain as:

$$\left[ (\mathbf{K} - \Omega^2 \mathbf{M}) + i(\Omega \mathbf{C} + \mathbf{D}) + F_{C,nl}(A, \Omega) \mathbf{g} \mathbf{g}^T \right] \mathbf{X}(\Omega) = \mathbf{F}(\Omega) \quad (9.5)$$

where  $F_{C,nl}(A, \Omega)$  is the sinusoidal input constant amplitude DF approximation of the nonlinear damping force [157].

Since the nonlinear damping force  $\mathbf{f}_{C,nl}(\mathbf{x}, \dot{\mathbf{x}})$  is a pure dissipative force, its sinusoidal input DF  $F_{C,nl}(A, \Omega)$  at constant amplitude  $A$  of oscillation across the nonlinearity, results in the form:

$$F_{C,nl}(A, \Omega) = i\Omega (c_{nl,0} + z_1 A c_{nl,1} + z_2 A^2 c_{nl,2} + \dots + z_T A^T c_{nl,T}) \quad (9.6)$$

where  $z_i$  are gain coefficients resulting from the DF approximation. Both  $z_i$  and  $T$  depend on the type of nonlinear damping.

The resulting equivalent linear damping coefficient  $c_{eq}$  under controlled constant amplitude of oscillation  $A$  across the nonlinearity becomes:

$$c_{eq} = c_{nl,0} + z_1 A c_{nl,1} + z_2 A^2 c_{nl,2} + \dots + z_T A^T c_{nl,T} \quad (9.7)$$

The nonlinear DSM  $[\mathbf{H}_{nl}^C(A, \Omega)]^{-1} \in \mathbb{C}^{N \times N}$  of the system under sinusoidal excitation at constant amplitude  $A$  across the nonlinearity can be written as:

$$[\mathbf{H}_{nl}^C(A, \Omega)]^{-1} = (\mathbf{K} - \Omega^2 \mathbf{M}) + i\Omega \left[ \mathbf{C} + \frac{\mathbf{D}}{\Omega} + (c_{nl,0} + z_1 A c_{nl,1} + \dots + z_T A^T c_{nl,T}) \mathbf{g} \mathbf{g}^T \right] \quad (9.8)$$

The nonlinear FRM  $\mathbf{H}_{nl}^C(A, \Omega)$  matrix can be directly measured through sweep test with constant amplitude of oscillation  $A$  across the nonlinearity, controlled to be constant in the entire frequency range of interest.

The imaginary part of the nonlinear DSM contains all the dissipation terms:

$$\Im([\mathbf{H}_{nl}^C(A, \Omega)]^{-1}) = \Omega \left[ \mathbf{C} + \frac{\mathbf{D}}{\Omega} + (c_0 + z_1 A c_1 + \dots + z_T A^T c_T) \mathbf{g} \mathbf{g}^T \right] \quad (9.9)$$

Substituting the DSM of the underlying linear undamped system  $(\mathbf{H}^N(\Omega))^{-1}$  Eq. (4.25) in Eq. (9.8):

$$[\mathbf{H}^N(\Omega)]^{-1} \mathbf{X}(\Omega) + [i\Omega \mathbf{C} + i\mathbf{D} + F_{C,nl}(A, \Omega) \mathbf{g} \mathbf{g}^T] \mathbf{X}(\Omega) = \mathbf{F}(\Omega) \quad (9.10)$$

Pre-multiplying Eq. (9.10) by  $\mathbf{H}^N(\Omega)$  yields:

$$\mathbf{X}(\Omega) = [\mathbf{I} + i\mathbf{G}(A, \Omega)]^{-1} \mathbf{H}^N(\Omega) \mathbf{F}(\Omega) \quad (9.11)$$

where  $\mathbf{G}(A, \Omega) \in \mathbb{R}^{N \times N}$  is the amplitude dependent transformation matrix:

$$\mathbf{G}(A, \Omega) = [\mathbf{H}^N(\Omega)] \left[ \Omega \mathbf{C} + \mathbf{D} + \Omega (c_{nl,0} + z_1 A c_{nl,1} + \dots + z_T A^T c_{nl,T}) \mathbf{g} \mathbf{g}^T \right] \quad (9.12)$$

The transformation matrix  $\mathbf{G}(A, \Omega)$  becomes amplitude dependent, instead in the linear identification it is only frequency dependent, as in Eq. (4.29),.

Comparing Eq. (9.5) and Eq. (9.10), the relationship between nonlinear damped FRM  $\mathbf{H}_{nl}(A, \Omega)$  and normal FRM  $\mathbf{H}^N(\Omega)$  matrices is given by:

$$\mathbf{H}^N(\Omega) = [\mathbf{I} + i\mathbf{G}(A, \Omega)] \mathbf{H}_{nl}(A, \Omega) \quad (9.13)$$

Eq. (9.13) can be subdivided in its real and imaginary parts:

$$\Re(\mathbf{H}^N(\Omega)) = \mathbf{H}_{nl,R}(A, \Omega) - \mathbf{G}(A, \Omega) \mathbf{H}_{nl,I}(A, \Omega) \quad (9.14)$$

$$\Im(\mathbf{H}^N(\Omega)) = \mathbf{H}_{nl,I}(A, \Omega) + \mathbf{G}(A, \Omega) \mathbf{H}_{nl,R}(A, \Omega) = \mathbf{0} \quad (9.15)$$

where  $\mathbf{H}_{nl,R} = \Re(\mathbf{H}_{nl})$  and  $\mathbf{H}_{nl,I} = \Im(\mathbf{H}_{nl})$ . Eq. (9.15) is true because  $\mathbf{H}^N(\Omega)$  is a real matrix, thus:

$$\mathbf{G}(A, \Omega) = -\mathbf{H}_{nl,I}(A, \Omega) [\mathbf{H}_{nl,R}(A, \Omega)]^{-1} \quad (9.16)$$

The normal FRM  $\mathbf{H}^N(\Omega)$  is obtained substituting Eq. (9.16) in Eq. (9.13):

$$\mathbf{H}^N(\Omega) = \mathbf{H}_{nl,R}(A, \Omega) + \mathbf{H}_{nl,I}(A, \Omega) [\mathbf{H}_{nl,R}(A, \Omega)]^{-1} \mathbf{H}_{nl,I}(A, \Omega) \quad (9.17)$$

Note that  $\mathbf{H}^N(\Omega)$  is not amplitude dependent, due to the definition of undamped DSM in Eq. (4.25):

$$\mathbf{H}^N(\Omega) = (\mathbf{K} - \Omega^2 \mathbf{M})^{-1} \quad (9.18)$$

This consideration is also physically reasonable, in fact the undamped linear system underlying the nonlinear damped system is always the same system for any amplitude of oscillation  $A$ , while the transformation matrix  $\mathbf{G}(A, \Omega)$  is amplitude dependent, because a different transformation matrix is necessary to obtain the linear undamped FRM from the nonlinear damped system at each oscillation amplitude  $A$ . The viscous  $\mathbf{C}$ , structural  $\mathbf{D}$  and the  $T$  terms of the

nonlinear damping force can be computed from Eq. (9.12), using the experimental FRM  $\mathbf{H}_m(A, \Omega)$  at constant amplitude  $A$  of oscillation across nonlinearity:

$$\begin{bmatrix} \Omega_1 \mathbf{H}^N(\Omega_1) & \mathbf{H}^N(\Omega_1) & \Omega_1 z_1 A \mathbf{H}^N(\Omega_1) & \cdots & \Omega_1 z_T A^T \mathbf{H}^N(\Omega_1) \\ \Omega_2 \mathbf{H}^N(\Omega_2) & \mathbf{H}^N(\Omega_2) & \Omega_2 z_1 A \mathbf{H}^N(\Omega_2) & & \Omega_2 z_T A^T \mathbf{H}^N(\Omega_2) \\ \vdots & \vdots & & & \vdots \\ \Omega_K \mathbf{H}^N(\Omega_K) & \mathbf{H}^N(\Omega_K) & \Omega_K z_1 A \mathbf{H}^N(\Omega_K) & \cdots & \Omega_K z_T A^T \mathbf{H}^N(\Omega_K) \end{bmatrix} \begin{bmatrix} \mathbf{C}_{lin} \\ \mathbf{D} \\ c_{nl,1} \mathbf{g} \mathbf{g}^T \\ \vdots \\ c_{nl,T} \mathbf{g} \mathbf{g}^T \end{bmatrix} = \begin{bmatrix} \mathbf{G}(A, \Omega_1) \\ \mathbf{G}(A, \Omega_2) \\ \vdots \\ \mathbf{G}(A, \Omega_K) \end{bmatrix} \quad (9.19)$$

where  $\Omega_i$   $1 < i < K$  are selected spectral lines. The matrix  $\mathbf{C}_{lin}$  is the sum of the linear viscous damping matrix  $\mathbf{C}$  and the zero-order term of the nonlinear damping force DF approximation:

$$\mathbf{C}_{lin} = \mathbf{C} + c_{nl,0} \mathbf{g} \mathbf{g}^T \quad (9.20)$$

The zero-order coefficient  $c_{nl,0}$  of the nonlinear dissipative DF and the linear viscous coefficient acting in parallel to nonlinear dampers cannot be identified separately, but only the sum of the two coefficients together can be identified.

Eq. (9.20) can be written in compact forms as:

$$\mathbf{V}(A) \begin{bmatrix} \mathbf{C}_{lin} \\ \mathbf{D} \\ c_{nl,1} \mathbf{g} \mathbf{g}^T \\ \vdots \\ c_{nl,t} \mathbf{g} \mathbf{g}^T \end{bmatrix} = \mathbf{Q}(A) \quad (9.21)$$

where  $\mathbf{V}(A) \in \mathbb{R}^{KN \times N(2+T)}$  and  $\mathbf{Q}(A) \in \mathbb{R}^{KN \times N}$  are the matrix of coefficients and the known terms matrix in Eq. (9.19). Eq. (9.19) has  $\infty^{T+1}$  solutions, because the nonlinear damping coefficients in Eq. (9.7) required at least  $T+1$  levels of oscillation amplitude  $A$  to be uniquely identified. Otherwise the nonlinear damping effect can be spread among the different orders coefficients arbitrary. To avoid the indeterminate problem, the unknowns can be identified combining  $T+1$  like-Eq. (9.21), at different amplitude  $A$ . The problem is written as:

$$\begin{bmatrix} \mathbf{V}(A_1) \\ \mathbf{V}(A_2) \\ \vdots \\ \mathbf{V}(A_{T+1}) \end{bmatrix} \begin{bmatrix} \mathbf{C}_{lin} \\ \mathbf{D} \\ c_{nl,1} \mathbf{g} \mathbf{g}^T \\ \vdots \\ c_{nl,T} \mathbf{g} \mathbf{g}^T \end{bmatrix} = \begin{bmatrix} \mathbf{Q}(A_1) \\ \mathbf{Q}(A_2) \\ \vdots \\ \mathbf{Q}(A_{T+1}) \end{bmatrix} \quad (9.22)$$

or in compact form:

$$\tilde{\mathbf{V}} \begin{bmatrix} \mathbf{C}_{lin} \\ \mathbf{D} \\ c_{nl,1} \mathbf{g} \mathbf{g}^T \\ \vdots \\ c_{nl,T} \mathbf{g} \mathbf{g}^T \end{bmatrix} = \tilde{\mathbf{Q}} \quad (9.23)$$

where  $\tilde{\mathbf{V}} \in \mathbb{R}^{KN(T+1) \times N(2+T)}$  and  $\tilde{\mathbf{Q}} \in \mathbb{R}^{KN(T+1) \times N}$  are the coefficients matrix and the known terms matrix in Eq. (9.22).

### 9.2.1 Layers formulation of the nonlinear damping force

The vector of the unknown damping coefficients  $\mathbf{u}$  defined in Eq. (4.11) is here updated with the coefficients of the nonlinear damping force to be identified:

$$\mathbf{u} = \left\{ \mathbf{c}_A^T \quad \mathbf{c}_R^T \quad \mathbf{d}_A^T \quad \mathbf{d}_R^T \quad c_{nl,1} \quad c_{nl,2} \quad \cdots \quad c_{nl,T} \right\}^T \quad (9.24)$$

Note that the zero order coefficient  $c_{nl,0}$  is not explicitly present in the unknowns vector  $\mathbf{u} \in \mathbb{R}_+^{2(N_A+NR)+T}$ , since it is identified together with the linear one and thus included in  $\mathbf{c}_A$  or  $\mathbf{c}_R$ , depending on system topology.

The viscous  $\mathbf{C}_{lin}$  and structural  $\mathbf{D}$  damping matrices are defined in Eq. (4.18) and Eq. (4.19).

The terms coming from the DF approximation of the nonlinear damping force are single Layer matrices  $\mathbf{C}_{nl,i}$ , with the pattern given by the location vector  $\mathbf{g}$ .

$$\mathbf{C}_{nl,i} = c_{nl,i} \mathbf{g} \mathbf{g}^T \text{ with } 1 \leq i \leq T \quad (9.25)$$

The pattern of the nonlinear term  $\mathbf{P}_{nl}$  is defined in addition to the absolute  $\mathbf{P}_p^A$  and relative  $\mathbf{P}_q^R$  patterns, given in Eq. (4.14):

$$\mathbf{P}_{nl} = \mathbf{g} \mathbf{g}^T \quad (9.26)$$

Substituting Eq. (9.26) and (9.24) in Eq. (9.25) the matrix terms of the nonlinear force  $\mathbf{C}_{nl,i}$  can be re-written as:

$$\mathbf{C}_{nl,i} = u_{2(N_A+NR)+i} \mathbf{P}_{nl} \text{ with } 1 \leq i \leq T \quad (9.27)$$

### 9.2.2 Nonlinearly damped system identification via Layers Method

The viscous  $\mathbf{C}$ , structural  $\mathbf{D}$  damping matrices, given in Eq. (4.18) and in Eq. (4.19), and the terms of the nonlinear damping force, given in Eq. (9.27), written by the Layers Method are substituted in Eq. (9.22):

$$\tilde{\mathbf{V}}\tilde{\mathbf{P}}\begin{bmatrix} [u_1\mathbf{I} \cdots u_{N_A}\mathbf{I} \ u_{N_A+1}\mathbf{I} \cdots u_{N_A+NR}\mathbf{I}]^T \\ [u_{1+NA+NR}\mathbf{I} \cdots u_{2NA+NR}\mathbf{I} \ u_{2NA+NR+1}\mathbf{I} \cdots u_{2(N_A+NR)}\mathbf{I}]^T \\ c_{nl,1} \\ \vdots \\ c_{nl,T} \end{bmatrix} = \tilde{\mathbf{Q}} \quad (9.28)$$

where  $\tilde{\mathbf{P}} \in \mathbb{R}^{N(2+T) \times N[2(N_A+NR)+T]}$  is the block diagonal matrix in Eq. (9.29)

$$\tilde{\mathbf{P}} = \text{diag} \left[ \begin{array}{c} \bar{\mathbf{P}} \quad \bar{\mathbf{P}} \quad \underbrace{\mathbf{P}_{nl} \cdots \mathbf{P}_{nl}}_T \end{array} \right] \quad (9.29)$$

Eq. (9.28) can be re-arrangement to make explicit the vector of unknown damping coefficients  $\mathbf{u}$ :

$$\begin{bmatrix} \tilde{\mathbf{V}}\tilde{\mathbf{P}}\mathbf{Z}_1 \\ \vdots \\ \tilde{\mathbf{V}}\tilde{\mathbf{P}}\mathbf{Z}_N \end{bmatrix} \mathbf{u} = \begin{bmatrix} \tilde{\mathbf{Q}}\mathbf{W}_1 \\ \vdots \\ \tilde{\mathbf{Q}}\mathbf{W}_N \end{bmatrix} \quad (9.30)$$

where  $\mathbf{W}_i$  is defined in Eq. (4.45) and  $\mathbf{Z}_i \in \mathbb{R}^{N[2(N_A+NR)+T] \times 2(N_A+NR)+T}$  with  $i = 1, 2, \dots, N$  is defined as:

$$\mathbf{Z}_i = \mathbf{0} \text{ and } (\mathbf{Z}_i)_{(y-1)N+i,y} = 1 \text{ with } y = 1, 2, \dots, 2(N_A + NR) + T \quad (9.31)$$

Eq. (9.30) can be written in compact form as:

$$\bar{\mathbf{V}}\mathbf{u} = \bar{\mathbf{Q}} \quad (9.32)$$

where  $\bar{\mathbf{V}} \in \mathbb{R}^{KN^2(T+1) \times 2(N_A+NR)+T}$  and  $\bar{\mathbf{Q}} \in \mathbb{R}^{KN^2(T+1) \times 1}$  are the matrix of coefficients and the known terms matrix in Eq. (9.30).

The solution of Eq. (9.32) is exactly as in the linear case, and the procedure from Eq. (4.50) to Eq. (4.57) can be replicated using the above defined  $\bar{\mathbf{V}}$ ,  $\mathbf{u}$  and  $\bar{\mathbf{Q}}$  matrices.

The stabilisation of the solution and the choice of the optimal solution  $\mathbf{u}^*$  are performed as in the linear case § 4.3.1, extending the stability check to the  $2(NA + NR) + T$  unknown damping coefficients.

### 9.3 Application to numerical nonlinearly damped system

The SLM extended to the nonlinear damping identification is here applied on a numerically generated five DOFs system, Figure 9.1. The system presents linear non-proportional viscous dissipations and a nonlinear amplitude dependent damper acting between the 4<sup>th</sup> and 5<sup>th</sup> DOFs.

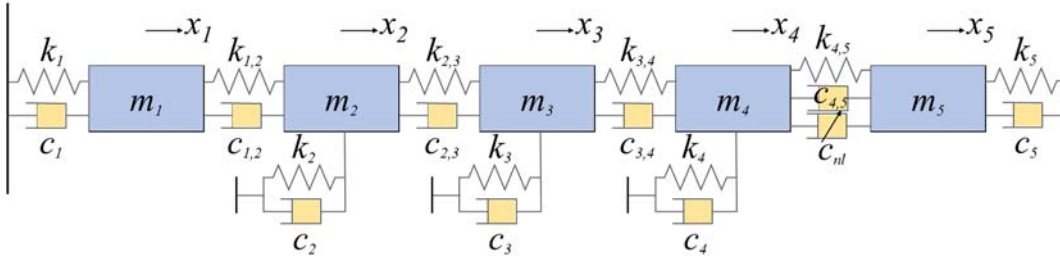


Figure 9.1 - Schematic of the nonlinear damped system.

The equation of motion of the systems is:

$$\mathbf{M}\ddot{\mathbf{x}} + \mathbf{C}\dot{\mathbf{x}} + \mathbf{K}\mathbf{x} + f_{c, nl_{4,5}}(x_4, x_5, \dot{x}_4, \dot{x}_5)\mathbf{g} = \mathbf{f}(t) \quad (9.33)$$

where

$$\begin{aligned} \mathbf{M} &= 10^{-2} \text{diag}([1 \quad 2 \quad 3 \quad 4 \quad 5]) \text{ kg} \\ \mathbf{K} &= 10^2 \begin{bmatrix} 15 & -5 & & & \\ -5 & 18 & -3 & & \\ & -3 & 21 & -8 & \\ & & -8 & 23 & -5 \\ & & & -5 & 15 \end{bmatrix} \text{ N/m} \\ \mathbf{C} &= \begin{bmatrix} 1 & & & & \\ & 0.5 & -0.5 & & \\ & -0.5 & 0.5 & & \\ & & & 0 & \\ & & & & 0 \end{bmatrix} + 10^{-6} \mathbf{M} + 4 \cdot 10^{-5} \mathbf{K} \text{ Ns/m} \\ \mathbf{g} &= [0 \quad 0 \quad 0 \quad 1 \quad -1]^T \end{aligned} \quad (9.34)$$

The dissipative nonlinear damping force  $f_{c, nl_{4,5}}$  is amplitude dependent and it is written as second order polynomial:

$$f_{c,nl_{4,5}} = (c_{nl,0} + c_{nl,1}|\xi| + c_{nl,2}\xi^2)\dot{\xi}, \quad \xi = x_4 - x_5, \quad \dot{\xi} = \dot{x}_4 - \dot{x}_5 \quad (9.35)$$

where the damping coefficients values are:

$$c_{nl,0} = 1 \text{ Ns/m}, \quad c_{nl,1} = 0 \text{ Ns/m}^2, \quad c_{nl,2} = 2 \cdot 10^7 \text{ Ns/m}^3 \quad (9.36)$$

The equation of motion Eq. (9.33) in frequency domain is:

$$\left[ (\mathbf{K} - \Omega^2 \mathbf{M}) + F_{c,nl_{4,5}}(A, \Omega) \mathbf{g} \mathbf{g}^T \right] \mathbf{X}(\Omega) = \mathbf{F}(\Omega) \quad (9.37)$$

where  $F_{c,nl_{4,5}}(A, \Omega)$  is the DF of the nonlinear damping force, given in Eq. (9.35):

$$F_{c,nl_{4,5}}(\Omega, A) = i\Omega(c_{nl,0} + c_{nl,1}z_1A + c_{nl,2}z_2A^2), \quad z_1 = \frac{4}{3\pi}, \quad z_2 = \frac{1}{4} \quad (9.38)$$

where  $A$  is the relative oscillation amplitude between 4<sup>th</sup> and 5<sup>th</sup> DOFs.

The nonlinear FRM  $\mathbf{H}_{nl}(A, \Omega)$  with constant amplitude  $A$  are necessary to apply the identification method presented in § 9.2.

The nonlinear receptance matrix  $\mathbf{H}_{nl}(A, \Omega)$  can be numerically computed using the Sherman–Morrison formula [130,158] from the linear receptance matrix  $\mathbf{H}(\Omega)$ :

$$\mathbf{H}_{nl}(A, \Omega) = \mathbf{H}(\Omega) - \frac{F_{c,nl_{4,5}}(\Omega, A) \mathbf{H}(\Omega) (\mathbf{e}_4 - \mathbf{e}_5)(\mathbf{e}_4 - \mathbf{e}_5)^T \mathbf{H}(\Omega)}{1 + F_{c,nl_{4,5}}(\Omega, A) (\mathbf{e}_4 - \mathbf{e}_5)^T \mathbf{H}(\Omega) (\mathbf{e}_4 - \mathbf{e}_5)} \quad (9.39)$$

where  $\mathbf{e}_4$ ,  $\mathbf{e}_5$  are respectively the 4<sup>th</sup> and 5<sup>th</sup> columns of the identity matrix of the dimension five and  $\mathbf{H}(\Omega)$  is computed using Eq. (5.1), from the eigenvectors of the underlying linear non-classically damped system.

The nonlinear numerical FRFs  $\mathbf{H}_{nl}(A, \Omega)$  are contaminated with a random noise of 10% of the FRF amplitude, to check robustness of the identification method against the noise effects.

The order of the nonlinear damping function Eq. (9.35) is  $T=2$ , therefore three nonlinear FRM  $\mathbf{H}_{nl}(\Omega, A)$  with different levels of the constant amplitude  $A$  are required for the identification.

An example FRF of the FRM  $\mathbf{H}_{nl}(\Omega, A)$  at constant amplitude  $A$  across the nonlinearity and with an additional Gaussian random noise is shown in Figure 9.2. The system response in Figure 9.2 is visibly nonlinear; the second mode shape peak is affected by the damping nonlinearity.



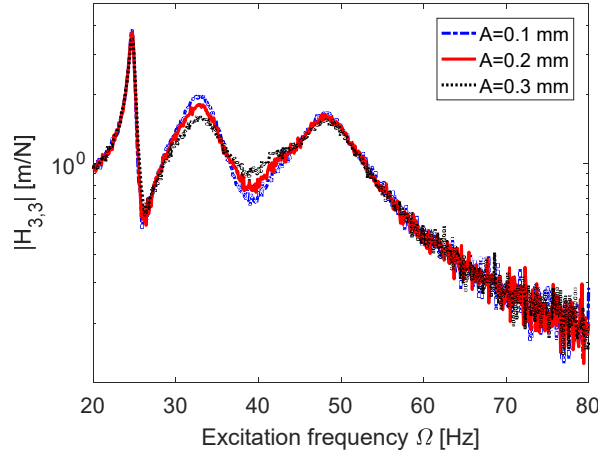


Figure 9.2 - Numerical noisy FRF with different oscillations amplitude.

The identification can be performed by simplifying Eq. (9.19) to remove the structural damping component:

$$\begin{bmatrix} \Omega_1 \mathbf{H}^N(\Omega_1) & \Omega_1 z_1 A \mathbf{H}^N(\Omega_1) & \Omega_1 z_2 A^2 \mathbf{H}^N(\Omega_1) \\ \Omega_2 \mathbf{H}^N(\Omega_2) & \Omega_2 z_1 A \mathbf{H}^N(\Omega_2) & \Omega_2 z_2 A^2 \mathbf{H}^N(\Omega_2) \\ \vdots & \vdots & \vdots \\ \Omega_K \mathbf{H}^N(\Omega_K) & \Omega_K z_1 A \mathbf{H}^N(\Omega_K) & \Omega_K z_2 A^2 \mathbf{H}^N(\Omega_K) \end{bmatrix} \begin{bmatrix} \mathbf{C}_{lin} \\ c_{nl,1} \mathbf{g} \mathbf{g}^T \\ c_{nl,2} \mathbf{g} \mathbf{g}^T \end{bmatrix} = \begin{bmatrix} \mathbf{G}(A, \Omega_1) \\ \mathbf{G}(A, \Omega_2) \\ \vdots \\ \mathbf{G}(A, \Omega_K) \end{bmatrix} \quad (9.40)$$

The layers involved for the creation of viscous  $\mathbf{C}$  and structural  $\mathbf{D}$  damping matrices are five absolute layers, one for each system DOF, and four relative dampers representing the connection between two consecutive DOFs.

Two additional layers are required to build the first  $\mathbf{C}_{nl,1}$  and second  $\mathbf{C}_{nl,2}$  order matrices terms of the nonlinear damping function, which are 2 relative dampers between the fourth and fifth DOFs. The zero-order coefficient is identified together with the relative damping  $c_{4,5}$ :

$$c_{4,5}^{id} = c_{4,5} + c_{nl,0} \quad (9.41)$$

The identified damping coefficients of the eleven layers and their regions of stability are mapped onto the  $(r_{\%}, \tilde{k})$  plane in

Figure 9.3 - Figure 9.13, together with the stabilisation diagram, computed using Eq. (4.67) and tolerance value  $\varepsilon = 1\%$ . Several asymptotes are present onto the  $(r_{\%}, \tilde{k})$  plane because five asymptotes exist for each level of oscillation. The asymptotes range values  $r_{\%asympote}$  are different for each oscillation amplitude  $A$ :

$$r_{\%asympote} = \begin{cases} 0.3718, 0.7323, 0.8127, 0.9977, 1.3023\% & A = 0.1 \text{ mm} \\ 0.2400, 0.5332, 0.8040, 1.2642, 1.2900\% & A = 0.2 \text{ mm} \\ 0.5478, 0.7020, 0.8012, 1.2769, 1.9026\% & A = 0.3 \text{ mm} \end{cases} \quad (9.42)$$

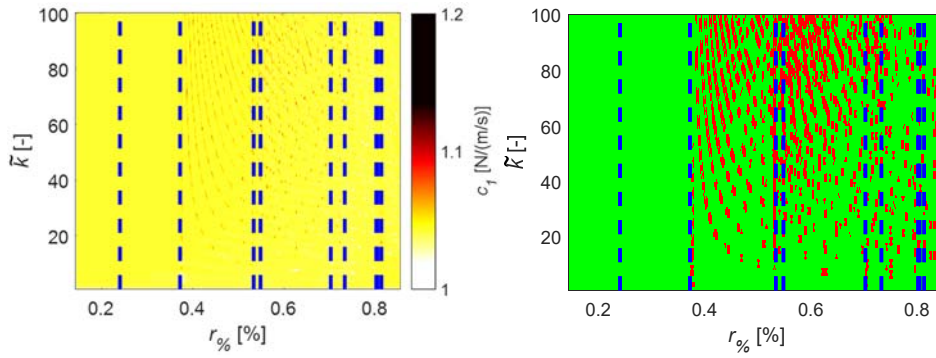


Figure 9.3 - Damping coefficient  $c_1$  : quantification (left) , stability (right).

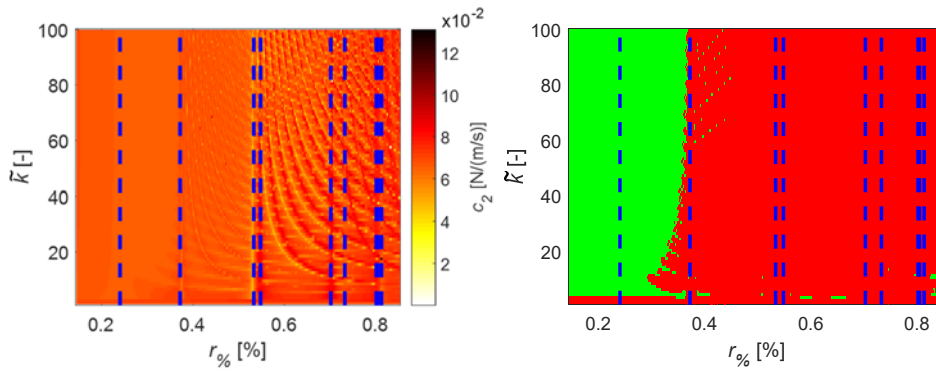


Figure 9.4 - Damping coefficient  $c_2$  : quantification (left) , stability (right).

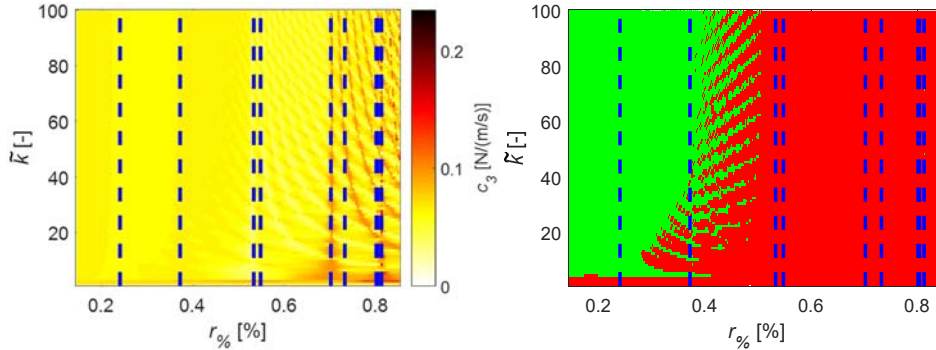


Figure 9.5 - Damping coefficient  $c_3$  : quantification (left) , stability (right).

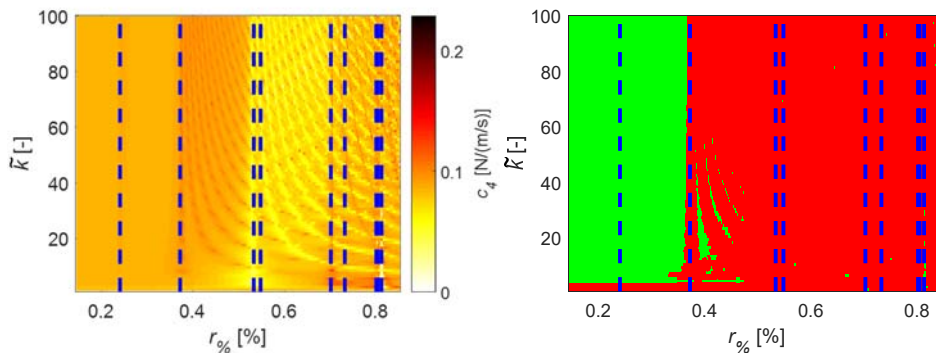


Figure 9.6 - Damping coefficient  $c_4$  : quantification (left) , stability (right).

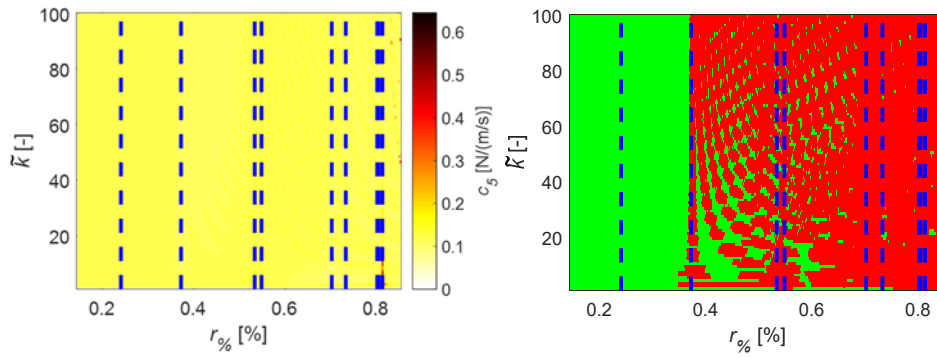


Figure 9.7 - Damping coefficient  $c_5$  : quantification (left) , stability (right).

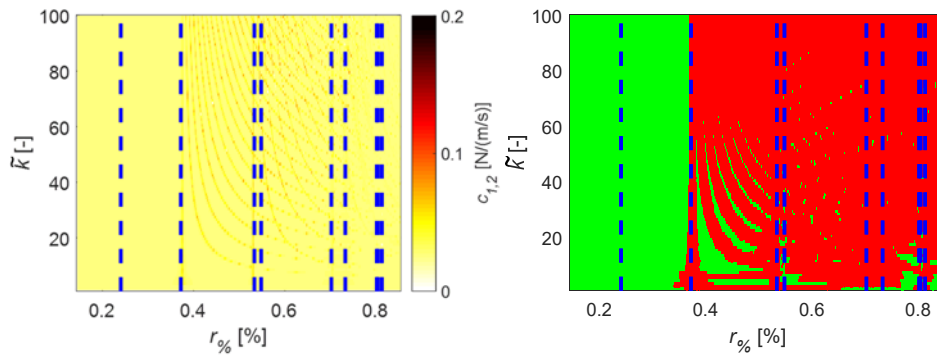


Figure 9.8 - Damping coefficient  $c_{1,2}$  : quantification (left) , stability (right).

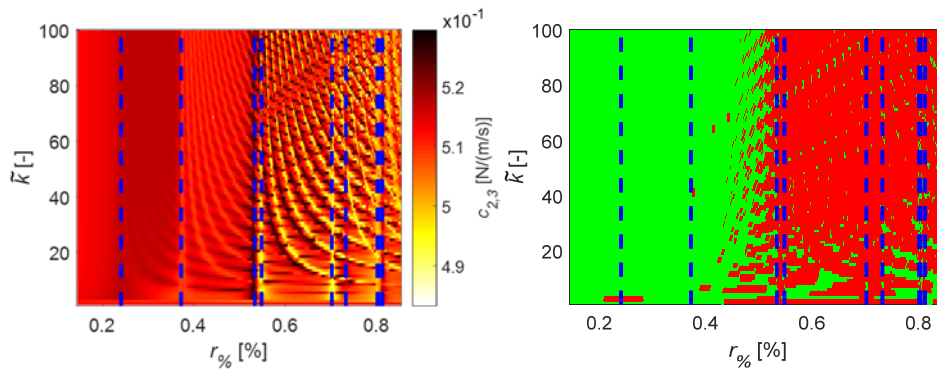


Figure 9.9 - Damping coefficient  $c_{2,3}$  : quantification (left) , stability (right).

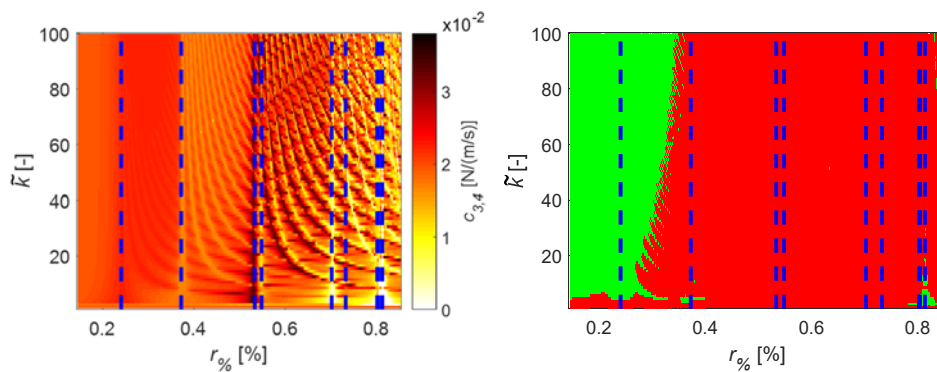
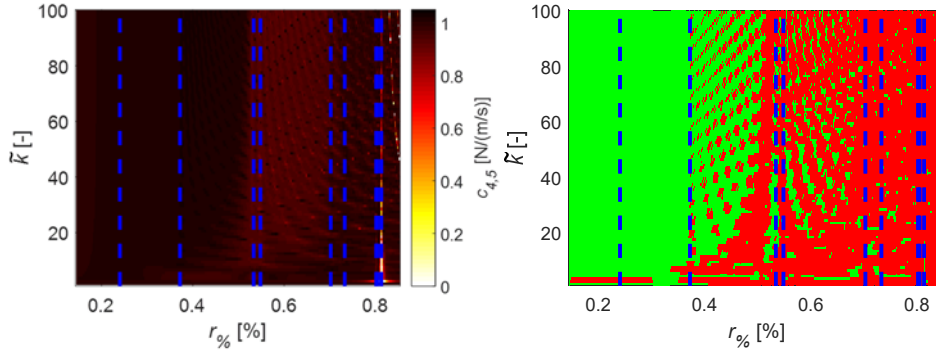
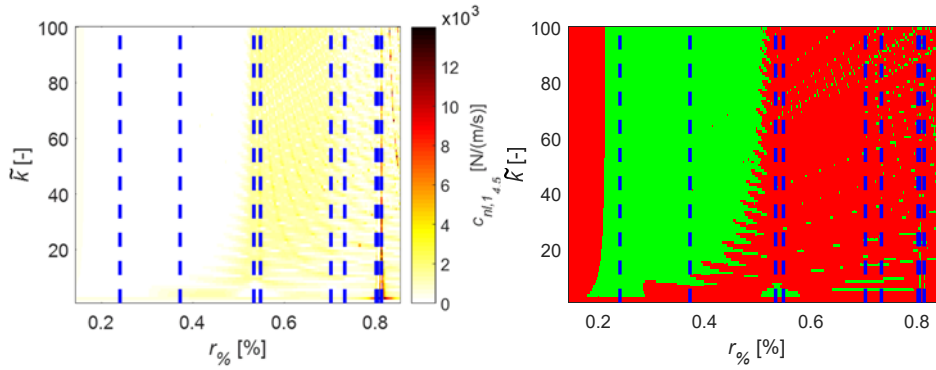
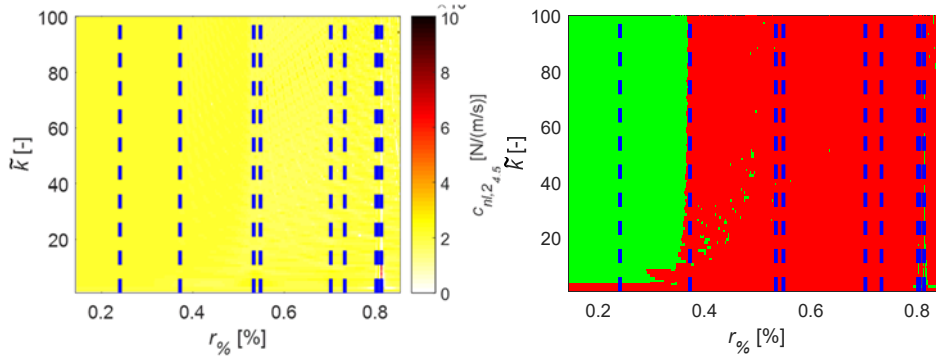


Figure 9.10 - Damping coefficient  $c_{3,4}$  : quantification (left) , stability (right).


 Figure 9.11 - Damping coefficient  $c_{4,5}^{id}$ : quantification (left) , stability (right).

 Figure 9.12 - Damping coefficient  $c_{nl,1}$ : quantification (left) , stability (right).

 Figure 9.13 - Damping coefficient  $c_{nl,2}$ : quantification (left) , stability (right).

The eleven identified damping coefficients are very close to the reference values and stable between the globally smallest two asymptotes. The optimal identified solution  $\mathbf{u}^*$  can be selected looking for  $(r_{\%}^*, \tilde{k}^*)$  satisfying Eq. (4.70). The global stabilisation diagram  $\bar{\mathbf{S}}$ , computed as in Eq. (4.68), and the error map  $\mathbf{E}$ , computed using Eq. (4.69), are shown in Figure 9.14.

The optimal solution  $\mathbf{u}^*$  is  $(r_{\%}^*, \tilde{k}^*) = (99, 0.3111\%)$  and present an extremely low inversion error  $E_{\%}^* = 0.0002\%$ , corresponding to the blue cross in Figure 9.14.

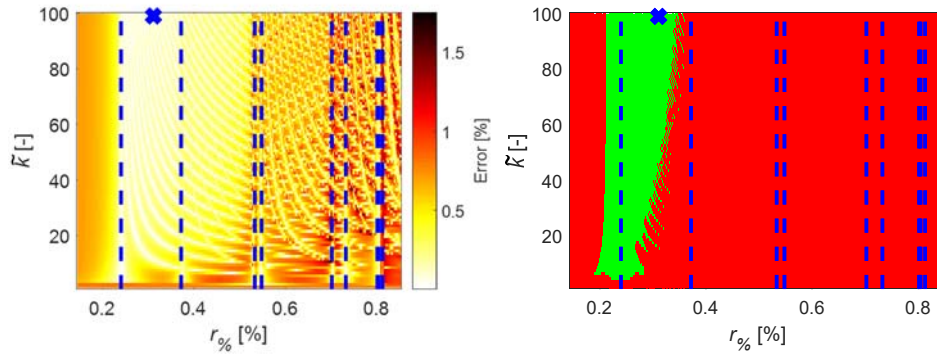


Figure 9.14 - Normalised residuum (left) and global stability diagram (right).

The identified damping matrices are shown in Figure 9.15. The damping coefficient values of the 11 layers are reported in Table 9.1. The spatial distribution of the damping is well identified and the damping values are in very good agreement with the expected ones. The identification results are quite close to the systems parameters.

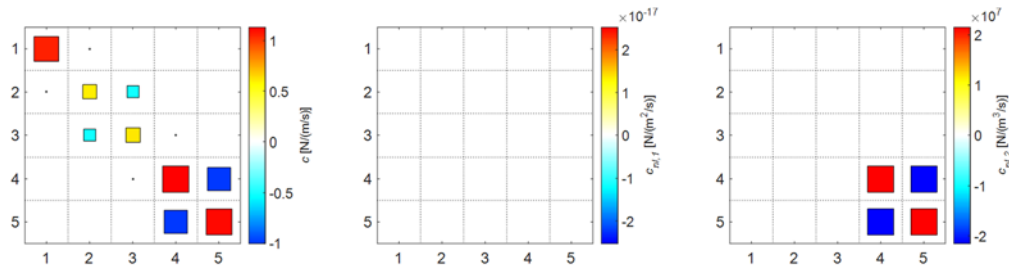

 Figure 9.15 - Identified damping matrices:  $C$  (left),  $C_{nl,1}$  (middle) and  $C_{nl,2}$  (right).

Table 9.1 - Identified damping coefficients values.

Coefficient	Actual [N/(m/s)]	Identified [N/(m/s)]
$c_1$	1.04	1.041
$c_2$	0.04	0.064
$c_3$	0.04	0.060
$c_4$	0.04	0.085
$c_5$	0.04	0.112
$c_{1,2}$	0.012	0.025
$c_{2,3}$	0.52	0.517
$c_{3,4}$	0.032	0.044
$c_{4,5} + c_0$	1.02	1.002
$c_{nl,1}$	0 N/(m <sup>2</sup> /s)	0.000 N/(m <sup>2</sup> /s)
$c_{nl,2}$	$2 \cdot 10^7$ N/(m <sup>3</sup> /s)	$2.15 \cdot 10^7$ N/(m <sup>3</sup> /s)

## 9.4 Conclusions

The SLM was here extended to the identification of nonlinear damped system with a single amplitude dependent nonlinearity, both absolute or relative. The type and location of the nonlinearity should be known or identified and written using sinusoidal input DF approximation. The DF approximation is generally a polynomial function depending on the oscillation amplitude across the nonlinearity. The order of the describe function approximation is quite important because it is related to the number of experimental stepped-sine test to be performed on the structure with different oscillation level. The viscous linear damping matrix is identified together with the coefficients of the nonlinearity. The identified nonlinear damping coefficient requires several experimental stepped sine oscillations to be identified, but once identified can be used in the system model to predict whatever type of vibrational behaviour.

The method is tested against noisy numerical generated data of a five DOFs system with a relative nonlinear damper. The method seems able to identify very well both the linear and nonlinear viscous damping coefficients.



# Chapter 10

## 10. Identification of a nonlinear magnetic damped system

In this chapter, the extension of the SLM for the damping identification in system with localised nonlinearity, presented in § 9, is applied on a lumped system with an amplitude depending nonlinear magnetic damper.

The nonlinear force is given by the interaction of permanent magnets with vibrating paramagnetic conductors. The results of the interaction can be summarised into two main effects: the dissipative interactions and the conservative ones.

The dissipative interactions are related to the ohmic losses created by eddy currents in the conductive moving parts. The main effect of these losses is to drain power from the mechanical vibration, thus reducing the oscillations amplitude. The resulting effect of magnetic field distribution is a nonlinear dependence of force on the oscillation amplitude. For instance as the conducting part is moving closer to the permanent magnet, the experienced magnetic field is higher, increasing locally the induced eddy currents and thus the force [199,200].

The conservative interactions are instead related to the magnetic field created by eddy currents. Even if this field is not high enough to alter the main field imposed by permanent magnets, its energy cannot be neglected [200] and its effect is to modify the elastic properties of the vibrating structure, changing its resonance frequencies.

The aim of this chapter is to identify the dissipative force arising from the magneto-dynamics interaction, validating the methodology introduced in § 9, and comparing the identified results with reference values.

The description of the test rig is presented in § 10.1, together with the experimental setup used to run the tests. The nonlinear damping force is analysed in § 10.2. The general SLM extended to the identification of nonlinear damping



force, presented in § 9, is adapted to the actual test-rig in § 10.3. The identified damping matrices of the system in different configuration are shown in § 10.4. Finally, the identified results are compared among them and with reference values in § 10.5.

### 10.1 Three DOFs magnetic damped test rig

The test-rig is a three DOFs vertical lumped mass-damper-spring system with plate-like springs, shown in Figure 10.1. Each mass is connected to its nearest neighbour through a “coupling spring”. Only the first mass is connected to the ground through a “ground spring”. The system possesses three horizontal translational DOFs, one for each mass and numbered 1-2-3 from the top to bottom in Figure 10.1.

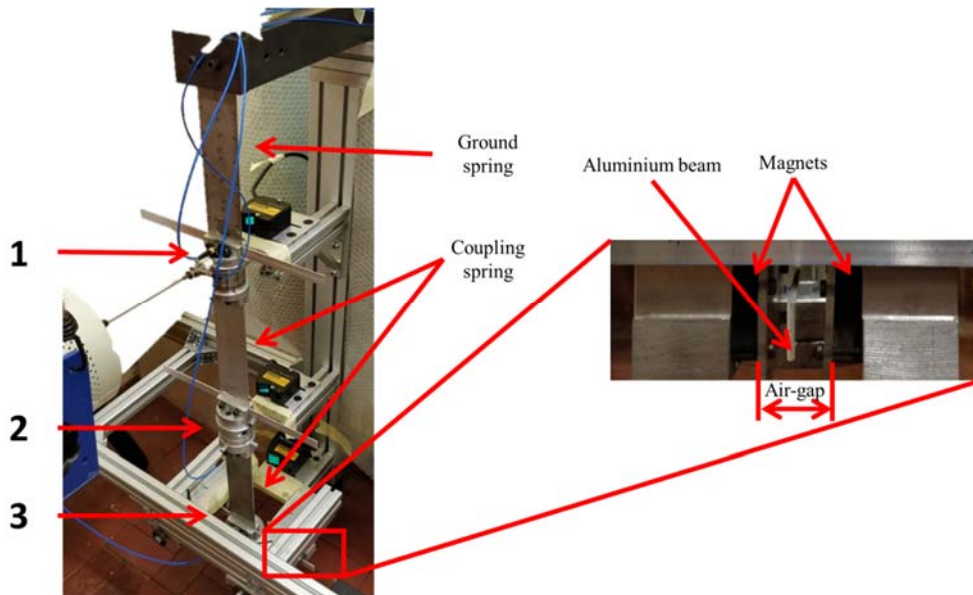


Figure 10.1 - Three DOFs magnetic damped test rig.

Each of the masses is equipped by two aluminium paramagnetic slabs (size  $l = 180 \text{ mm}$ ,  $w = 15 \text{ mm}$  and thickness  $h = 2 \text{ mm}$ ), one for each side.

The aluminium beams of the third DOF vibrate inside the air-gap between two couple of  $\text{Sm}_2\text{Co}_{17}$  permanent magnet in repulsion. The four magnets have dimensions  $2a = 11 \text{ mm}$ ,  $2b = 35 \text{ mm}$ ,  $2c = 30 \text{ mm}$  and residual magnetic induction  $B_r = 1.0 \text{ T}$ .

The structure holding the magnets are in aluminium to not modify the magneto- static field. The air-gap  $\Delta$  between each couple of magnets can be adjusted continuously.

The magnetic damping is created using the effect of a paramagnetic material, aluminium slab, vibrating inside a magnetic field.

The identification is performed with two different air-gaps  $\Delta$  between the magnets:  $\Delta = 17$  mm and  $\Delta = 22$  mm.

### 10.1.1 Experimental setup

Experimental amplitude-controlled sweeps tests are carried out on the test-rig, using LMS SCADAS mobile and Siemens LMS Test.Lab. The amplitude of oscillation across the nonlinearity, which location is known, is maintained constant in the frequency range between  $\Delta f = 0.5 \div 28.5$  Hz. Three sweeps with different amplitude of oscillation are performed for each configuration of the test rig, exciting the first DOF with a shaker Dongling ESD-045.

The FRFs in term of displacement are obtained measuring the system response with three displacement laser sensors (Keyence LK-H052, LK-H082 and LK-H152), one for each system DOF. The excitation force is measured with a load cell PCB 208C02. The system is also equipped with PCB 356A15 triaxle accelerometers, which are used in the pre-test phase to perform EMA of the undamped system. The EMA is required to understand the frequency band of interest and check that only bending mode are present in that frequency range.

## 10.2 Nonlinear damping force

The magnetic damping force given by two magnets in repulsion. It is dissipative nonlinear force, with a very small conservative component [201].

Bonisoli et al. presented in [201] the analytical formulation of the nonlinear damping coefficient filled by a paramagnetic conductor of thickness  $h$  and resistivity  $r_e$  inside the magnetic field generated by two permanent magnet of dimensions  $2a \times 2b \times 2c$  with an air-gap  $\Delta$ :

$$c_{eq} = \frac{b^2 c^2 h}{2r_e} \left( \frac{dB_{m,y_3}}{dy_3} \right)^2 \quad (10.1)$$

where  $\frac{dB_{m,y_3}}{dy_3}$  is the magnetic induction gradient, which is function of the air-gap  $\Delta$  and the position of the oscillating slab  $y_3(t)$ .

In [201] the analytical formulation for the magnetic induction gradient  $\frac{dB_{m,y_3}}{dy_3}$  is presented, and it can be fitted by a quadratic function:

$$\frac{dB_{m,y_3}}{dy} = \chi + \gamma y_3^2 \quad (10.2)$$

where  $\chi$  and  $\gamma$  are the coefficients of the fitting polynomial.

The nonlinear damping force, considering oscillation  $y_3(t) \ll 1$  m, becomes:

$$f_{c,nl,3}(y_3, \dot{y}_3) = c_{eq} \dot{y}_3 = \frac{b^2 c^2 h}{2r_e} (\chi + \gamma y_3^2)^2 \dot{y}_3 = \frac{b^2 c^2 h}{2r_e} (\chi^2 + 2\chi\gamma y_3^2 + o(y_3^2)) \dot{y}_3 \quad (10.3)$$

The amplitude depending nonlinear damping function  $f_{c,nl,3}(y_3, \dot{y}_3)$  in Eq. (10.3) can be written in a more compact form as:

$$f_{c,nl,3}(y_3, \dot{y}_3) = c_{nl,0} + c_{nl,1}|y| + c_{nl,2}y^2 \quad (10.4)$$

where  $c_{nl,0}$ ,  $c_{nl,1}$  and  $c_{nl,2}$  are the coefficients of the nonlinear damping function to be identified. These coefficients are defined as:

$$c_{nl,0} = \frac{b^2 c^2 h}{2r_e} \chi^2 \quad (10.5)$$

$$c_{nl,1} = 0 \quad (10.6)$$

$$c_{nl,2} = \frac{b^2 c^2 h}{r_e} \chi\gamma \quad (10.7)$$

The definition of the coefficients in Eq. (10.5), Eq. (10.6) and Eq. (10.7) are not of interest in the identification, because the aim is to identify the coefficients  $c_{nl,i}$  of the nonlinear damping force. Eq. (10.6) is instead considered an indicator of the identification goodness: if the magnetic damper is symmetric with respect to the aluminium beam,  $c_{nl,1}$  should result close to zero.

### 10.3 Nonlinear SLM application

The sinusoidal input DF approximation of Eq. (10.4), in the form presented in Eq. (9.6), becomes:

$$F_{c,nl,3}(\Omega, A) = i\Omega(c_{nl,0} + c_{nl,1}z_1 A + c_{nl,2}z_2 A^2), \quad z_1 = \frac{4}{3\pi}, \quad z_2 = \frac{1}{4} \quad (10.8)$$

where  $A$  is the oscillations amplitude across the nonlinearity  $y_3(t) = A \sin(\omega t)$ .

Eq. (10.4) defines the order  $T=2$  on the nonlinearity, and therefore the number of different and constant amplitude  $A$   $T+1=3$  necessary for the identification. The chosen amplitudes of oscillation  $A$  are:

$$A = 0.25, 0.5, 1 \text{ mm} \quad (10.9)$$

The SLM for nonlinear damping identification is adapted to second order nonlinearity  $T=2$  and non-proportional viscous damping  $\mathbf{C}$ , thus Eq. (9.19) becomes:

$$\begin{bmatrix} \Omega_1 \mathbf{H}^N(\Omega_1) & \Omega_1 z_1 A \mathbf{H}^N(\Omega_1) & \Omega_1 z_2 A^2 \mathbf{H}^N(\Omega_1) \\ \Omega_2 \mathbf{H}^N(\Omega_2) & \Omega_2 z_1 A \mathbf{H}^N(\Omega_2) & \Omega_2 z_2 A^2 \mathbf{H}^N(\Omega_2) \\ \vdots & \vdots & \vdots \\ \Omega_K \mathbf{H}^N(\Omega_K) & \Omega_K z_1 A \mathbf{H}^N(\Omega_K) & \Omega_K z_2 A^2 \mathbf{H}^N(\Omega_K) \end{bmatrix} \begin{bmatrix} \mathbf{C}_{lin} \\ c_{nl,1} \mathbf{g} \mathbf{g}^T \\ c_{nl,2} \mathbf{g} \mathbf{g}^T \end{bmatrix} = \begin{bmatrix} \mathbf{G}(A, \Omega_1) \\ \mathbf{G}(A, \Omega_2) \\ \vdots \\ \mathbf{G}(A, \Omega_K) \end{bmatrix} \quad (10.10)$$

The location of the nonlinearity is known, it is an absolute damper located on the third DOF therefore the selection vector  $\mathbf{g}$  is defined as:

$$\mathbf{g} = [0 \quad 0 \quad 1]^T \quad (10.11)$$

The Layers used for the identification are: three absolute layers, one on each DOF and two relative layers linking the first and second DOFs  $c_{1,2}$  and second and third DOFs  $c_{2,3}$ . The absolute layer on the first DOF is necessary to identify the damping coefficients  $c_1$  due to the clamp and the shaker used for the excitation; the absolute damper on the third DOF  $c_3$  is necessary to identify the linear part of the nonlinear damping force, while the absolute damper on the second DOF  $c_2$  could be avoided, but it is inserted for completeness. It identified values should be close to zero. The relative layers represent the dissipation due to the links between consecutive masses.

## 10.4 Identification results

The extended SLM, presented in § 9, is applied to perform the identification of system with nonlinear damping. The results of the identification in the two configurations of air-gap are presented in § 10.4.1 and § 10.4.2.

### 10.4.1 Nonlinear damping with 17 mm air-gap

In this configuration the nonlinear damper is prepared with an air-gap  $\Delta = 17$  mm. The first row only of the FRM  $\mathbf{H}_{nl}^{Exp}(A, \Omega)$  is measured with the three levels of amplitude oscillations of the third DOF in Eq. (10.9), shown in Figure 10.2. The complete FRM  $\mathbf{H}_{syn}(A, \Omega)$  is synthesised using Eq. (5.1) and the consideration in § 5.1. The amplitude of the sinusoidal oscillation across the nonlinearity is very well controlled. At the maximum oscillation amplitude,  $A = 1$  mm, the reference is not followed at higher frequencies, since saturation limits are imposed on the shaker amplifier for security reason. The system synthesised FRM  $\mathbf{H}_{syn}(A, \Omega)$  are in very good agreement with the experimental

FRM  $\mathbf{H}^{Exp}(A, \Omega)$ . The peak in the experimental FRFs at 8 Hz circa is not a system resonance, it is a resonance of the support; while the peak before the first natural frequency is given by excitation problems, i.e. the shaker is not able to work properly at very low excitation frequency. The two mentioned peaks are therefore not identified as system mode shapes and removed in the synthesised FRM  $\mathbf{H}_{nl, syn}(A, \Omega)$ .

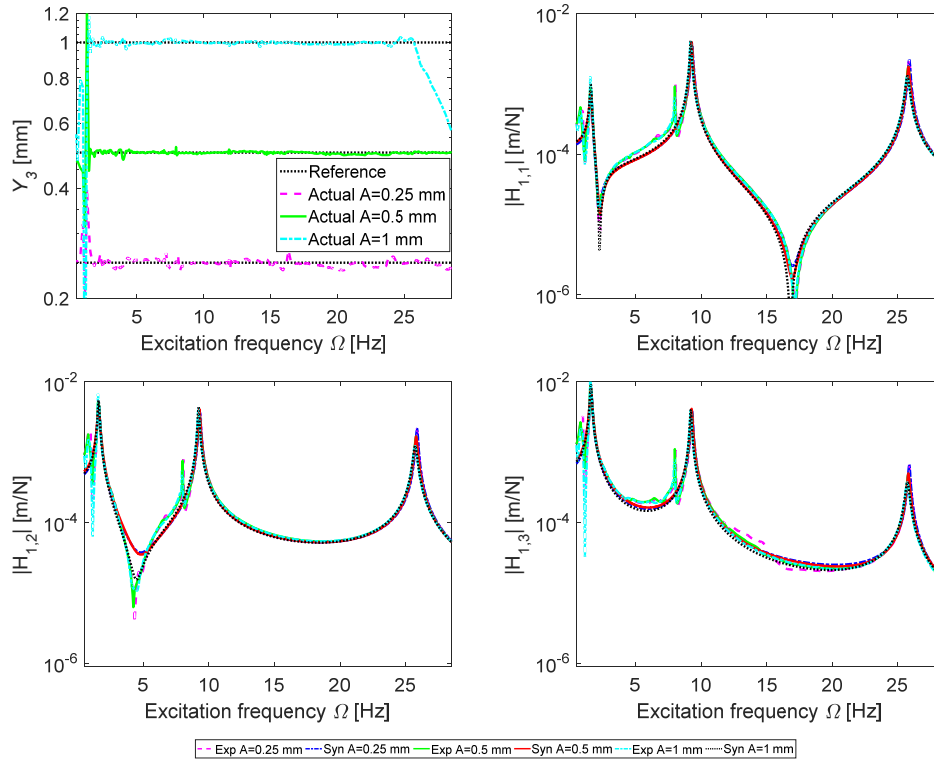


Figure 10.2 - Measured and synthesised FRFs changing oscillation amplitude.

Zooms of the natural frequency ranges are shown in Figure 10.3, to better understand the effect of the nonlinear damping.

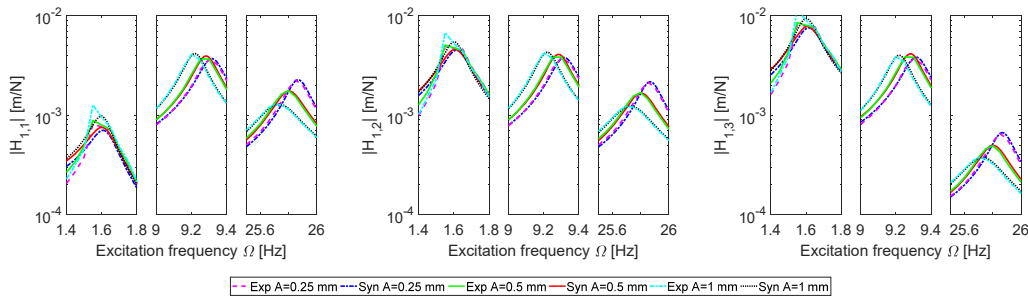


Figure 10.3 - Effects of nonlinearity with air-gap  $\Delta = 17$  mm.

The amplitude of the third peak decreases and moves at lower frequency when oscillation amplitude  $A$  of the third DOF increases. This is the effect of

increased damping. The second mode shapes peak decreases also its frequency, while the first one is almost invariant.

Several asymptotes are present onto the  $(r_%, \tilde{k})$ , plane because three asymptotes exist for each level of oscillation. The asymptotes range values  $r_{\% \text{asymptote}}$  are different for each oscillation amplitude  $A$  across the nonlinearity:

$$r_{\% \text{asymptote}} = \begin{cases} 0.1187, 0.1290, 2.2823\% & A = 0.25 \text{ mm} \\ 0.1017, 0.1119, 2.1342\% & A = 0.5 \text{ mm} \\ 0.0816, 0.1742, 0.7758\% & A = 1 \text{ mm} \end{cases} \quad (10.12)$$

The identified damping coefficients of the seven layers and their regions of stability are mapped onto the  $(r_%, \tilde{k})$  plane in Figure 10.4 - Figure 10.10, together with the stabilisation diagram computed using Eq. (4.67) and tolerance  $\varepsilon = 10\%$ .

The expected asymptotes, given in Eq. (10.12), are highlighted in blue dashed vertical lines and the stabilisation diagrams show stable and unstable regions.

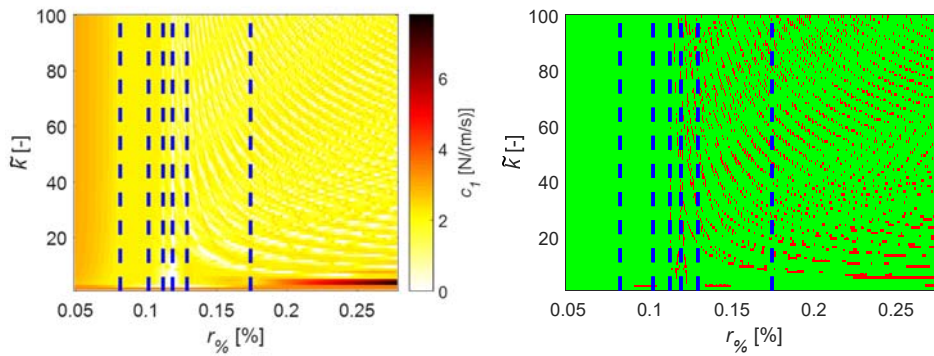


Figure 10.4 - Damping coefficient  $c_1$  : quantification (left) , stability (right).

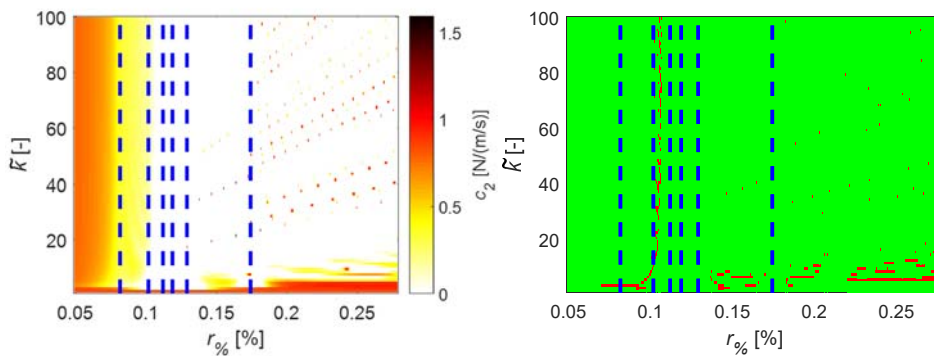


Figure 10.5 - Damping coefficient  $c_2$  : quantification (left) , stability (right).

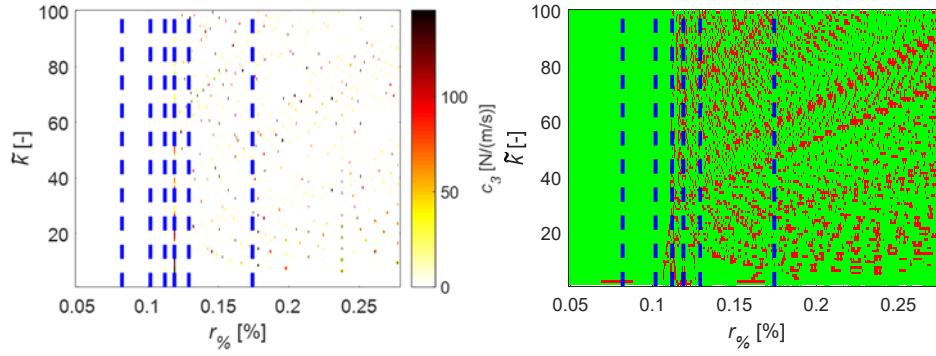


Figure 10.6 - Damping coefficient  $c_3^{id}$  : quantification (left) , stability (right).

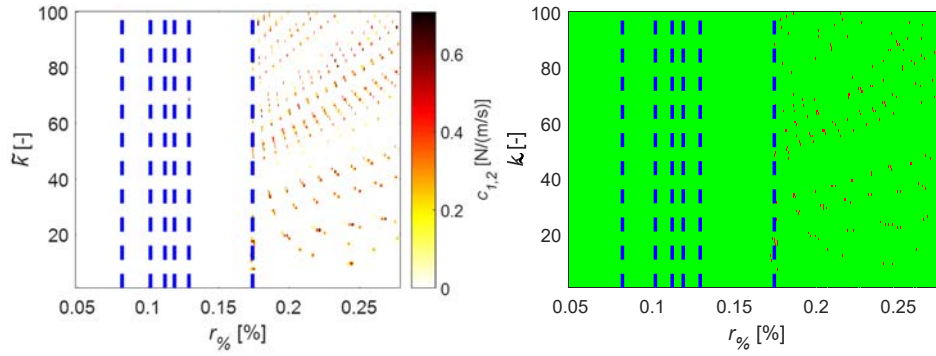


Figure 10.7 - Damping coefficient  $c_{1,2}$  : quantification (left) , stability (right).

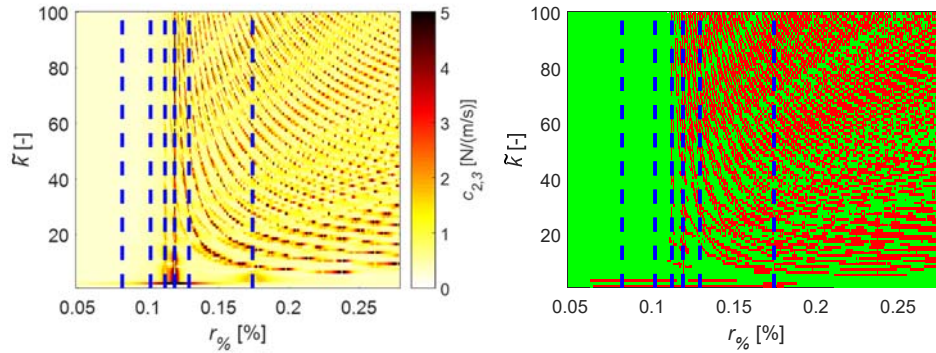


Figure 10.8 - Damping coefficient  $c_{2,3}$  : quantification (left) , stability (right).

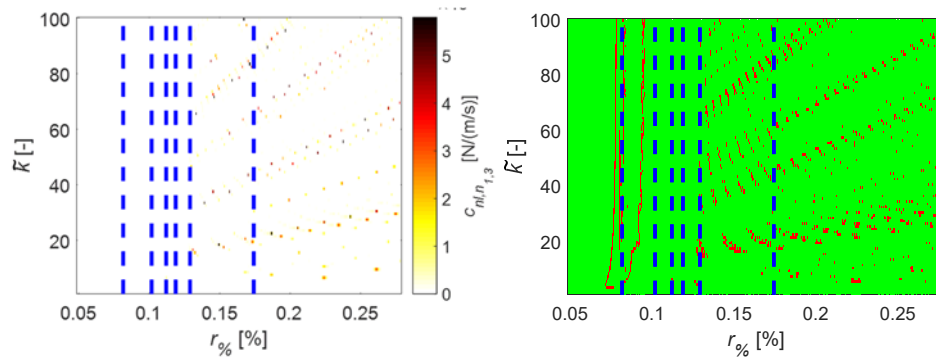


Figure 10.9 - Damping coefficient  $c_{nl,1}$  : quantification (left) , stability (right).

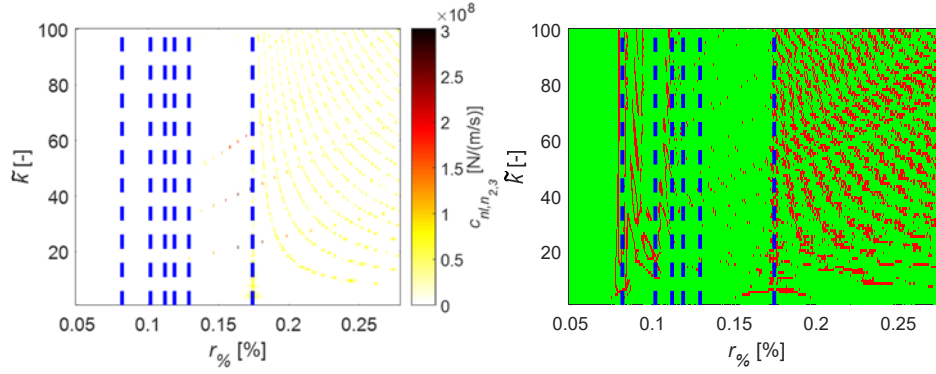


Figure 10.10 - Damping coefficient  $c_{nl,2}$ : quantification (left) , stability (right).

The damping coefficients are well identified in the range between the higher among the first asymptotes and the higher among the second asymptotes.

The optimal identified solution  $\mathbf{u}^*$  can be selected looking for  $(r_{\%}^*, \tilde{k}^*)$  satisfying Eq. (4.70). The global stabilisation diagram  $\bar{\mathbf{S}}$ , computed as in Eq. (4.68), and the error map  $\mathbf{E}$ , computed using Eq. (4.69), are shown in Figure 10.11. The identification is globally stable in a region close to the first asymptote, in the same region also the normalised residuum  $E_{\%}$  reaches a minimum value.

In the same region also the normalised residuum is low. But in that region not all the three first asymptotes are reached; therefore, the minimum error is found in a region which is spotted globally stable. The optimal identified solution  $\mathbf{u}^*$  is the one with minimum residuum at  $(r_{\%}^*, \tilde{k}^*) = (11, 0.1658\%)$  and a low inversion error  $E_{\%}^* = 0.5359\%$ , corresponding to the blue cross in Figure 10.11.

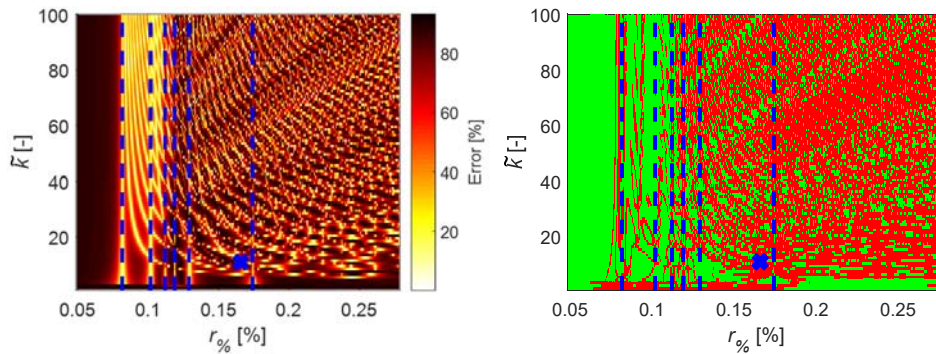


Figure 10.11 - Normalised residuum (left) and global stability diagram (right).

The identified damping matrices are shown in Figure 10.12. The damping coefficient values of the seven layers are reported in Table 10.1. The spatial distribution of the damping is well identified.



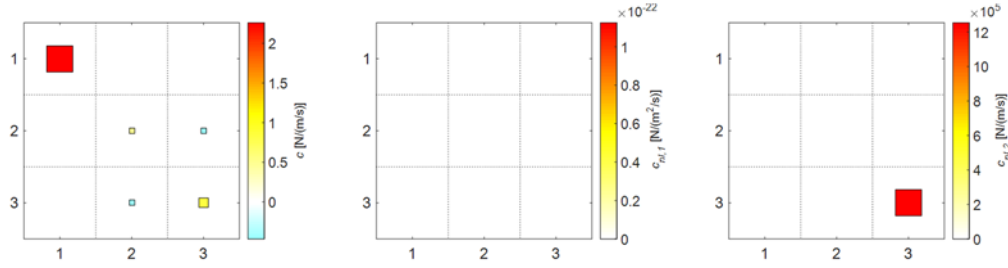


Figure 10.12 - Identified damping matrices:  $C_{lin}$  (left),  $C_{nl,1}$  (middle) and  $C_{nl,2}$  (right).

The SLM extended to nonlinear damping identify a linear viscous damping matrix  $C_{lin}$  with a big dissipation on the first DOF, probably due to the shaker. The identification of the shaker as a localised damped in already found in literature [89,202]. The relative damper  $c_{2,3}$  between the second and third DOFs is also identified. Finally, the nonlinear damper is identified with a small linear coefficient  $c_3^{id} = c_{nl,0} + c_3$  and a quite big second order coefficient  $c_{nl,2}$ .

The absolute damper on second DOF  $c_2$  is null as expected, because there is no link between it and the fixed frame. The first order coefficient of the nonlinear damping function  $c_{nl,1}$  result to be zero, as expected from Eq. (10.6).

Table 10.1 - Identified damping coefficients values, air-gap  $\Delta = 17$  mm .

Coefficient	Identified [N/(m/s)]
$c_1$	2.2592
$c_2$	0.000
$c_3$	0.3516
$c_{1,2}$	0.0000
$c_{2,3}$	0.4669
$c_{nl,1}$	0.000 N/(m <sup>2</sup> /s)
$c_{nl,2}$	$1.25 \cdot 10^6$ N/(m <sup>3</sup> /s)

#### 10.4.2 Nonlinear damping with 22 mm air-gap

In this configuration the nonlinear damper is prepared with an air-gap  $\Delta = 22$  mm . The first row only of the FRM  $\mathbf{H}_{nl}^{Exp}(A, \Omega)$  is measured with the three levels of amplitude oscillations of the third DOF in Eq. (10.9), shown in Figure 10.13. The complete FRM  $\mathbf{H}_{syn}(A, \Omega)$  is synthesised using Eq. (5.1) and the consideration in § 5.1.

The amplitude of the sinusoidal oscillation across the nonlinearity is very well controlled. At the maximum oscillation amplitude,  $A = 1$  mm , the reference is not followed at higher frequencies since a saturation limit is imposed on the shaker amplifier for security reason. The system synthesised FRM  $\mathbf{H}_{nl,syn}(A, \Omega)$  is in very

good agreement with the experimental FRM  $\mathbf{H}_{nl}^{Exp}(A, \Omega)$ . As in the previous case the peak in the experimental FRFs at 8 Hz and 0.5 Hz circa are not system resonances and removed in the synthesised FRM  $\mathbf{H}_{nl, syn}(A, \Omega)$ .

Zooms of the natural frequency ranges are shown in Figure 10.14, to better understand the effect of the nonlinear damping. The amplitude of the third peak decreases and moves at lower frequency when oscillation amplitude  $A$  of the third DOF increases. The second mode shapes peak also decreases its frequency, while the first one is almost invariant.

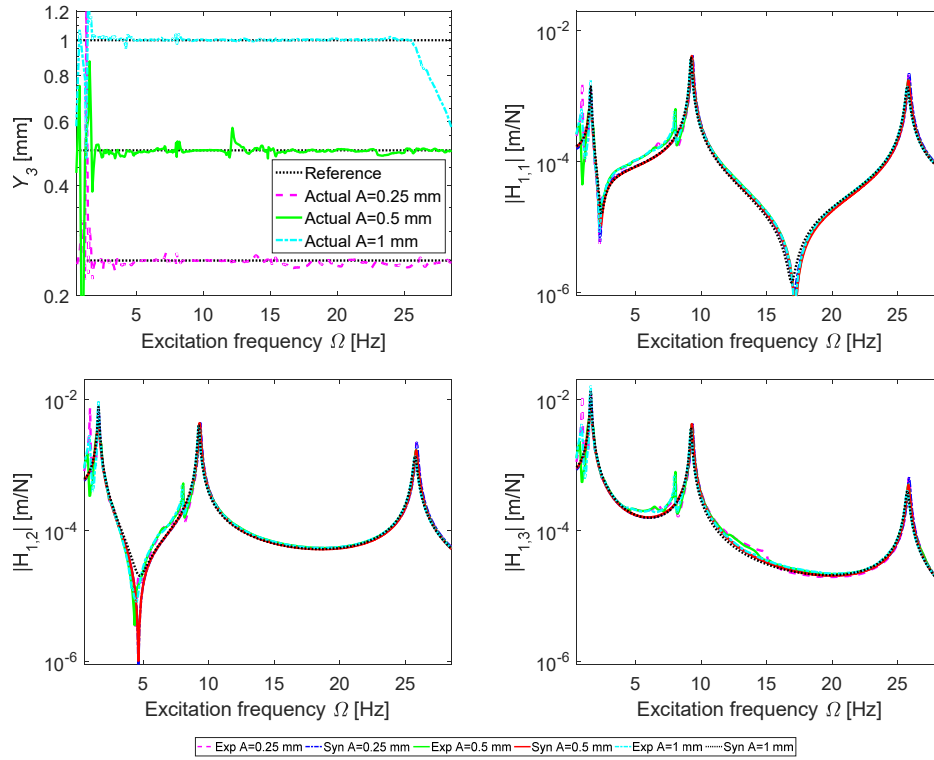


Figure 10.13 - Measured and synthesised FRFs changing oscillation amplitude.

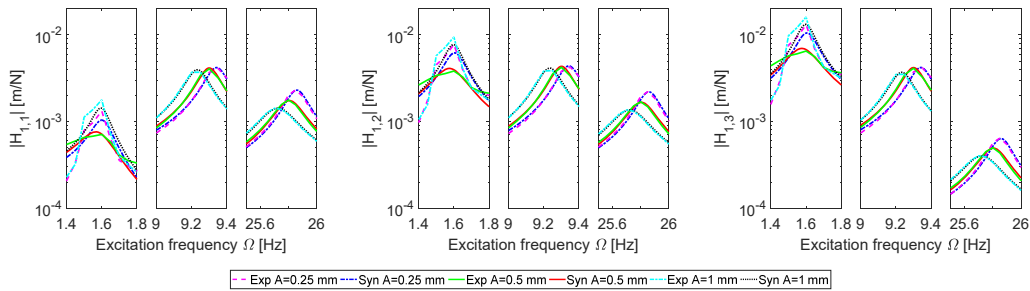


Figure 10.14 - Effects of nonlinearity with air-gap 22 mm.

Several asymptotes are present onto the  $(r_{\%}, \tilde{k})$  plane because three asymptotes exist for each level of oscillation. The range values  $r_{\% asymptote}$  are different for each oscillation amplitude  $A$  across the nonlinearity.

The asymptotes levels are computed using Eq. (4.71):

$$r_{\% \text{asymptote}} = \begin{cases} 0.0597, 0.1125, 0.2661\% & A = 0.25 \text{ mm} \\ 0.1260, 0.1451, 0.5949\% & A = 0.5 \text{ mm} \\ 0.0789, 0.1592, 0.5583\% & A = 1 \text{ mm} \end{cases} \quad (10.13)$$

The identified damping coefficients of the seven layers and their regions of stability are mapped onto the  $(r_{\%}, \tilde{k})$  plane in Figure 10.15 - Figure 10.21, together with the stabilisation diagram computed using Eq. (4.67) and a tolerance value  $\varepsilon = 10\%$ .

The expected asymptotes, in Eq. (10.13), are highlighted in blue dashed vertical lines and the stabilisation diagrams show stable (green) and unstable (red) regions of  $(r_{\%}, \tilde{k})$  plane. The damping coefficients are well identified in the range between the higher among the first asymptotes and the higher among the second asymptotes.

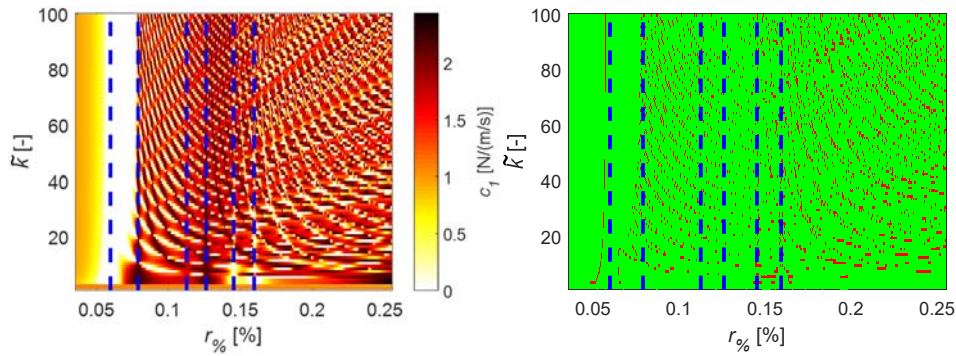


Figure 10.15 - Damping coefficient  $c_1$  : quantification (left) , stability (right).

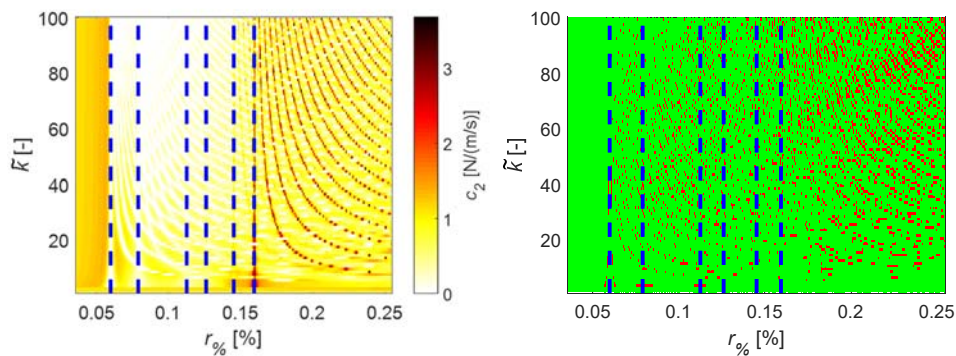
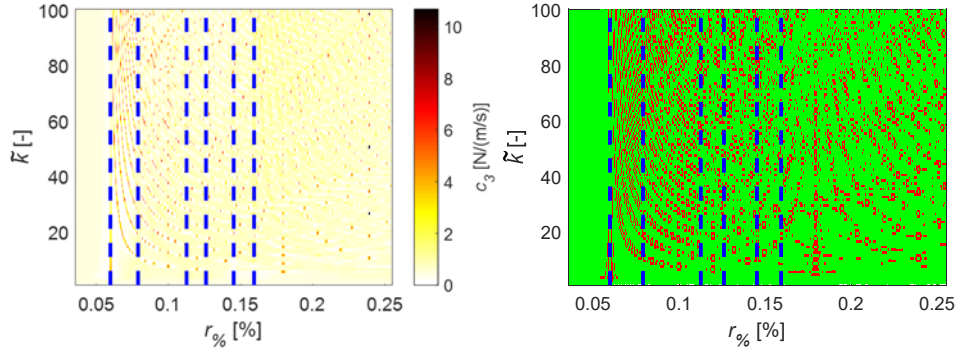
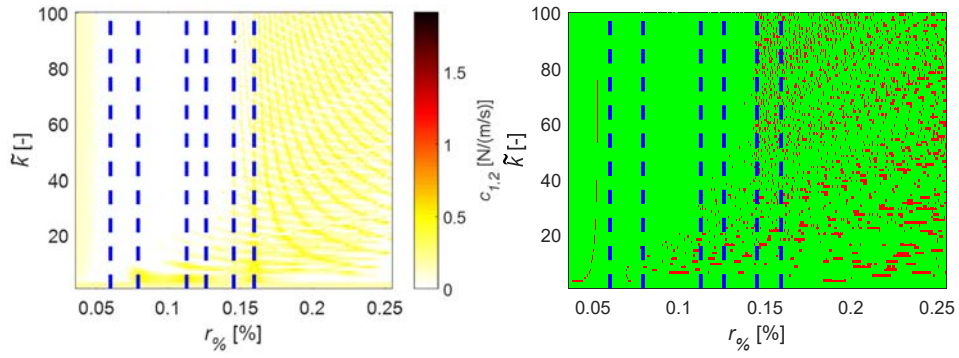
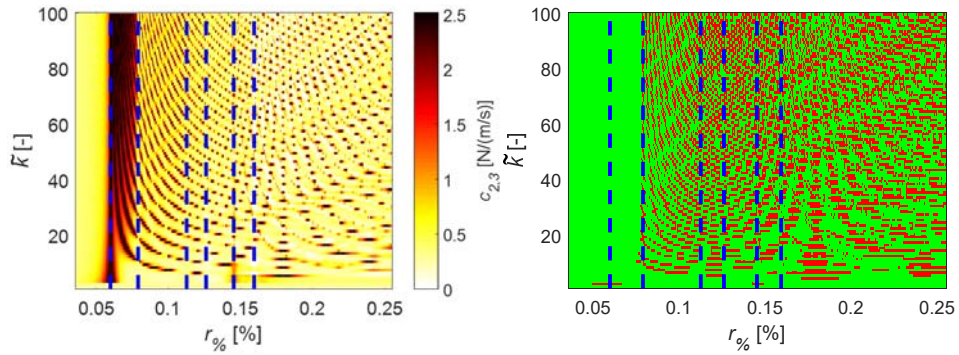
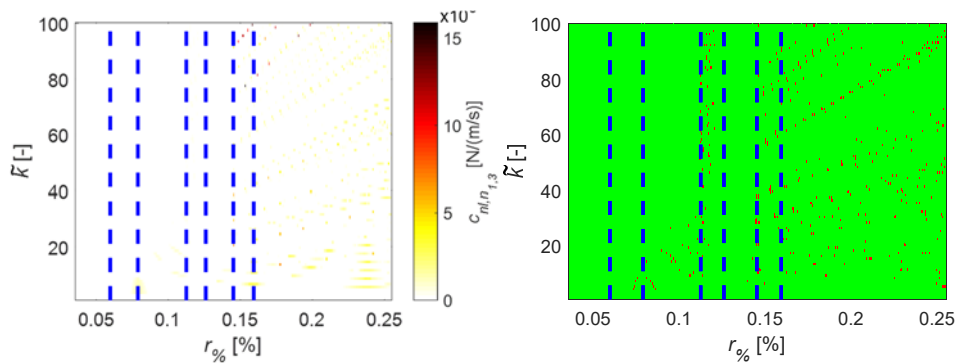
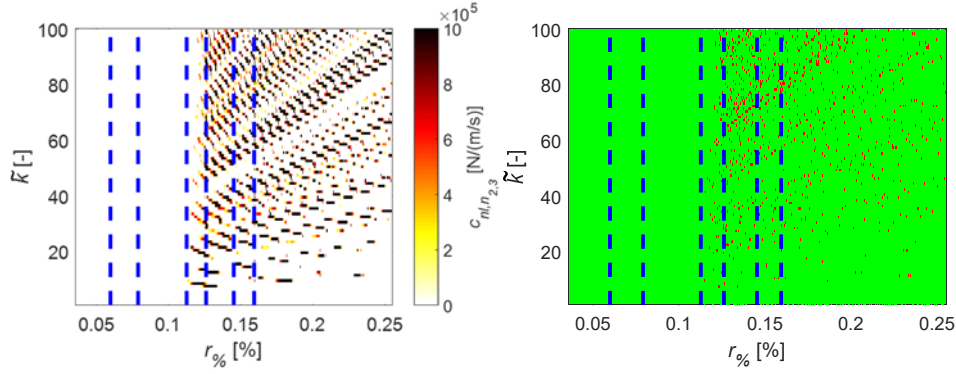


Figure 10.16 - Damping coefficient  $c_2$  : quantification (left) , stability (right).


 Figure 10.17 - Damping coefficient  $c_3^{id}$  : quantification (left) , stability (right).

 Figure 10.18 - Damping coefficient  $c_{1,2}$  : quantification (left) , stability (right).

 Figure 10.19 - Damping coefficient  $c_{2,3}$  : quantification (left) , stability (right).

 Figure 10.20 - Damping coefficient  $c_{nl,1}$  : quantification (left) , stability (right).


 Figure 10.21 - Damping coefficient  $c_{nl,2}$ : quantification (left) , stability (right).

The optimal identified solution  $\mathbf{u}^*$  can be selected looking for  $(r_{\%}^*, \tilde{k}^*)$  satisfying Eq. (4.70). The global stabilisation diagram  $\bar{\mathbf{S}}$ , computed as in Eq. (4.68), and the error map  $\mathbf{E}$ , computed using Eq. (4.69), are shown in Figure 10.22. The identification is globally stable in a region close to the first asymptote, in the same region also the normalised residuum  $E_{\%}$  reaches a minimum value. But in that region not all the three first asymptotes are reached; therefore, the minimum error is found in a region which is spotted globally stable. The optimal identification couple  $(r_{\%}^*, \tilde{k}^*)$  is the one with minimum residuum at  $(r_{\%}^*, \tilde{k}^*) = (45, 0.1171\%)$  and a low inversion error  $E_{\%}^* = 0.3591\%$ , corresponding to the blue cross in Figure 10.22.

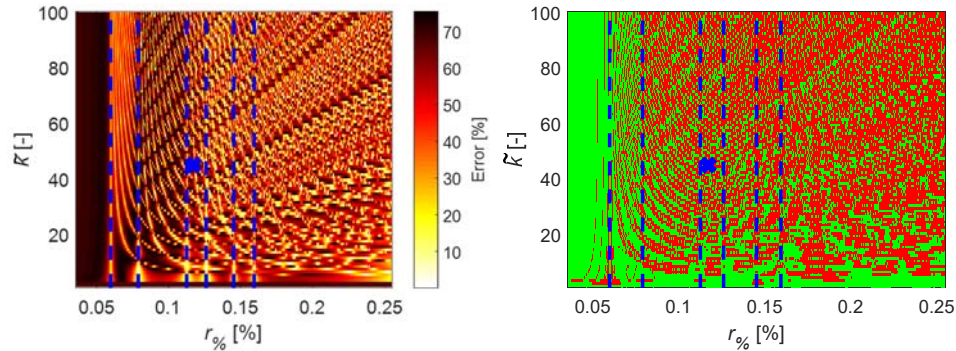
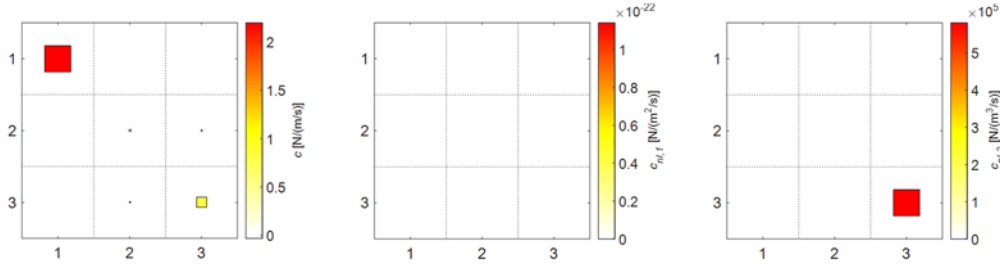


Figure 10.22 - Normalised residuum (left) and global stability diagram (right).

The identified damping matrices are shown in Figure 10.23. The damping coefficient values of the seven layers are reported in Table 10.1. The spatial distribution of the damping is well identified.


 Figure 10.23 - Identified damping matrices:  $C_{lin}$  (left),  $C_{nl,1}$  (middle) and  $C_{nl,2}$  (right).

The SLM extended to nonlinear damping identify a linear viscous damping matrix  $C_{lin}$  with a topology coherent with the expected one. As for the other configuration, a big dissipation on the first DOF and a small the relative damper  $c_{2,3}$  between the second and third DOFs are identified. Finally, the nonlinear damper is identified with a linear coefficient  $c_3^{id} = c_{nl,0} + c_3$  and a quite big second order coefficient  $c_{nl,2}$ . The absolute damper on second DOF  $c_2$  is null as expected, because there is no link between it and the fixed frame. The first order coefficient of the nonlinear damping function  $c_{nl,1}$  result zero, as expected from Eq. (10.6).

 Table 10.2 - Identified damping coefficients values, air-gap  $\Delta = 22$  mm .

Coefficient	Identified [N/(m/s)]
$c_1$	2.1954
$c_2$	0.1416
$c_3$	0.8177
$c_{1,2}$	0.0000
$c_{2,3}$	0.0292
$c_{nl,1}$	0.000 N/(m <sup>2</sup> /s)
$c_{nl,2}$	$5.81 \cdot 10^5$ N/(m <sup>3</sup> /s)

## 10.5 Identification results comparison

The results of the nonlinear damping identification are compared in terms of equivalent damping coefficient  $c_{eq}$ . From Eq. (10.8) it can be defined as:

$$c_{eq} = c_{nl,0} + c_{nl,1} \frac{4}{3\pi} A + c_{nl,2} \frac{1}{4} A^2 \quad (10.14)$$

The  $c_{nl,0}$  cannot be identified alone, but it is identified together with the linear damping coefficients. Because no other dampers are acting on the system, it is assumed to be:

$$c_{nl,0} \approx C_{lin}(3,3) \quad (10.15)$$

The equivalent damping for the two configurations, computed using Eq. (10.14) are shown in Figure 10.24.

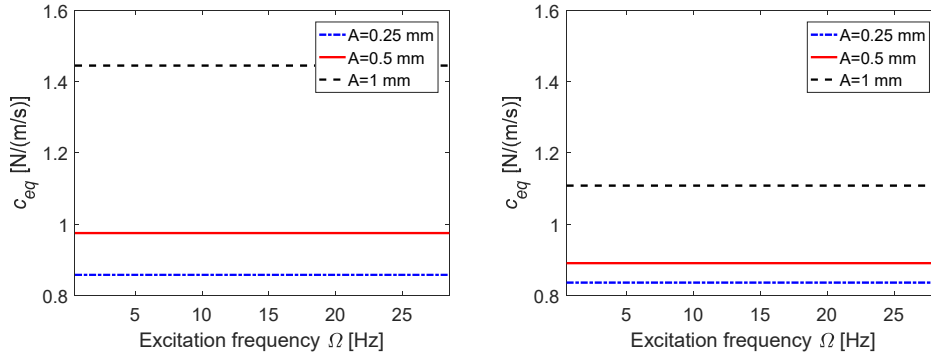


Figure 10.24 - Equivalent identified damping coefficients: configurations  $\Delta = 17$  mm (left) and  $\Delta = 22$  mm (right).

The equivalent damping coefficient  $c_{eq}$  results to be higher when a low air-gap is present between the magnets, as analytically predicted in [201].

The comparison between the coefficients is shown in Table 10.3. The identified linear damping coefficients  $c_{nl,0}$  are almost the same in the two configurations, while the second order damping coefficient  $c_{nl,1}$  is an order of magnitude lower in the configuration with larger air-gap  $\Delta$ .

Table 10.3 - Comparison between identified damping coefficients  $c_{nl,i}$  of the nonlinear damping force.

Coefficient	$\Delta = 17$ mm	$\Delta = 22$ mm
$c_{nl,0}$	0.8175 N/(m/s)	0.8369 N/(m/s)
$c_{nl,1}$	0.000 N/(m <sup>2</sup> /s)	0.000 N/(m <sup>2</sup> /s)
$c_{nl,2}$	$1.25 \cdot 10^6$ N/(m <sup>3</sup> /s)	$5.81 \cdot 10^5$ N/(m <sup>3</sup> /s)

The equivalent damping coefficients  $c_{eq}$  are compared literature values, in Table 10.4 and Figure 10.25.

In [201] Bonisoli et al. shows the identified damping coefficients of an aluminium beam, with dimensions  $w = 30$  mm and thickness  $h = 3$  mm, vibrating in the air-gap between the same couple of permanent magnet used in this chapter.

The global width of the beam is the same, because in the setup under analysis two aluminium beam of width 15 mm vibrates inside two couple of permanent magnets, therefore global frontal area is the same.

The thickness  $h$  is different: 3 mm in the literature values and 2 mm in this chapter. The identified damping coefficients should be slightly lower in this configuration, because the eddy currents are lower in a thinner beam.



The air-gap are also slightly different:  $\Delta = 18$  mm and  $\Delta = 21$  mm in [201] while  $\Delta = 17$  mm and  $\Delta = 22$  mm in the actual work.

Table 10.4 - Comparison of identified  $c_{eq}$  damping values with literature.

Air-gap $\Delta$ [mm]	Identified $c_{eq}$ [N/(m/s)]			Bonisoli et al. [201]
	Nonlinear SLM			
	Amplitude $A$ [mm]			
	0.25	0.5	1	
17	0.8577	0.9752	1.4454	1.48 ( $\Delta$ = 18 mm )
22	0.8359	0.8904	1.1084	1.09 ( $\Delta$ = 21 mm )

The identification condition are different: in [201] only the magnetic field nonlinearity are considered; the oscillation amplitude is not taken into account, since the beam was excited with random force, thus a mean value is obtained for different air-gaps. In this work the amplitude dependent nonlinearity is also considered. The identified damping values using the SLM for nonlinear damping force identification are perfectly coherent with the literature reference values, considering also the differences in the setups.

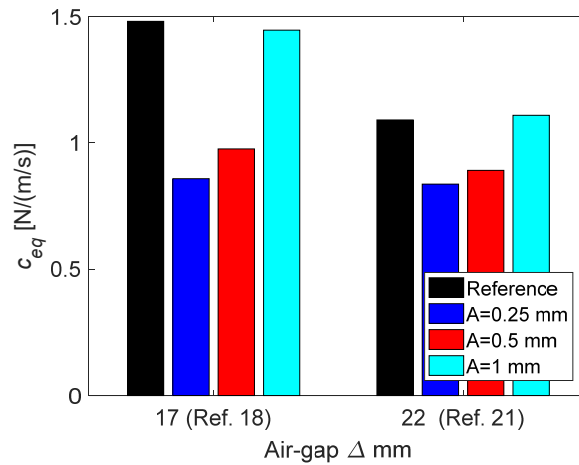


Figure 10.25 - Reference and identified equivalent damping coefficients.

## 10.6 Conclusions

The SLM extend to the identification of nonlinear system was applied in this chapter to the identification of a three DOF test-rig with a magnetic damping nonlinearity as absolute damper on a DOF of the system. The time domain analytical function of the magnetic nonlinearity was derived from literature and its describing function computed. The order of the describing function result to be 2, therefore three sweeps with different amplitude of oscillation across the nonlinearity were performed to measure the data required by the nonlinear SLM.



The nonlinearity is quite soft, however shift in the peaks frequency of the FRF with different oscillation amplitudes are visible.

The magnetic nonlinearity was identified in two configurations, changing the air-gap between the magnets. The identified results are coherent, i.e. the equivalent viscous damping increase increasing the oscillation amplitude and decreasing the air gap.

The identified values were compared to literature identified values, in which the dependence of the damping coefficient from the oscillation amplitude was neglected. The identified values are in good agreement with the reference values. The proposed identification gives more accurate results with respect to the literature, since the actual identification include also the amplitude dependence. This experimental campaign gives encouraging results and validates the SLM extended to nonlinear damping forces.

### **10.7 Identification of nonlinear system and active design of vibrational behaviour**

The direct spatial damping identification of linear and nonlinear system has been experimentally performed on different test-rig using the proposed SLM and SLM extended to nonlinear system identification.

The method gives good result in term of damping identification, localisation and quantification. The three DOF test-rig presented in chapter § 6 has been identified in term of dissipation in several different configuration and the SLM seems a good solution to the first research question of the thesis, even for nonlinear system.

The second research question of the thesis will be developed in the next chapter. Once the system is identified in terms of dissipation, its behaviour is modified by means of input to the system, so that it behaves as convenient, without structural modifications. The aim is to design the vibrational behaviour of systems with non-smooth nonlinearities. The nonlinear configuration of the test-rig will be used to perform the linearisation and active vibration control of the system in the undamped configuration identified in chapter § 7.3.1.

# Chapter 11

## 11. Feedback linearisation of non-smooth nonlinear systems

The system behaviour can be controlled in terms of dissipations to assign a new desired damping layout. The desired pole can be assigned to the system, therefore also natural frequencies can be modified.

In this chapter input-output partial feedback linearisation is demonstrated experimentally for the first time on a system with non-smooth nonlinearity, a laboratory three DOFs lumped mass system with a piecewise-linear spring.

In the tested system the output DOF is located away from the nonlinearity so that the partial feedback linearisation possesses nonlinear internal dynamics. The dynamic behaviour of the linearised part is specified by eigenvalue assignment and an investigation of the zero dynamics is carried out to confirm stability of the overall system.

A tuned numerical model is developed for use in the controller and to produce numerical outputs for comparison with experimental closed-loop results. A new limitation of the feedback linearisation method is discovered in the case of lumped mass systems - that the input and output must share the same DOFs.

The work presented in this chapter is motivated by the need to generalise the experimental validation of feedback linearisation to non-smooth nonlinear systems, beyond the special case of [203], to include the more complicated general case when the zero dynamics are nonlinear.

Partial feedback linearisation is applied to a non-smooth, nonlinear three DOFs mass-spring system. In the present work the structural non-smooth stiffness and damping nonlinearity are located at a different DOF from the input.

A brief explanation of the theory behind input-output feedback linearisation and its applications was presented in § 3.3.2. The extension of feedback

linearisation to non-smooth nonlinear systems and the limitations in the case of lumped mass system are presented in § 11.1.

The test-rig used in this study is presented in § 6.3 with a full description of the system and its main characteristics. In § 11.3, an analytical/numerical model is developed, and experimental tests on the linear and nonlinear configuration of the system, aimed at tuning the model parameters and validating it, are presented. In § 11.4, feedback linearisation is applied theoretically to the system and the stability of the internal dynamics is checked.

Finally, in § 11.5 both experimental and numerical results are presented, including the zero dynamics.

The result presented in this chapter are summarised in [182,203,204]

### 11.1 Feedback linearisation of non-smooth nonlinear systems

The application of the feedback linearisation control to non-smooth nonlinear systems is an area open to research, possibly because the smoothness of the nonlinearity was originally said to be a requirement for the application of feedback linearisation. Tao and Kokotovic [205] proved this constraint to be unnecessary at least in cases where the non-smooth nonlinearity is in the input and has a dead zone, piecewise, backlash or hysteresis characteristic - for these cases they also developed adaptive methods.

The feedback linearisation theory presented in § 3.3.2 was extended for the application in a subclass of non/smooth nonlinear system by Jiffri et al. in [154]

Jiffri et al. [154] developed the theory of complete and partial feedback linearisation to nonlinear aeroelastic systems with structural non-smooth nonlinearity and demonstrated how flutter control of a wing might be achieved using a simulated example. In [203] this theory was applied experimentally to a non-smooth nonlinear system with the nonlinearity at the same DOF as the input, thereby causing the zero dynamics of the system to be linear (i.e. a special case of partial feedback linearisation in which the entire system is linearised).

A condition for the applicability of feedback-linearisation is the continuous differentiability of the transformation matrix  $\mathbf{T}(\mathbf{v})$ , which can be also nonlinear. This is linked to the smoothness of the expressions  $\underline{\mathbf{f}}$  and  $\underline{\mathbf{G}}$ . The smoothness of  $\underline{\mathbf{f}}$  is governed by the smoothness of the nonlinear force  $\mathbf{f}_{nl}(\mathbf{v})$ .

The case of non-smooth nonlinearity  $\mathbf{f}_{nl}(\mathbf{v})$  is now considered. In [154] it is shown as the smoothness of  $\underline{\mathbf{f}}$  can be relaxed, and input-output feedback linearisation can be still applicable.

In the case of structural system,  $\underline{\mathbf{G}}$  is a constant, Eq. (3.110) and the velocity in Eq. (3.107) do not directly depend on the nonlinear force  $\mathbf{f}_{nl}(\mathbf{v})$ .

These special features let to have a transformation matrix  $\mathbf{T}$  which is constant and non-singular, when the displacement  $\mathbf{x}$  are chosen as output. Therefore, the nature of the transformation is not affected by the non-smoothness of the nonlinearity.

If complete input-output feedback linearisation is applied, the entire open-loop dynamics will be replaced by the assigned smooth dynamics. In the case of partial input-output feedback linearisation, the behaviour of the linearised coordinates  $\chi$  will depend on the type of nonlinearity. If the nonlinearity is non-smooth but continuous both displacement and velocity of the linearised coordinates will be smooth. If the nonlinearity is not continuous, the system will present some type of non-smoothness in the global system dynamics. The stable internal dynamics will be affected by the nonlinearity, at non-smooth or discontinuous behaviour could be present until the internal dynamics decay.

### 11.1.1 Limitations for lumped mass systems

A sufficient condition for partial feedback linearisation is that input appears explicitly after differentiating the output a finite number of times, known as the relative degree and denoted by  $r$ .

For reasons of simplicity a single-input single-output (SISO) will be now considered. Then, without loss of generality an  $N$  DOFs lumped mass system with input at the first coordinate may be chosen. The output is assumed to be at the  $\kappa^{\text{th}}$  coordinate and the non-smooth nonlinearity at the  $\pi^{\text{th}}$  coordinate.

Using the nomenclature introduced in § 3.3.2 the expression for the state space model may be re-written as:

$$\underline{\mathbf{f}}(\mathbf{v}) = \left\{ \begin{array}{c} [\mathbf{0} \quad \mathbf{I}] \mathbf{v} \\ -\mathbf{M}^{-1} (\mathbf{K} [\mathbf{I} \quad \mathbf{0}] \mathbf{v} + \mathbf{C} [\mathbf{0} \quad \mathbf{I}] \mathbf{v} + \mathbf{f}_{nl}) \end{array} \right\}; \quad (f_{nl})_{\pi} \neq 0 \quad (11.1)$$

and

$$\underline{\mathbf{G}} = \left\{ \begin{array}{c} \mathbf{0}_{N \times 1} \\ \mathbf{M}^{-1} \mathbf{B} \end{array} \right\}; \quad \mathbf{M}^{-1} = \begin{bmatrix} 1/m_{11} & & & \\ & 1/m_{22} & & \\ & & \ddots & \\ & & & 1/m_{NN} \end{bmatrix}; \quad \mathbf{B} = \begin{pmatrix} 1 \\ 0 \\ \vdots \\ 0 \end{pmatrix}_{N \times 1} \quad (11.2)$$

Thus,

$$\underline{G}_j = 0; \quad \underline{G}_{j=N+1} = 1/m_{11}; \quad j = 1, \dots, 2N \quad (11.3)$$

The presence of the input in the  $i^{\text{th}}$  derivative of the output depends upon the nonzero entries of the term  $\underline{\mathbf{G}} \in \mathbb{R}^{2N \times 1}$ .

Then, by carrying out differentiation of the output:

$$\chi_1 = y = v_{\kappa=1} \quad (11.4)$$

$$\chi_2 = \dot{\chi}_1 = \dot{y} = \dot{v}_{\kappa=1} = v_{N+\kappa=N+1} \quad (11.5)$$

$$\chi_3 = \dot{\chi}_2 = \ddot{\chi}_1 = \ddot{y} = \dot{v}_{N+\kappa=N+1} = \underline{f}_{N+\kappa=N+1}(\mathbf{v}) + \underline{G}_{N+\kappa=N+1}u(t) \quad (11.6)$$

Therefore a transformation matrix  $\mathbf{T}$  can be formed between linear and nonlinear coordinate systems and the first coordinate can be linearised as in Eq. (3.138).

If the DOF of the output is different from the DOF to which the input is delivered ( $\kappa \neq 1$ ), then

$$\chi_1 = y = x_{\kappa} \quad (11.7)$$

$$\chi_2 = \dot{\chi}_1 = \dot{y} = \dot{x}_{\kappa} = x_{N+\kappa} \quad (11.8)$$

$$\chi_3 = \dot{\chi}_2 = \ddot{\chi}_1 = \ddot{y} = \dot{v}_{N+\kappa} = f_{N+\kappa}(\mathbf{v}) + g_{N+\kappa}(\mathbf{v})u(t) = f_{N+\kappa}(\mathbf{v}) \quad (11.9)$$

because  $g_{N+\kappa}(\mathbf{v}) = 0$ .

$$\chi_4 = \dot{\chi}_3 = \frac{\partial}{\partial t}(f_{N+\kappa}(\mathbf{v})) = \frac{\partial}{\partial t} \left( -\frac{1}{m_{\kappa\kappa}} (\mathbf{K}_{\kappa,1:N} [\mathbf{I} \quad \mathbf{0}] \mathbf{v} + \mathbf{C}_{\kappa,1:N} [\mathbf{0} \quad \mathbf{I}] \dot{\mathbf{v}}) \right) + \frac{\partial}{\partial t} \left( -\frac{1}{m_{\kappa\kappa}} f_{nl_{\kappa}} \right) \quad (11.10)$$

If  $\kappa = \pi$  differentiation of the nonlinear term is required and therefore feedback linearisation is not feasible. If  $\kappa \neq \pi$ , then in principle differentiation can continue but the transformation matrix  $\mathbf{T}$  is found not to allow the required separation of the linearised subsystem from the nonlinear internal dynamics, and therefore, once again, feedback linearisation is found not to be feasible.

Therefore, in a lumped-mass system, with no inertial coupling, it is necessary to have the input at the same DOFs as the output for partial feedback linearisation.

## 11.2 Active control experimental setup

The state space feedback linearisation extended to non-smooth nonlinearities is performed on the nonlinear configuration of the three DOFs test rig described in § 6.3. The real time linearisation control was implemented in dSPACE using a nested controller with a model-based outer loop that provides an actuator command, applied in an inner proportional derivative (PD) control loop that sets the measured force applied at the first DOF. Three laser displacement sensors (Keyence LK-500 and LK-G402 and microepsilon OptoNCDT 1402-100) were arranged to measure the horizontal displacements of the three masses and provide the dSPACE inputs, Figure 11.1.

Control actuation was achieved using an LDS V406 permanent magnet shaker with an LDS PA100 amplifier, Figure 11.1. The shaker force was measured by a PCB 208C02 load cell with a PCB 442C04 ICP signal conditioner.

The system was instrumented separately for:

- open-loop modal hammer test on linear system (setting springs removed);
- stepped sine of the open-loop nonlinear system
- closed-loop modal hammer test on linearised system (with setting springs).

The first two of these tests were required to tune the numerical model used in the third test. The tests were carried out using an LMS SCADAS III, an instrumented hammer PCB 086C03 and three Kistler accelerometers KShear 8728A500.

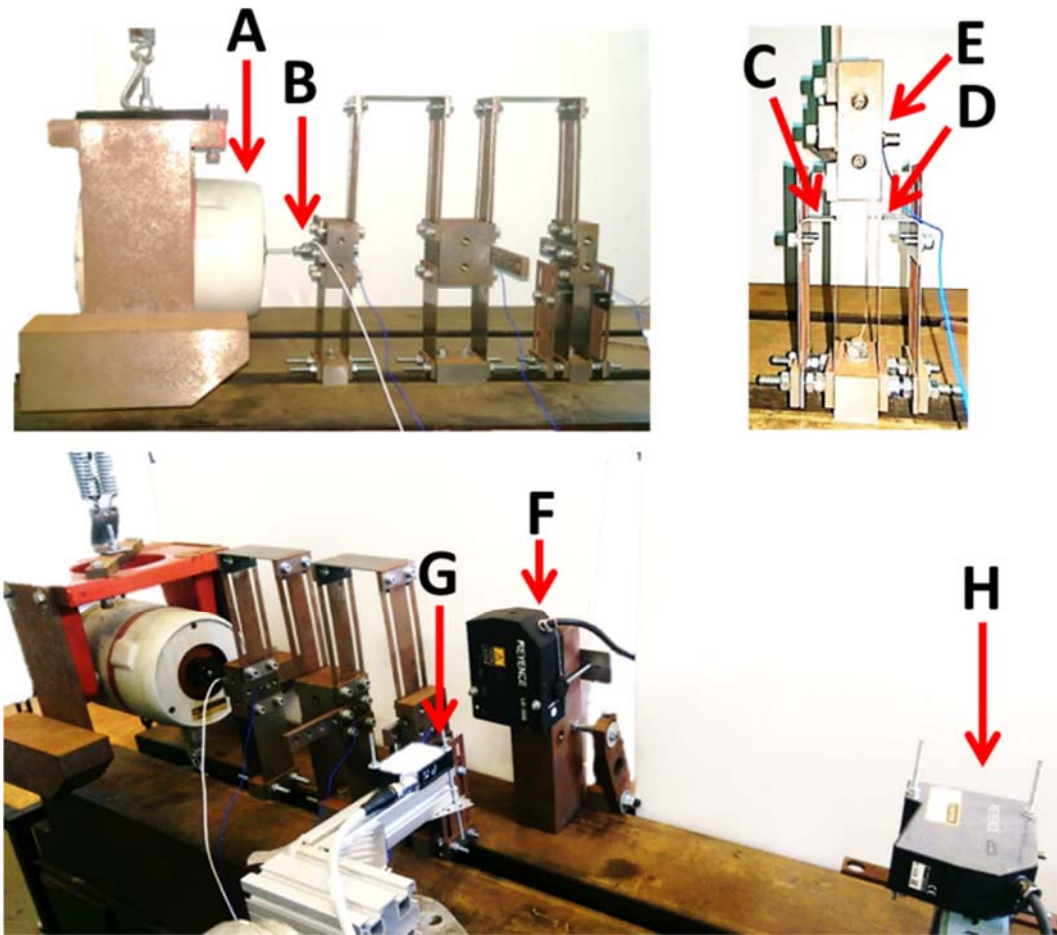


Figure 11.1 - Close-loop experimental setup: A) suspended shaker, B) Load cell, C) left gap  $g_1$ , D) right gap  $g_2$ , E) Accelerometers (one for each DOF), F) laser on  $x_1$ , G) laser on  $x_2$  and H) laser on  $x_3$ .

During closed-loop control the external input was provided by hammer excitation and modal properties of the linearised system were determined. The shaker was used to produce the linearising control input  $\mathbf{u}(t)$  in real time.

Displacements were measured using the laser sensors and velocities obtained by differentiation of the filtered displacement signals. Both displacement and force signals were filtered using a second-order Butterworth filter with a cut-off frequency of  $f_{co} = 21 \text{ Hz}$ , to remove high frequency noise and disturbances but without removing frequencies components related to the natural frequencies  $f_n$  of the system or to the desired natural frequency  $f_{n,d}$  of the linearised portion, which is at maximum  $f_{n,d} = 19 \text{ Hz}$ .

### 11.3 System model

The test rig presented in § 6.3 may be represented schematically as the three DOFs lumped parameter system shown in Figure 11.2. The masses are assumed to be rigid and the springs massless. The nonlinear spring is located at the third mass, while the input is delivered at the first DOF.

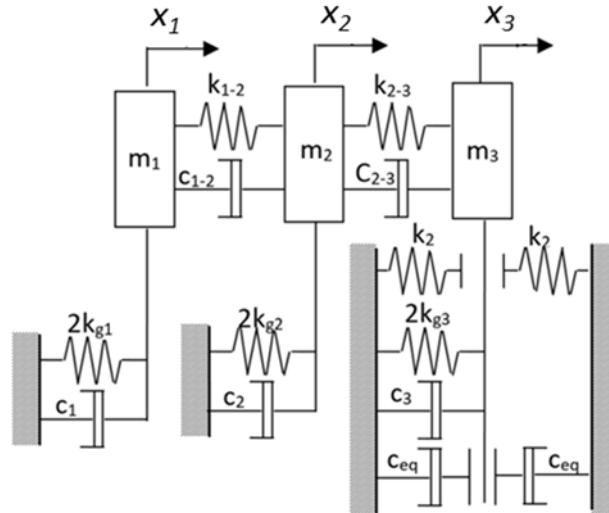


Figure 11.2 - Schematic of the three DOFs non-smooth nonlinear system.

In theory the nonlinear spring introduces piecewise nonlinear behaviour in the stiffness, but in practice nonlinear damping is also present, because of friction and impacts.

The equation of motion may be written in the time domain as:

$$\mathbf{M}\ddot{\mathbf{x}} + \mathbf{C}\dot{\mathbf{x}} + \mathbf{K}\mathbf{x} + \mathbf{f}_{Knl} + \mathbf{f}_{Cnl} = \mathbf{f}(t) \quad (11.11)$$

where  $\mathbf{x}$  contains the displacements associated with the three DOFs,  $\mathbf{M}$ ,  $\mathbf{C}$  and  $\mathbf{K}$  are the mass, viscous damping and stiffness matrices respectively,  $\mathbf{f}_{Knl}$  is the vector of nonlinear forces due to the nonlinear stiffness,  $\mathbf{f}_{Cnl}$  is the vector of

nonlinear forces due to nonlinear damping and  $\mathbf{f}(t)$  is the excitation applied to the system.

The structure and parameters pertaining to the above quantities may be expressed in the form:

$$\begin{aligned} \mathbf{x} &= \{x_1 \quad x_2 \quad x_3\}^T \\ \dot{\mathbf{x}} &= \{\dot{x}_1 \quad \dot{x}_2 \quad \dot{x}_3\}^T \quad \mathbf{f}(t) = \begin{Bmatrix} 1 \\ 0 \\ 0 \end{Bmatrix} u(t) \quad \mathbf{M} = \text{diag}(m_1, m_2, m_3) \\ \ddot{\mathbf{x}} &= \{\ddot{x}_1 \quad \ddot{x}_2 \quad \ddot{x}_3\}^T \end{aligned} \quad (11.12)$$

$$\mathbf{K} = \begin{bmatrix} 2k_{g,1} + k_{12} & -k_{12} & 0 \\ -k_{12} & 2k_{g,2} + k_{12} + k_{23} & -k_{23} \\ 0 & -k_{23} & 2k_{g,3} + k_{23} \end{bmatrix}; \quad \mathbf{C} = \alpha \mathbf{M} + \beta \mathbf{K};$$

The nonlinear spring stiffness, shown in Figure 6.6, may be written formally defined as:

$$k_{g,nl} = \begin{cases} 2k_{g,3} + k_2 & x_3 \leq -g_1 \\ 2k_{g,3} & -g_1 \leq x_3 \leq g_2 \\ 2k_{g,3} + k_2 & x_3 \geq g_2 \end{cases} \quad (11.13)$$

and the nonlinear stiffness force in Eq. (11.11) is then given by:

$$\mathbf{f}_{Knl} = \begin{cases} \mathbf{K}_{nl}(\mathbf{x} - \{0, 0, -g_1\}^T) & \text{if } x_3 < -g_1 \\ \mathbf{0} & \text{if } -g_1 \leq x_3 \leq g_2 \\ \mathbf{K}_{nl}(\mathbf{x} - \{0, 0, g_2\}^T) & \text{if } x_3 > g_2 \end{cases}; \quad \mathbf{K}_{nl} = \begin{bmatrix} 0 & 0 & 0 \\ 0 & 0 & 0 \\ 0 & 0 & k_2 \end{bmatrix} \quad (11.14)$$

Energy is dissipated in two ways, firstly as friction between the slider and the grounding spring, so that the damping is proportional to the nonlinear stiffness force. Then, secondly there is energy lost at impact with a portion of the total momentum passing into the higher vibration modes of the system. The nonlinear damping force is modelled equivalently by taking into consideration the physical assumptions just described; it acts only when the slider and the setting spring are in contact and may be written as:

$$f_{Cnl,3} = \varepsilon |f_{Knl,3}| \text{sgn}(\dot{x}_3) \quad (11.15)$$

where  $\varepsilon$  is a correction factor to take account of friction and the impact restitution factor, while  $|f_{Knl,3}|$  is the contact force. The nonlinear damping becomes:



$$\mathbf{f}_{Cnl} = \mathbf{C}_{nl} |\mathbf{f}_{Knl}| \text{sgn}(\dot{x}_3); \quad \mathbf{C}_{nl} = \begin{bmatrix} 0 & 0 & 0 \\ 0 & 0 & 0 \\ 0 & 0 & \varepsilon \end{bmatrix} \quad (11.16)$$

Tuning of the system parameters was found to be necessary to converge the model upon the linear and nonlinear dynamics of the system. The linear viscous damping matrix  $\mathbf{C}$  is chosen as a classical dissipation proportional to mass  $\mathbf{M}$  and stiffness  $\mathbf{K}$  matrices. This because the linear system is slightly different with respect to the one identified in § 7.3.1. The dampers are removed; hence masses are different. The system is almost undamped and as seen in § 7.3.1 the identification of dissipation in very low damped system with SLM is affected not very small inversion error. Moreover, using a non-proportional viscous damping identified matrix adds a pointless complication to the control aim.

### 11.3.1 Tuning the linear parameters

The set of linear parameters consists of the three masses of the system, the stiffness of the coupling and grounding springs and the proportional coefficients of the viscous damping model. An experimental hammer test was carried out on the linear system, with the setting springs removed, to determine the complete experimental receptance matrix with a frequency resolution of 0.05 Hz and averaging over five impulses using instrumented hammer. Natural frequencies  $\omega_{n,i}$ , damping ratios  $\zeta_i$  and mode shapes  $\phi_i$  were extracted using the PolyMAX algorithm [175]. An optimisation procedure using an Immune Network Model Optimisation method [206] was used to minimise the difference between the experimental linear FRM  $\mathbf{H}^{Exp}(\Omega)$  and those produced by the tuned numerical model  $\mathbf{H}_{syn}(\Omega)$ , computed using Eq. (5.1) in the range 5 ÷ 15 Hz. Ten independent parameters, the three masses ( $m_1$ ,  $m_2$  and  $m_3$ ), five stiffnesses ( $k_{g,1}$ ,  $k_{g,2}$ ,  $k_{g,3}$ ,  $k_{12}$  and  $k_{23}$ ) and two proportional viscous coefficients ( $\alpha$  and  $\beta$ ), were optimised using the objective function  $f$ :

$$f = \sum_{i=1}^3 \sum_{j=1}^3 \sum_k (FRF_{i,j,num} - FRF_{i,j,exp})^2 \quad (11.17)$$

where  $i$  and  $j$  denote the DOF of the system and  $k$  is the spectral-line index.

The optimised parameters are shown in Table 11.1, where  $(\tilde{\bullet})$  denotes a nominal parameter value and  $(\bullet)_i = g_{c,i}(\tilde{\bullet})_i$  is a tuned (optimised) parameter.

The correction factors,  $g_{c,i}$ , close to unitary value, are deemed to be physical.

Table 11.1 - Parameters of the linear system.

Parameter		Correction factor	
$\tilde{k}_{g,1}$	3617.4 N/m	$g_{c,1}$	0.87002700422
$\tilde{k}_{g,2}$	3617.4N/m	$g_{c,2}$	0.87688563969
$\tilde{k}_{g,3}$	3617.4N/m	$g_{c,3}$	1.10706672391
$\tilde{k}_{12}$	1735.5 N/m	$g_{c,4}$	0.60358398562
$\tilde{k}_{23}$	1735.5 N/m	$g_{c,5}$	0.72601010491
$\tilde{m}_1$	1.3297 kg	$g_{c,6}$	0.89057572011
$\tilde{m}_2$	2.4234 kg	$g_{c,7}$	0.95570410127
$\tilde{m}_3$	0.9065 kg	$g_{c,8}$	1.29994609954
$\tilde{\alpha}$	0.2605	$g_{c,9}$	0.92654104990
$\tilde{\beta}$	2.7948e-5	$g_{c,10}$	1.00575218718

The springs are found to be slightly softer than the numerical stiffnesses and the masses of the springs, neglected in the analysis, are spread across the three lumped masses of the system. The FRM, shown in Figure 11.3, confirm that the system is indeed linear and the tuned model is in very good agreement with experimental results, showing only small discrepancies at very low levels of response. Figure 11.4 shows that natural frequencies determined from the tuned model are very close to measured values and mode shapes are in excellent agreement (MAC > 99.5%).

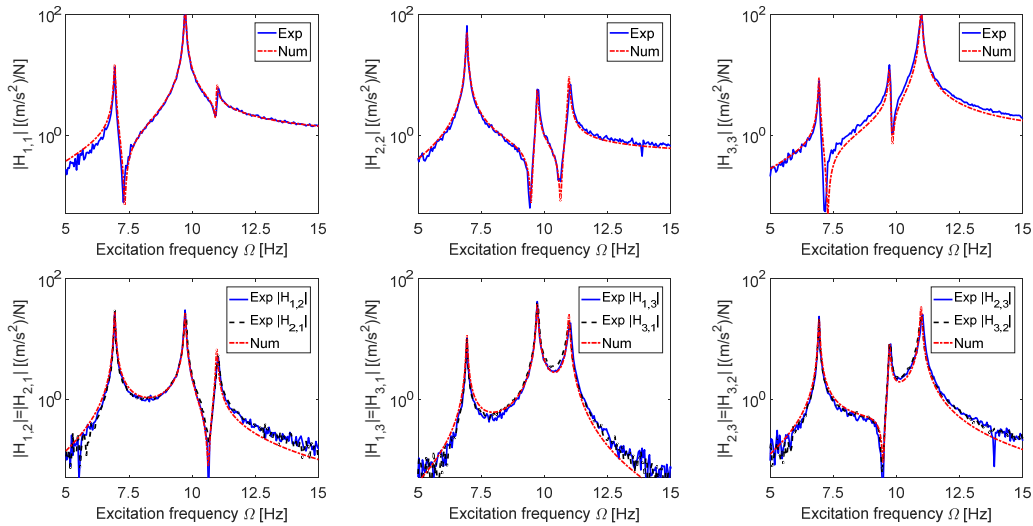


Figure 11.3 - Experimental and numerical FRM comparison.

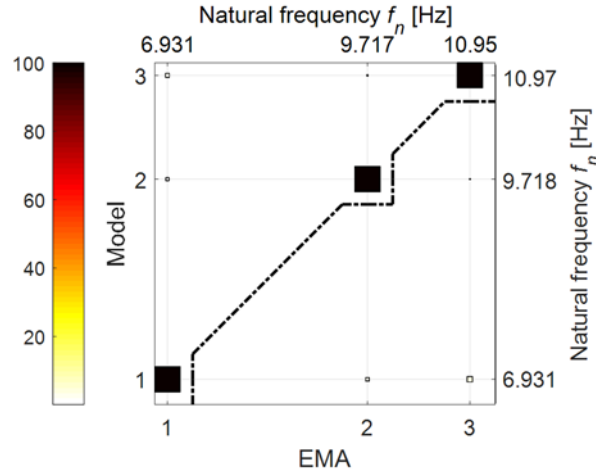


Figure 11.4 - MAC between numerical and experimental mode shapes.

### 11.3.2 Tuning the nonlinear parameters

The parameters  $k_2$  and  $\varepsilon$  concerning the nonlinear stiffness and damping forces were tuned using data from stepped sine tests, carried out forwards and backwards in the range  $5 \div 15$  Hz in steps of 0.05 Hz.

Constant-amplitude  $f_0$  force excitation was delivered by a suspended and balanced shaker, with different constant amplitudes for each of four experiments performed. The results obtained from each experiment were averaged over three tests at the same level of force amplitude.

The effect of the hardening nonlinearity is clear in the FRFs  $\mathbf{H}_{1,3}$  shown in Figure 11.5. The excitation force was controlled to remain within a band of  $\pm 0.05$  N with respect to the desired value.

When the force amplitude increases, the peak of the third mode becomes increasingly distorted, the resonant amplitude decreases and the jump frequency increases. Minor peaks at around 8 Hz, which do not appear in the linear test, are the effect of the shaker added mass linked to the system through the stinger [207].

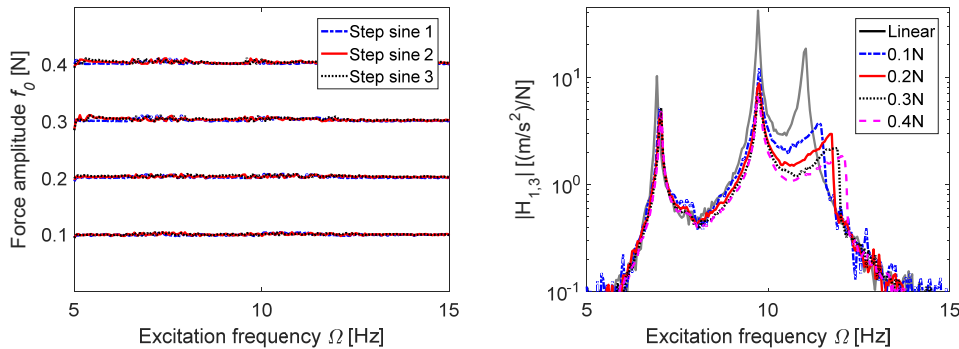


Figure 11.5 - Nonlinear experimental FRF for different levels of excitation: excitation force amplitude (left), nonlinear system responses (right).

Numerical nonlinear FRFs were obtained from the envelope of the time domain response of the system, excited at the first DOF with a sine-sweep in which the excitation frequency  $\Omega(t)$  varied linearly with time, but slowly compared to the natural periods of the system.

The FRFs were found to be sensitive to the nonlinear parameters only in the frequency range of the third mode, most affected by the nonlinear DOF.

The jump frequency is mainly influenced by the coefficient  $\varepsilon$  and by increasing  $\varepsilon$  the jump was found to occur at lower frequencies as a result of increased damping. The setting-spring stiffness  $k_2$  was found to affect the slope of the FRFs around the nonlinear mode and the onset of nonlinearity was determined according to the sizes of the gaps  $g_1$  and  $g_2$ , measured using a feeler gauge. Manually tuned parameters  $\varepsilon = 0.3954$ ,  $k_2 = 1722.6$  N were found to produce numerical FRM in very close agreement with measured values.

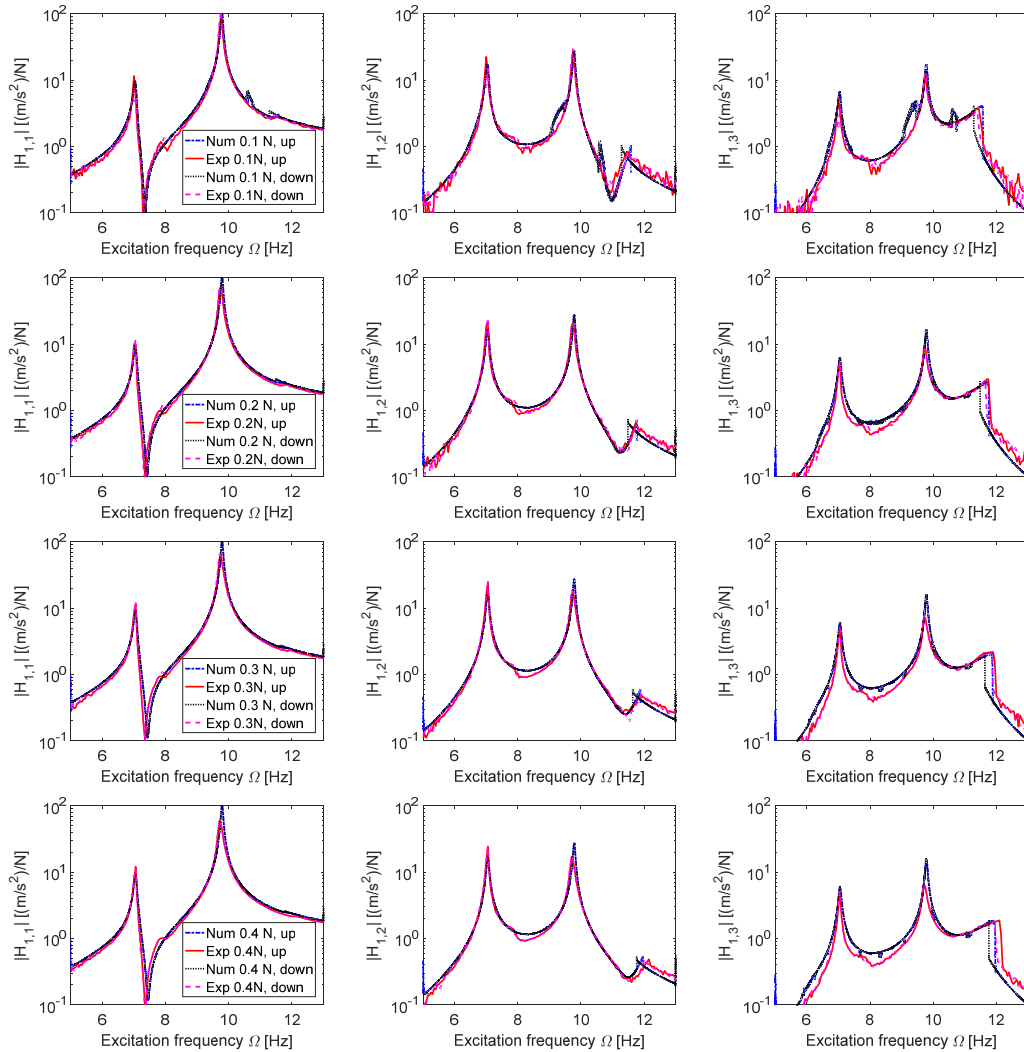


Figure 11.6 - Experimental vs. numerical FRFs, changing force amplitude:  $f_0 = 0.1$  N -1<sup>st</sup> row,  $f_0 = 0.2$  N -2<sup>nd</sup> row,  $f_0 = 0.3$  N -3<sup>rd</sup> row,  $f_0 = 0.4$  N -4<sup>th</sup> row.

The comparison between experimental and numerical FRFs obtained with both upward and downward stepped-sines at four different levels of excitation is shown in Figure 11.6. The FRF obtained for downward stepped-sine tests are very similar to those obtained during upward excitation; some differences are visible only in the jump frequencies, as is usual in nonlinear hardening systems. The comparison between experimental and numerical results confirms that the mathematical model is sufficiently accurate to describe the nonlinear behaviour of the system.

## 11.4 Application of partial feedback linearisation

The theory of feedback linearisation for systems with non-smooth nonlinearity, presented in § 11.1, is applied for the linearisation of the system presented in § 6.3.

The system under analysis is a lumped mass system, therefore the partial input output feedback linearisation is feasible only if the output and the input are the same DOF, as shown in § 11.1.1.

The nonlinear system described in Eq. (11.11) may be cast in first order form:

$$\dot{\mathbf{v}} = \underline{\mathbf{f}}(\mathbf{v}) + \underline{\mathbf{G}}u(t) \quad (11.18)$$

where

$$\begin{aligned} \underline{\mathbf{f}}(\mathbf{v}) &= \left\{ \begin{bmatrix} \mathbf{0} & \mathbf{I} \end{bmatrix} \mathbf{v} \\ -\mathbf{M}^{-1} \left( \begin{bmatrix} \mathbf{K} & \mathbf{C} \end{bmatrix} \mathbf{v} + \mathbf{f}_{Knl} \left( \begin{bmatrix} \mathbf{I} & \mathbf{0} \end{bmatrix} \mathbf{v} \right) + \mathbf{f}_{Cnt} (v_3, v_6) \right) \end{bmatrix} \right\} \\ \underline{\mathbf{G}} &= \left\{ \begin{bmatrix} \mathbf{0}_{(3 \times 1)} \\ \mathbf{M}^{-1} \mathbf{B} \end{bmatrix} \right\}; \quad \mathbf{B} = \begin{pmatrix} 1 \\ 0 \\ 0 \end{pmatrix} \end{aligned} \quad (11.19)$$

The displacement at the first DOF,  $x_1 = v_1$ , is chosen as the output  $y$ , for the input-output linearisation procedure, while the nonlinearity is located in the third DOF.

$$y = x_1 = v_1 \quad (11.20)$$

The complete set of equations representing the partially linearised system is obtained by combining the output equation with its  $r$  time-derivatives, where  $r$  is the relative degree of the SISO system, i.e. the number of times it is necessary to differentiate the output before the input term appears explicitly. Denoting the coordinates of the linearised system as  $\chi_{i=1,2}$ :

$$\chi_1 = y = v_1 \quad (11.21)$$

$$\chi_2 = \dot{\chi}_1 = \dot{y} = \dot{v}_1 = v_4 \quad (11.22)$$

$$\dot{\chi}_2 = \ddot{\chi}_1 = \ddot{y} = \ddot{v}_1 = \dot{v}_4 = \underline{f}_4(\mathbf{v}) + \underline{G}_4 u(t) \quad (11.23)$$

where  $\underline{f}_4(\mathbf{v})$  and  $\underline{G}_4 \neq 0$ , are the 4<sup>th</sup> rows of the vectors  $\underline{\mathbf{f}}(\mathbf{v})$  and  $\underline{\mathbf{G}}$  respectively. Thus, the relative degree of the system is  $r = 2$ , from which it is evident that the linearisation of the system is partial because  $r$  is less than the dimension of the state vector  $\mathbf{v}$ .

The transformation matrix  $\mathbf{T}_{pl}$  between the linear  $\chi$  and nonlinear systems of coordinates  $\mathbf{v}$  may be obtained from Eq. (11.21) and Eq. (11.22) as:

$$\begin{Bmatrix} \chi_1 \\ \chi_2 \end{Bmatrix} = \mathbf{T}_{pl} \mathbf{v} = \begin{bmatrix} 1 & 0 & 0 & 0 & 0 & 0 \\ 0 & 0 & 0 & 1 & 0 & 0 \end{bmatrix} \mathbf{v} \quad (11.24)$$

The system in linear coordinates becomes:

$$\begin{Bmatrix} \dot{\chi}_1 \\ \dot{\chi}_2 \end{Bmatrix} = \begin{bmatrix} 0 & 1 \\ 0 & 0 \end{bmatrix} \begin{Bmatrix} \chi_1 \\ \chi_2 \end{Bmatrix} + \begin{Bmatrix} 0 \\ 1 \end{Bmatrix} \bar{u}(t); \quad \bar{u}(t) = f_4(\mathbf{v}) + g_4(\mathbf{v})u(t) \quad (11.25)$$

where  $\bar{u}(t)$  is the artificial input, which may be chosen to specify the dynamics of the linearised system by eigenvalue assignment:

$$\bar{u}(t) = \varsigma_1 \chi_1 + \nu_1 \chi_2 = -\omega_{n,d}^2 \chi_1 - 2\zeta_d \omega_{n,d} \chi_2 \quad (11.26)$$

where  $\omega_{n,d}$  and  $\zeta_d$  are the desired natural frequency and damping ratio of the linearised DOF. It is found by substituting Eq. (11.26) into Eq. (11.25) that:

$$\begin{Bmatrix} \dot{\chi}_1 \\ \dot{\chi}_2 \end{Bmatrix} = \begin{bmatrix} 0 & 1 \\ -\omega_{n,d}^2 & -2\zeta_d \omega_{n,d} \end{bmatrix} \begin{Bmatrix} \chi_1 \\ \chi_2 \end{Bmatrix} \quad (11.27)$$

### 11.4.1 Internal dynamics

It is generally not possible to control the entire dynamics of a MDOF system using a single output. In the present case the system described in Eq. (11.27) has dimension 2 whereas the full system has dimension 6. Thus, there remains an unlinearised portion of dimension 4, which represent the system internal dynamics.

The full transformation matrix  $\mathbf{T}$ , where  $\chi = \mathbf{T} \mathbf{v}$ , should be chosen under the conditions (a) that it is non-singular and (b) the dynamics associated with the additional co-ordinates are orthogonal to  $\underline{\mathbf{G}}$ . The latter condition ensures that the internal dynamics are obtained in the normal form, where the system inputs do not appear.

A matrix  $\mathbf{T}$  satisfying these conditions is given by Eq. (3.138):

$$\mathbf{T} = \begin{bmatrix} 1 & 0 & 0 & 0 & 0 & 0 \\ 0 & 0 & 0 & 1 & 0 & 0 \\ 0 & 1 & 0 & 0 & 0 & 0 \\ 0 & 0 & 1 & 0 & 0 & 0 \\ 0 & 0 & 0 & 0 & 1 & 0 \\ 0 & 0 & 0 & 0 & 0 & 1 \end{bmatrix} \quad (11.28)$$

The nonlinear internal dynamics in linearised coordinates  $\chi_{id}$  is written as:

$$\dot{\chi}_{id} = \begin{Bmatrix} \dot{\chi}_3 \\ \dot{\chi}_4 \\ \dot{\chi}_5 \\ \dot{\chi}_6 \end{Bmatrix} = \begin{bmatrix} 0 & 0 & 0 & 0 & 1 & 0 \\ 0 & 0 & 0 & 0 & 0 & 1 \\ \frac{k_{1,2}}{m_2} & -\frac{c_{2,1}}{m_2} & -\frac{2k_{g,2} + k_{1,2} + k_{2,3}}{m_2} & \frac{k_{2,3}}{m_2} & -\frac{c_{2,2}}{m_2} & -\frac{c_{2,3}}{m_2} \\ 0 & -\frac{c_{3,1}}{m_3} & \frac{k_{2,3}}{m_3} & -\frac{k_{2,3} + 2k_{g,3}}{m_3} & -\frac{c_{3,2}}{m_3} & -\frac{c_{3,3}}{m_3} \end{bmatrix} \begin{Bmatrix} \chi_1 \\ \chi_2 \\ \chi_3 \\ \chi_4 \\ \chi_5 \\ \chi_6 \end{Bmatrix} + \quad (11.29)$$

$$+ [0 \ 0 \ 0 \ -1/m_3]^T (f_{Knl_3}(\chi_4) + f_{Cnl_3}(\chi_4, \dot{\chi}_4))$$

where  $c_{i,j}$  is the element located at  $i^{\text{th}}$  row and  $j^{\text{th}}$  column of the viscous damping matrix  $\mathbf{C}$ .

The so-called zero dynamics are found by setting to zero the coordinates  $\chi_1$  and  $\chi_2$ , corresponding to the linearised state variables:

$$\dot{\chi}_{zd} = \begin{Bmatrix} \dot{\chi}_3 \\ \dot{\chi}_4 \\ \dot{\chi}_5 \\ \dot{\chi}_6 \end{Bmatrix} = \begin{bmatrix} 0 & 0 & 1 & 0 \\ 0 & 0 & 0 & 1 \\ -\frac{2k_{g,2} + k_{1,2} + k_{2,3}}{m_2} & \frac{k_{2,3}}{m_2} & -\frac{c_{2,2}}{m_2} & -\frac{c_{2,3}}{m_2} \\ \frac{k_{2,3}}{m_3} & -\frac{k_{2,3} + 2k_{g,3}}{m_3} & -\frac{c_{3,2}}{m_3} & -\frac{c_{3,3}}{m_3} \end{bmatrix} \begin{Bmatrix} \chi_3 \\ \chi_4 \\ \chi_5 \\ \chi_6 \end{Bmatrix} + \quad (11.30)$$

$$+ [0 \ 0 \ 0 \ -1/m_3]^T (f_{Knl_3}(\chi_4) + f_{Cnl_3}(\chi_4, \dot{\chi}_4))$$

Stability of the complete system is ensured when the zero dynamics are stable. Proof of the stability of the zero dynamics may be found in § 11.4.2.

A numerical demonstration of the stability is shown in Figure 11.7, obtained solving Eq. (11.30) for different initial conditions.

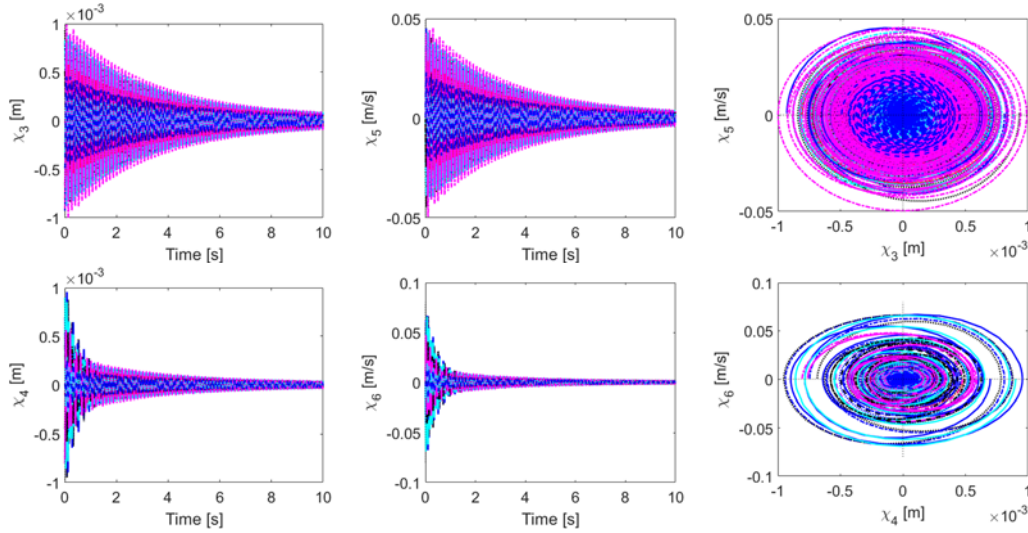


Figure 11.7 - Several numerical simulations of the zero dynamics.

### 11.4.2 Stability of the zero dynamics

The application of partial feedback linearisation requires stability of the zero dynamics for the overall stability of the system. A physical argument can be made in the present case to support the proposition that the system is stable.

The piecewise-linear nature of the system means that if its displacement lies outside the central region  $-g_1 < \chi_4 < g_2$ , then it will be driven within that region when enough energy has been dissipated through damping. Once inside the central region the system is linear with a zero-equilibrium state.

However, for purposes of completeness a brief mathematical derivation will now be provided.

The zero dynamics of Eq. (11.30) may be written as:

$$\dot{\chi}_{zd} = \mathbf{A}\chi_{zd} + \mathbf{b}f_{nl} \quad (11.31)$$

with the obvious definition of matrix  $\mathbf{A}$ , vectors  $\mathbf{b}$  and  $f_{nl}$ .

The equilibrium points of Eq. (11.31) are found that satisfy:

$$\mathbf{A}\chi_{eq} + \mathbf{b}f_{nl} = \mathbf{0} \quad (11.32)$$

The nonlinearity is piecewise linear, so that

$$f_{nl} = \begin{cases} k_2(\chi_4 - (-g_1)) & \chi_4 < -g_1 \\ 0 & -g_1 < \chi_4 < g_2 \\ k_2(\chi_4 - g_2) & \chi_4 > g_2 \end{cases} \quad (11.33)$$

Using the substitution  $\chi_4 = \mathbf{e}_2^T \chi_{eq}$  and  $\mathbf{e}_2 = \mathbf{I}_{(.,2)}^{4 \times 4}$ :



$$f_{nl} = \begin{cases} k_2 \mathbf{e}_2^T \boldsymbol{\chi}_{eq} + k_2 g_1 & \chi_4 < -g_1 \\ 0 & -g_1 < \chi_4 < g_2 \\ k_2 \mathbf{e}_2^T \boldsymbol{\chi}_{eq} - k_2 g_2 & \chi_4 > g_2 \end{cases} \quad (11.34)$$

The equilibrium point must be found in each of the three regions.

In the central region,  $-g_1 < \chi_4 < g_2$ , from Eq. (11.31) and Eq. (11.33):

$$\mathbf{A} \boldsymbol{\chi}_{eq} = \mathbf{0} \quad (11.35)$$

Since  $\mathbf{A}$  is full rank, then,

$$\boldsymbol{\chi}_{eq} = \mathbf{0} \quad (11.36)$$

In the first outer region,  $\chi_4 < -g_1$ , from Eq. (11.31) and Eq. (11.33)

$$\mathbf{A} \boldsymbol{\chi}_{eq} + \mathbf{b} (k_2 \mathbf{e}_2^T \boldsymbol{\chi}_{eq} + k_2 g_1) = \mathbf{0} \quad (11.37)$$

$$\boldsymbol{\chi}_{eq} = -[\mathbf{A} + \mathbf{b} k_2 \mathbf{e}_2^T]^{-1} \mathbf{b} k_2 g_1 \quad (11.38)$$

This leads to an equilibrium solution

$$\boldsymbol{\chi}_{eq} = -\{0.0788 \quad 0.2606 \quad 0 \quad 0\}^T g_1 \quad (11.39)$$

It is clear that  $-0.2606 > -1$  and therefore there is not acceptable in the domain  $\chi_4 < -g_1$ .

And the second outer region,  $\chi_4 > g_2$ , from Eq. (11.31) and Eq. (11.33):

$$\mathbf{A} \boldsymbol{\chi}_{eq} + \mathbf{b} (k_2 \mathbf{e}_2^T \boldsymbol{\chi}_{eq} - k_2 g_2) = \mathbf{0} \quad (11.40)$$

$$\boldsymbol{\chi}_{eq} = [\mathbf{A} + \mathbf{b} k_2 \mathbf{e}_2^T]^{-1} \mathbf{b} k_2 g_2 \quad (11.41)$$

This leads to:

$$\boldsymbol{\chi}_{eq} = \{0.0788 \quad 0.2606 \quad 0 \quad 0\}^T g_2 \quad (11.42)$$

It is clear that  $0.2606 < 1$  and therefore the solution is not acceptable in the domain  $\chi_4 > g_2$ .

The stability of each of the three equilibrium points in each of the three ranges was investigated in [154]. They discovered theoretically and in numerous simulations that the two non-zero equilibria were stable only in case of zero stiffness in the central region (i.e. free play). Otherwise, as in the present case, the two non-zero equilibria were found to be points of neutral stability.

Thus, the only equilibrium point to be considered is  $\chi_{eq} = \mathbf{0}$  and, since the zero dynamics are non-smooth, its stability will be analysed with a general Lyapunov approach for non-smooth systems [208],

$$V = \frac{1}{2} \chi_{zd}^T \mathbf{P} \chi_{zd}; \quad \mathbf{P} \succ 0, \quad \mathbf{P}^T = \mathbf{P} \quad (11.43)$$

It may be shown using the calculus of the Filippov differential inclusion [209], applied in non-smooth feedback linearisation, as in [154], that

$$\dot{V} = \chi_{zd}^T \mathbf{P} (\mathbf{A} \chi_{zd} + \mathbf{b} f_{nl}) \quad (11.44)$$

In the three regions Eq. (11.44) can be expressed as:

$$\dot{V} = \begin{cases} \chi_{zd}^T \mathbf{P} (\mathbf{A} \chi_{zd} + \mathbf{b} \{k_2 [\chi_4 - (-g_1)] + \varepsilon \operatorname{sgn}(\chi_6) |k_2 [\chi_4 - (-g_1)]|\}) \\ \chi_{zd}^T \mathbf{P} \mathbf{A} \chi_{zd} \\ \chi_{zd}^T \mathbf{P} (\mathbf{A} \chi_{zd} + \mathbf{b} [k_2 (\chi_3 - g_2) + \varepsilon \operatorname{sgn}(\chi_6) |k_2 (\chi_3 - g_2)|]) \end{cases} \quad (11.45)$$

Therefore, stability is governed by the negative definiteness of each of the three expressions in Eq. (11.45), and inside the central region by:

$$\mathbf{P} \mathbf{A} \prec 0 \quad (11.46)$$

Since a matrix  $\mathbf{P}$  can always be found to satisfy Eq. (11.46) the system is found to have a stable zero equilibrium.

### 11.4.3 Dynamics of the partially linearised system

The equation describing the complete dynamics of the partially linearised system can be expressed using Eq. (11.27) and Eq. (11.29) as,

$$\dot{\chi} = \begin{Bmatrix} \dot{\chi}_1 \\ \dot{\chi}_2 \\ \dot{\chi}_3 \\ \dot{\chi}_4 \\ \dot{\chi}_5 \\ \dot{\chi}_6 \end{Bmatrix} = \begin{bmatrix} 0 & 1 & 0 & 0 & 0 & 0 \\ -\omega_{n,d}^2 & -2\zeta_d \omega_{n,d} & 0 & 0 & 0 & 0 \\ 0 & 0 & 0 & 0 & 1 & 0 \\ 0 & 0 & 0 & 0 & 0 & 1 \\ \frac{k_{1,2}}{m_2} & \frac{c_{2,1}}{m_2} & -\frac{2k_{g,2} + k_{1,2} + k_{2,3}}{m_2} & \frac{k_{2,3}}{m_2} & -\frac{c_{2,2}}{m_2} & -\frac{c_{2,3}}{m_2} \\ 0 & \frac{c_{3,1}}{m_3} & \frac{k_{2,3}}{m_3} & -\frac{k_{2,3} + 2k_{g,3}}{m_3} & -\frac{c_{3,2}}{m_3} & -\frac{c_{3,3}}{m_3} \end{bmatrix} \begin{Bmatrix} \chi_1 \\ \chi_2 \\ \chi_3 \\ \chi_4 \\ \chi_5 \\ \chi_6 \end{Bmatrix} + [0 \ 0 \ 0 \ 0 \ 0 \ -1/m_3]^T (f_{Knl_3}(\chi_4) + f_{Cnl_3}(\chi_4, \dot{\chi}_4)) \quad (11.47)$$

It is seen that the linearised part is given entirely in terms of the first two states and is therefore independent of states  $\chi_3 - \chi_6$ . The nonlinear internal dynamics depend upon the full system of states including  $\chi_1, \chi_2$  of the linearised sub-system.

This effect is also apparent when the system in Eq. (11.47) is re-written in second order form:

$$\begin{aligned} & \begin{bmatrix} 1 & 0 & 0 \\ 0 & m_2 & 0 \\ 0 & 0 & m_3 \end{bmatrix} \begin{Bmatrix} \ddot{z}_1 \\ \ddot{z}_2 \\ \ddot{z}_3 \end{Bmatrix} + \begin{bmatrix} 2\zeta_d \omega_{n,d} & 0 & 0 \\ -\beta k_{12} & \alpha m_2 + \beta(k_{g,2} + k_{12} + k_{23}) & -\beta k_{23} \\ 0 & -\beta k_{23} & \alpha m_3 + \beta(k_{g,3} + k_{23}) \end{bmatrix} \begin{Bmatrix} \dot{z}_1 \\ \dot{z}_2 \\ \dot{z}_3 \end{Bmatrix} + \\ & + \begin{bmatrix} \omega_{n,d}^2 & 0 & 0 \\ -k_{12} & k_{g,2} + k_{12} + k_{23} & -k_{23} \\ 0 & -k_{23} & k_{g,3} + k_{23} \end{bmatrix} \begin{Bmatrix} z_1 \\ z_2 \\ z_3 \end{Bmatrix} + \begin{Bmatrix} 0 \\ 0 \\ f_{Knl_3} \end{Bmatrix} + \begin{Bmatrix} 0 \\ 0 \\ f_{Cnl_3} \end{Bmatrix} = \begin{Bmatrix} 0 \\ 0 \\ 0 \end{Bmatrix} \quad (11.48) \end{aligned}$$

The system damping  $\mathbf{C}$  and stiffness  $\mathbf{K}$  matrices have lost the property of symmetry, typical of controlled systems. The first DOF is a SDOF system with the assigned natural frequency  $\omega_{n,d}$  with damping ratio  $\zeta_d$ . The other two DOFs belongs to a 3 DOFs system with nonlinear dynamics and their dynamics depend also on the controlled DOF.

## 11.5 Partial feedback linearisation results

In this section experimental and numerical results from the three DOFs, non-smooth, nonlinear, closed-loop system are presented and compared.

The experimental setup was the described in § 11.2 including the use of dSPACE for implementation of the controller and LMS Test.Lab for external hammer excitation of the linearised system.

The first DOF should be linear when the controller is switched on and therefore an impact modal test is entirely appropriate.

The closed-loop test procedure begins with the system in static equilibrium. Desired  $\omega_{n,d}$  and  $\zeta_d$  are set and the controller is switched on. Hammer excitation is delivered at the first mass and displacement and accelerations are measured at all three masses. The shaker delivers the control force  $u(t)$  according to the commanded input determined by the dSPACE model (at 10 kHz processing speed) and regulated by the PD controller. The duration of a single test from the moment of impact is 10 seconds, experimental FRFs are obtained in LMS Test.Lab by averaging over five tests and modal parameters of the linearised system are determined.

A schematic of the closed-loop control is shown in Figure 11.8 with the outer dSPACE control loop and the inner PD controller, which was tuned separately on a sinusoidal signal with gains that were feasible for the working frequency range of the system. Further details on the input force control can be found in § 11.5.2. The purpose of the saturation term is to prevent damage to the shaker caused by hitting the stops at the end of its stroke.

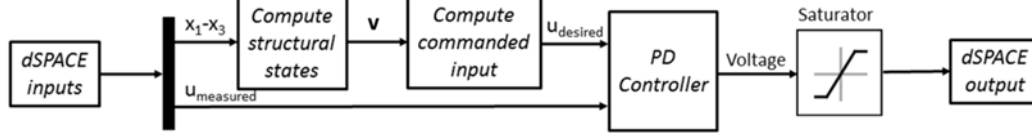


Figure 11.8 - Schematic of the control strategy.

Numerical closed-loop FRFs were obtained for purpose of comparison by exciting the partially linearised model with a slowly varying sine-swept force applied at the first DOF.

The equation of motion includes both the external excitation  $f(t) = \sin(\Omega(t)t)$  and the control force  $u(t)$ :

$$\mathbf{M}\ddot{\mathbf{x}} + \mathbf{C}\dot{\mathbf{x}} + \mathbf{K}\mathbf{x} + \mathbf{f}_{knl} + \mathbf{f}_{cnl} = \mathbf{B}(f(t) + u(t)) \quad (11.49)$$

where  $\Omega(t)$  changes linearly with time at a slow rate compared to the natural frequencies of the system.

Experiments and numerical simulations were repeated for four different values of desired natural frequencies  $f_{n,d}$  and for each twelve desired damping ratios  $\zeta_d$ :

$$f_{n,d} = \{9.7 \quad 13.5 \quad 16 \quad 19\} \text{ Hz} \quad (11.50)$$

$$\zeta_d = \{0.5 \quad 1 \quad 5 \quad 10 \quad 15 \quad 20 \quad 25 \quad 30 \quad 35 \quad 40 \quad 45 \quad 50\} \% \quad (11.51)$$

During all the tests, the nonlinear springs are known to act on the system until the motion decays to amplitudes lower than the gaps values. The experimental closed-loop FRFs of the linearised DOFs are shown in Figure 11.9.

The controller is capable of assign the desired dynamics in almost all cases. It completely cancels out the dynamics of the third mode, while a small part of the dynamics of the first mode at 6.9 Hz is not completely cancelled out but decreases when the desired natural frequency and damping ratio increases. The not complete cancellation of the first mode is due to imperfections in the tuned model.

The experimental closed-loop FRFs, shown Figure 11.9 (left), match the numerical ones, shown in Figure 11.9 (right), very closely. Like the experimental results, the simulated FRFs show the complete cancellation of the third mode while the first mode is not completely cancelled especially in the FRFs with low

damping. In this case, it is due to the numerical differentiation of displacements to obtain velocities in the numerical model, to replicate what is done also in the experimental application. The response of the linearised system at low frequencies is seen to be higher in the numerical simulation than in the experiments due to the motion of the shaker in the low frequency range.

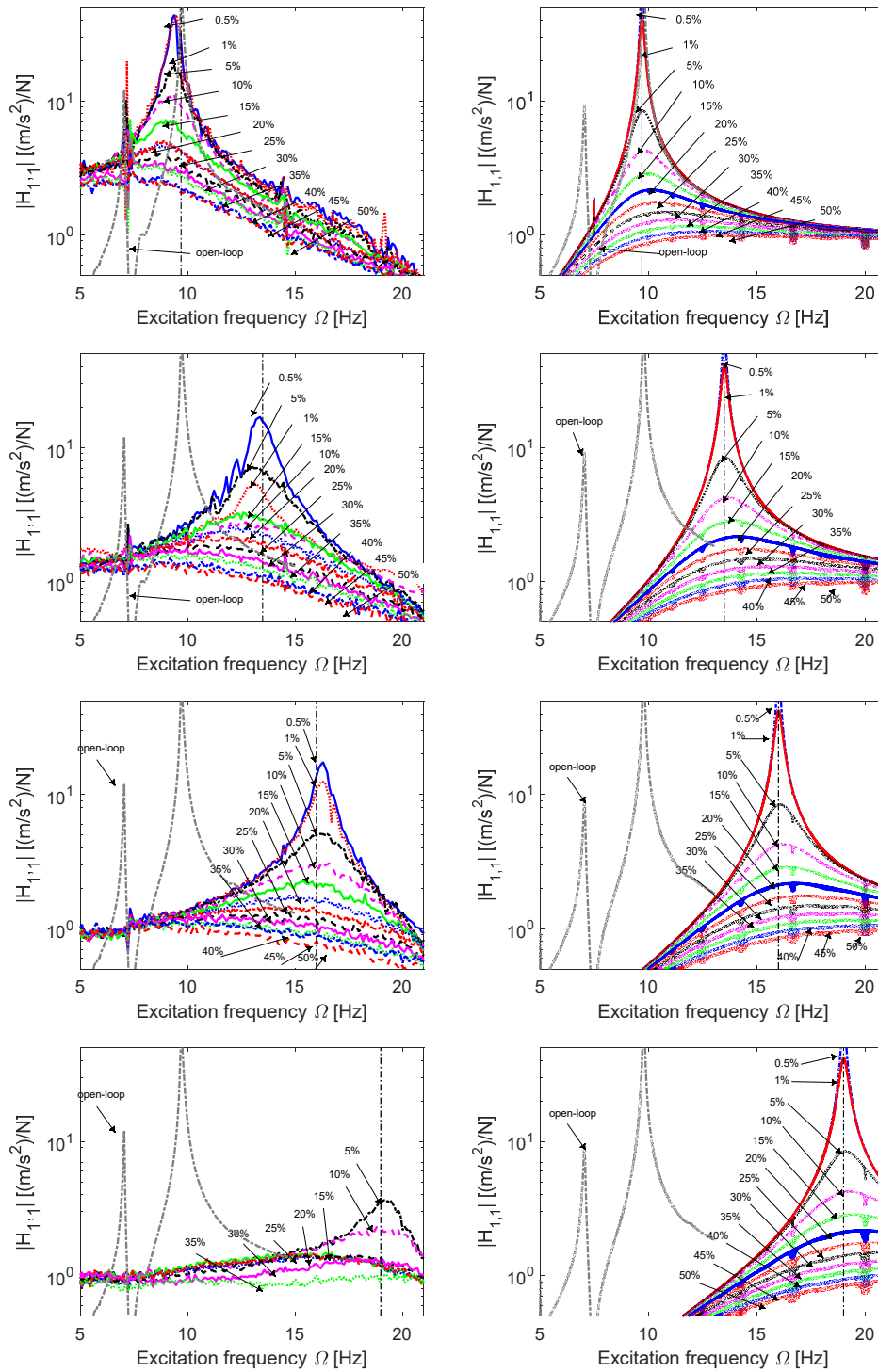


Figure 11.9 - Closed-loop FRFs: experimental (left) and numerical (right).

The natural frequencies and damping ratios of the closed-loop system were extracted using the ML-MM and are compared to assigned values in Figure 11.10.

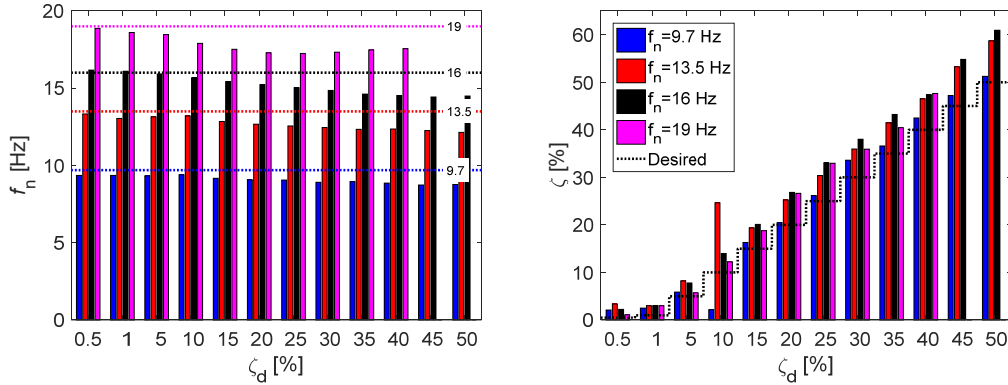


Figure 11.10 - Feedback linearisation, desired  $f_{n,d} = 9.7, 13.5, 16, 19$  Hz: actual natural frequencies (left) and actual damping ratios (right).

The closed-loop feedback linearisation is capable of correctly apply the natural frequency and damping ratio in all cases, even if changing the natural frequency of a system by eigenvalue assignment is usually a very challenging task. In the case in which only the damping ratio is different with respect to the open loop system, i.e.  $f_{n,d} = 9.7$  Hz denoted by the blue bars in Figure 11.10, the actual damping values are very well aligned with the desired ones, while the natural frequencies are slightly lower than expected. In the case of  $f_{n,d} = 13.5$  Hz (red bars in Figure 11.10) the experimental natural frequencies are slightly lower than the desired one, while damping ratios overestimate the desired values. The same phenomena is visible when the assigned natural frequency is  $f_{n,d} = 16$  Hz (black bars in Figure 11.10) and  $f_{n,d} = 19$  Hz. In the last case when  $\zeta_d$  is very high the eigenvalue is not identified. The controller is not able to assign very low values of damping, less than 2%, probably due to internal damping in the shaker.

The result of numerical feedback linearisation, including force saturation, is provided in Figure 11.11. The FRFs display the saturation effect of a truncated peak, which leads to an inaccurate estimate of the damping ratio.

A comparison between numerical and experimental FRFs for the four assigned natural frequencies with  $\zeta_n = 5\%$  are shown in Figure 11.12. The experimental trend is again very similar to the numerical one, but there are discrepancies in the vibration amplitude especially at low frequencies. The reason is that the numerical FRFs are obtained by swept-sine tests, while the experimental ones are determined from hammer tests. The closed-loop control is capable to linearise the output and the FRFs are close to a single DOF system. Also, the assigned natural frequencies are located exactly at the  $-90^\circ$  phase point, as in Figure 11.13, and the slope of the phase decreases with increasing the damping ratio.

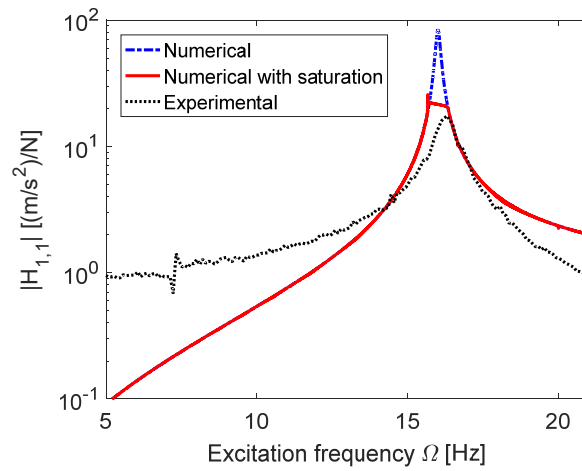


Figure 11.11 - Effect of the output saturation on close-loop dynamics.

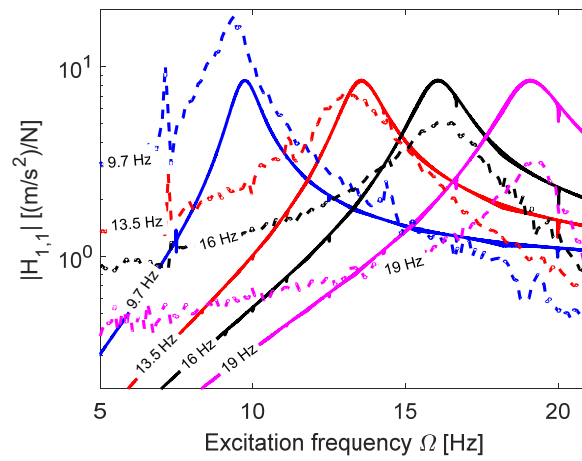


Figure 11.12 - Comparison between experimental (dashed line) and numerical (solid line) closed-loop FRFs with  $\zeta_d = 5\%$ .

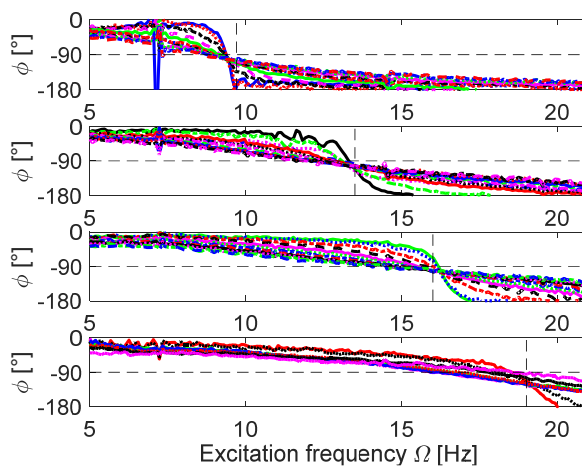


Figure 11.13 - Experimental closed loop FRFs phases.

The experimental time domain response  $\chi_1$  to the impact in the case of desired natural frequency  $f_{n,d} = 16$  Hz are shown in Figure 11.14. They behave as a SDOF system, which confirms that the linearised part of the partially linearised system is independent of the internal dynamics. The decay time of the response clearly decreases when the damping ratio is increased.

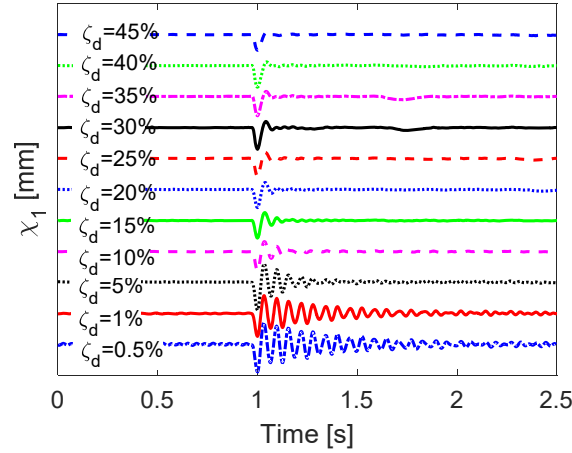


Figure 11.14 - Time domain  $\chi_1$ ,  $f_n = 16$  Hz

### 11.5.1 Internal dynamics

The FRFs of the internal dynamics with  $\zeta_d = 5\%$  are shown in Figure 11.15, together with the open-loop FRF, obtained from a frequency sweep (up to 15 Hz) with amplitude controlled force at  $f_0 = 0.4$  N.

The numerical internal dynamics FRF shows three major peaks: one corresponding to the desired natural frequency (highlighted with a dash-dot black vertical line), which is the effect of the linearised DOF on the internal dynamics  $\chi_{id}$ , and the other two related to resonances of the nonlinear internal dynamics. A jump due to the hardening effect can be seen in the numerical FRFs  $\mathbf{H}_{1,3}$ , because the internal dynamics is nonlinear, the jump is also present in the experimental open-loop response under slow sweep.

The experimental close-loop results follow the same trend but do not catch the jump because they are the results of an impulsive test. Moreover, the experimental FRFs show higher order harmonic components, due to the nonlinearity.

The FRFs obtained with higher damping ratios (not shown) display very similar behaviour with the peak of the desired eigenvalue less visible when the damping ratio increases.



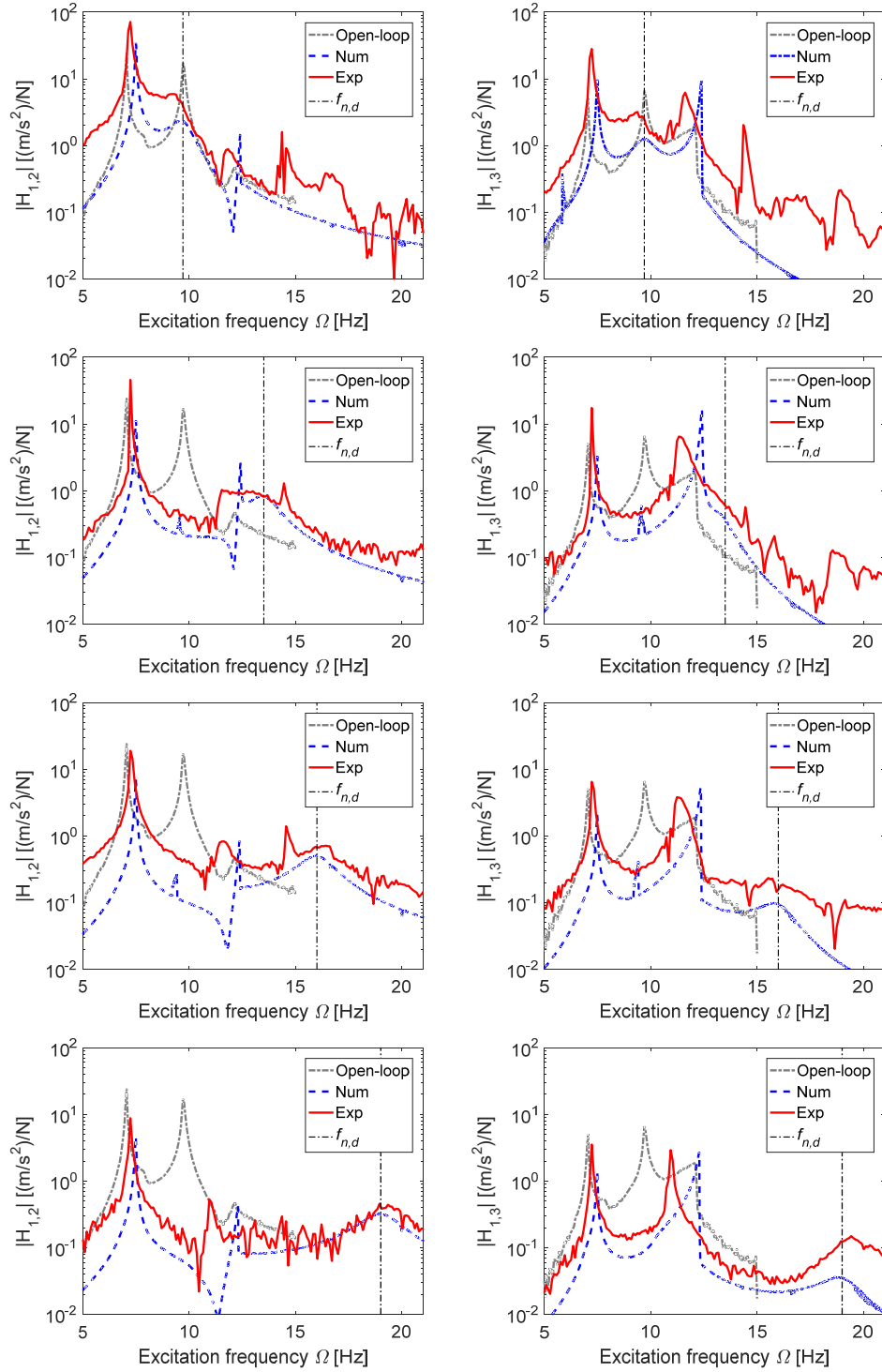


Figure 11.15 - Internal dynamics numerical and experimental closed loop FRFs.

The time domain responses of the internal dynamics are shown in Figure 11.16. The amplitude of the responses is much smaller than those of the linearised DOF. The scales of  $\chi_3$  and  $\chi_4$  respectively in Figure 11.16 are amplified by factors of two and four times that of the linearised DOF  $\chi_1$  in Figure 11.14.

The responses show a multi-harmonic behaviour as expected. The decay time is much longer than the decay time of the linearised DOF but was found to be completely decayed at around 30 seconds.

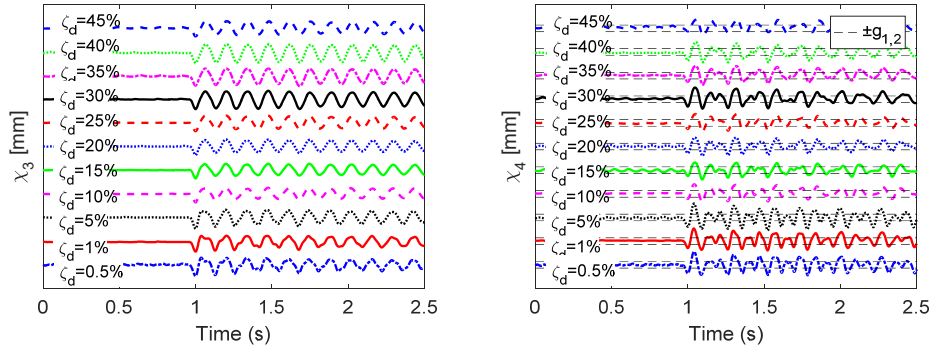


Figure 11.16 - Experimental time domain response of the internal dynamics  $f_{n,d} = 16$  Hz and increasing values of damping:  $\chi_3$  (left) and  $\chi_4$  (right).

### 11.5.2 Control of the input force

Outer loop control gives the reference input force to the system, which should be provided by the shaker. The force provided by the shaker is directly proportional to the current in the electromagnetic coils, while the reference of the outer loop is an output voltage from dSPACE to the amplifier.

Therefore, an inner PD controller is necessary to regulate the shaker force in real time. In this case the proportional and derivative coefficients of the controller were tuned manually to reproduce sine waves in the range of interest from  $4 \div 21$  Hz. The three natural frequencies  $f_n$  of the system and the assigned frequencies  $f_{n,d}$  were all within this range and it was found that the resulting controller was able to deliver the inputs commanded by outer-loop linearising controller with good accuracy as shown in Figure 11.17 and Figure 11.18.

The output of the PD controller is a voltage to drive the shaker and it is subject to a saturation term in dSPACE to ensure the safety of the hardware.

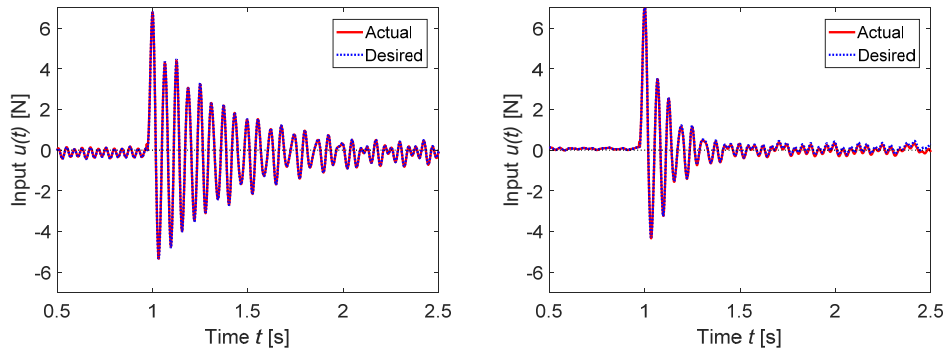


Figure 11.17 - Commanded and achieved input  $u(t)$  with  $f_{n,d} = 16$  Hz:  $\zeta_d = 0.5\%$  (left) and  $\zeta_d = 5\%$  (right).

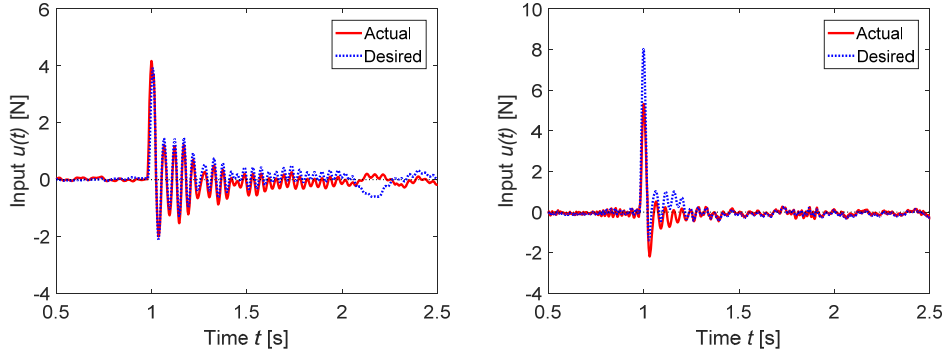


Figure 11.18 - Commanded and achieved input for  $f_{n,d} = 19$  Hz:  
 $\zeta_d = 5\%$  (left) and  $\zeta_d = 35\%$  (right).

The figures show typical command signals from the outer-loop feedback linearising controller and achieved force inputs, the latter being measured by the load cell and provided to the system. The system is initially at rest and excitation is delivered at  $t = 1$  second with the controller switched on.

In Figure 11.17 the actual input reproduces the command signal very well, measured modal parameters are very close to the assigned ones and partial feedback linearisation is successfully applied.

In Figure 11.18 the physical input is slightly different from the assigned one and, in the case of low damping (Figure 11.18, left), the discrepancy is acceptable and the controller is still able to assign the correct modal parameters. When the assigned damping is high (Figure 11.18, right) the discrepancy between actual and desired input becomes evident, due to the voltage saturation, and the controller is no longer effective in assigning the desired damping.

## 11.6 Conclusions

The dynamics behaviour of the non-smooth nonlinear system has been designed in this chapter using the state space feedback linearisation. This chapter validate the theory of state space feedback linearisation for systems with non-smooth nonlinearities and it is here applied for the first time.

A limitation of feedback linearisation for non-smooth nonlinearities applied to lumped parameter systems was discovered, in particular the linearisation is feasible only if the input is located in the same degree of freedom of the output.

The first DOF of the non-smooth nonlinear system was linearised and its behaviour controlled in terms of natural frequency and damping ratio.

The linearised DOF act as a SDOF system, although it is physically connected to the remaining DOFs. The natural frequency and damping ratio are very well assigned: four different level of natural frequency and twelve level of damping ratio were assigned. The internal dynamics remains nonlinear and its behaviour is quite aligned with simulations. The actual modal properties, extracted using ML-ML-MM algorithm, are very close to the desired modal properties in almost all

the cases. Generally assigned natural frequency are slightly lower than desired one, while damping ratio are higher than desired one. This is due to the effect of the shaker saturation, which affect the close loop FRF and the modal parameters extraction.



# Chapter 12

## 12. Feedback linearisation via method of receptances

In this chapter the feedback linearisation via method of receptance is experimentally applied on the three DOFs non-smooth nonlinear system, presented in § 6.3 and linearise through classical feedback linearisation in § 11.4 and in [203,204]. The classical feedback linearisation theory, discussed in § 3.3.2, requires the system model as input. Moreover, in the case of partial feedback linearisation the stability of the internal dynamics is a necessary condition. Significant effort was required in § 11.3 to tune the numerical model, in both the linear and nonlinear parameters, to obtain a model enough accurate to successfully achieve the desired closed-loop dynamics and detailed and complex analysis was carried out to establish the stability of zero dynamics in § 11.4.2.

Receptance based feedback linearisation, presented in § 3.3.3 could be implemented on a non-smooth nonlinear system without the necessity of a conventional system matrix model and allows also an alternative way to test the stability of the internal dynamics. The porpoise of this chapter is to experimentally apply the feedback linearisation via method of receptances on the three DOFs non-smooth nonlinear test-rig and to replicate the closed-loop results already obtained with classical feedback linearisation in § 11.5 and [204].

This chapter is organized as follows. In § 12.1 the system model, based on measured receptance data, and the complex DF with stiffness and damping terms is presented. The preliminary tests and the result of the experimental implementation of the receptance-based feedback linearisation method are presented § 12.2, both in the frequency and time domain.

The work presented in this chapter is summarised in [210].

## 12.1 Non-smooth system receptance-based model

The system under analysis is the non-smooth nonlinear configuration of the three DOFs system presented in § 6.3. The form of the non-smooth nonlinearity is a piecewise stiffness (and damping) nonlinearity formed by the closure and opening of two gaps on either side of a linear spring. The stiffness is increased when the gap closes on one side and between the gaps the stiffness is linear. Friction is present during the periods that either gap is closed; its effect is represented by a Coulomb-type damping force proportional to the absolute stiffness force and directed in opposition to velocity. The effects of an instantaneous impact are neglected.

The system may be represented as shown in Figure 11.2 as a three DOFs arrangement of lumped masses connected by springs and light dampers. It is seen that one of the two springs labelled  $k_2$  becomes active when the motion of mass  $m_3$  is great enough to close the gap. The dampers  $c_{eq}$  represent Coulomb friction when the gap  $g = g_1 = g_2$  is closed and account for energy lost (transferred to higher modes of the setting spring) at impact occurring at the instant the gap is closed.

One advantage of the receptance method is that the mathematical model of the mass  $\mathbf{M}$ , viscous damping  $\mathbf{C}$  and stiffness  $\mathbf{K}$  matrices is unnecessary and instead the system is represented by experimentally acquired receptance measurements. Thus, the underlying linear system, for small displacements such that the gaps remain open, is given by:

$$\mathbf{H}(i\Omega)\mathbf{f}(t) = \mathbf{x}(t) \quad (12.1)$$

and in the Laplace ‘ $s$ ’ domain by modal synthesis using Eq. (5.1):

$$\mathbf{H}(s) = \sum_{j=1}^3 \frac{\boldsymbol{\Psi}_j \boldsymbol{\Psi}_j^T}{a_j (s - \lambda_j)} + \frac{\boldsymbol{\Psi}_j^* \boldsymbol{\Psi}_j^{*T}}{a_j^* (s - \lambda_j^*)}; \quad s = i\Omega \quad (12.2)$$

where  $\boldsymbol{\Psi}_j$  is the  $j^{th}$  eigenvector,  $\lambda_j$  is the  $j^{th}$  pole and  $a_j$  is the  $j^{th}$  modal constant, identified in § 11.3.1.  $(\bullet)^*$  denotes complex conjugation.

If the displacement of  $m_3$  is such that the gap becomes closed, then the system behaviour is nonlinear and an amplitude-dependent linearised receptance model may be obtained by swept sine testing:

$$\mathbf{H}_{nl}(X_3, i\Omega)\mathbf{f}(t) = \mathbf{x}(t) \quad (12.3)$$

where:

$$x_3 = X_3 \sin \Omega t; \quad \Omega = \dot{\Omega} t \quad (12.4)$$

where  $\dot{\Omega}$  is the rate of variation of the excitation frequency  $\Omega$ , which is very slow compared to the system natural frequency.

Eq. (12.3) and Eq. (12.4) are the equivalent of the analytic DF representation of nonlinear elastic force  $f_{Knl,3}$ , given in Eq. (11.14), and nonlinear damping force  $f_{Cnl,3}$ , given in Eq. (11.15), acting on the third DOF  $m_3$ . The formulation of the nonlinear force is analytical known from § 11.3.

The sinusoidal input DF at constant amplitude of oscillation across the nonlinearity  $X_3$  of the piecewise linear elastic force  $f_{Knl,3}$  can be found in [157]:

$$F_{Knl}(X_3, \Omega) = k_2 [1 - \alpha(\chi)] \quad (12.5)$$

where  $\alpha(\chi)$  is defined as:

$$\alpha(\chi) = \begin{cases} -1 & \chi < -1 \\ \frac{2}{\pi} \left( \sin^{-1}(\chi) + \chi \sqrt{1 - \chi^2} \right) & |\chi| \leq 1, \\ 1 & \chi > 1 \end{cases} \quad \chi = \frac{g}{X_3} \quad (12.6)$$

The nonlinear damper force  $f_{Cnl,3}$ , given in Eq. (11.15), was represented in § 11.3 using a Coulomb model:

$$f_{Cnl,3} = \varepsilon |f_{Knl,3}| \operatorname{sgn}(\dot{x}_3) \quad (12.7)$$

where  $f_{Knl,3}$  is defined in Eq. (11.14).

The DF for the nonlinear damper is not present in literature and therefore developed in § 12.1.1. The DF of Eq. (12.7) result to be:

$$F_{Cnl}(X_3, \Omega) = -i \frac{2\varepsilon k_2}{\pi} (1 - \beta(\chi))^2 \quad (12.8)$$

where  $\beta(\chi)$  is defined as:

$$\beta(\chi) = \begin{cases} -1 & \chi < -1 \\ \chi & |\chi| \leq 1, \\ 1 & \chi > 1 \end{cases} \quad \chi = \frac{g}{X} \quad (12.9)$$

The global DF  $F_{nl}(X_3)$  of the nonlinear force  $f_{nl,3}(t) = f_{Knl,3}(t) + f_{Cnl,3}(t)$ , including stiffness and damping is:



$$F_{nl}(X_3, \Omega) = F_{Knl}(X_3, \Omega) + F_{Cnl}(X_3, \Omega) = k_2 \left\{ [1 - \alpha(\chi)] - i \frac{2\varepsilon}{\pi} [1 - \beta(\chi)]^2 \right\} \quad (12.10)$$

or, when written in the Laplace 's' domain:

$$F_{nl}(X_3, s) = k_2 \left\{ [1 - \alpha(\chi)] - s \frac{2\varepsilon}{\pi\Omega} [1 - \beta(\chi)]^2 \right\} \quad (12.11)$$

If the linear receptance FRM  $\mathbf{H}(s)$ , Eq. (12.1), is available and the DF known, then the amplitude-dependent receptance, Eq. (12.3), may be computed by using the Sherman-Morrison formula for absolute localised nonlinearity:

$$\mathbf{H}_{nl}(X_3, s) = \mathbf{H}(s) - \frac{F_{nl}(X_3, s) \mathbf{H}(s) \mathbf{e}_i \mathbf{e}_i^T \mathbf{H}(s)}{1 + F_{nl}(X_3, s) \mathbf{e}_i^T \mathbf{H}(s) \mathbf{e}_i} \quad (12.12)$$

where  $\mathbf{e}_i$  is the unit vector given by the  $i^{th}$  column of the identity matrix  $\mathbf{I}$  and  $i$  denotes the location of the nonlinearity, in this case  $i = 3$ .

### 12.1.1 Describing function of the nonlinear damping force

The nonlinear damping force is given in Eq. (12.7), is represented in the force-displacement plane is shown in Figure 12.1. The force  $F$  in the  $y$  axis represent the amplitude of the nonlinear damping force, while  $x$  is the instantaneous displacement of the nonlinear DOF  $x_3(t)$ , defined in Eq. (12.4), and  $A = X_3$  is the amplitude of the oscillation. The displacement  $x_3(t)$  in the  $x$  axis as a function of the angle  $\psi$  of an oscillation cycle is represented in the bottom graph.

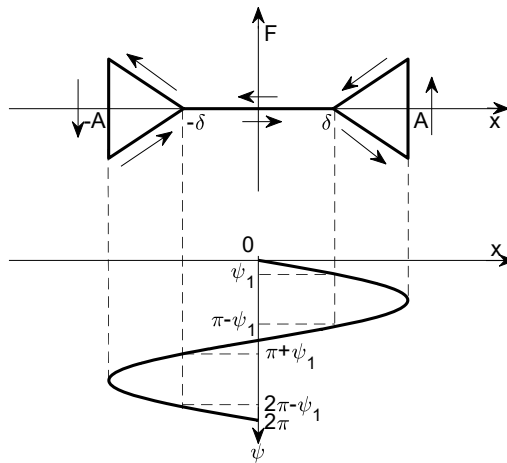


Figure 12.1 - Nonlinear damping force.

The area inside the curve in the  $F-x_3$  plane represents the work, which is proportional to energy. Because the damping force  $f_{Cnl,3}$  dissipate energy from the system, the cycle is in the counter-clockwise direction.

The DF of  $f_{Cnl,3}(x_3, \dot{x}_3)$  is defined as [157]:

$$F_{Cnl}(A, \Omega) = n_p + in_q \text{ or } F_{Cnl}(A, s) = n_p + \frac{n_q}{\Omega} s \quad (12.13)$$

Since in this case the cycle is in the counter-clockwise direction:

$$\begin{aligned} n_p &= \frac{1}{\pi A} \int_{2\pi}^0 f_{Cnl,3}(A \sin \psi, \Omega A \cos \psi) \sin \psi d\psi \\ &= -\frac{1}{\pi A} \int_0^{2\pi} f_{Cnl,3}(A \sin \psi, \Omega A \cos \psi) \sin \psi d\psi \end{aligned} \quad (12.14)$$

$$\begin{aligned} n_q &= -\frac{1}{\pi A} \int_{2\pi}^0 f_{Cnl,3}(A \sin \psi, \Omega A \cos \psi) \cos \psi d\psi = \\ &= -\frac{1}{\pi A} \int_0^{2\pi} f_{Cnl,3}(A \sin \psi, \Omega A \cos \psi) \cos \psi d\psi \end{aligned} \quad (12.15)$$

As this is a non-conservative (dissipative) force, the in-phase term  $n_p$  is expected to be zero.

Defining the switching point, the angle  $\psi_1$  at which the gap  $\delta$  is closed:

$$A \sin \psi_1 = \delta \quad (12.16)$$

Applying the definition Eq. (12.14) the in phase term  $n_p$  results to be:

$$\begin{aligned} n_p &= -\frac{1}{\pi A} \int_0^{\psi_1} (\varepsilon |0| \operatorname{sgn}(\Omega A \cos \psi)) \sin \psi d\psi \\ &\quad - \frac{1}{\pi A} \int_{\psi_1}^{\pi-\psi_1} (\varepsilon |k_2 (A \sin \psi - \delta)| \operatorname{sgn}(\Omega A \cos \psi)) \sin \psi d\psi \\ &\quad - \frac{1}{\pi A} \int_{\pi-\psi_1}^{\pi+\psi_1} (\varepsilon |0| \operatorname{sgn}(\Omega A \cos \psi)) \sin \psi d\psi \\ &\quad - \frac{1}{\pi A} \int_{\pi+\psi_1}^{2\pi-\psi_1} (\varepsilon |k_2 (A \sin \psi + \delta)| \operatorname{sgn}(\Omega A \cos \psi)) \sin \psi d\psi \\ &\quad - \frac{1}{\pi A} \int_{2\pi-\psi_1}^{2\pi} (\varepsilon |0| \operatorname{sgn}(-\Omega A \cos \psi)) \sin \psi d\psi = \end{aligned} \quad (12.17)$$

Simplifying the region in which the force is null:

$$\begin{aligned}
 n_p = & -\frac{1}{\pi A} \int_{\psi_1}^{\pi-\psi_1} \varepsilon k_2 (A \sin \psi - \delta) \operatorname{sgn}(\Omega A \cos \psi) \sin \psi d\psi \\
 & -\frac{1}{\pi A} \int_{\pi+\psi_1}^{2\pi-\psi_1} -\varepsilon k_2 (A \sin \psi + \delta) \operatorname{sgn}(\Omega A \cos \psi) \sin \psi d\psi
 \end{aligned} \quad (12.18)$$

The “sgn” function may be eliminated by casting Eq. (12.18) as follows:

$$n_p = -\frac{1}{\pi A} \left[ \int_{\psi_1}^{\frac{\pi}{2}} \varepsilon k_2 (A \sin \psi - \delta) \sin \psi d\psi + \int_{\frac{\pi}{2}}^{\pi-\psi_1} -\varepsilon k_2 (A \sin \psi - \delta) \sin \psi d\psi + \right. \\
 \left. \int_{\pi+\psi_1}^{\frac{3}{2}\pi} \varepsilon k_2 (A \sin \psi + \delta) \sin \psi d\psi + \int_{\frac{3}{2}\pi}^{2\pi-\psi_1} -\varepsilon k_2 (A \sin \psi + \delta) \sin \psi d\psi \right] \quad (12.19)$$

Computing the integrals, as expected, it is found that:

$$n_p = 0 \quad (12.20)$$

The term in quadrature  $n_q$  is computed by applying Eq. (12.15). Simplifying the region in which the integrand function is zero results in:

$$\begin{aligned}
 n_q = & -\frac{1}{\pi A} \int_{\psi_1}^{\pi-\psi_1} (\varepsilon k_2 (A \sin \psi - \delta) \operatorname{sgn}(\Omega A \cos \psi)) \cos \psi d\psi \\
 & -\frac{1}{\pi A} \int_{\pi+\psi_1}^{2\pi-\psi_1} (-\varepsilon k_2 (A \sin \psi + \delta) \operatorname{sgn}(\Omega A \cos \psi)) \cos \psi d\psi
 \end{aligned} \quad (12.21)$$

Eliminating the “sgn” function as before:

$$n_q = -\frac{1}{\pi A} \left[ \int_{\psi_1}^{\frac{\pi}{2}} \varepsilon k_2 (A \sin \psi - \delta) \cos \psi d\psi + \int_{\frac{\pi}{2}}^{\pi-\psi_1} -\varepsilon k_2 (A \sin \psi - \delta) \cos \psi d\psi + \right. \\
 \left. \int_{\pi+\psi_1}^{\frac{3}{2}\pi} +\varepsilon k_2 (A \sin \psi + \delta) \cos \psi d\psi + \int_{\frac{3}{2}\pi}^{2\pi-\psi_1} -\varepsilon k_2 (A \sin \psi + \delta) \cos \psi d\psi \right] \quad (12.22)$$

Computing all the integrals, the in-quadrature term  $n_q$  becomes:

$$n_q = -\frac{2\varepsilon k_2}{\pi} \left(1 - \frac{\delta}{A}\right)^2 \quad (12.23)$$

The DF for the nonlinear damping force  $f_{Cnl,3}(t)$  when  $A > \delta$  is:

$$F_{Cnl,3}(A, \Omega) = n_p + in_q = 0 + i \left( -\frac{2\varepsilon k_2}{\pi} \left( 1 - \frac{\delta}{A} \right)^2 \right) = -i \frac{2\varepsilon k_2}{\pi} \left( 1 - \frac{\delta}{A} \right)^2 \quad (12.24)$$

or in compact form as:

$$F_{Cnl,3}(A, \Omega) = -i \frac{2\varepsilon k_2}{\pi} \left( 1 - g \left( \frac{\delta}{A} \right) \right)^2 \quad (12.25)$$

where

$$g(\chi) = \begin{cases} -1 & \chi < -1 \\ \frac{\delta}{A} & |\chi| \leq 1, \\ 1 & \chi > 1 \end{cases} \quad \chi = \frac{\delta}{A} \quad (12.26)$$

## 12.2 Experimental linearisation via method of receptances

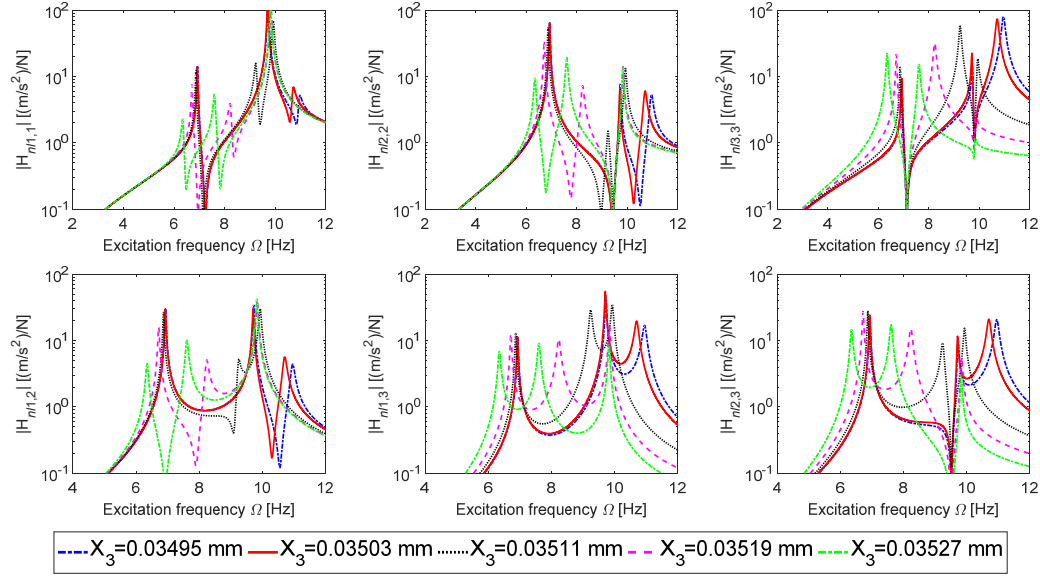
### 12.2.1 Zero dynamics stability

Experimental receptance FRM  $\mathbf{H}^{Exp}(\Omega)$  and synthesized FRM  $\mathbf{H}_{syn}(\Omega)$  of the underlying linear system are presented in Figure 11.3, where very close agreement can be observed.

The nonlinear FRM  $\mathbf{H}_{nl}(X_3, \Omega)$  at constant amplitude of oscillation across the nonlinearity is computed using Eq. (12.12), where the DF of the nonlinear force is given in Eq. (12.25). The parameters of the nonlinearity, having been identified previously in § 11.3 and [204], are  $\varepsilon = 0.3954$  and  $k_2 = 1722.6 \text{ N/m}$ .

The nonlinear FRM  $\mathbf{H}_{nl}(X_3, \Omega)$  obtained for different values of  $X_3$  are shown in Figure 12.2.

The amplitude of oscillation  $X_3$  across the nonlinearity is very effective on the FRFs. The peaks move a lot in frequency for very small change of amplitude  $X_3$ . In Figure 12.2 the blue lines represent the FRM of the linear system, because  $X_3 < g$ , therefore the nonlinearity is not yet activated. Increasing the oscillation amplitude  $X_3$ , the three modes moves toward lower frequency and decreases their amplitude.


 Figure 12.2 - Nonlinear FRM  $\mathbf{H}_{nl}(X_3, \Omega)$  changing oscillation amplitude  $X_3$ .

The evaluation of the zero dynamics  $\mathbf{z}_{zd}$  stability requires the partition of the nonlinear FRM  $\mathbf{H}_{nl}(X_3, \Omega)$  on the basis of controlled and uncontrollable DOFs in the linearised set of coordinates  $\mathbf{z}$ .

The transformation matrix  $\mathbf{T}$  in Eq. (3.147), which meets the requirement in Eq. (3.148) is the identity matrix  $\mathbf{I}$ :

$$\mathbf{z} = \mathbf{T}\mathbf{x}; \quad \mathbf{T} = \mathbf{I}; \quad \mathbf{z} = \mathbf{x} \quad (12.27)$$

and as consequence from Eq. (3.150):

$$\tilde{\mathbf{H}}_{nl}(\mathbf{Z}_3, s) = \mathbf{H}_{nl}(X_3, s) \quad (12.28)$$

The experimental active feedback linearisation implementation is a SISO system: the physical input  $u(t)$  is given to the first DOF and the output  $y = x_1$ . The force distribution matrix  $\mathbf{B}$  in Eq. (3.142) can be written as:

$$\mathbf{B} = \begin{bmatrix} B_1 \\ \mathbf{B}_2 \end{bmatrix}; \quad B_1 = 1; \quad \mathbf{B}_2 = \begin{bmatrix} 0 \\ 0 \end{bmatrix} \quad (12.29)$$

The vector of the linearised coordinates can be writes as:

$$\mathbf{z} = \begin{bmatrix} z_1 \\ \mathbf{z}_2 \end{bmatrix}; \quad \mathbf{z}_2 = \begin{bmatrix} z_2 \\ z_3 \end{bmatrix} \quad (12.30)$$

where  $z_1$  is the controllable DOF and  $\mathbf{z}_2$  is the vector of the uncontrollable DOFs. The nonlinear FRM  $\tilde{\mathbf{H}}_{nl}(\mathbf{Z}_3, s)$  is therefore portioned in:

$$\tilde{\mathbf{H}}_{nl}(Z_3, s) = \begin{bmatrix} (\tilde{H}_{nl}(Z_3, s))_{11} & (\tilde{\mathbf{H}}_{nl}(Z_3, s))_{12} \\ (\tilde{\mathbf{H}}_{nl}(Z_3, s))_{21} & (\tilde{\mathbf{H}}_{nl}(Z_3, s))_{22} \end{bmatrix} \quad (12.31)$$

where

$$\begin{aligned} (\tilde{H}_{nl}(Z_3, s))_{11} &= \tilde{\mathbf{H}}_{nl}(Z_3, s)(1, 1) \in \mathbb{C}^{1 \times 1} \\ (\tilde{\mathbf{H}}_{nl}(Z_3, s))_{12} &= \tilde{\mathbf{H}}_{nl}(Z_3, s)(1, 2:3) \in \mathbb{C}^{1 \times 2} \\ (\tilde{\mathbf{H}}_{nl}(Z_3, s))_{21} &= \tilde{\mathbf{H}}_{nl}(Z_3, s)(2:3, 1) \in \mathbb{C}^{2 \times 1} \\ (\tilde{\mathbf{H}}_{nl}(Z_3, s))_{22} &= \tilde{\mathbf{H}}_{nl}(Z_3, s)(2:3, 2:3) \in \mathbb{C}^{2 \times 2} \end{aligned} \quad (12.32)$$

The transfer function matrix of the zero dynamics, determined by using the amplitude-dependent receptances in Eq. (3.162), is shown in Figure 12.3.

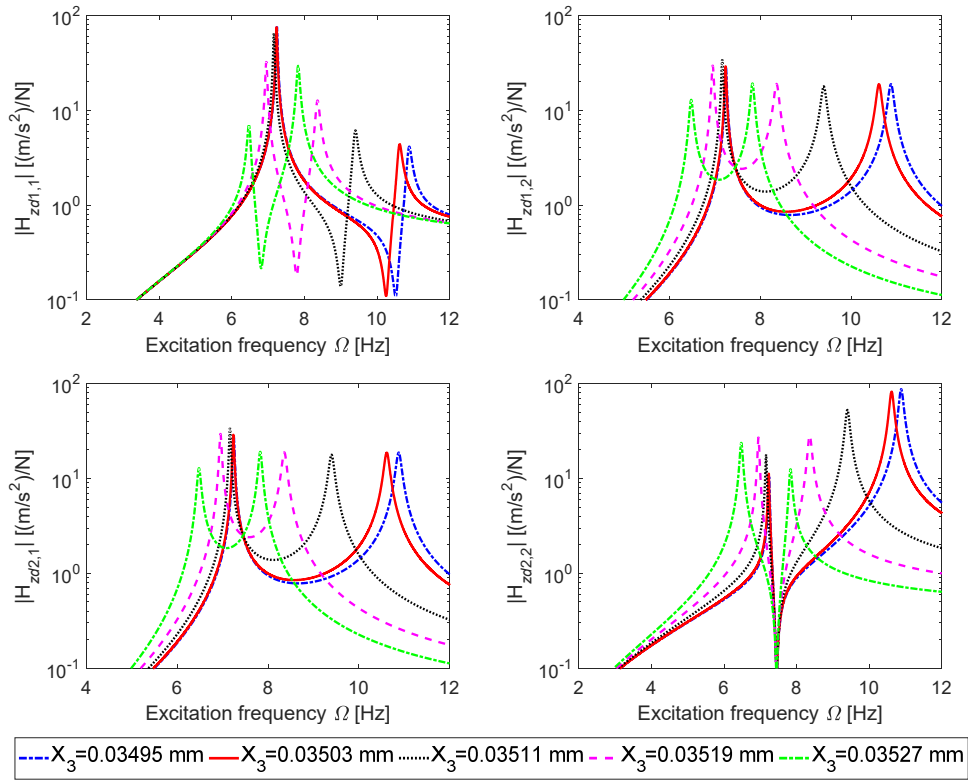


Figure 12.3 - Zero dynamics FRM changing  $X_3$  amplitude.

The zero dynamics result to be a two DOFs system, therefore the stability of its four poles must be proved.

The poles of the zero dynamics are extracted from the zero dynamics transfer function by using rational fractional polynomials method [211]. The zero dynamics  $\mathbf{z}_{zd}$  poles  $\lambda_i$  loci in function of the vibration amplitude  $Z_3$  are shown in

Figure 12.4 and in Figure 12.5, where a zoomed view close to the gap at  $X_3 = Z_3 = 0.035$  mm can be seen.

The real part of the zero dynamics poles, Figure 12.4 (left) and Figure 12.5 (left), is always negative changing the vibration amplitude  $X_3$ , therefore the four poles of the zero dynamics are stable, at least in the amplitude oscillation range of interest.

Having established that the zero dynamics are stable, input-output feedback linearisation by the method of receptances and pole placement may be carried out.

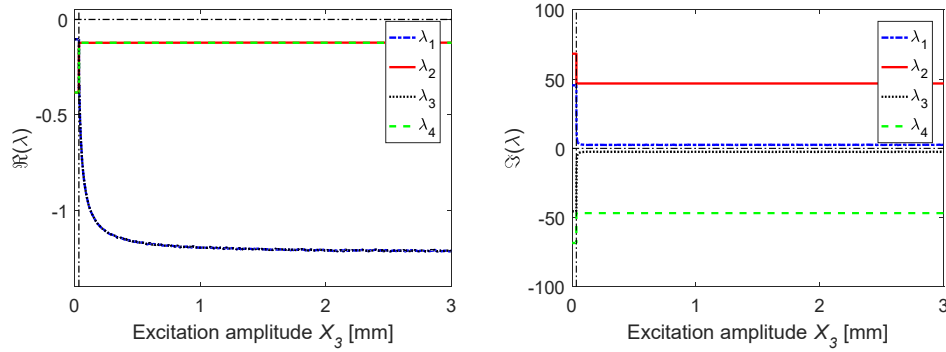


Figure 12.4 - Zero dynamics poles: real (left) and imaginary (right) parts.

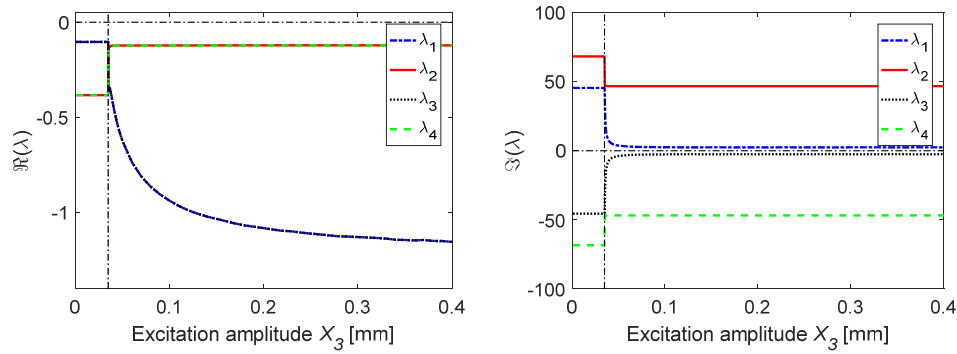


Figure 12.5 - Zoomed view of poles: real (left) and imaginary (right) parts.

### 12.2.2 Computation of the actual input

The experimental implementation of the feedback linearisation via the method of receptance requires the time domain computation of the physical input  $u(t)$ , computed using Eq. (3.155). The physical input  $u(s)$ , in Laplace domain ‘ $s$ ’, can be written for this example as:

$$u(s) = B_1^{-1} \left[ \tilde{u}(s) + \left( \left( \tilde{\mathbf{H}}_{nl}(Z_3, s) \right)^{-1} \right)_{11} z_1(s) + \left( \left( \tilde{\mathbf{H}}_{nl}(Z_3, s) \right)^{-1} \right)_{12} z_2(s) - s^2 z_1(s) \right] \quad (12.33)$$

Remembering  $\mathbf{T} = \mathbf{I}$ , the terms in Eq. (12.33) can be computed as:

$$\left(\tilde{\mathbf{H}}_{nl}(Z_3, s)\right)^{-1} = \mathbf{Z}_{nl}(X_3, s) = \mathbf{Z}(s) + \mathbf{e}_3 \mathbf{e}_3^T \mathbf{Z}_{nl}(F_{nl}(X_3, s), \mathbf{Z}(s)) \quad (12.34)$$

where  $\mathbf{e}_3$  is the third column of the identity matrix  $\mathbf{I}$  of dimension three.

The nonlinear DSM  $\mathbf{Z}_{nl}(X_3, s)$  differs from the linear one  $\mathbf{Z}(s)$  only in the term where the nonlinearity is acting, therefore the terms required in Eq. (12.33) becomes:

$$\left(\left(\tilde{\mathbf{H}}_{nl}(Z_3, s)\right)^{-1}\right)_{11} = \left(\mathbf{Z}_{nl}(X_3, s)\right)_{11} = \left(\mathbf{Z}(s)\right)_{11} = a_{11}s^2 + b_{11}s + c_{11} \quad (12.35)$$

$$\left(\left(\tilde{\mathbf{H}}_{nl}(Z_3, s)\right)^{-1}\right)_{12} = \left(\mathbf{Z}_{nl}(X_3, s)\right)_{12} = \left(\mathbf{Z}(s)\right)_{12} = \begin{bmatrix} a_{12}s^2 + b_{12}s + c_{12} \\ a_{13}s^2 + b_{13}s + c_{13} \end{bmatrix}^T \quad (12.36)$$

where the coefficients  $a_{ij}, b_{i,j}, c_{i,j}$  can be fitted from the linear DSM  $\mathbf{Z}$ , computed inverting the synthesised FRM  $\mathbf{H}_{syn}(s)$ .

The nonlinearity does not appear in the computation of the input, therefore if nonlinearities are not located in the controllable DOFs, the form of the nonlinearity is not required for the application of the receptance based input-output partial feedback linearisation.

Elements of the DSM  $\mathbf{Z}(s)$  in Eq. (12.35) and (12.36) are shown in Figure 12.6, where numerical inversion of the FRM  $\mathbf{H}_{syn}(\Omega)$  and the fitting with second order polynomial in Eq. (12.35) and Eq. (12.36) are shown to be in almost perfect agreement. The fitted coefficients are reported in Table 12.1.

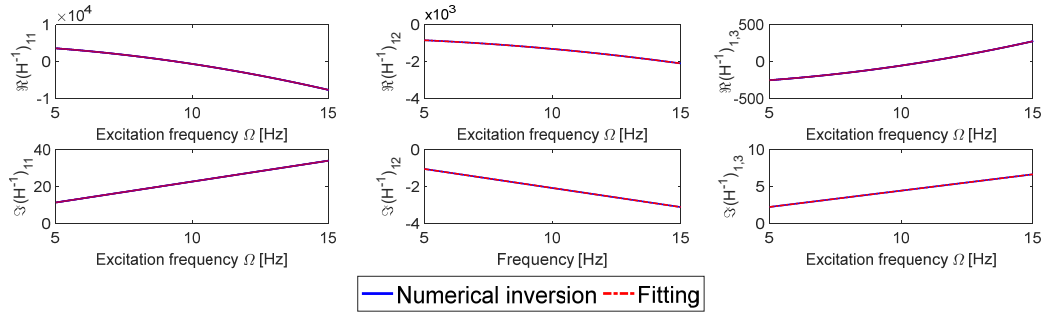


Figure 12.6 - Fitting of the required DSM  $\mathbf{Z}$  terms.

Table 12.1 - Coefficients of the fitted DSM  $\mathbf{Z}$  terms.

Coefficient	Value	Coefficient	Value	Coefficient	Value
$a_{11}$	1.4332	$b_{11}$	0.3622	$c_{11}$	5032.2
$a_{12}$	0.1584	$b_{12}$	-0.0330	$c_{12}$	-707.4
$a_{13}$	-0.0666	$b_{13}$	0.0707	$c_{13}$	-320.9

The physical input in Eq. (12.33) becomes:



$$u(s) = \left[ \tilde{u}(s) + (a_{11}s^2 + b_{11}s + c_{11})z_1(s) + \begin{bmatrix} a_{12}s^2 + b_{12}s + c_{12} \\ a_{13}s^2 + b_{13}s + c_{13} \end{bmatrix}^T \begin{bmatrix} z_2(s) \\ z_3(s) \end{bmatrix} - s^2 z_1(s) \right] \quad (12.37)$$

or

$$u(s) = \begin{bmatrix} \tilde{u}(s) + (a_{11} - 1)s^2 z_1(s) + b_{11}s z_1(s) + c_{11} z_1(s) + \\ + a_{12}s^2 z_2(s) + b_{12}s z_2(s) + c_{12} z_2(s) + \\ + a_{13}s^2 z_3(s) + b_{13}s z_3(s) + c_{13} z_3(s) \end{bmatrix} \quad (12.38)$$

Performing inverse Laplace transform on Eq. (12.38) and expanding the virtual input  $\tilde{u}(t)$ , given Eq. (3.157), it is possible to write down the time domain implementation of the required physical input  $u(t)$ :

$$u(t) = \begin{bmatrix} (a_{11} - 1) & a_{12} & a_{13} \end{bmatrix} \ddot{\mathbf{z}}(t) + \begin{bmatrix} b_{11} - 2\zeta_d \omega_{n,d} & b_{12} & b_{13} \end{bmatrix} \dot{\mathbf{z}}(t) + \begin{bmatrix} c_{11} - \omega_{n,d}^2 & c_{12} & c_{13} \end{bmatrix} \mathbf{z}(t) \quad (12.39)$$

Eq. (12.39) is the time domain implementation of the physical input to the system, required to cancel out the complete open loop dynamics and assign the desired poles  $\mu_d = -\zeta_d \omega_{n,d} \pm i \omega_{n,d} \sqrt{1 - \zeta_d^2}$  to the controlled DOF  $z_1$ .

### 12.2.3 Close loop results

In this section experimental results produced by the receptance-based partial feedback linearisation approach described in § 3.3.3 are presented and compared to numerically-produced results from a  $\mathbf{M}$ ,  $\mathbf{C}$ ,  $\mathbf{K}$  model described in § 11.5 and in [204].

Inspection of Eq. (3.153) shows that the dynamics of the controlled DOFs are independent of the internal dynamics, but the dynamics of uncontrolled DOFs (the internal dynamics) depend upon all the DOFs of the system, as already shown in § 11.5.1.

The experimental close loop is implemented with the same strategy described in § 11.2. Two nested close loops are implemented. The outer loop is a PD controller to achieve the correct reference input computed using the inner loop. The difference with respect § 11.5, lies in the inner loop, in which is now implemented the receptance based partial feedback linearisation and the physical input  $u(t)$  is computed in real time from the sensor measures. A schematic representation of the control is given in Figure 12.7.

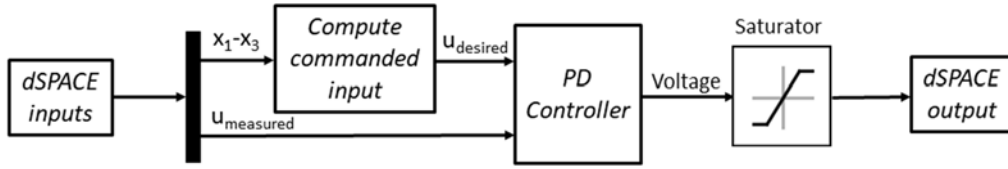


Figure 12.7 - Schematic of the control logic.

Also using the presented receptance based feedback linearisation, the closed-loop receptance  $\mathbf{H}_{11}(\Omega)$  has only a single DOF and a single natural frequency.

The test procedure is the same already described in § 11.5, where classical feedback linearisation is performed: with the controller switched on, the response of the controlled system to an impact hammer test at the first DOF is used to characterize the dynamics of the linearised part of the closed-loop system.

In the present example the controller was used to assign the desired natural frequency  $\omega_{n,d}$  and damping ratio  $\zeta_{n,d}$  of the linearised DOF, i.e. the first DOF.

Displacements were recorded for 10 seconds from the moment of impact, and experimental FRFs obtained by averaging over 5 tests.

Experiments and numerical simulations were repeated for three different values of desired natural frequencies and twelve damping ratios:

$$f_{n,d} = \{13.5 \ 16 \ 19\} \text{ Hz} \quad (12.40)$$

$$\zeta_{n,d} = \{0.5 \ 1 \ 5 \ 10 \ 15 \ 20 \ 25 \ 30 \ 35 \ 40 \ 45 \ 50\} \% \quad (12.41)$$

Not all the damping values were achievable because, for higher values of desired natural frequencies  $f_{n,d}$  and very low values of desired damping ratios  $\zeta_{n,d}$ , the shaker saturated and was not able to deliver the required input force to the system.

The experimental closed-loop FRFs of the linearised DOF are shown in Figure 12.8. It is seen that the controller was able to assign the desired dynamics in almost all cases. The open-loop dynamics of the system was completely cancelled out, thus confirming the accuracy of the extracted open-loop receptances. It was observed that when the assigned values of natural frequency were low, a small portion of the dynamics of the first mode was not completely cancelled out, most likely due to imperfect synthesis of measured FRFs. Experimental results appear to be in very good agreement with their numerical counterparts shown in Figure 12.8. Successful linearisation is evident also from the expected presence of just a single peak in the closed-loop response. The response of the linearised system at low frequencies is higher in the experiments than in numerical simulation, most likely due to motion of the shaker in the low frequency range.

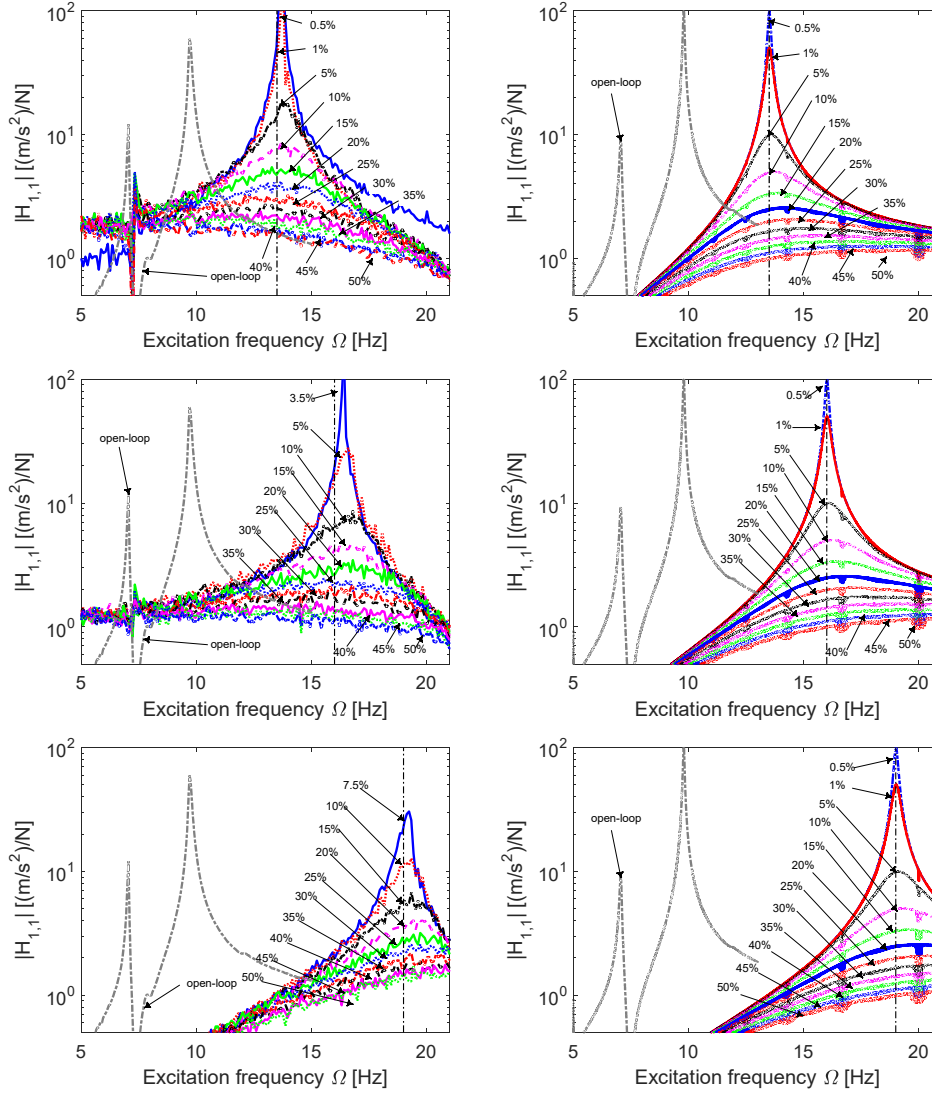


Figure 12.8 - Close-loop FRF: experimental (left) and numerical (right).

The natural frequencies and damping ratios of the closed-loop system are compared to assigned values in Figure 12.9. The poles are identified using ML-MM algorithm. Successful assignment of the desired natural frequency  $\omega_{n,d}$  through feedback linearisation is possible in almost all the cases in which a pole is identified. When the desired natural frequency is  $f_{n,d} = 13.5$  Hz (red bars in Figure 12.9) the actual natural frequency is very close to the assigned value in all performed tests. The assigned damping ratio slightly more than the desired one. In the case of  $f_{n,d} = 16$  Hz (black bars in Figure 12.9) the minimum achievable damping ratio is  $\xi_d = 3.5\%$ , because the shaker saturates for lower values. The experimental natural frequencies are all well aligned with assigned values in the cases in which tests can be performed, while the damping ratios are slightly less than the desired values at low values and slightly more for higher damping ratio. In the last case  $f_{n,d} = 19$  Hz (green bars in Figure 12.9) the effect of actuator

saturation is clearly visible - the minimum damping ratio assignable is  $\xi_d = 7.5\%$ . It is seen that also in this case the controller continues to assign natural frequencies very well, while the damping ratios present the same phenomena of  $f_{n,d} = 16$  Hz.

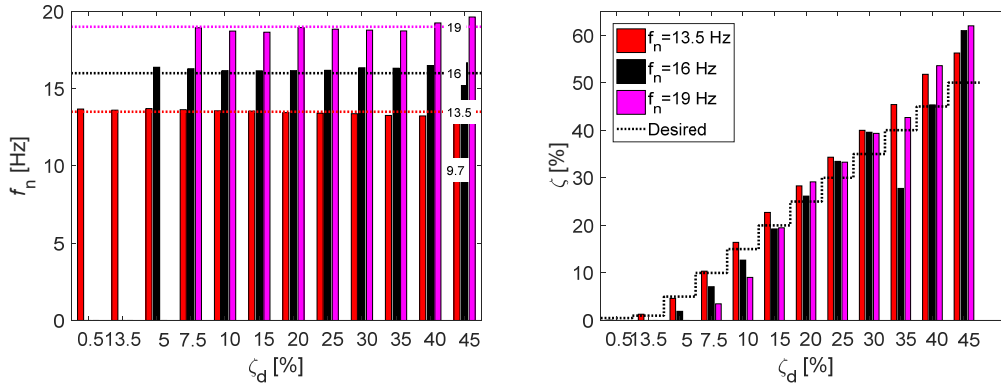


Figure 12.9 - Desired and actual poles of the linearised system.

Analysing the phases of the linearised DOF, the assigned natural frequencies are located very close to the  $-90^\circ$  phase point, as in Figure 12.10. The slope of the phase decreases with increasing damping ratio, thereby confirming the expected increased damping.

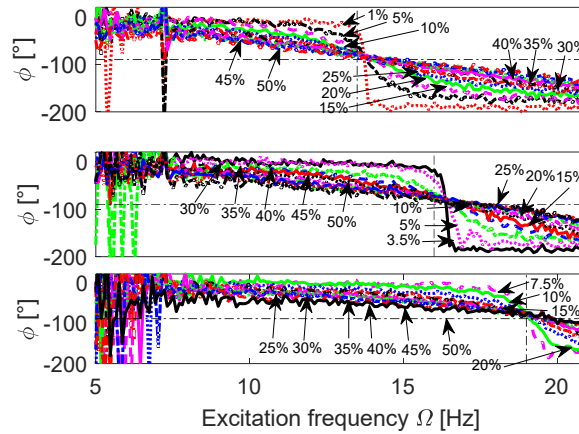


Figure 12.10 - Experimental closed loop FRFs phases.

The experimental time-domain responses of the controlled  $z_1$  and uncontrolled  $z_2$  and  $z_3$  DOFs reflect the observations seen in the above frequency domain plots.

Results for the three different assigned natural frequencies are shown in Figure 12.11, Figure 12.12 and Figure 12.13. A single harmonic, very close to the assigned frequency is visible in the  $z_1$  response (left plot in Figure 12.11, Figure 12.12 and Figure 12.13), which is now a SDOF system.

The decay time of the controlled DOF  $z_1$  response clearly decreases when the damping ratio is increased, which reflects successful assignment of the damping, and when desired natural frequency increase, as expected in a SDOF system. The  $z_2$  and  $z_3$  time-domain plots of the internal dynamics (middle and right-hand plots in Figure 12.11, Figure 12.12 and Figure 12.13), with smaller amplitude-scale than  $z_1$ , exhibit multi-harmonic behaviour. Although the decay time for  $z_2$  and  $z_3$  is clearly much longer than that of  $z_1$ , the system was found to be completely at rest after 15 seconds.

In Figure 12.11, Figure 12.12 and Figure 12.13 right it is possible to note that the amplitude of vibration was sufficient to induce nonlinearity by gap closure in all the tests, until the motion decayed sufficiently for the gaps to remain open.

Although the first DOF is linearised by the controller, the internal dynamics (second and third DOFs) remains nonlinear. The FRFs pertaining to the second and third DOFs, for the various values of natural frequencies and damping ratios assigned to the first (controlled) DOF are shown in Figure 12.14 and Figure 12.15 for the experimental and numerical cases. The expected multi-mode dynamic behaviour is evident from these plots; there are two fixed resonances at natural frequencies corresponding to the first and third open loop modes, and a third peak corresponding to the dynamics assigned to the first DOF. The clearly visible jump in the numerical simulations of  $\mathbf{H}_{1,3}(\Omega)$  is not visible in the experimental results because the FRFs were obtained from hammer tests.

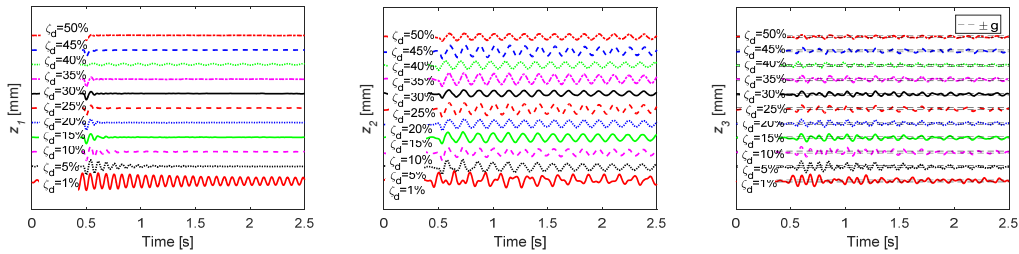


Figure 12.11 - Time domain responses for  $f_{n,d} = 13.5$  Hz :

$z_1$  (left),  $z_2$  (middle) and  $z_3$  (right).

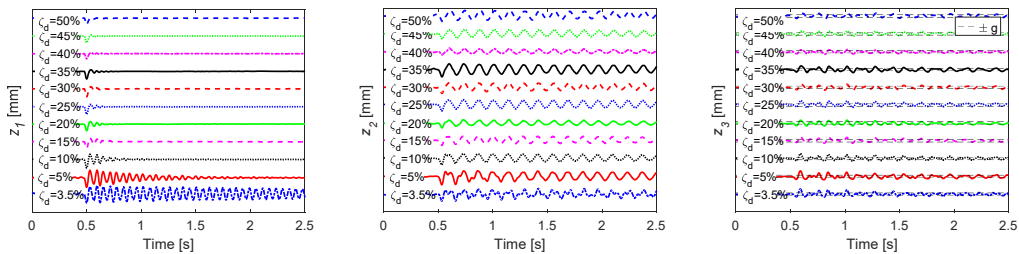


Figure 12.12 - Time domain responses for  $f_{n,d} = 16$  Hz :

$z_1$  (left),  $z_2$  (middle) and  $z_3$  (right).

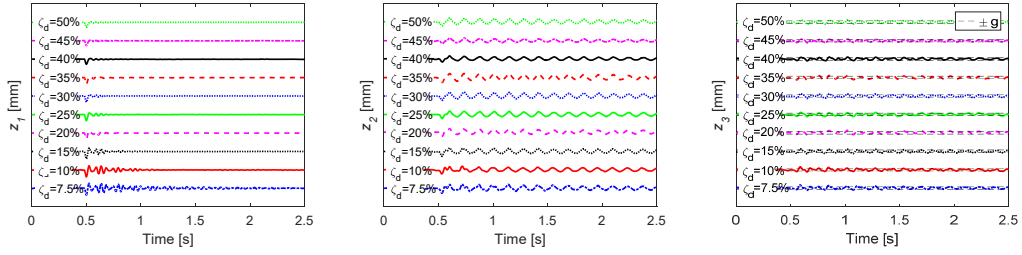


Figure 12.13 - Time domain responses for  $f_{n,d} = 19$  Hz :  
 $z_1$  (left),  $z_2$  (middle) and  $z_3$  (right).

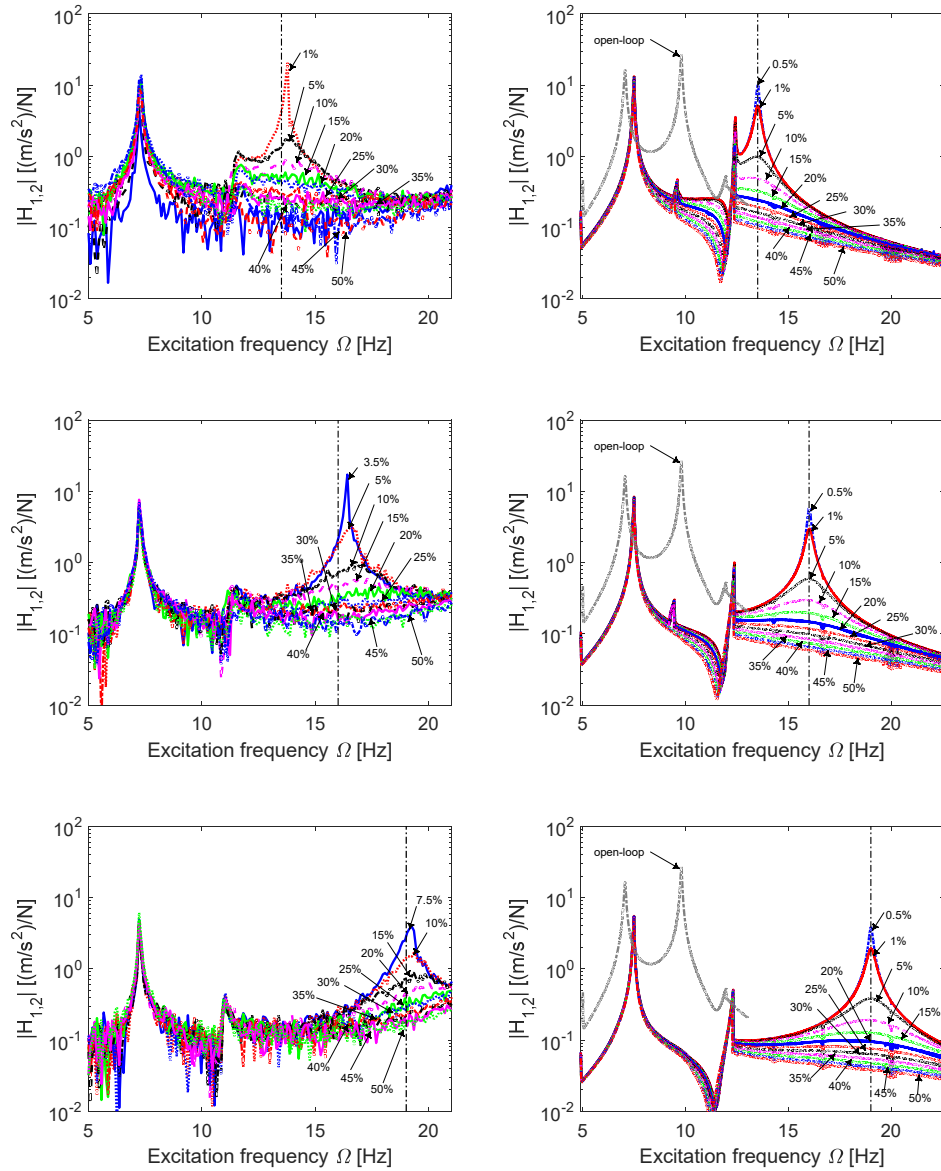


Figure 12.14 - Close-loop internal dynamics  $H_{1,2}$  :  
 experimental (left) and numerical (right).

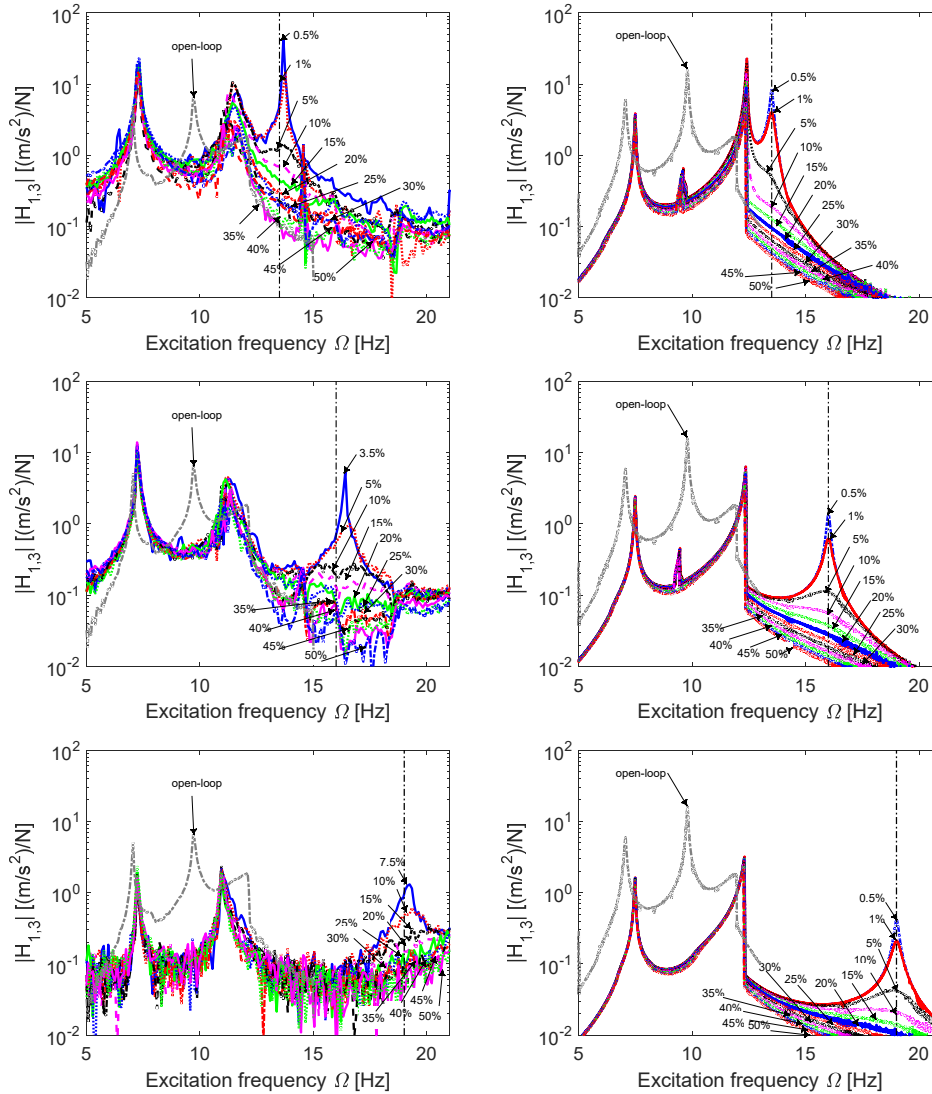


Figure 12.15 - Close-loop internal dynamics  $\mathbf{H}_{1,3}$ :  
experimental (left) and numerical (right).

### 12.3 Comparison between classic and receptance based feedback linearisation

The results achieved in the feedback linearisation of a non-smooth nonlinear system are discussed in this section, in term of assigned modal properties. The result using state space feedback linearisation were discussed in § 11.5 while the results obtained using feedback linearisation via method of receptance were presented in § 12.2.

The achieved results in terms of FRF of the close loop system are quite similar. The two biggest differences are: 1) the receptance based feedback linearisation is not able to control the system when the desired pole is located at the same natural frequency of the open loop frequency and only the damping ratio is changed, while the classical feedback linearisation successfully assigns the this



desired dynamics, although the dynamics of the first mode is not perfectly removed; 2) the receptance based feedback linearisation successfully assigns the poles when the desired natural frequency is 19 Hz, almost double the original natural frequency, while classical feedback linearisation is not able to control the system when the desired damping ratio is low and however control the system with difficulties. The second difference is probably due to the advantages of the receptances method-based feedback linearisation in terms of real time experimental feedback quantities, since also the accelerations are necessary to close the control loop. A comparison of the results can be analysed looking at the errors between the assigned and desired natural frequencies and damping ratio. The errors in terms of natural frequency  $E_{\omega\%}$  and damping ratios  $E_{\zeta\%}$ , computed as in Eq. (12.42), are shown in Figure 12.16 in function of the desired modal parameters  $\omega_{n,d}$  and  $\zeta_{n,d}$ , where the 'X' crosses represent not measured cases.

$$E_{\omega\%} = 100 \frac{\omega_n - \omega_{n,d}}{\omega_{n,d}} \quad \text{and} \quad E_{\zeta\%} = 100 \frac{\zeta_n - \zeta_{n,d}}{\zeta_{n,d}} \quad (12.42)$$

The errors in natural frequency placement are small, lower than 10%. Classical feedback linearisation assigns an underestimation of the desired natural frequency in almost all the cases, with bigger errors when higher damping ratio values are assigned. The errors  $E_{\omega\%}$  of the receptance based version of the feedback linearisation are much smaller and around zero. The errors  $E_{\zeta\%}$  regarding the damping ratio are much higher, as expected due to higher uncertainties in the damping identification. Classical feedback linearisation is not able to assign very low damping values. When only the damping ratio is required to be controlled in the system, i.e.  $\omega_{n,d} = 9.7$  Hz the damping ratio is very accurately assigned, while in almost all the other cases the assigned damping ratio is 20% higher with respect to the desired one. Receptances based feedback linearisation is able to assign quite well the damping ratio, and the errors are around the zero, generally in the range  $\pm 10\%$ .

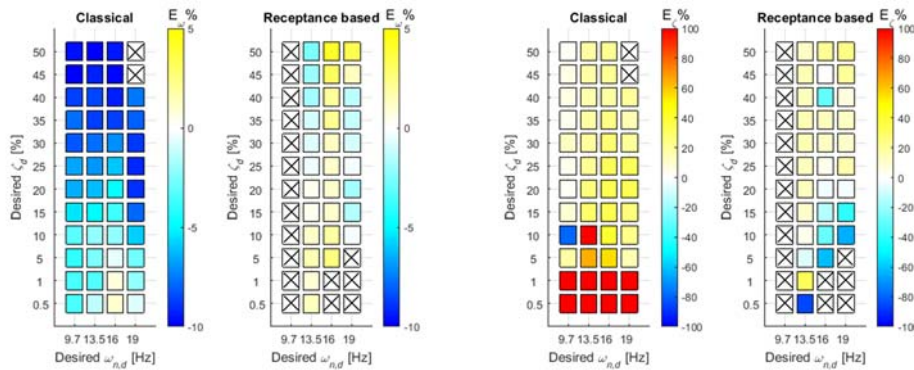


Figure 12.16 - Error in the assigned natural frequency (left) and damping ratio (right) using the two methods.



### 12.4 Conclusions

The partial input-output feedback linearisation by the method of receptances was applied to the non-smooth three DOFs system to replicate the results already achieved in § 11 using classical state space feedback linearisation.

The method of receptances does not require the structural matrix of the system, but only the open loop FRM. The partial feedback linearisation can be applied without a previous accurate identification of the system. It provides also a useful method to check the stability of the close loop system requiring only the open loop receptance at different levels of oscillation across the nonlinearity.

The receptance based model of the non-smooth nonlinear system is presented, including the sinusoidal input DF approximation of the nonlinear forces. The DF approximation of the non-smooth nonlinear damping force was not tabulated and developed in this chapter.

Stability of the internal dynamic was assessed using the receptance based method and the system result to be stable in the oscillation range of interest.

The input to the system was computed in Laplace domain and then implemented in time domain. In this particular example only the first row of the nonlinear FRM is necessary to compute the control force. Linearisation of the output was experimentally performed on the non-smooth nonlinear system, validating the theory of [156].

The behaviour of the controlled DOF, both in time and frequency domain, is clearly a SDOF system oscillating with the assigned pole. The internal dynamic instead results a three DOFs system, it presents the two unchanged pole of the structure and the assigned one.

The comparison between the achieved results using state space and receptance based feedback linearisation is finally shown. The receptance based feedback linearisation is able to assign both damping ratio and natural frequency better than classical feedback linearisation

# Chapter 13

## 13. Conclusions

The identification of damping matrices in dynamic system is a grey area in the literature. Usually equivalent models, which are not always meaningful physically, are used in order to preserve the mathematical linearity of the problem. In this dissertation the focus was on the spatial identification of damping matrices in mechanical systems, with a particular attention for the fidelity of the identified model to the real physics of the system. The identification of physical damping matrix is very useful to understand the system oscillatory behaviour and passive or active modification may be applied to the system to assign desired behaviour in terms of natural frequency, modal damping and mode shapes. Since in recent years, optimised and flexible damping layouts in mechanical structures are more and more required, the second part of the dissertation aims to address a second research objective: once the system is identified its dynamic behaviour is adjusted in real time to meet the working condition requirement in term of damping distribution and natural frequencies, assigning desired damping layouts to the system. The control of the system is not limited to only damping but also to the system resonance frequency.

The literature review proposed in Chapter 3, presents several proposed FRM-based methods and active control method for vibration suppression. The reviewed damping identification methods can be collected into two main classes: the inverse receptance method and the inverse modal parameters method. The identification results can be far from the physics of the system, because usually dampers between DOFs not physically linked and/or negative damping coefficients are identified. The identified solution is only an energetically equivalent distribution of damping. Among all the method, one of the most promising methods seems to be the Chen-Ju-Tsuei method.

The review of active control strategy is focused in particular on the method of receptance, state space feedback linearisation and receptance based feedback

linearisation which will be used in the second part of the thesis to design the vibrational behaviour of structure.

The requirement for physical identification of damping matrices is addressed in Chapter 4 by the formulation of damping matrices via the Layers Method. The layer formulation of the viscous and structural damping matrices is combined with the Chen-Ju-Tsuei method in the Stabilised Layers Method, which introduces physical connectivity constraints so that the damping matrices are represented by the sum of a defined number of damping layers. The method allows a reduction in the required number of unknowns in the inverse problem with respect the classical Chen-Ju-Tsuei method and the identification of a damping matrix closest to the real topology of the system among the infinite energy-equivalent solutions is obtained.

When the method is applied to experimental results, damping value maps and stabilisation diagrams are developed based on a number of spectral lines within a frequency band arranged symmetrically around the peaks of measured receptances (where the damping effect is most pronounced). The stabilisation diagram exploits the physical evidence that the damping level and distribution in the system, i.e. the identified damping matrices, cannot change when the identification is performed using slightly different location and quantity of experimental frequency domain data.

The application of solution stabilisation required many closely spaced spectral lines around the measured damped peaks; this is not feasible using only experimental data. The problem can be overcome using synthesised FRM, which allow computing the system response for all the required spectral lines. Methods to optimise the modal data extraction and the synthesis of FRM are presented in Chapter 5, together with techniques to identify complete damping matrices from spatially incomplete measures.

A configurable lumped parameter three DOFs system is presented in Chapter 6. The system is designed to validate both SLM and the active control method applied to non-smooth nonlinear system.

The SLM method has been validated in Chapter 7, against the damped configuration of the configurable three DOFs system. The SLM shows a good accuracy in the identification of ten different damping levels and distributions. Both relative and absolute dampers are identified, localised and quantified. The results are consistent across different setups and in good agreement with reference values.

The potential of the method is assessed in the dissipation identification of a passenger car chassis; an industrial application and a huge structure. In this case a numerical expansion and filtering method was applied to the experimental mode shapes to expand the incomplete eigenvectors and identify the complete damping matrices of the system using 285 DOFs and 786 unknowns damping coefficients.

The viscous and hysteretic damping of the system has been localised and quantified with the SLM. The damping identification process maps the sources of

---

damping of the structure. The comparison between the identified viscous damping coefficients values of the front shock absorbers with the reference values is in very good agreement.

The SLM is expanded to the identification of system with localised nonlinear damping forces in Chapter 9. In this case the location and type of nonlinearity should be previously known, either analytically or through nonlinearity identification techniques. The identification is also in this case performed on the nonlinear FRM, which is obtained using the sinusoidal input DF approximation of the nonlinearity. The identification of the damping coefficients of the nonlinearity requires the measure of the nonlinear FRM of the system under slow sweeps at constant amplitude of oscillation across the nonlinearity. The number of required sweeps depends on the order of the nonlinear DF. The nonlinearity is identified using controlled displacement amplitude sweeps, however the identified damping coefficients can be used in the system model to predict other dynamic behaviour.

The method SLM for nonlinear damping identification is experimentally applied for the identification of a system with adjustable nonlinear magnetic damping, in Chapter 10. The damping nonlinearity is well identified: the identified damping coefficients results in equivalent damping coefficients very close to the literature values at different amplitude of oscillations and with different configurations of the magnetic damper.

The modification of the damping layout of systems to achieve active vibration suppression in mechanical system is the second research question developed in this thesis. The real time control is experimentally applied to the non-smooth nonlinear configuration three DOFs system. A piecewise linear spring is added located at the third DOF of the system; the system becomes a non-smooth nonlinear system.

Two different strategies are used for the control aim: the first one described in Chapter 11, which requires the system model, and the second one described in Chapter 12, which make use of the open loop system response to control its behaviour.

An experimental investigation of input-output partial feedback linearisation on the three DOFs nonlinear system is reported in Chapter 11.

The input and output share the same first DOF, resulting in non-smooth, nonlinear zero dynamics that are shown to be stable, causing the entire system to be stable when the eigenvalues of the linearised part are positively damped. Successful partial feedback linearisation is achieved with the linearised first DOF displaying a single mode, while the other modes are almost completely cancelled out, except small effects caused by slight imperfections in the tuned model. The desired damping layout on the linearised DOF is achieved for several different damping values. The uncontrollable internal dynamics are shown to be stable with three main peaks and further nonlinear resonance effects. Excellent agreement is achieved between experimental and numerical results, except for saturation of the

shaker which occurs when the assigned eigenvalues are too far away from the open-loop natural frequencies and damping ratios.

Chapter 12 presents the experimental investigation of a control approach that combines partial feedback linearisation with the receptance method. The method is able to achieve the same result presented in Chapter 11 without the necessity of a system model, thereby eliminating errors due to inaccuracies in the numerical representation of the system. The stability of the internal dynamics can be also studied using a receptance-based method, which make use of only the FRM of the open loop system. As in the previous control, partial feedback linearisation is successfully achieved, with the linearised DOF displaying a single mode at the assigned natural frequency and with the desired damping layout, while the other modes are almost completely cancelled out, except for small discrepancies when the assigned natural frequency is low. The agreement between desired and actual values of natural frequencies and damping ratios is very good, except for a few cases when a pole cannot be identified, or the shaker saturates. The results achieved using receptance based feedback linearisation are more accurate than state space feedback linearisation.

### 13.1 Future developments

The results obtained in this dissertation leave some open questions, on which may be convenient to investigate.

#### *Integration of the SLM with others identification methods.*

The SLM has been integrated in this dissertation with the Chen-Ju-Tsuei identification method. It could be easily integrated with other methods, for example the Lee-Kim's method, Arora's method, Leuridan-Brown-Allemang's method and Minas-Inman's method. The method may be applied also for the methods requiring the modal identification from experimental FRM such as Adhikari's and Phani-Woodhouse's methods.

Extending the Layers approach to also mass and stiffness matrix, it could be applied also to the instrumented variable method.

#### *Identification of other type of elements.*

In this dissertation the absolute and relative damping elements are used to identify systems. This could be enough for the identification of physical matrices, but other elementary elements could be implemented to identify even more realistic results reducing unknowns number. The usual elementary element used in FEM (FE method) codes suit very well to this aim. For example, the structure of a Euler-Bernoulli/Timoshenko beam or a Kirchhoff-Love/Mindlin-Reissner plate can be implemented as elementary matrix to identify beam or plate like structures. These new elements should be introduced to identify the damping distribution from only the measured FRM and geometry. The elementary matrix

---

must depend only on geometry of each layer, such as the length of a beam element, while all the other properties of a FEM elementary matrix, such as material properties, are included in the unknown damping coefficient to be identified.

*Mitigation effect of SLM on modal truncation.*

Most of the damping identification methods, when applied to continuous system, suffer modal truncation, i.e. the result in term of localisation and quantification of damping distribution is strictly related to the frequency range considered. Usually, the localisation of the damper is less defined when fewer mode shapes are considered in the identification.

The effects of the SLM in the identification of continuous systems with different level of modal truncation could be studied in depth to investigate advantages of the Layers Method also with respect the localisation and quantification of damping in these cases.

*Combination of SLM and full field measures.*

The SLM has been implemented for small controllable system, such as lumped parameters system and industrial cases such as BIW car chassis. In both cases the damping matrix identification is limited to a finite number of DOFs which can be feasibly measured with standard sensors.

The identification of the damping matrices could be much more spatially defined if optical full field measures are used as experimental data. This requires the implementation of the SLM for the elaboration of large amounts of data, being the order of magnitude more than the most complex system tested with standard modal analysis. The identification results could be very interesting.

*Identification of general nonlinear damped system.*

The identification method presented in Chapter 9, is capable of identify the nonlinear damping force, when only a single nonlinearity is acting on the system and its location is known. The method could be extended to general nonlinear damped systems, in the cases of more nonlinear dampers acting on the system and with unknown location. The method may be developed using random excitation DF.

*Extension of the SLM to the identification of stiffness and mass matrices.*

The SLM is implemented for the identification of viscous structural and nonlinear damping matrices, which are related to the imaginary part of the FRM. The same concepts of layers could be used for writing and identifying the mass and stiffness matrices from the real part of the complex FRM and compare advantages and disadvantages with standard and consolidated inertial and elastic properties by spatial identification methods.

### *Adaptive state space feedback linearisation active control*

The state space feedback linearisation for non-smooth nonlinear system requires the model of the system and the effectiveness of the controller depend on the model accuracy. The model could be inaccurate in both the linear and nonlinear parts and in the location of the nonlinearity.

Real time adaptative control strategies could be implemented to correct the system model, which doesn't necessarily correct the model physically, but it corrects the control force.

# 14. List of publications

## Journal publications

- [5] D. Lisitano, E. Bonisoli, J.E. Mottershead, Experimental direct spatial damping identification by the stabilised layers method, *J. Sound Vib.* 437 (2018) 325–339. doi:10.1016/J.JSV.2018.08.055.
- [4] E. Bonisoli, D. Lisitano, A. Vigliani, Damping identification and localisation via layer method: experimental application to a vehicle chassis focused on shock absorbers effects, *Mech. Syst. Signal Process.* 116 (2019) 194–216. doi:10.1016/j.ymssp.2018.06.013.
- [3] D. Lisitano, S. Jiffri, E. Bonisoli, J.E. Mottershead, Experimental feedback linearisation of a vibrating system with a non-smooth nonlinearity, *J. Sound Vib.* 416 (2018). doi:10.1016/j.jsv.2017.11.047.
- [2] D. Lisitano, S. Jiffri, E. Bonisoli, J.E. Mottershead, Experimental feedback linearisation of a non-smooth nonlinear system by the method of receptances, *Math. Mech. Solids.* (2018). doi:10.1177/1081286517744601.
- [1] E. Bonisoli, M. Brino, M. Scapolan, D. Lisitano, Stochastic modelling and experimental outcomes of modal analysis on automotive wheels, *Int. J. Mech. Control.* 16 (2015).

## Conference proceedings

- [12] G. Iuso, G. Virone, G. Cafiero, E. Bonisoli, D. Lisitano, S. Venturini, Aeroelastic-structural coupling in antenna prototype for windy open-space, submitted to VIII International Conference on Computational Methods for Coupled Problems in Science and Engineering, Siteg, SP, 2019.
- [11] E. Bonisoli, C. Delprete, F. Freschi, D. Lisitano, M. Repetto, Identification of nonlinear magnetic damping in vibrating coupled structures, submitted to 22nd International Conference on the Computation of Electromagnetic Fields, Paris, FR, 2019.
- [10] D. Lisitano, S. Jiffri, E. Bonisoli, J.E. Mottershead, Experimental partial feedback linearisation: comparison between two active control strategies on a non-smooth nonlinear system, submitted to Int. Conf. Struct. Eng. Dyn. Viana do Castelo, Port., 2017.
- [9] D. Anastasio, D. Lisitano, S. Marchesiello, E. Bonisoli, J.E. Mottershead, Subspace system identification of a non-smooth nonlinearity under random excitation, submitted to submitted to Int. Conf. Struct. Eng. Dyn. Viana do Castelo, Port., 2017.



#### 14. List of publications

---

- [8] E. Bonisoli, D. Lisitano, L. Dimauro, L. Peroni, A proposal of dynamic behaviour design based on mode shape tracing: numerical application to a motorbike frame, in: 37th IMAC, A Conf. Expo. Struct. Dyn., Orlando, FL, USA, 2019.
- [7] E. Bonisoli, D. Lisitano, C. Conigliaro, Experimental-numerical comparison of contact nonlinear dynamics through multi-level linear mode shapes, in: 37th IMAC, A Conf. Expo. Struct. Dyn., Orlando, FL, USA, 2019.
- [6] D. Lisitano, E. Bonisoli, J.E. Mottershead, Stabilised layer method for linear and nonlinear spatial non classical damping identification, in: D. Moens, W. Desmet, B. Pluymers, W. Rottiers (Eds.), 28th Int. Conf. Noise Vib. Eng. ISMA 2018 7th Int. Conf. Uncertain. Struct. Dyn. USD 2018;, KU Leuven - Departement Werktuigkunde, 2018: pp. 991–1003.
- [5] E. Bonisoli, D. Lisitano, L. Dimauro, Experimental and numerical mode shape tracing from components to whole motorbike chassis, in: D. Moens, W. Desmet, B. Pluymers, W. Rottiers (Eds.), Int. Conf. Noise Vib. Eng. - ISMA-USD2018, KU Leuven - Departement Werktuigkunde, Leuven (Be), 2018: pp. 3597–3604.
- [4] E. Bonisoli, M. Casazza, D. Lisitano, L. Dimauro, Parametric experimental modal analysis of a modern violin based on a guarneri del gesù model, in: Rotating Mach. Vibro-Acoustics Laser Vibrometry, Vol. 7, Springer, 2019: pp. 219–230. doi:10.1007/978-3-319-74693-7\_21.
- [3] D. Lisitano, C. Zhen, S. Jiffri, E. Bonisoli, J.E. Mottershead, An example of feedback linearization in a non-smooth system, in: Int. Conf. Struct. Eng. Dyn. Ericeira, Port., 2017.
- [2] E. Bonisoli, Lisitano, Domenico, A. Vigliani, Experimental evaluation of the influence of shock-absorbers on white-body chassis modal behaviour, in: Int. Conf. Structural Eng. Dyn. ICEDyn, Ericeira (PT), 2017.
- [1] D. Lisitano, S. Jiffri, E. Bonisoli, E. Mottershead, Active control of a non-smooth nonlinear system using feedback linearisation, in: EACS 2016 – 6th Eur. Conf. Struct. Control, Sheffield, n.d.: pp. 1–13.

# 15. References

- [1] S.G. Kelly, Fundamentals of Mechanical Vibrations, McGraw-hill, 2000.
- [2] J.P. Den Hartog, Mechanical Vibration, McGraw-hill, 1947.
- [3] D.J. Inman, Engineering Vibration, Pearson, 2014.
- [4] D. Bastow, G. Howard, Car Suspension and Handling, Pentech press, 1993.
- [5] D.M.W. Hoffman, In-line internal combustion engine dynamics and vibration, University of michigan, 1999.
- [6] A. Fuchs, E. Nijman, H.H. Pribsch, Automotive NVH Technology, Springer international publishing, 2015.
- [7] F. Chen, C.A. Tan, R.L. Quaglia, Disc Brake Squeal: Mechanism, Analysis, Evaluation, and Reduction/prevention, SAE international, 2006.
- [8] K. Cheng, Machining Dynamics: Fundamentals, Applications and Practices, Springer london, 2008.
- [9] S. Iwnicki, Handbook of Railway Vehicle Dynamics, CRC press, 2006.
- [10] C.R. Farrar, K. Worden, Structural Health Monitoring: A Machine Learning Perspective, Wiley, 2012.
- [11] D. Ignazio, A.M.H. Ferri, Active Control Of Aircraft Cabin Noise, World scientific publishing company, 2015.
- [12] Y.C. Fung, An Introduction to the Theory of Aeroelasticity, Dover publications, 2002.
- [13] D. Gakkai, Earthquake Resistant Design for Civil Engineering Structures, Earth Structures and Foundations in Japan, The society, 1960.
- [14] H. Bachmann, W. Ammann, Vibrations in Structures: Induced by Man and Machines, International association for bridge and structural engineering, 1987.
- [15] S. Priya, D.J. Inman, Energy Harvesting Technologies, Springer us, 2008.
- [16] S.H. Crandall, The role of damping in vibration theory, J. Sound Vib. 11 (1970) 3-IN1. doi:10.1016/S0022-460X(70)80105-5.
- [17] L. Gaul, The influence of damping on waves and vibrations, Mech. Syst. Signal Process. 13 (1999) 1–30. doi:10.1006/MSSP.1997.0185.
- [18] R. Hooke, Lectiones Cutlerianæ, Or, A Collection of Lectures, Physical, Mechanical, Geographical, & Astronomical: Made Before the Royal Society on Several Occasions at Gresham Colledge : to which are Added Divers Miscellaneous Discourses, John martyn, 1679.
- [19] I. Newton, J. Streater, Philosophiæ naturalis principia mathematica, Jussu societatis regiae ac typis josephi streater. prostant venales apud sam. smith ad insignis principis walliae in coemiterio d. pauli, aliosq, 1687.
- [20] S.D. Poisson, Mémoire sur les équations générales de l'équilibre et du mouvement des corps solides élastiques et des fluides., J. l'cole Polytech. (1831) 13–139.
- [21] G.G. Stokes, On the Effect of the Internal Friction of Fluids on the Motion of Pendulums, Pitt press, 1851.

- [22] J.C. Maxwell, The Bakerian Lecture: On the Viscosity or Internal Friction of Air and other Gases, *Proc. R. Soc. London.* 15 (1866) 14–17.
- [23] R.E.D. Bishop, The Treatment of Damping Forces in Vibration Theory, *J. R. Aeronaut. Soc.* 59 (1955) 738–742. doi:10.1017/S0368393100117122.
- [24] Lord Rayleigh, *The theory of sound - Second edition revised and enlarged*, Macmillan and co., New York, 1896.
- [25] S. Adhikari, J. Woodhouse, Quantification of non-viscous damping in discrete linear systems, *J. Sound Vib.* 260 (2003) 499–518. doi:10.1016/S0022-460X(02)00952-5.
- [26] M. Brumat, J. Slavič, Design of damping layout using spatial-damping identification methods, *Int. J. Mech. Sci.* 127 (2017) 41–46. doi:10.1016/J.IJMECSCI.2016.07.041.
- [27] S. Subramanian, R. Surampudi, K.R. Thomson, S. Vallurupalli, Optimization of damping treatment for structure borne noise reduction, SAE technical paper, 2003.
- [28] D.J. Mead, *Passive vibration control*, John Wiley & sons inc, 1999.
- [29] M. Česnik, J. Slavič, M. Boltežar, Uninterrupted and accelerated vibrational fatigue testing with simultaneous monitoring of the natural frequency and damping, *J. Sound Vib.* 331 (2012) 5370–5382. doi:10.1016/J.JSV.2012.06.022.
- [30] H.-S. Yan, L.-C. Hsieh, Conceptual design of gear differentials for automotive vehicles, *J. Mech. Des.* 116 (1994) 565–570.
- [31] M. Hinterstoißer, K. Michaelis, B. Höhn, Influence factors on gearbox power loss, *Ind. Lubr. Tribol.* 63 (2011) 46–55. doi:10.1108/00368791111101830.
- [32] F. Fahy, J. Walker, *Fundamentals of Noise and Vibration*, Taylor & francis, 1998.
- [33] N.H. Fletcher, T.D. Rossing, *The Physics of Musical Instruments*, Springer new york, 2013.
- [34] D.J. Inman, *Vibration with Control*, Wiley, 2006. <https://books.google.it/books?id=DbRCBLfkzhkC>.
- [35] N.M.M. Maia, J.M.M. Silva, *Theoretical and Experimental Modal Analysis*, Research studies press, Somerset, 1997.
- [36] G. Genta, *Vibration Dynamics and Control*, Springer us, 2008. <https://books.google.it/books?id=CvIAF7UkXhYC>.
- [37] J.L. Lagrange, *Mécanique analytique*, Ve courcier, 1811.
- [38] W.E. Boyce, R.C. DiPrima, *Elementary Differential Equations and Boundary Value Problems*, 10th Edition, Wiley, 2012.
- [39] K. Marynowski, T. Kapitaniak, Kelvin–Voigt versus Bürgers internal damping in modeling of axially moving viscoelastic web, *Int. J. Non. Linear. Mech.* 37 (2002) 1147–1161. doi:10.1016/S0020-7462(01)00142-1.
- [40] T.K. Caughey, M.E.J. O’Kelly, Classical normal modes in damped linear dynamic systems, *J. Appl. Mech.* 32 (1965) 583–588.
- [41] K.A. Foss, *Coordinates which uncouple the equations of motion of damped linear dynamic systems*, Massachusetts inst. of tech. cambridge, 1956.
- [42] T.K. Caughey, M.E.J. O’Kelly, Effect of Damping on the Natural Frequencies of Linear Dynamic Systems, *J. Acoust. Soc. Am.* 33 (1961) 1458–1461. doi:10.1121/1.1908470.
- [43] T. Kailath, *Linear systems*, Prentice-hall, 1980.

- 
- [https://books.google.it/books?id=EmVzugEACAAJ&dq=Linear+Systems+kailath&hl=it&sa=X&ved=0ahUKEwjMge6o2p\\_hAhXnwsQBHQBVDCAQ6AEIODAC](https://books.google.it/books?id=EmVzugEACAAJ&dq=Linear+Systems+kailath&hl=it&sa=X&ved=0ahUKEwjMge6o2p_hAhXnwsQBHQBVDCAQ6AEIODAC) (accessed March 26, 2019).
- [44] B.C. Kuo, Automatic control systems, Prentice-hall, 1982. [https://books.google.it/books?id=27dSAAAAMAAJ&q=Automatic+Control+Systems+kuo+gholoaraghi&dq=Automatic+Control+Systems+kuo+gholoaraghi&hl=it&sa=X&ved=0ahUKEwiU2oPC2p\\_hAhUH3qQKHVVNBkYQ6AEIMTAB](https://books.google.it/books?id=27dSAAAAMAAJ&q=Automatic+Control+Systems+kuo+gholoaraghi&dq=Automatic+Control+Systems+kuo+gholoaraghi&hl=it&sa=X&ved=0ahUKEwiU2oPC2p_hAhUH3qQKHVVNBkYQ6AEIMTAB) (accessed March 26, 2019).
  - [45] S.M. Shinnars, Modern control system theory and design, J. wiley, 1998.
  - [46] J. Ackermann, Parameter space design of robust control systems, IEEE Trans. Automat. Contr. 25 (1980) 1058–1072. doi:10.1109/TAC.1980.1102505.
  - [47] A. Laub, W. Arnold, Controllability and observability criteria for multivariable linear second-order models, IEEE Trans. Automat. Contr. 29 (1984) 163–165. doi:10.1109/TAC.1984.1103470.
  - [48] D. Bender, A. Laub, Controllability and observability at infinity of multivariable linear second-order models, IEEE Trans. Automat. Contr. 30 (1985) 1234–1237. doi:10.1109/TAC.1985.1103869.
  - [49] A.N. Andry, E.Y. Shapiro, J. c. Chung, Eigenstructure Assignment for Linear Systems, IEEE Trans. Aerosp. Electron. Syst. AES-19 (1983) 711–729. doi:10.1109/TAES.1983.309373.
  - [50] G.P. (Guo P. Liu, R. Patton, Eigenstructure assignment for control system design, John wiley sons, 1998. <https://dl.acm.org/citation.cfm?id=551440> (accessed March 26, 2019).
  - [51] B.N. Datta, S. Elhay, Y.M. Ram, Orthogonality and partial pole assignment for the symmetric definite quadratic pencil, Linear Algebra Appl. 257 (1997) 29–48. doi:10.1016/S0024-3795(96)00036-5.
  - [52] Y. Ram, Pole assignment for the vibrating rod, Q. J. Mech. Appl. Math. 51 (1998) 461–476. doi:10.1093/qjmam/51.3.461.
  - [53] B.N. Datta, Y.M. Ram, D.R. Sarkissian, Spectrum Modification for Gyroscopic Systems, ZAMM. 82 (2002) 191–200. doi:10.1002/1521-4001(200203)82:3<191::AID-ZAMM191>3.0.CO;2-L.
  - [54] O.C. Zienkiewicz, R.L. Taylor, D. Fox, The Finite Element Method for Solid and Structural Mechanics, in: O.C. Zienkiewicz, R.L. Taylor, D.B.T.-T.F.E.M. for S. and S.M. (Seventh E. Fox (Eds.), Butterworth-heinemann, Oxford, 2014. doi:<https://doi.org/10.1016/B978-1-85617-634-7.00016-8>.
  - [55] T.J.R. Hughes, The Finite Element Method: Linear Static and Dynamic Finite Element Analysis, Dover publications, 2012.
  - [56] M. Prandina, J.E. Mottershead, E. Bonisoli, An assessment of damping identification methods, J. Sound Vib. 323 (2009) 662–676. doi:10.1016/j.jsv.2009.01.022.
  - [57] M. Brumat, J. Slavič, M. Boltežar, Spatial damping identification in the frequency domain—A theoretical and experimental comparison, J. Sound Vib. 376 (2016) 182–193. doi:10.1016/j.jsv.2016.04.006.
  - [58] A. Srikantha Phani, J. Woodhouse, Viscous damping identification in linear vibration, J. Sound Vib. 303 (2007) 475–500. doi:10.1016/J.JSV.2006.12.031.
  - [59] N. Barbieri, P.R. Novak, R. Barbieri, Experimental identification of
-

- damping, *Int. J. Solids Struct.* 41 (2004) 3585–3594. doi:10.1016/J.IJSOLSTR.2004.02.006.
- [60] M. Okuma, Q. Shi, T. Oho, Development of the experimental spatial matrix identification method (theory and basic verification with a frame structure), *J. Sound Vib.* 219 (1999) 5–22. doi:10.1006/JSVI.1998.1821.
- [61] S.Y. Chen, M.S. Ju, Y.G. Tsuei, Estimation of mass, stiffness and damping matrices from frequency response functions, *J. Vib. Acoust.* 118 (1996) 78–82. <http://dx.doi.org/10.1115/1.2889638>.
- [62] J.H. Lee, J. Kim, Identification of damping matrices from measured frequency response functions, *J. Sound Vib.* 240 (2001) 545–565. doi:10.1006/jsvi.2000.3248.
- [63] S.Y. Chen, M.S. Ju, Y.G. Tsuei, A Simple Method for Extracting Normal Modes, in: 14th Bienn. Conf. Mech. Vib. Noise, Vib. Shock. Damage, Identif. Mech. Syst., ASME, Albuquerque, 1993: pp. 1–8.
- [64] S.Y. Chen, M.S. Ju, Y.G. Tsuei, Extraction of normal modes for highly coupled incomplete systems with general damping, *Mech. Syst. Signal Process.* 10 (1996) 93–106. doi:10.1006/mssp.1996.0006.
- [65] J.H. Lee, J. Kim, Development and Validation of a New Experimental Method To Identify Damping Matrices of a Dynamic System, *J. Sound Vib.* 246 (2001) 505–524. doi:10.1006/jsvi.2001.3670.
- [66] V. Arora, S.P. Singh, T.K. Kundra, Damped model updating using complex updating parameters, *J. Sound Vib.* 320 (2009) 438–451. doi:10.1016/J.JSV.2008.08.014.
- [67] V. Arora, S.P. Singh, T.K. Kundra, Finite element model updating with damping identification, *J. Sound Vib.* 324 (2009) 1111–1123. doi:10.1016/J.JSV.2009.02.048.
- [68] V. Arora, Structural damping identification method using normal FRFs, *Int. J. Solids Struct.* 51 (2014) 133–143. doi:10.1016/j.ijsolstr.2013.09.017.
- [69] V. Arora, Direct structural damping identification method using complex FRFs, *J. Sound Vib.* 339 (2015) 304–323. doi:10.1016/j.jsv.2014.08.040.
- [70] C.-P. Fritzen, Identification of Mass, Damping, and Stiffness Matrices of Mechanical Systems, *J. Vib. Acoust. Stress. Reliab. Des.* 108 (1986) 9–16. <http://dx.doi.org/10.1115/1.3269310>.
- [71] J.-H. Wang, Mechanical parameters identification, with special consideration of noise effects, *J. Sound Vib.* 125 (1988) 151–167. doi:10.1016/0022-460X(88)90423-3.
- [72] J.E. Mottershead, C.D. Foster, An instrumental variable method for the estimation of mass, stiffness and damping parameters from measured frequency response functions, *Mech. Syst. Signal Process.* 2 (1988) 379–390. doi:10.1016/0888-3270(88)90061-1.
- [73] S. Adhikari, J. Woodhouse, Identification of damping: part 1, viscous damping, *J. Sound Vib.* 243 (2001) 43–61. doi:10.1006/JSVI.2000.3391.
- [74] D.L. Cronin, Eigenvalue and eigenvector determination for nonclassically damped dynamic systems, *Comput. Struct.* 36 (1990) 133–138. doi:10.1016/0045-7949(90)90182-2.
- [75] S. Adhikari, J. Woodhouse, Identification of damping: part 3, symmetry-preserving methods, *J. Sound Vib.* 251 (2002) 477–490. doi:10.1006/JSVI.2001.4023.
- [76] A. Srikantha Phani, J. Woodhouse, Experimental identification of viscous

- 
- damping in linear vibration, *J. Sound Vib.* 319 (2009) 832–849. doi:10.1016/J.JSV.2008.06.022.
- [77] J. Woodhouse, Linear damping models for structural vibration, *J. Sound Vib.* 215 (1998) 547–569. doi:10.1006/JSVI.1998.1709.
  - [78] P. Lancaster, Expressions for Damping Matrices in Linear Vibration Problems, *J. Aerosp. Sci.* 28 (1961) 256. doi:10.2514/8.8949.
  - [79] P. Lancaster, Inversion of Lambda-Matrices and Application to the Theory of Linear Vibrations, *Arch. Ration. Mech. Anal.* 6 (1960) 105–114. doi:10.1007/bf00276157.
  - [80] D.F. Pilkey, D.J. Inman, An iterative approach to viscous damping matrix identification, in: n.d.
  - [81] A. Bajrić, J. Høgsberg, Identification of damping and complex modes in structural vibrations, *J. Sound Vib.* 431 (2018) 367–389. doi:10.1016/J.JSV.2018.05.048.
  - [82] J. Leuridan, D. Brown, R. Allemang, Direct system parameter identification of mechanical structures with application to modal analysis, in: 23rd Struct. Struct. Dyn. Mater. Conf., American institute of aeronautics and astronautics, 1982. doi:10.2514/6.1982-767.
  - [83] M. Link, Theory of a method for identifying incomplete system matrices from vibration test data, *Z. Flugwiss. Weltraumforsch.* 9 (1985).
  - [84] T. Kasai, M. Link, Identification of non-proportional modal damping matrix and real normal modes, *Mech. Syst. Signal Process.* 16 (2002) 921–934. doi:10.1006/MSSP.2001.1478.
  - [85] M. Link, A. Vollen, Identification of structural system parameters from dynamic response data, *Z. Flugwiss. Weltraumforsch.* 2 (1978) 165–174.
  - [86] C. Minas, D.J. Inman, Identification of a nonproportional damping matrix from incomplete modal information, *J. Vib. Acoust.* 113 (1991) 219–224. <http://dx.doi.org/10.1115/1.2930172>.
  - [87] F. Ablitzer, C. Pézerat, J.-M. Génevaux, J. Bégué, Identification of stiffness and damping properties of plates by using the local equation of motion, *J. Sound Vib.* 333 (2014) 2454–2468. doi:10.1016/J.JSV.2013.12.013.
  - [88] M. Prandina, J.E. Mottershead, E. Bonisoli, Damping identification in multiple degree-of-freedom systems using an energy balance approach, *J. Phys. Conf. Ser.* 181 (2009) 12006. doi:https://doi.org/10.1088/1742-6596/181/1/012006.
  - [89] M. Prandina, Spatial damping identification, University of Liverpool, 2010.
  - [90] M.J. Roemer, D.J. Mook, Mass, Stiffness, and Damping Matrix Identification: An Integrated Approach, *J. Vib. Acoust.* 114 (1992) 358–363. <http://dx.doi.org/10.1115/1.2930270>.
  - [91] J.-G. Beliveau, Identification of viscous damping in structures from modal information, *ASME J. Appl. Mech.* 43 (1976). doi:10.1080/08035259950169585.
  - [92] J. Slavič, M. Boltežar, Damping identification with the Morlet-wave, *Mech. Syst. Signal Process.* 25 (2011) 1632–1645. doi:10.1016/J.YMSSP.2011.01.008.
  - [93] J. Slavič, I. Simonovski, M. Boltežar, Damping identification using a continuous wavelet transform: application to real data, *J. Sound Vib.* 262 (2003) 291–307. doi:10.1016/S0022-460X(02)01032-5.
-

- [94] M. Mihalec, J. Slavič, M. Boltežar, Synchrosqueezed wavelet transform for damping identification, *Mech. Syst. Signal Process.* 80 (2016) 324–334. doi:10.1016/J.YMSSP.2016.05.005.
- [95] M. Dalenbring, Damping function estimation based on measured vibration frequency responses and finite-element displacement modes, *Mech. Syst. Signal Process.* 13 (1999) 547–569. doi:10.1006/MSSP.1999.1221.
- [96] S.R. Ibrahim, Computation of Normal Modes from Identified Complex Modes, *AIAA J.* 21 (1983) 446–451. doi:10.2514/3.60118.
- [97] S. Mondal, S. Chakraborty, Identification of non-proportional viscous damping matrix of beams by finite element model updating, *J. Vib. Control.* 24 (2016) 2134–2148. doi:10.1177/1077546316678528.
- [98] M.I. Friswell, D.J. Inman, D.F. Pilkey, Direct Updating of Damping and Stiffness Matrices, *AIAA J.* 36 (1998) 491–493. doi:10.2514/2.396.
- [99] R.M. Lin, D.J. Ewins, Analytical model improvement using frequency response functions, *Mech. Syst. Signal Process.* 8 (1994) 437–458. doi:10.1006/MSSP.1994.1032.
- [100] M. Imregun, W.J. Visser, D.J. Ewins, Finite element model updating using frequency response function data: I. Theory and initial investigation, *Mech. Syst. Signal Process.* 9 (1995) 187–202. doi:10.1006/MSSP.1995.0015.
- [101] M. Imregun, K.Y. Sanliturk, D.J. Ewins, Finite element model updating using frequency response function data: II. Case study on a medium-size finite element model, *Mech. Syst. Signal Process.* 9 (1995) 203–213. doi:10.1006/MSSP.1995.0016.
- [102] S. Pradhan, S.V. Modak, A method for damping matrix identification using frequency response data, *Mech. Syst. Signal Process.* 33 (2012) 69–82. doi:10.1016/J.YMSSP.2012.07.002.
- [103] A.D. Nashif, D.I.G. Jones, J.P. (John P. Henderson, *Vibration damping*, Wiley, 1985.
- [104] R.E. Kalman, P.L. Falb, M.A. Arbib, *Topics in mathematical system theory*, McGraw-hill, 1969. <https://books.google.it/books?id=PAIRAAAAMAAJ>.
- [105] G.S. Miminis, C.C. Paige, An algorithm for pole assignment of time invariant multi-input linear systems, in: 1982 21st IEEE Conf. Decis. Control, 1982: pp. 62–67. doi:10.1109/CDC.1982.268401.
- [106] G. Miminis, Deflation in eigenvalue assignment of descriptor systems using state feedback, *IEEE Trans. Automat. Contr.* 38 (1993) 1322–1336. doi:10.1109/9.237645.
- [107] W. Wonham, On pole assignment in multi-input controllable linear systems, *IEEE Trans. Automat. Contr.* 12 (1967) 660–665. doi:10.1109/TAC.1967.1098739.
- [108] J. Kautsky, N.K. Nichols, P. Van Dooren, Robust pole assignment in linear state feedback, *Int. J. Control.* 41 (1985) 1129–1155. doi:10.1080/0020718508961188.
- [109] K. Sobel, E. Shapiro, A.N. Andry, Eigenstructure assignment, *Int. J. Control.* 59 (1994) 13–37. doi:10.1080/00207179408923068.
- [110] B.N. Datta, S. Elhay, Y.M. Ram, D.R. Sarkissian, PARTIAL EIGENSTRUCTURE ASSIGNMENT FOR THE QUADRATIC PENCIL, *J. Sound Vib.* 230 (2000) 101–110. doi:10.1006/JSVI.1999.2620.
- [111] G.R. Duan, Parametric Eigenstructure Assignment in Second-Order

- 
- Descriptor Linear Systems, *IEEE Trans. Automat. Contr.* 49 (2004) 1789–1795. doi:10.1109/TAC.2004.835580.
- [112] M.T. Chu, Y.-C. Kuo, W.-W. Lin, On Inverse Quadratic Eigenvalue Problems with Partially Prescribed Eigenstructure, *SIAM J. Matrix Anal. Appl.* 25 (2004) 995–1020. doi:10.1137/S0895479803404484.
- [113] N.K. Nichols, J. Kautsky, Robust Eigenstructure Assignment in Quadratic Matrix Polynomials: Nonsingular Case, *SIAM J. Matrix Anal. Appl.* 23 (2001) 77–102. doi:10.1137/S0895479899362867.
- [114] Y.M. Ram, Pole-Zero Assignment of Vibratory Systems by State Feedback Control, *J. Vib. Control.* 4 (1998) 145–165. doi:10.1177/107754639800400204.
- [115] U. Prells, J.E. Mottershead, M.I. Friswell, On pole-zero placement by unit-rank modification, *Mech. Syst. Signal Process.* 17 (2003) 611–633. doi:10.1006/MSSP.2002.1529.
- [116] E.K. Chu, Pole assignment for second-order systems, *Mech. Syst. Signal Process.* 16 (2002) 39–59. doi:10.1006/MSSP.2001.1439.
- [117] J. Tang, K.W. Wang, Vibration Confinement via Optimal Eigenvector Assignment and Piezoelectric Networks, *J. Vib. Acoust.* 126 (2004) 27. doi:10.1115/1.1597213.
- [118] Y.J. Huang, T.C. Kuo, A state tracking control algorithm with pole assignment, *Electr. Eng. (Archiv Fur Elektrotechnik)*. 85 (2003) 267–273. doi:10.1007/s00202-003-0169-3.
- [119] W.R. Ferng, W.-W. Lin, D.J. Pierce, C.-S. Wang, Nonequivalence transformation of  $H_2$ -matrix eigenproblems and model embedding approach to model tuning, *Numer. Linear Algebr. with Appl.* 8 (2001) 53–70. doi:10.1002/1099-1506(200101/02)8:1<53::AID-NLA228>3.0.CO;2-3.
- [120] J.E. Mottershead, Y.M. Ram, Receptance Method in Active Vibration Control, *AIAA J.* 45 (2007) 562–567. doi:10.2514/1.24349.
- [121] Y.M. Ram, J.E. Mottershead, Multiple-input active vibration control by partial pole placement using the method of receptances, *Mech. Syst. Signal Process.* 40 (2013) 727–735. doi:10.1016/J.YMSSP.2013.06.008.
- [122] M. Ghandchi Tehrani, J.E. Mottershead, A.T. Shenton, Y.M. Ram, Robust pole placement in structures by the method of receptances, *Mech. Syst. Signal Process.* 25 (2011) 112–122. doi:10.1016/J.YMSSP.2010.04.005.
- [123] M. Ghandchi Tehrani, R.N.R. Elliott, J.E. Mottershead, Partial pole placement in structures by the method of receptances: Theory and experiments, *J. Sound Vib.* 329 (2010) 5017–5035. doi:10.1016/J.JSV.2010.06.018.
- [124] K.V. Singh, L.A. McDonough, J. Mottershead, J. Cooper, Active Aeroelastic Control Using the Receptance Method, in: *Vol. 8 Dyn. Syst. Control. Parts A B*, ASME, 2010: pp. 137–146. doi:10.1115/IMECE2010-38877.
- [125] K. V. Singh, L.A. McDonough, Optimization of Control Surface Parameters with Augmented Flutter Boundary Constraints, in: *AIAA Atmos. Flight Mech. Conf.*, American institute of aeronautics and astronautics, Reston, Virginia, 2014. doi:10.2514/6.2014-2050.
- [126] M. Ghandchi Tehrani, L. Wilmschurst, S.J. Elliott, Receptance method for active vibration control of a nonlinear system, *J. Sound Vib.* 332 (2013)
-



- 4440–4449. doi:10.1016/J.JSV.2013.04.002.
- [127] A. Isidori, *Nonlinear Control Systems*, Springer london, 2013.
  - [128] H.K. Khalil, *Nonlinear Systems*, Pearson education, limited, 2013.
  - [129] M. Vidyasagar, *Nonlinear Systems Analysis: Second Edition*, Society for industrial and applied mathematics, 2002.
  - [130] G.H. Golub, C.F. Van Loan, *Matrix Computations*, Johns hopkins university press, 1996.
  - [131] B. d’Andréa-Novel, G. Bastin, G. Campion, Dynamic feedback linearization of nonholonomic wheeled mobile robots, in: *Proc. 1992 IEEE Int. Conf. Robot. Autom.*, 1992: pp. 2527–2532 vol.3. doi:10.1109/ROBOT.1992.220061.
  - [132] A. de Luca, P. Lucibello, A general algorithm for dynamic feedback linearization of robots with elastic joints, in: *Proceedings. 1998 IEEE Int. Conf. Robot. Autom. (Cat. No.98CH36146)*, 1998: pp. 504–510 vol.1. doi:10.1109/ROBOT.1998.677024.
  - [133] G. Oriolo, A. De Luca, M. Vendittelli, WMR control via dynamic feedback linearization: design, implementation, and experimental validation, *IEEE Trans. Control Syst. Technol.* 10 (2002) 835–852. doi:10.1109/TCST.2002.804116.
  - [134] B. d’Andréa-Novel, G. Campion, G. Bastin, Control of Nonholonomic Wheeled Mobile Robots by State Feedback Linearization, *Int. J. Rob. Res.* 14 (1995) 543–559. doi:10.1177/027836499501400602.
  - [135] F. Piltan, H. Rezaie, B. Boroomand, A. Jahed, Design Robust Backstepping on-line Tuning Feedback Linearization Control Applied to IC Engine, in: 2012.
  - [136] W. Mielczarski, A.M. Zajaczkowski, Nonlinear field voltage control of a synchronous generator using feedback linearization, *Automatica*. 30 (1994) 1625–1630. doi:10.1016/0005-1098(94)90102-3.
  - [137] J. Chiasson, Dynamic feedback linearization of the induction motor, *IEEE Trans. Automat. Contr.* 38 (1993) 1588–1594. doi:10.1109/9.241583.
  - [138] O. Akhrif, F.-. Okou, L.-. Dessaint, R. Champagne, Application of a multivariable feedback linearization scheme for rotor angle stability and voltage regulation of power systems, *IEEE Trans. Power Syst.* 14 (1999) 620–628. doi:10.1109/59.761889.
  - [139] T.K. Boukas, T.G. Habetler, High-performance induction motor speed control using exact feedback linearization with state and state derivative feedback, *IEEE Trans. Power Electron.* 19 (2004) 1022–1028. doi:10.1109/TPEL.2004.830042.
  - [140] F. Alonge, M. Cirrincione, M. Pucci, A. Sferlazza, Input–output feedback linearizing control of linear induction motor taking into consideration the end-effects. Part II: Simulation and experimental results, *Control Eng. Pract.* 36 (2015) 142–150. doi:10.1016/J.CONENGPRAC.2014.09.013.
  - [141] F. Alonge, M. Cirrincione, M. Pucci, A. Sferlazza, Input–output feedback linearizing control of linear induction motor taking into consideration the end-effects. Part I: Theoretical analysis, *Control Eng. Pract.* 36 (2015) 133–141. doi:10.1016/J.CONENGPRAC.2014.08.009.
  - [142] W.K. Na, B. Gou, Feedback-Linearization-Based Nonlinear Control for PEM Fuel Cells, *IEEE Trans. Energy Convers.* 23 (2008) 179–190. doi:10.1109/TEC.2007.914160.

- 
- [143] T. Kimura, S. Hara, T. Fujita, T. Kagawa, Feedback linearization for pneumatic actuator systems with static friction, *Control Eng. Pract.* 5 (1997) 1385–1394. doi:10.1016/S0967-0661(97)00135-4.
  - [144] G. Vossoughi, M. Donath, Dynamic Feedback Linearization for Electrohydraulically Actuated Control Systems, *J. Dyn. Syst. Meas. Control.* 117 (1995) 468–477. <http://dx.doi.org/10.1115/1.2801102>.
  - [145] A. Mokhtari, A. Benallegue, B. Daachi, Robust feedback linearization and GH/sub /spl infin// controller for a quadrotor unmanned aerial vehicle, in: 2005 IEEE/RSJ Int. Conf. Intell. Robot. Syst., 2005: pp. 1198–1203. doi:10.1109/IROS.2005.1545112.
  - [146] D. Lee, H. Jin Kim, S. Sastry, Feedback linearization vs. adaptive sliding mode control for a quadrotor helicopter, *Int. J. Control. Autom. Syst.* 7 (2009) 419–428. doi:10.1007/s12555-009-0311-8.
  - [147] Y. Choi, H. Ahn, Nonlinear Control of Quadrotor for Point Tracking: Actual Implementation and Experimental Tests, *IEEE/ASME Trans. Mechatronics.* 20 (2015) 1179–1192. doi:10.1109/TMECH.2014.2329945.
  - [148] S. Jiffri, P. Paoletti, J.E. Cooper, J.E. Mottershead, Feedback linearisation for nonlinear vibration problems, *Shock Vib.* 2014 (2014).
  - [149] J. Ko, A.J. Kurdila, T.W. Strganac, Nonlinear Control of a Prototypical Wing Section with Torsional Nonlinearity, *J. Guid. Control. Dyn.* 20 (1997) 1181–1189. doi:10.2514/2.4174.
  - [150] S. Jiffri, S. Fichera, J.E. Mottershead, A. Da Ronch, Experimental Nonlinear Control for Flutter Suppression in a Nonlinear Aeroelastic System, *J. Guid. Control. Dyn.* 40 (2017) 1925–1938. doi:10.2514/1.G002519.
  - [151] C.F. Castillo-Berrio, V. Feliu-Batlle, Vibration-free position control for a two degrees of freedom flexible-beam sensor, *Mechatronics.* 27 (2015) 1–12. doi:10.1016/J.MECHATRONICS.2015.01.005.
  - [152] K. Nanos, E.G. Papadopoulos, On the dynamics and control of flexible joint space manipulators, *Control Eng. Pract.* 45 (2015) 230–243. doi:10.1016/J.CONENGPRAC.2015.06.009.
  - [153] N. Jacobson, *Lie Algebras*, Dover publications, 2013.
  - [154] S. Jiffri, P. Paoletti, J.E. Mottershead, Feedback Linearization in Systems with Nonsmooth Nonlinearities, *J. Guid. Control. Dyn.* 39 (2016) 814–825. doi:10.2514/1.G001220.
  - [155] A. Preumont, *Vibration Control of Active Structures: An Introduction*, Springer netherlands, 2011.
  - [156] C. Zhen, S. Jiffri, D. Li, J. Xiang, J.E. Mottershead, Feedback linearisation of nonlinear vibration problems: A new formulation by the method of receptances, *Mech. Syst. Signal Process.* 98 (2018) 1056–1068. doi:10.1016/J.YMSSP.2017.05.048.
  - [157] A. Gelb, W.E. Vander Velde, *Multiple-input describing functions and nonlinear system design*, McGraw-hill, 1968.
  - [158] J.E. Mottershead, Y.M. Ram, Inverse eigenvalue problems in vibration absorption: Passive modification and active control, *Mech. Syst. Signal Process.* 20 (2006) 5–44. doi:10.1016/J.YMSSP.2005.05.006.
  - [159] A. Nassirharand, H. Karimi, Nonlinear controller synthesis based on inverse describing function technique in the MATLAB environment, *Adv.*
-

- Eng. Softw. 37 (2006) 370–374.  
doi:10.1016/J.ADVENGSOFT.2005.09.009.
- [160] A. Nassirharand, Matlab software for inversion of describing functions, Adv. Eng. Softw. 40 (2009) 600–606.  
doi:10.1016/J.ADVENGSOFT.2008.11.003.
- [161] D. Lisitano, E. Bonisoli, J.E. Mottershead, Experimental direct spatial damping identification by the Stabilised Layers Method, J. Sound Vib. 437 (2018) 325–339. doi:10.1016/J.JSV.2018.08.055.
- [162] E. Bonisoli, D. Lisitano, A. Vigliani, Damping identification and localisation via Layer Method: Experimental application to a vehicle chassis focused on shock absorbers effects, Mech. Syst. Signal Process. 116 (2019) 194–216. doi:10.1016/j.ymssp.2018.06.013.
- [163] J.E. Mottershead, M. Link, M.I. Friswell, The sensitivity method in finite element model updating: A tutorial, Mech. Syst. Signal Process. 25 (2011) 2275–2296. doi:10.1016/J.YMSSP.2010.10.012.
- [164] J.E. Mottershead, M.I. Friswell, Model Updating In Structural Dynamics: A Survey, J. Sound Vib. 167 (1993) 347–375.  
doi:10.1006/JSVI.1993.1340.
- [165] A.S. Householder, Principles of numerical analysis, McGraw-hill, 1953.
- [166] C.L. Lawson, R.J. Hanson, Solving Least Squares Problems, Society for industrial and applied mathematics, New Jersey, 1974.
- [167] J.E. Calvert, W.L. Voxman, Linear Programming, Harcourt brace jovanovich, 1989.
- [168] A. Grama, V. Kumar, A. Gupta, G. Karypis, Introduction to Parallel Computing, Addison-wesley, 2003.
- [169] J.C. Maxwell, L. On the calculation of the equilibrium and stiffness of frames, London, Edinburgh, Dublin Philos. Mag. J. Sci. 27 (1864) 294–299. doi:10.1080/14786446408643668.
- [170] S. Timoshenko, J.N. Goodier, J.N. Goodier, Theory of Elasticity, McGraw-hill, 1951.
- [171] R. Pintelon, J. Schoukens, System Identification: A Frequency Domain Approach, Wiley, 2012.
- [172] W. Heylen, S. Lammens, P. Sas, Modal Analysis Theory and Testing, Division of production engineering, machine design and automation, katholieke universiteit leuven, 1994.
- [173] A. Arda Ozdemir, S. Gumussoy, Transfer Function Estimation in System Identification Toolbox via Vector Fitting, IFAC-PapersOnLine. 50 (2017) 6232–6237. doi:10.1016/J.IFACOL.2017.08.1026.
- [174] P. Guillaume, P. Verboven, S. Vanlanduit, Frequency-domain maximum likelihood identification of modal parameters with confidence intervals, in: Proc. Int. Semin. Modal Anal., Katholieke universiteit leuven, 1998: pp. 359–366.
- [175] B. Peeters, H. Van der Auweraer, P. Guillaume, J. Leuridan, The PolyMAX Frequency-Domain Method: A New Standard for Modal Parameter Estimation?, Shock Vib. 11 (2004) 395–409.  
doi:https://doi.org/10.1155/2004/523692.
- [176] M. El-Kafafy, B. Peeters, P. Guillaume, T. De Troyer, Constrained maximum likelihood modal parameter identification applied to structural dynamics, Mech. Syst. Signal Process. 72–73 (2016) 567–589.

- 
- doi:10.1016/j.ymssp.2015.10.030.
- [177] E. Balmes, Experimental/analytical predictive models of damped structural dynamics, (1993).
- [178] E. Balmés, New results on the identification of normal modes from experimental complex modes, *Mech. Syst. Signal Process.* 11 (1997) 229–243. doi:10.1006/MSSP.1996.0058.
- [179] M. Ouisse, E. Foltête, Identification of Reduced Models from Optimal Complex Eigenvectors in Structural Dynamics and Vibroacoustics, in: *Vib. Struct. Acoust. Anal.*, Springer, 2011: pp. 303–327. doi:https://doi.org/10.1007/978-94-007-1703-9\_11.
- [180] M. Ouisse, E. Foltête, On the properness condition for modal analysis of non-symmetric second-order systems, *Mech. Syst. Signal Process.* 25 (2011) 601–620. doi:10.1016/J.YMSSP.2010.08.017.
- [181] Airpot-Corporation, Dashpots • Actuators • Shock Absorbers, (n.d.). www.airpot.com.
- [182] D. Lisitano, S. Jiffri, E. Bonisoli, E. Mottershead, Active control of a non-smooth nonlinear system using feedback linearisation, in: *EACS 2016 – 6th Eur. Conf. Struct. Control*, Sheffield, n.d.: pp. 1–13.
- [183] E. Bonisoli, Lisitano, Domenico, A. Vigliani, Experimental evaluation of the influence of shock-absorbers on white-body chassis modal behaviour, in: *Int. Conf. Strucutural Eng. Dyn. ICEDyn*, Ericeira (PT), 2017.
- [184] E. Bonisoli, C. Delprete, C. Rosso, Proposal of a modal-geometrical-based master nodes selection criterion in modal analysis, in: *Link. Model. Exp. Vol. 2. Conf. Proc. Soc. Exp. Mech. Ser.*, Springer, New York, 2011: pp. 606–620. doi:https://doi.org/10.1007/978-1-4419-9305-2\_20.
- [185] M. Guiggiani, *The Science of Vehicle Dynamics*, (2014). doi:10.1007/978-94-017-8533-4.
- [186] C. Braccesi, F. Cianetti, Development of selection methodologies and procedures of the modal set for the generation of flexible body models for multi-body simulation, *Proc. Inst. Mech. Eng. Part K J. Multi-Body Dyn.* 218 (2004) 19–30. doi:10.1243/146441904322926913.
- [187] M. El-Kafafy, B. Peeters, P. Guillaume, Optimal Modal Parameter Estimation for Highly Challenging Industrial Cases, in: *Conf. Proc. Soc. Exp. Mech. Ser.*, 2017.
- [188] C.R. Hua, Y. Zhao, Z.W. Lu, H. Ouyang, Random vibration of vehicle with hysteretic nonlinear suspension under road roughness excitation, *Adv. Mech. Eng.* 10 (2018) 1687814017751222. doi:10.1177/1687814017751222.
- [189] P. Vacher, B. Jacquier, A. Bucharles, Extensions of the MAC criterion to complex modes, in: n.d.
- [190] C. Schedlinski, M. Link, A survey of current inertia parameter identification methods, *Mech. Syst. Signal Process.* 15 (2001) 189–211. doi:10.1006/MSSP.2000.1345.
- [191] R.S. Pappa, K.B. Elliott, A. Schenk, Consistent-mode indicator for the eigensystem realization algorithm, *J. Guid. Control. Dyn.* 16 (1993) 852–858. doi:10.2514/3.21092.
- [192] K. Levenberg, A method for the solution of certain non-linear problems in least square, *Q. Appl. Math.* 2 (1944) 164–168.
-

- <http://www.jstor.org/stable/43633451>.
- [193] D.W. Marquardt, An Algorithm for Least-Squares Estimation of Nonlinear Parameters, *J. Soc. Ind. Appl. Math.* 11 (1963) 431–441. <http://www.jstor.org/stable/2098941>.
  - [194] S. Cafferty, K. Worden, G. Tomlinson, Characterization of Automotive Shock Absorbers Using Random Excitation, *Proc. Inst. Mech. Eng. Part D J. Automob. Eng.* 209 (1995) 239–248. doi:10.1243/PIME\_PROC\_1995\_209\_211\_02.
  - [195] C. Surace, K. Worden, G.R. Tomlinson, On the Non-Linear Characteristics of Automotive Shock Absorbers, *Proc. Inst. Mech. Eng. Part D J. Automob. Eng.* 206 (1992) 3–16. doi:10.1243/PIME\_PROC\_1992\_206\_156\_02.
  - [196] D. Lisitano, E. Bonisoli, J.E. Mottershead, Stabilised Layer Method for linear and nonlinear spatial non classical damping identification, in: D. Moens, W. Desmet, B. Pluymers, W. Rottiers (Eds.), 28th Int. Conf. Noise Vib. Eng. ISMA 2018 7th Int. Conf. Uncertain. Struct. Dyn. USD 2018,, KU leuven - departement werktuigkunde, 2018: pp. 991–1003.
  - [197] A.H. Nayfeh, D.T. Mook, *Nonlinear Oscillations*, Wiley, 1995.
  - [198] S.J. Elliott, M.G. Tehrani, R.S. Langley, Nonlinear damping and quasi-linear modelling, *Philos. Trans. R. Soc. A Math. Phys. Eng. Sci.* 373 (2015). <http://rsta.royalsocietypublishing.org/content/373/2051/20140402.abstract>.
  - [199] B. Pionbo, E. Bonisoli, M. Ruzzene, A theoretical model and experimental validation of the oscillations of a para- or dia-magnetic beam subject to the effects of passive magnetic elements, in: *Proc. 1st AIMETA Int. Tribol. Conf*, L'Aquila, Italy, 2000.
  - [200] E. Bonisoli, F. Freschi, M. Repetto, Nonlinear coupling of the phantom effect in magneto-dynamic vibrations, in: *25th Symp. Electromagn. Phenom. Nonlinear Circuits*, 2018.
  - [201] E. Bonisoli, A. Vigliani, Passive effects of rare-earth permanent magnets on flexible conductive structures, *Mech. Res. Commun.* 33 (2006) 302–319. doi:10.1016/J.MECHRESCOM.2005.08.011.
  - [202] M. Prandina, J.E. Mottershead, E. Bonisoli, Location and identification of damping parameters, in: *IMAC XXVII Conf. Expo. Struct. Dyn.*, Orlando, FL, USA, 2009.
  - [203] D. Lisitano, C. Zhen, S. Jiffri, E. Bonisoli, J.E. Mottershead, An example of feedback linearization in a non-smooth system, in: *Int. Conf. Struct. Eng. Dyn.* Ericeira, Port., 2017.
  - [204] D. Lisitano, S. Jiffri, E. Bonisoli, J.E. Mottershead, Experimental feedback linearisation of a vibrating system with a non-smooth nonlinearity, *J. Sound Vib.* 416 (2018). doi:10.1016/j.jsv.2017.11.047.
  - [205] G. Tao, P. V Kokotović, Adaptive control of systems with unknown non-smooth non-linearities, *Int. J. Adapt. Control Signal Process.* 11 (1998) 81–100. doi:10.1002/(SICI)1099-1115(199702)11:1<81::AID-ACS396>3.0.CO;2-A.
  - [206] L.N. de Castro, J. Timmis, An artificial immune network for multimodal function optimization, in: *Proc. 2002 Congr. Evol. Comput. CEC'02 (Cat. No.02TH8600)*, 2002: pp. 699–704 vol.1. doi:10.1109/CEC.2002.1007011.
  - [207] D. Cloutier, D.P. Avitabile, R. Bono, M. Peres, Shaker/stinger effects on

- 
- measured frequency response functions, (n.d.).
- [208] D. Shevitz, B. Paden, Lyapunov stability theory of nonsmooth systems, *IEEE Trans. Automat. Contr.* 39 (1994) 1910–1914. doi:10.1109/9.317122.
  - [209] B. Paden, S. Sastry, A calculus for computing Filippov’s differential inclusion with application to the variable structure control of robot manipulators, *IEEE Trans. Circuits Syst.* 34 (1987) 73–82. doi:10.1109/TCS.1987.1086038.
  - [210] D. Lisitano, S. Jiffri, E. Bonisoli, J.E. Mottershead, Experimental feedback linearisation of a non-smooth nonlinear system by the method of receptances, *Math. Mech. Solids*. (2018). doi:10.1177/1081286517744601.
  - [211] M.H. Richardson, D.L. Formenti, Global curve fitting of frequency response measurements using the rational fraction polynomial method, *Proceeding 3rd IMAC*. (1985) 390–397.

